

**UNIVERSIDADE FEDERAL DO PARÁ
INSTITUTO DE GEOCIÊNCIAS
PROGRAMA DE PÓS-GRADUAÇÃO EM GEOLOGIA E GEOQUÍMICA**

TESE DE DOUTORADO Nº 172

**EVOLUÇÃO CRUSTAL DO SETOR SUL DA PROVÍNCIA
BORBOREMA: DOMÍNIO MACURURÉ, SISTEMA
OROGÊNICO SERGIPANO, NORDESTE DO BRASIL**

Tese apresentada por:

FÁBIO DOS SANTOS PEREIRA

Orientador: Prof. Dr. Jean Michel Lafon (UFPA)

Coorientadora: Prof.^a Dr.^a Maria de Lourdes da Silva-Rosa (UFS)

**BELÉM
2023**

Dados Internacionais de Catalogação na Publicação (CIP) de acordo com ISBD
Sistema de Bibliotecas da Universidade Federal do Pará
Gerada automaticamente pelo módulo Ficat, mediante os dados fornecidos pelo(a) autor(a)

P436e Pereira, Fábio dos Santos.
Evolução crustal do setor Sul da Província Borborema : Domínio
Macururé, Sistema Orogênico Sergipano, Nordeste do Brasil / Fábio dos
Santos Pereira. — 2023.
xx, 239 f. : il. color.

Orientador(a): Prof. Dr. Jean Michel Lafon
Coorientação: Prof^a. Dra. Maria de Lourdes da Silva Rosa Tese
(Doutorado) - Universidade Federal do Pará, Instituto de
Geociências, Programa de Pós-Graduação em Geologia e Geoquímica,
Belém, 2023.

1. Sistema Orogênico Sergipano. 2. Província Borborema.
3. Gondwana Ocidental. 4. Orogenia Brasileira. 5. Geocronologia. I. Título.

CDD 558.13



Universidade Federal do Pará
Instituto de Geociências
Programa de Pós-Graduação em Geologia e Geoquímica

**EVOLUÇÃO CRUSTAL DO SETOR SUL DA PROVÍNCIA
BORBOREMA: DOMÍNIO MACURURÉ, SISTEMA
OROGÊNICO SERGIPANO, NORDESTE DO BRASIL**

Tese apresentada por

FÁBIO DOS SANTOS PEREIRA

**Como requisito parcial à obtenção de Grau de Doutor em Ciências na Área de GEOQUÍMICA E
PETROLOGIA e Linha de Pesquisa GEOCRONOLOGIA E GEOQUÍMICA ISOTÓPICA**

Data de Aprovação: 29 / 09 / 2023

Banca Examinadora:

Prof. Dr. Jean Michel Lafon
(Orientador – UFPA)

Documento assinado digitalmente



IGNEZ DE PINHO GUIMARAES

Data: 02/10/2023 12:33:54-0300

Verifique em <https://validar.iti.gov.br>

Prof.^a Dr. Ignez de Pinho Guimarães
(Membro – UFPE)

Prof. Dr. Valdecir de Assis Janasi
(Membro – USP)

Prof. Dr. Moacir José B. Macambira
(Membro – ITV)

Prof. Dr. Candido Augusto V. Moura
(Membro – UFPA)

Dedico este trabalho às duas mulheres que tornaram esse sonho possível. Célia Regina dos Santos e Maria de Lourdes da Silva Rosa, espero um dia poder retribuir tudo que vocês fizeram e fazem por mim.

AGRADECIMENTOS

Expresso meus mais sinceros agradecimentos a todas as pessoas e entidades que tornaram esse trabalho possível.

A Coordenação de Aperfeiçoamento de Pessoal de Nível Superior (CAPES) pela bolsa concedida (Processo 88887.356733/2019-00).

Ao Conselho Nacional de Desenvolvimento Científico e Tecnológico (CNPq), cujos financiamentos possibilitaram a obtenção da maior parte dos dados apresentados nesse volume (Processos 312393/2020-2, 42625/2018-7, 311023/2021-5, 310740/2021-5, 403797/2016-0)

Ao Programa de Pós-Graduação em Geologia e Geoquímica (PPGG) da Universidade Federal do Pará (UFPA) pela infraestrutura disponibilizada para realização desse trabalho.

Ao Laboratório de Laminação da Faculdade de Geologia da UFPA, em nome dos técnicos e amigos Joelma Lobo e Bruno Veras, pelas incontáveis vezes em que precisei de um serviço às pressas e fui prontamente atendido com um sorriso no rosto e uma conversa gostosa.

Ao Laboratório de Geologia Isotópica (Pará-Iso) da UFPA pela infraestrutura laboratorial que possibilitou a aquisição dos dados isotópicos.

Ao Laboratório de Microscopia Eletrônica de Varredura da UFPA, em nome do Prof. Cláudio Lamarão e da técnica Gisele Marques.

Ao Laboratório de Análises Mineraias da Superintendência Regional de Belém do Serviço Geológico do Brasil (LAMIN/CPRM), especialmente a dedicada Jenny Ortega, pela captura de imagens em catodoluminescência de zircões detríticos.

Ao Condomínio de Laboratórios das Geociências da Universidade Federal de Sergipe (CLGeo/UFS) pela viabilização das análises geoquímicas de rocha total e imageamento por microscopia eletrônica de varredura.

A João Alberto Pinto, pelo suporte durante as análises U-Pb em titanita.

A Dra. Anelise Bertotti por ter facilitado os trabalhos de campo aos plútons Capela e Dores, bem como pela disponibilização das lâminas delgadas, análises geoquímicas e isotópicas desses corpos.

Aos professores Dr. João Marinho Milhomem Neto e Dr. Paulo Sergio de Sousa Gorayeb por todo aprendizado compartilhado durante o estágio supervisionado em petrologia metamórfica.

Aos meus mestres Dr. Jean-Michel Lafon, Dra. Maria de Lourdes da Silva Rosa e Dr. Herbet Conceição, exemplos de profissionalismo e dedicação à vida acadêmica, que sempre apoiaram meus projetos e não mediram esforços para torná-los realidade.

Aos amigos da sala 7 e agregados Bruna Karine Nogueira, Renata Veras, Luísa Barros, Renan Fernandes, Allan Lima, Mozaniel Santos, Yasmin Ferro, Camila Vilar e Ivan Barrera, por todo acolhimento, momentos de descontração e discussões geológicas regadas a café. Vocês foram imprescindíveis nessa jornada.

Aos programas sociais implementados durante os mandatos do Presidente Luiz Inácio Lula da Silva, por permitirem que o filho de um sapateiro com uma dona de casa se tornasse DOUTOR.

Muito obrigado a todos!

RESUMO

O Sistema Orogênico Sergipano (SOS), localizado no setor sul da Província Borborema, é parte de um extenso orógeno Brasileiro/Pan-Africano estruturado durante a amalgamação do supercontinente Gondwana, que se prolonga pela parte central da África até Camarões. Seis domínios compõem o SOS: Estância, Vaza Barris, Macururé, Marancó, Poço Redondo e Canindé. O Domínio Macururé estende-se por cerca de 350 km desde a costa de Sergipe até a cidade de Macururé na Bahia e compõe-se por uma sequência de quartzitos sobrepostos por um espesso pacote de filitos, xistos, metarritmitos e metagrauvacas, com intercalações de níveis de anfíbolitos e rochas calciossilicáticas. Essas rochas foram metamorfizadas em condições das fácies xisto verde a anfíbolito e intrudidas por abundantes granitos e rochas máficas. Nesse trabalho, novos dados geoquímicos, geocronológicos U-Pb (zircão e titanita) e isotópicos (Rb-Sr, Sm-Nd e Pb-Pb em rocha total e Lu-Hf em zircão) das principais unidades constituintes do Domínio Macururé permitiram refinar a estratigrafia local e avançar no entendimento sobre as fontes e processos envolvidos na geração das rochas magmáticas. Dados isotópicos U-Pb em zircões detríticos extraídos de quartzitos forneceram dois picos principais entre 1980-1950 e 1000-910 Ma, consistentes com a Orogenia Riacciana (2,2-1,9 Ga) e o evento Cariris Velhos (1,0-0,9 Ga). As idades paleoproterozoicas são similares aquelas observadas no embasamento da Província Borborema, que está representado na área de estudo pelo Domo Jirau do Ponciano e pelo Complexo Arapiraca. Valores negativos a positivos de $\epsilon\text{Hf}_{(t)}$ de -15,6 a +0,5 e idades modelo Hf- T_{DM}^C entre 2,5 e 3,5 Ga foram obtidos para os grãos dessa população, sugerindo extensivo retrabalhamento de crosta arqueana durante os períodos Riacciano-Orosiriano. Os grãos de idade cedo neoproterozoica mostram composição de Hf subcondrítica a supercondrítica com valores de $\epsilon\text{Hf}_{(t)}$ entre -12,3 e +7,7 e idades modelo crustais Hf- T_{DM}^C de 2,5 a 1,3 Ga, sugerindo adição de material juvenil e retrabalhamento de crostas preexistentes durante o evento Cariris Velhos. Contribuições menos abundantes do Mesoproterozoico (1120-1040 Ma) e Neoproterozoico tardio (880-740 Ma) sugerem que a deposição dos sedimentos do Domínio Macururé ocorreu antes da Orogenia Brasileira. Três grupos de rochas magmáticas puderam ser individualizados com base em aspectos de campo, petrográficos e geoquímicos. (i) As rochas plutônicas mais antigas da região são dioritos e gabros, com subordinada ocorrência de hornblenditos cumuláticos. Elas geralmente apresentam foliação tectônica bem desenvolvida, marcada pela orientação de plagioclásio, hornblenda e biotita, bem como evidências de deformação no estado sólido, o que sugere uma colocação em estágio pré- a cedo-colisional entre 643 e 628 Ma. Dados geoquímicos de elementos maiores e traços revelam uma natureza magnesianas e afinidade com as suítes cálcio-alcálicas de alto potássio e shoshoníticas. Os espectros de elementos terras raras (ETR) e multielementares mostram enriquecimento em

ETR leves e elementos litófilos de grande íon (LILE), com importantes anomalias negativas em Ti-Nb-Ta, que são tipicamente associadas a ambientes de subducção. Os dados isotópicos de rocha total indicam uma assinatura evoluída com razões subcondríticas de Nd ($\epsilon\text{Nd}_{(t)} = -2,0$ a $-5,2$) e radiogênicas de Sr ($^{87}\text{Sr}/^{86}\text{Sr}_{(t)} = 0,708-0,710$) e Pb ($^{206}\text{Pb}/^{204}\text{Pb} = 18,50-19,18$; $^{207}\text{Pb}/^{204}\text{Pb} = 15,69-15,77$; $^{208}\text{Pb}/^{204}\text{Pb} = 38,54-40,04$), implicando derivação a partir de uma fonte mantélica enriquecida. As elevadas razões $^{87}\text{Sr}/^{86}\text{Sr}_{(t)}$ e Rb/Sr em associação com as baixas razões Sr/Th e Ba/Rb sugerem que o enriquecimento da fonte mantélica ocorreu em resposta a introdução de sedimentos através de processos de subducção, levando a formação de flogopita como principal fase metassomática. Idades modelo Hf- T_{DM}^{C} entre 2,47 e 2,09 Ga sugerem que o enriquecimento do manto litosférico abaixo da Província Borborema Sul ocorreu durante os eventos acrescionários da Orogenia Riacciana. A incorporação de sedimentos pelos peridotitos mantélicos provocou aumento das razões elementares Rb/Sr e (U-Th)/Pb, e diminuição das razões Sm/Nd e Lu/Hf, resultando na assinatura crustal das rochas máficas. (ii) Granodioritos, monzogranitos e sienogranitos leucocráticos com biotita e muscovita ocorrem como *stocks* e *sheets*. Essas rochas exibem foliação magmática definida pela orientação de micas e enclaves surmicáceos, que é paralela à xistosidade das encaixantes, sugerindo colocação sincrônica ao evento colisional entre 630 e 624 Ma. Os leucogranitos são metaluminosos a fortemente peraluminosos, de natureza cálcio-alcálica de alto potássio e assinatura magnésiana a ferrosa. Os valores de $\epsilon\text{Nd}_{(t)}$ e idades modelo Nd- T_{DM} sobrepõem aos das rochas encaixantes, sugerindo derivação a partir de protólitos predominantemente sedimentares. (iii) Monzonitos, quartzo-monzonitos, granodioritos e granitos constituem o grupo magmático mais jovem, que apresenta idades de cristalização entre 625 e 603 Ma. Essas rochas são majoritariamente isotrópicas e cortam a foliação regional, indicando uma colocação tardia em relação ao evento colisional. O caráter metaluminoso, magnésiano, filiação cálcio-alcálica de alto potássio e shoshonítica são similares as composições de líquidos obtidos em experimentos de fusão de protólitos basálticos moderadamente enriquecidos em elementos incompatíveis. Dados isotópicos Lu-Hf fornecem valores de $\epsilon\text{Hf}_{(t)}$ entre -8,3 a -4,0 e idades modelo Hf- T_{DM}^{C} oscilando de 1,77 a 2,03 Ga, indicando retrabalhamento de crosta continental antiga, possivelmente relacionada ao evento Cariris Velhos. A integração dos dados geoquímicos e isotópicos com aqueles disponíveis na literatura permite inferir que a evolução geodinâmica neoproterozoica do SOS ao longo da margem ocidental do Gondwana pode ser explicada por uma extensão litosférica do embasamento da Província Borborema, seguido por inversão da bacia e colisão continental.

Palavras-chave: Orogenia Brasileira/Pan-Africana, Gondwana Ocidental, Província Borborema

ABSTRACT

The Sergipano Orogenic System (SOS), located in the southern Borborema Province, is part of a large Brasiliano/Pan-African orogen structured during the Gondwana supercontinent assembly, which spread out to central Africa up to Cameroon. Six domains compose the SOS, namely Estância, Vaza Barris, Macururé, Marancó, Poço Redondo, and Canindé. The Macururé Domain stretches 350 km from the Sergipe coast to Macururé City, Bahia state. It consists of a succession of quartzites overlaying by a thick package of phyllites, schists, metarhytmities, and metagraywacke, with intercalations of amphibolite and calc-silicate rocks. The rocks were metamorphosed under greenschist-amphibolite facies and intruded by numerous late Cryogenian-Ediacaran granites and mafic plutons. In this work, new geochemical, U-Pb geochronological (zircon and titanite), and isotopic (whole-rock Rb-Sr, Sm-Nd, and Pb-Pb and in situ zircon Lu-Hf) results from the main units composing the Macururé Domain allowed to refine the local stratigraphy and improve the comprehension about sources and processes involved in the generation of the magmatic rocks. U-Pb isotope analyses on detrital zircon from quartzites yielded two main peaks in the ranges of 1980-1950 Ma and 1000-910 Ma, consistent with the Rhyacian Orogeny (2.2-1.9 Ga) e Cariris Velhos event (1.0-0.9 Ga). Paleoproterozoic dates overlap those observed in the Província Borborema basement, represented in the study area by the Jirau do Ponciano Dome and Arapiraca Complex. Negative to slightly positive $\epsilon\text{Hf}(t)$ values between -15.6 and +0.5 and $\text{Hf-T}_{\text{DM}}^{\text{C}}$ model ages from 2.5 to 3.5 Ga characterize this population, suggesting extensive reworking of the Archean crust during the Rhyacian-Orosirian periods. Early Neoproterozoic zircon grains display sub- to superchondritic Hf isotope composition (-12.3 to +7.7) and $\text{Hf-T}_{\text{DM}}^{\text{C}}$ model ages from 2.5 to 1.3 Ga, implying the addition of juvenile material and reworking of preexistent crusts during the Cariris Velhos event. Less abundant Mesoproterozoic (1120-1040 Ma) and late Neoproterozoic (880-740 Ma) zircon populations suggest that the sediment deposition took place before the Brasiliano Orogeny. The groups of magmatic rocks were individualized based on field, petrographic, and geochemical features. (i) The oldest plutonic rocks in the area are diorites and gabbros, with minor cumulate hornblendites. They generally show evidence of solid-state deformation and well-developed tectonic foliation, defined by the plagioclase, hornblende, and biotite orientations. These features point to emplacement in a pre- to early-collisional stage between 643 and 628 Ma. Geochemical data reveal a magnesian nature and affinities with the high-K calc-alkaline and shoshonite magmatic series. REE and multielement spectra exhibit enrichment in light REE and large ion lithophile elements, with deep troughs at Ti-Nb-Ta, typically interpreted as a

subduction setting signature. Whole-rock isotope data indicate an evolved signature with subchondritic Nd ($\epsilon\text{Nd}_{(t)} = -2.0$ a -5.2) e radiogenic Sr ($^{87}\text{Sr}/^{86}\text{Sr}_{(t)} = 0.708$ - 0.710), and Pb ($^{206}\text{Pb}/^{204}\text{Pb} = 18.50$ - 19.18 ; $^{207}\text{Pb}/^{204}\text{Pb} = 15.69$ - 15.77 ; $^{208}\text{Pb}/^{204}\text{Pb} = 38.54$ - 40.04), indicating derivation from an enriched mantle source. High $^{87}\text{Sr}/^{86}\text{Sr}_{(t)}$ and Rb/Sr ratios, together with low Sr/Th and Ba/Rb ratios, suggest that the enrichment episode occurred in response to the introduction of sedimentary components in the mantle via subduction processes, leading to the formation of phlogopite as the main metasomatic phase. Hf- T_{DM}^{C} model ages between 2.47 and 2.09 Ga suggest that the enrichment of the lithospheric mantle beneath the southern Borborema Province occurred during the accretionary events of the Rhyacian Orogeny. Incorporating sediments by the mantle peridotites may have led to increasing Rb/Sr, (U-Th)/Pb coupled with decreasing Sm/Nd and Lu/Hf ratios, which resulted in the time-integrated crustal signature observed in the mafic rocks. (ii) Biotite- and muscovite-bearing leucocratic granodiorites, monzogranites, and syenogranites outcrop as stocks and sheets. They show magmatic foliation marked by the orientation of micas and surmicaceous enclaves, parallel to the schistosity of country rocks, indicating synchronous emplacement to the collisional event between 630 and 624 Ma. Leucogranites are metaluminous to strongly peraluminous, high-K calc-alkaline, and magnesian to ferroan. $\epsilon\text{Nd}_{(t)}$ values and Nd- T_{DM} model ages overlap those of their host rocks, suggesting derivation from mostly sedimentary protholiths. (iii) The younger group consists of monzonites, quartz-monzonites, granodiorites, and granites, with crystallization ages from 625 to 603 Ma. They are predominantly isotropic and truncate the regional foliation of the country rocks, indicating a late emplacement relative to the collisional event. The metaluminous and magnesian signatures, with high-K calc-alkaline and shoshonite affiliations, resemble the composition of experimental liquids obtained by partial melting of basalt protoliths moderately enriched in incompatible elements. Lu-Hf isotope data provided subchondritic $\epsilon\text{Hf}_{(t)}$ values between -8.3 and 4.0 with Hf- T_{DM}^{C} model ages from 1.77 to 2.03, indicating the reworking of ancient continental crust, possibly related to the Cariris Velhos event. The geochemical and isotopic data of this study, together with those available in the literature allows us to infer that the Neoproterozoic geodynamic evolution of the SOS along the western Gondwana margin can be explained by a lithospheric extension of the Borborema Province basement, followed by basin inversion, and continental collision.

Keywords: Brasiliano/Pan-African Orogeny, Western Gondwana, Borborema Province.

LISTA DE ILUSTRAÇÕES

CAPÍTULO I Introdução

Figura I.1- Mapa de localização da área de estudo destacando as principais vias de acesso e municípios.....	3
Figura I.2- Contexto geológico.....	5
Figura I.3- Mapa de pontos com localização das amostras utilizadas nesse estudo.....	9

CAPÍTULO II Late Cryogenian-Ediacaran magmatism in southern Borborema Province, NE Brazil: ages, sources, petrogenesis, and tectonic setting

Figure II.1- Geological setting of the study area	21
Figure II.2- Geochronological map of the eastern segment of the SOS.....	25
Figure II.3- Field aspects and mesoscopic features of the studied plutons.	34
Figure II.4- Petrographic aspects of the plutonic rocks from the Macururé Domain.....	35
Figure II.5- Geochemical diagrams for major elements.....	40
Figure II.6- Harker diagrams for major and trace elements of the plutonic rocks from the Macururé Domain.....	41
Figure II.7- REE and multielement patterns for plutonic rocks from the Macururé Domain, normalized to chondrite and primitive mantle.....	42
Figure II.8- CL images of representative zircon crystals from the studied plutons, with their corresponding $^{206}\text{Pb}/^{238}\text{U}$ dates in Ma, $\epsilon\text{Hf}(t)$, and $\text{Hf-T}_{\text{DM}}^{\text{C}}$	44
Figure II.9- Concordia diagrams, chondrite-normalized REE zircon patterns, and Ti-in-zircon thermometry for the plutons Camará, Glória Norte, and Santa Helena.....	45
Figure II.10- Hf isotope signature for the Camará, Santa Helena, and Glória Norte plutons ..	46
Figure II.11- BSE images of representative titanite crystals from the Dores, Pedra Furada, and Glória Norte plutons	49
Figure II.12- Tera-Wasserburg plot for titanite crystals from the Dores, Pedra Furada, and Glória Norte plutons	50
Figure II.13- Summary of geochronological data for the SOS.....	53
Figure II.14- Origin of the Camará pluton	59
Figure II.15- Petrogenetic diagrams for the syn- and late-collisional granitoids	63
Figure II.16- Geological evolution of the study area.....	73

CAPÍTULO III Constraints on the source and petrogenesis of early Ediacaran shoshonitic mafic magmatism and high-K calc-alkaline granitoids in the Sergipano Orogenic System, Borborema Province, Brazil

Figure III.1- Geological setting	95
Figure III.2- Field and petrographic aspects of the Capela pluton	99
Figure III.3- Geochemical diagrams for the Capela pluton samples	103
Figure III.4- Chondrite-normalized REE and primitive mantle-normalized trace element patterns of the Capela pluton samples	104
Figure III.5- Variation diagrams for selected oxides against SiO ₂	105
Figure III.6- Cathodoluminescence images of the dated zircon crystals from the samples SOS-696F and SOS-696G with their respective ²⁰⁶ Pb/ ²³⁸ U date, εHf _(t) , and Hf-T _{DM} ^C	106
Figure III.7- Zircon U–Pb and Lu–Hf isotope results	107
Figure III.8- Whole-rock Sr–Nd–Pb isotope composition	112
Figure III.9- Petrogenetic discrimination diagrams for rocks from the Capela pluton	115
Figure III.10- Initial ⁸⁷ Sr/ ⁸⁶ Sr and ¹⁴³ Nd/ ¹⁴⁴ Nd isotope ratios of rocks from the Capela pluton, host schists, and the average of Rhyacian and Cariris Velhos remnants in the SOS..	119
Figure III.11- Elemental and isotopic constraints on mantle source	121
Figure III.12- Origin of the granitoids associated with the Capela pluton	126
Figure III.13- Conceptual model for generation and assembly of the Capela pluton.	130
Supplementary Figure 1- Ultramafic rocks major elements normalized to the average amphibole composition.....	156
Supplementary Figure 2- Nb anomaly expressed as Nb/Nb* parameter versus MgO.....	156
Supplementary Figure 3- Nb anomaly expressed as Nb/Nb* parameter versus ⁸⁷ Sr/ ⁸⁶ Sr _(630 Ma)	156

CAPÍTULO VI Detrital zircon U–Pb-Hf geochronology and geochemical constraints on the provenance and tectonic setting of the Macururé Complex, southern Borborema Province, NE Brazil

Figure IV.1- Geological background of the study area	160
Figure IV.2- Simplified stratigraphy of the SOS based on available geochronological data for igneous and metasedimentary rocks	163
Figure IV.3- Rocks of the study area.....	170
Figure IV.4- Whole-rock geochemical data for paraderived metamorphic rocks of the Macururé	

Domain	172
Figure IV.5- Harker diagrams for selected major oxides (wt.%) from the metasedimentary rocks of the Macururé Complex	173
Figure IV.6- Concordia and KDE plots of the analyzed quartzites from the Macururé Complex.....	175
Figure IV.7- Lu-Hf isotope composition on detrital zircon from quartzite samples of the Macururé Complex, compared with zircon data of the main tectonic event recorded in the Borborema Province	177
Figure IV.8- Geochemical constraints on the source	181
Figure IV.9- Cumulative age proportion plotted against the difference between the crystallization age for a detrital zircon grain and the depositional age of the succession	184

LISTA DE TABELAS

CAPÍTULO II Late Cryogenian-Ediacaran magmatism in southern Borborema Province, NE Brazil: ages, sources, petrogenesis, and tectonic setting

Table II.1- Summary of available U-Pb and whole-rock Sm-Nd isotopic data for Neoproterozoic plutonic units of the SOS.	23
Table II.2- ICP-MS and laser instrumentation parameters for U-Pb analysis in titanite.....	30
Table II.3- Summary of modal compositions of the studied plutons.	33
Table II.4- Major and trace element modeling for generation of the high-K Santa Helena granodiorite by partial melting of a basaltic amphibolite.	66

CAPÍTULO III Constraints on the source and petrogenesis of early Ediacaran shoshonitic mafic magmatism and high-K calc-alkaline granitoids in the Sergipano Orogenic System, Borborema Province, Brazil

Table III.1- Lu–Hf isotope analysis of zircon crystals from the Capela pluton.	108
Table III.2- SHRIMP U–Pb zircon data for sample SOS-696G.....	110
Table III.3- Whole-rock Sr, Nd, and Pb isotope compositions.	111
Table III.4- Parameters of the components used for petrogenetic modeling. Elemental and isotopic compositions relative to average values from <i>n</i> analyses. Values in parentheses correspond to the entire variation range.	120
Table III.5- Major and trace element modeling for generation of the granitoids of the Capela pluton by partial melting of a basaltic amphibolite source.....	128
Supplementary Table S1- Summary of whole-rock geochemical data	152
Supplementary Table S2- Fractional crystallization model for major and trace elements.....	155

CAPÍTULO VI Detrital zircon U–Pb–Hf geochronology and geochemical constraints on the provenance and tectonic setting of the Macururé Complex, southern Borborema Province, NE Brazil

Table IV.1- Petrographic aspects of the metasedimentary rocks from the Macururé Complex. Mineral abbreviation names follow the recommendation of Warr (2021).	169
Table IV.2- Summary of U-Pb and Lu-Hf analyses on detrital zircon from quartzite samples of the Macururé Complex.	176

Supplementary Table S1- Major and trace elements data for metasedimentary rocks of the Macururé Complex	196
Supplementary Table S2- U-Pb data for detrital zircon grains from quartzite samples of the Macururé Domain	198
Supplementary Table S3- Lu-Hf data for detrital zircon grains from quartzite samples of the Macururé Domain	210

SUMÁRIO

DEDICATÓRIA	iv
AGRADECIMENTOS	v
RESUMO	vii
ABSTRACT	ix
LISTA DE ILUSTRAÇÕES	xi
LISTA DE TABELAS	xiv
CAPÍTULO I INTRODUÇÃO	1
1.1 APRESENTAÇÃO.....	1
1.2 LOCALIZAÇÃO E ACESSOS.....	2
1.3 CONTEXTO GEOLÓGICO REGIONAL.....	3
1.4 OBJETIVOS.....	7
2 MATERIAIS E MÉTODOS	8
2.1 TRABALHOS DE CAMPO E AMOSTRAGEM.....	8
2.2 DESCRIÇÃO PETROGRÁFICA	9
2.3 ESTUDO MINERALOQUÍMICO.....	10
2.4 GEOQUÍMICA DE ROCHA TOTAL.....	10
2.5 GEOCRONOLOGIA	11
2.5.1 Datação U-Pb em zircão e titanita por SHRIMP	11
2.5.2 Datação U-Pb em zircão por LA-SF-ICP-MS	12
2.5.3 Datação U-Pb em titanita por LA-Q-ICP-MS	12
2.5.4 Datação U-Pb em zircão detrítico por LA-Q-ICP-MS	13
2.6 ANÁLISES Lu-Hf EM ZIRCÃO.....	13
2.7 ELEMENTOS TRAÇOS EM ZIRCÃO.....	14
2.8 ANÁLISES ISOTÓPICAS Sm-Nd, Rb-Sr E Pb-Pb EM ROCHA TOTAL	15
2.9 ELABORAÇÃO DA TESE	16

CAPÍTULO II LATE CRYOGENIAN-EDIACARAN MAGMATISM IN SOUTHERN BORBOREMA PROVINCE, NE BRAZIL: AGES, SOURCES, PETROGENESIS, AND TECTONIC SETTING	17
ABSTRACT	18
1 INTRODUCTION	19
2 GEOLOGICAL SETTING	20
2.1 MACURURÉ DOMAIN AND ASSOCIATED BRASILIANO PLUTONISM	24
3 SAMPLING AND ANALYTICAL METHODS	27
3.1 PETROGRAPHY, MINERAL COMPOSITIONS, AND IMAGING.....	27
3.2 WHOLE-ROCK GEOCHEMISTRY	27
3.2.1 Geochemical modeling	28
3.3 U-Pb GEOCHRONOLOGY	29
3.3.1 Zircon dating	29
3.3.2 Titanite dating	30
3.4 ZIRCON Lu-Hf ISOTOPE ANALYSES	31
3.5 ZIRCON TRACE ELEMENTS	32
4 RESULTS	33
4.1 FIELD RELATIONSHIPS AND SAMPLE DESCRIPTION	33
4.1.1 Early-collisional magmatism	35
4.1.2 Syn-collisional magmatism	37
4.1.3 Late-collisional magmatism	38
4.2 WHOLE-ROCK GEOCHEMISTRY	39
4.3 U-Pb DATING AND Lu-Hf ANALYSES.....	43
4.3.1 Early-collisional Camará pluton (sample SOS-626)	43
4.3.2 Late-collisional Glória Norte pluton (sample FDS-12)	46
4.3.3 Late-collisional Santa Helena pluton (sample SOS-1281)	47
4.4 ZIRCON TRACE ELEMENT COMPOSITION	47
4.5 TITANITE U-Pb AGES	48

4.5.1	Early-collisional Dores pluton (sample SOS-910).....	48
4.5.2	Syn-colisional Pedra Furada pluton (sample SOS-1257).....	51
4.5.3	Late-collisional Glória Norte pluton (sample FDS-12).....	51
5	DISCUSSION	52
5.1	A REAPPRAISAL OF THE AGE OF THE MAGMATIC EPISODES	52
5.1.1	Stage I: 643-628 Ma	54
5.1.2	Stage II: 630-624 Ma	54
5.1.3	Stage III: 625-603 Ma	55
5.1.4	Significance of the range 590-570 Ma	56
5.2	POTENTIAL SOURCES AND MAGMA EVOLUTION.....	57
5.2.1	Origin of the Camará pluton	57
5.2.2	Hybrid crustal sources for the leucogranites	62
5.2.3	Amphibolite lower crust producing granodiorites and monzonites.....	64
5.3	Hf ISOTOPES ON ZIRCON.....	66
5.3.1	Subcontinental lithospheric mantle (SCLM) beneath the southern Borborema Province	67
5.3.2	Role of crustal reworking.....	69
5.4	GEODYNAMIC IMPLICATIONS.....	70
5.5	A POSSIBLE MODEL.....	72
6	CONCLUSIONS	74
	 CAPÍTULO III CONSTRAINTS ON THE SOURCE AND PETROGENESIS OF EARLY EDIACARAN SHOSHONITIC MAFIC MAGMATISM AND HIGH-K CALC-ALKALINE GRANITOIDS IN THE SERGIPANO OROGENIC SYSTEM, BORBOREMA PROVINCE, BRAZIL	90
	ABSTRACT	92
1	INTRODUCTION	93
2	GEOLOGICAL BACKGROUND	94
3	THE MACURURÉ MAFIC SUITE: CAPELA PLUTON	97

3.1	ULTRAMAFIC UNIT.....	98
3.2	MAFIC UNIT.....	98
3.3	GRANITOID UNIT.....	100
3.4	ENCLAVES.....	101
3.5	PEGMATITES.....	101
4	SAMPLING AND ANALYTICAL PROCEDURES.....	102
5	MAJOR AND TRACE ELEMENT DATA.....	102
6	ZIRCON U–Pb DATING AND Lu–Hf ISOTOPE COMPOSITION.....	105
6.1	PLAGIOCLASE-BEARING BIOTITE HORNBLENDITE (SAMPLE SOS-696F).....	105
6.2	BIOTITE-HORNBLLENDE MELANOGABBRO (SAMPLE SOS-696G).....	109
7	WHOLE-ROCK ISOTOPE GEOCHEMISTRY.....	109
8	DISCUSSION.....	113
8.1	AGE VARIATION IN THE CAPELA PLUTON.....	113
8.2	ROLE OF FRACTIONAL CRYSTALLIZATION.....	114
8.3	EVOLUTION OF CUMULATES.....	116
8.4	CRUSTAL CONTAMINATION VERSUS ENRICHMENT OF THE MANTLE SOURCE.....	117
8.5	CONSTRAINTS ON MANTLE SOURCE.....	120
8.6	MANTLE ENRICHMENT HISTORY.....	124
8.7	ORIGIN OF GRANITIDS.....	125
8.8	TOWARD AN INTEGRATED MODEL.....	128
9	CONCLUSIONS.....	130
CAPÍTULO IV DETRITAL ZIRCON U–Pb-Hf GEOCHRONOLOGY AND GEOCHEMICAL CONSTRAINTS ON THE PROVENANCE AND TECTONIC SETTING OF THE MACURURÉ COMPLEX, SOUTHERN BORBOREMA PROVINCE, NE BRAZIL.....		157
1	INTRODUCTION.....	158
2	GEOLOGICAL SETTING.....	159

2.1	BORBOREMA PROVINCE.....	159
2.2	SERGIPANO OROGENIC SYSTEM	161
2.2.1	Canindé Domain	161
2.2.2	Poço Redondo and Marancó domains	163
2.2.3	Macururé Domain	164
2.2.4	Vaza Barris Domain	164
2.2.5	Estância Domain	165
3	ANALYTICAL APPROACH	165
3.1	WHOLE-ROCK GEOCHEMISTRY	165
3.2	ZIRCON U-Pb DATING	166
3.3	LA-ICP-MS ZIRCON Lu-Hf ISOTOPE ANALYSES.....	167
4	GEOLOGICAL CONTEXT OF THE STUDY AREA	168
5	MAJOR AND TRACE ELEMENTS	171
6	U-Pb AND Lu-Hf DETRITAL ZIRCON GEOCHRONOLOGY	174
2.1	SAMPLE SOS-1254.....	174
6.2	SAMPLE SOS-1260.....	177
6.3	SAMPLE SOS-1274.....	178
3	PRELIMINARY DISCUSSION	179
7.1	DEPOSITIONAL AGES.....	179
7.2	SOURCE CHARACTERISTICS.....	180
7.3	POTENTIAL SOURCE AREAS	182
7.4	TECTONIC SETTING.....	183
7.5	CRUSTAL GROWTH AND REWORKING	184
8	FINAL REMARKS	185
	CAPÍTULO V CONCLUSÕES.....	214
	REFERÊNCIAS.....	217

CAPÍTULO I INTRODUÇÃO

1.1 APRESENTAÇÃO

O Sistema Orogênico Sergipano (SOS) é uma faixa móvel neoproterozoica de forma aproximadamente triangular e orientação WNW-ESE situada no setor extremo sul da Província Borborema, entre o Cráton São Francisco (CSF) e o Domínio Pernambuco-Alagoas (PEAL), Nordeste do Brasil. O SOS se estende desde o litoral dos estados de Sergipe e Alagoas, até a cidade de Curaçá, no norte do estado da Bahia, perfazendo uma área de cerca de 45.000 km² (Brito Neves *et al.*, 2000).

Na sua porção sergipana, o SOS constitui-se pelos domínios tectono-estratigráficos Canindé, Poço Redondo, Marancó, Macururé, Vaza Barris e Estância (Davison & Santos, 1989). De acordo com Oliveira *et al.* (2010), a evolução do SOS iniciou-se com a quebra de um continente paleoproterozoico, seguido pela formação de um arco continental envolvendo os domínios Marancó e Poço Redondo (980-960 Ma) e de um rifte continental representado pelo Domínio Canindé (700-640 Ma). Os domínios Estância, Vaza Barris e Macururé são interpretados como margens passivas do CSF e do PEAL. A convergência desses dois blocos continentais durante o evento Brasileiro/Pan-Africano culminou na amalgamação dos seis domínios, resultando na atual configuração do SOS. Nesse contexto, o Domínio Macururé se destaca dos demais domínios por ter sido estruturado unicamente o evento Brasileiro e por alojar um significativo número de intrusões graníticas e máficas-ultramáficas que registram os principais estágios evolutivos do orógeno Sergipano.

O Domínio Macururé é constituído essencialmente por micaxistos granatíferos, filitos e quartzitos. Embora este seja o maior domínio em extensão areal no SOS, as determinações geocronológicas em zircões detríticos são escassas (Van Schmus *et al.*, 2011; Oliveira *et al.*, 2015b; Neves *et al.*, 2019), o que dificulta o estabelecimento de correlações com possíveis fontes de detritos, a determinação do contexto tectônico de deposição e a idade máxima de sedimentação.

O panorama geocronológico das rochas ígneas do Domínio Macururé também não está bem delineado. De modo geral, as rochas plutônicas da região são enquadradas nos intervalos de idade de 630-618 Ma e 590-570 Ma, sendo o primeiro período definido por dados U-Pb em zircão e segundo com base em dados U-Pb em titanita. Bueno *et al.* (2009) e Oliveira *et al.* (2010, 2015a) propuseram que os granitoides mais antigos do Domínio Macururé são pré-colisionais e foram formados em um ambiente de margem continental ativa do tipo Andina. Por outro lado, os mais jovens são interpretados como granitos sin-colisionais de derivação crustal

que marcariam o episódio de colisão e espessamento crustal no SOS, similarmente aos leucogranitos himalaianos. Datações U-Pb em zircão obtidas por Pereira *et al.* (2020) indicam a colocação de plútons máficos com assinatura de arco continental no Domínio Macururé em torno de 630 Ma, compatível com o modelo evolutivo de Oliveira *et al.* (2010). Contudo, novos U-Pb em zircão obtidos por Conceição (2019) e Lisboa *et al.* (2019) para rochas graníticas do Domínio Macururé indicam a colocação de leucogranitos a cerca de 625 Ma e o início do estágio pós-colisional em torno de 588 Ma. Essas novas idades estão em desacordo daquelas propostas no modelo geotectônico mais amplamente aceito para a área, indicando haver necessidade de adequações nos episódios magmáticos. Esses intervalos estão melhor definidos no PEAL (Silva Filho *et al.*, 2014, 2016) e na faixa Riacho do Pontal (Caxito *et al.*, 2016), terrenos contíguos ao SOS.

As fontes e os processos petrogenéticos envolvidos na produção dos magmas máficos e félsicos também são assunto de debate. Oliveira *et al.* (2015a) propõem que os granitoides mais antigos do Domínio Macururé são resultado da mistura de uma crosta inferior basáltica com um componente crustal superior. Em relação à petrogênese dos tipos leucograníticos, Conceição *et al.* (2016) assinalam que a variedade composicional encontrada nessas intrusões é produto da mistura de um componente mantélico (representado por enclaves máficos de afinidade shoshonítica) e outro crustal metassedimentar. Por outro lado, Pereira *et al.* (2020) sugerem que as rochas da associação ultrabásica-básica-intermediária do Domínio Macururé foram produzidas pela fusão de um manto subcontinental litosférico metassomatizado e evoluíram por cristalização fracionada. Em grande parte, essas considerações são apoiadas em dados geoquímicos de rocha total, visto que dados isotópicos têm ocorrência bastante restrita na área. Nesse sentido, os isótopos de Sr, Nd e Hf figuram como importantes ferramentas petrológicas que permitiriam traçar a composição isotópica das fontes, bem como quantificar misturas entre componentes e definir episódios de acreção ou retrabalhamento crustal.

1.2 LOCALIZAÇÃO E ACESSOS

A área de estudo localiza-se na porção leste do Domínio Macururé, setor centro-norte do estado de Sergipe, estando compreendida nas folhas topográficas Gracho Cardoso (SC.24-Z-B-I), Propriá (SC.24-Z-B-II), Pão de Açúcar (SC.24-X-D-IV) e Carira (SC.24-Z-A-III). Partindo-se da capital Aracaju, o acesso a área pode ser realizado pelas rodovias BR-101 e BR-235 (Fig. 1). O acesso aos municípios de interesse pode ser feito por rodovias estaduais pavimentadas e não pavimentadas. Uma densa rede de estradas vicinais recobre a zona rural dessa região, o que permite acessar a maioria dos afloramentos.

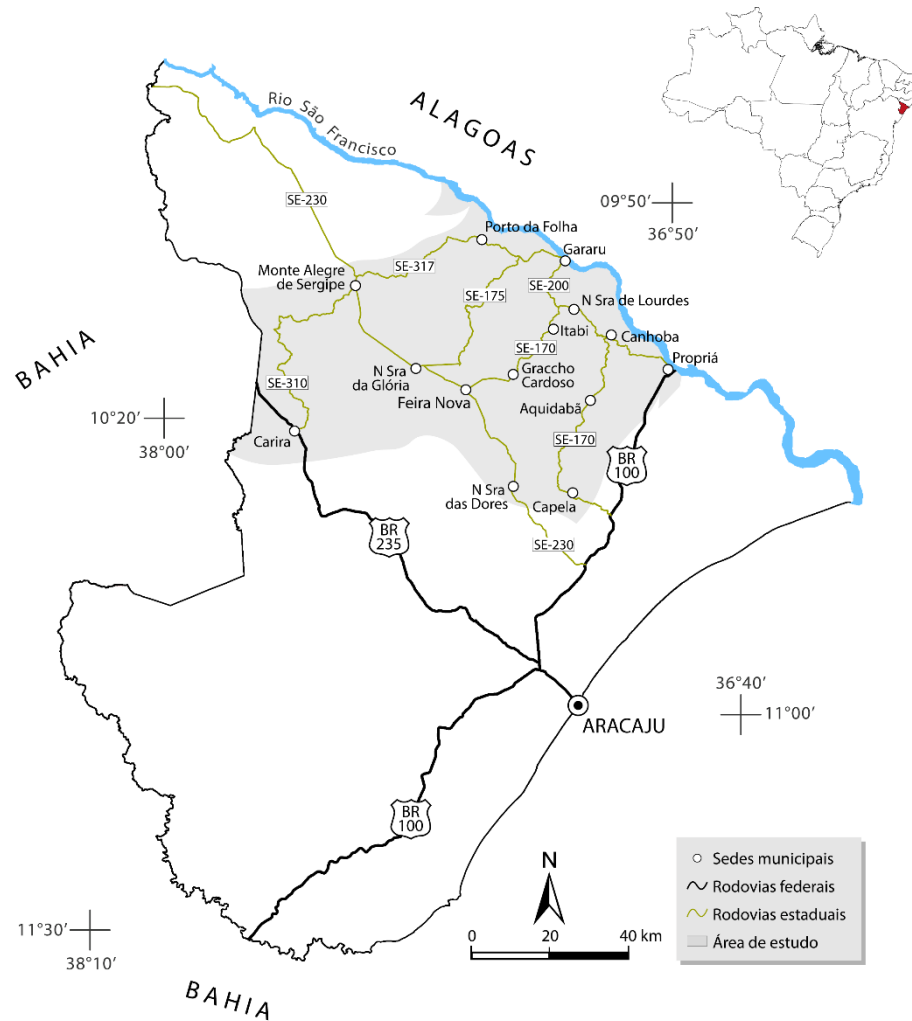


Figura I.1- Mapa de localização da área de estudo destacando as principais vias de acesso e municípios.

1.3 CONTEXTO GEOLÓGICO REGIONAL

A Província Borborema (Almeida *et al.*, 1981) é uma unidade geotectônica situada na região Nordeste do Brasil, que foi formada a partir da convergência dos crátons Amazônico, Oeste África-São Luís e São Francisco-Congo durante a aglutinação do Gondwana Oeste (Fig. 2A). Ela é constituída por um embasamento gnáissico-migmatítico paleoproterozoico (2,5-2,0 Ga) a arqueano (3,4-2,7 Ga), recoberto por sequências metassupracrustais mesoproterozoicas a neoproterozoicas (Brito Neves *et al.*, 2000; Van Schmus *et al.*, 2008). Adicionalmente, os eventos Cariris Velhos (1,0-0,9 Ga) e Brasileiro/Pan-Africano (650-530 Ma) afetaram a província, sendo este último responsável por metamorfismo de baixo a alto grau, colocação de abundantes granitoides e desenvolvimento de um expressivo sistema de zonas de cisalhamento transcorrentes de escala continental.

As zonas de cisalhamento de Patos e Pernambuco têm tendência E-W e dividem a Província Borborema nas subprovíncias norte, central e sul (Van Schmus *et al.*, 2008, 2011). A subprovíncia sul situa-se entre o Lineamento Pernambuco e o Cráton de São Francisco e compreende o PEAL e as faixas orogênicas Sergipana e Riacho do Pontal (Fig. 2B). A Faixa Sergipana ou, formalmente, Sistema Orogrênico Sergipano é limitado a norte pelo PEAL e a sul pelo CSF, representando o segmento oeste do orógeno Oubanguides em reconstruções *pré-drift*, que se estende até o NW da África (Trompette, 1997; Caxito *et al.*, 2020).

Diferentes modelos têm sido propostos para explicar a evolução tectônica do SOS. Ele foi inicialmente interpretado como um geossinclinal (Humphrey & Allard, 1969; Silva Filho *et al.*, 1979), como uma colagem de terrenos alóctones (Davison & Santos, 1989) e como um cinturão de dobras e empurrões desenvolvido pela inversão de uma margem passiva desenvolvida na borda norte da paleoplaca São Francisco (D'el-Rey Silva, 1999). O modelo mais recente é creditado a Oliveira *et al.* (2010, 2017), que propõem que o SOS corresponde ao produto da colisão continental entre o PEAL e a antiga placa São Francisco, durante a Orogenia Brasileira/Pan-Africana.

De acordo com Davison & Santos (1989), o SOS pode ser subdividido nos domínios Estância, Vaza-Barris, Macururé, Marancó, Poço Redondo e Canindé (Fig. 2C). Esses domínios têm histórias de sedimentação e evoluções tectônicas distintas, sendo separados entre si por zonas de cisalhamento regionais. Os domínios Vaza-Barris e Macururé exibem janelas estruturais do embasamento arqueano-paleoproterozoico, onde afloram os domos de Simão Dias, Itabaiana e Jirau do Ponciano.

Os domínios meridionais Estância, Vaza Barris e Macururé consistem majoritariamente de rochas metassedimentares e são interpretados como o registro de margens passivas do CSF e do PEAL (Oliveira *et al.*, 2010). Os domínios setentrionais Marancó, Poço Redondo e Canindé são considerados terrenos alóctones, que foram acretados à margem norte da paleoplaca São Francisco durante o Brasiliano (Oliveira, 2017). A existência de um outro domínio, denominado Rio Coruripe, foi proposta para a porção alagoana do SOS (Silva Filho & Torres, 2002; Mendes & Brito, 2016), no entanto, ainda é uma questão em aberto se ele representa um domínio a parte ou a continuação dos domínios Macururé (Oliveira *et al.*, 2006) ou Canindé (Neves *et al.*, 2016). Mais recentemente, Tesser *et al.* (2021) sugeriram que o Complexo Arapiraca representa um segmento paleoproterozoico desmembrado do Cráton de São Francisco durante um evento de rifteamento.

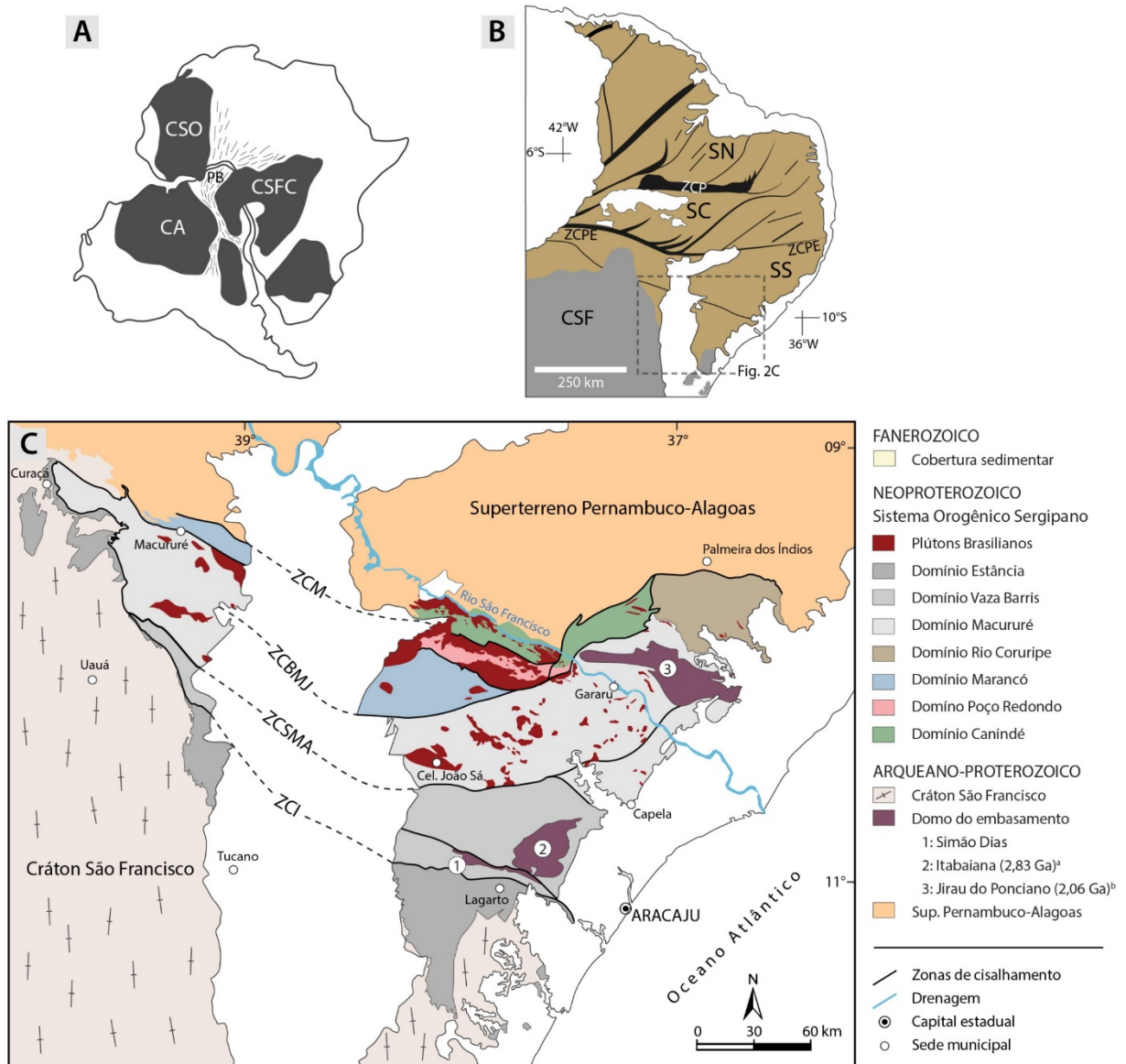


Figura I.2- Contexto geológico. (A) Reconstrução pré-*drift* da América do Sul-África mostrando a localização da Província Borborema (PB) e dos crátons Amazônico (CA), São Luís-Oeste África (CSO) e São Francisco-Congo (CSFC). (B) Subdivisão da Província Borborema nas subprovíncias norte (SN), central (SC) e sul (SS), limitadas pelas zonas de cisalhamento de Patos (ZCP) e Pernambuco (ZCPE), de acordo com Van Schmus *et al.* (2008, 2011). (C) Mapa geológico simplificado da área demarcada em (B) mostrando a compartimentação tectônica do Sistema Orogênico Sergipano. ZCI = zona de cisalhamento Itaporanga, ZCSMA = zona de cisalhamento São Miguel do Aleixo, ZCBMJ = zona de cisalhamento Belo Monte-Jeremoabo, ZCM = zona de cisalhamento Macururé.

O Domínio Macururé limita-se a sul com o domínio Vaza-Barris e a norte com os domínios Marancó, Poço Redondo e Canindé pelas zonas de cisalhamento sinistrais de São Miguel do Aleixo e Belo Monte-Jeremoabo. Este domínio é composto pela sequência metassedimentar do Complexo Macururé e por uma suíte intrusiva brasileira de granitoides e rochas máfico-ultramáficas.

O Complexo Macururé é predominantemente metapelítico e exibe grande variação faciológica. Na região predominam biotita xistos granatíferos, filitos, metarenitos e quartzitos, com subordinadas ocorrências de grauvacas, rochas vulcânicas e lentes de anfibólito, intercalados com níveis de mármore, calciossilicáticas e formações ferríferas (Santos *et al.*, 1998; Oliveira *et al.*, 2010). Essas rochas assentam sobre o Domo Jirau do Ponciano (2,07-2,05 Ga; Lima *et al.*, 2019), que aflora na região sudeste de Alagoas e é considerado embasamento do domínio. A sequência sedimentar do Grupo Macururé é interpretada como uma cunha turbidítica neoproterozoica (D'el-Rey Silva, 1999; Oliveira *et al.*, 2017), com base na presença de estruturas indicativas de deposição em águas profundas (Davison & Santos, 1989). Dados U-Pb de zircões detríticos fornecem picos paleoproterozoicos e mesoproterozoicos, não sendo identificados cristais mais jovens que 900 Ma (Van Schmus *et al.*, 2011; Oliveira *et al.*, 2015b; Neves *et al.*, 2019), o que posiciona a idade máxima de sedimentação desse domínio no Toniano. O metamorfismo regional alcançou fácies anfibólito, sob intermediárias pressões e altas temperaturas (Davison & Santos, 1989; Silva *et al.*, 1995). A única estimativa de idade de metamorfismo disponível para o domínio é uma isócrona Sm-Nd de dois pontos (granada/rocha total) para um micaxisto próximo a cidade de Gararu, que fornece uma idade de 573 ± 1 Ma (Oliveira *et al.*, 2010). Idades Ar-Ar em anfibólito (625 ± 3 Ma) e muscovita (612 ± 7 Ma, 591 ± 4 Ma e 581 ± 2 Ma) em zonas de cisalhamento do SOS indicam que os eventos de deformação variaram ao longo do orógeno (Oliveira *et al.*, 2010).

Rochas ígneas plutônicas são abundantes no Domínio Macururé. Bueno *et al.* (2009) dividiram os granitoides em pré-colisionais (628-625 Ma) e sin-colisionais (590-570 Ma), em relação ao principal evento deformacional que afetou este setor do SOS (D₂). Os granitos do primeiro grupo mostram evidências de deformação no estado sólido relacionada a D₂, enquanto os do segundo absorvem parte ou toda deformação D₂ e preservam suas estruturas magmáticas paralelas às estruturas das encaixantes. Oliveira *et al.* (2010, 2015a) propuseram que os granitos mais velhos foram formados em ambientes de arco magmático continental, ao passo que os mais jovens foram gerados durante o evento colisional.

Conceição *et al.* (2017), utilizando dados geoquímicos e geocronológicos disponíveis na literatura, propuseram que os corpos intrusivos na porção sergipana do Domínio Macururé poderiam ser reunidos nos grupos magmáticos:

- (1) Básico-ultrabásico toleítico a cálcio-alcálico (~630 Ma);
- (2) Intermediário a básico cálcio-alcálico de alto potássio (~630 Ma);
- (3) Granodiorítico cálcio-alcálico de alto potássio (625-618 Ma);
- (4) Monzonítico shoshonítico (619-588 Ma);

(5) Leucogranítico cálcio-alcálico de alto potássio (584-571 Ma).

As intrusões dos grupos 1 e 2 foram agrupadas por Pereira *et al.* (2020) na Suíte Máfica Macururé. Ela constitui-se por pequenos corpos tabulares (1-20 km²) de gabros, dioritos e hornblenditos, com subordinados termos félsicos, colocados contemporaneamente por volta de 630 Ma (Bueno *et al.*, 2009; Pereira *et al.*, 2020). As intrusões afloram na margem leste do Domínio Macururé e ocorrem estruturados segundo a foliação regional das encaixantes. As rochas desse grupo exibem uma foliação de baixo ângulo, paralela à foliação regional. Evidências de deformação no estado sólido compatíveis com condições metamórficas das fácies xisto verde a anfíbolito, associado aos aspectos de campo, sugerem a colocação pré a cedocolisional dessas intrusões (Pereira *et al.*, 2020).

Os granodioritos do grupo 3 têm como principais representantes o batólito Coronel João Sá (625 ± 2 Ma; Long *et al.*, 2005) e o *stock* Lagoa do Roçado (618 ± 2 Ma; Silva, 2014). As rochas dessas intrusões não apresentam evidências de deformação e incluem abundantes enclaves máficos microgranulares e xenólitos anfíbolíticos.

Os plútons Fazenda Lagoas (623 ± 4 Ma; Fernandes *et al.*, 2020), Propriá (615 ± 6 Ma; Santos *et al.*, 2019) e Glória Norte (588 ± 5 Ma; Lisboa *et al.*, 2019) figuram como expoentes do magmatismo monzonítico shoshonítico. As rochas desses plútons não exibem evidências de deformação no estado sólido e truncam as estruturas regionais. O *stock* Glória Norte destaca-se das demais intrusões do SOS por alojar abundantes enclaves ultrapotássicos lamprofíricos e cumuláticos (Fontes *et al.*, 2018).

Os leucogranitos do grupo 5 ocorrem como *stocks* arredondados e *sheets* que se colocam paralelamente a foliação dos xistos do Domínio Macururé ou como diques. Esses corpos são constituídos por biotita granitos e biotita-muscovita granitos, por vezes ricos em granada, que hospedam enclaves máficos surmicáceos e microgranulares de afinidade shoshonítica. Idades U-Pb SHRIMP em zircão dão conta da colocação desses magmas em torno de 625 Ma (Conceição, 2019). Por outro lado, idades U-Pb ID-TIMS em titanita variam entre 571 e 584 Ma (Bueno *et al.*, 2009).

1.4 OBJETIVOS

Essa pesquisa se propôs a contribuir para o entendimento da evolução geodinâmica do setor sul da Província Borborema durante o Neoproterozoico através do aporte de novos dados geoquímicos, geocronológicos e isotópicos para as rochas magmáticas e metassedimentares do setor leste do Domínio Macururé. Para tanto, adotou-se como objetivos específicos:

- Caracterizar o ambiente de formação das rochas magmáticas com base em dados geoquímicos e isotópicos de rocha total.
- Definir os principais estágios magmáticos por meio de datação U-Pb em zircão.
- Investigar as fontes e quantificar os processos petrogenéticos responsáveis pela geração das rochas ígneas por meio de dados geoquímicos de elementos maiores e traços, e composição isotópica de Sr-Nd em rocha total e de Hf em zircão.
- Caracterizar a proveniência e o contexto geotectônico de deposição das rochas metassedimentares do Complexo Macururé através de geoquímica de rocha total e geocronologia U-Pb de zircões detríticos.
- Identificar episódios de crescimento e retrabalhamento crustal através de dados Lu-Hf em zircão das rochas magmáticas e metassedimentares.

2 MATERIAIS E MÉTODOS

Os procedimentos metodológicos adotados para alcançar os objetivos delineados para esta pesquisa são descritos abaixo de forma simplificada. Maiores detalhes sobre as técnicas empregadas são fornecidos nos capítulos seguintes.

2.1 TRABALHOS DE CAMPO E AMOSTRAGEM

Foi realizada uma campanha de campo entre os dias 02 e 05 de março de 2020, com o objetivo de reconhecer a geologia da área de estudo, verificar as relações de contato entre as intrusões e suas encaixantes, bem como coletar amostras para os estudos laboratoriais. Durante as atividades de campo, foram visitados e descritos 33 afloramentos e coletadas 43 amostras representativas das principais unidades do Domínio Macururé (Fig. 3). As coordenadas de cada ponto foram aferidas empregando o sistema Universal Transversa de Mercator (UTM) e o *South American Datum 1969* (SAD69) como referência. Algumas amostras provenientes de campanhas de campo anteriores realizadas junto ao Laboratório de Petrologia Aplicada à Pesquisa Mineral da Universidade Federal de Sergipe (LAPA/UFS) também foram utilizadas nesse estudo, a fim de compor um panorama geológico completo da região.

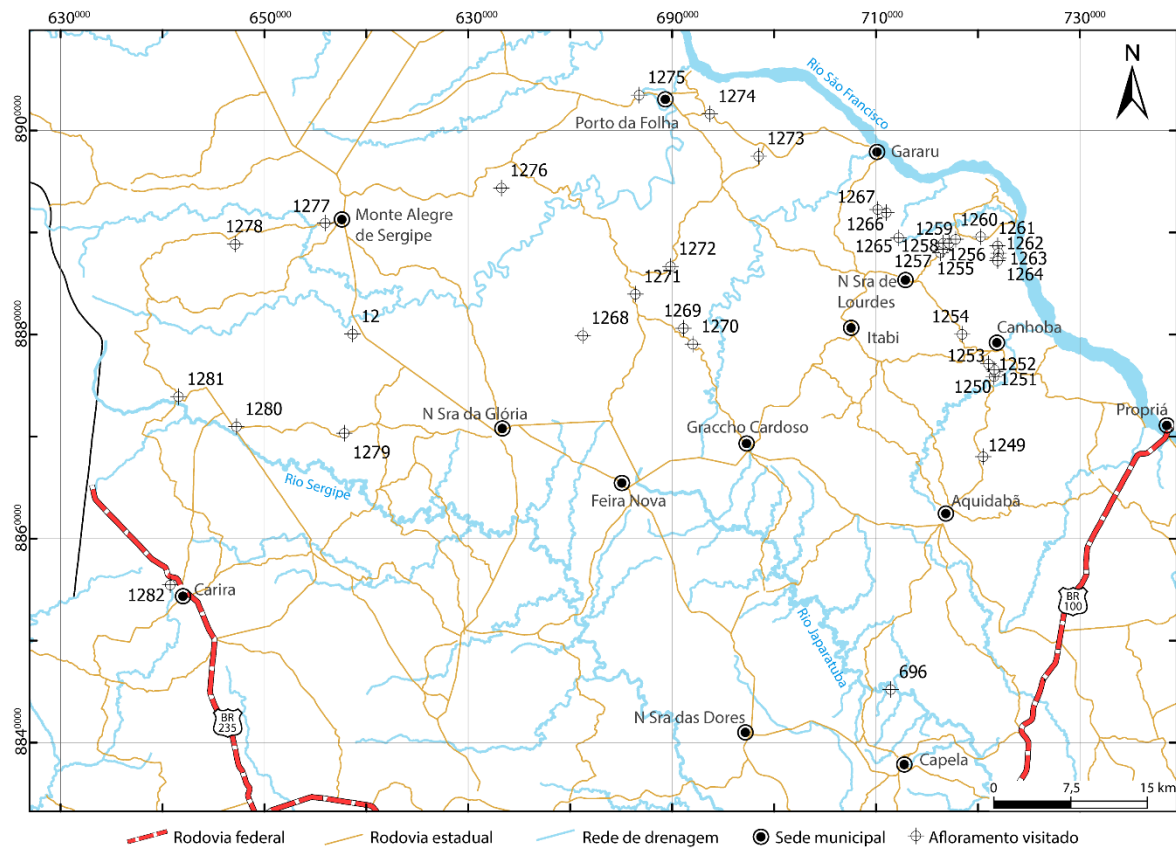


Figura I.3- Mapa de pontos com localização das amostras utilizadas nesse estudo.

2.2 DESCRIÇÃO PETROGRÁFICA

As amostras selecionadas para o estudo petrográfico foram reduzidas a tamanhos de aproximadamente 10 cm para confecção de lâminas delgado-polidas. As lâminas foram produzidas na Oficina de Laminação do Instituto de Geociências da Universidade Federal do Pará (IG/UFPa) e descritas no Laboratório de Petrografia do PPGG. A análise petrográfica consistiu na descrição das texturas e estruturas gerais da rocha, seguida pela caracterização de cada fase mineral, considerando atributos como cor, pleocroísmo, tamanho, contatos, inclusões, feições deformacionais e alterações secundárias. A composição modal das rochas foi determinada por contagem de aproximadamente 1000 pontos com espaçamento regular, de modo a cobrir toda a área da lâmina. As rochas magmáticas foram nomeadas conforme recomendações da Subcomissão sobre Sistemática de Rochas Ígneas da União Internacional de Ciências Geológicas – IUGS (Streckeisen, 1976; Le Maitre *et al.*, 2002). A nomenclatura das rochas metamórficas seguiu as diretrizes da Subcomissão de Sistematização das Rochas Metamórficas da IUGS, resumidas por Fettes & Desmons (2014). A abreviatura dos nomes dos minerais seguiu as sugestões de Warr (2021).

2.3 ESTUDO MINERALOQUÍMICO

Foram realizadas análises químicas pontuais semiquantitativas nos principais minerais constituintes das amostras estudadas por espectrometria de energia dispersiva (EDS). As lâminas foram metalizadas com ouro. A localização e análise dos cristais foram executadas por meio de um microscópio eletrônico de varredura (MEV) Tescan Vega LMU3, no Laboratório de Microanálises do Condomínio de Laboratórios Multiusuários das Geociências na Universidade Federal de Sergipe (CLGeo/UFS). Este equipamento tem acoplado detectores de sinais de elétrons retroespalhados, elétrons secundários e catodoluminescência. As composições químicas dos cristais foram determinadas com um detector de energia dispersiva modelo X-Act, da Oxford Instruments. O *software* Quant foi empregado na aquisição e tratamento automático dos dados químicos. Os espectros de energia obtidos foram analisados individualmente, com a finalidade de eliminar picos falsos, interferências de energia e sobreposições de picos (Newbury, 2009). As condições analíticas adotadas foram tensão de 15 kV e intensidade de corrente variando de 15 a 17 nA, que produz um feixe de elétrons com diâmetro entre 280 e 430 nm. O tempo médio de contagem variou de 30 a 60 s.

2.4 GEOQUÍMICA DE ROCHA TOTAL

Os elementos maiores foram dosados a partir de pastilhas prensadas por espectrometria de fluorescência de raios-X (FRX) utilizando um equipamento Shimadzu XRF-1800 instalado no Laboratório de Geoquímica do CLGeo/UFS. O procedimento de obtenção das pastilhas compreendeu as etapas de britagem, moagem, quartejamento, pulverização, homogeneização e compactação. Após a cominuição mecânica em britadores de mandíbula, as amostras foram pulverizadas em moinho de panela de tungstênio até atingir uma fração próxima a 200 mesh. O pó de rocha foi seco em estufa por cerca de 2 h a 120 °C. O pó seco foi misturado com ácido bórico (H_3BO_3) na proporção de 3:1 (3 partes de amostra para 1 de ácido). A mistura foi homogeneizada e depositada em discos metálicos de aço. A compactação das pastilhas foi realizada em uma prensa hidráulica a 60 kN por 30 s. O conteúdo de água e de elementos voláteis foi determinado através de calcinação em forno mufla a 1000 °C por 2 h. A precisão e acurácia das análises foi avaliada por comparação com a leitura de materiais de referência certificados (*e.g.* DTS-2b, AVG-2, QLO-1A) e por leituras em duplicata de amostras representativas. As concentrações dos elementos traços foram determinadas por espectrometria de massa com plasma indutivamente acoplado (ICP-MS) nos laboratórios comerciais ALS e GEOSOL. O protocolo de preparação de amostras da ALS inclui fusão com borato de lítio,

seguida por dissolução ácida. Por outro lado, os procedimentos analíticos empregados pela GEOSOL envolvem a fusão por peróxido de sódio antes da análise das concentrações elementares. O tratamento dos dados e confecção dos diagramas geoquímicos foram realizados com o pacote Geochemical Data toolkit (Janoušek *et al.*, 2006) em ambiente R.

2.5 GEOCRONOLOGIA

Foram realizadas datações U-Pb em titanita e zircão. A concentração desses minerais envolveu as etapas de (i) deslamagem, para retirada da fração mais fina, (ii) peneiramento úmido, para aproveitamento da fração granulométrica entre 250 e 75 μm , (iii) bateia em água, para concentração dos minerais pesados, e (iv) separação magnética com imã de mão e separador isodinâmico Frantz. Os grãos extraídos foram colados ordenadamente em fitas dupla face para preparação das pastilhas em resina epóxi no Laboratório de Laminação do IG/UFPA. As pastilhas foram polidas para revelar as partes internas dos cristais e metalizadas com ouro para imageamento por microscopia eletrônica de varredura.

As imagens de catodoluminescência para o zircão e de elétrons retroespalhados para a titanita foram obtidas em dois laboratórios. No CLGeo/UFS utilizou-se o mesmo equipamento empregado na determinação da composição pontual dos minerais. As condições de operação foram 20 kV de voltagem, 10-20 nA de corrente e diâmetro do feixe entre 0,4 e 1,0 μm . No LAMIN/CPRM-Belém, as imagens foram obtidas por meio de um microscópio eletrônico de varredura Zeiss EVO LS-15 operando a 15 kV e 10 nA, com distância de trabalho de 12 mm.

2.5.1 Datação U-Pb em zircão e titanita por SHRIMP

Uma amostra de zircão e uma de titanita foram datadas pelo método U-Pb no Laboratório de Geocronologia de Alta Resolução do Instituto de Geociências da Universidade de São Paulo (IGc/USP) com uma microsonda iônica de alta resolução e sensibilidade (SHRIMP IIe). Os concentrados desses minerais foram obtidos pelas técnicas convencionais de britagem, moagem, peneiramento, mesa vibratória, separação magnética, separação gravimétrica (bromofórmio $\rho = 2,85 \text{ g/cm}^3$ e diiodometano $\rho = 3,32 \text{ g/cm}^3$) e seleção manual.

Os grãos escolhidos foram montados em discos de resina epóxi, juntamente com fragmentos dos matéria de referência TEMORA 2 e Khan. Após o polimento dos *mounts*, os cristais de zircão foram imageados por catodoluminescência e os de titanita por elétrons retroespalhados a fim de investigar suas estruturas internas e selecionar os alvos para análise.

Nas análises U-Pb em zircão, a concentração de U foi determinada com base no zircão de referência SL13 (238 ppm; Williams, 1997). As razões isotópicas de U-Pb foram normalizadas em relação ao valor correspondente à idade do zircão TEMORA 2 ($416,8 \pm 0,2$ Ma; Black *et al.*, 2004). O padrão primário de titanita Khan foi empregado para determinação dos conteúdos de U e das razões isotópicas de U e Pb, assumindo uma idade de referência de 520 Ma. A redução dos dados isotópicos brutos foi realizada usando o programa SQUID (Ludwig, 2009a). Mais detalhes sobre os procedimentos analíticos são apresentados por Sato *et al.* (2014) e Sato *et al.* (2016).

2.5.2 Datação U-Pb em zircão por LA-SF-ICP-MS

A datação U-Pb em zircão de três amostras de rochas magmáticas foi realizada no Laboratório de Geocronologia da Universidade Federal de Ouro Preto (UFOP) usando um ICP-MS *sector field* Element 2 da Thermo Finnigan, acoplado a um sistema de ablação a laser Photon Machines 193 nm ArF Excimer (LA-SF-ICP-MS). Os protocolos analíticos adotados são descritos por Santos *et al.* (2022). Os dados foram adquiridos em modo *peak jumping* com 20 s de leitura de *background*, 20 s de ablação e 30 μm de diâmetro do *spot*. As condições do laser foram frequência de 10 Hz e 4 J/cm² de fluência. O fracionamento elementar induzido pelo laser e a discriminação instrumental de massa foram corrigidos com base nas razões do zircão de referência GJ-1 (608.5 ± 1.5 Ma; Jackson *et al.*, 2004). Os zircões Blue Berry e Plešovice foram usados como materiais de referência secundários para checar a reprodutibilidade das análises. O *software* U-Pb SATURN (Silva *et al.*, 2022) foi utilizado na redução dos dados brutos. Nenhuma correção para chumbo comum foi aplicada.

2.5.3 Datação U-Pb em titanita por LA-Q-ICP-MS

Duas amostras de rochas magmáticas foram selecionadas para datação U-Pb em titanita. As análises foram obtidas no Laboratório de Geologia Isotópica da Universidade Federal do Pará (Pará-Iso/UFPA), utilizando um espectrômetro de massa com plasma indutivamente acoplado quadrupolo iCAP-Q da Thermo Fisher acoplado a um sistema de ablação a laser Nd:YAG LSX-213 G2 CETAC (LA-Q-ICP-MS). A análise de cada *spot* consistiu em 20 s de leitura do *background*, 40 s de aquisição de dados e 30 s para limpeza da célula de ablação. O material ablado foi transferido utilizando He como gás de arraste, que foi misturado com Ar antes da introdução no ICP-MS. As massas ²⁰²Hg, ²⁰⁴(Pb + Hg), ²⁰⁶Pb, ²⁰⁷Pb, ²⁰⁸Pb, ²³²Th and ²³⁸U foram medidas. Os dados brutos foram reduzidos e corrigidos para o *background* e fracionamento isotópico em uma planilha MS Excel. A titanita Khan foi empregada como

material de referência primário, usado para calcular as concentrações de U, Th e Pb, e normalizar as razões $^{206}\text{Pb}/^{238}\text{U}$, considerando uma idade de referência de 520 Ma (Heaman, 2009). A titanita Tory Hill (Fisher *et al.*, 2020) foi analisada como material de referência secundário para monitorar a reprodutibilidade das medidas isotópicas. O detalhamento dos procedimentos experimentais de datação U-Pb em titanita por LA-Q-ICP-MS no Laboratório Pará-Iso encontra-se em Pinto (2023).

2.5.4 Datação U-Pb em zircão detrítico por LA-Q-ICP-MS

Três amostras de quartzitos do Complexo Macururé foram selecionadas para datação U-Pb de zircão detrítico. Aproximadamente 5 kg de amostra foi moída e pulverizada até uma fração areia média, utilizando britador de mandíbula e moinho de panela de tungstênio.

As análises isotópicas foram realizadas no Pará-Iso/UFPA, utilizando o mesmo espectrômetro de massa e sistema de ablação a laser empregado nas análises dos cristais de titanita. O sinal das massas $^{204}(\text{Pb} + \text{Hg})$, ^{206}Pb , ^{207}Pb , ^{208}Pb , ^{238}U e ^{232}Th foram medidos durante as análises. O sinal do isótopo ^{235}U foi calculado assumindo $^{238}\text{U}/^{253}\text{U} = 138,77$. Os dados foram adquiridos durante 40 s de ablação após 20 s de leitura do *background*. Os parâmetros analíticos do laser foram diâmetro do *spot* de 25 μm , frequência de 10 Hz e fluência de 4 J/cm^2 . A redução *offline* dos dados brutos foi realizada em planilha Excel modificada de Milhomem Neto & Lafon (2019). Nessa planilha, a proporção de ^{206}Pb comum é calculada com base nos valores medidos de ^{204}Pb corrigidos para ^{204}Hg em cada ponto analítico, usando a composição de chumbo prevista pelo modelo de Stacey & Kramers (1975).

O fracionamento elementar induzido pelo laser e a discriminação instrumental de massa foram corrigidas por meio da normalização pelo zircão de referência GJ-1 ($608,5 \pm 1,5$ Ma; Jackson *et al.*, 2004). Os zircões Blue Berry ($560,0 \pm 0,4$ Ma; Santos *et al.*, 2017) e 91500 ($1065,4 \pm 0,3$ Ma; Wiedenbeck *et al.*, 1995) foram aplicados como materiais de referência secundários para monitorar a confiabilidade e reprodutibilidade do método. As constantes de decaimento utilizadas são aquelas recomendadas por Steiger & Jäger (1977).

2.6 ANÁLISES Lu-Hf EM ZIRCÃO

As análises isotópicas de Lu-Hf em zircão foram realizadas no Pará-Iso/UFPA e no Laboratório de Geocronologia da Universidade Federal de Ouro Preto (UFOP). Os protocolos analíticos desses laboratórios são descritos por Milhomem Neto & Lafon (2019) e Santos *et al.* (2022), respectivamente. O equipamento utilizado no Pará-Iso para análise dos cristais de zircão

magmáticos foi um ICP-MS multicoletor Thermo Finnigan Neptune, acoplado a uma microsonda de ablação a laser CETAC Nd:YAG 213 nm modelo LSX-213 G2. Para os zircões detríticos, utilizou-se um sistema de ablação a laser de fonte gasosa Photon Machines 193 nm ArF Excimer acoplado ao espectrômetro Neptune. As condições analíticas foram as seguintes: diâmetro do *spot* de 40 ou 50 μm , 10-12 Hz de frequência, 50-60% de potência e 60 s de contagem. Na UFOP, as amostras foram analisadas usando um ICP-MS multicoletor Thermo Scientific Neptune Plus em conjunto com sistema de ablação Photon Machines 193 ($\lambda = 193$ nm) ArF excimer. Os dados foram coletados durante 60 s de ablação com um *spot* de 40 μm e taxa de repetição de 8 Hz.

Os grãos de zircão utilizados para análise Lu-Hf foram aqueles previamente analisados pelo método U-Pb, no mesmo domínio em que a idade foi obtida. Em cristais cujas determinações U-Pb foram feitas por SHRIMP, as análises de Hf foram realizadas sobre o *spot*. Sempre que possível, as composições isotópicas de Hf foram medidas apenas em cristais com idade U-Pb concordantes e subconcordantes para zircões de rochas magmáticas (< 5% discordância) e detríticos (< 10% de discordância).

As razões isotópicas foram recalculadas para as idades de cristalização das amostras (rochas magmáticas) ou dos grãos individuais (zircões detríticos) considerando a constante de decaimento $1,867 \times 10^{-11}$ anos⁻¹ (Söderlund *et al.*, 2004). Para o cálculo do parâmetro petrogenético épsilon Hf (ϵHf) e da idade modelo em dois estágios (Hf- T_{DM}^{C}) utilizou-se os valores do reservatório condrítico uniforme (CHUR) de Bouvier *et al.* (2008) e do manto empobrecido (DM) de Andersen *et al.* (2009). As razões $^{176}\text{Lu}/^{177}\text{Hf}$ de 0,015 (Griffin *et al.*, 2002, 2004) e 0,022 (Pietranik *et al.*, 2008) foram assumidas para a média da crosta continental e para uma crosta máfica, respectivamente.

2.7 ELEMENTOS TRAÇOS EM ZIRCÃO

As concentrações de elementos traços em cristais de zircão foram determinadas em três amostras de rochas plutônicas datadas por U-Pb. O equipamento utilizado foi um ICP-MS *sector field* Element 2 da Thermo Finnigan, acoplado a um sistema de ablação a laser Photon Machines 193 nm ArF Excimer no Laboratório de Geocronologia da UFOP. As condições do laser foram 6 Hz de taxa de repetição, 10-12 J/cm² de fluência e um diâmetro de *spot* de 20 μm . As leituras foram realizadas em modo de baixa resolução, com 15 s de *background* e 30 s de aquisição de dados. O software GLITTER foi utilizado para redução dos dados brutos,

empregando o NIST 612 como material de referência primário. Os materiais de referência BCR e BHVO foram usados como padrões secundários.

2.8 ANÁLISES ISOTÓPICAS Sm-Nd, Rb-Sr E Pb-Pb EM ROCHA TOTAL

As análises isotópicas de rocha total foram realizadas no Laboratório de Geologia Isotópica (LGI) do Centro de Estudos em Petrologia e Geoquímica (CPGq) da Universidade Federal do Rio Grande do Sul (UFRGS). Cerca de 100 µg de pó de amostra foi misturado com uma solução traçadora mista ^{149}Sm - ^{150}Nd em bombas Savillex. A mistura foi atacada com os ácidos HNO_3 , HF e HCl em chapa quente até a completa dissolução da amostra. Em seguida, realizou-se a separação dos elementos químicos pelas técnicas convencionais de cromatografia de troca iônica em colunas de teflon. A primeira etapa consistiu na separação do Sr e elementos terras raras (ETR) usando uma resina catiônica Bio-Rad AG50W-X8. Os elementos Sm e Nd foram separados dos demais ETR utilizando a resina HDEHP LN. A separação do Pb foi realizada com uma resina aniônica Dowex Bio-Rad AG-1X8. Os concentrados dos elementos de interesse foram secos em chapa quente e dissolvidos em solução HNO_3 , para então serem depositados em filamentos de arranjo duplo de Re. A alíquota coletada de Pb foi depositada em filamentos simples de Re usando uma mistura de H_3PO_4 e sílica gel. Todas as razões isotópicas foram medidas em um espectrômetro de massa por ionização térmica com multicoleção modelo Triton Plus da Thermo Scientific.

A composição isotópica de Sr foi determinada com base em uma média de 120 leituras com intensidade de 1,0 V para o ^{88}Sr . As razões $^{86}\text{Sr}/^{88}\text{Sr}$ foram normalizadas para 0,1194. As $^{87}\text{Rb}/^{86}\text{Sr}$ foram calculadas com base nos conteúdos elementares de Rb e Sr das análises geoquímicas de rocha total. As análises isotópicas de Sm-Nd foram realizadas com uma média de 100 leituras com uma intensidade de 1,0 V para o ^{146}Nd . A razão $^{146}\text{Nd}/^{144}\text{Nd}$ igual a 0,7219 foi utilizada para a normalização das razões. As razões isotópicas Pb-Pb foram obtidas através de 50 medidas com uma intensidade média de 0,5 V para o isótopo ^{206}Pb . As razões foram corrigidas para o fracionamento em 0,1% amu^{-1} com base na análise da solução de referência NBS-982 “Equal Atoms”.

Os valores condriticos de $^{143}\text{Nd}/^{144}\text{Nd} = 0,512638$ e $^{147}\text{Sm}/^{144}\text{Nd} = 0,1967$ (Othman *et al.*, 1984) foram usados para o cálculo do parâmetro petrogenético épsilon Nd (ϵNd). As idades modelo de Sm-Nd (Nd-T_{DM}) foram calculadas de acordo com DePaolo (1981). Os cálculos cronométricos aplicaram as constantes de decaimento recomendadas por Steiger & Jäger (1977) e Wasserburg *et al.* (1981).

2.9 ELABORAÇÃO DA TESE

Essa etapa consistiu na reunião dos dados obtidos nas etapas anteriores para a elaboração do volume final da tese. Os resultados são apresentados nos capítulos a seguir na forma de três artigos científicos originais.

O primeiro artigo, intitulado “*Late Cryogenian-Ediacaran magmatism in southern Borborema Province, NE Brazil: ages, sources, petrogenesis, and tectonic setting*”, foi publicado no periódico *Geoscience Frontiers*. Nessa contribuição são apresentados novos dados petrográficos, geoquímicos, geocronológicos U-Pb em zircão e titanita e Lu-Hf em zircão, com a finalidade de redefinir os episódios magmáticos no SOS e caracterizar as fontes e processos petrogenéticos envolvidos na geração dos principais tipos de rochas magmáticas do Domínio Macururé.

O segundo artigo, intitulado “*Constraints on the source and petrogenesis of early Ediacaran shoshonitic mafic magmatism and high-K calc-alkaline granitoids in the Sergipano Orogenic System, Borborema Province, Brazil*”, foi submetido ao periódico *Precambrian Research* e encontra-se em fase de revisão. Por meio de dados geoquímicos e isotópicos de Sr-Nd-Pb em rocha total e Lu-Hf em zircão do plúton máfico-ultramáfico Capela, foi possível melhor compreender a natureza do manto litosférico subcontinental abaixo do setor sul da Província Borborema. Adicionalmente, propõe-se que a colocação desses magmas máficos na base da crosta foi um importante mecanismo para a geração de magmas félsicos contemporâneos.

O terceiro artigo, intitulado “*Detrital zircon U-Pb-Hf geochronology and geochemical constraints on the provenance and tectonic setting of the Macururé Complex, southern Borborema Province, NE Brazil*”, ainda se encontra em fase de elaboração e pretende-se submetê-lo ao periódico *International Geology Review*. Nesse trabalho são apresentados os primeiros dados isotópicos combinados U-Pb e Lu-Hf em zircões detríticos do Complexo Macururé. Em conjunto com determinações geoquímicas de elementos maiores e traços em rocha total, será possível compreender a idade e natureza das fontes de detritos, caracterizar o ambiente tectônico de deposição dos protólitos sedimentares e entender os processos de geração e retrabalhamento de crosta continental durante a amalgamação do supercontinente Gondwana Ocidental.

CAPÍTULO II LATE CRYOGENIAN-EDIACARAN MAGMATISM IN SOUTHERN BORBOREMA PROVINCE, NE BRAZIL: AGES, SOURCES, PETROGENESIS, AND TECTONIC SETTING

Artigo publicado em: Geoscience Frontiers

DOI: [10.1016/j.gsf.2023.101626](https://doi.org/10.1016/j.gsf.2023.101626)

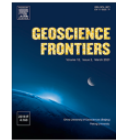
Geoscience Frontiers 14 (2023) 101626



Contents lists available at ScienceDirect

Geoscience Frontiers

journal homepage: www.elsevier.com/locate/gsf



Research Paper

Late Cryogenian–Ediacaran magmatism in southern Borborema Province, NE Brazil: Ages, sources, petrogenesis, and tectonic setting



Fábio Santos Pereira^{a,c,*}, Herbert Conceição^b, Maria de Lourdes Silva Rosa^b, Moacyr Moura Marinho^c, Colombo Celso Gaeta Tassinari^d, João Marinho Milhomem Neto^e, Jean-Michel Lafon^e

^a Programa de Pós-Graduação em Geologia e Geoquímica (PPGG), Instituto de Geociências, Universidade Federal do Pará (UFPA), 66075-110 Belém, Pará, Brazil

^b Programa de Pós-Graduação em Geociências e Análise de Bacias (PGAB), Universidade Federal de Sergipe (UFS), 49100-000 São Cristóvão, Sergipe, Brazil

^c Instituto de Geociências, Universidade Federal da Bahia (UFBA), 40170-290 Salvador, Bahia, Brazil

^d Instituto de Geociências, Universidade de São Paulo (USP), 05508-900 São Paulo, Brazil

^e Laboratório de Geologia Isotópica (Pará-Iso), IG-UFPA, 66075-110 Belém, Pará, Brazil

ARTICLE INFO

Article history:

Received 18 January 2023

Revised 11 March 2023

Accepted 25 April 2023

Available online 2 May 2023

Handling Editor: Damian Nance

Keywords:

Brasiliano/Pan-African Orogeny

Western Gondwana

Zircon and titanite U-Pb dating

Hf isotope data

Magma source

ABSTRACT

The Sergipano Orogenic System (SOS) in southern Borborema Province (NE Brazil) hosts voluminous Neoproterozoic plutonism related to the Brasiliano/Pan-African Orogeny. This paper presents comprehensive whole-rock geochemical data, titanite U-Pb ages, and the first combined zircon U-Pb and Lu-Hf isotope results for plutonic rocks from the Macururé Domain to constrain their sources, petrogenesis, and tectonic setting. Three magmatic episodes are recognized and record the evolutionary stages of the orogen. (i) Early-collisional magmatism (643–628 Ma) comprises gabbros and diorites with minor tonalites characterized by well-developed tectonic foliation and evidence of solid-state deformation. These rocks are magnesian, high-K calc-alkaline, LILE- and LREE-enriched and provide subchondritic $\varepsilon_{\text{Hf}}(t)$ values (−6.5 to −4.7) and Orosirian Hf- T_{DM}^{M} model ages (1.83–1.94 Ga). Such features indicate derivation from a lithospheric mantle source metasomatized by incorporating crustal components through subduction processes prior to magma generation, possibly related to the Rhyacian Orogeny (2.20–1.96 Ga). Extensive mixing/mingling between basaltic and crust-derived magmas took place at lower crustal depths, producing coeval hybrid diorites and quartz-diorites. (ii) Syn-collisional magmatism (630–624 Ma) encompasses biotite- and muscovite-bearing granodiorites and monzogranites, preserving their structures parallel to the schistosity of the country rocks. These rocks are leucocratic, weakly metaluminous to peraluminous, and contain abundant surmicaceous enclaves. Petrographic features and geochemical composition suggest an origin related to the partial melting of graywacke protoliths with a subordinate igneous component. (iii) Late-collisional magmatism (625–600 Ma) includes undeformed and isotropic monzonites and granodiorites, which truncate the regional foliation. These rocks are consistently metaluminous and magnesian, showing affinities with the high-K calc-alkaline to shoshonite series. Trace element modeling with subchondritic $\varepsilon_{\text{Hf}}(t)$ values (−8.3 to −4.1) and Paleoproterozoic Hf- T_{DM}^{M} model ages (1.77–2.03 Ga) demonstrate that reworking of ancient lower mafic crust played an important role at this time. The integration of our data with previously published results leads us to conclude that the geodynamic evolution of the SOS along the western Gondwana margin is better explained by large-scale lithospheric extension followed by basin inversion and continental collision.

© 2023 China University of Geosciences (Beijing) and Peking University. Published by Elsevier B.V. on behalf of China University of Geosciences (Beijing). This is an open access article under the CC BY-NC-ND license (<http://creativecommons.org/licenses/by-nc-nd/4.0/>).

1. Introduction

Granitoids are efficient geodynamic indicators that trace orogen evolution episodes when precisely characterized and dated. Calc-alkaline diorites to granites are a typical association of magmatic arcs and form vast batholiths elongated parallel to the trench (Barbarin, 1999; Frost et al., 2001a). Above the subduction zone, batches of magma derived from the mantle wedge can remain

* Corresponding author at: Programa de Pós-Graduação em Geologia e Geoquímica (PPGG), Instituto de Geociências (IG), Universidade Federal do Pará (UFPA), 66075-110 Belém, Pará, Brazil.

E-mail address: fabio.pereira@ig.ufpa.br (F.S. Pereira).

<https://doi.org/10.1016/j.gsf.2023.101626>

1674-9871/© 2023 China University of Geosciences (Beijing) and Peking University. Published by Elsevier B.V. on behalf of China University of Geosciences (Beijing). This is an open access article under the CC BY-NC-ND license (<http://creativecommons.org/licenses/by-nc-nd/4.0/>).

ABSTRACT

The Sergipano Orogenic System (SOS), southern Borborema Province (NE Brazil), hosts a voluminous Neoproterozoic plutonism related to the Brasiliano/Pan-African Orogeny. This paper presents comprehensive whole-rock geochemical data, titanite U-Pb ages, and the first combined zircon U-Pb and Lu-Hf isotope results for the plutonic rocks from the Macururé Domain to constrain their sources, petrogenesis, and tectonic setting. Three magmatic episodes are recognized and record the evolutionary stages of the orogen. (i) Early-collisional magmatism (643-628 Ma) comprises gabbros and diorites with minor tonalites characterized by well-developed tectonic foliation and evidence of solid-state deformation. These rocks are magnesian, high-K calc-alkaline, LILE- and LREE-enriched, and provide subchondritic $\epsilon\text{Hf}_{(t)}$ values (-6.0 to -4.1) and Orosirian Hf- T_{DM}^{C} model ages (1.83-1.94 Ga). Such features indicate derivation from a lithospheric mantle source metasomatized by incorporating crustal components through subduction process prior to magma generation, possibly related to the Rhyacian Orogeny (2.20-1.96 Ga). Extensive mixing/mingling between basaltic and crustal-derived magmas took place at lower crustal depths, producing the coeval hybrid diorites and quartz-diorites. (ii) Syn-collisional magmatism (630-624 Ma) encompasses biotite- and muscovite-bearing granodiorites and monzogranites, preserving their structures parallel to the schistosity of the country rocks. These rocks are leucocratic, weakly metaluminous to peraluminous, and contain abundant surmicaceous enclaves. Petrographic features and geochemical composition suggest an origin related to the partial melting of graywacke protoliths with a subordinate igneous component. (iii) Late-collisional magmatism (625-600 Ma) includes undeformed and isotropic monzonites and granodiorites, which truncate the regional foliation. These rocks are consistently metaluminous and magnesian, showing affinities with the high-K calc-alkaline to shoshonite series. Trace element modeling with subchondritic $\epsilon\text{Hf}_{(t)}$ values (-8.3 to -4.1) and Paleoproterozoic Hf- T_{DM}^{C} model ages (1.77-2.03 Ga) demonstrate that reworking of ancient lower mafic crust played an important role at this time. The integration of our data with previously published results leads us to conclude that the geodynamic evolution of the SOS along the western Gondwana margin is better explained by a large-scale lithospheric extension followed by basin inversion and continental collision.

Keywords: Brasiliano/Pan-African Orogeny, Western Gondwana, Zircon and titanite U-Pb dating, Hf isotope data, Magma source

1 INTRODUCTION

Granitoids are efficient geodynamic indicators that trace orogen evolution episodes when precisely characterized and dated. Calc-alkaline diorites to granites are a typical association of magmatic arcs and form vast batholiths elongated parallel to the trench (Barbarin, 1999; Frost et al., 2001a). Above the subduction zone, batches of magma derived from the mantle wedge can remain trapped at the interface between the upper mantle and crust, favoring the differentiation and mixing with crustal melts produced by contact with large volumes of hot mafic magma. The emplacement of peraluminous granitoids (including S-type granites) tends to be associated with thickened areas, making them a useful temporal indicator for the onset of convergence between continental landmasses (Barbarin, 1999; Chappell and White, 2001). On the other hand, high-K calc-alkaline to shoshonite granitoids are especially common during periods of orogen relaxation or transition from compressional to extensional regimes when the collision is ending (Pe-Piper et al., 2009; Couzinié et al., 2016; Orejana et al., 2020).

The Brasiliano/Pan-Africano Orogeny in the Borborema Province, northeastern Brazil, is characterized by extensive magmatism, the development of continental-scale shear zones, and metamorphism. The Sergipano Orogenic System (SOS) lies in the southernmost segment of the Borborema Province and exposes large volumes of intrusive rocks. Until the last decade, the magmatism in the SOS was grouped into two intervals: 630-618 Ma and 590-570 Ma (Bueno et al., 2009; Oliveira et al., 2010, 2015a). However, newly acquired data demonstrate a quasi-continuum of crystallization ages from 640 to 600 Ma, marking shifts in the composition of igneous rocks from (1) high-K calc-alkaline gabbros and diorites (Santos, 2016; Pereira et al., 2020) to (2) muscovite- and biotite-bearing leucogranites (Conceição, 2019), and (3) high-K calc-alkaline to shoshonite granodioritic-monzonitic intrusions (Soares et al., 2019; Sousa et al., 2019; Fernandes et al., 2020). These new findings suggest that the magmatic episodes in SOS need to be refined in light of new data to unravel the geodynamic evolution of the southern Borborema Province.

In this work, we present a comprehensive study of the three main groups of plutonic rocks in the Macururé Domain, representing the central segment of the SOS. We report new whole-rock geochemical data, zircon and titanite U-Pb dating, and the very first zircon Lu-Hf isotope results for all SOS. These data allow us to improve the range of magmatic episodes, access the sources and petrogenetic processes involved in magma genesis, and discuss the crustal evolution during the Brasiliano/Pan-Africano Orogeny.

2 GEOLOGICAL SETTING

The Borborema Province in northeastern Brazil resulted from the convergence between the Amazonian, São Luís-West Africa, and São Francisco-Congo cratons, culminating with the Western Gondwana assembly during the Brasiliano/Pan-African Orogeny (Almeida et al., 1981; Caxito et al., 2020a) (Fig. 1a). Its basement comprises Paleoproterozoic orthogneisses and scarce Archean nuclei, which occur as inliers all over the Borborema Province (Brito Neves et al., 2000; Van Schmus et al., 2008; Rosa et al., 2020). Metavulcanosedimentary sequences and orthogneisses related to the Cariris Velhos event (1.0-0.9 Ga) have been recognized in the central and southern sectors of the province (Carvalho, 2005; Caxito et al., 2014; Guimarães et al., 2016). Metasedimentary successions deposited during the middle-late Neoproterozoic cover the basement rocks. In addition, an extensive Brasiliano/Pan-African magmatism ca. 650-530 Ma is recorded by several stocks, batholiths, and dike swarms throughout the entire province.

The Brasiliano magmatism in the whole Borborema Province has been divided into five stages according to their structural, geochemical, geochronological, and isotopic features. Based on the terminology of Van Schmus et al. (2011), with some modifications in the age ranges, Caxito et al. (2020a) proposed the following magmatic episodes: Stage I (640-620 Ma) encompasses pre-collisional plutons emplaced before the development of the main thrust foliation in the supracrustal belts; Stage II (625-590 Ma) includes leucogranites and two-mica granites whose emplacement coincides with metamorphism peak and deformation related to the Brasiliano event; Stage III (590-575 Ma) comprises syn-collisional to syn-transcurrent granitic to syenitic and locally shoshonitic plutons; Stage IV (575-550 Ma) contains late- and post-collisional plutons coeval to regional strike-slip deformation; and Stage V (550-530 Ma) is generally composed of non-deformed plutons, except those emplaced along shear zones.

The Patos and Pernambuco shear zones divide the Borborema Province into the Northern, Central, and Southern subprovinces (Van Schmus et al., 2008, 2011). The southern subprovince spreads between the Pernambuco shear zone and the São Francisco Craton (SFC), comprising the Pernambuco-Alagoas Domain (PEAL) and, from west to east, the Rio Preto, Riacho do Pontal, and Sergipano orogenic belts (Fig. 1b). The latter stands between the PEAL and SFC and is considered as the western segment of the Central African Orogen in pre-drift reconstructions (Caxito et al., 2020a).

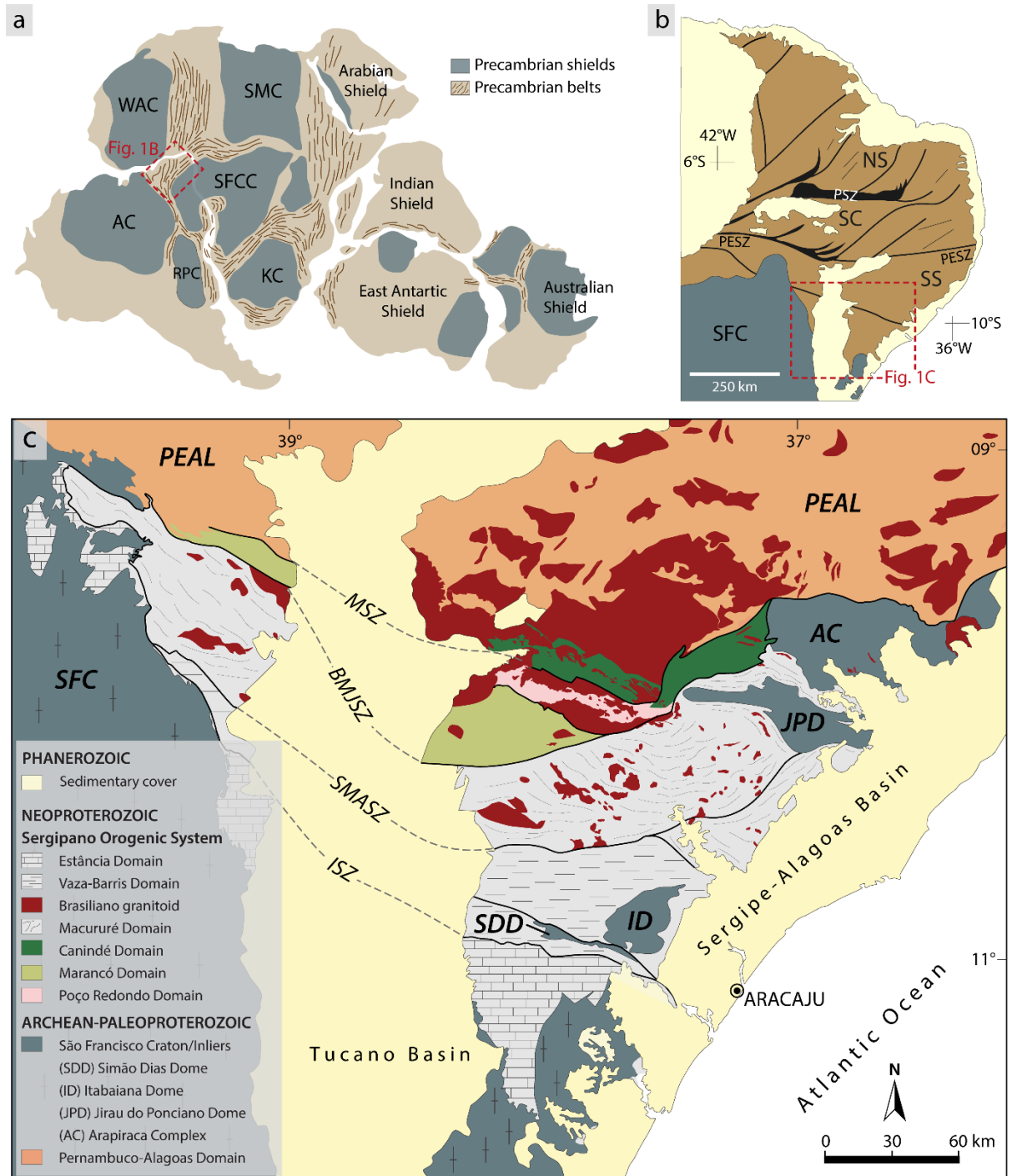


Figure II.1- Geological setting of the study area. (a) Gondwana supercontinent with the distribution of the Archean-Proterozoic cratons and Neoproterozoic orogenic belts (Gray et al., 2007). AC = Amazonian Craton, KC = Kalahari Craton, RPC = Rio de La Plata Craton, SFCC = São Francisco-Congo Craton, SMC = Sahara Metacraton, WAC = West Africa-São Luís Craton. (b) Division of the Borborema Province in the Northern (NS), Central (SC), and Southern (SS) subprovinces (Van Schmus et al., 2008), limited by the Patos (PSZ) and Pernambuco (PESZ) shear zones. (c) Tectonic compartmentation of the SOS (modified from Davison and Santos, 1989). SFC = São Francisco Craton, PEAL = Pernambuco-Alagoas Domain, MSZ = Macururé shear zone, BMJSZ = Belo Monte-Jeremoabo shear zone, SMASZ = São Miguel do Aleixo shear zone, ISZ = Itaporanga shear zone.

The geodynamical model widely accepted for the evolution of this region describes the SOS as the product of a continental collision between the PEAL and the São Francisco paleoplate over the Cryogenian-Ediacaran periods (Oliveira et al., 2010, 2017). Conversely, another model proposes that the Borborema Province and SFC were part of a large continental landmass formed by Paleoproterozoic accretionary-collisional processes, which underwent intracontinental stretching during the Neoproterozoic (Neves, 2003, 2021; Neves et al., 2015). The existence of a continuous basement since Paleoproterozoic times is also argued by Caxito et al. (2020a) and Ganade et al. (2021). However, these authors suggest that decratonization and hyperextension of this basement induce the opening of oceanic basins during the Neoproterozoic, which were then involved in typical Wilson cycles of subduction-collision.

The SOS contains six domains (Fig. 1c) with distinct sedimentation stories and tectonic evolution, namely the Estância, Vaza-Barris, Macururé, Marancó, Poço Redondo, and Canindé domains (Davison and Santos, 1989). The Estância, Vaza-Barris, and Macururé domains largely consist of metasedimentary rocks interpreted as ancient passive margins (Davison and Santos, 1989; Oliveira et al., 2010). In contrast, the Marancó, Poço Redondo, and Canindé domains have been considered allochthonous terranes accreted to the northern margin of the São Francisco paleoplate (Oliveira et al., 2017). From south to north, these domains are bounded by the Itaporanga, São Miguel do Aleixo, Belo Monte-Jeremoabo, and Macururé shear zones. A compilation of geochronological U-Pb results and whole-rock Sm-Nd isotope signature of the plutonic units of the SOS is presented in Table 1.

The Marancó Domain comprises 950 Ma A-type granites and clastic metasedimentary rocks interleaved with basic to intermediate volcanic levels. The Poço Redondo Domain includes a 980 Ma migmatitic basement that was intruded by granitoids between 636 and 617 Ma (Carvalho, 2005; Oliveira et al., 2015a; Lima, 2016; Sousa et al., 2019). The Tonian magmatic rocks are synchronous with the Cariris Velhos event (1.0-0.9 Ga), first recognized in the central subprovince of the Borborema Province (Brito Neves et al., 1995; Kozuch, 2003; Santos et al., 2010). There is no consensus about the tectonic setting of these granitoids, which have been associated with accretionary (e.g., Oliveira et al., 2010) or extensional (e.g., Guimarães et al., 2012) tectonics. Whole-rock Sm-Nd data for Cariris Velhos rocks into SOS provided negative to slightly positive values of $\epsilon\text{Nd}_{(0.98-0.95 \text{ Ga})}$ from -2.5 to +1.0 and Nd- T_{DM} model ages of 1.48-1.63 Ga (Table 1). The suprachondritic to slightly subchondritic ϵNd values allied to Mesoproterozoic Nd- T_{DM} ages were assigned to variable mixing of mantle and crustal-derived sources (Carvalho, 2005).

Table II.1- Summary of available U-Pb and whole-rock Sm-Nd isotopic data for Neoproterozoic plutonic units of the SOS.

Plutonic unit	Lithology	Mineral/Method	Approach	U-Pb age (Ma)	Nd-T _{DM} (Ga)	εNd(t)
MACURURÉ DOMAIN						
Aquidabã	Gabbro	Zrn SHRIMP	Concordant age	636 ± 4 ^(a)		
Capela	Hornblendite	Zrn SHRIMP	Concordant age	631 ± 3 ^(a)		
Fazenda Alvorada	Quartz monzonite	Zrn SHRIMP	Concordant age	630 ± 4 ^(b)		
Campo Grande	Monzodiorite	Zrn SHRIMP	Concordant age	629 ± 9 ^(a)		
Camará	Tonalite	Zrn SHRIMP	Lower intercept age	628 ± 12 ^(c)	1.71 ^(o)	-7.5 ^(o)
Glória Sul	Leucogranite	Zrn SHRIMP	Concordant age	627 ± 7 ^(d)	1.86-1.26 ^(o)	-5.7 to -1.6 ^(o)
Altos Verdes	Quartz diorite	Zrn ID-TIMS	Concordant age	625 ± 4 ^(e)		
Coronel João Sá	Granodiorite	Zrn ID-TIMS	Concordant age	625 ± 2 ^(f)	1.7-1.5 ^(t)	-6.9 to -4.8 ^(t)
Glória Sul	Leucogranite	Zrn SHRIMP	Concordant age	624 ± 11 ^(d)		
Fazenda Lagoas	Granodiorite	Zrn SHRIMP	Concordant age	623 ± 4 ^(g)		
Coronel João Sá	Granodiorite	Ttn ID-TIMS	Weighed mean age	621 ± 1 ^(f)		
Lagoa do Roçado	Granodiorite	Zrn SHRIMP	Concordant age	618 ± 4 ^(h)		
Propriá	Syenogranite	Zrn SHRIMP	Concordant age	615 ± 6 ⁽ⁱ⁾		
Mocambo	Quartz diorite	Zrn SHRIMP	Concordant age	614 ± 7 ⁽ⁱ⁾		
Graccho Cardoso	Quartz diorite	Zrn SHRIMP	Concordant age	603 ± 8 ^(k)		
Glória Norte	Quartz monzonite	Zrn SHRIMP	Concordant age	588 ± 5 ^(l)	1.36 ^(o)	-3.8 ^(o)
Angico	Leucogranite	Ttn ID-TIMS	Upper intercept age	584 ± 10 ^(e)	1.23 ^(o)	-3.6 ^(o)
Pedra Furada	Leucogranite	Ttn ID-TIMS	Upper intercept age	571 ± 9 ^(e)	1.39 ^(o)	-5.0 ^(o)
MARANCÓ DOMAIN						
Serra Negra	Granite gneiss	Zrn SHRIMP	Concordant age	952 ± 2 ^(m)	1.53-1.63 ^(m)	-2.5 to -1.1 ^(m)
POÇO REDONDO DOMAIN						
Poço Redondo Complex	Tonalitic paleosome	Zrn SHRIMP	Concordant age	980 ± 4 ^(m)	1.48-1.49 ^(m)	-1.4 to +1.0 ^(m)
Poço Redondo Complex	Gneiss	Zrn LA-ICP-MS	Concordant age	957 ± 12 ⁽ⁿ⁾		
Indiscriminate granitoid	Granite	Zrn LA-ICP-MS	Concordant age	636 ± 4 ⁽ⁿ⁾		
Sítios Novos	Granite	Zrn SHRIMP	Concordant age	631 ± 4 ^(o)	1.51 ^(o)	-5.5 ^(o)
Poço Redondo	Granite	Zrn SHRIMP	Concordant age	623 ± 7 ^(o)	1.57-1.40 ^(o)	-5.5 to -4.2 ^(o)
Queimada Grande	Granodiorite	Zrn SHRIMP	Concordant age	618 ± 4 ^(o)	1.32-1.18 ^(o)	-2.5 to -1.1 ^(o)
Rio Jacaré	Granodiorite	Zrn SHRIMP	Concordant age	617 ± 4 ^(p)		
Curitiba	Granitoid	Zrn ID-TIMS	Upper intercept age	617 ± 7 ^(q)	1.5 ^(q)	-11.2 ^(q)
CANINDÉ DOMAIN						
Novo Gosto	Amphibolite	Zrn LA-ICP-MS	Concordant age	743 ± 3 ^(r)		+0.4 to +4.9 ^(r)
Garrote	Metasyenogranite	Zrn LA-ICP-MS	Upper intercept age	720 ± 29 ⁽ⁿ⁾		
Canindé Gabbroic Complex	Metadolerite	Zrn LA-ICP-MS	Upper intercept age	718 ± 23 ⁽ⁿ⁾		
Canindé Gabbroic Complex	Metadolerite	Zrn LA-ICP-MS	Concordant age	716 ± 3 ⁽ⁿ⁾		
Canindé Gabbroic Complex	Metagabbro	Zrn LA-ICP-MS	Concordant age	719 ± 2 ⁽ⁿ⁾		
Boa Esperança	Metasyenogranite	Zrn LA-ICP-MS	Upper intercept age	708 ± 8 ⁽ⁿ⁾		
Canindé Gabbroic Complex	Gabbro	Zrn LA-ICP-MS	Concordant age	703 ± 2 ^(s)		+1.3 to +4.3 ^(s)
Gentileza	Metavolcanic	Zrn LA-ICP-MS	Concordant age	701 ± 5 ⁽ⁿ⁾		
Canindé Velho	Diorite	Zrn SHRIMP	Concordant age	640 ± 4 ^(t)		
Lajedinho	Monzodiorite	Zrn SHRIMP	Concordant age	619 ± 3 ^(o)	1.22-1.14 ^(o)	-1.1 to -0.1 ^(o)
Santa Maria	Monzogranite	Zrn SHRIMP	Concordant age	611 ± 4 ^(u)		

Zrn = zircon; Ttn = titanite. Nd-T_{DM} ages following the depleted mantle evolution model of DePaolo (1988). Data source: ^aPereira et al. (2020), ^bSantos (2021), ^cBueno et al. (2009), ^dConceição (2019), ^eLima (2021), ^fLong et al. (2005), ^gFernandes et al. (2020), ^hSilva (2014), ⁱSantos et al. (2019), ^jOliveira (2020), ^kSousa (2020), ^lLisboa et al. (2019), ^mCarvalho (2005), ⁿPassos et al. (2022), ^oOliveira et al. (2015b), ^pSousa et al. (2019), ^qLima (2016), ^rPassos et al. (2021), ^sPinto et al. (2020), ^tSantos (2016), ^uSoares et al. (2019a).

Metasedimentary rocks, tholeiite metabasalts, layered gabbros, and A-type granites constitute the Canindé Domain (Oliveira et al., 2010, 2017). Several tectonic interpretations have been proposed for this area, firstly considered an ophiolitic complex (Silva Filho et al., 1979). According to Oliveira et al. (2010), this association of rocks formed in a continental rift

that evolved to an ocean between 715 and 640 Ma. More recent subduction-based models suggest that the Canindé Domain represents island arc/back-arc (Lima et al., 2018) and continental arc/back-arc systems (Pinto et al., 2020; Passos et al., 2021, 2022). The Nd isotopic signature of the mafic-ultramafic Canindé layered intrusion and amphibolites from the Novo Gosto unit points to an episode of generation of juvenile crust ($\epsilon\text{Nd}_{(0.74-0.70 \text{ Ga})} = +0.4$ to $+4.9$) from a relatively depleted to enriched mantle source (Pinto et al., 2020; Passos et al., 2021).

Structural windows from the Archean-Paleoproterozoic basement have been identified within the metavolcanosedimentary sequence of SOS, which are exposed in the domes of Simão Dias (2.86 Ga; Oliveira, 2012), Itabaiana (2.83 Ga; Rosa et al., 2020), Jirau do Ponciano (ca. 2.0 Ga; Lima et al., 2019), and Arapiraca Complex (ca. 2.0 Ga; Tesser et al. 2021).

The whole-rock Sm-Nd data for the Cryogenian-Ediacaran granitoids into Canindé, Poço Redondo, Marancó, and Macururé domains yielded negative values of $\epsilon\text{Nd}_{(0.63-0.57 \text{ Ga})}$ (-7.5 to -1.6) and variable Nd- T_{DM} model ages (1.86-1.23 Ga), indicating that reworking of ancient crust was the primary process of crustal evolution (Oliveira et al., 2015a).

2.1 MACURURÉ DOMAIN AND ASSOCIATED BRASILIANO PLUTONISM

The Macururé Domain is limited to the south by the São Miguel do Aleixo shear zone and to the north by the Belo Monte-Jeremoabo shear zone (Fig. 2). It is divided into two branches, separated by the Phanerozoic Tucano Basin. The Macururé Domain comprises the metasedimentary succession of the Macururé Complex and a Cryogenian-Ediacaran intrusive suite (Bueno et al., 2009; Oliveira et al., 2010, 2015a; Pereira et al., 2020).

The Macururé Complex is mainly composed of greenschist to amphibolite facies meta-turbiditic rocks (Davison and Santos, 1989; Silva et al., 1995). In the eastern sector, garnet-bearing biotite schists, phyllites, metasandstones, metagraywackes, and quartzites predominate, with minor intercalations of metavolcanic acid rocks, and lenses of amphibolite, marble, and calc-silicate rocks (Santos et al., 1998; Oliveira et al., 2010). These lithologies lie above the Jirau do Ponciano Dome, interpreted as the basement of the domain. U-Pb detrital zircon data demonstrate a heterogeneous provenance for the Macururé Complex, dominated by Paleoproterozoic (2.1-1.9 Ga), late Mesoproterozoic (ca. 1.1 Ga), and early Neoproterozoic (1.0-0.92 Ga) sources (Van Schmus et al., 2011; Oliveira et al., 2015b; Neves et al., 2019). The lack of zircon crystals younger than 850 Ma suggests that the sedimentary succession deposition occurred before the Brasiliano Orogeny.

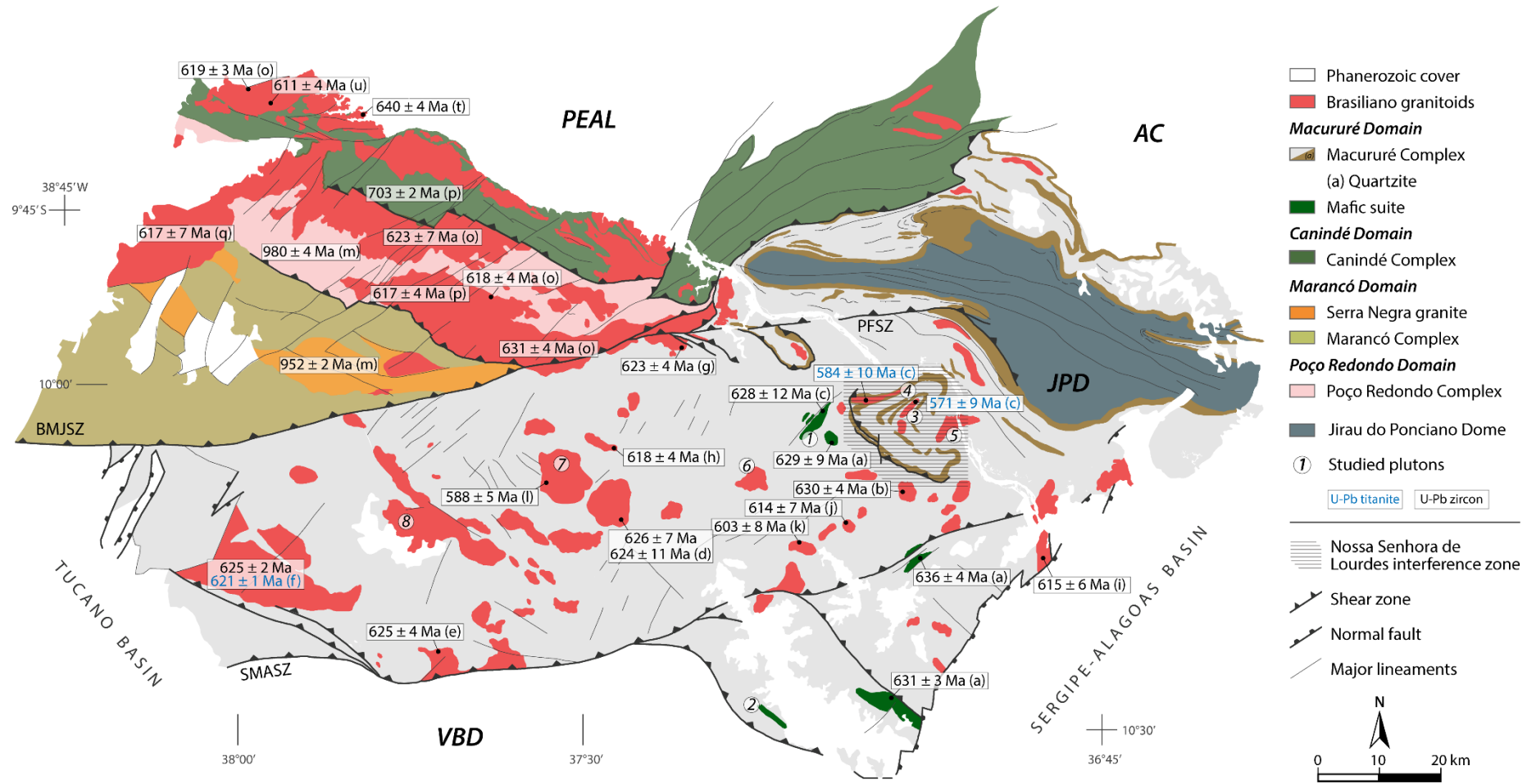


Figure II.2- Geochronological map of the eastern segment of the SOS. Age references are those shown in Table 1. AC = Arapiraca Complex, JPD = Jirau do Ponciano Dome, PEAL = Pernambuco-Alagoas Domain, VBD = Vaza-Barris Domain, BMJSZ = Belo Monte-Jeremoabo shear zone, PFSZ = Porto da Folha shear zone, SMASZ = São Miguel do Aleixo shear zone. Plutons: 1 – Camará, 2 – Dorés, 3 – Pedra Furada, 4 – Angico, 5 – Areias, 6 – Várzea Nova, 7 – Glória Norte, 8 – Santa Helena.

Large volumes of Neoproterozoic plutonic rocks occur in the Macururé Domain, represented by several stocks and some batholiths. According to field relationships and radiometric dating, these granitoids were classified as pre-collisional (628-625 Ma) and syn-collisional (590-570 Ma) relative to the main collisional event in the SOS (Bueno et al., 2009). These authors described the first group as composed of calc-alkaline granodiorites-tonalites displaying a penetrative foliation and evidence of solid-state deformation. The emplacement age of this group was constrained by the U-Pb zircon dating of the Camará (628 ± 12 Ma; Bueno et al., 2009) and Coronel João Sá (625 ± 2 Ma; Long et al., 2005) plutons. The syn-collisional group consists of leucocratic granites that outcrop as tabular bodies and preserve magmatic structures parallel to the country rocks. The U-Pb ID-TIMS titanite ages for the Angico (584 ± 10 Ma) and Pedra Furada (571 ± 9 Ma) plutons constrain the emplacement of this magmatic group (Bueno et al., 2009). Both plutons outcrop into the Nossa Senhora de Lourdes interference structure, which is a mushroom-fold interference pattern that records the main ductile deformational events in the SOS (Fig. 2). Oliveira et al. (2015b, 2010) suggested that the older granites were produced in an Andean-type magmatic arc, while the younger ones mark the collision-between the SFC and PEAL in a Himalayan-like setting.

Recent U-Pb dating of other plutonic rocks revealed a nearly continuous spectrum of ages throughout the Brasiliano Orogeny instead of two distinct magmatic episodes as previously proposed (Bueno et al., 2009; Oliveira et al., 2010, 2015a). Small elongated bodies of mafic-ultramafic rocks emplaced at ca. 636-629 Ma were recognized by Pereira et al. (2020) and grouped into the Macururé Mafic Suite. The first U-Pb zircon dating of a leucogranite in the SOS yielded crystallization ages of 627 ± 7 Ma and 624 ± 11 Ma for the Glória Sul pluton (Conceição 2019). These ages are around 50 Ma older than those obtained by Bueno et al. (2009) for titanites from the Pedra Furada and Angico leucogranites. The youngest U-Pb zircon age in the Macururé Domain was obtained for the Glória Norte pluton (588 ± 5 Ma), whose shoshonitic and ultrapotassic affinities mark a post-collisional stage in the SOS (Lisboa et al., 2019). Furthermore, several granitoids with high-K calc-alkaline to shoshonite affinities were emplaced earlier during the period 623-603 Ma (Silva, 2014; Santos et al., 2019; Fernandes et al., 2020; Oliveira, 2020).

3 SAMPLING AND ANALYTICAL METHODS

The samples of this work were collected from 34 depictive outcrops of the main types of plutonic rocks in the Macururé Domain. The investigated units include mafic rocks (Camará and Dores plutons), leucogranite bodies (Pedra Furada, Angico, Areias, and Várzea Nova plutons), and undeformed granitoids (Glória Norte and Santa Helena plutons). Petrographic descriptions were performed on 19 samples from the mafic intrusions, 14 from leucogranites, and 6 from undeformed granitoids. Twenty-five of these samples were selected for whole-rock geochemical analyses. Zircon crystals from Camará (SOS-626), Glória Norte (FDS-12), and Santa Helena (SOS-1281) plutons were used for U-Pb dating, Lu-Hf isotope analysis, and trace elements composition. Titanite U-Pb dating was carried out in samples of the Dores (SOS-910), Pedra Furada (SOS-1257), and Glória Norte (FDS-12) plutons.

3.1 PETROGRAPHY, MINERAL COMPOSITIONS, AND IMAGING

The modal composition of 29 samples was determined by counting an average of 1000 points by thin section (Supplementary Table S1). Mineral modes of 10 other samples were obtained by visual estimation under the microscope. Mineral abbreviations follow the recommendations of Warr (2021). The investigation of mineral composition was performed with an energy dispersive X-ray spectrometer (EDS) Oxford Instruments model x-act, coupled to a scanning electron microscope (SEM) Tescan model LMU Vega3, at the Condomínio Laboratorial das Geociências, Universidade Federal de Sergipe (CLGeo-UFS). Operation conditions were 15 kV of accelerating voltage and 15-17 nA of beam current, producing an electron beam of 280-430 nm in diameter. Natural minerals and synthetic oxides were used for equipment calibration. The ZAF (atomic number-absorption-fluorescence) correction procedure was applied to chemical data treatment. Cathodoluminescence (CL) and backscattered electron (BSE) imaging were carried out at the same laboratory with the following analytical conditions: 20 kV of acceleration voltage, 10-20 nA of beam current, and electron beam diameter between 0.4-1.0 μm .

3.2 WHOLE-ROCK GEOCHEMISTRY

The major element contents of 18 samples were determined from pressed pellets by X-ray spectrometry fluorescence (XRF) using a Shimadzu XRF-1800 installed in CLGeo-UFS. All samples were mechanically crushed and milled to a granulometric fraction lower than 100 mesh. The preparation of pressed pellets for XRF analysis followed the procedures outlined

below. About 2.5 g of the sample powder was mixed with 0.8 g of boric acid (H_3BO_3). The mixture was homogenized, deposited in steel disks, and compacted in a hydraulic press at 60 kN/30 s. The XRF was calibrated using 26 geochemical standards, comprising a wide range of rock types. The quality control was monitored by analyzing three duplicate samples and reference materials. The precision was better than 1% for all analyzed oxides. Loss of mass on ignition (LOI) was determined in dried rock powder (120 °C) by calcination in a muffle furnace at 1000 °C for 2 h. Trace element analysis of 10 samples was performed at ALS Laboratories, Lima, Peru. These samples were chosen to represent all compositional variation in the area, considering the alteration degree indicated by the LOI values. The selected package (MEMS81™) includes lithium borate fusion prior to acid dissolution and inductively coupled plasma mass spectrometry (ICP-MS) analysis. Analytical procedures are available at <https://www.alsglobal.com/>.

Additionally, major and trace elements of 10 other samples from the Camará pluton were analyzed by major and trace elements by XRF and ICP-MS at the SGS GEOSOL laboratory in Vespasiano, Minas Gerais, Brazil. Analytical protocols were those of the XRF79C and IMS95A packages, whose detailed description can be accessed at <https://www.sgsgeosol.com.br/>. The geochemical diagrams were made using the Geochemical Data Toolkit software (Janoušek et al., 2006). The whole-rock geochemical results are listed in Supplementary Table S2.

3.2.1 Geochemical modeling

Our modeling included two steps: first, mass-balance using the software GENESIS 4.0 (Teixeira, 2005) to determine modal and geochemical compositions of the residual assemblage based on major elements. Second, trace element modeling constrained by the calculated mineral proportions. During mass-balance calculations, the minor oxides MnO and P_2O_5 are omitted, and all iron is reported as FeO. The adjustment accuracy between theoretical and observed data is expressed by the sum of the squared residuals Σr^2 , where the lower value of $\Sigma r^2 < 1$ indicates a better correlation between the model and data. An in-house Excel spreadsheet was used to calculate the modeled trace element concentrations by applying the equilibrium partial melting equation $C_i/C_0 = 1/(F + D - FD)$ (Wilson, 1989). Binary mixing calculations follow the equation $C_m = X_1C_1 + (1 - X_1)C_2$, where the concentration of the considered component (C) is weighted by the proportion (X) of end-members in the mixing. The mineral/liquid partition coefficients used for trace element modeling are those from the GERM database (<https://kdd.earthref.org/KdD/>) and Rollinson (1993).

3.3 U-Pb GEOCHRONOLOGY

The zircon and titanite concentrates were obtained by the conventional crushing, grinding, panning, and magnetic separation procedures. Titanite grains remained in the non-magnetic fraction (1.0-1.5 A) with zircon. The best zircon and titanite grains were hand-picked using a binocular microscope, mounted in individual epoxy discs (~ 25 mm), polished, and gold-coated. These grains were imaged under CL (zircon) and BSE (titanite) to reveal the internal structures of the crystals and choose the target areas to be analyzed.

Uranium decay constants used for age calculations are those recommended by Steiger and Jäger (1977). The graphic representation of the U-Pb data was made using the Excel Add-in Isoplot 4.15 (Ludwig, 2009a), with error ellipses reflecting 2σ uncertainty.

3.3.1 Zircon dating

U-Pb isotopic analyses on zircon from samples SOS-626 (diorite), FDS-12 (monzonite), and SOS-1281 (granodiorite) were carried out with an Element 2 Thermo Finnigan ICP-MS equipped with a Photon-Machines 193 nm ArF Excimer laser ablation system at Departamento de Geologia, Universidade Federal de Ouro Preto (DEGEO/UFOP). The analytical procedures are those described by Santos et al. (2022). Data were acquired in peak jumping mode with 20 s background measurement, 20 s zircon ablation, and 30 μm spot size. Laser conditions were 10 Hz frequency and 4 J/cm^2 fluency. Laser-induced elemental fractionation and instrumental mass discrimination are corrected by normalizing to the reference zircon GJ-1 (608.5 ± 1.5 Ma; Jackson et al., 2004). Blue Berry (BB) and Plešovice reference zircons were used as secondary standards to check the reliability and reproducibility of the analyses. BB zircon provided a Concordia age of 560.1 ± 2.2 Ma (2σ , $n = 22$, MSWD = 1.6), in agreement with the ID-TIMS age of 560.0 ± 0.4 Ma reported by Santos et al. (2017). A Concordia age of 338.3 ± 1.5 Ma (2σ , $n = 20$, MSWD = 0.53) was obtained for the Plešovice zircon, which is consistent with the ID-TIMS age of 337.3 ± 0.4 Ma admitted to this reference material (Sláma et al., 2008).

Raw data reduction was performed with the U-Pb SATURN software (Silva et al., 2022). No correction for common lead was applied. Only concordant to sub-concordant analyses were considered for Concordia ages (discordance degree $\leq 3\%$), avoiding the spots with uncertainties on isotopic ratios beyond 5% at 2σ . All reported uncertainties (2σ) were propagated by quadratic addition of the external reproducibility obtained from the reference material GJ-1 during the analytical session (2σ %) and the within-run precision of each analysis

(2 SD%). The U-Pb results for unknown and reference zircons are listed in Supplementary Table S3 and Supplementary Table S4.

3.3.2 Titanite dating

One diorite (SOS-910), one monzonite (FDS-12), and one leucogranite (SOS-1257) were selected for titanite dating. U-Pb isotope measurements from the samples SOS-910 and FDS-12 were conducted by LA-Q-ICP-MS, using a quadrupole Thermo Fisher iCAP-Q mass spectrometer coupled to a laser system Nd:YAG LSX-213 G2 CETAC at the Laboratório de Geologia Isotópica, Universidade Federal do Pará (Pará-Iso/UFPa). Each spot analysis consisted of 20 s background measurements, followed by 40 s data acquisition and 30 s for cleaning the sample cell and plumbing lines. Table 2 summarizes the analytical parameters of the mass spectrometer and laser. Ablated material was transferred in He carrier gas mixed with Ar prior to introduction into the ICP-MS. Masses ^{202}Hg , $^{204}(\text{Pb} + \text{Hg})$, ^{206}Pb , ^{207}Pb , ^{208}Pb , ^{232}Th and ^{238}U were measured. Raw data reduction and corrections for background and laser-induced elemental fractionation were performed using an in-house MS Excel spreadsheet. The primary reference material was the Khan titanite, used to calculate the U, Th, and Pb concentrations and normalize the $^{206}\text{Pb}/^{238}\text{U}$ ratios, considering a reference age of 520 Ma (Heaman, 2009). Tory Hill titanite was analyzed as a secondary reference material to verify the reproducibility of the isotopic measurements. Regression from initial common Pb ($^{207}\text{Pb}/^{206}\text{Pb}_{(1039 \text{ Ma})} = 0.92$; Stacey and Kramers, 1975) through uncorrected data yielded an age of $1028 \pm 9 \text{ Ma}$ (2σ , MSWD = 3.1), identical within analytical uncertainty to ID-TIMS age of $1039 \pm 23 \text{ Ma}$ reported by Fisher et al. (2020). Titanite U-Pb data are given in Supplementary Table S5.

Table II.2- ICP-MS and laser instrumentation parameters for U-Pb analysis in titanite.

ICP-MS	iCAP-Q
Mass analyzer	Quadrupole
RF power	1550 W
Cooling gas	Ar 16.0 L min ⁻¹
Auxiliary gas	Ar 1.0 L min ⁻¹
Isotopes	^{202}Hg , $^{204}(\text{Pb} + \text{Hg})$, ^{206}Pb , ^{207}Pb , ^{208}Pb , ^{232}Th , ^{238}U
Laser	Nd:YAG LSX-213 G2 CETAC
Wavelength	213 nm
Carrier gas	He 0.8 L min ⁻¹
Frequency	10 Hz
Fluency	4-5 J/cm ²
Energy	55%
Spot size	50 μm
Ablation time	40 s

An appropriate choice of initial Pb composition is challenging for samples with a high content of common lead, like titanite. For titanites with low common Pb ($f_{206} < 10\%$), the choice of initial Pb composition will have a slight effect on calculated ages (Frost et al., 2001b; Aleinikoff et al., 2002). In this case, we estimate the initial $^{207}\text{Pb}/^{206}\text{Pb}$ through the terrestrial Pb evolution model of Stacey and Kramers (1975). For the titanites that display $f_{206} > 10\%$, the ages were calculated by (1) free regression of uncorrected data in the Tera-Wasserburg diagram, where the y-intercept corresponds to the initial $^{207}\text{Pb}/^{206}\text{Pb}$; (2) weighted average of individual $^{206}\text{Pb}/^{238}\text{U}$ dates assuming this initial $^{207}\text{Pb}/^{206}\text{Pb}$.

In addition to the quadrupole dataset, the sample SOS-1257 (leucogranite) was analyzed by the Sensitive High-Resolution Ion Microprobe – SHRIMP IIe at Instituto de Geociências of the Universidade de São Paulo (IGc-USP), using the analytical methods described by Sato et al. (2016). Operation conditions were a diameter beam of 30 μm and an O^{-2} beam density of $\sim 3\text{-}5$ ηA . Data reduction was performed using SQUID software (Ludwig, 2009b).

3.4 ZIRCON Lu-Hf ISOTOPE ANALYSES

LA-ICP-MS Lu-Hf analyses were obtained on the zircon crystals from the three samples previously dated by the U-Pb method in the same internal domain where the U-Pb isotopic analysis was performed. This step was executed at DEGEO/UFOP. The isotope ratios were measured using an MC-ICP-MS Thermo Finnigan Neptune Plus, coupled to a Photon-Machines 193 nm ArF Excimer laser ablation system, following the analytical protocols of Santos et al. (2022). Data were obtained in static mode during 60 s of ablation, with a spot size of 50 μm .

The isotopes of Lu, Hf, and Yb were measured concomitantly. Isotope ratios of Yb and Hf were normalized by assuming the values of $^{173}\text{Yb}/^{171}\text{Yb} = 1.12346$ (Thirlwall and Anczkiewicz, 2004) and $^{179}\text{Hf}/^{177}\text{Hf} = 0.7325$ (Patchett and Tatsumoto, 1981), according to the exponential law. Natural abundances for isotopes ^{175}Lu ($^{176}\text{Lu}/^{175}\text{Lu} = 0.02659$; Chu et al., 2002) and ^{173}Yb ($^{176}\text{Yb}/^{173}\text{Yb} = 0.786956$; Thirlwall and Anczkiewicz, 2004) were adopted to correct the isobaric interferences. $^{176}\text{Hf}/^{177}\text{Hf}$ ratios measured in unknown crystals were normalized based on the average values of $^{176}\text{Hf}/^{177}\text{Hf}$ obtained from the Mud Tank reference zircon and its respective certified ratios (Woodhead and Hergt, 2005). Five reference zircons were used as secondary standards to monitor the external reproducibility of the method. During the period of data acquisition, repeated analyses yielded $^{176}\text{Hf}/^{177}\text{Hf}$ ratios (± 2 SD) of 0.282507 ± 43 for Mud Tank ($n = 30$), 0.282672 ± 44 for TEMORA 2 ($n = 26$), 0.282310 ± 38 for 91500 ($n = 20$), 0.281677 ± 31 for BB ($n = 29$), and 0.282022 ± 65 for GJ-1 ($n = 20$). These results

agree with recommended values (Woodhead and Hergt, 2005; Morel et al., 2008; Santos et al., 2017). The isotopic data for reference zircons are listed in Supplementary Table S6 and shown in Supplementary Figure S1.

Hafnium isotope compositions were measured only on zircon crystals with concordant to subconcordant U-Pb age ($\leq 5\%$ of discordance). Isotope ratios were recalculated back to the crystallization age using the decay constant $1.867 \times 10^{-11} \text{ years}^{-1}$ (Söderlund et al., 2004). Present-day values for the chondritic uniform reservoir (CHUR; Bouvier et al., 2008) and the depleted mantle (DM; Andersen et al., 2009) were used to calculate the epsilon hafnium parameter (ϵHf) and the two-stage depleted mantle model ages ($\text{Hf-T}_{\text{DM}}^{\text{C}}$), respectively. The $^{176}\text{Lu}/^{177}\text{Hf}$ ratio equal to 0.015 is assumed as a continental crust average for $\text{Hf-T}_{\text{DM}}^{\text{C}}$ calculation (Griffin et al., 2002). Results for zircon crystals from studied plutonic rocks constitute Supplementary Table S7.

3.5 ZIRCON TRACE ELEMENTS

Trace elements concentrations were measured on zircon from the three samples dated by U-Pb, using a Thermo Finnigan ICP-MS sector field Element 2 coupled to a Photon Machines 193 nm ArF Excimer laser at DEGEO/UFOP. Laser conditions were a repetition rate of 6 Hz, 10-12 J/cm² of energy density, and a spot size of 25 μm . The measurements were performed in low-resolution mode, with 15 s background and 30 s data acquisition. Data reduction was carried out with GLITTER software using the NIST 612 glass as the primary standard. The basaltic glasses BCR and BHVO were used as secondary standards. Trace element data for zircon and reference materials are shown in Supplementary Table S8.

The crystallization temperature of the zircon was calculated by the revised Ti-in-zircon calibration of Ferry and Watson (2007). All studied samples contain modal quartz, suggesting that $a\text{SiO}_2$ could be assumed as 1. Rutile was not identified in any of the samples, indicating that TiO_2 saturation was not achieved, such that the $a\text{TiO}_2$ must be lower than the unit. The main titanium-bearing phases in the investigated samples are titanite and ilmenite, which constrain TiO_2 activity to high values (Watson et al., 2006). Therefore, we estimate an $a\text{TiO}_2 = 0.6$ for the calculation.

4 RESULTS

4.1 FIELD RELATIONSHIPS AND SAMPLE DESCRIPTION

According to field relationships, the studied magmatic rocks from the Macururé Domain can be classified in relation to the main deformation event as pre- to early-collisional, syn-collisional, and late-collisional.

Pre- to early-collisional plutons (now referred to as early-collisional) show solid-state deformation and well-marked foliation or lineation related to the main collisional event. This magmatism is represented in the study area by the Dores and Camará plutons, along with Capela, Aquidabã, and Campo Grande mafic stocks (Pereira et al., 2020)

The syn-collisional Pedra Furada, Angico, Areias, and Várzea Nova plutons were emplaced synchronously with the collisional event, preserving their igneous structures parallel to the foliation of the country rocks.

In contrast, the late-collisional plutons truncate the structures of the country rocks and have no tectonic foliation related to the collisional event. When present, rock foliation results from magmatic flux, which orients mafic minerals and enclaves. The Santa Helena and Glória Norte plutons are associated with this stage.

Table 3 presents the modal composition of the studied rocks. Field and petrographic aspects are shown in figures 3 and 4.

Table II.3- Summary of modal compositions of the studied plutons.

Minerals (vol%)	Early-collisional plutons		Syn-collisional plutons		Late-collisional plutons	
	Gb-Dio	Ton	Grd-Ton	Mzg	Mzd-Grd	Mzg
Quartz	2.0 – 15.0	12.4 – 28.6	26.9 – 37.4	24.6 – 33.8	11.9 – 22.9	17.4 – 22.9
Plagioclase	41.7 – 71.0	24.5 – 50.0	30.5 – 38.0	26.1 – 34.3	34.2 – 36.6	25.1 – 36.6
Microcline	0.0 – 0.7	0.4 – 4.3	5.6 – 14.5	20.2 – 31.9	17.9 – 19.4	18.2 – 25.4
Biotite	7.0 – 28.1	13.4 – 28.1	0.0 – 12.5	0.6 – 7.2	4.0 – 15.8	4.0 – 10.7
Muscovite*	0.0 – 3.0	0.0 – 1.2	0.4 – 18.9	3.0 – 15.8	0.0 – 9.2	0.0 – 9.2
Amphibole	0.0 – 20.0	0.0 – 12.5	–	–	0.0 – 13.7	0.0 – 11.4
Clinopyroxene	0.0 – 5.0	0.0 – 10.0	–	–	0.0 – 2.7	0.0 – 0.4
Titanite	0.8 – 2.2	0.1 – 0.7	0.4 – 2.9	0.1 – 1.0	0.8 – 1.7	1.3 – 1.7
Epidote*	0.0 – 5.6	3.2 – 14.5	0.1 – 5.5	0.6 – 2.6	1.8 – 5.0	3.5 – 4.8
Garnet	0.0 – 7.0	–	0.0 – 1.0	–	–	–
Allanite	0.0 – 0.2	0.3 – 0.5	0.0 – 0.8	0.0 – 0.4	tr	0.0 – 0.2
Apatite	0.0 – 0.4	0.0 – 0.3	0.0 – 0.4	0.1 – 0.3	0.0 – 0.5	0.0 – 0.9
Zircon	tr	tr	tr	tr	tr	tr
Opaque minerals	0.0 – 1.0	0.1 – 0.2	tr	0.0 – 0.4	0.0 – 0.3	tr
Chlorite	–	–	–	0.0 – 1.9	0.0 – 1.1	0.0 – 4.6
Tourmaline	0.0 – 1.0	–	–	–	–	–
Carbonate	0.0 – 0.2	0.2 – 0.8	0.0 – 1.9	0.0 – 1.0	–	0.0 – 1.8

Gb = gabbro, Dio = diorite, Ton = tonalite, Grd = granodiorite, Mzg = monzogranite, Mzd = monzodiorite. *Includes the magmatic and secondary varieties, “tr” mineral identified but not counted, “–” not determined.

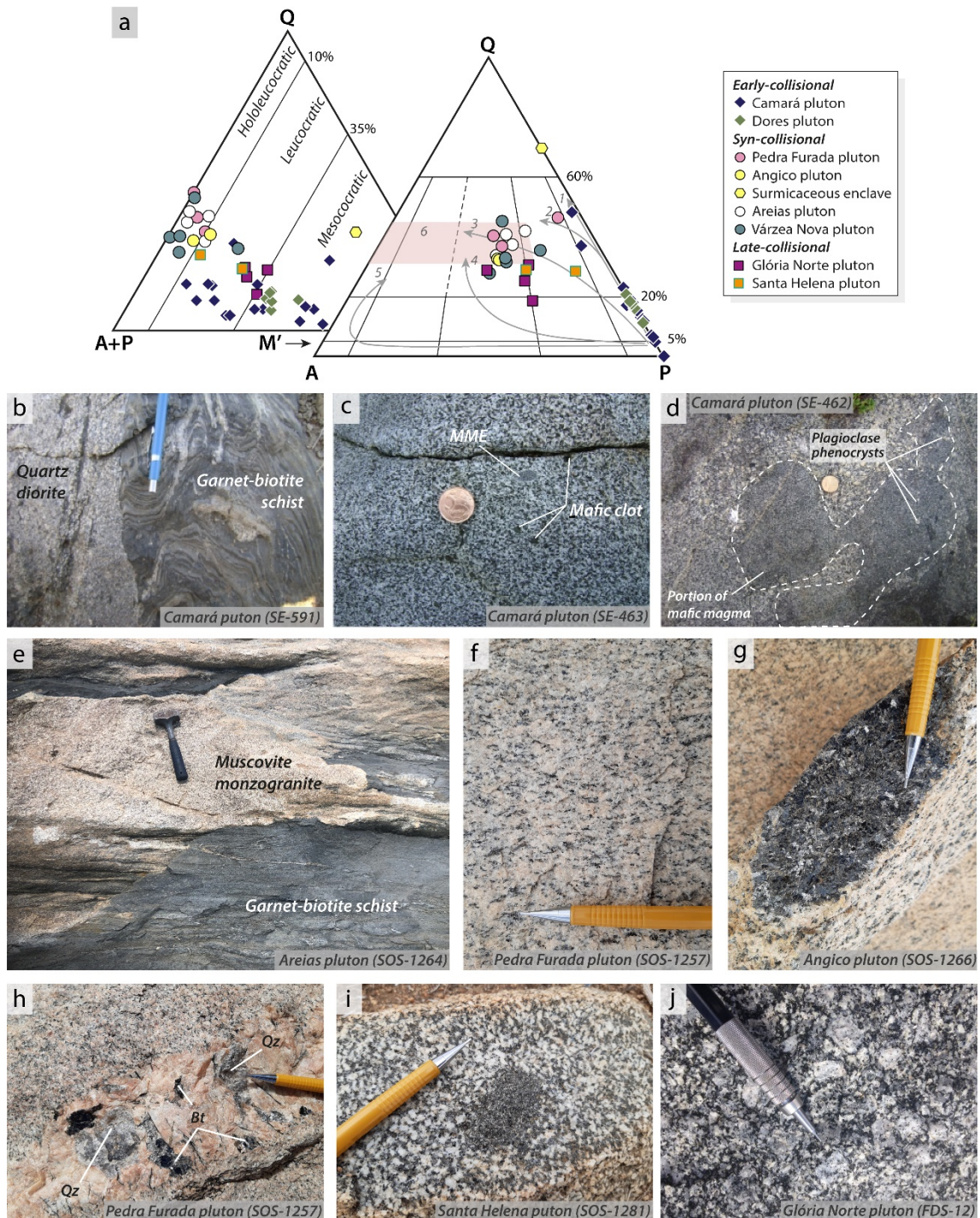


Figure II.3- Field aspects and mesoscopic features of the studied plutons. (a) QAP and Q(A+P)M' plots (le Maitre et al., 2002). Evolutionary trends of granitoid series according to Lameyre and Bowden (1982): 1 – tholeiitic, 2 – low-K calc-alkaline, 3 – medium-K calc-alkaline, 4 – high-K calc-alkaline, 5 – alkaline, and 6 – field of crustal granitoids. (b) Quartz diorite from the Camará pluton intrudes the Macururé micaschists along the axial planes of the folds. (c) Equigranular foliated diorite from Camará pluton, hosting centimeter MME and mafic clots. (d) Disrupted fine-grained diorite MME wrapped into porphyritic granodiorite. Plagioclase phenocrysts into MME suggest the coexistence and interaction between mafic and felsic magmas. (e) Areias leucogranite intruding schists of the Macururé Complex along the foliation. (f) Biotite-muscovite monzogranite of the Pedra Furada pluton with a foliation defined by the orientation of the micas. (g) Surmicaceous enclave within medium-grained pink monzogranite in Angico pluton. (h) Pegmatite vein cross-cutting the Pedra Furada leucogranite. (i) Equigranular granodiorite from Santa Helena pluton hosting a microgranular mafic enclave. (j) Typical porphyritic texture of the Glória Norte monzonites, displaying plagioclase and potassic feldspar phenocrysts.

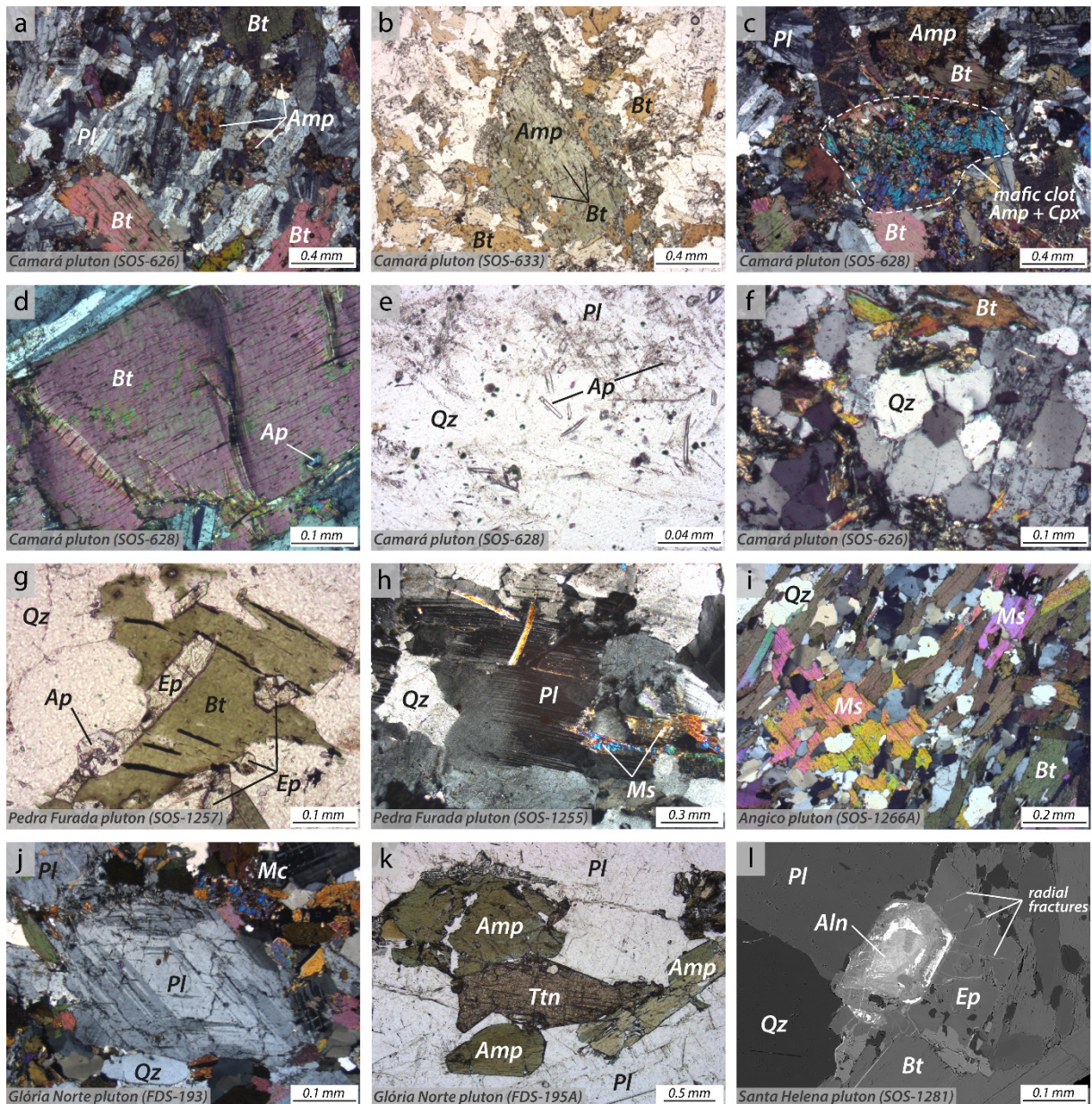


Figure II.4- Petrographic aspects of the plutonic rocks from the Macururé Domain. (a) Lath-shaped plagioclase oriented parallel to rock foliation. (b) Hornblende being transformed to biotite along cleavage planes. (c) Mafic clot containing hornblende and clinopyroxene. (d) Kink band in biotite with the inclusion of stubby apatite. (e) Acicular apatite enclosed within quartz. (f) Polygonal quartz aggregates. (g) Inclusions of apatite and epidote into green biotite. (h) Deformation twinning in plagioclase. (i) Biotite blades in a surmicaceous enclave outline a strong foliation truncated by large muscovite crystals. (j) Concentric zoning in plagioclase phenocryst. (k) Euhedral titanite in association with hornblende crystals. (l) BSE image of metamictic allanite within epidote crystals, promoting the formation of radial fractures.

4.1.1 Early-collisional magmatism

The Dores stock (5 km²) is an elongated NW-SE intrusion outcropping at the southern segment of the Macururé Domain, with the major axis parallel to the São Miguel do Aleixo shear zone (Fig. 2). This pluton comprises mesocratic light to dark-gray quartz diorites and tonalites (Fig. 3a), showing equigranular texture and medium granulation. The mafic minerals

define an NW-SE low-angle foliation dipping to NE. The essential mineralogy includes plagioclase (41.7-50.9 vol%), quartz (6.2-12.4 vol%), and small microcline (0.2-0.5 vol%). Biotite (20.1-28.1 vol%), hornblende (6.7-17.1 vol%), and clinopyroxene (0.3-1.1 vol%) are the mafic minerals. Garnet is found as disseminated anhedral crystals, composing less than 2.0 vol%. Titanite, epidote, apatite, and opaque minerals are accessory phases.

The Camará pluton (15 km²) occurs in the northeastern area of the Macururé Domain and intrudes garnet-biotite schists (Fig. 2). This body has an N-S elongated shape and comprises leucocratic to mesocratic ($M' = 13-59$) gabbros, quartz diorites, and tonalites (Fig. 3a). The contact with the country rocks is penetrative, with the mafic rocks emplaced as sills in the schistosity or along the axial planes of the folds (Fig. 3b). In the margin with schists, the diorites show sparse garnet crystals. The rocks of the Camará pluton are equigranular, gray- to black-colored, and fine- to medium-grained (Fig. 3c). Locally, the leucogabbros exhibit cumulate texture with plagioclase phenocrysts and small hornblende and quartz intercumulus. The rocks from the Camará pluton are composed of plagioclase (24.5-71.0 vol%), quartz (2.0-28.6 vol%), hornblende (1.0-43.0 vol%), and biotite (7.0-28.0 vol%), with minor microcline (0.7-4.3 vol%) and clinopyroxene (1.0-10.0 vol%). The accessory phases are titanite, epidote, apatite, allanite, zircon, and opaque minerals.

Microgranular mafic enclaves (MME), mafic clots, and metasedimentary xenoliths are common in Camará pluton. The MME show disaggregated rims in contact with a felsic host, indicating a disequilibrium reaction (Fig. 3d). Plagioclase phenocrysts within the MME suggest mechanical transfer from the felsic magma to the mafic magma (Fig. 3d). Even at the outcrop scale, the rocks show a gradation from gabbros to tonalites passing through intermediate compositions. All these features suggest hybridization between mafic and felsic magmas.

Lath-shaped plagioclase crystals display a preferred orientation aligned along the rock foliation (Fig. 4a), lenticular deformation twinning, and strong undulose extinction. Epidote, carbonate, and white mica are secondary phases related to the destabilization of plagioclase. Green hornblende is the main mafic mineral, which transforms into tremolite needles and fine-grained biotite along cleavages (Fig. 4b). Large clinopyroxene and amphibole crystals form subrounded aggregates resembling mafic clots (Fig. 4c). Reddish biotite often shows smooth kink bands and includes euhedral zircon and apatite (Fig. 4d). The presence of stubby (Fig. 4d) and acicular (Fig. 4e) apatite suggests two growth generations. Magmatic epidote containing allanite cores wrapped by biotite become progressively more common toward tonalitic rocks. In gabbros and diorites, polygonal aggregates of quartz occupy interstices between plagioclase prisms (Fig. 4f). Well-formed to anhedral garnet crystals (1.0-4.0 mm) developed parallel

(Dores pluton) or above the rock foliation (Camará pluton) indicate syn- and post-kinematic growth with respect to ductile deformation. Occasionally, prismatic green tourmaline up to 1.0 mm in size occurs associated with biotite in Camará pluton, suggesting some hydrothermal alteration.

4.1.2 Syn-collisional magmatism

This group comprehends small intrusions (4-10 km²) emplaced into garnet-biotite schists and phyllites from the Macururé Domain. The Pedra Furada, Angico, and Areias plutons are NNE-SSE trending tabular bodies outcropping in the surroundings and within the Nossa Senhora de Lourdes interference zone (Fig. 2). The Várzea Nova pluton occurs in the central-east area of the domain as a 5 km long E-W subrounded stock (Fig. 2).

These bodies are composed of pink- to gray-colored granodiorites and monzogranites, which fall in the field of crustal leucogranites from Lameyre and Bowden (1982) (Fig. 3a). These rocks are equigranular, leucocratic to hololeucocratic ($M' = 0.1-21.5$), and fine- to medium-grained (Fig. 3f). The orientation of micas, surmicaceous enclaves, and biotite schlieren define the foliation (Fig. 3g). Quartz-feldspathic pegmatite veins cross-cutting the granites are common in the Pedra Furada pluton (Fig. 3h), reflecting the interaction with autometasomatic fluids during the final stages of magmatic crystallization.

The leucocratic granitoids consists of plagioclase (24.6-37.4 vol%), quartz (11.2-38.0 vol%), microcline (5.6-31.9 vol%), biotite (0.6-12.0 vol%), and muscovite (0.4-15.8 vol%). The accessory phases include epidote, titanite, garnet, apatite, allanite, zircon, and opaque minerals. The microcline is perthitic and may display micrographic vermicular intergrowth of quartz. Plagioclase commonly exhibits lenticular deformational twinning and strong undulose extinction (Fig. 4f). Undulose extinction is also present in quartz and microcline, while green biotite and muscovite show deformation by kinking. Epidote has straight contact with biotite and reentrant with quartz and feldspars (Fig. 4g). Titanite crystals are brownish or colorless, euhedral to subhedral, and enclosed in plagioclase and biotite. Muscovite may occur as primary large subhedral crystals dispersed on the rock and as an alteration product of biotite. Other secondary transformations include chloritization of biotite and plagioclase alteration to carbonate and white mica.

The surmicaceous enclaves show similar composition to their host rocks (Fig. 4i), differing when the higher volume of biotite (ca. 40 vol%) and muscovite (ca. 20 vol%).

4.1.3 Late-collisional magmatism

The Santa Helena pluton (110 km²) occurs in the central part of the Macururé Domain and comprises two main petrographic facies (Fig. 3a). In the southern sector grayish biotite-bearing muscovite monzogranites dominate, with feldspar phenocrysts immersed in a fine-grained matrix. The monzogranites contain plagioclase (ca. 37 vol%), quartz (ca. 23 vol%), microcline (ca. 19 vol%), with abundant muscovite (ca. 9 vol%) and minor biotite (ca. 4 vol%). Dark-gray hornblende-bearing biotite granodiorites, medium-grained and equigranular outcrop in the northern sector (Fig. 4h). The paragenesis of the granodiorites consists of plagioclase (ca. 44 vol%), quartz (ca. 21 vol%), biotite (ca. 20 vol%), and microcline (ca. 8 vol%), with minor amounts of hornblende and clinopyroxene. Titanite, epidote, allanite, apatite, zircon, and opaque minerals are the accessory phases. These rocks are isotropic and display rare centimeter biotitic surmicaceous and mafic microgranular enclaves.

The Glória Norte pluton (45 km²) has a rounded shape and intrudes the metasedimentary rocks of the Macururé Domain along its central segment (Fig. 2). It is chiefly formed by porphyritic quartz monzodiorites, quartz monzonites, granodiorites, and monzogranites (Fig. 4i), containing plagioclase and microcline phenocrysts immersed in a fine-grained matrix. These rocks are gray-colored, leucocratic ($M' = 25.1-34.8$), and host three enclave types: mafic microgranular, lamprophyre, and cumulate (Lisboa et al., 2019). Locally, these rocks show a remarkable magmatic foliation indicated by the orientation of enclaves and feldspar phenocrysts. The essential mineralogy consists of plagioclase (25.1-34.2 vol%), microcline (14.9-25.4 vol%), and quartz (11.9-20.7 vol%). Biotite (9.6-16.3 vol%), hornblende (7.5-13.4 vol%), and clinopyroxene (0.1-2.7 vol%) are the main varietal minerals. The accessories are titanite, epidote, allanite, zircon, apatite, and opaque minerals.

Plagioclase shows concentric compositional zoning, with idiomorphic zones parallel to the crystal faces (Fig. 4j). Hornblende exhibits greenish-brown cores and green rims, suggesting some compositional zoning. Titanite is an abundant minor phase, occurring as large euhedral crystals, sometimes with simple and lamellar twinnings (Fig. 4k). Allanite inclusions are common in epidote, often showing a radial fracture pattern around the allanite crystal (Fig. 4l). Deformation evidence is provided by quartz, which displays a weak undulose extinction, as well as by the biotite showing rare kink bands. Secondary alteration is incipient, limited to the plagioclase transformation in epidote, carbonate, and white mica.

4.2 WHOLE-ROCK GEOCHEMISTRY

Because the petrographic investigations showed that the primary mineral assemblage was affected by secondary transformations (especially the samples from the Capela pluton), their chemical effects on the samples were evaluated before the petrogenetic interpretations. Firstly, the low values of LOI varying from 0.02 to 1.60 wt% suggest that the formation of hydrated secondary phases was small. In the ternary diagram FMW (Ohta and Arai, 2007), the studied rocks follow the trend of the unaltered igneous rocks, indicating that they have not undergone a substantial secondary alteration (except for the sample SOS-1264A; Supplementary Figure S3). These results, together with the consistent trends in variation diagrams and REE patterns without significant cerium anomalies ($Ce/Ce^* = 0.72-1.32$), demonstrate the relative immobility of most elements. Hence, despite evidence for secondary transformations, the relation between elements remained preserved in the rocks, and their chemical composition may be used to make petrogenetic inferences.

Early-collisional magmatism: rocks from the Camará pluton are the most primitive of the investigated samples. In the total alkalis versus silica diagram, their compositions spread from gabbroic diorite to granodiorite fields, with silica contents ranging between 50.95 and 66.74 wt% (Fig. 5a). Gabbros and diorites show higher sums of $Fe_2O_3^* + MgO$ (10.30-19.76 wt%) compared to the granodiorites (4.32-9.13 wt%). The magnesium number [$Mg\# = \text{molar } Mg^{2+}/(Mg^{2+} + Fe^{2+})$] ranges from 0.27 to 0.65. The alkalis sum ($Na_2O + K_2O = 3.86-7.49$ wt%) and K_2O/Na_2O ratios (0.61-1.19) vary considerably, increasing toward most evolved compositions. These rocks are metaluminous to weakly peraluminous, displaying A/CNK [molar $A_2O_3/(CaO + Na_2O + K_2O)$] index from 0.72 to 1.08 (Fig. 5b). One sample exhibited an anomalously high A/CNK ratio of 1.46 (SOS-630B).

Syn-collisional magmatism: the rocks from this group lie in the fields of quartz-monzonites and granites (Fig. 5a). The samples show a similar distribution of major elements, with uniform high-silica contents (68.31-74.46 wt%) and low to moderate Mg# (0.14-0.54). They are metaluminous to peraluminous, with A/CNK values between 0.96 and 1.20 (Fig. 5b). This group has the highest contents of $Na_2O + K_2O$ (6.62-10.25 wt%), with most K_2O/Na_2O ratios higher than unity (0.94-1.56).

Late-collisional magmatism: this group comprehends intermediate to acid rocks showing compositions of monzonite, quartz-monzonite, and granite (Fig. 5a). The silica contents vary from 60.77 to 70.47 wt%, along Mg# values between 0.40 and 0.57. All samples from this group are metaluminous ($A/CNK = 0.83-1.00$; Fig. 5b) and display high $Na_2O + K_2O$

varying between 7.09 and 9.08 wt%. The K_2O/Na_2O ratios are considerably higher in Glória Norte (1.22-1.53) than in Santa Helena (0.78-0.97) rocks.

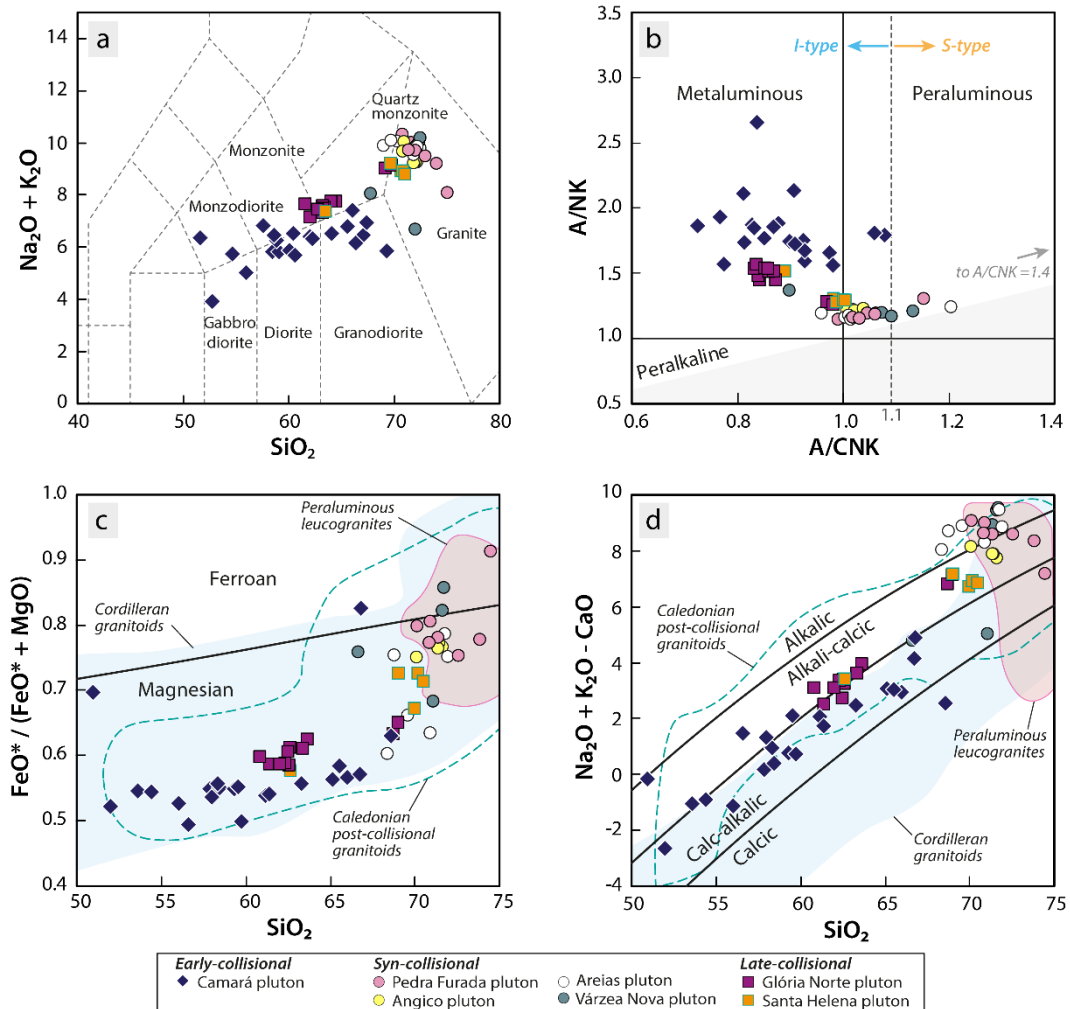


Figure II.5- Geochemical diagrams for major elements. (a) SiO_2 vs. $Na_2O + K_2O$ (Middlemost, 1994). (b) A/CNK [molar $Al_2O_3/(CaO + Na_2O + K_2O)$] vs. A/NK [molar $Al_2O_3/(Na_2O + K_2O)$] diagram (Shand, 1943), with the boundary of I- and S-type granites ($A/CNK = 1.1$) from Chappell and White (2001). (c) SiO_2 vs. $FeO^*/(FeO^* + MgO)$ and (d) SiO_2 vs. $(Na_2O + K_2O - CaO)$ from Frost et al. (2001), with the fields of Cordilleran granitoids, peraluminous leucogranites, and Caledonian granitoids.

Rocks of all plutons have bulk compositions consistent with those of magnesian granitoids, with a few higher- SiO_2 granites trespassing the ferroan granitoids field (Fig. 5c). When plotted in the modified alkali-lime index diagram, the samples lie within calc-alkalic and alkali-calcic fields, except the leucogranites which spread along calc-alkalic and alkali-calcic areas (Fig. 5d). In both diagrams, early- and late-collisional plutons have geochemical behavior akin to Cordilleran and Caledonian granitoids (Frost et al., 2001a). In contrast, the syn-collisional group overlaps with the area of peraluminous leucogranites.

In Harker diagrams, TiO_2 , MgO , Fe_2O_3^* , CaO , and P_2O_5 negatively correlate with SiO_2 (Fig. 6). Al_2O_3 , Na_2O , and K_2O show scatter patterns against SiO_2 but have an ascending trend toward more evolved compositions. In the SiO_2 vs. K_2O diagram with fields of Peccerillo and Taylor (1976), the studied rocks fall within the high-K calc-alkaline and shoshonite series. Regarding trace element concentrations, V, Cr, and Sr show negative correlations with silica, whereas Rb concentration increases with differentiation. The contents of Sr, Ba, and Zr decrease with increasing SiO_2 in the same plutonic unit. Contrastingly, the Camará rocks exhibit non-uniform near-flat trends for these incompatible elements.

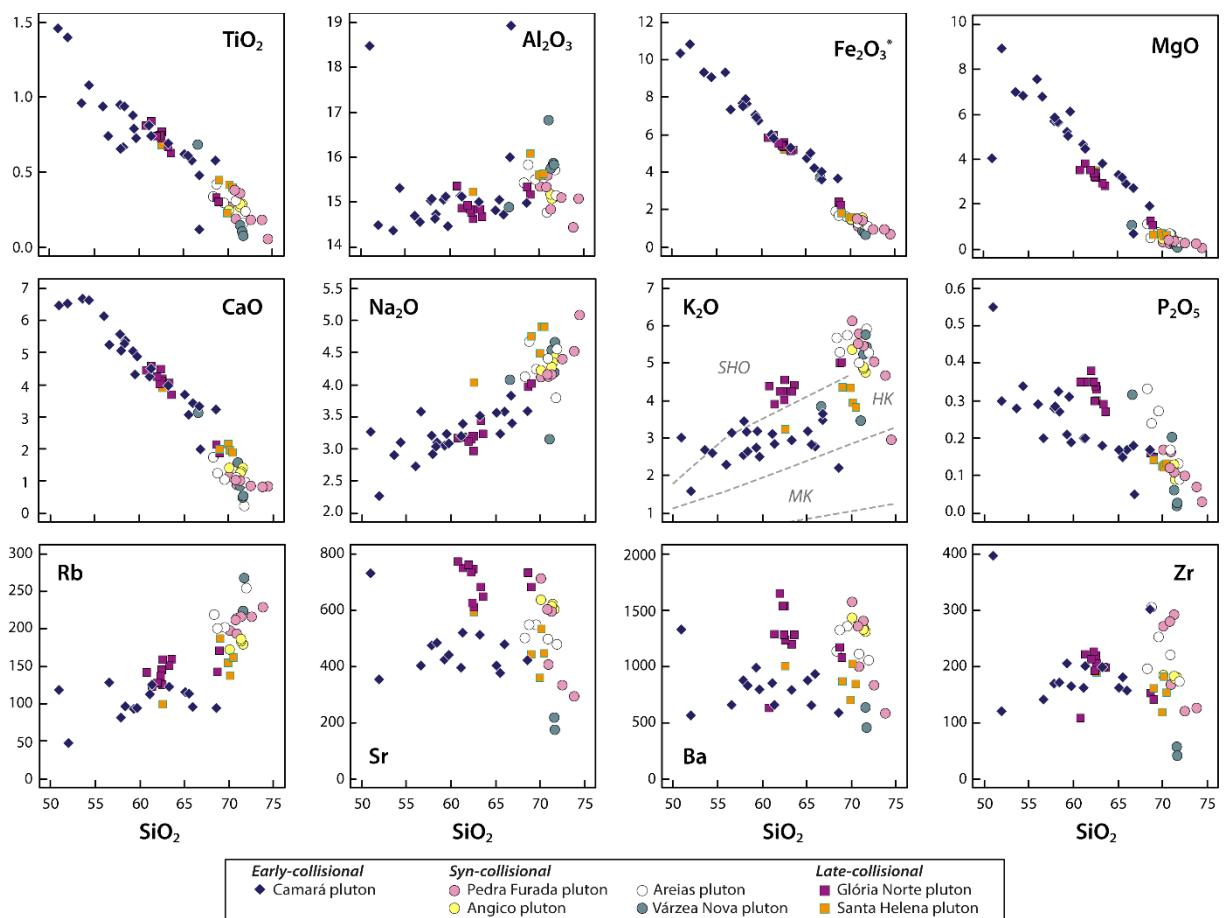


Figure II.6- Harker diagrams for major (wt%) and trace (ppm) elements of the plutonic rocks from the Macururé Domain. Fields of medium-K calc-alkaline (MK), high-K calc-alkaline (HK), and shoshonite (SHO) series, according to Peccerillo and Taylor (1976).

All studied rocks show an enrichment of light REE (LREE) compared to heavy REE (HREE) (Fig. 7). The REE contents in Camará rocks decrease from more primitive (ca. 420 ppm) to more evolved samples (ca. 130 ppm). Their patterns are almost flat to LREE-enriched, with $(\text{Ce}/\text{Yb})_{\text{CN}} = 3\text{-}43$, where CN refers to chondrite-normalized values. These samples show a moderate to slight negative Eu anomaly ($\text{Eu}/\text{Eu}^* = 0.6\text{-}0.9$).

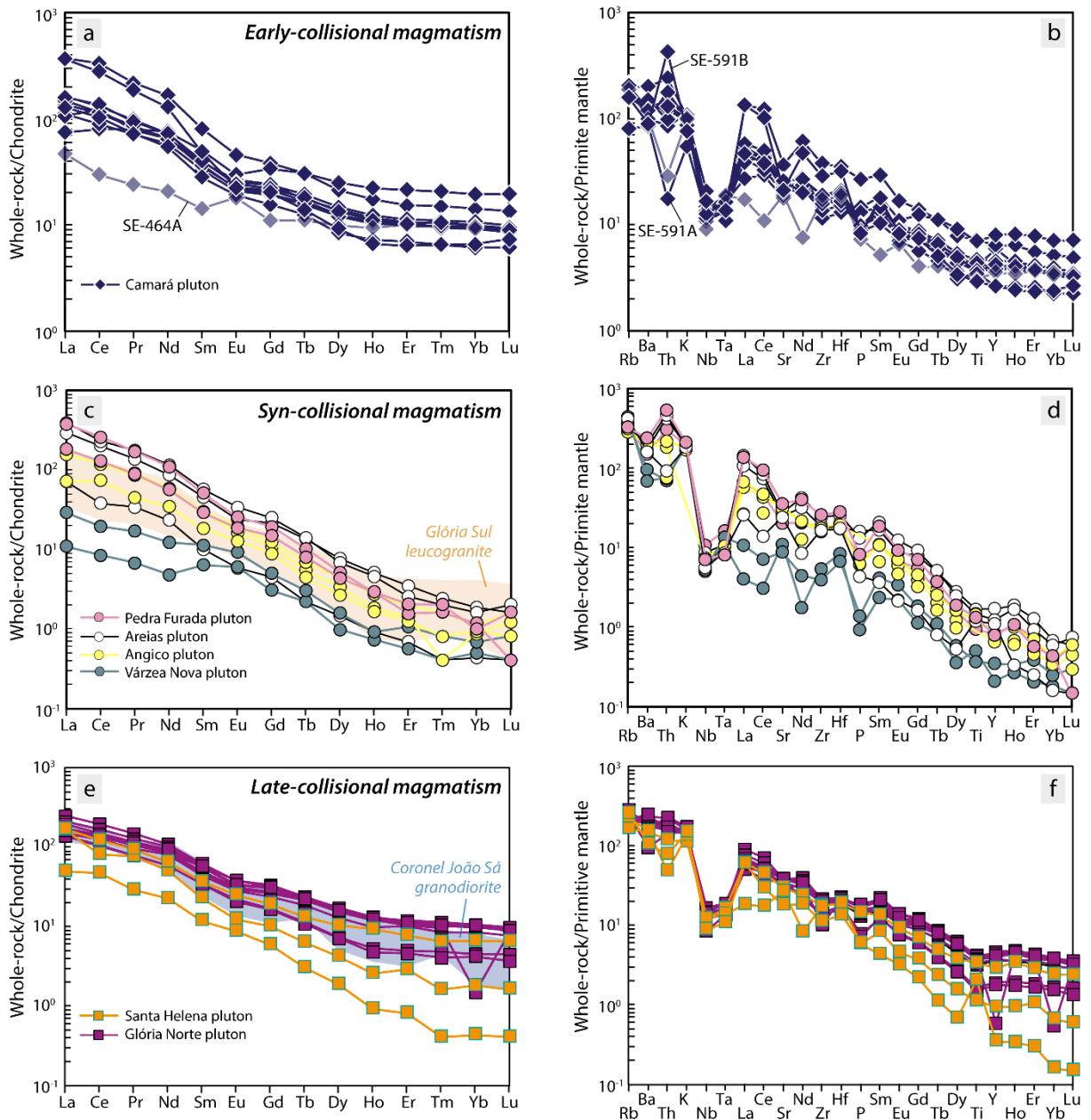


Figure II.7- REE (a, c, and e) and multielement (b, d, and f) patterns for plutonic rocks from the Macururé Domain, normalized to chondrite and primitive mantle (McDonough and Sun, 1995), respectively. The data for the Glória Sul leucogranite and Coronel João Sá granodiorite are from Conceição (2019) and Long et al. (2005). The outlier SE-464A indicated in (a) and (b) is a late cumulate of plagioclase.

The Pedra Furada, Angico, and Areias leucogranite intrusions compose a cohesive group regarding trace elements. They have similar highly-fractionated patterns with $(Ce/Yb)_{CN} = 79-220$, variable REE sums (57.4-329.9 ppm), and weak negative to non-existent Eu anomaly ($Eu/Eu^* = 0.8-1.0$). The samples from Várzea Nova pluton differ from the others by the lowest REE total (13.1-30.2 ppm), positive Eu anomalies ($Eu/Eu^* = 1.2-1.4$), and moderate $(Ce/Yb)_{CN} = 17-27$.

The late-collisional granitoids show a decrease in REE contents with differentiation (Glória Norte = 268.8-144.5 ppm, Santa Helena = 170.3-58.1 ppm). These patterns are characterized by high LREE/HREE ratios, with $(\text{Ce}/\text{Yb})_{\text{CN}} = 13\text{-}109$ and lack or weak negative Eu anomalies ($\text{Eu}/\text{Eu}^* = 0.8\text{-}1.0$).

Figure 7 shows the incompatible trace element concentrations normalized to the primitive mantle (McDonough and Sun, 1995). The patterns depicted by all samples share similar features: enrichment of large ion lithophile elements (LILE) relative to high field strength elements (HFSE) and HREE, deep troughs at Nb-Ta, and moderate negative anomaly in Ti. The Camará pluton rocks differ from the other syn- and late-collisional plutons by the greater concentration of less incompatible elements. Negative anomalies in Sr and P are well-defined for most rocks.

Zirconium saturation temperatures were calculated based on the calibration of Watson and Harrison (1983) for samples with $M \leq 1.9$ [$M = \text{cationic} (\text{Na} + \text{K} + 2\text{Ca})/(\text{Al} \times \text{Si})$]. The higher temperatures were obtained for the samples from Camará, Glória Norte, and Santa Helena plutons, ranging from 772 to 871 °C. Leucogranites yielded a wide temperature range from 673 to 849 °C.

4.3 U-Pb DATING AND Lu-Hf ANALYSES

4.3.1 Early-collisional Camará pluton (sample SOS-626)

A population of 39 zircon crystals was analyzed for U-Pb dating, totaling 45 spots. The zircon crystals are pale pink colored and show sizes between 189 and 397 μm . They exhibit euhedral to subhedral shapes and bipyramidal habit, with length/width ratios of 1:1 to 4:1. Opaque mineral inclusions are rare. All crystals show oscillatory zoning under CL and Th/U ratios from 0.5 to 0.9 (Fig. 8). A data set of 34 concordant analytical points provided a Concordia age of 643 ± 2 Ma (MSWD = 0.91; Fig. 9a).

Twenty zircon crystals analyzed for Lu-Hf show concordance between 98 and 100%. The $^{176}\text{Hf}/^{177}\text{Hf}_{(643 \text{ Ma})}$ ratios vary from 0.282202 to 0.282254, resulting in subchondritic values of $\epsilon\text{Hf}_{(643 \text{ Ma})}$ between -6.0 and -4.1, with a weighted average value of -5.8 ± 0.2 (95% conf., MSWD = 1.4). These crystals yield homogenous Orosirian Hf- T_{DM}^{C} model ages ranging from 1.83 to 1.94 Ga (Fig. 10).

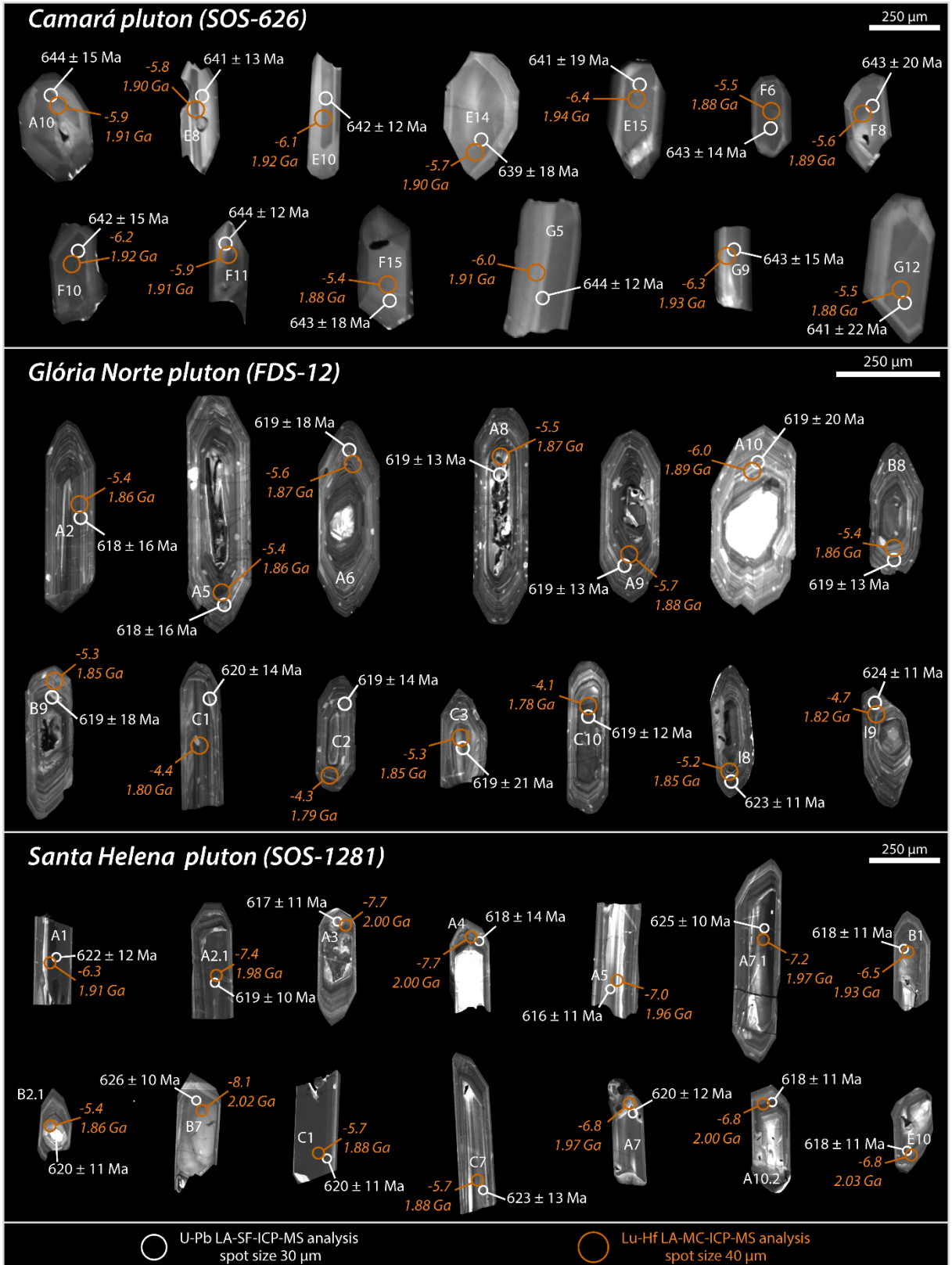


Figure II.8- CL images of representative zircon crystals from the studied plutons, with their corresponding $^{206}\text{Pb}/^{238}\text{U}$ dates in Ma, $\epsilon\text{Hf}(t)$, and $\text{Hf-T}_{\text{DM}}^{\text{C}}$.

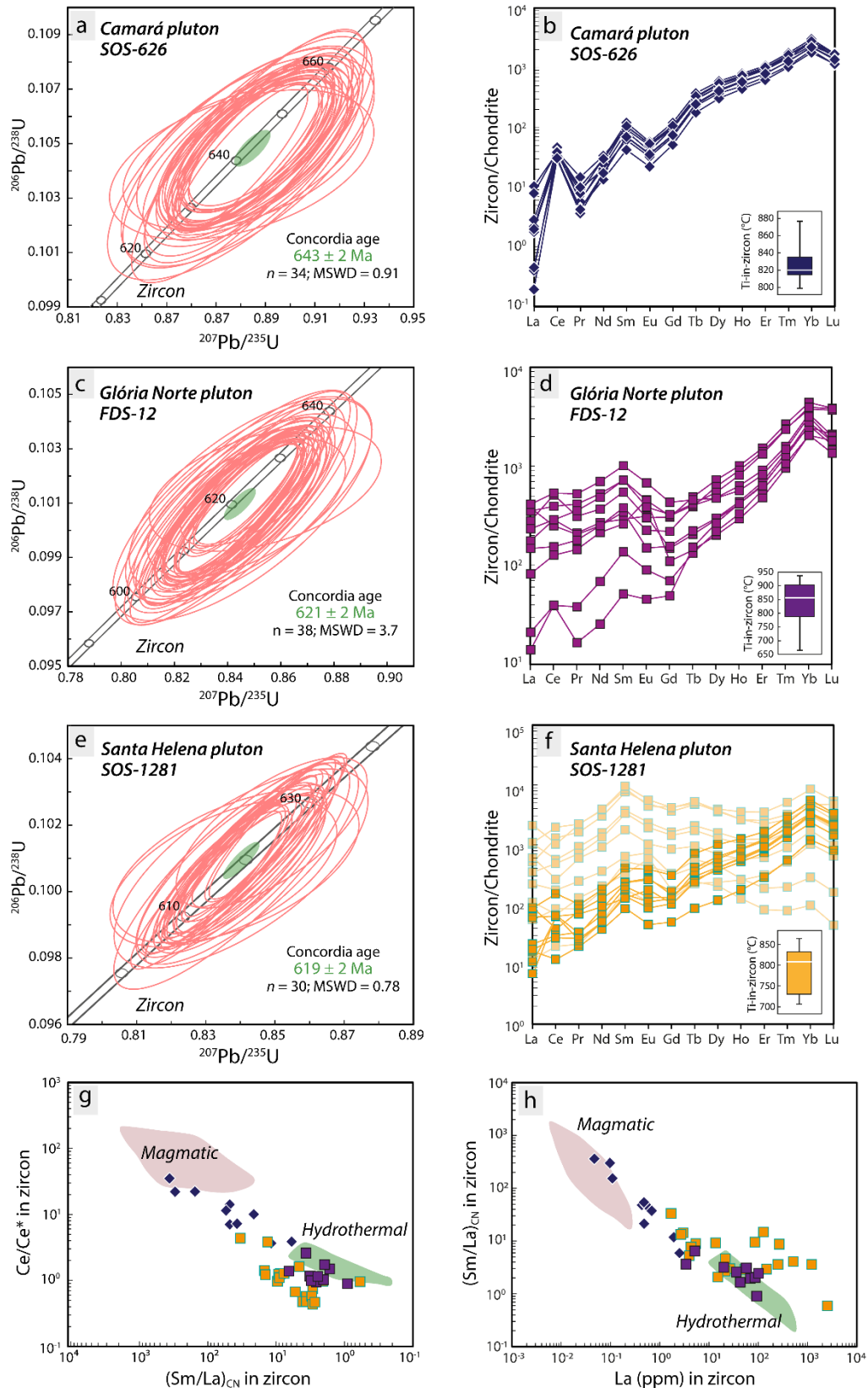


Figure II.9- Concordia diagrams, chondrite-normalized REE zircon patterns, and Ti-in-zircon thermometry for the plutons (a, b) Camará, (c, d) Glória Norte, and (e, f) Santa Helena. Discrimination diagrams for magmatic and hydrothermal zircon, according to Hoskin (2005). (g) $(\text{Sm}/\text{La})_{\text{CN}}$ vs. Ce/Ce^* (where $\text{Ce}/\text{Ce}^* = \text{Ce}_{\text{CN}}/(\text{La}_{\text{CN}} + \text{Pr}_{\text{CN}})^{1/2}$) and (h) La vs. $(\text{Sm}/\text{La})_{\text{CN}}$. The “CN” subscript indicates chondrite-normalized (McDonough and Sun, 1995).

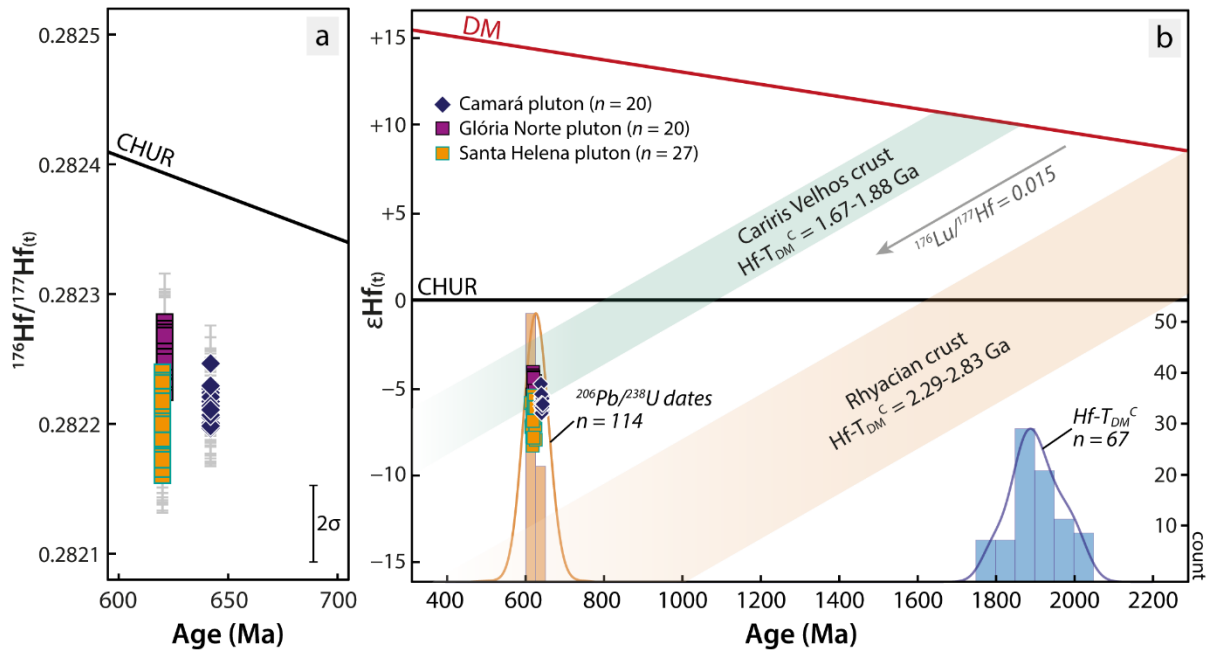


Figure II.10- Hf isotope signature for the Camará, Santa Helena, and Glória Norte plutons. (a) $^{176}\text{Hf}/^{177}\text{Hf}(t)$ vs. age (Ma). (b) $\epsilon\text{Hf}(t)$ vs. age (Ma). Kernel density estimation (KDE) plots for zircon crystallization dates ($^{206}\text{Pb}/^{238}\text{U}$) and $\text{Hf-T}_{\text{DM}}^{\text{C}}$ model ages from studied samples. Calculation of evolution trends assuming a $^{176}\text{Lu}/^{177}\text{Hf}$ ratio of 0.015 for the average continental crust (Griffin et al., 2002). Lu-Hf isotope data for Cariris Velhos and Rhyacian crusts are from Caxito et al. (2020), Costa et al. (2018), and Lima et al. (2021).

4.3.2 Late-collisional Glória Norte pluton (sample FDS-12)

A total of 38 crystals were analyzed for U-Pb, totaling 45 spots. The zircon population is composed of colorless and limpid crystals, with 210-575 μm in size. These crystals are euhedral, with elongated shapes (length/width = 2:1 to 4:1) and pyramidal endings (Fig. 8). Most zircons show well-defined oscillatory zoning, mainly at the borders, but some cores display complex zoning patterns with chaotic (crystals A5, A8, B9) and convolute structures (crystal I8). Subrounded unzoned bright nuclei also can be observed (crystals A6, A10). All chosen domains for analysis U-Pb display oscillatory zoning and Th/U ratios between 0.2 and 1.4. A cluster of 38 analytical points produced a Concordia age of $621 \pm 2\text{ Ma}$ (MSWD = 3.7; Fig. 9c).

Lu-Hf analyses were performed in 20 sub-concordant zircon crystals (concordance = 97-99%). Calculated $^{176}\text{Hf}/^{177}\text{Hf}_{(621\text{ Ma})}$ ratios range from 0.282230 to 0.282286, resulting in negative $\epsilon\text{Hf}_{(621\text{ Ma})}$ values between -6.0 and -4.1, with a weighted average value of -5.1 ± 0.3 (95% conf., MSWD = 5.1). These crystals provided Statherian-Orosirian $\text{Hf-T}_{\text{DM}}^{\text{C}}$ model ages ranging from 1.77 to 1.89 Ga (Fig. 10).

4.3.3 Late-collisional Santa Helena pluton (sample SOS-1281)

The analyzed zircon population is composed of 33 crystals, encompassing 35 spots. The selected crystals are pale pink colored to colorless, slightly translucent, and have sizes between 184 and 740 μm . They are euhedral to subhedral and show elongated or equant shapes (length/width = 1:1 to 4:1). Most crystals exhibit oscillatory zoning, but chaotically zoned (crystal A3) domains are also present, with convolute structures blurring the magmatic zoning (crystals A7, A10) (Fig. 8). The Th/U relation of the analyzed zircons ranges from 0.1 to 1.5. A set of 30 analytical points provided a Concordia age of 620 ± 2 Ma (MSWD = 0.78; Fig. 9e).

Lu-Hf isotope ratios were measured in 27 zircon crystals, whose concordance degrees vary between 98 and 101%. The $^{176}\text{Hf}/^{177}\text{Hf}_{(620\text{ Ma})}$ ratios are subchondritic and oscillate between 0.282168 and 0.282253, corresponding to $\epsilon\text{Hf}_{(620\text{ Ma})}$ values from -8.3 to -5.4, with a weighted mean of -7.0 ± 0.3 (95% conf., MSWD = 7.8). The Hf- T_{DM}^{C} model ages are Orosirian and range from 1.83 to 2.03 Ga (Fig. 10).

4.4 ZIRCON TRACE ELEMENT COMPOSITION

The zircon crystals from Camará pluton are compositionally homogenous regarding U (95.7-164.3 ppm, average 129.7 ± 24.8 ppm) and Th (79.9-174.0 ppm, average 129.0 ± 30.9 ppm), showing Th/U ratios between 0.82 and 1.12 (average 0.99 ± 0.10). The REE sums vary from 592-1036 ppm, with an average of 834 ± 132 ppm. Chondrite-normalized REE patterns increase steeply from La (LREE = 47 ± 9 ppm) to Lu (HREE = 786 ± 125 ppm), with Sm/La_{CN} ratios between 6 and 362 (Fig. 9b). Moderate positive Ce anomalies ($\text{Ce}/\text{Ce}^* = 3.7\text{-}35.1$) and negative Eu anomalies ($\text{Eu}/\text{Eu}^* = 0.44\text{-}0.52$) are also observed, which is typical of magmatic unaltered igneous zircons (Hoskin and Schaltegger, 2003). The Ti concentration in these grains varies from 31 to 57 ppm, providing temperatures between 799 and 877 $^{\circ}\text{C}$ (median of 820 $^{\circ}\text{C}$, $n = 9$). One analysis has an anomalously high Ti concentration of 142 ppm and was excluded from consideration.

Zircon crystals from Glória Norte monzonite are characterized by an unusual, almost flat LREE pattern ($\text{Sm}/\text{La}_{\text{CN}} = 1\text{-}6$), lacking the typical positive anomaly in Ce ($\text{Ce}/\text{Ce}^* = 0.9\text{-}2.6$) (Fig. 9d). A weak negative to strong positive Eu anomaly (0.80-2.72) is discernible. From Gd to Lu, the ascending slope of REE patterns is similar to those observed in HREE-enriched magmatic zircon (Hoskin and Schaltegger, 2003). They show high U (319.9-588.2 ppm, average 450.2 ± 80.2 ppm) and Th (126.5-512.5 ppm, average 281.6 ± 119.0 ppm) contents, resulting in Th/U ratios ranging from 0.29 to 1.07 (average 0.62 ± 0.22). The Ti contents in

these zircons vary between 7 and 92 ppm, recording a wide range of crystallization temperatures from 665 to 936 °C (median of 857 °C, $n = 10$).

Zircon crystals from Santa Helena granodiorite show a wide compositional variation concerning U (158.7-644.2 ppm, average 326.9 ± 132.3 ppm), Th (49.0-585.2; average 197.5 ± 150.3), and Th/U ratios (0.12-1.50, average 0.64 ± 0.40). Two zircon populations are distinguished based on REE composition. Most crystals contain extremely high LREE concentrations, about 100 times compared to a typical magmatic zircon (Hoskin and Schaltegger, 2003). This behavior results in flatter chondrite-normalized REE patterns (Fig. 9f). In contrast, the second population encompasses those HREE-enriched crystals ($\text{Lu/La}_{\text{CN}} = 16-446$), with discrete fractionating between LREE ($\text{Sm/La}_{\text{CN}} = 2-33$) and varying Ce ($\text{Ce/Ce}^* = 0.5-3.8$) and Eu ($\text{Eu/Eu}^* = 0.7-1.5$) anomalies. Although there is a significant difference concerning trace element composition, there is no distinction between them morphologically. The concentration of Ti varies from 11 to 51 ppm, which results in Ti-in-zircon crystallization temperatures between 706 and 864 °C (median of 808 °C, $n = 12$).

4.5 TITANITE U-Pb AGES

4.5.1 Early-collisional Dores pluton (sample SOS-910)

Titanite from this sample occurs as dark to pale brown euhedral grains, with lengths ranging from 315 to 550 μm . Most crystals show oscillatory or sectorial zoning under BSE images (Fig. 11). Inclusions of tiny apatite and zircon are frequent. Analyzed grains have elevated contents of U (171.6-310.8 ppm, 217.8 ± 36.3 ppm on average) and low Th (12.3-29.8 ppm, 18.0 ± 4.6 ppm on average), resulting in Th/U ratios of around 0.1 (0.08 ± 0.01 on average). The proportion of common ^{206}Pb is low, with most values of f_{206} less than 1.5%. Thus, the model of Stacey and Kramers (1975) is appropriate for correcting isotope data. When plotted in a Tera-Wasserbug diagram, the uncorrected analytical points describe a discordant array with an intercept on Concordia at 610 ± 36 Ma ($n = 21$, MSWD = 1.6) and an initial $^{207}\text{Pb}/^{206}\text{Pb} = 1.05$ (Fig. 12a). A weighted average of $^{206}\text{Pb}/^{238}\text{U}$ individual dates corrected for common lead gave an age of 628 ± 5 Ma ($n = 21$, MSWD = 1.4), identical to that obtained from uncorrected data (629 ± 5 Ma; $n = 21$, MSWD = 1.4).

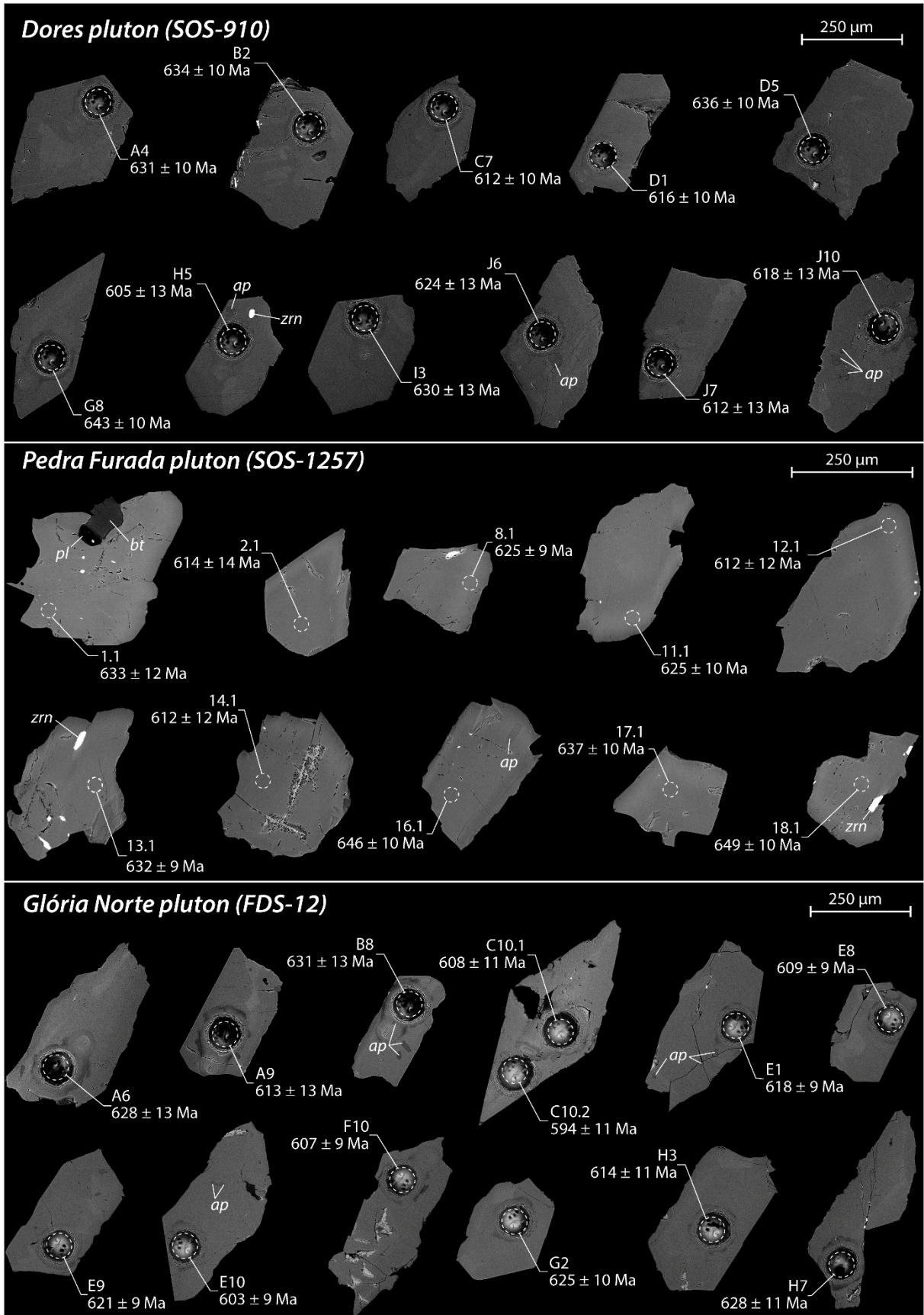


Figure II.11- BSE images of representative titanite crystals from the Dores, Pedra Furada, and Glória Norte plutons, containing inclusions of typical magmatic minerals. $^{206}\text{Pb}/^{238}\text{U}$ dates corrected for common Pb.

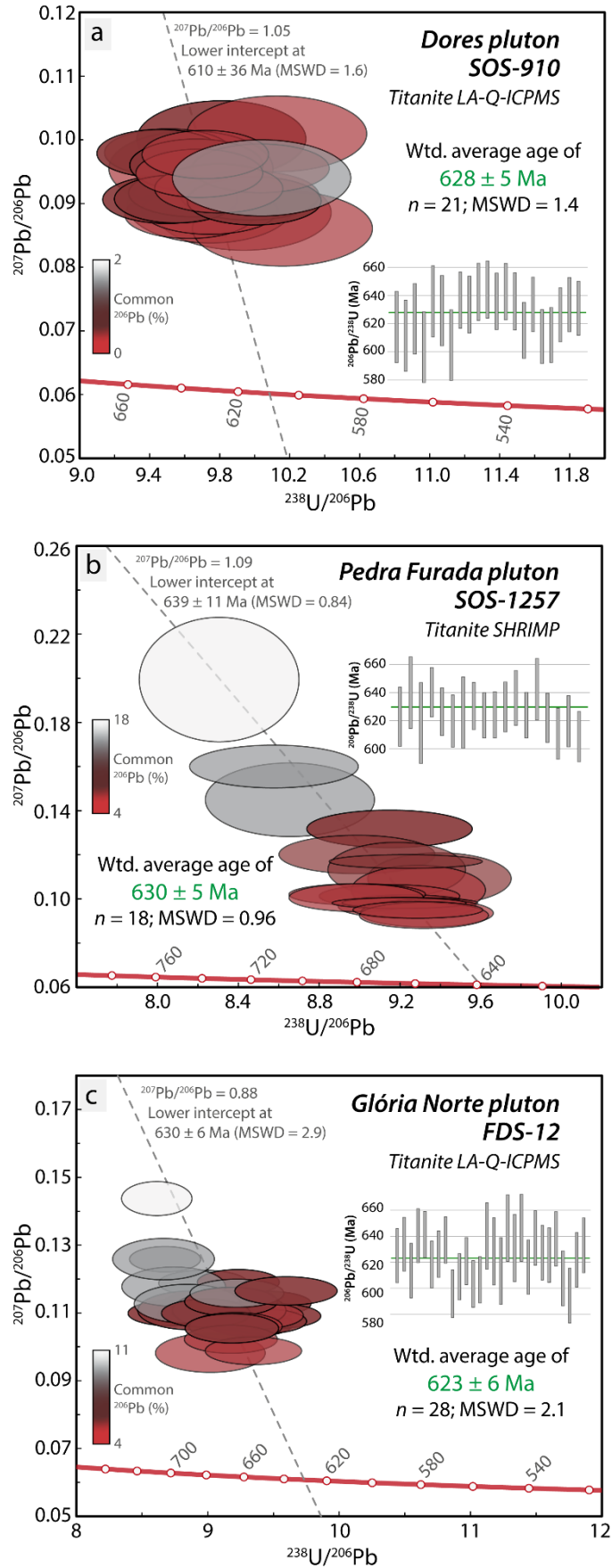


Figure II.12- Tera-Wasserburg plot for titanite crystals from the (a) Dores, (b) Pedra Furada, and (c) Glória Norte plutons. Error ellipses shaded according to the percentage of common ^{206}Pb .

4.5.2 Syn-colisional Pedra Furada pluton (sample SOS-1257)

Two titanite populations were identified based on their textures under transmitted light and BSE images. The first population encompasses limpid and dark-brown colored titanites, interpreted as unaltered magmatic crystals. These crystals are compositionally homogeneous in BSE images, showing a discrete or no concentric zoning. Moreover, they may contain inclusions of magmatic minerals, such as zircon, apatite, biotite, and plagioclase. The second population comprises translucent milky-yellow and pale-brown colored titanites containing surface corrosion pits. They show a “spongy” texture in BSE images, giving the crystals a porous appearance (Supplementary Figure S4). The main secondary minerals formed from titanite replacement are Fe-Ti oxides and Ca-carbonates. Patches of fresh titanite occur preserved within altered porous zones. All these features point to altered magmatic titanite.

Eighteen titanite crystals belonging to the unaltered magmatic population were analyzed for U-Pb dating (Fig. 11). The selected crystals are euhedral to subhedral, with some inclusions of zircon and rare fractures. They show variable chemical composition regarding U (106.3-335.1 ppm, 228.9 ± 68.5 ppm on average), Th (102.7-458.1 ppm, 192.6 ± 82.4 ppm on average), and Th/U (0.63-1.41, 0.87 ± 0.21 on average). The abundances of common ^{206}Pb vary from 4.2 to 17.3%. Most analyzes are concordant or near concordant (generally less than 10% of discordance). In the Tera-Wasserburg diagram with common Pb-uncorrected ratios, the analytical points define a linear array with an inferior intercept at 639 ± 11 Ma (MSWD = 0.84) and a y-intercept of initial $^{207}\text{Pb}/^{206}\text{Pb}$ of 1.09 (Fig. 12b). The ^{204}Pb -corrected $^{206}\text{Pb}/^{238}\text{U}$ apparent ages vary between 612 and 649 Ma. A $^{206}\text{Pb}/^{238}\text{U}$ weighted average age of 631 ± 6 Ma ($n = 13$, MSWD = 1.19) can be calculated when filtering those crystals with a common ^{206}Pb and discordance degree less or equal to 10%. This result is identical to the $^{206}\text{Pb}/^{238}\text{U}$ weighted average age of 630 ± 5 Ma ($n = 18$, MSWD = 0.93) obtained when considering the entire dataset. Because the two ages overlap within analytical uncertainty, we interpreted the latter as the most conservative age estimate due to the lower error and MSWD.

4.5.3 Late-collisional Glória Norte pluton (sample FDS-12)

Titanite is dark brown colored, euhedral to subhedral, and dominated by crystals of 330-630 μm length. Uranium and thorium contents vary between 57.5-163.7 ppm (99.6 ± 26.4 ppm on average) and 146.3-551.0 ppm (294.2 ± 100.5 ppm on average), respectively. The Th/U ratios range from 1.18 to 3.99, with an average value of 2.99 ± 0.64 . Dated titanite crystals show fainty concentric zoning and apatite inclusions (Fig. 11). Relatively low abundances of

common ^{206}Pb characterize these crystals, showing f_{206} values between 4.5 and 10.3%, except for an outlier with 14.0%. In a Tera-Wasserburg plot, uncorrected U-Pb results do not display enough spread to define a precise free regression. Anchored regression to $^{207}\text{Pb}/^{206}\text{Pb}_{(620\text{ Ma})} = 0.88$ (Stacey and Kramers, 1975) yields a lower intercept of 630 ± 6 Ma ($n = 28$, MSWD = 2.9). Common lead-corrected $^{206}\text{Pb}/^{238}\text{U}$ dates vary from 595 to 646 Ma, with a weighted average age of 623 ± 6 Ma ($n = 28$, MSWD = 2.1; Fig. 12c).

5 DISCUSSION

5.1 A REAPPRAISAL OF THE AGE OF THE MAGMATIC EPISODES

The U-Pb data in this study define a new geochronological framework for SOS and improve the age ranges of the magmatic episodes during the Brasiliano Orogeny. Zircon dating was conducted in three samples whose grains show oscillatory zoning and Th/U ratios from 0.1 to 1.5, consistent with a magmatic origin (Rubatto, 2017). The values of MSWD for the Camará and Santa Helena plutons agree with those recommended by Spencer et al. (2016) for the considered dataset at 2σ uncertainty. Conversely, the Glória Norte data show overdispersion indicated by an MSWD = 3.7 ($n = 38$), implying a geological source of scattering. Some crystals from Santa Helena and Glória Norte samples show a disruption of concentric oscillatory zoning (Fig. 8). Because these zones show the same age as the preserved domains, they probably reflect late-magmatic modifications related to aqueous fluids during the final stages of magmatic crystallization (Corfu, 2003; and references therein). In the discriminant plots for magmatic and hydrothermal zircon, analyzed crystals define a trend from magmatic to the hydrothermal field (Fig. 9g and 9h), corroborating the influence of autometasomatic fluids (Hoskin and Schaltegger, 2003; Hoskin, 2005). Similarly, the preservation of internal zoning and inclusions typical of igneous minerals supports that titanite grains grew in a magmatic environment (Frost et al., 2001b). Hence, we infer that U-Pb isotope data on zircon and titanite record the crystallization ages of the Camará, Dores, Pedra Furada, Glória Norte, and Santa Helena plutons.

The U-Pb ages obtained in this work are compared with those available for Brasiliano plutonic rocks from the Poço Redondo and Canindé domains (Fig. 13a). The well-documented ages for magmatism in the SOS extended from 636 to 603 Ma. Our new U-Pb results, with the reassessment of some of the available ages for the area, allow us to constrain the Brasiliano magmatism in the SOS between 643 and 603 Ma during three transitional stages:

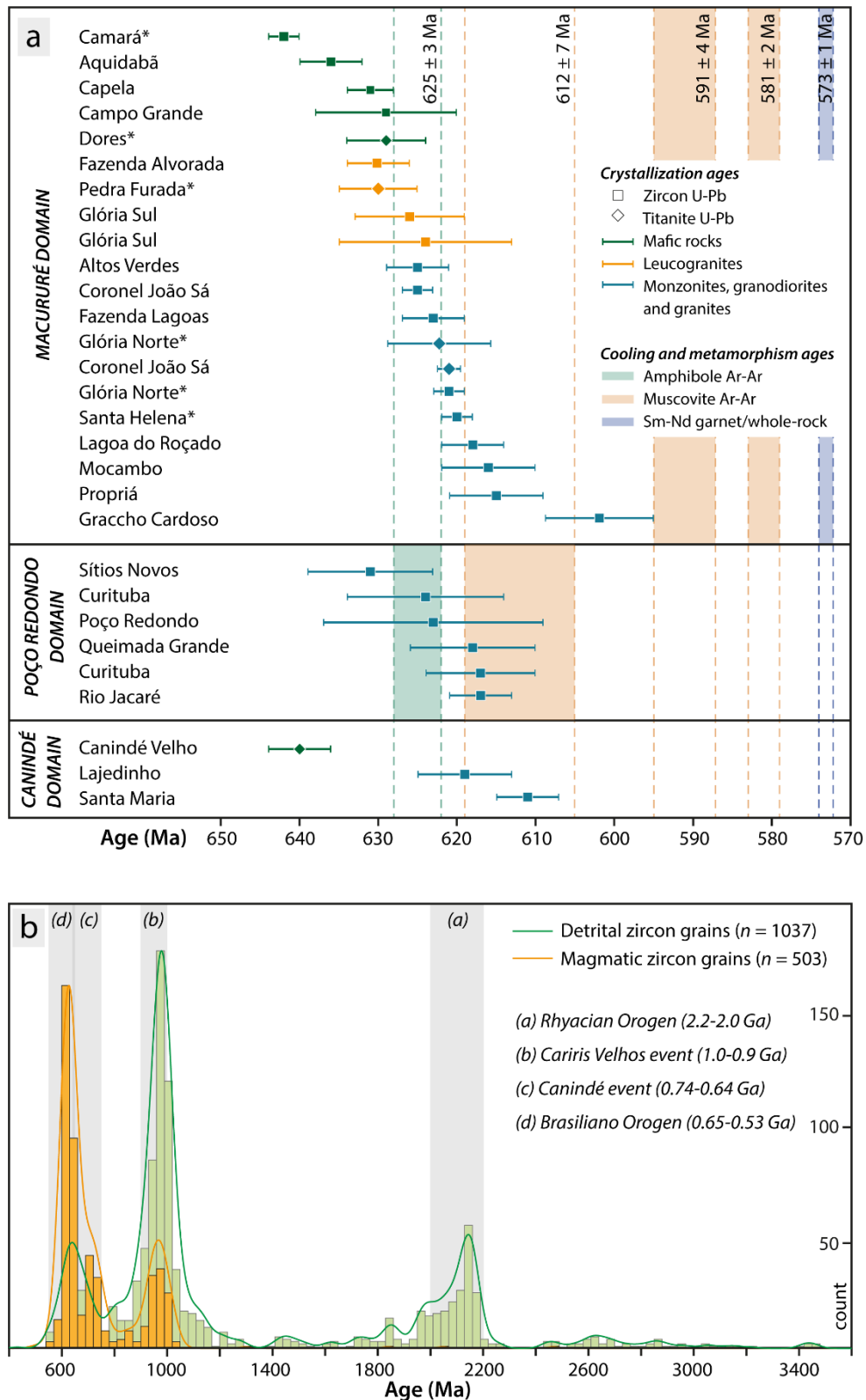


Figure II.13- (a) Summary of geochronological data for the SOS, including U-Pb data obtained in this work (denoted by the asterisk). References for crystallization age are in Table 1. Cooling and metamorphic ages are from Oliveira et al. (2010). (b) KDE of compiled zircon data for igneous and supracrustal rocks in the SOS. Detrital zircon data are from Lima et al. (2018), Neves et al. (2019), Oliveira et al. (2015c), Passos et al. (2022) and Van Schmus et al. (2011). Magmatic zircon data from references in Table 1. U-Pb data filtered by discordance ($\leq 10\%$ for detrital and $\leq 5\%$ for magmatic zircon) and $\text{Th}/\text{U} > 0.1$. According to Spencer et al. (2016), the $^{206}\text{Pb}/^{238}\text{U}$ and $^{207}\text{Pb}/^{206}\text{Pb}$ ages were used when < 1500 Ma and > 1500 Ma, respectively.

5.1.1 Stage I: 643-628 Ma

The ages of about 636-629 Ma were obtained for the Macururé Mafic Suite, encompassing a series of small basic-intermediate stocks that have experienced regional deformation (Pereira et al., 2020). The Camará pluton belongs to this rock association and had been dated before by Bueno et al. (2009), which obtained a lower intercept age of 628 ± 12 Ma. The newly acquired U-Pb zircon age for this pluton allows us to establish that its emplacement occurred at 643 ± 2 Ma, around 15 Ma earlier than previously proposed (Fig. 13a). The new U-Pb titanite age of 628 ± 5 Ma obtained for the diorite of the Dores pluton defines the lower limit for emplacement of this magmatic group. Together with the crystallization ages of the Aquidabã (636 ± 4 Ma), Capela (631 ± 3 Ma), and Campo Grande (629 ± 9 Ma) plutons from the Macururé Mafic Suite, these results reinforce that the mantle contribution was prevalent during the early magmatic stages of Brasiliano Orogeny in the SOS.

The Sítios Novos granite (631 ± 4 Ma) and Canindé Velho diorite (640 ± 4 Ma) also record this interval in the Poço Redondo and Canindé domains, respectively (Oliveira et al., 2015a; Santos, 2016). Silva Filho et al. (2016) obtained a U-Pb age of 632 ± 5 Ma for the early-to syn-collisional Serra do Catu batholith, located at the interface between the SOS and PEAL, indicating that this period was broadly contemporaneous across adjacent domains.

5.1.2 Stage II: 630-624 Ma

The titanite age of 630 ± 5 Ma obtained for the leucogranite of the Pedra Furada pluton coincides with the age range determined on zircon for the Glória Sul leucogranite (627-624 Ma; Conceição, 2019). These findings indicate that leucogranite emplacement was coeval with the latest manifestations of the mafic magmatism in the Macururé Domain, overlapping with the crystallization ages of the Campo Grande and Dores plutons (Fig. 13a).

Previous TIMS analyses on titanite multigrain fractions yielded ages of 571 ± 9 Ma and 584 ± 10 Ma for the Pedra Furada and Angico plutons, respectively (Bueno et al., 2009). These authors concluded that the segregation of small volumes of peraluminous melts at 590-570 Ma was associated with the SFC-PEAL collision. Later, Ganade de Araujo et al. (2013) proposed that the tectonic evolution of the Borborema Province throughout the late Neoproterozoic resulted from two subsequent collisions: the first one would involve the Parnaíba Block and the basement of the Borborema Province (620-610 Ma), whereas the second one was the consequence of the SFC-PEAL convergence along the SOS (590-580 Ma). However, the titanite grains dated by Bueno et al. (2009) are discordant or reversely discordant, showing

heterogeneous compositions (U, Th, Pb, Th/U) and very high common Pb contents ($^{206}\text{Pb}/^{204}\text{Pb} < 80$). Because of the reactive nature and wide stability range, ages determined in titanite can reflect a variety of processes, including magmatic crystallization, solid-state growth, hydrothermal alteration, or regional cooling (Frost et al., 2001b; Kohn, 2017). Thus, obtaining a representative age by dissolution methods becomes challenging without textural control. A careful textural study has demonstrated that Pedra Furada titanite records late-magmatic transformations, resulting in the formation of secondary oxides and carbonates (Supplementary Figure S4). Considering the textural complexity of the Pedra Furada titanite, we envisage that such younger ages could represent a mixture of igneous and altered domains resulting in mixed geologically meaningless ages. However, in an alternative scenario, the interval 570-590 Ma can reflect a regional resetting metamorphic event in SOS, as discussed below.

Oliveira et al. (2010) determined an Ar-Ar age of 625 ± 3 Ma on amphiboles from a metabasalt of the Marancó Domain. This age indicates when the orogen reached metamorphic conditions consistent with lower amphibolite facies (hornblende blocking temperature 530 ± 30 Ma; Rollinson, 1993), probably recording the collision onset in the region.

5.1.3 Stage III: 625-603 Ma

The Glória Norte (621 ± 2 Ma) and Santa Helena (620 ± 2 Ma) plutons were intruded synchronously with other late-collisional intrusions in the Macururé Domain (Long et al., 2005; Silva, 2014; Fernandes et al., 2020; Oliveira, 2020; Sousa, 2020; Lima, 2021) (Fig. 13a). These bodies generally display subrounded shapes, preserved igneous fabric, and incipient or no evidence of solid-state deformation (except those plutons emplaced along shear zones).

The Glória Norte monzonite was previously dated by Lisboa et al. (2019), which determined the zircon U-Pb SHRIMP Concordia age of 588 ± 5 Ma. The $^{206}\text{Pb}/^{238}\text{U}$ dates in their dataset show a large dispersion from 670 to 565 Ma. These authors interpreted the younger ages as a Pb loss event, while the older ones would reflect xenocryst grains sequestered during magma ascension. Nevertheless, no detrital zircon younger than 850 Ma is recorded in the supracrustal sequence of the Macururé Domain (Van Schmus et al., 2011; Oliveira et al., 2015b; Neves et al., 2019). Moreover, the high Ti-in-zircon and Zr saturation temperatures preclude a xenocryst origin or inheritance from the magma source (Watson and Harrison, 1983; Miller et al., 2003). As discussed above, the zircon crystals of the Glória Norte pluton archive late-magmatic transformations evidenced by textural aspects under CL images, anomalously LREE-rich patterns, and high MSWD values. So, we argue that the zircon age of 621 ± 2 Ma is a

reasonable estimation for the emplacement of the Glória Norte magmas, which is identical within error to those obtained in titanite from the same sample (623 ± 6 Ma).

Several granitoid intruding the Poço Redondo and Canindé domains show zircon U-Pb crystallization ages covering this age range, namely: Queimada Grande (618 ± 4 Ma), Curitiba (617 ± 7 Ma), Rio Jacaré (617 ± 4 Ma), Lajedinho (619 ± 3 Ma), and Santa Maria (611 ± 4 Ma) plutons (Oliveira et al., 2015a; Lima, 2016; Soares et al., 2019; Sousa et al., 2019). Oliveira et al. (2010) obtained a muscovite Ar-Ar age of 612 ± 7 Ma from garnet mica schist and ascribed it to the exhumation of the Poço Redondo and Marancó domains.

5.1.4 Significance of the range 590-570 Ma

The period 590-570 Ma has been the subject of debate among researchers in the study area. This range was initially reported for the emplacement of syn-collisional leucogranites (Bueno et al., 2009; Oliveira et al., 2015a) and then for post-collisional monzonites (Lisboa et al., 2019). Our U-Pb dataset in zircon and titanite for these intrusions supports that their emplacement took place earlier, around 630-620 Ma.

Compiled detrital zircon data for supracrustal sequences of the SOS reveals three main age clusters consistent with the main tectonic events in the Borborema Province (Fig. 13b). The most prominent peak correlates with the Cariris Velhos event. Two smaller peaks relate to Rhyacian (2.22-1.96 Ga) and Brasiliano (650-530 Ma) orogenies. The sedimentary deposits from Canindé, Vaza-Barris, and Estância domains show an important contribution of Cryogenian-Ediacaran detritus (Oliveira et al., 2015b; Passos et al., 2022). The youngest age peak of detrital zircon matches the main period of magma generation in the SOS, indicating syn-orogenic sedimentation. The uppermost formations of the Estância Domain are interpreted as peripheral foreland deposits and contain zircon ages ranging from 600 to 540 Ma (Oliveira et al., 2015b). These younger grains represent a small proportion (ca. 2.5%) of dated zircons but demonstrate that 600-540 Ma sources were available for erosion, possibly derived from PEAL.

Geochronological constraints on this episode also come from Ar-Ar, Sm-Nd, and U-Pb isotope determinations in metamorphic minerals. A two-point (whole-rock/garnet) Sm-Nd isochron from a garnet mica schist near to Nossa Senhora de Lourdes interference zone yielded an age of 573 ± 1 Ma, interpreted as a metamorphism age (Oliveira et al., 2010). Oliveira et al. (2010) obtained Ar-Ar ages of 591 ± 4 Ma and 581 ± 2 Ma in muscovite of quartzites from the eastern and western segments of the Macururé Domain, respectively. Such ages can reflect the

uplift and cooling of the orogen, implying that this event varied across the belt. Recrystallized metamorphic zircon grains in the Canindé Domain provided ages in this interval (569-582 Ma; Passos et al., 2022).

In the PEAL, the time interval of 580-550 correlates with metamorphic overgrowth in zircon from supracrustal sequences and orthogneisses (Silva Filho et al., 2014, 2021). Several plutons in this domain with U-Pb ages within the 590-570 Ma range have been interpreted as marking the transition from a contractional to a transcurrent regime at the final stage of the Brasiliano Orogeny (Neves et al., 2008; Silva Filho et al., 2016).

In summary, despite our data not supporting a magmatic episode during 590-570 Ma in the Macururé Domain, this seems to be a pervasive metamorphic (reheating?) event in the SOS and adjoining terranes.

5.2 POTENTIAL SOURCES AND MAGMA EVOLUTION

5.2.1 Origin of the Camará pluton

Lithochemical data for the Camará pluton reveal a continuous trend from gabbro to granodiorite compositions (Fig. 5a). These rocks show potassic affinity and plot in the high-K calc-alkaline association field (Fig. 6). Low-silica contents combined with high Mg# in the gabbros and diorites indicate a significant involvement of mantle components once such compositions can not be obtained from the partial melting of crustal rocks (Rushmer, 1991; Patiño Douce and Beard, 1995; Sisson et al., 2005). Even the most primitive members exhibit high LILE/HFSE ratios and negative Nb-Ta anomalies. Two main scenarios could be explored to explain these crustal signatures. Firstly, these geochemical features would be acquired by crustal contamination of basaltic magmas sourced from a depleted mantle. Secondly, these LILE-rich compositions would reflect the partial melting of an enriched mantle source.

The first hypothesis seems to be a compelling argument to explain such enriched character once some degree of crustal contamination is expected when mantle-derived magmas ascend and emplace into the crust due to their high liquidus temperatures. The Nb/U and Ce/Pb ratios are not considerably affected by partial melting or fractional crystallization, such that they reflect the values of the source (Hofmann et al., 1986). Basic to intermediate rocks from the Camará pluton have low Nb/U (3.3-9.2, average of 6 ± 2), similar to those of the continental crust (4.4-25; Rudnick and Gao, 2003). In contrast, the widely variable Ce/Pb ratios (3.0-70.4, average of 25 ± 19) cover the range observed in the crust (3.7-5.0; Rudnick and Gao, 2003) and mid-ocean ridge basalts and ocean island basalts (25 ± 5 ; Hofmann et al., 1986). These geochemical features suggest the involvement of crustal components via crustal assimilation or

source contamination. Although the role of crustal assimilation can not be ruled out (as discussed in the following section), we argue that the crustal fingerprint of the mafic rocks requires enrichment of the mantle source before the partial melting. This statement is supported by the fact that the abundances of incompatible trace elements (e.g., LILE, LREE, Th, Zr, U) in the most primitive samples from the Camará pluton are significantly higher than those of the continental crust (Rudnick and Gao, 2003).

The flat HREE patterns with $(\text{Ho}/\text{Yb})_{\text{CN}}$ ranging from 1.0 to 1.3 suggest shallower melting depths in the spinel stability field because the melting of garnet mantle facies results in large HREE fractionating (Rollinson, 1993). In addition, weak negative Eu anomalies in the chondrite-normalized REE patterns indicate the absence of residual plagioclase and reinforce the presence of spinel as the main Al-bearing mineral phase in the mantle where the melting took place (Fig. 7). Pereira et al. (2020) proposed that the enriched nature of the basaltic magmas from the Macururé mafic suite resulted from the partial melting of a lherzolite lithospheric mantle, previously fertilized by incompatible elements during a subduction event.

The nature of the contaminant agent of the mantle has been traced through trace element ratios. In the Th/Yb vs. Ba/La diagram, the samples show high Th/Yb and low Ba/La ratios (Fig. 14a). Because LILE are more fluid soluble than REE and HFSE, the vertical trend reveals that the enrichment in the mantle was controlled by the input of subducted sediments (or sediment melts) rather than slab-derived fluids (Woodhead et al., 2001). This melt influx may cause modal metasomatism, inducing the formation of unusual K-, REE- and LILE-rich minerals (in particular, pargasite and phlogopite). The increasing Rb/Sr ratio at a narrow range of Ba/Rb ratio suggests that phlogopite was the main hydrous phase in the source (Fig. 14b; Furman and Graham, 1999). Relative to anhydrous peridotite, the appearance of phlogopite increases the concentration of volatiles and incompatible elements, making it more susceptible to melting due to a lower solidus (Menzies et al., 1987; Wilson, 1989; Conceição and Green, 2004).

Figure 14c shows partial melting curves of three mantle sources progressively more enriched: depleted MORB mantle (Workman and Hart, 2005), metasomatized spinel lherzolite (Kourim et al., 2021), and phlogopite-pargasite lherzolite (Menzies et al., 1987). In a Yb_{CN} vs. $(\text{Ce}/\text{Yb})_{\text{CN}}$ space, the melting trajectories for these compositions are quite distinctive. The geochemical data for Camará rocks are consistent with a modest melting rate of ca. 8-10% of a metasomatized spinel lherzolite, leaving a harzburgite residue (58% olivine + 25% orthopyroxene + 12% clinopyroxene + 5% spinel).

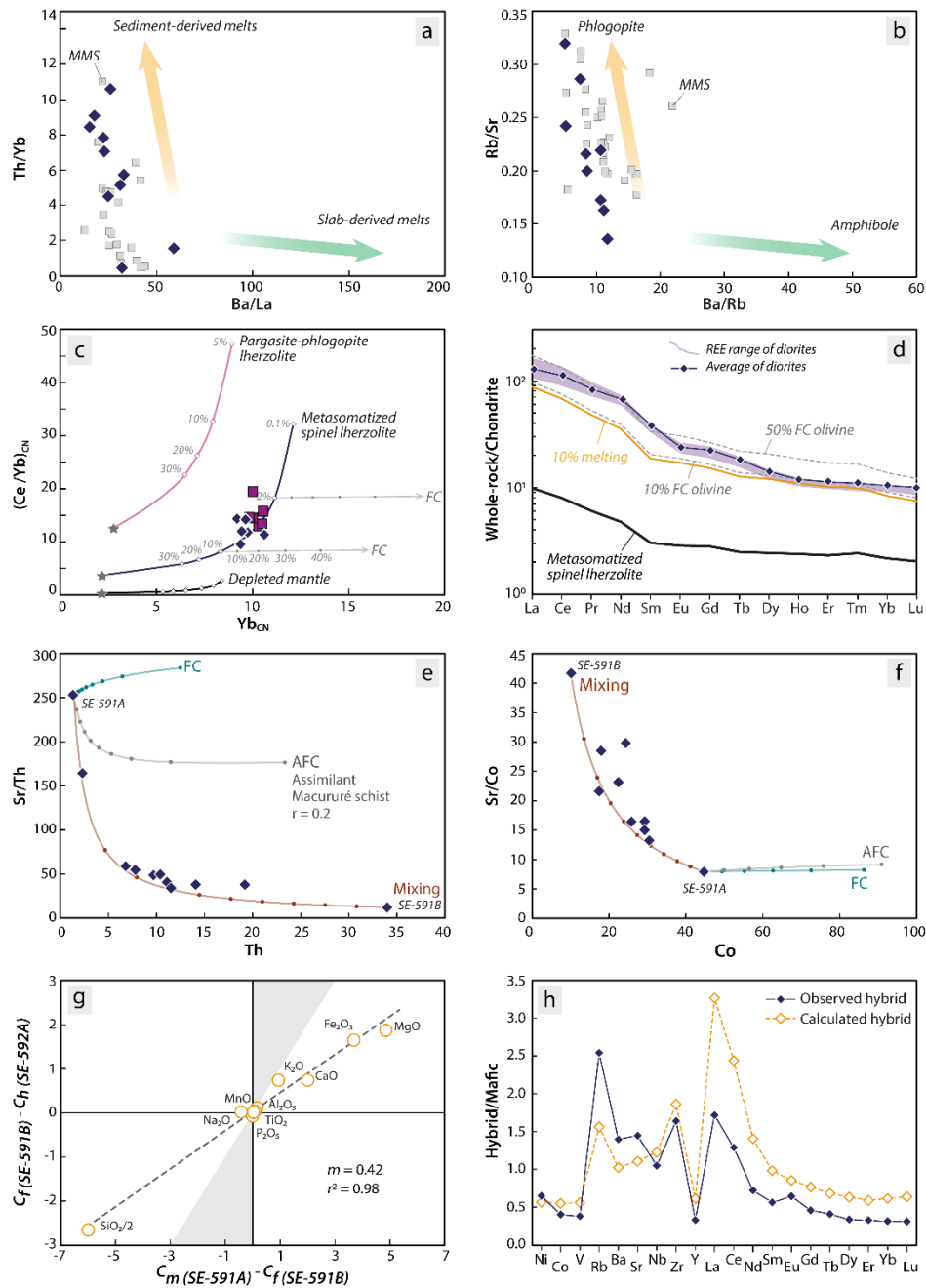


Figure II.14- Origin of the Camará pluton. (a) Ba/La vs. Th/Yb, according to Woodhead et al. (2001). (b) Ba/Rb vs. Rb/Sr ratios with the indication of the compositional variations resulting from partial melting of phlogopite- or amphibole-bearing mantle source (Furman and Graham, 1999). Macururé mafic suite (MMS) data shown in (a) and (b) are from Pereira et al. (2020). (c) Chondrite-normalized Sm/Yb vs. Yb diagram with melting curves for different potential mantle sources: depleted MORB mantle (Workman and Hart, 2005), metasomatized spinel lherzolite (ST0804; Kourim et al., 2021) and pargasite-phlogopite lherzolite (RS1; Menzies et al., 1987). Gray arrows correspond to the paths of fractional crystallization of olivine. (d) REE chondrite-normalized patterns for 10% batch melting of a metasomatized spinel lherzolite (ST0804; Kourim et al., 2021), followed by 10-50% olivine fractionating (dashed lines). Residue composition: 58% olivine + 25% orthopyroxene + 12% clinopyroxene + 5% spinel. Chondrite values are from McDonough and Sun (1995). (e) Th vs. Sr/Th and (f) Co vs. Sr/Co with trends of fractional crystallization (FC), assimilation and fractional crystallization (AFC), and mixing. (g) Major oxides mixing model testing the hypothesis that the hybrid diorite ($C_h = SE-592A$) can be generated by mixing between a mafic magma ($C_m = SE-591A$) and a differentiated magma ($C_f = SE-591B$). The shaded region represents the domain where mixing is not verified. m = fraction of mafic magma in the mixture. r^2 = correlation coefficient. (h) Calculated and observed trace elements normalized to the mafic member.

Primary magmas derived from mantle peridotites are believed to be basaltic rather than andesitic, with low SiO₂ (< 50 wt%) and high Mg# (> 0.7), Ni (> 400 ppm), and Cr (> 1000 ppm) (Wilson, 1989). However, liquids as silica-rich as andesite may be obtained straight from a metasomatized mantle source (Conceição and Green, 2004; Condamine and Médard, 2014). The studied basic-intermediate rocks have moderate Mg# and compatible trace elements, suggesting some olivine fractionation. We argue that the enriched parental basaltic magma of the Camará pluton was produced by partial melting of a fertile spinel lherzolite source and evolved by fractional crystallization. As shown in Fig. 14d, the REE patterns of the diorites are reproduced through 10-50% fractional crystallization of olivine. Olivine fractionation at mantle depths or during the magma ascent does not modify the Ce/Yb ratios but depletes the magma in MgO and Ni, leading to more evolved compositions.

5.2.1.1 Mechanisms of differentiation

Field, petrographic and geochemical relationships suggest more than one geological process operating to produce the compositional variation of the Camará pluton. In order to quantify the role of these petrogenetic processes, we carried out modeling tests.

Initially, we investigate if the most evolved granodiorite (sample SE-591B, 68.58 wt% SiO₂) could be produced from an andesitic magma (sample SE-591A, 51.97 wt% SiO₂) by fractional crystallization. The best fit was obtained for 63% fractional crystallization ($F = 37\%$), with a cumulate composed of 68.4% amphibole + 22.4% biotite + 7.0% clinopyroxene + 2.2% ilmenite. The relatively high $\Sigma r^2 = 1.5$ suggests that the model cannot adequately describe the observed compositions. The nonparallelism of REE patterns between intermediate and acid rocks implies distinct sources for andesitic and dacitic magmas.

The presence of metasedimentary xenoliths and the development of garnet in contact with schists suggests some crustal assimilation. The Assimilation and Fractional Crystallization (AFC) model describes the effects of the assimilation of wall rocks during fractional crystallization (DePaolo, 1981). AFC modeling requires applying parameters for fractional crystallization as parent magma (SE-591A), daughter magma (SE-591B), the modal composition of the cumulate (71.2% amphibole + 23% biotite + 4.3% clinopyroxene + 1.5% titanite) and degree of crystallization ($(1 - F) = 0.65$). The composition of garnet-biotite schist from the Macururé Complex (sample FDS-68A) was used as a possible contaminant, assuming an assimilation rate/crystallization rate of 0.2. As shown in Fig. 14e, the assimilation of surrounding rocks cannot explain the compositional variation in the Camará pluton. Because the contents of incompatible elements (e.g., Rb, Ba, Sr) are much higher than those observed

in country rocks, the effects of contamination would dilute these trace elements, making their bulk-rock composition “immune” to crustal contamination. Thus, contamination by country rocks could play an important role locally, but it can not explain all compositional variation observed in this intrusion.

As previously mentioned, several petrographic and geochemical observations point to magma mixing/mingling as a critical process in generating the compositional variation in the studied rocks. The richness of MME, sometimes containing plagioclase phenocrysts, besides abundant mafic clots, is interpreted as evidence for hybridization at various scales between mafic and felsic magmas (Barbarin and Didier, 1991). Mixed apatite morphologies (stubby and acicular) have been ascribed to the magma mixing/mingling process (Baxter and Feely, 2002). The presence of stubby apatite records the earlier crystallization phase of the felsic magma, while the acicular variety reflects the rapid cooling of mafic magma when incorporated by a cooler magma. In Harker diagrams, major elements show linear trends instead the inflections typical of rock associations linked by fractional crystallization. In a Th vs. Sr/Th diagram, the role of magma mixing becomes more evident (Fig. 14e). All samples arrange between the mafic and felsic members and fit the hyperbolic trend of the mixing line.

A simple two-component mixing test was applied to estimate the proportion of mafic and felsic components needed to account for the composition of the hybridized rocks. We evaluate if mixing between andesitic (sample SE-591A) and dacitic (sample SE-591B) magmas could produce the intermediate composition of the SE-592A sample. In the case of perfect mixing, all data spread along a straight line, where the slope m provides the proportion of mafic end-member (Fourcade and Allegre, 1981). In terms of major oxides, a mafic component proportion of 0.42 may reproduce the composition of the sample SE-592A, with a linear correlation (r^2) of 0.98 (Fig. 14g). Mafic/felsic proportion can be used to estimate the abundance of trace elements in the hybrid sample. Figure 14h displays the calculated and observed trace element compositions normalized to the mafic member. The best fits were obtained for the major and compatible trace elements, whereas the highly incompatible Rb, Ba, and Sr do not match well. Decoupling of elements between calculated and observed compositions suggests another process besides mixing. Discrepancies for LREE and HREE could result from the accumulation of REE-bearing phases, such as allanite and zircon. In the last instance, the selected compositions for mixing calculations might not necessarily represent the real mafic and felsic end-member. Although the interpretation of the magmatic evolution of the Camará pluton is not unique, most features support mixing/mingling between mantle- and crustal-derived magmas as the process responsible for all observed compositions.

5.2.2 Hybrid crustal sources for the leucogranites

The biotite- and two-mica granitoids have high-silica contents (66.61-74.46 wt%), weakly metaluminous to moderately peraluminous affinities ($A/CNK = 0.90-1.20$), potassic character ($K_2O > Na_2O - 2$), and normative corundum higher than 1%. They are magnesian ($Mg\# = 0.14-0.54$) akin to Cordilleran granitoids, magmatism characteristic of active margin environments. Available Nd isotope data for leucogranites ($\epsilon Nd_{(630\text{ Ma})} = -3.5$ to -2.9 ; $Nd-T_{DM} = 1.30-1.23$ Ga) cover the range reported for their country rocks ($\epsilon Nd_{(630\text{ Ma})} = -7.0$ to -0.6 ; $Nd-T_{DM} = 1.79-1.29$ Ga), suggesting that Macururé schists would be a potential source for these rocks (Oliveira et al., 2015b, 2015a). Inherited zircons are abundant in these leucogranites and record the same ages found in the detrital zircons of the Macururé Complex (Oliveira et al., 2015b; Conceição, 2019), supporting a crustal sedimentary derivation. Moreover, the presence of surmicaceous enclaves is evidence of a significant continental crust contribution.

Leucogranites show Nb/U ratios between 1.2 and 2.6, as low as those recorded in the upper continental crust ($Nb/U = 4.4$; Rudnick and Gao, 2003). The steep REE patterns strongly suggest the presence of garnet as a melting residue. At the same time, the positive correlation between the Gd/Yb and La/Yb indicates variation in the amount of garnet in the source. Weak negative Eu anomalies suggest the absence of residual plagioclase.

Oliveira et al. (2015a) proposed that the leucogranites generation involved high degrees of partial melting of the Macururé micaschists. However, experimental liquids obtained by dehydration-melting of muscovite schists are strongly peraluminous, alkali-rich, and CaO-poor (Patiño Douce, 1999), which is not the case with the studied rocks. Therefore, the leucogranite compositions require a magma source that is less aluminous and richer in feldspars. When compared with liquids obtained from melting experiments (Fig. 15), the leucogranite chemical composition is similar to those of melts of metagraywackes, with some samples spreading along the pelitic field (Patiño Douce, 1999).

Although our data indicate a significant sedimentary contribution to leucogranite genesis, several lines of evidence rule out a pure sediment-derived origin: (i) lack of aluminous silicates besides biotite and muscovite, such as cordierite, garnet, and tourmaline, typical of S-type granites; (ii) relatively high $Mg\#$ even at high SiO_2 contents; (iii) weakly metaluminous character of the most primitive samples; (iv) higher near-liquidus temperatures correlate with those of “hot granites” which require a significant influx of heat or participation of mantle-derived magmas (Miller et al., 2003); (v) abundance of titanite and allanite, typical accessory phases of I-type magmas (Chappell and White, 2001; Clemens, 2018). Thus, we infer that the generation of these compositions requires that both metasedimentary and metaigneous rocks were involved in the partial melting.

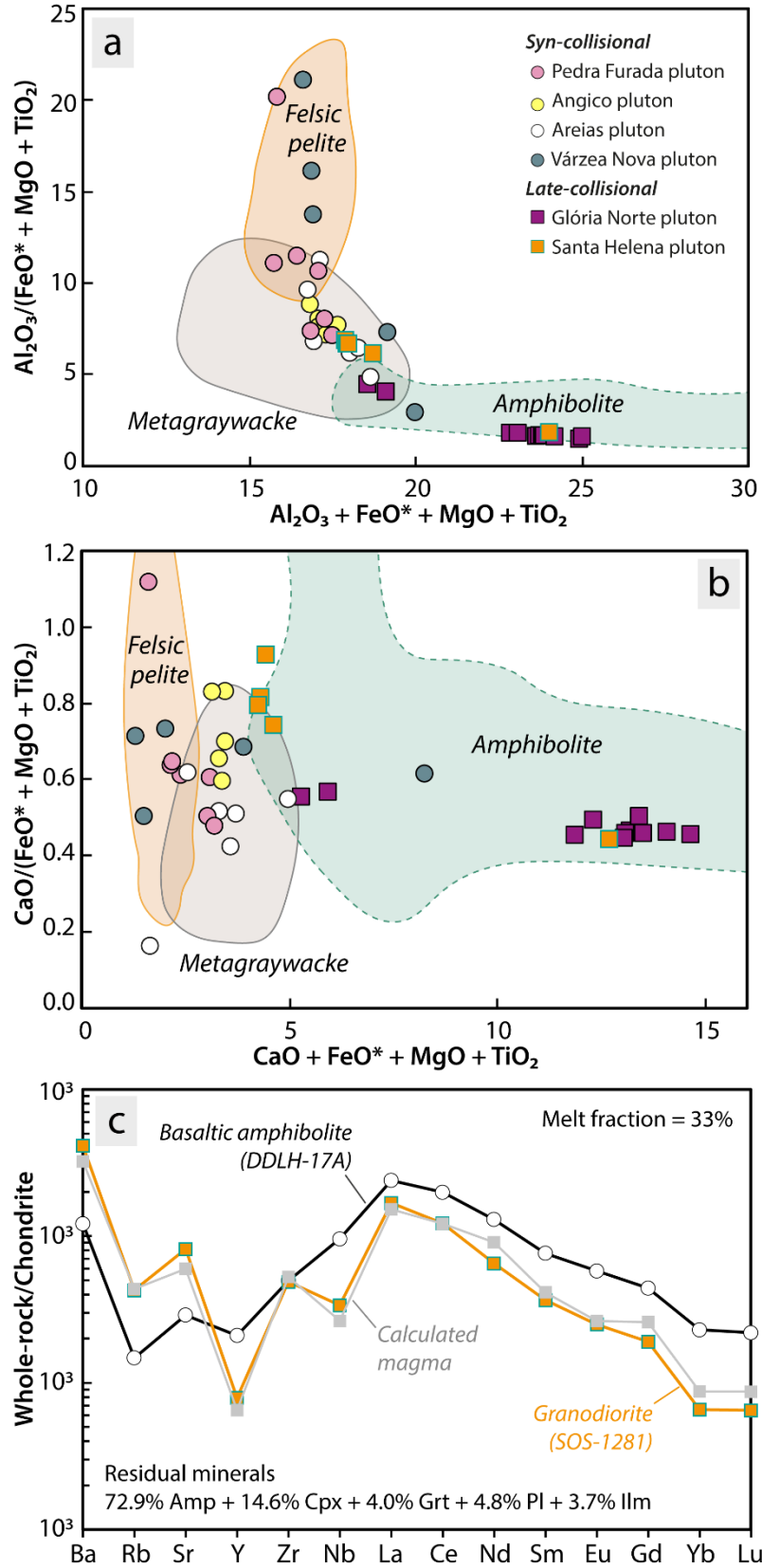


Figure II.15- (a) $Al_2O_3 + FeO^* + MgO + TiO_2$ vs. $Al_2O_3 / (FeO^* + MgO + TiO_2)$ and (b) $CaO + FeO^* + MgO + TiO_2$ vs. $CaO / (FeO^* + MgO + TiO_2)$ showing fields of experimental melts derived from amphibolites, metagraywackes and felsic pelites (Patiño Douce, 1999). (c) Trace element model for the Santa Helena granodiorite generation by partial melting of a metabasaltic amphibolite.

The existence of peraluminous granites showing I-type affinities generated by partial melting of dominantly metasedimentary sources was predicted from thermodynamic modeling by Clemens et al. (2011). The modeling assumed a two-component source consisting of aluminous graywacke and andesite. They observed that melts produced by partial melting of graywacke-dominated sources (> 80%) at high temperatures (> 825°C) would coexist with restitic garnet and orthopyroxene and thus retain all S-type magma features. In contrast, most melts generated by other mixtures between these two components would coexist with restitic clinopyroxene and inherit I-type chemistry. Because basic-intermediate volcanic rocks are common within orogenic sequences, we propose that syn-collisional leucogranites resulted from a heterogeneous source comprising metasedimentary and mantle-derived protoliths.

5.2.3 Amphibolite lower crust producing granodiorites and monzonites

The intrusion of high-K granodiorites and shoshonite monzonites marks the period around 620 Ma in the SOS. The samples of the Glória Norte and Santa Helena plutons are all metaluminous ($A/CNK = 0.83-1.00$), amphibole-rich, and magnesian ($Mg\# = 0.40-0.57$). Their geochemical characteristics resemble those reported for I-type granitoids sourced from metaigneous rocks (Chappell and White, 2001).

The shoshonitic and high-K calc-alkaline rocks follow parallel trends in Harker diagrams, evolving from monzodiorites and quartz monzonites to granites (Fig. 6). The main chemical difference is the higher K_2O contents in Glória Norte rocks compared to those of the Santa Helena pluton. They display similar chondrite-normalized REE patterns, progressively poorer in REE toward most evolved compositions (Fig. 7). The distinct geochemical behavior between these plutons can result from different sources or degrees of partial melting.

The shoshonitic signature, allied to the abundance of lamprophyre enclaves outlined by Lisboa et al. (2019), suggests the participation of an enriched mantle in the genesis of the Glória Norte pluton. Models based on modal melting of spinel lherzolite source indicate that Glória Norte monzonites could be derived from a small degree of partial melting ca. 2-5% (Fig. 14c). Experimental data demonstrate that potassic high-silica melts could be obtained by a fertile mantle source in equilibrium with phlogopite on spinel stability field (Condamine and Médard, 2014). Such liquids overall contain higher $Mg\# (> 0.7)$ and compatible element contents than those observed in the Glória Norte monzonites ($Mg\# = 0.52-0.54$, $Ni = 20-37$ ppm). These lower values can indicate the progressive magma depletion by fractional crystallization of mafic

phases (as proposed above for the Camará intrusion) or that the source area was not the mantle but mantle-derived rocks.

The monzonites and granodiorites fall within the area of liquids produced from amphibolite compositions (Fig. 15; Patiño Douce, 1999), suggesting a basaltic source. Experimental dehydration-melting of amphibolite starts between 850-1000°C (Rushmer, 1991; Patiño Douce and Beard, 1995). This temperature range is compatible with our estimates for near-liquidus temperatures inferred from Zr saturation and Ti-in-zircon systematics. However, melts derived from low-K mafic sources contain low-K and high Na₂O/K₂O, contrasting with the potassic character of the Santa Helena and Glória Norte plutons. Experimental data from Sisson et al. (2005) demonstrated that slightly peraluminous to metaluminous potassium-rich rocks could be obtained from hydrous medium- to high-K basaltic sources. Such rock types are common in subduction-related magmatic arcs and essential constituents of the lower continental crust (Rudnick and Gao, 2003; Sisson et al., 2005), making it a strong candidate for source rock.

The hypothesis of generation of the Santa Helena parental magma by partial melting of a LILE-enriched amphibolite has been tested. In the absence of direct information about amphibolite rocks in the Macururé Domain, we assume the basalt composition of the sample DDLH-17A from the Novo Gosto unit, Canindé Domain, as a possible source ($K_2O/Na_2O = 0.45$, $Mg\# = 0.54$, $(Ce/Yb)_{CN} = 8.6$; Passos et al., 2021). The chondrite-normalized REE spectra of the late-collisional plutons are characterized by almost flat HREE patterns and slight negative Eu anomalies (Fig. 7), suggesting no involvement of garnet and plagioclase as a melting residue. However, when adding minor amounts of these phases, statistically acceptable Σr^2 values are reached. The most suitable model for major elements was obtained with 33% partial melting ($\Sigma r^2 = 0.255$), leading to a residue composed of amphibole (72.88%), clinopyroxene (14.66%), plagioclase (4.79%), garnet (4.00%), and ilmenite (3.67%). Trace elements calculations performed with residual assemblage and melt fraction constrained by mass balance also provided good fits, as shown in Table 4 and Fig. 15. Although the derivation of the potassic late-collisional rocks straight from the mantle may not be ruled out, the geochemical modeling suggests an incompatible-element enriched amphibolite source. A similar crustal model has been postulated by Pe-Piper et al. (2009) for post-orogenic shoshonites from the Limnos area, Greece.

Table II.4- Major and trace element modeling for generation of the high-K Santa Helena granodiorite by partial melting of a basaltic amphibolite.

<i>Major elements (wt%)</i>	DDLH-17A^a Amphibolite^b <i>C₀</i>	Residue <i>C_s</i>	Mineral compositions					Calculated melt <i>C_i'</i>	SOS-1281 Granodiorite^b <i>C_i</i>
			Amp^c 72.88%	Cpx^c 14.66%	Pl^c 4.79%	Grt^c 4.00%	Ilm^d 3.67%		
SiO ₂	51.20	45.10	44.98	50.56	50.24	38.84		63.77	64.06
TiO ₂	2.10	2.99	1.49	0.27		0.03	50.00	0.30	0.70
Al ₂ O ₃	12.48	11.09	11.19	2.52	30.46	21.51		15.31	15.58
FeO*	12.38	16.13	15.29	12.15		27.15	50.00	4.77	4.77
MgO	8.21	10.66	12.01	10.04		5.51		3.22	3.54
CaO	9.61	12.41	10.88	22.59	14.39	6.31		3.92	3.96
Na ₂ O	2.77	1.42	1.60	0.42	3.42			5.50	4.11
K ₂ O	1.25	0.29	0.39		0.04			3.20	3.29
Trace elements (ppm)									
Ba	293							779	995
Rb	34							100.4	98.5
Sr	210							435	592
Y	33							10.3	12.4
Zr	190							202	187
Nb	23							6.4	8.1
La	56.8							36.1	39.9
Ce	122.0							74.5	75.1
Nd	59.3							41.5	29.8
Sm	11.3							6.12	5.43
Eu	3.26							1.49	1.41
Gd	8.8							5.16	3.79
Yb	3.7							1.41	1.06
Lu	0.54							0.21	0.16

^a Enriched basaltic amphibolite from the Novo Gosto unit, Canindé Domain (Passos et al., 2021).

^b Major oxides recalculated to 100%.

^c Mineral compositions from Weaver et al. (1982).

^d Assumed simplified composition.

5.3 Hf ISOTOPES ON ZIRCON

All analyzed zircon grains display subchondritic Hf composition, with $\epsilon\text{Hf}(t)$ values typically lower than -4.0. The obtaining $^{176}\text{Hf}/^{177}\text{Hf}$ involved accurate correction for the interferent ^{176}Yb . Intrasample ϵHf variability in our dataset cannot be assigned to inappropriate Yb-correction once there is no correlation between $^{176}\text{Hf}/^{177}\text{Hf}$ and $^{176}\text{Yb}/^{177}\text{Hf}$, as shown in Supplementary Figure S2. In addition, the $^{176}\text{Yb}/^{177}\text{Hf}$ ratios on zircon are lower than 0.10, agreeing with the recommendations of Griffin et al. (2002). Because observed intrasample variations do not exceed three ϵHf -units, they are probably more related to errors on epsilon than geological factors.

Whole-rock Nd- T_{DM} model ages available for the studied plutons (Oliveira et al., 2015a) are younger than the zircon Hf- T_{DM}^{C} model ages, with differences between them reaching 500

Ma. These discrepancies result from the fact of whole-rock Nd- T_{DM} represents the average model ages of the sources involved in the magma generation (Arndt and Goldstein, 1987). In contrast, a single zircon population from a magmatic unit can exhibit an extensive range of Hf compositions, recording the contribution of distinct sources (Roberts and Spencer, 2015).

Despite this advantage, there are some caveats to using and interpreting Hf- T_{DM}^C model ages due to dependence on variables that cannot be precisely determined, such as the model of Hf isotopic evolution through time for the depleted mantle or $^{176}\text{Lu}/^{177}\text{Hf}$ ratio of the parental magma (Roberts and Spencer, 2015; Vervoort and Kemp, 2016; Spencer et al., 2020). Although we consider the Hf model ages as approximate mantle extraction ages, the Lu-Hf isotope data point out the significant participation of ancient crustal components for the Brasiliano magmatism in the Macururé Domain as elsewhere in the southern Borborema Province (Caxito et al., 2016; Silva Filho et al., 2016).

5.3.1 Subcontinental lithospheric mantle (SCLM) beneath the southern Borborema Province

Mafic rocks provide an excellent opportunity to constrain the nature of mantle sources. The zircon crystals from Camará diorite show simple internal structures without core-rim variations and provide a uniform population of concordant U-Pb data (Fig. 9a). These features indicate a single event of zircon generation during magma crystallization and that the obtained initial $^{176}\text{Hf}/^{177}\text{Hf}$ is representative of the magma composition. Despite the evidence of magma mixing, the zircon grains from the Camará sample show a narrow range of $\epsilon\text{Hf}_{(t)}$ values (2 ϵHf -units; Fig. 10), which characterizes a magma with homogeneous Hf composition and a closed-system behavior (e.g., Griffin et al., 2002; Shaw and Flood, 2009).

The diorite of the Camará pluton provided negative values of the $\epsilon\text{Hf}_{(643\text{ Ma})}$ between -6.1 and -4.1, differing from those expected for a depleted mantle reservoir at the time of magma generation (Fig. 10). The Hf- T_{DM}^C model ages show a slight variation between 1.83 and 1.94 Ga. It was thought that mafic magmas from the Macururé Mafic Suite represent the first pulses during the construction of a magmatic arc involving the Macururé-Marancó-Poço Redondo-Canindé domains (Oliveira et al., 2010; Pereira et al., 2020). Interestingly, even the most primitive samples of the SOS hold evolved isotopic compositions, suggesting an underlying thick lithospheric mantle, once a thin or absent lithospheric mantle would result in juvenile magmatism (Chapman et al., 2017). According to Ganade et al. (2021), the Brasiliano Orogeny added only around 15% of the new continental crust in the Borborema Province, suggesting the

predominance of crustal reworking with subordinate juvenile magma input. However, this approach does not consider the contribution of unambiguous mantle-derived rocks that display elemental and isotopic crustal signatures due to the incorporation of crustal materials, as is the case of the Camará pluton.

The upper mantle beneath Borborema Province shows a heterogeneous composition, ranging from isotopically depleted to enriched. To the north in SOS, a depleted mantle is sampled by metabasites of the Canindé Domain (Pinto et al., 2020; Passos et al., 2021, 2022). The Sr and Nd isotope signature for these basaltic rocks follow the mantle array and have been interpreted as recording: (i) the ascent of a young convecting mantle in the context of continental rifting (Oliveira and Tarney, 1990; Oliveira et al., 2010) or (ii) a metasomatized mantle by subduction-related fluids in a continental arc/back-arc environment (Pinto et al., 2020; Passos et al., 2021, 2022).

Contrastingly, our Lu-Hf data for the Camará pluton point to a derivation from an enriched mantle source, where the isotope composition seems governed by non-radiogenic hafnium of ancient crustal components introduced via subduction. The recycling of pelagic sediments and turbidites exerts a critical role in modifying the isotopic composition of the mantle wedge due to the insertion of old zircons having high unradiogenic Hf-Nd contents (Hao et al., 2022). The model of sediment reworking has been claimed as an efficient mechanism for originating the crustal fingerprint retained by rocks in orogenic systems worldwide (Couzinié et al., 2016; Hao et al., 2022). Thus, the incompatible-enriched character combined with subchondritic $\epsilon\text{Hf}(t)$ values in the Camará pluton is consistent with a mantle source contaminated by sediment melts during ancient subduction events.

Although the model ages are not quantitatively significant, they provide clues to the timing of the metasomatic event, yielding minimum ages for the mixing episode (Menzies et al., 1987; Orejana et al., 2020). Zircon crystals from Camará diorite yielded Orosirian Hf- T_{DM}^{C} model ages that may be interpreted as the time when the isotopic heterogeneity developed in the mantle source. Thus, the SCLM enrichment may have been achieved throughout the Rhyacian Orogeny and persisted until the Brasiliano cycle.

The pre-Brasiliano crust in the SOS comprises (1) Mesoarchean orthogneisses from the Itabaiana and Simão Dias domes (2.86-2.85 Ga; Oliveira, 2012; Rosa et al., 2020), (2) Paleoproterozoic orthogneisses and ultrahigh-temperature metamorphic rocks from the Jirau do Ponciano Dome and Arapiraca Complex (ca. 2.0 Ga; Lima et al., 2019; Spalletta and Oliveira, 2017; Tesser et al., 2021), (3) Tonian migmatitic orthogneisses and granitoids in the Poço Redondo and Marancó domains (1000-960 Ma; Carvalho, 2005; Passos et al., 2022), and (4)

Tonian-Cryogenian mafic rocks and granitoids from the Canindé Domain (740-700 Ma; Pinto et al., 2020; Passos et al., 2021, 2022). Both formation events of the Cariris Velhos remnants and in the Canindé Domain accreted juvenile material to the SOS during the Neoproterozoic. Whether the mantle source enrichment took place during these episodes or earlier, the presented data do not allow a straightforward conclusion. Nevertheless, the sedimentary protoliths of the Macururé Domain were deposited above the Paleoproterozoic basement, exposed in the Jirau do Ponciano Dome, which was formed through accretionary-collisional tectonics (Oliveira et al., 2010; Lima et al., 2019). In this context, the recognition of mantle-derived rocks showing Paleoproterozoic Hf- T_{DM}^C model ages is compatible with a Rhyacian basement and its lithospheric mantle. Therefore, our data favor that the mantle root beneath the Macururé Domain survived since the Paleoproterozoic and was partially melted to produce LILE-enriched mafic melts during the Brasiliano Orogeny.

5.3.2 Role of crustal reworking

The Santa Helena granodiorite shows $\epsilon Hf_{(620 \text{ Ma})}$ values ranging from -8.3 to -4.1, and the Hf- T_{DM}^C model ages between 1.83 and 2.03 Ga. Regarding Nd isotope composition, the Santa Helena pluton shows uniform negative $\epsilon Nd_{(620 \text{ Ma})}$ ranging from -7.3 to -6.3, and Nd- T_{DM} model ages between 1.55 and 1.54 Ga (Oliveira et al., 2015a). Zircon grains from the Glória Norte monzonite also display evolved Hf isotope compositions, with $\epsilon Hf_{(621 \text{ Ma})}$ (-6.0 to -4.1) and Hf- T_{DM}^C model ages (1.77-1.89 Ga). Based on whole-rock Nd isotopic data, the late-collisional granitoids could be formed from a Mesoproterozoic juvenile crust generated about 1.4-1.5 Ga or may represent a hybrid composition resulting from a mixture between a Tonian source with a minor Paleoproterozoic-Archean contribution.

Due to the absence of Hf isotope determinations in the SOS, our data were compared to those available in other domains of Borborema Province in order to access the composition of the pre-Brasiliano crust (Fig. 10). Zircon Lu-Hf data for the Rhyacian basement provide sub- to suprachondritic values of $\epsilon Hf_{(t)}$ varying from -2.5 to +6.0 (Costa et al., 2018; J. v Lima et al., 2021). This period was marked by both intense crustal growth and reworking of Archean components, showing Hf- T_{DM}^C model ages between 2.29 and 2.83 Ga. Available data for Cariris Velhos crust encompass moderately juvenile to slightly evolved rocks ($\epsilon Hf_{(t)} = -1.5$ to +2.5), with Orosirian-Statherian Hf- T_{DM}^C model ages ranging from 1.67 to 1.88 Ga (Caxito et al., 2020b). Hf isotope composition of the zircons from Santa Helena and Glória Norte plutons lies between evolutionary trends for Cariris Velhos and Rhyacian crusts. This way, their isotope

composition probably reflects derivation from a source containing a mixture of Tonian and Paleoproterozoic sources, dominated by a Cariris Velhos-like component. Moreover, the consistency of isotopic signatures between the Camará, Glória Norte, and Santa Helena plutons may indicate an isotopically coupled lithospheric mantle and lower crust throughout the Brasiliano Orogeny.

5.4 GEODYNAMIC IMPLICATIONS

Neves (2021, 2003) has proposed that the Borborema Province and São Francisco-Congo Craton were part of a single paleocontinent since the end of Rhyacian Orogeny underwent subsequent extensional events in a dominantly intracontinental setting from late Paleoproterozoic to late Neoproterozoic. The assumption of a continuous paleocontinent is also claimed by Ganade et al. (2021) and Tesser et al. (2021), which proposed that intermittent rifting events weakened the cratonic margin and favored decratonization processes and terrane dispersion. The decratonization led to the opening of oceanic basins, which were then involved in complete Wilson cycles of subduction and collision. In this model, the Archean-Paleoproterozoic inliers within the supracrustal sequence in SOS are remnants of the dismembered terranes from SFC.

The emplacement setting of the Cariris Velhos-related fragments in the SOS is controversial. An Andine-type active margin was inferred for protoliths of the Poço Redondo migmatites (Oliveira et al., 2010). Extension of this block would have given rise to the A-type Serra Negra granites (Carvalho, 2005; Oliveira et al., 2010). However, both migmatite and granite share similar extension-related geochemical signatures (Guimarães et al., 2016).

In the Canindé Domain, rifting could have started at ca. 715 Ma and lasted until ca. 640 Ma just before the onset of the Brasiliano Orogeny, as suggested by the emplacement of bimodal igneous association, continental mafic volcanic rocks, gabbroic layered intrusion and rapakivi granites (Oliveira and Tarney, 1990; Oliveira et al., 2017). However, other researchers have argued that the Canindé Domain represents the remnants of a continental arc/back-arc system rather than a rift (Pinto et al., 2020; Passos et al., 2021).

The SOS experienced continuous magmatic activity from 640 to 600 Ma related to Western Gondwana assembly (Fig. 13). Different tectonic models have been used to interpret this ~40 Ma time frame, including subduction and extension. Early- and late-collisional plutons have similar enrichment in incompatible elements and negative anomalies of Ta-Nb-Ti, typically related to subduction environments. In the tectonic discrimination diagram, these

samples lie in the volcanic arc field, overlapping the area of post-collisional granites (Supplementary Figure S5). The consumption of an ocean in an Andean-type setting evolving into a Himalayan-type collision, which culminated with slab break-off, has been proposed to explain the signatures of the magmatic rocks (Oliveira et al., 2010, 2015a, 2017). However, the advance of geochemical and isotopic knowledge about magmatic rocks has favored an extensional model as the main process controlling the Cryogenian-Ediacaran evolution of this area.

One of the most intriguing features of the SOS is the dominance of potassic rocks throughout the Brasiliano event, which makes it difficult to insert into classic models of orogenies. Unlike expected in a magmatic arc, the typical calc-alkaline signature of Andean-type rocks is nonexistent in the SOS. The overwhelming majority of magmatic rocks have high-K calc-alkaline, shoshonitic, and even ultrapotassic affinities (Lisboa et al., 2019; Sousa et al., 2019; Fernandes et al., 2020; Pereira et al., 2020). This rock association is more consistent with a post-collisional setting (Wilson, 1989; Couzinié et al., 2016), which can be readily ruled out due to the crystallization ages. As documented in this work, whole-rock Sm-Nd and zircon Lu-Hf isotope data indicate that Brasiliano juvenile components are virtually absent in the SOS, such that gabbroic-dioritic rocks have consistently enriched mantle signatures and Paleoproterozoic model ages (Fig. 10). This “reworking-dominated” scenario is incompatible with the fact that magmatic arcs are the major sites of crustal growth (Chapman et al., 2017). Furthermore, exposures of high-grade metamorphic rocks and ophiolite complexes are missing. Thus, the SOS has no undoubted evidence of a Neoproterozoic subduction episode.

Recent works in the PEAL interface zone with the SOS have proposed a Cryogenian-Ediacaran continental arc for the composite Santa do Ipanema batholith build-up by continuous amalgamations over 30 Ma (Ferreira et al., 2021). According to Ferreira et al. (2021), the plutons older than 625 Ma have slightly negative to slightly positive ϵ_{Nd} values, while the younger plutons show more negative ones, indicating that mantle contribution decreased with time. Unlike the Macururé Domain, a juvenile component is present in this area and plutonic rocks form vast batholiths as expected along active margins (Barbarin, 1999; Frost et al., 2001a; Chapman et al., 2017). Whether an ocean has existed on SOS during the late Cryogenian-Ediacaran, it was consumed by the dipping-northward subduction zone (present coordinates) below the PEAL.

An alternative interpretation proposed here considers that establishing the Canindé rift was the driving force behind the extensional tectonics in the SOS. The volume of basic magmatism in the Canindé Domain would require a sizeable thermal event to remobilize the

subcontinental lithosphere (Oliveira and Tarney, 1990). This event would affect the whole SFC margin and create favorable conditions to melt the lithospheric mantle and the overlying crust. In this context, the geochemical and isotopic signatures of the magmatic rocks might be inherited from their sources. Hence, the 640-600 Ma potassic magmatism in the Macururé Domain seems more linked to an extensional environment than to subduction.

5.5 A POSSIBLE MODEL

We propose that the development of the SOS and associated magmatism may be assigned to a four-stage geodynamic evolution as follows:

Stage I: After successive rifting events, the extended and weakened crust of the southern Borborema Province acted as the depocentre for basins receiving detritus from the eroded Paleoproterozoic and Tonian uplifted continental blocks (Fig. 16a). On the side of the PEAL, the sedimentary succession from the Macururé Complex was deposited, while sedimentation of the basal units from the Estância and Vaza-Barris domains took place at the SFC edge (Van Schmus et al., 2011; Oliveira et al., 2015b; Neves et al., 2019).

Stage II: Partial melting of the subduction-modified Paleoproterozoic lithospheric mantle enabled the production of primary basaltic magmas, later emplaced as sills and stocks around 640 Ma (Fig. 16b). In Macururé Domain, the magmatic activity included the generation of LILE-enriched ultrabasic to intermediate bodies displaying potassic affinities (Pereira et al., 2020). Mixing between the mantle and crustal magmas at infracrustal depths resulted in a wide composition range of magmatic rocks. The Camará (643 ± 2 Ma) and Dores (628 ± 5 Ma) plutons are related to this period, together with other plutons composing the Macururé Mafic Suite. With the shift from extension to compression in response to far-field stresses transferred from elsewhere in Western Gondwana, the basins were inverted and involved in the orogeny.

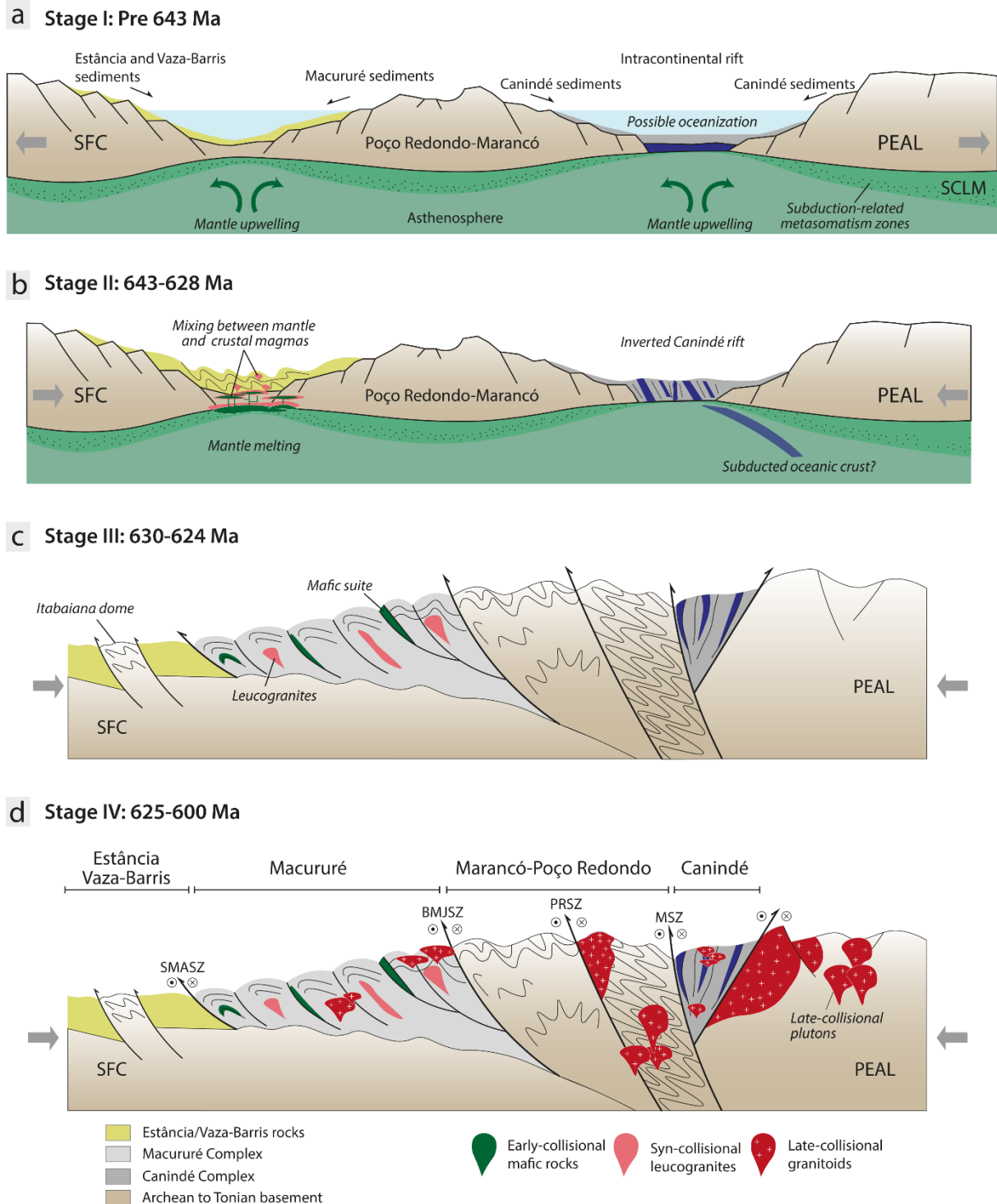


Figure II.16- Geological evolution of the study area. (a) Tonian and Cryogenian rifting events weakened the northern edge of the SFC, which acted as the basement for sedimentary basins. (b) Decompression melting allowed partial melting of the Paleoproterozoic lithospheric mantle and generation of parental magmas from the Macururé Mafic Suite. The emplacement of basaltic magmas at lower crustal depths facilitated the production of crustal melts and mixing at varying proportions. (c) Anatexis of the sedimentary protholiths from the Macururé Complex produced biotite- and muscovite-bearing leucogranites, emplaced along the schistosity of the country rocks. (d) The intrusion of undeformed granitoids cross-cutting the regional foliation, followed by the sedimentation of foreland deposits, demarcated the final stages of the Brasiliano/Pan-African Orogeny in the SOS. SMASZ = São Miguel do Aleixo Shear Zone, BMJSZ = Belo Monte-Jeremoabo Shear Zone, PRSZ = Poço Redondo Shear Zone, MSZ = Macururé Shear Zone, SFC = São Francisco Craton, PEAL = Pernambuco-Alagoas Domain.

Stage III: When SFC and PEAL landmasses collided, the subsequent crustal shortening and thickening favored the development of large-scale shear zones and metamorphism coupled with magma production (Fig. 16c). Sedimentary basins, microcontinental blocks, and rift slices were amalgamated and thrust toward the SFC margin. We postulate that the emplacement of syn-collisional leucogranites within the Macururé Domain records the beginning of the SFC-PEAL collision, limiting this event between 630-624 Ma (Conceição, 2019). This range coincides with the addition of mantle-derived rocks in the SOS, leading us to infer that these hotter magmas could trigger the anatexis of the Macururé sedimentary pile. Conceição et al. (2016) described the presence of mafic microgranular enclaves with shoshonitic affinity hosted by the Glória Sul leucogranite, reinforcing the assumption that the generation of mantle- and crustal-derived magmas were broadly contemporary.

Stage IV: A large volume of magma was produced between 625-600 Ma, characterizing the late-collisional stage in SOS (Fig. 16d). Several stocks and batholiths intruded into Poço Redondo, Canindé, and Macururé domains, including monzonite, granodiorite, and granite compositions. Generally, these rocks are isotropic, without solid-state deformation evidence, and truncate the foliation of the country rocks. Mantle material played an important role in forming rocks at this time, represented by abundant mafic enclaves and syn-plutonic dikes enclosed in granitoids, showing affiliation with shoshonitic and ultrapotassic suites (Lisboa et al., 2019; Fernandes et al., 2020; Sousa et al., 2022). Plutonic activity associated with large shear zones sealed the boundaries of the domains and marked the end of the tectonic collage. Part of this material was available for erosion, providing detritus for the uppermost units from the Vaza-Barris and Estância domains, interpreted as foreland basins (Oliveira et al., 2015b).

6 CONCLUSIONS

The data presented in this work allow constraining the evolution of the eastern segment of the SOS, southern Boroborema Province. Field relationships, U-Pb geochronology, whole-rock geochemistry, and Hf isotopes allowed recognition of three magmatic groups in the Macururé Domain related to the main stages of the Brasiliano/Pan-Africano Orogeny: (i) early-collisional; (ii) syn-collisional; and (iii) late-collisional.

Early-collisional Camará pluton comprises basic to acid rocks, magnesian, high-K calc-alkaline, LILE- and LREE-enriched, emplaced at 643 ± 2 Ma. Geochemical features indicate that the gabbroic-dioritic rocks were derived from a shallower lithospheric mantle at the spinel stability field. The lithospheric mantle beneath southern Boroborema Province seems to be

previously enriched by the introduction of crustal material via subduction associated with the Rhyacian Orogeny. Such enrichment resulted in more radiogenic Hf values, yielding Orosirian Hf-T_{DM}^C model ages. Magma mixing with crustal-derived melts took place at infracrustal depths, producing a wide compositional variation.

The emplacement of biotite-muscovite leucogranites occurred around 630 Ma, marking the onset of the SFC-PEAL collision. These rocks are magnesian to ferrous, potassic, and metaluminous to peraluminous. Petrographic, elemental, and isotopic features argue for derivation from crustal sources dominated by metagraywackes with minor metaigneous components.

Late-collisional Santa Helana and Glória Norte plutons were contemporarily intruded at ca. 620 Ma. These rocks are metaluminous, magnesian, and show affinities with the high-K calc-alkaline to shoshonite magmatic series. Their geochemical signatures are consistent with derivation from a lower-crustal K-rich amphibolite source, pointing to the reworking of ancient crusts related to Cariris Velhos and Rhyacian events.

Cryogenian-Ediacaran magmatic rocks from the SOS have a unimodal age frequency distribution, spanning from 643 to 603 Ma. The absence of ages around 590-570 Ma on zircon and titanite suggests that previously reported dates in this interval can represent a regional metamorphic overprinting related to the final stages of the Brasiliano Orogeny.

In light of geochemical, geochronological, and isotope data, we suggest that the evolution of the SOS during the Brasiliano/Pan-Africano Orogeny may be explained by a lithosphere extension followed by basin inversion and continental collision.

ACKNOWLEDGMENTS

This study was financed in part by the Coordenação de Aperfeiçoamento de Pessoal de Nível Superior – Brazil (CAPES) – Finance Code 001. The research was supported with funding from Conselho Nacional de Desenvolvimento Científico e Tecnológico (CNPq; Jean Michel Lafon – grants 312393/2020-2 and 42625/2018-7; Maria de Lourdes Silva Rosa – grant 311023/2021-5; Herbet Conceição – grant 310740/2021-5). The authors thank João Alberto Evangelista Pinto (PPGG/UFPA) for the technical support during the analytical routine in the Pará-Iso. We especially thank Fabrício de Andrade Caxito and Sérgio Pacheco Neves for their comments that greatly improved the manuscript.

REFERENCES

- Aleinikoff, J.N., Wintsch, R.P., Fanning, C.M., Dorais, M.J., 2002. U–Pb geochronology of zircon and polygenetic titanite from the Glastonbury Complex, Connecticut, USA: an integrated SEM, EMPA, TIMS, and SHRIMP study. *Chemical Geology* 188, 125–147.
- Almeida, F.F.M., Hasui, Y., Brito Neves, B.B., Fuck, R.A., 1981. Brazilian structural provinces: An introduction. *Earth-Science Reviews* 17, 1–29.
- Andersen, T., Andersson, U.B., Graham, S., Åberg, G., Simonsen, S.L., 2009. Granitic magmatism by melting of juvenile continental crust: new constraints on the source of Palaeoproterozoic granitoids in Fennoscandia from Hf isotopes in zircon. *Journal of the Geological Society* 166, 233–247.
- Arndt, N.T., Goldstein, S.L., 1987. Use and abuse of crust-formation ages. *Geology* 15, 893–895.
- Barbarin, B., 1999. A review of the relationships between granitoid types, their origins and their geodynamic environments. *Lithos* 46, 605–626.
- Barbarin, B., Didier, J., 1991. Macroscopic features of mafic microgranular enclaves. *Enclaves and Granite Petrology*. Elsevier, Amsterdam, 253–262.
- Baxter, S., Feely, M., 2002. Magma mixing and mingling textures in granitoids: examples from the Galway Granite, Connemara, Ireland. *Mineralogy and Petrology* 76, 63–74.
- Bouvier, A., Vervoort, J.D., Patchett, P.J., 2008. The Lu–Hf and Sm–Nd isotopic composition of CHUR: Constraints from unequilibrated chondrites and implications for the bulk composition of terrestrial planets. *Earth and Planetary Science Letters* 273, 48–57.
- Brito Neves, B.B., Santos, E.J., Van Schmus, W.R., 2000. Tectonic history of the Borborema Province. In: Cordani, U.G., Milani, E.J., Thomaz Filho, A., Campos, D.A. (Eds.), *Tectonic Evolution of South America*. 31st International Geological Congress, Rio de Janeiro, 151–182.
- Brito Neves, B.B., Van Schmus, W.R., Santos, E.J., Campos Neto, M.C., Kozuch, M., 1995. O evento Carirís Velhos na Província Borborema: intergração de dados, implicações e perspectivas. *Revista Brasileira de Geociências* 25, 279–296.
- Bueno, J.F., Oliveira, E.P., McNaughton, N.J., Laux, J.H., 2009. U–Pb dating of granites in the Neoproterozoic Sergipano Belt, NE-Brazil: implications for the timing and duration of

continental collision and extrusion tectonics in the Borborema Province. *Gondwana Research* 15, 86–97.

Carvalho, M.J., 2005. Evolução tectônica do Domínio Marancó-Poço Rendido: registro das orogêneses Cariris Velhos e Brasiliana na Faixa Sergipana, NE do Brasil. Ph.D. thesis. Universidade de Campinas, Campinas.

Caxito, F.A., Santos, L.C.M.L., Ganade, C.E., Bendaoud, A., Fettous, E., Bouyo, M.H., 2020a. Toward an integrated model of geological evolution for NE Brazil-NW Africa: The Borborema Province and its connections to the Trans-Saharan (Benino-Nigerian and Tuareg shields) and Central African orogens. *Brazilian Journal of Geology* 50, e20190122.

Caxito, F.A., Santos, L.C.M.L., Uhlein, A., Dantas, E.L., Alkmim, A.R., Lana, C., 2020b. New U-Pb (SHRIMP) and first Hf isotope constraints on the Tonian (1000-920 Ma) Cariris Velhos event, Borborema Province, NE Brazil. *Brazilian Journal of Geology* 50, e20190082.

Caxito, F.A., Uhlein, A., Dantas, E.L., 2014. The Afeição augen-gneiss Suite and the record of the Cariris Velhos Orogeny (1000–960 Ma) within the Riacho do Pontal fold belt, NE Brazil. *Journal of South American Earth Sciences* 51, 12–27.

Caxito, F.A., Uhlein, A., Dantas, E.L., Stevenson, R., Salgado, S.S., Dussin, I.A., Sial, A.N., 2016. A complete Wilson Cycle recorded within the Riacho do Pontal Orogen, NE Brazil: implications for the Neoproterozoic evolution of the Borborema Province at the heart of West Gondwana. *Precambrian Research* 282, 97–120.

Chapman, J.B., Ducea, M.N., Kapp, P., Gehrels, G.E., DeCelles, P.G., 2017. Spatial and temporal radiogenic isotopic trends of magmatism in Cordilleran orogens. *Gondwana Research* 48, 189–204.

Chappell, B.W., White, A.J.R., 2001. Two contrasting granite types: 25 years later. *Australian Journal of Earth Sciences* 48, 489–499.

Chu, N.C., Taylor, R.N., Chavagnac, V., Nesbitt, R.W., Boella, R.M., Milton, J.A., German, C.R., Bayon, G., Burton, K., 2002. Hf isotope ratio analysis using multi-collector inductively coupled plasma mass spectrometry: an evaluation of isobaric interference corrections. *Journal of Analytical Atomic Spectrometry* 17, 1567–1574.

Clemens, J.D., 2018. Granitic magmas with I-type affinities, from mainly metasedimentary sources: the Harcourt batholith of southeastern Australia. *Contributions to Mineralogy and Petrology* 173, 1–20.

- Clemens, J.D., Stevens, G., Farina, F., 2011. The enigmatic sources of I-type granites: The peritectic connexion. *Lithos* 126, 174–181.
- Conceição, J.A., 2019. Magmatismo leucogranítico do Domínio Macururé, Sistema Orogênico Sergipano, NE do Brasil. Ph.D. thesis. Universidade Federal da Bahia, Salvador.
- Conceição, J.A., Rosa, M.L.S., Conceição, H., 2016. Sienogranitos leucocráticos do Domínio Macururé, Sistema Orogênico Sergipano, Nordeste do Brasil: Stock Glória Sul. *Brazilian Journal of Geology* 46, 63–77.
- Conceição, R. V., Green, D.H., 2004. Derivation of potassic (shoshonitic) magmas by decompression melting of phlogopite+pargasite lherzolite. *Lithos* 72, 209–229.
- Condamine, P., Médard, E., 2014. Experimental melting of phlogopite-bearing mantle at 1 GPa: Implications for potassic magmatism. *Earth and Planetary Science Letters* 397, 80–92.
- Corfu, F., 2003. Atlas of zircon textures. *Reviews in Mineralogy and Geochemistry* 53, 469–500.
- Costa, F.G., Klein, E.L., Lafon, J.M., Milhomem Neto, J.M., Galarza, M.A., Rodrigues, J.B., Naleto, J.L.C., Corrêa Lima, R.G., 2018. Geochemistry and U–Pb–Hf zircon data for plutonic rocks of the Troia Massif, Borborema Province, NE Brazil: Evidence for reworking of Archean and juvenile Paleoproterozoic crust during Rhyacian accretionary and collisional tectonics. *Precambrian Research* 311, 167–194.
- Couzinié, S., Laurent, O., Moyen, J.F., Zeh, A., Bouilhol, P., Villaros, A., 2016. Post-collisional magmatism: Crustal growth not identified by zircon Hf–O isotopes. *Earth and Planetary Science Letters* 456, 182–195.
- Davison, I., Santos, R.A., 1989. Tectonic evolution of the Sergipano Fold Belt, NE Brazil, during the Brasiliano Orogeny. *Precambrian Research* 45, 319–342.
- DePaolo, D.J., 1988. Neodymium Isotope Geochemistry: An Introduction. Springer-Verlag, Berlin.
- DePaolo, D.J., 1981. Trace element and isotopic effects of combined wallrock assimilation and fractional crystallization. *Earth and Planetary Science Letters* 53, 189–202.
- Fernandes, D.M., Lisboa, V.A.C., Rosa, M.L.S., Conceição, H., 2020. Petrologia e idade do Stock Fazenda Lagoas, Domínio Macururé, Sistema Orogênico Sergipano, NE-Brasil. *Geologia USP. Série Científica* 20, 39–60.

- Ferreira, V.P., Neves, C.H.S., Silva, T.R., Lima, M.M.C., Sial, A.N., da Silva Filho, A.F., 2021. Neoproterozoic high magmatic addition rate episode building a composite batholith in northeastern Brazil, and implications for the western Gondwana assembly. *Precambrian Research* 363, 106331.
- Ferry, J.M., Watson, E.B., 2007. New thermodynamic models and revised calibrations for the Ti-in-zircon and Zr-in-rutile thermometers. *Contributions to Mineralogy and Petrology* 154, 429–437.
- Fisher, C.M., Bauer, A.M., Luo, Y., Sarkar, C., Hanchar, J.M., Vervoort, J.D., Tapster, S.R., Horstwood, M., Pearson, D.G., 2020. Laser ablation split-stream analysis of the Sm-Nd and U-Pb isotope compositions of monazite, titanite, and apatite – Improvements, potential reference materials, and application to the Archean Saglek Block gneisses. *Chemical Geology* 539, 119493.
- Fourcade, S., Allegre, C.J., 1981. Trace elements behavior in granite genesis: A case study The calc-alkaline plutonic association from the Querigut complex (Pyrénées, France). *Contributions to Mineralogy and Petrology* 1981 76:2 76, 177–195.
- Frost, B.R., Barnes, C.G., Collins, W.J., Arculus, R.J., Ellis, D.J., Frost, C.D., 2001a. A geochemical classification for granitic rocks. *Journal of Petrology* 42, 2033–2048.
- Frost, B.R., Chamberlain, K.R., Schumacher, J.C., 2001b. Spinel (titanite): phase relations and role as a geochronometer. *Chemical Geology* 172, 131–148.
- Furman, T., Graham, D., 1999. Erosion of lithospheric mantle beneath the East African Rift system: geochemical evidence from the Kivu volcanic province. *Lithos* 48, 237–262.
- Ganade, C.E., Weinberg, R.F., Caxito, F.A., Lopes, L.B.L., Tesser, L.R., Costa, I.S., 2021. Decratonization by rifting enables orogenic reworking and transcurrent dispersal of old terranes in NE Brazil. *Scientific Reports* 2021 11:1 11, 1–13.
- Ganade de Araujo, C.E., Weinberg, R.F., Cordani, U.G., 2013. Extruding the Borborema Province (NE-Brazil): a two-stage Neoproterozoic collision process. *Terra Nova* 26, 157–168.
- Gray, D.R., Foster, D.A., Maas, R., Spaggiari, C. v., Gregory, R.T., Goscombe, B., Hoffmann, K.H., 2007. Continental growth and recycling by accretion of deformed turbidite fans and remnant ocean basins: Examples from Neoproterozoic and Phanerozoic orogens. *Memoir of the Geological Society of America* 200, 63–92.

- Griffin, W.L., Wang, X., Jackson, S.E., Pearson, N.J., O'Reilly, S.Y., Xu, X., Zhou, X., 2002. Zircon chemistry and magma mixing, SE China: In-situ analysis of Hf isotopes, Tonglu and Pingtan igneous complexes. *Lithos* 61, 237–269.
- Guimarães, I.P., Lara de Brito, M.F., Lages, G.A., Silva Filho, A.F., Santos, L., Brasilino, R.G., 2016. Tonian granitic magmatism of the Borborema Province, NE Brazil: A review. *Journal of South American Earth Sciences* 68, 97–112.
- Guimarães, I.P., Van Schmus, W.R., de Brito Neves, B.B., Bretas Bittar, S.M., Silva Filho, A.F., Armstrong, R., 2012. U–Pb zircon ages of orthogneisses and supracrustal rocks of the Cariris Velhos belt: Onset of Neoproterozoic rifting in the Borborema Province, NE Brazil. *Precambrian Research* 192–195, 52–77.
- Hao, H., Campbell, I.H., Park, J.W., 2022. Nd-Hf isotopic systematics of the arc mantle and their implication for continental crust growth. *Chemical Geology* 602, 120897.
- Heaman, L.M., 2009. The application of U–Pb geochronology to mafic, ultramafic and alkaline rocks: An evaluation of three mineral standards. *Chemical Geology* 261, 43–52.
- Hofmann, A.W., Jochum, K.P., Seufert, M., White, W.M., 1986. Nb and Pb in oceanic basalts: new constraints on mantle evolution. *Earth and Planetary Science Letters* 79, 33–45.
- Hoskin, P.W.O., 2005. Trace-element composition of hydrothermal zircon and the alteration of Hadean zircon from the Jack Hills, Australia. *Geochimica et Cosmochimica Acta* 69, 637–648.
- Hoskin, P.W.O., Schaltegger, U., 2003. The composition of zircon and igneous and metamorphic petrogenesis. *Reviews in Mineralogy and Geochemistry* 53, 27–62.
- Jackson, S.E., Pearson, N.J., Griffin, W.L., Belousova, E.A., 2004. The application of laser ablation-inductively coupled plasma-mass spectrometry to in situ U–Pb zircon geochronology. *Chemical Geology* 211, 47–69.
- Janoušek, V., Farrow, C.M., Erban, V., 2006. Interpretation of whole-rock geochemical data in igneous geochemistry: introducing Geochemical Data Toolkit (GCDkit). *Journal of Petrology* 47, 1255–1259.
- Kohn, M.J., 2017. Titanite petrochronology. *Reviews in Mineralogy and Geochemistry* 83, 419–441.
- Kourim, F., Wang, K.L., Beinlich, A., Chieh, C.J., Dygert, N., Lafay, R., Kovach, V., Michibayashi, K., Yarmolyuk, V., Iizuka, Y., 2021. Metasomatism of the off-cratonic

lithospheric mantle beneath Hangay Dome, Mongolia: Constraints from trace-element modelling of lherzolite xenoliths. *Lithos* 400–401, 106407.

Kozuch, M., 2003. Isotopic and trace element geochemistry of early Neoproterozoic gneissic and metavolcanic rocks in the Cariris Velhos orogen of the Borborema Province, Brazil, and their bearing on tectonic setting. Ph.D. thesis. University of Kansas, Lawrence.

Lameyre, J., Bowden, P., 1982. Plutonic rock types series: discrimination of various granitoid series and related rocks. *Journal of Volcanology and Geothermal Research* 14, 169–186.

le Maitre, R.W., Streckeisen, A., Zanettin, B., le Bas, M.J., Bonin, B., Bateman, P. (Eds.), 2002. *Igneous Rocks: a classification and glossary of terms, recommendations of the International Union of Geological Sciences Subcommittee on the Systematics of Igneous Rocks*, 2nd ed. Cambridge University Press, Cambridge.

Lima, A.L.R., 2021. Petrologia do Stock Altos Verdes, Domínio Macururé, Província Borborema. M.S. dissertation. Universidade Federal de Sergipe, São Cristóvão.

Lima, D.R., 2016. Caracterização petrológica e geoquímica do pluton Curitiba, Domínio Poço Redondo-Marancó, Cinturão Sergipano. M.S. dissertation. Universidade Federal de Pernambuco, Recife.

Lima, H.M., Pimentel, M.M., Fuck, R.A., Santos, L.C.M.L., Dantas, E.L., 2018. Geochemical and detrital zircon geochronological investigation of the metavolcanosedimentary Araticum complex, Sergipano Fold Belt: Implications for the evolution of the Borborema Province, NE Brazil. *Journal of South American Earth Sciences* 86, 176–192.

Lima, H.M., Pimentel, M.M., Santos, L.C.M.L., Dantas, E.L., 2019. Isotopic and geochemical characterization of the metavolcano-sedimentary rocks of the Jirau do Ponciano Dome: A structural window to a Paleoproterozoic continental arc root within the Southern Borborema Province, Northeast Brazil. *Journal of South American Earth Sciences* 90, 54–69.

Lima, M.M.C., Ferreira, V.P., Silva, T.R., Sial, A.N., Carvalho, B.M.B., 2021. Crustal growth during Western Gondwana amalgamation and onset of the Brasiliano orogeny: Insights from geochemistry and Pb–Sr–Nd–O isotopes from granites in northeastern Brazil. *Lithos* 396–397, 106223.

Lima, J. v, Guimarães, I.P., Neves, S.P., Basei, M.A.S., Silva Filho, A.F., Brainer, C.C.G., 2021. Post-collisional, high-Ba-Sr Teixeira Batholith granites: Evidence for recycling of

- Paleoproterozoic crust in the Alto Pajeú domain, Borborema Province – NE-Brazil. *Lithos* 404–405, 106469.
- Lisboa, V.A.C., Conceição, H., Rosa, M.L.S., Fernandes, D.M., 2019. The onset of post-collisional magmatism in the Macururé Domain, Sergipano Orogenic System: The Glória Norte Stock. *Journal of South American Earth Sciences* 89, 173–188.
- Long, L.E., Castellana, C.H., Sial, A.N., 2005. Age, origin and cooling history of the Coronel João Sá Pluton, Bahia, Brazil. *Journal of Petrology* 46, 255–273.
- Ludwig, K., 2009a. User's Manual for Isoplot 3.70, Spec. Pub. ed. Berkeley Geochronology Center, Berkeley.
- Ludwig, K., 2009b. SQUID 2: A User's Manual, Spec. Pub. ed, Berkeley Geochronology Center. Berkeley.
- McDonough, W.F., Sun, S.S., 1995. The composition of the Earth. *Chemical Geology* 120, 223–253.
- Menzies, M.A., Rogers, N., Tindle, A.G., Hawkesworth, C.J., 1987. Metasomatic and enrichment processes in lithospheric peridotites, an effect of asthenosphere-lithosphere interaction. In: Menzies, M.A., Hawkesworth, C.J. (Eds.), *Mantle Metasomatism*. Academic Press, London, 313–361.
- Middlemost, E.A.K., 1994. Naming materials in the magma/igneous rock system. *Earth-Science Reviews* 37, 215–224.
- Miller, C.F., McDowell, S.M., Mapes, R.W., 2003. Hot and cold granites? Implications of zircon saturation temperatures and preservation of inheritance. *Geology* 31, 529–532.
- Morel, M.L.A., Nebel, O., Nebel-Jacobsen, Y.J., Miller, J.S., Vroon, P.Z., 2008. Hafnium isotope characterization of the GJ-1 zircon reference material by solution and laser-ablation MC-ICPMS. *Chemical Geology* 255, 231–235.
- Neves, S.P., 2021. Comparative geological evolution of the Borborema Province and São Francisco Craton (eastern Brazil): Decratonization and crustal reworking during West Gondwana assembly and implications for paleogeographic reconstructions. *Precambrian Research* 355, 106119.

- Neves, S.P., 2003. Proterozoic history of the Borborema province (NE Brazil): Correlations with neighboring cratons and Pan-African belts and implications for the evolution of western Gondwana. *Tectonics* 22, 1–14.
- Neves, S.P., Bruguier, O., Bosch, D., da Silva, J.M.R., Mariano, G., 2008. U–Pb ages of plutonic and metaplutonic rocks in southern Borborema Province (NE Brazil): Timing of Brasiliano deformation and magmatism. *Journal of South American Earth Sciences* 25, 285–297.
- Neves, S.P., Bruguier, O., Silva, J.M.R., Mariano, G., Silva Filho, A.F., Teixeira, C.M.L., 2015. From extension to shortening: Dating the onset of the Brasiliano Orogeny in eastern Borborema Province (NE Brazil). *Journal of South American Earth Sciences* 58, 238–256.
- Neves, S.P., Silva, J.M.R., Bruguier, O., 2019. The metasedimentary Macururé Complex (Sergipano Belt, Borborema Province, Brazil) in southern Alagoas state: geology and geochronology. *Journal of the Geological Survey of Brazil* 2, 17–25.
- Ohta, T., Arai, H., 2007. Statistical empirical index of chemical weathering in igneous rocks: A new tool for evaluating the degree of weathering. *Chemical Geology* 240, 280–297.
- Oliveira, E.P., 2012. Geologia da Faixa Sergipana no Estado da Bahia. In: Barbosa, J., Mascarenhas, J.F., Correa Gomes, L.C., Dominguez, J.M.L., S, S.J. (Eds.), *Geologia Da Bahia. Pesquisa e Atualização*. Companhia Baiana de Pesquisa Mineral, 179–190.
- Oliveira, E.P., Bueno, J.F., McNaughton, N.J., Silva Filho, A.F., Nascimento, R.S., Donatti-Filho, J.P., 2015a. Age, composition, and source of continental arc- and syn-collision granites of the Neoproterozoic Sergipano Belt, Southern Borborema Province, Brazil. *Journal of South American Earth Sciences* 58, 257–280.
- Oliveira, E.P., McNaughton, N.J., Windley, B.F., Carvalho, M.J., Nascimento, R.S., 2015b. Detrital zircon U–Pb geochronology and whole-rock Nd-isotope constraints on sediment provenance in the Neoproterozoic Sergipano Orogen, Brazil: from early passive margins to late foreland basins. *Tectonophysics* 662, 183–194.
- Oliveira, E.P., Tarney, J., 1990. Petrogenesis of the Canindé de São Francisco complex: A major Late Proterozoic gabbroic body in the Sergipe Foldbelt, northeastern Brazil. *Journal of South American Earth Sciences* 3, 125–140.

- Oliveira, E.P., Windley, B.F., Araújo, M.N.C., 2010. The Neoproterozoic Sergipano Orogenic Belt, NE Brazil: a complete plate tectonic cycle in Western Gondwana. *Precambrian Research* 181, 64–84.
- Oliveira, E.P., Windley, B.F., McNaughton, N.J., Bueno, J.F., Nascimento, R.S., Carvalho, M.J., Araújo, M.N.C., 2017. The Sergipano Belt. In: Heilbron, M., Cordani, U.G., Alkmim, F.F. (Eds.), *São Francisco Craton, Eastern Brazil: Tectonic Genealogy of a Miniature Continent*. Springer International Publishing, Cham, 241–254.
- Oliveira, I.R., 2020. Petrogênese dos stocks Mocambo e Frutuoso, Domínio Macururé, Sistema Orogênico Sergipano. M.S. dissertation. Universidade Federal de Sergipe, São Cristóvão.
- Orejana, D., Villaseca, C., Kristoffersen, M., 2020. Geochemistry and geochronology of mafic rocks from the Spanish Central System: Constraints on the mantle evolution beneath central Spain. *Geoscience Frontiers* 11, 1651–1667.
- Passos, L.H., Fuck, R.A., Chemale, F., Lenz, C., Pimentel, M.M., Machado, A., Pinto, V.M., 2021. Neoproterozoic (740-680 Ma) arc-back-arc magmatism in the Sergipano Belt, southern Borborema Province, Brazil. *Journal of South American Earth Sciences* 109, 103280.
- Passos, L.H., Fuck, R.A., Junior, F.C., Lenz, C., Porcher, C.C., Pinto, V.M., Santos, L.C.M. de L., 2022. Neoproterozoic pre-collisional events recorded in the Sergipano belt, Southern Borborema Province, West Gondwana. *International Geology Review* 64, 1–19.
- Patchett, P.J., Tatsumoto, M., 1981. A routine high-precision method for Lu-Hf isotope geochemistry and chronology. *Contributions to Mineralogy and Petrology* 75, 263–267.
- Patiño Douce, A.E., 1999. What do experiments tell us about the relative contributions of crust and mantle to the origin of granitic magmas? Geological Society, London, Special Publications 168, 55–75.
- Patiño Douce, A.E., Beard, J.S., 1995. Dehydration-melting of Biotite Gneiss and Quartz Amphibolite from 3 to 15 kbar. *Journal of Petrology* 36, 707–738.
- Peccerillo, A., Taylor, S.R., 1976. Geochemistry of eocene calc-alkaline volcanic rocks from the Kastamonu area, Northern Turkey. *Contributions to Mineralogy and Petrology* 58, 63–81.
- Pe-Piper, G., Piper, D.J.W., Koukouvelas, I., Dolansky, L.M., Kokkalas, S., 2009. Postorogenic shoshonitic rocks and their origin by melting underplated basalts: The Miocene of Limnos, Greece. *Geological Society of America Bulletin* 121, 39–54.

- Pereira, F.S., Rosa, M.L.S., Conceição, H., Bertotti, A.L., 2020. Age, composition, and source of the Macururé Mafic Suite, Southern Borborema Province, Brazil. *Brazilian Journal of Geology* 50, e20190105.
- Pinto, V.M., Koester, E., Debruyne, D., Chemale, F., Marques, J.C., Porcher, C.C., Passos, L.H., Lenz, C., 2020. Petrogenesis of the mafic-ultramafic Canindé layered intrusion, Sergipano Belt, Brazil: Constraints on the metallogenesis of the associated Fe–Ti oxide ores. *Ore Geology Reviews* 122, 103535.
- Roberts, N.M.W., Spencer, C.J., 2015. The zircon archive of continent formation through time. *Geological Society, London, Special Publications* 389, 197–225.
- Rollinson, H., 1993. *Using geochemical data: evaluation, presentation, interpretation*. Longman, Essex.
- Rosa, M.L.S., Conceição, J.A., Marinho, M.M., Pereira, F.S., Conceição, H., 2020. U-Pb SHRIMP dating of the Itabaiana Dome: a Mesoarchean basement inlier (2.83 Ga) in the Sergipano Orogenic System, Borborema Province. *Brazilian Journal of Geology* 50, e20190106.
- Rubatto, D., 2017. Zircon: the metamorphic mineral. *Reviews in Mineralogy and Geochemistry* 83, 261–295.
- Rudnick, R.L., Gao, S., 2003. Composition of the continental crust. *Treatise on Geochemistry* 1–64.
- Rushmer, T., 1991. Partial melting of two amphibolites: contrasting experimental results under fluid-absent conditions. *Contributions to Mineralogy and Petrology* 107, 41–59.
- Santos, C., Zincone, S.A., Queiroga, G.N., Bersan, S.M., Lana, C.C., Oliveira, E.P., 2022. Evidence for change in crust formation process during the Paleoproterozoic in the São Francisco Craton (Gavião Block): Coupled zircon Lu-Hf and U-Pb isotopic analyses and tectonic implications. *Precambrian Research* 368, 106472.
- Santos, E.J., Schmus, W.R. van, Kozuch, M., Neves, B.B. de B., 2010. The Cariris Velhos tectonic event in Northeast Brazil. *Journal of South American Earth Sciences* 29, 61–76.
- Santos, I.S., Conceição, H., Rosa, M.L.S., Marinho, M.M., 2019. Magmatismos shoshonítico e cálcio-alcalino de alto potássio pós-orogênico (615 Ma) na porção leste do Domínio Macururé, Sistema Orogênico Sergipano: Stocks Propriá, Amparo do São Francisco e Fazenda Alvorada. *Geologia USP. Série Científica* 19, 9–116.

- Santos, L.Q.S., 2021. Petrogênese do Stock Fazenda Alvorada, Domínio Macururé, Sistema Orogênico Sergipano. M.S. dissertation. Universidade Federal de Sergipe, São Cristóvão.
- Santos, L.R., 2016. Petrologia do Stock Canindé Velho, Sistema Orogênico Sergipano, NE Brasil. M.S. dissertation. Universidade Federal de Sergipe, São Cristóvão.
- Santos, M.M., Lana, C., Scholz, R., Buick, I., Schmitz, M.D., Kamo, S.L., Gerdes, A., Corfu, F., Tapster, S., Lancaster, P., Storey, C.D., Basei, M.A.S., Tohver, E., Alkmim, A., Nalini, H., Krambrock, K., Fantini, C., Wiedenbeck, M., 2017. A New Appraisal of Sri Lankan BB Zircon as a Reference Material for LA-ICP-MS U-Pb Geochronology and Lu-Hf Isotope Tracing. *Geostandards and Geoanalytical Research* 41, 335–358.
- Santos, R.A., Martins, A.A.M., Neves, J.P., Leal, R.A., 1998. Programa de Levantamentos Geológicos Básicos do Brasil: Geologia e recursos minerais do Estado de Sergipe. Escala 1:250.000. Texto explicativo do mapa geológico do Estado de Sergipe. CPRM/DIEDIG/DEPAT;CODISE, Salvador.
- Sato, K., Junior, O.S., Basei, M.A.S., Tassinari, C.C.G., Onoe, A.T., 2016. SHRIMP U-Th-Pb Analyses of titanites: Analytical techniques and examples of Terranes of the South-Southeast of Brazil - Geoscience Institute of the University of São Paulo. *Geologia USP - Serie Cientifica* 16, 3–18.
- Shand, S.J., 1943. *The Eruptive Rocks*, 2nd ed. John Wiley, New York.
- Shaw, S.E., Flood, R.H., 2009. Zircon Hf Isotopic Evidence for Mixing of Crustal and Silicic Mantle-derived Magmas in a Zoned Granite Pluton, Eastern Australia. *Journal of Petrology* 50, 147–168.
- Silva, C.C., 2014. Petrologia e geocronologia do stock granodiorítico Lagoa do Roçado, Domínio Macururé, Faixa Sergipana-SE. M.S. dissertation. Universidade Federal de Sergipe, São Cristóvão.
- Silva Filho, A.F., Guimarães, I.P., Armstrong, R.A., Silva, J.R.M., Schmus, W.R., Farias, D.S., Ferreira, V.P., Amorim, J.V.A., Souza, K., Cocentino, L.M., 2021. A major neoproterozoic crustal boundary in the Borborema province of ne Brazil. *International Geology Review* 64, 1981–2007.
- Silva Filho, A.F., Guimarães, I.P., Santos, L., Armstrong, R., Van Schmus, W.R., 2016. Geochemistry, U–Pb geochronology, Sm–Nd and O isotopes of ca. 50 Ma long ediacaran high-

K syn-collisional magmatism in the Pernambuco Alagoas Domain, Borborema Province, NE Brazil. *Journal of South American Earth Sciences* 68, 134–154.

Silva Filho, A.F., Guimarães, I.P., Van Schmus, W.R., Armstrong, R.A., Rangel da Silva, J.M., Osako, L.S., Cocentino, L.M., 2014. SHRIMP U–Pb zircon geochronology and Nd signatures of supracrustal sequences and orthogneisses constrain the Neoproterozoic evolution of the Pernambuco–Alagoas domain, southern part of Borborema Province, NE Brazil. *International Journal of Earth Sciences* 103, 2155–2190.

Silva Filho, M.A., Bomfim, L.F.C., Santos, R.A., Leal, R.A., Santana, A.C., Filho, P.A.B., 1979. *Geologia da Geossinclinal Sergipana e do seu embasamento - Alagoas, Sergipe e Bahia: Projeto Baixo São Francisco/Vaza-Barris*. DNPM/CPRM, Brasília.

Silva, J.M.R., Campos Neto, M.C., Brito Neves, B.B., 1995. Deformação e metamorfismo principais de uma parte da Faixa Sul-Alagoana (Complexo Macururé), Sistema de Dobramentos Sergipano, Nordeste do Brasil. *Revista Brasileira de Geociências* 25, 343–350.

Silva, J.P.A., Lana, C., Mazoz, A., Buick, I., Scholz, R., 2022. U-Pb Saturn: New U-Pb/Pb-Pb Data Reduction Software for LA-ICP-MS. *Geostandards and Geoanalytical Research* 1–18.

Sisson, T.W., Ratajeski, K., Hankins, W.B., Glazner, A.F., 2005. Voluminous granitic magmas from common basaltic sources. *Contributions to Mineralogy and Petrology* 148, 635–661.

Sláma, J., Košler, J., Condon, D.J., Crowley, J.L., Gerdes, A., Hanchar, J.M., Horstwood, M.S.A., Morris, G.A., Nasdala, L., Norberg, N., Schaltegger, U., Schoene, B., Tubrett, M.N., Whitehouse, M.J., 2008. Plešovice zircon — A new natural reference material for U–Pb and Hf isotopic microanalysis. *Chemical Geology* 249, 1–35.

Soares, H.S., Sousa, C.S., Rosa, M.L.S., Conceição, H., 2019. Petrologia dos stocks Santa Maria, Monte Pedral, Bom Jardim, Boa Esperança e Niterói, Suíte Intrusiva Serra do Catu, estado de Sergipe, NE Brasil. *Revista Geologia USP. Série Científica* 19, 63–84.

Söderlund, U., Patchett, P.J., Vervoort, J.D., Isachsen, C.E., 2004. The ^{176}Lu decay constant determined by Lu–Hf and U–Pb isotope systematics of Precambrian mafic intrusions. *Earth and Planetary Science Letters* 219, 311–324.


Sousa, C.S., Soares, H.S., Rosa, M.L.S., Conceição, H., 2022. Injection of enriched lithospheric mantle magmas explains the formation of microgranular enclaves in the Rio Jacaré Batholith, Borborema Province, Brazil. *Brazilian Journal of Geology* 52, e2022033.


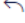
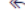
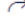
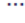
- Sousa, C.S., Soares, H.S., Rosa, M.L.S., Conceição, H., 2019. Petrologia e geocronologia do Batólito Rio Jacaré, Domínio Poço Redondo, Sistema Orogênico Sergipano, NE do Brasil. *Geologia USP. Série Científica* 19, 171–194.
- Sousa, E.S., 2020. Petrologia do magmatismo ediacarano na porção central do Domínio Macururé: stocks Graccho Cardoso e Queimadinha. M.S. dissertation. Universidade Federal de Sergipe, São Cristóvão.
- Spalletta, B.M., Oliveira, E.P., 2017. Idades LA-SF-ICPMS em zircão dos quartzitos da Formação Santa Cruz, Orógeno Sergipano, Alagoas. XXVII Simpósio de Geologia Do Nordeste. Sociedade Brasileira de Geologia, João Pessoa.
- Spencer, C.J., Kirkland, C.L., Roberts, N.M.W., Evans, N.J., Liebmann, J., 2020. Strategies towards robust interpretations of in situ zircon Lu–Hf isotope analyses. *Geoscience Frontiers* 11, 843–853.
- Spencer, C.J., Kirkland, C.L., Taylor, R.J.M., 2016. Strategies towards statistically robust interpretations of in situ U–Pb zircon geochronology. *Geoscience Frontiers* 7, 581–589.
- Stacey, J.S., Kramers, J.D., 1975. Approximation of terrestrial lead isotope evolution by a two-stage model. *Earth and Planetary Science Letters* 26, 207–221.
- Steiger, R.H., Jäger, E., 1977. Subcommittee on geochronology: convention on the use of decay constants in geo- and cosmochronology. *Earth and Planetary Science Letters* 36, 359–362.
- Teixeira, L., 2005. GENESIS 4.0: Modelos geoquímicos.
- Tesser, L.R., Ganade, C.E., Weinberg, R.F., Basei, M.A.S., Moraes, R., Batista, L.A., 2021. Ultrahigh-temperature Palaeoproterozoic rocks in the Neoproterozoic Borborema Province, implications for São Francisco Craton dispersion in NE Brazil. *Journal of Metamorphic Geology*.
- Thirlwall, M.F., Anczkiewicz, R., 2004. Multidynamic isotope ratio analysis using MC–ICP–MS and the causes of secular drift in Hf, Nd and Pb isotope ratios. *International Journal of Mass Spectrometry* 235, 59–81.
- Van Schmus, W.R., Kozuch, M., Brito Neves, B.B., 2011. Precambrian history of the Zona Transversal of the Borborema Province, NE Brazil: Insights from Sm–Nd and U–Pb geochronology. *Journal of South American Earth Sciences* 31, 227–252.

- Van Schmus, W.R., Oliveira, E.P., Silva Filho, A.F., Toteu, S.F., Penaye, J., Guimarães, I.P., Silva Filho, A.F., Toteu, S.F., Penaye, J., Guimarães, I.P., 2008. Proterozoic links between the Borborema Province, NE Brazil, and the Central African fold belt. *Geological Society Special Publication* 294, 69–99.
- Vervoort, J.D., Kemp, A.I.S., 2016. Clarifying the zircon Hf isotope record of crust–mantle evolution. *Chemical Geology* 425, 65–75.
- Warr, L.N., 2021. IMA–CNMNC approved mineral symbols. *Mineralogical Magazine* 85, 291–320.
- Watson, E.B., Harrison, T.M., 1983. Zircon saturation revisited: temperature and composition effects in a variety of crustal magma types. *Earth and Planetary Science Letters* 64, 295–304.
- Watson, E.B., Wark, D.A., Thomas, J.B., 2006. Crystallization thermometers for zircon and rutile. *Contributions to Mineralogy and Petrology* 151, 413–433.
- Weaver, B.L., Tarney, J., Windley, B.F., Leake, B.E., 1982. Geochemistry and petrogenesis of Archaean metavolcanic amphibolites from Fiskenaesset, S. W. Greenland. *Geochimica et Cosmochimica Acta* 46, 2203–2215.
- Wilson, M., 1989. *Igneous Petrogenesis: a Global Tectonic Approach*. Springer Netherlands, Dordrecht.
- Woodhead, J.D., Hergt, J.M., 2005. A preliminary appraisal of seven natural zircon reference materials for in situ Hf isotope determination. *Geostandards and Geoanalytical Research* 29, 183–195.
- Woodhead, J.D., Hergt, J.M., Davidson, J.P., Eggins, S.M., 2001. Hafnium isotope evidence for ‘conservative’ element mobility during subduction zone processes. *Earth and Planetary Science Letters* 192, 331–346.
- Workman, R.K., Hart, S.R., 2005. Major and trace element composition of the depleted MORB mantle (DMM). *Earth and Planetary Science Letters* 231, 53–72.

CAPÍTULO III CONSTRAINTS ON THE SOURCE AND PETROGENESIS OF EARLY EDIACARAN SHOSHONITIC MAFIC MAGMATISM AND HIGH-K CALC-ALKALINE GRANITOIDS IN THE SERGIPANO OROGENIC SYSTEM, BORBOREMA PROVINCE, BRAZIL

Artigo submetido em: Precambrian Research (05/07/2023)

PRECAM-D-23-00270 - Confirming your submission to Precambrian Research 

 Precambrian Research <em@editorialmanager.com>    
Para: Você Qua, 05/07/2023 20:11

This is an automated message.

Constraints on the source and petrogenesis of early Ediacaran shoshonitic mafic magmatism and high-K calc-alkaline granitoids in the Sergipano Orogenic System, Borborema Province, Brazil

Dear Mr Pereira,

We have received the above referenced manuscript you submitted to Precambrian Research. It has been assigned the following manuscript number: PRECAM-D-23-00270.

To track the status of your manuscript, please log in as an author at <https://www.editorialmanager.com/precam/>, and navigate to the "Submissions Being Processed" folder.

Thank you for submitting your work to this journal.

Kind regards,
Precambrian Research

Constraints on the source and petrogenesis of early Ediacaran shoshonitic mafic magmatism and high-K calc-alkaline granitoids in the Sergipano Orogenic System, Borborema Province, Brazil

Fábio Santos Pereira^{a,b,*}, Jean-Michel Lafon^b, Maria de Lourdes da Silva Rosa^c, Herbet Conceição^c, Anelise Losangela Bertotti^d, João Marinho Milhomem Neto^b, Cristiano Lana^e, Edinei Koester^f

^a Pós-Graduação em Geologia e Geoquímica, Instituto de Geociências, Universidade Federal do Pará, Rua Augusto Corrêa 01, 66075-110 Belém, Pará, Brazil

^b Laboratório de Geologia Isotópica, Instituto de Geociências, Universidade Federal do Pará, Rua Augusto Corrêa 01, Rua Augusto Corrêa, 01, 66075-110 Belém, Pará, Brazil

^c Pós-Graduação em Geociências e Análise de Bacias, Universidade Federal de Sergipe, Avenida Marechal Rondon S/N, 49100-000 São Cristóvão, Sergipe, Brazil

^d Departamento de Geologia, Universidade Federal de Pernambuco, Cidade Universitária, Avenida da Arquitetura S/N, 50740-550 Recife, Pernambuco, Brazil

^e Applied Isotope Research Group, Departamento de Geologia, Universidade Federal de Ouro Preto, Rua Diogo de Vasconcelos 122, 35400-000 Ouro Preto, Minas Gerais, Brazil

^f Instituto de Geociências, Universidade Federal do Rio Grande do Sul, Avenida Bento Gonçalves 9500, 91570-900 Porto Alegre, Rio Grande do Sul, Brazil

*Corresponding author: Programa de Pós-Graduação em Geologia e Geoquímica, Instituto de Geociências, Universidade Federal do Pará, 66075-110 Belém, Pará, Brazil

E-mail address: fabio.pereira@ig.ufpa.br (F.S. Pereira)

ABSTRACT

The Ediacaran Capela pluton (ca. 630 Ma) intruded the metasedimentary succession of the Sergipano Orogenic System along the oriental segment of the Macururé Domain, southern Borborema Province, during the early-collisional stage of the Brasiliano/Pan-African Orogeny. This magmatic body exhibits a wide diversity of rocks, comprising hornblendites, gabbro-norites, gabbros, diorites, granodiorites, and granites. Shoshonitic mafic rocks and high-K calc-alkaline granitoids show significant enrichments in LILE and LREE and depletions in HFSE. Ultramafic and mafic rocks display a conspicuous crustal signature, yielding subchondritic $\epsilon\text{Nd}_{(t)}$ (-5.2 to -2.0) and zircon $\epsilon\text{Hf}_{(t)}$ (-6.5 to -2.2), along with variable radiogenic Sr ($^{87}\text{Sr}/^{86}\text{Sr}_{(t)} = 0.708\text{-}0.710$) and Pb ($^{206}\text{Pb}/^{204}\text{Pb} = 18.50\text{-}19.18$, $^{207}\text{Pb}/^{204}\text{Pb} = 15.69\text{-}15.77$, $^{208}\text{Pb}/^{204}\text{Pb} = 38.54\text{-}39.62$) isotopic compositions. The dominant factors controlling the geochemical features of the mafic magmas were the enriched signature of the lithospheric mantle source and partial melting degree. Mantle source metasomatism is thought to have occurred by incorporating subducted sediments into the mantle wedge before the onset of the Brasiliano Orogeny. Geochemical modeling demonstrates that low partial melting degrees (5-10%) of phlogopite-bearing lithospheric mantle in the spinel stability field metasomatized by 5-10% subducted sediments may account for the main characteristics of the Capela pluton. Introducing sedimentary material into the mantle caused a decrease in Sm/Nd and Lu/Hf ratios while increasing the Rb/Sr, U/Pb, and Th/Pb ratios, which led to the time-integrated evolved isotopic signature observed in mafic rocks. The coeval high-K calc-alkaline granitoids are metaluminous to slightly peraluminous. The isotopic compositions of Nd ($\epsilon\text{Nd}_{(t)} = -3.6$ to -3.4 , $\text{Nd-T}_{\text{DM}} \sim 1.3$ Ga), Sr ($^{87}\text{Sr}/^{86}\text{Sr}_{(t)} = 0.705\text{-}0.711$), and Pb ($^{206}\text{Pb}/^{204}\text{Pb} = 18.60\text{-}18.85$, $^{207}\text{Pb}/^{204}\text{Pb} = 15.72\text{-}15.73$, $^{208}\text{Pb}/^{204}\text{Pb} = 38.64\text{-}39.17$) isotopes partially overlap those of the ultramafic-mafic rocks. Their petrological and isotopic features are consistent with derivation from an ancient amphibolitic lower crustal source, probably related to the Tonian Cariris Velhos event. We argue that the ascension and emplacement of hydrous mantle-derived magmas as successive sills into the lower crust produced a deep hot zone beneath the Sergipano Orogenic System during the onset of the Brasiliano/Pan-African Orogeny. Aqueous fluid released from such potassic mafic magmas favored the partial melting of surrounding rocks, producing contemporary granitic magma.

Keywords: Subduction-modified lithospheric mantle; Potassic magmatism; Water-rich mafic magma; Crustal anatexis; Western Gondwana; Sr–Nd–Pb–Hf isotopes

1 INTRODUCTION

The study of mafic rocks is an indirect way to access the processes of depletion and enrichment affecting the mantle. The enrichment mechanisms are particularly challenging to outline because the recycling of crustal components in the mantle results in mafic magmas with elemental and isotopic evolved signatures similar to those acquired through crustal contamination (Couzinié et al., 2016; Guo et al., 2006; Turner et al., 1996; Xu et al., 2017).

Subduction-modified lithospheric mantle sources can give rise to basic-intermediate rocks showing affinities with the high-K calc-alkaline, shoshonite, and ultrapotassic series (Becker et al., 1999; Couzinié et al., 2016; Foley, 1992; Hawkesworth et al., 1997). Such rock associations have distinctive enrichment in alkalis, large ion lithophile elements (LILE), and light rare earth elements (LREE), along with depletion in Nb-Ta-Ti (Fowler et al., 2008; Morrison, 1980; Murphy, 2020). In addition to its notable importance in the tectonic reconstruction of ancient orogens, mantle-derived magmas play a significant role in the formation of granitoids. The emplacement of underplating basaltic magma yields the heat source and fluids to trigger the partial melting of the lower crust, producing substantial amounts of crustal and hybrid mantle-crust magmas (Annen et al., 2015, 2006; Hildreth and Moorbath, 1988; Moyen et al., 2021; Weinberg and Hasalová, 2015).

The late Cryogenian-Ediacaran magmatism of the Macururé Domain, Sergipano Orogenic System (SOS), NE Brazil, is dominated by granitoids with subordinate stocks of gabbros and diorites (Bueno et al., 2009; Lisboa et al., 2019; Oliveira et al., 2015a; Pereira et al., 2020). The occurrence of mafic rocks was first reported by Silva Filho et al. (1979), who grouped them with the metasedimentary host rocks into the Macururé Group. They remained thus clustered in the following regional cartography works (Santos et al., 1998; Teixeira, 2014) due to the absence of geochronological and geochemical data that would allow their positioning concerning the regional framework. Recent works focused on petrographic, mineral, and whole-rock chemistry, and U–Pb dating has revealed that basaltic magma emplacement occurred between 643 and 628 Ma, coeval with the early stages of felsic magmatism (630–600 Ma) in the SOS (Conceição, 2014; Long et al., 2005; Oliveira et al., 2015a; Pereira et al., 2023).

The Capela pluton is the main mafic intrusion of the Macururé Domain and consists of coexisting hornblendites, gabbros, diorites, and granites. In this contribution, we report elemental and Sr–Nd–Pb isotope geochemistry on whole-rock and zircon Lu–Hf isotopes for mafic rocks and granitoids to constrain the petrogenetic processes and sources involved in magma genesis. We evaluate the role of the metasomatized subcontinental lithospheric mantle

in the generation of shoshonitic mafic magmas, and we propose that this mafic magmatism triggered partial melting of the lower crust and produced the associated high-K calc-alkaline granitoids.

2 GEOLOGICAL BACKGROUND

The SOS is part of the southernmost segment of the Borborema Province, a Brasiliano/Pan-African orogenic belt located in NE Brazil, which extends throughout West Africa (Caxito et al., 2020a; Neves et al., 2015; Trompette, 1997). The build-up of the Borborema Province took place during the Western Gondwana assembly resulting from the convergence of the São Francisco-Congo, West Africa, and Amazonian cratons (Fig. 1a).

The Borborema Province has been compartmentalized into northern, transversal, and southern subprovinces, which are bounded by the continental-scale Pernambuco and Patos shear zones (Van Schmus et al., 2008). The SOS extends between the São Francisco craton (SFC) and Pernambuco-Alagoas Domain (PEAL), composing the southern subprovince with the PEAL and Riacho do Pontal orogen. It consists of a triangular-shaped belt formed by the collision of the PEAL with the SFC (Oliveira et al., 2010; Pereira et al., 2023). Six domains compose the SOS (Davison and Santos, 1989), from north to south: Canindé, Poço Redondo, Marancó, Macururé, Vaza Barris, and Estância (Fig. 1b). These domains display distinct tectonic evolutions and are limited by the Macururé, Belo Monte-Jeremoabo, São Miguel do Aleixo and Itaporanga shear zones. The São Miguel do Aleixo shear zone defines a major crustal boundary north of which voluminous Brasiliano magmatism occurs in the Macururé, Marancó, Poço Redondo and Canindé domains.

The pre-Brasiliano crust in the SOS is represented by:

- (i) Structural windows from the Meosoarchean and Rhyacian-Orosirian basements pulled away from the SFC (Ganade et al., 2021). These ancient remnants crop out in the Itabaiana (2.83 Ga; Rosa et al., 2020), Simão Dias (2.85 Ga; Oliveira, 2012), Jirau do Ponciano domes (ca. 2.0 Ga; Lima et al., 2019), and the Arapiraca complex (ca. 2.0 Ga; Tesser et al., 2021), which are mainly exposed within the supracrustal sequences of the Vaza-Barris and Macururé domains (Fig. 1b).

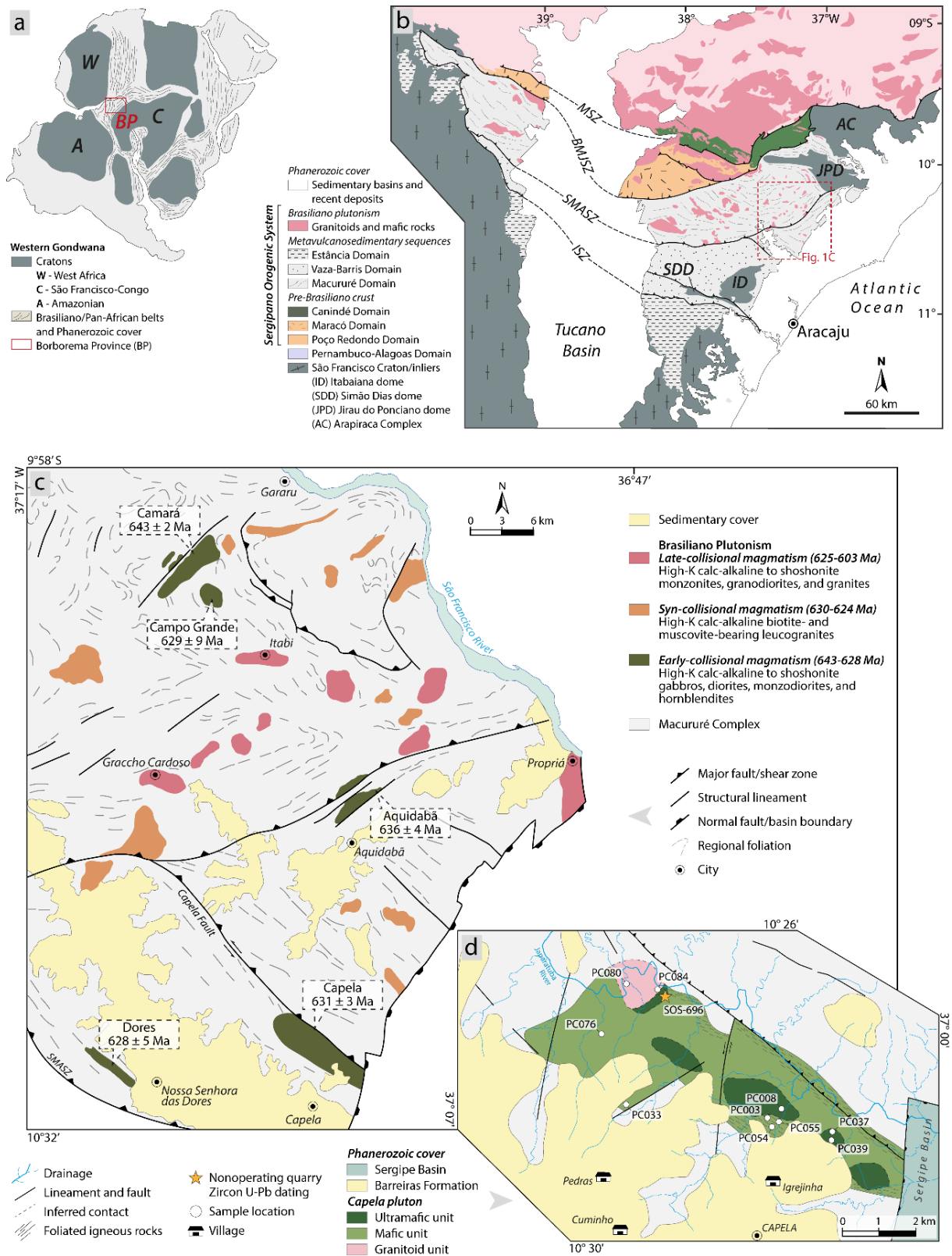


Figure III.1- Geological setting. (a) Predrift reconstruction of South America-Africa along the West Gondwana paleocontinent with Archean/Proterozoic cratons and Brasiliano/Pan-African fold belts. (b) Sketch of the SOS and adjacent region, displaying their geological domains separated by the shear zones from Itaporanga (ISZ), São Miguel do Aleixo (SMASZ), Belo Monte-Jeremoabo (BMJSZ), and Macururé (MSZ). (c) Simplified geological map of the eastern Macururé Domain showing the occurrence zone of mafic rocks (modified from Pereira et al., 2020a). (d) Geological map of the Capela pluton with sample locations.

- (ii) The 980-960 Ma migmatitic complex in the Poço Redondo Domain and 950 Ma A-type orthogneisses in the Marancó Domain related to the Cariris Velhos event (1.0-0.9 Ga), primarily recognized in the transversal zone of the Borborema Province (Brito Neves et al., 1995; Santos et al., 2010). Oliveira et al. (2010) proposed that the protoliths of the Poço Redondo migmatites were emplaced in a magmatic arc developed at the edge of the PEAL, whereas the A-type crustal melts were produced in a context of the extension of this continental block. Conversely, Guimarães et al. (2016) argued that the Tonian migmatites and gneisses in the SOS show geochemical signatures consistent with an extensional setting. Whole-rock Sm–Nd isotope data for Cariris Velhos granitoids of both domains provide weakly negative to positive $\epsilon\text{Nd}_{(t)}$ values (-2.5 to +1.0) and Nd- T_{DM} model ages between 1.48 and 1.63 Ga (Carvalho, 2005).
- (iii) A late Tonian-Cryogenian bimodal igneous association, metavolcanic-sedimentary rocks, gabbroic layered intrusion, and granitoids compose the Canindé Domain. Oliveira et al. (2010) interpreted this association as a rift sequence that started at approximately 715 Ma and could have lasted until 640 Ma. However, other researchers argued that a continental arc/back-arc system could have existed between 740 and 680 Ma (Passos et al., 2022). Regardless of the tectonic setting, the metabasites and gabbroic rocks from the Canindé Domain record a period of crustal growth in the SOS, evidenced by suprachondritic $\epsilon\text{Nd}_{(t)}$ values between +0.4 and +4.9 (Passos et al., 2021; Pinto et al., 2020).

The supracrustal sequence of the Macururé Domain that unconformably recovers the Paleoproterozoic basement consists of two units deposited before the onset of the Brasiliano Orogeny (Oliveira et al., 2015b, 2010). The basal Santa Cruz Formation is formed of quartzites, mainly exposed around the Jirau do Ponciano Dome. The quartzites underlie a thick turbidite-type unit composed of garnet-bearing micaschists, phyllites, and metagraywackes, with intercalations of marble, calc-silicate rocks, and amphibolites (Davison and Santos, 1989; Oliveira et al., 2010; Santos et al., 1998). This sequence records greenschist- to amphibolite-facies metamorphism (Davison and Santos, 1989).

Numerous granitoids and mafic rocks intruded the metasedimentary rocks of the Macururé Domain between 643 and 600 Ma (Bueno et al., 2009; Long et al., 2005; Oliveira et al., 2015a; Pereira et al., 2020). Pereira et al. (2023) recognized three groups of plutonic rocks related to the evolutive stages of the Brasiliano Orogeny (Fig. 1c):

Pre- to early-collisional plutons (643-628 Ma) comprise gabbros and diorites, with minor tonalites and ultramafic rocks showing solid-state deformation associated with the main deformational event in the SOS. These intrusions belong to the Macururé Mafic Suite (Pereira, 2019; Pereira et al., 2020). The injection of such mafic magmas has been attributed to generating coeval high-K crustal granitoids (Pereira et al., 2023).

Syn-collisional plutons include pink- to gray-colored biotite- and muscovite-bearing leucogranites. This magmatism comprises stocks and sheets emplaced along the schistosity of the country rock, preserving their magmatic structures parallel to the regional foliation (Bueno et al., 2009). Such leucogranites are restricted to the Macururé Domain and constrain the PEAL-SFC collisional event at 630-624 Ma (Conceição, 2019; Pereira et al., 2023).

Late-collisional plutons of undeformed monzonites, granodiorites, and granites occur as rounded to subrounded stocks and batholiths, which truncate the structures of the country rocks. Zircon and titanite U–Pb dating yields crystallization ages from 625 to 600 Ma for this group (Long et al., 2005; Pereira et al., 2023 and references therein).

The predominantly potassic character is the most conspicuous feature of the Neoproterozoic magmatism in the SOS. These rocks invariably show affinities with the high-K calc-alkaline, shoshonitic, or even ultrapotassic series (Lisboa et al., 2019; Pereira et al., 2023, 2020; Sousa et al., 2022).

3 THE MACURURÉ MAFIC SUITE: CAPELA PLUTON

The Macururé Mafic Suite encompasses a set of small ultrabasic-basic-intermediate intrusions along the eastern branch of the Macururé Domain (Pereira, 2019). They include the Capela, Dores, Aquidabã, Campo Grande, and Camará plutons, which provide zircon and titanite U–Pb crystallization ages between 643 and 628 Ma (Pereira et al., 2020, 2023). These 5- to 12-km-long bodies are elongated parallel to the regional foliation (Fig. 1c).

Geochemical data reveal affinities with high-K calc-alkaline and shoshonitic magma associations and uniform enrichment in LILE and LREE. Zircon crystals from the Camará pluton provided $\epsilon_{\text{Hf}}(643 \text{ Ma})$ from -6.5 to -4.7 and Siderian Hf- T_{DM}^{C} model ages (assuming a mafic crust with $^{176}\text{Lu}/^{177}\text{Hf} = 0.022$), reflecting the long-lasting incorporation of crustal material in the mantle source (Pereira et al., 2023).

The Capela pluton is a WNW–ESE-elongated intrusion parallel to the regional fabric of the metasedimentary host rocks (Fig. 1d). It is the best-characterized intrusion in the suite and includes ultrabasic, basic, intermediate, and acid terms. Because its outcrops are generally

sparse and small, inferring field relationships between different units is challenging. Even so, gradational contacts between ultramafic and mafic rocks can be noticed, with more than one rock type occurring at the same outcrop.

The metamorphism recorded by the country rocks also affected the Capela pluton, causing the transformation of the primary assemblage and solid-state deformation. Actinolite, biotite, and titanite developed along hornblende cleavages are consistent with greenschist facies. Chloritization of hornblende and biotite records retrograde conditions. Considerable amounts of epidote and carbonate in ultramafic-mafic rocks seem to be related to plagioclase destabilization, which fills interstices and fractures with quartz.

For descriptive purposes, the rocks from the Capela pluton are divided as follows.

3.1 ULTRAMAFIC UNIT

This unit encompasses medium- to coarse-grained plagioclase-bearing hornblendites and biotite hornblendites, intimately associated with the gabbros and diorites (Fig. 2a). The hornblendites are composed almost entirely of euhedral to subhedral hornblende prisms (Fig. 2b), suggesting their early crystallization. Interstitial plagioclase, biotite, quartz, and microcline traces crystallized late. Garnet crystals are mainly subhedral and contain plagioclase and amphibole inclusions. Titanite, ilmenite, sulfides, zircon, and apatite are common accessory minerals. Diopside occurs in some samples as relict grains within hornblende but is uncommon. The monomineralic character combined with the fine-grained interstitial matrix suggests a cumulate origin for the hornblendites.

3.2 MAFIC UNIT

The mafic unit comprises the most outcropping area, corresponding chiefly to melanocratic hornblende gabbros, diorites, and subordinate gabbro-norites. The gradational contacts with ultramafic rocks are marked by decreasing hornblende and increasing plagioclase amounts. They are fine- to medium-grained and often show well-developed foliation, defined by the orientations of plagioclase, hornblende, and biotite.

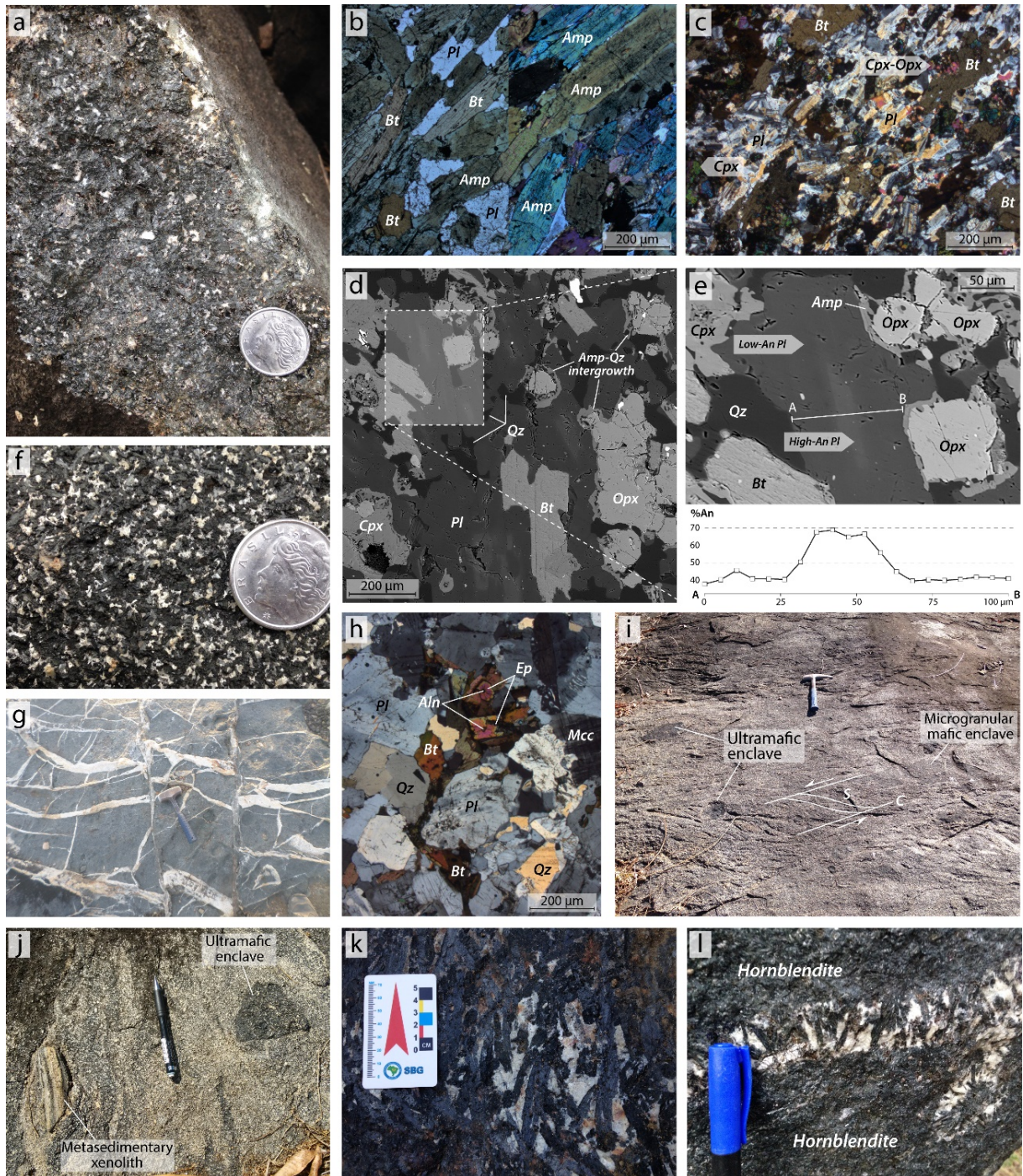


Figure III.2- Field and petrographic aspects of the Capela pluton. (a) Medium-grained biotite hornblendite with interstitial plagioclase. (b) Cumulate texture in hornblendite identified by large idiomorphic amphibole cumulus with minor biotite and plagioclase. (c) Alignment of plagioclase laths in gabbronorite defining a magmatic foliation. (d) Backscattering image of gabbronorite showing sub- to euhedral clinopyroxene and orthopyroxene rimmed by amphibole-quartz intergrowth. (e) Outlined polygon in (d) illustrates the variation in anorthite content (%An) across a patchy zoned plagioclase lath. (f) Medium-grained ‘salt-and-pepper’ equigranular hornblende gabbro. (g) Vein network of aplitic granite cross-cutting hornblende gabbro. (h) Epidote crystals enclosed by biotite in fine-grained granite. (i) Mafic and ultramafic enclaves in gabbro outcrop in the northern sector of the intrusion showing S/C fabric, which indicates a sinistral shearing kinematic. (j) Sharp contacts of metasedimentary xenolith and ultramafic cumulate enclave with the host diorite. (k) Detail of mafic pegmatite pond where amphibole crystals show a linear fabric. (l) Large hornblende crystals in a pegmatite vein grew perpendicularly to hornblendite layer walls wrapped in a quartz-feldspathic groundmass.

Equigranular fine-grained gabbronorite with dominant orthopyroxene and clinopyroxene (Fig. 2c) differs considerably from the other gabbroic-dioritic rocks, where hornblende is the dominant mafic mineral. The crystallization sequence deduced from microtextural observations indicates the early crystallization of ilmenite, orthopyroxene, clinopyroxene, and plagioclase. Biotite and quartz grew late. Exsolution lamellae of orthopyroxene are present in clinopyroxene crystals. Patchy-zoned plagioclase laths contain skeletal calcic cores enclosed by low-anorthite plagioclase (Fig. 2d and 2e). Hornblende rims pyroxene crystals, showing symplectite intergrowth with quartz. These features suggest that the reaction of pyroxenes with the melt produced hornblende. Apatite occurs as stubby and acicular crystals. Such inferences indicate that the gabbronorite is the most primitive facies of the pluton.

Medium-grained gabbros and diorites contain hornblende and biotite as the main ferromagnesian phases (Fig. 2f). Their mineralogy includes considerable amounts of plagioclase laths with varying fine-grained microcline and quartz contents. Sericitization of feldspar is weak to moderate and produces epidote and white mica. Subhedral to euhedral green hornblende encases rare clinopyroxene relicts and can contain retrogressed biotite and titanite along cleavages. Dark brown to reddish biotite occurs as fresh plates associated with hornblende, displaying minor transformation to chlorite. Euhedral to subhedral garnet crystals make straight contact with plagioclase, amphibole, and biotite, suggesting equilibrium crystallization. The accessory minerals are titanite, apatite, zircon, ilmenite, and, less commonly, allanite. Evidence for solid-state deformation comes from quartz with undulose extinction, mechanical twinning in plagioclase, and kinked biotite.

3.3 GRANITOID UNIT

All the rocks mentioned above were invaded by biotite monzogranite and aplite dikes. Backveining felsic rocks into mafic rocks indicates that the latter crystallized before the former attained the solidus (Fig. 2g).

In addition to these late intrusions, extensive exposures of biotite granodiorites and biotite monzogranites crop out toward the northern part of the pluton (Fig. 1d). These felsic rocks are gray, equigranular, and fine- to medium-grained. They have monotonous mineralogy containing plagioclase, microcline, and quartz, with minor amounts of biotite and hornblende, the main mafic phases (Fig. 2h). Garnet is present as anhedral granular crystals disseminated by the rock. Euhedral epidote is enclosed by biotite and possesses allanite cores. Other accessory phases are titanite, apatite, zircon, and ilmenite.

Locally, gabbros and hornblendites wrap small muscovite-bearing tonalite pockets (< 1.0 m).

3.4 ENCLAVES

The Capela pluton carries abundant enclaves (*lato sensu*), which are divided into mafic microgranular enclaves (MME), ultramafic enclaves (UME), and metasedimentary xenoliths. These enclaves are hosted by gabbroic-dioritic rocks aligned with their fabric.

The MME are dioritic to tonalitic in composition and show subrounded morphologies, mostly elliptical (Fig. 2i). Enclave-host rock contacts are lobate to gradational, suggestive of a liquid-liquid interaction. Plagioclase phenocrysts embedded in a groundmass suggest mechanical transfer from the host rock. Disrupted MME grading into biotite schlieren seems to reflect progressive stages of disaggregation and hybridization.

The UME have mineralogy and texture akin to the cumulate hornblendites. They are composed of coarse-grained amphibole prisms, biotite, and small amounts of interstitial plagioclase and quartz (Fig. 2i and 2j). The contacts with the hosts typically are straight and sharp, resembling brecciated blocks of hornblendites incorporated into the gabbros. These UME range in size from tiny clots to meter-scale blocks.

Centimeter xenoliths of garnet-biotite schists and calc-silicate rocks are common at intrusion margins. The contacts of the xenoliths with mafic hosts grade from sharp to ameboid and gradational, indicating variable degrees of assimilation (Fig. 2j). Leucocratic bands rimming and crossing these metasedimentary fragments indicate that they underwent some partial melting.

3.5 PEGMATITES

Hornblende-plagioclase pegmatites occur as centimeter-thick dikes and ponds associated with ultramafic rocks (Fig. 2k). They have large hornblende crystals (2-12 cm) and an interstitial white groundmass containing plagioclase and minor amounts of biotite, quartz, and microcline. Idiomorphic hornblende grows perpendicular to layer walls or radially, defining comb layering or rosettes (Fig. 2l). These textures are typically described in appinite complexes (Murphy, 2020, 2013).

4 SAMPLING AND ANALYTICAL PROCEDURES

The analytical techniques used in this work included 1) X-ray fluorescence (XRF) and inductively coupled plasma–mass spectrometry (ICP–MS) for whole-rock major and trace element analyses; 2) sensitive high-resolution ion microprobe (SHRIMP) for zircon U–Pb dating; 3) laser ablation multicollector inductively coupled plasma–mass spectrometry (LA-MC-ICP–MS) for zircon Lu–Hf analyses; and 4) thermal ionization mass spectrometry (TIMS) for whole-rock Sr–Nd–Pb isotope analyses. Detailed analytical procedures are available in Supplementary Material.

5 MAJOR AND TRACE ELEMENT DATA

Whole-rock major and trace elements of the analyzed samples and previously published data for the Capela pluton are listed in Supplementary Table S1.

In a total alkalis versus silica diagram (Fig. 3a), the compositions of the analyzed samples spread from ultrabasic to acidic fields, plotting across the subalkaline and alkaline series (Irvine and Baragar, 1971; Middlemost, 1994). The rocks are metaluminous to slightly peraluminous (Fig. 3b; Shand, 1943) and show K_2O/Na_2O ratios of around unity, indicating a potassic affinity. In SiO_2 and Na_2O versus K_2O diagrams (Peccerillo and Taylor, 1976; Turner et al., 1996), most samples plot along the shoshonite magma series, with exception of the high-silica granitoids, which lie across the medium- and high-K calc-alkaline fields (Fig. 3c and 3d). High alkali-sum, K_2O/Na_2O , low TiO_2 , high but variable Al_2O_3 , and enrichment in LILE and LREE also suggest a geochemical affinity with the shoshonite association for the mafic rocks (Morrison, 1980).

The rocks of the ultramafic unit show SiO_2 values ranging from 40.24 to 44.96 wt%, with variable Al_2O_3 (9.61-19.40 wt.%) contents. In the total alkalis versus silica diagram (Fig. 3a), these samples lie along fooid gabbro and gabbro fields, with high alkali sums ($Na_2O + K_2O = 3.39-6.95$ wt%). The Mg number parameter [$Mg\# = \text{molar Mg}/(\text{Mg} + \text{Fe}^{2+})$] ranges from 0.49 to 0.72. The high CaO (5.50-10.98 wt%), MgO (5.61-13.08 wt%), and FeO^* (10.94-17.41 wt%) contents evidence the cumulative character of these samples. Chondrite-normalized (CN) rare earth element (REE) patterns show concave LREE-enriched downward curvature ($La/Yb_{CN} = 3.8-6.2$), characterized by almost flat LREE ($La/Sm_{CN} = 0.8-1.2$) and fractionated HREE ($Gd/Yb_{CN} = 2.9-3.8$), with weak negative Eu anomalies ($Eu/Eu^* = 0.7-0.8$) (Fig. 4a).

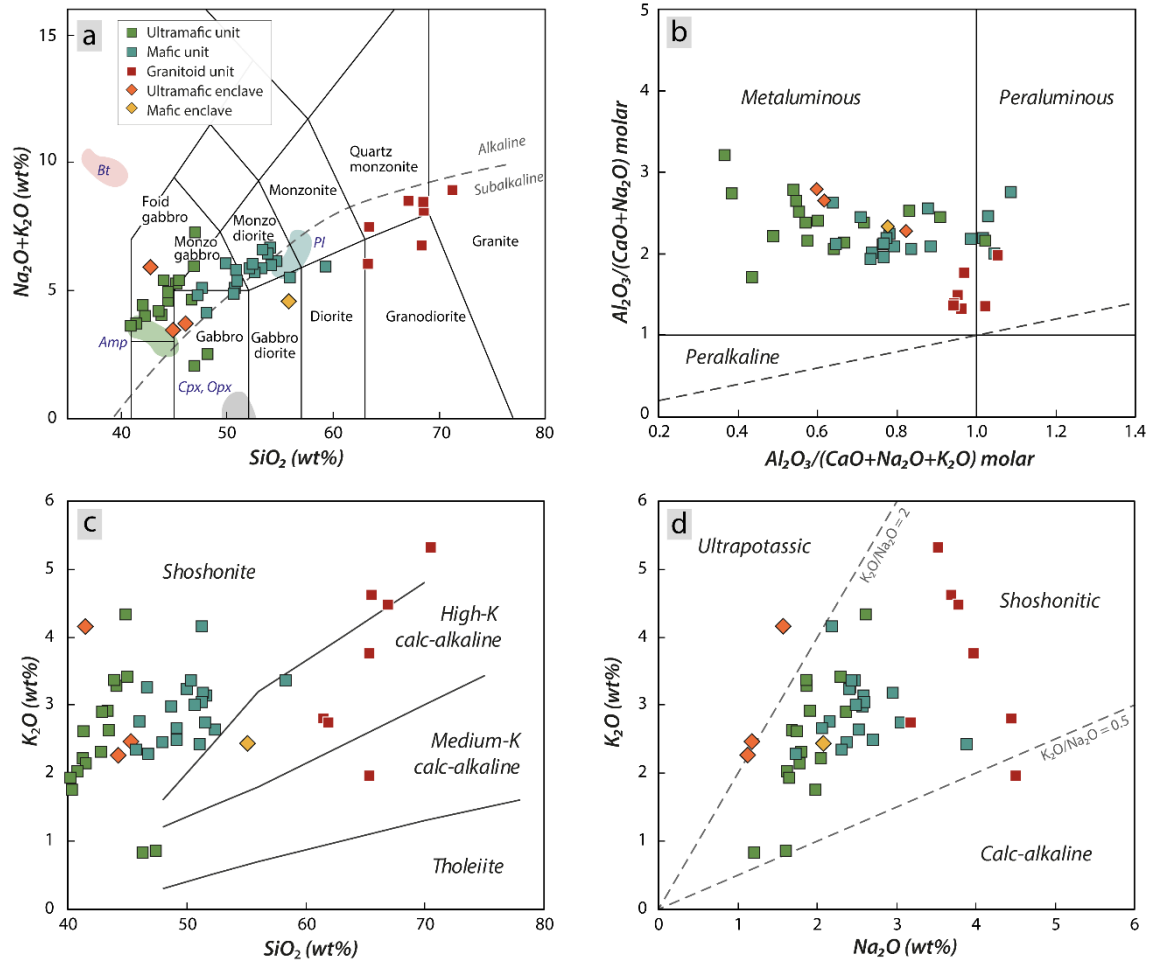


Figure III.3- Geochemical diagrams for the Capela pluton samples. (a) Total alkalis ($\text{Na}_2\text{O} + \text{K}_2\text{O}$) vs. SiO_2 (Middlemost, 1994) with boundary of subalkaline and alkaline series (Irvine and Baragar, 1971). Mineral compositional poles were taken from samples SOS-925 (hornblendite) and SOS-940 (gabbro diorite) analyzed by Pereira (2019). (b) Alumina saturation index $A/CNK = \text{molar Al}_2\text{O}_3/(\text{CaO} + \text{Na}_2\text{O} + \text{K}_2\text{O})$ vs. $A/NK = \text{molar Al}_2\text{O}_3/(\text{Na}_2\text{O} + \text{K}_2\text{O})$ (Shand, 1943). (c) SiO_2 vs. K_2O (Peccerillo and Taylor, 1976) and (d) Na_2O vs. K_2O (Turner et al., 1996) plots.

The rocks from the mafic unit show compositions of gabbro, monzogabbro, gabbro diorite, monzodiorite, and diorite (Fig. 3a), with SiO_2 contents of 45.75-58.29 wt%, variable MgO concentrations (9.02-1.98 wt%), and Mg# ranging from 0.64 to 0.35. Chondrite-normalized REE patterns show LREE enrichment ($\text{La}/\text{Yb}_{\text{CN}} = 3.1-37.2$) and faint fractionation among HREE ($\text{Gd}/\text{Yb}_{\text{CN}} = 1.1-3.2$) (Fig. 4b). Small negative Eu anomalies occur in mafic rocks akin to the ultramafic unit ($\text{Eu}/\text{Eu}^* = 0.6-0.9$).

The granitoid unit comprises granodiorites, quartz monzonites, and granites (Fig. 3a), displaying SiO_2 contents of 61.44-70.49 wt% and low values of MgO (0.59-2.80 wt%), CaO (2.08-3.96 wt%), and TiO_2 (0.16-0.57 wt%), with Mg# between 0.53 and 0.36. They display the most fractionated REE patterns among the analyzed samples ($\text{La}/\text{Yb}_{\text{CN}} = 37.0-41.3$;

La/Sm_{CN} = 4.6-5.2; Gd/Yb_{CN} = 4.8-5.1), with smooth negative Eu anomalies (Eu/Eu* = 0.8; Fig. 4c).

Incompatible trace element compositions normalized to the primitive mantle (PM) of McDonough and Sun (1995) are shown in Fig. 4. All samples display significant enrichments in LILE and LREE compared to HREE and HFSE. Normalized concentrations of fluid-soluble elements such as Rb, Ba, Sr, and U are dozens of times greater than those of PM. The multielement patterns of the ultramafic rocks show uniform negative anomalies of Rb, Nb, Sr, Zr, and Ti (Fig. 4d). In contrast, the samples of the mafic and granitoid units exhibit prominent negative troughs at Nb and Ti (Fig. 4e and 4f). In mafic rocks, the high contents of Ba, Sr, and LREE and relatively low contents of Rb, Nb, and HREE match the features described in apinitite suites worldwide (Fowler et al., 2008; Murphy, 2020, 2013).

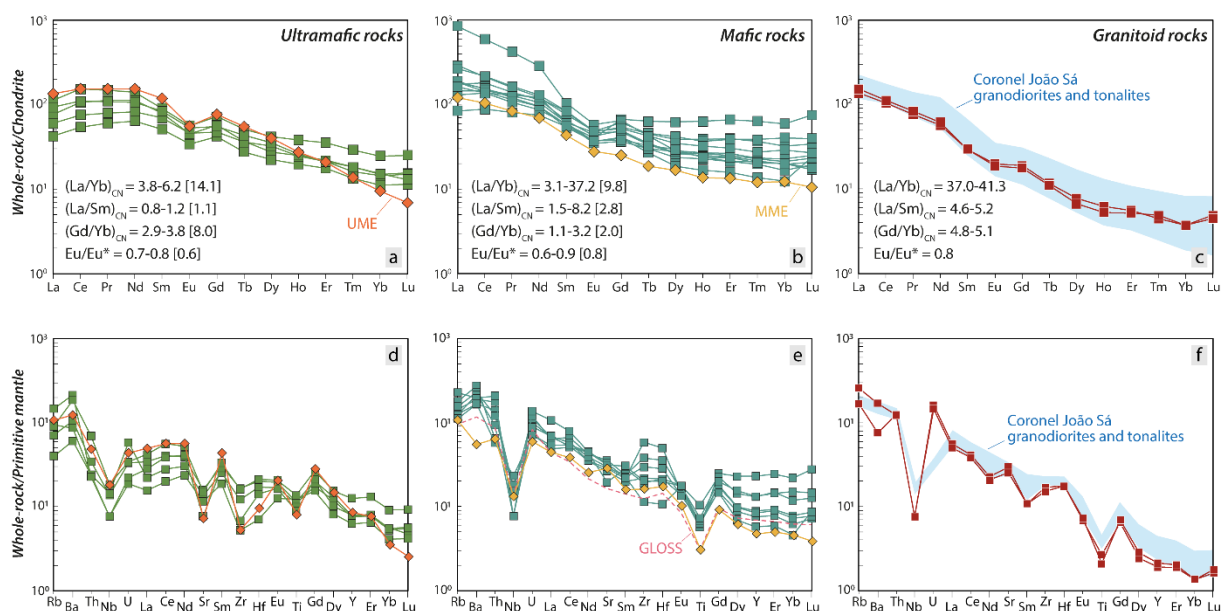


Figure III.4- Chondrite-normalized REE and primitive mantle-normalized trace element patterns of the Capela pluton samples. Values in square brackets refer to those from associated enclaves. Normalization values are from McDonough and Sun (1995). Trace element data for the GLOSS average (Plank and Langmuir, 1998) and Coronel João Sá pluton (Long et al., 2005) are also shown.

The samples from the ultramafic, mafic, and granitoid units appear to plot along a common evolutionary trend when selected major elements are plotted against SiO₂ (Fig. 5). The abundances of MgO, FeO_t, CaO, and TiO₂ decrease toward more evolved compositions, while Na₂O correlates positively with SiO₂. Al₂O₃ and K₂O have nonuniform trends versus silica but with an ascending inclination.

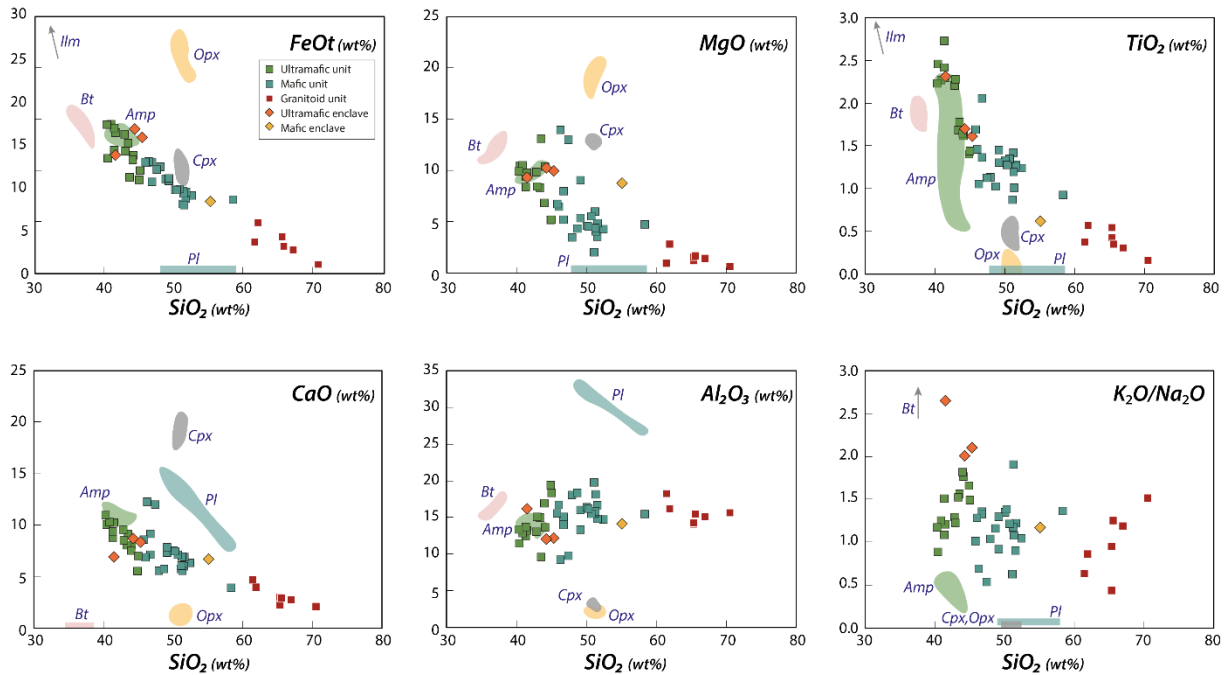


Figure III.5- Variation diagrams for selected oxides against SiO_2 . Colored fields indicate the compositional variation of the minerals clinopyroxene (Cpx), orthopyroxene (Opx), amphibole (Amp), biotite (Bt), and plagioclase (Pl).

6 ZIRCON U–Pb DATING AND Lu–Hf ISOTOPE COMPOSITION

6.1 PLAGIOCLASE-BEARING BIOTITE HORNBLENDITE (SAMPLE SOS-696F)

The zircon crystals are pale brown to colorless and exhibit subhedral prismatic shapes with pyramidal endings (Fig. 6a). Their sizes vary from 114 to 302 μm , with length/width ratios between 1:1 and 3:1. Some crystals show fractures and rare inclusions. All crystals display oscillatory zoning and Th/U ratios ranging from 0.35 to 1.14. Pereira et al. (2020) obtained a concordia age of $631 \pm 3 \text{ Ma}$ ($n = 11$, 2σ , $\text{MSWD} = 1.8$) for this sample (Fig. 7a). This dataset produces a $^{206}\text{Pb}/^{238}\text{U}$ weighted average age of $631 \pm 3 \text{ Ma}$ ($n = 12$, 2σ , $\text{MSWD} = 0.93$).

Lu–Hf isotope compositions were determined in fifteen concordant to subconcordant zircon crystals (95–108% concordance; Table 1). The calculated $^{176}\text{Hf}/^{177}\text{Hf}_{(630 \text{ Ma})}$ ratios range from 0.282204 to 0.282324, corresponding to subchondritic $\epsilon\text{Hf}_{(630 \text{ Ma})}$ values from -6.5 to -2.2 (Fig. 7e and 7f), with a weighted mean value of -3.6 ± 0.7 (95% conf.). The $\text{Hf-T}_{\text{DM}}^{\text{C}}$ model ages oscillate between 2.10 and 2.47 Ga.

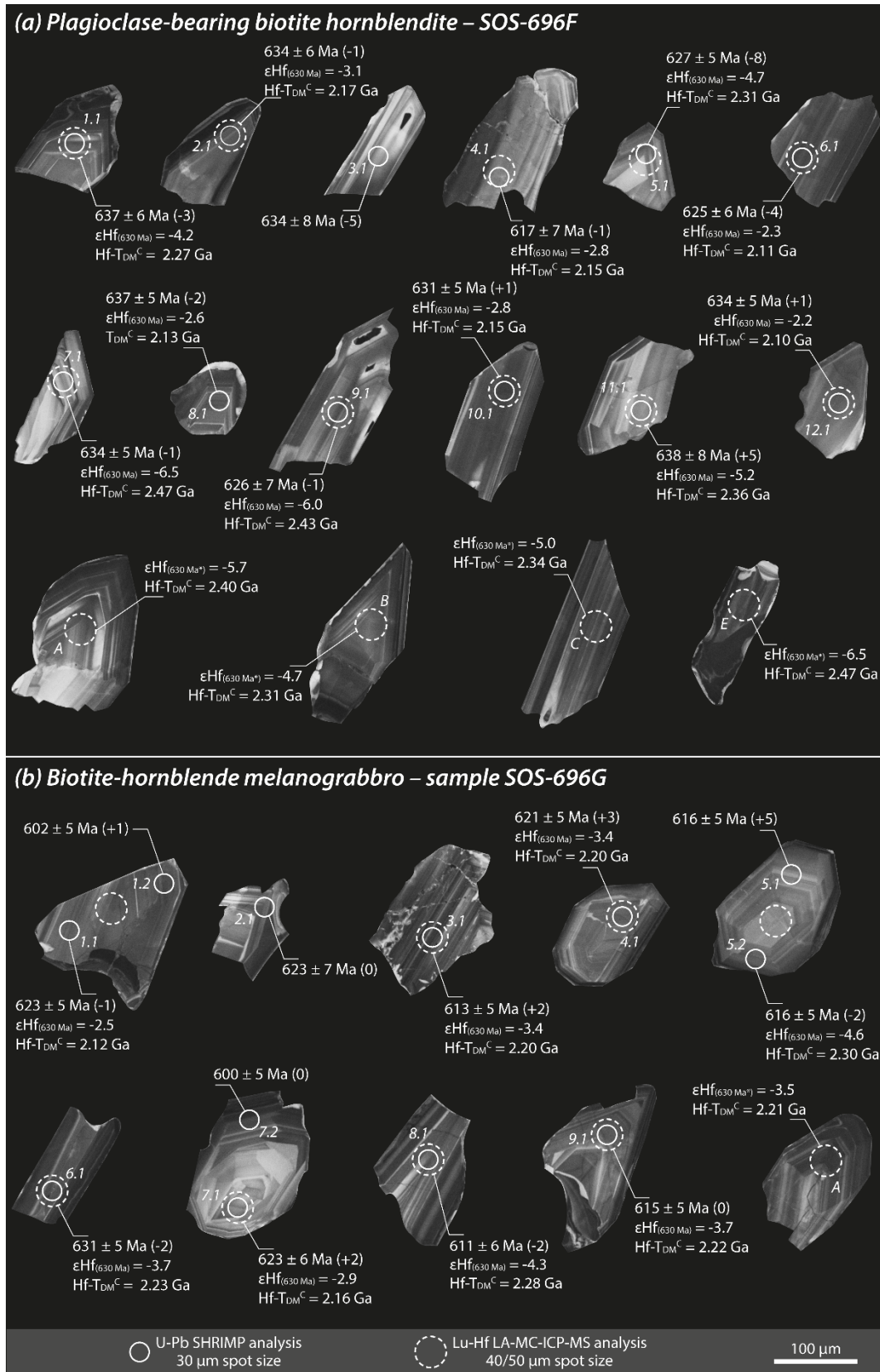


Figure III.6- Cathodoluminescence images of the dated zircon crystals from the samples SOS-696F (a) and SOS-696G (b) with their respective $^{206}\text{Pb}/^{238}\text{U}$ date, ϵHf_t , and $\text{Hf-T}_{\text{DM}}^{\text{C}}$. The discordance percentage in parentheses was quantified using the $^{207}\text{Pb}/^{206}\text{Pb}$ and $^{206}\text{Pb}/^{238}\text{U}$ dates (Spencer et al., 2016). Asterisks represent unanalyzed crystals for U-Pb.

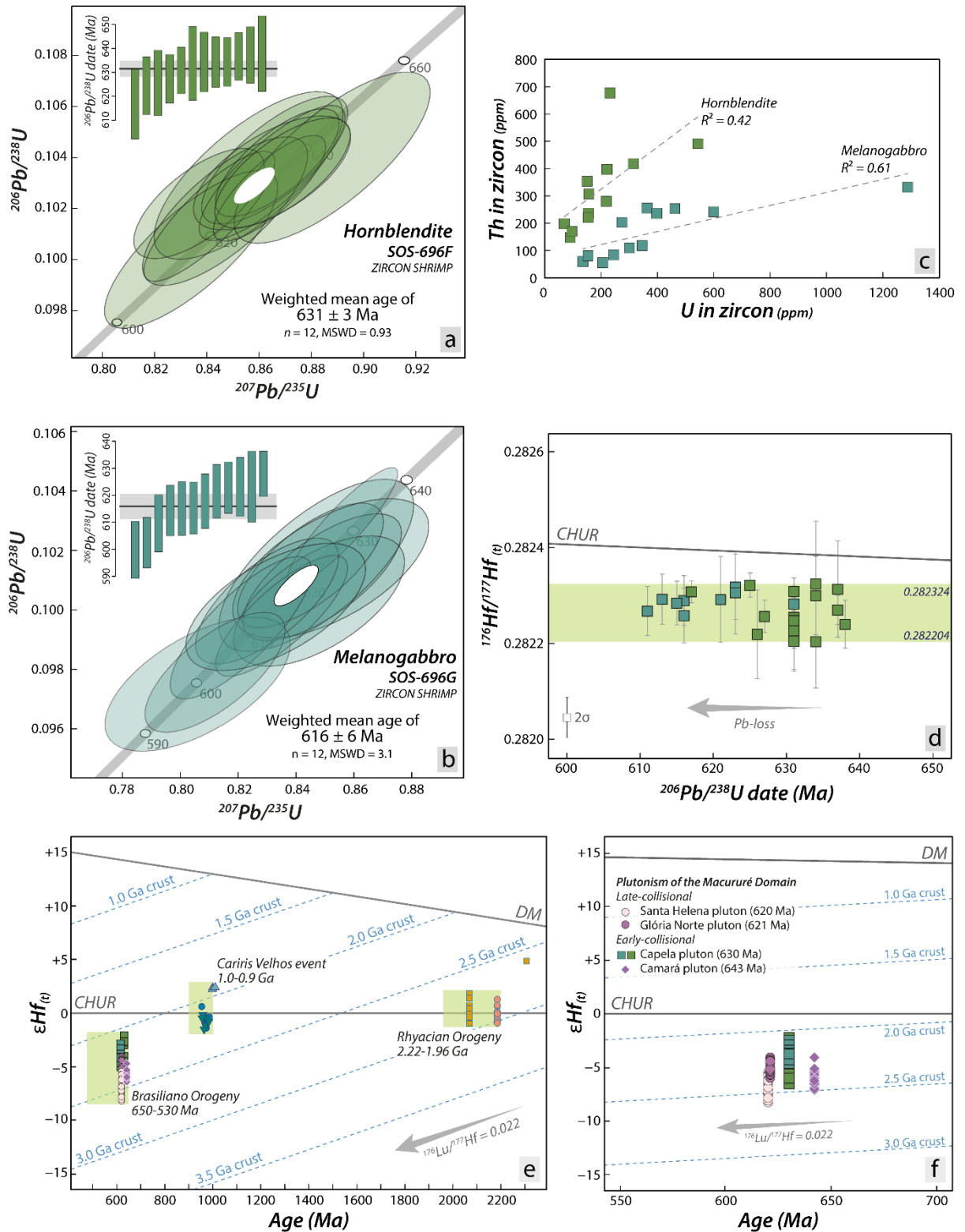


Figure III.7- Zircon U–Pb and Lu–Hf isotope results. Concordia diagrams for (a) plagioclase-bearing biotite hornblendite and (b) biotite-hornblende melanogabbro from the Capela pluton. (c) Variation in U and Th contents of dated zircon crystals. (d) $^{176}\text{Hf}/^{177}\text{Hf}$ vs. $^{206}\text{Pb}/^{238}\text{U}$ date. (e) $\epsilon\text{Hf}(t)$ vs. U–Pb age. Lu–Hf data for granitoids and mafic rocks related to the Rhyacian (Costa et al., 2018), Cariris Velhos (Caxito et al., 2020b), and Brasiliano (Pereira et al., 2023) tectonothermal events are given for comparison.

Table III.1- Lu–Hf isotope analysis of zircon crystals from the Capela pluton.

Spot ID	$^{176}\text{Hf}/^{177}\text{Hf}$	2 SE	$^{176}\text{Lu}/^{177}\text{Hf}$	2SE	$^{176}\text{Yb}/^{177}\text{Hf}$	2 SE	$^{178}\text{Hf}/^{177}\text{Hf}$	$\epsilon\text{Hf}_{(0)}$	$^{176}\text{Hf}/^{177}\text{Hf}_{(t)}$	$\epsilon\text{Hf}_{(630\text{ Ma})}$	2 SE	T_{DM}^{C} (Ma)
<i>Plagioclase-bearing biotite hornblendite (sample SOS-696F)</i>												
696F 1.1	0.282279	0.000031	0.000800	0.000005	0.02037	0.00016	1.467221	-17.9	0.282269	-4.2	1.1	2267
696F 2.1	0.282320	0.000083	0.001709	0.000105	0.06652	0.00298	1.467191	-16.5	0.282300	-3.1	2.9	2174
696F 4.1	0.282315	0.000024	0.000669	0.000008	0.01701	0.00022	1.467189	-16.6	0.282307	-2.8	0.8	2150
696F 5.1	0.282261	0.000034	0.000423	0.000003	0.01199	0.00010	1.467207	-18.5	0.282256	-4.7	1.2	2309
696F 6.1	0.282334	0.000026	0.001041	0.000006	0.02828	0.00023	1.467210	-16.0	0.282321	-2.3	0.9	2107
696F 7.1	0.282214	0.000098	0.000883	0.000008	0.03237	0.00036	1.467255	-20.2	0.282204	-6.5	3.5	2470
696F 8.1	0.282319	0.000101	0.000456	0.000024	0.02717	0.00086	1.467164	-16.5	0.282313	-2.6	3.6	2132
696F 9.1	0.282229	0.000094	0.000853	0.000055	0.04132	0.00207	1.467216	-19.7	0.282218	-6.0	3.3	2425
696F 10.1	0.282322	0.000029	0.001139	0.000007	0.03143	0.00027	1.467234	-16.4	0.282308	-2.8	1.0	2148
696F 11.1	0.282247	0.000051	0.000644	0.000059	0.05485	0.00276	1.467295	-19.0	0.282240	-5.2	1.8	2359
696F 12.1	0.282335	0.000131	0.000929	0.000006	0.02405	0.00021	1.466825	-15.9	0.282324	-2.2	4.7	2098
696F A	0.282235	0.000081	0.000697	0.000049	0.05778	0.00348	1.467311	-19.4	0.282227	-5.7	2.9	2399
696F B	0.282263	0.000066	0.000708	0.000053	0.04793	0.00241	1.467281	-18.5	0.282254	-4.7	2.3	2314
696F C	0.282254	0.000049	0.000582	0.000036	0.04726	0.00235	1.467260	-18.8	0.282247	-5.0	1.8	2336
696F E	0.282222	0.000064	0.001461	0.000224	0.08281	0.00884	1.467283	-19.9	0.282205	-6.5	2.3	2467
<i>Biotite-hornblende melanogabbro (sample SOS-696G)</i>												
696G 1.1	0.282330	0.000069	0.001016	0.000022	0.08811	0.00158	1.467264	-16.1	0.282318	-2.5	2.5	2118
696G 3.1	0.282303	0.000053	0.000974	0.000055	0.07247	0.00278	1.467288	-17.0	0.282291	-3.4	1.9	2199
696G 4.1	0.282303	0.000090	0.000968	0.000009	0.02271	0.00026	1.467319	-17.0	0.282291	-3.4	3.2	2199
696G 5.1	0.282264	0.000058	0.000541	0.000060	0.03942	0.00227	1.467284	-18.4	0.282258	-4.6	2.1	2304
696G 6.1	0.282292	0.000021	0.000832	0.000006	0.02169	0.00019	1.467214	-17.4	0.282282	-3.7	0.7	2228
696G 7.1	0.282313	0.000087	0.000600	0.000054	0.04108	0.00181	1.467271	-16.7	0.282306	-2.9	3.1	2155
696G 8.1	0.282278	0.000052	0.000920	0.000150	0.06924	0.00674	1.467260	-17.9	0.282267	-4.3	1.9	2275
696G 9.1	0.282292	0.000046	0.000746	0.000006	0.01729	0.00016	1.467157	-17.4	0.282284	-3.7	1.7	2223
696G 10.1	0.282299	0.000053	0.000857	0.000035	0.06215	0.00140	1.467286	-17.2	0.282289	-3.5	1.9	2207

6.2 BIOTITE-HORNBLLENDE MELANOGABBRO (SAMPLE SOS-696G)

Nine zircon crystals were analyzed for U–Pb, totaling 12 spots. The selected crystals are light brown to colorless, anhedral to subhedral, and exhibit prismatic shapes (Fig. 6b). Occasionally, they show pyramidal endings and fractures. Their sizes vary between 125 and 227 μm , with length/width ratios of 1:1 and 1:2. All analyzed crystals show oscillatory zoning. Some crystals show boundaries between distinct zones marked by a thin bright layer in CL images. Th/U ratios range from 0.27 to 0.77 (Table 2).

The $^{206}\text{Pb}/^{238}\text{U}$ and $^{207}\text{Pb}/^{206}\text{Pb}$ dates are concordant to subconcordant (95-102% concordance). Two crystals (spots 1.1/1.2 and 7.1/7.2) yield core-rim age variations, with older cores at ~ 620 Ma and younger edges at ~ 600 Ma (Fig. 6b). In the concordia diagram, the error ellipses overlap into analytical error and spread from 600 to 630 Ma (Fig. 7b), resulting in a high MSWD value of 3.1 for a $^{206}\text{Pb}/^{238}\text{U}$ weighted average age of 616 ± 6 Ma ($n = 9$, 95% conf.). A $^{206}\text{Pb}/^{238}\text{U}$ weighted average age of 618 ± 4 Ma ($n = 9$, 2σ , MSWD = 0.73) is calculated when the dates of the older crystal and the two younger rims are disregarded.

Lu–Hf isotope compositions of nine zircon crystals yield nonradiogenic $^{176}\text{Hf}/^{177}\text{Hf}_{(630 \text{ Ma})}$ ratios between 0.282258 and 0.282318 (Table 1), equivalent to negative $\epsilon\text{Hf}_{(630 \text{ Ma})}$ values ranging from -4.6 to -2.5 (weighted mean of -3.7 ± 0.5 , 95% conf.). The Hf- T_{DM}^{C} model ages vary from 2.12 to 2.30 Ga (Fig. 7e and 7f).

7 WHOLE-ROCK ISOTOPE GEOCHEMISTRY

The whole-rock Sr, Nd, and Pb isotope analyses are reported in Table 3 and Fig. 8. The initial $^{87}\text{Sr}/^{86}\text{Sr}$ and $^{143}\text{Nd}/^{144}\text{Nd}$ ratios were back-calculated to a crystallization age of 630 Ma.

Values of $^{87}\text{Sr}/^{86}\text{Sr}_{(630 \text{ Ma})}$ and $\epsilon\text{Nd}_{(630 \text{ Ma})}$ for ultramafic rocks range from 0.707876 to 0.709168 and from -4.3 to -2.2, respectively. The lead isotope ratios $^{206}\text{Pb}/^{204}\text{Pb}$, $^{207}\text{Pb}/^{204}\text{Pb}$, and $^{208}\text{Pb}/^{204}\text{Pb}$ range from 18.51-18.79, 15.71-15.74, and 38.58-39.51, respectively.

The rocks from the mafic unit have $^{87}\text{Sr}/^{86}\text{Sr}_{(630 \text{ Ma})}$ ratios ranging from 0.708160 to 0.710092, $\epsilon\text{Nd}_{(630 \text{ Ma})}$ values from -5.2 to -2.0, and significant variations in $^{206}\text{Pb}/^{204}\text{Pb}$ (18.50-19.18), $^{207}\text{Pb}/^{204}\text{Pb}$ (15.69-15.77), and $^{208}\text{Pb}/^{204}\text{Pb}$ (38.54-45.42).

The two analyzed granitoids display the lowest and highest radiogenic $^{87}\text{Sr}/^{86}\text{Sr}_{(630 \text{ Ma})}$ ratios of 0.705413 and 0.710827, respectively, with negative $\epsilon\text{Nd}_{(630 \text{ Ma})}$ from -3.6 to -3.4, Nd- T_{DM} model ages of 1.26 and 1.32 Ga. The $^{206}\text{Pb}/^{204}\text{Pb}$ and $^{208}\text{Pb}/^{204}\text{Pb}$ ratios vary between 18.60 and 18.65 and 38.64 and 39.17, respectively, at a uniform $^{207}\text{Pb}/^{204}\text{Pb}$ composition of 15.73.

Table III.2- SHRIMP U–Pb zircon data for sample SOS-696G.

Spot ID	U (ppm)	Th (ppm)	$^{232}\text{Th}/^{238}\text{U}$	$^{206}\text{Pb}_c$ (%)	Isotope ratios							Dates (Ma)		
					$^{206}\text{Pb}/^{206}\text{Pb}$	1 σ (%)	$^{207}\text{Pb}/^{235}\text{U}$	1 σ (%)	$^{206}\text{Pb}/^{238}\text{U}$	1 σ (%)	Rho	$^{206}\text{Pb}/^{238}\text{U} \pm 1\sigma$	$^{207}\text{Pb}/^{206}\text{U} \pm 1\sigma$	Disc. (%)
696G 1.1	363	255	0.73	0.04	0.06040	0.8	0.845	1.2	0.1015	0.83	0.7	623 \pm 5	618 \pm 18	-1
696G 1.2	397	236	0.61	0.09	0.06018	0.8	0.812	1.2	0.0979	0.83	0.7	602 \pm 5	610 \pm 18	+1
696G 2.1	345	118	0.35	0.20	0.06048	1.1	0.847	1.6	0.1015	1.15	0.7	623 \pm 7	621 \pm 23	0
696G 3.1	461	253	0.57	0.01	0.06069	0.7	0.835	1.1	0.0998	0.82	0.8	613 \pm 5	628 \pm 14	+2
696G 4.1	274	203	0.77	0.04	0.06093	0.9	0.849	1.3	0.1011	0.85	0.7	621 \pm 5	637 \pm 20	+3
696G 5.1	206	55	0.27	0.05	0.06131	1.1	0.848	1.4	0.1003	0.88	0.6	616 \pm 5	650 \pm 24	+5
696G 5.2	301	109	0.37	0.02	0.06000	0.8	0.830	1.2	0.1003	0.85	0.7	616 \pm 5	604 \pm 18	-2
696G 6.1	1288	332	0.27	-	0.06040	0.4	0.856	0.9	0.1028	0.78	0.9	631 \pm 5	618 \pm 09	-2
696G 7.1	136	59	0.45	0.04	0.06088	1.3	0.852	1.6	0.1014	0.93	0.6	623 \pm 6	635 \pm 29	+2
696G 7.2	154	80	0.54	0.04	0.05996	1.3	0.806	1.6	0.0975	0.93	0.6	600 \pm 5	602 \pm 29	0
696G 8.1	600	242	0.42	0.06	0.05988	0.7	0.821	1.2	0.0994	0.97	0.8	611 \pm 6	599 \pm 14	-2
696G 9.1	245	84	0.36	0.18	0.06038	1.3	0.833	1.5	0.1001	0.86	0.6	615 \pm 5	617 \pm 27	0

Table III.3- Whole-rock Sr, Nd, and Pb isotope compositions.

Sample	Rock	[Rb] ppm	[Sr] ppm	⁸⁷ Rb/ ⁸⁶ Sr	⁸⁷ Sr/ ⁸⁶ Sr ^a	⁸⁷ Sr/ ⁸⁶ Sr _(t)	[Sm] ppm	[Nd] ppm	¹⁴⁷ Sm/ ¹⁴³ Nd	¹⁴³ Nd/ ¹⁴⁴ Nd ^b	¹⁴³ Nd/ ¹⁴⁴ Nd _(t)	εNd _(t)	εNd ₍₀₎	T _{DM} (Ga)	²⁰⁶ Pb/ ²⁰⁴ Pb	²⁰⁷ Pb/ ²⁰⁴ Pb	²⁰⁸ Pb/ ²⁰⁴ Pb
<i>Ultramafic unit</i>																	
PC-008A	Hornblendite	54	300	0.5213	0.713853(6)	0.709168	13.63	64.42	0.1279	0.512176(6)	0.511647	-9.0	-3.5	-	18.509	15.712	39.509
PC-037A	Hornblendite	76	519	0.4240	0.712245(17)	0.708434	12.23	52.74	0.1402	0.512261(10)	0.511682	-7.4	-2.8	-	18.778	15.744	38.903
PC-084A	Hornblendite	24	228	0.3048	0.710615(16)	0.707876	9.58	36.56	0.1584	0.512366(7)	0.511712	-5.3	-2.2	-	18.592	15.709	38.580
SOS-696F	Hornblendite	43	315	0.3916	0.712000(8)	0.708481	12.73	51.45	0.1496	0.512226(7)	0.511608	-8.0	-4.3	-	-	-	-
<i>Mafic unit</i>																	
PC-003B	Gabbro	86	573	0.4346	0.712624(9)	0.708718	11.61	64.80	0.1083	0.512140(5)	0.511693	-9.7	-2.6	-	18.887	15.720	39.544
PC-033A	Gabbro	87	1020	0.2470	0.711404(16)	0.709184	8.83	44.48	0.1201	0.512178(6)	0.511683	-9.0	-2.8	-	19.178	15.689	45.421
PC-039A	Gabbro	88	152	1.6785	0.724644(6)	0.709560	11.18	53.82	0.1256	0.512189(11)	0.511670	-8.8	-3.0	-	18.633	15.740	38.544
PC-054A	Diorite	108	383	0.8169	0.716205(6)	0.708864	11.07	52.20	0.1283	0.512091(9)	0.511562	-10.7	-5.2	-	18.709	15.688	38.761
PC-055A	Diorite	93	706	0.3815	0.712924(6)	0.709496	15.62	131.80	0.0717	0.511944(6)	0.511648	-13.5	-3.5	-	19.021	15.770	39.622
PC-076A	Diorite	74	591	0.3626	0.711418(11)	0.708160	10.48	53.16	0.1192	0.512214(5)	0.511722	-8.3	-2.0	-	18.502	15.692	38.807
PC-084E	Diorite	137	650	0.6105	0.715578(4)	0.710092	8.42	53.53	0.0951	0.512048(5)	0.511656	-11.5	-3.3	-	18.876	15.767	40.043
<i>Granitoid unit</i>																	
PC-080A	Granodiorite	155	506	0.8876	0.718803(6)	0.710827	5.49	33.56	0.0988	0.512049(10)	0.511641	-11.5	-3.6	1.32	18.602	15.726	38.640
PC-084C	Granodiorite	101	592	0.4939	0.709852(14)	0.705413	5.31	35.37	0.0908	0.512028(7)	0.511653	-11.9	-3.4	1.26	18.850	15.731	39.172

All samples lie in the enriched quadrant in an $^{87}\text{Sr}/^{86}\text{Sr}_{(t)}$ versus $^{143}\text{Nd}/^{144}\text{Nd}_{(t)}$ plot (Fig. 8a). Radiogenic lead isotope ratios imply a melt source enriched in Th and U relative to Pb, akin to the upper crust signature (Zartman and Doe, 1981). In the Pb isotope diagrams (Fig. 8b and 8c), the samples plot across the field of Global Subducting Sediment (GLOSS; Plank and Langmuir, 1998), close to the Enriched Mantle II (EM-II; Hofmann, 2007) endmember and overlap the compositions of post-collisional potassic and ultrapotassic rocks from North Tibet (Guo et al., 2006). The lead isotopes for evolved samples broadly coincide with those from mafic and ultramafic units.

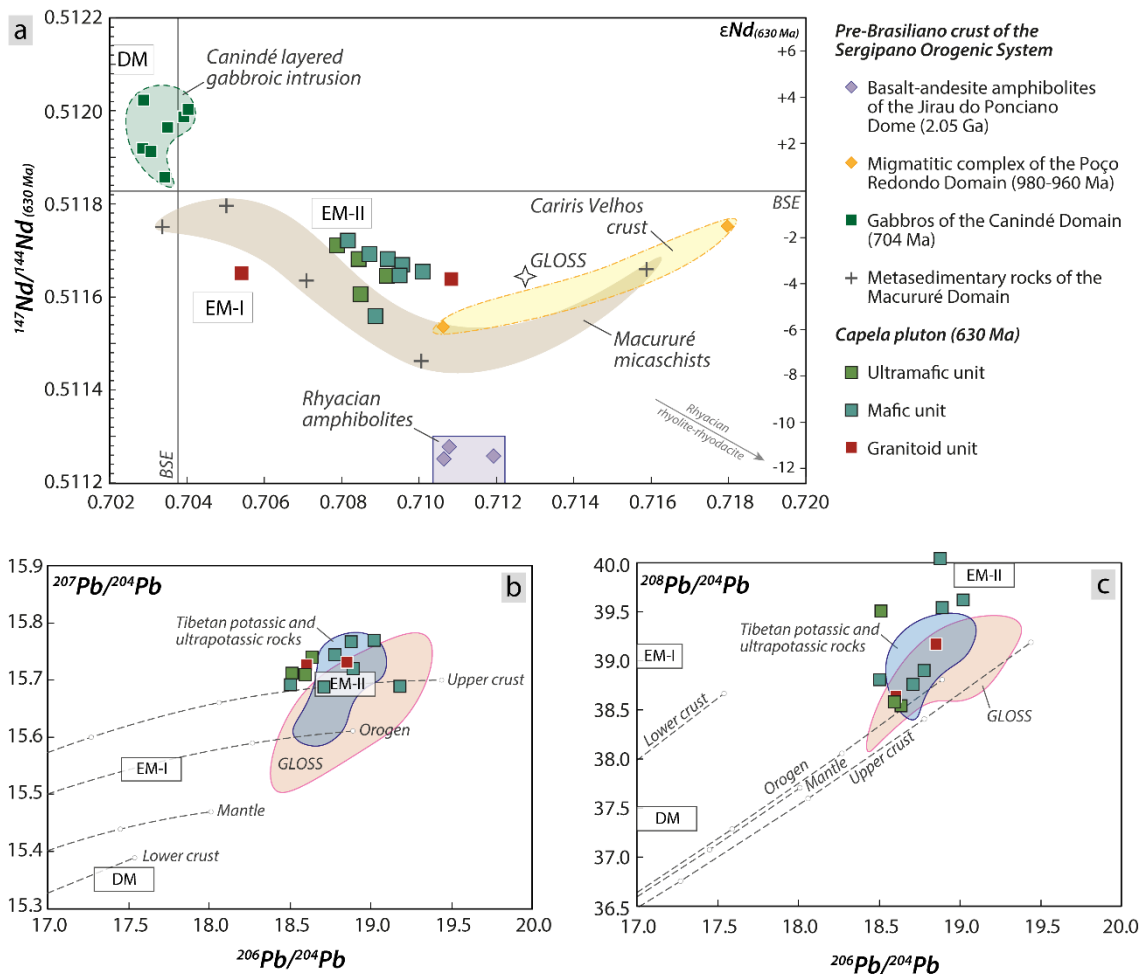


Figure III.8- Whole-rock Sr–Nd–Pb isotope composition. (a) $^{87}\text{Sr}/^{86}\text{Sr}_{(t)}$ vs. $^{143}\text{Nd}/^{144}\text{Nd}_{(t)}$ plot with fields of the Rhyacian (Lima et al., 2019) and Cariris Velhos (Oliveira et al., 2015a) crusts of the SOS. The compositions of the Canindé gabbroic layered intrusion (Pinto et al., 2020) and Macururé micaschists (Oliveira et al., 2015a) are also compared. GLOSS and DM compositions were taken from Plank and Langmuir (1998) and Workman and Hart (2005). Recalculation of the Bulk Silicate Earth (BSE) values to 630 Ma based on the constants $^{86}\text{Sr}/^{87}\text{Sr} = 0.7045$, $^{87}\text{Rb}/^{87}\text{Sr} = 0.0816$, $^{143}\text{Nd}/^{144}\text{Nd} = 0.512638$ and $^{147}\text{Sm}/^{144}\text{Nd} = 0.1967$ (Faure, 2001). (b) $^{207}\text{Pb}/^{204}\text{Pb}$ vs. $^{206}\text{Pb}/^{204}\text{Pb}$ and (c) $^{208}\text{Pb}/^{204}\text{Pb}$ vs. $^{206}\text{Pb}/^{204}\text{Pb}$ with evolution curves for the lower crust, mantle, orogen and upper crust (Zartman and Doe, 1981). The DM, EM-I, and EM-II coordinates are from Hofmann (2007). Fields of post-collisional potassic and ultrapotassic rocks in the northern Tibetan Plateau from Guo et al. (2006).

8 DISCUSSION

8.1 AGE VARIATION IN THE CAPELA PLUTON

This work provides a new SHRIMP zircon U–Pb age of 616 ± 6 Ma for a melanogabbro, different from the age of 631 ± 3 Ma previously obtained for a hornblendite at the same quarry (Pereira et al., 2020). The dated crystals from both samples are morphologically and texturally similar (Fig. 6), showing undisturbed oscillatory concentric zonations that suggest an igneous nature (Corfu, 2003). The variation in the Th/U ratios also suggests an igneous origin (Rubatto, 2017). Zircon grains from the hornblendite and gabbro have similar U concentrations but variable Th (Fig. 7c), producing distinctive higher Th/U ratios in the former.

The U–Pb data of the gabbro sample show low common lead, low uncertainties above isotope ratios, and concordant to subconcordant $^{206}\text{Pb}/^{238}\text{U}$ and $^{206}\text{Pb}/^{207}\text{Pb}$ dates (Table 2), indicating that the SHRIMP results are accurate. Nonetheless, the obtained MSWD value is higher than that recommended by Spencer et al. (2016) to infer if the U–Pb data represent a single population [$\text{MSWD} \leq 1 + 2\sqrt{2}/(n - 1)$, where n refers to the analysis number], implying a composite population. An acceptable value of MSWD of 0.73 is only achieved when the grain with the older date and two rims with younger dates are eliminated, providing a weighted mean age of 618 ± 4 Ma. Considering this age, the data return an intersample variation of ~ 13 Ma that may be interpreted as an incremental pluton assembly in a deep-seated magma chamber, where zircon crystals record a long-lived history of recycling and multistage growth. From this perspective, the oldest date of 631 Ma determined in the gabbro, identical to the crystallization age of the hornblendite, would correspond to antecryst grain incorporated from previous magma batches in a growing crystal mush (Coleman et al., 2004; Miller et al., 2007).

However, an age of 618 Ma is inconsistent with the evidence of plastic deformation documented by Capela rocks, as the 625–600 Ma period was marked by the emplacement of isotropic granodiorites and monzonites in a late-collisional setting (Pereira et al., 2023). Then, a preferred scenario to reconcile the U–Pb data and geological evidence is that magmatic crystallization of the gabbro occurred at ~ 630 Ma, and the data overdispersion represents an ancient Pb-loss event. In a population of cogenetic zircons, the lead loss is identifiable on a plot of $^{176}\text{Hf}/^{177}\text{Hf}_{(t)}$ against the U–Pb dates because the U–Pb and Lu–Hf systems are decoupled during zircon alteration such that the $^{176}\text{Hf}/^{177}\text{Hf}_{(t)}$ ratio is not modified by subsequent alteration processes that affect the U–Pb system (Gerdes and Zeh, 2009). The uniform $^{176}\text{Hf}/^{177}\text{Hf}_{(t)}$ ratios at variable $^{206}\text{Pb}/^{238}\text{U}$ dates (Fig. 7d) imply that zircon grains from hornblendite and gabbro grew from an isotopically homogenous magma, which remained undisturbed during the

secondary process that caused zircon Pb-loss. This inference is corroborated by the presence of rejuvenated rims at ~600 Ma and has been evidenced for other plutons in the SOS (Pereira et al., 2023 and reference therein). In this context, the age of 631 ± 3 Ma remains the most conservative estimate for the magmatic crystallization of the Capela pluton.

8.2 ROLE OF FRACTIONAL CRYSTALLIZATION

Evidence for fractional crystallization first came from petrographic observations. Normal-zoned plagioclase laths record subtle changes in magma composition (Pereira et al., 2019). Mesocumulate and orthocumulate hornblendites suggest settling early crystallized amphibole at the bottom of a deep-seated magma chamber (Annen et al., 2015). In addition, the predominance of hornblende and biotite as primary phases in mafic-ultramafic rocks, combined with the presence of ponds and dikes of mafic pegmatites, is indicative of crystallization from a water-rich magma (Castro et al., 2003; Couzinié et al., 2016; Murphy, 2020, 2013).

In a logarithmic plot of incompatible versus compatible elements, rocks related by partial melting describe subhorizontal trends, while those related by fractional crystallization tend to produce a subvertical alignment (Cocherie, 1986). The investigated samples depict a steep inclination on a projection of Rb against V and Dy (Fig. 9a and 9b), suggesting that fractional crystallization was an important process leading to magma differentiation.

Bivariate log-log vector plots permit monitoring the changes in trace element composition of the residual melt resulting from extracting particular mineral phases (Rollinson, 1993). Unlike the expected behavior for fractional crystallization-related suites, the mafic and felsic rocks display similar contents of highly incompatible elements Sr and Ba (Fig. 9c). The early crystallization of mafic minerals leads to higher Sr and Ba contents, whereas plagioclase involvement appears to be subordinate. Amphibole and accessory phases such as titanite, zircon, and apatite control the LREE and HREE supply (Fig. 9d). The compatible elements V and Cr are strongly sensitive to amphibole, clinopyroxene, and ilmenite removal (Fig. 9e and 9f).

Different models have been tested to quantify the role of fractional crystallization in Capela magmas. Mass balance calculations assumed the least differentiated (SOS-940) and more evolved (PC080A) samples as representing the initial (C_0) and final liquids (C_L), respectively. The best adjustment for major elements ($\sum R^2 = 0.056$) was obtained for 85% fractional crystallization ($F = 15\%$), with a cumulate consisting of 28.03% plagioclase + 26.88% amphibole + 24.49% biotite + 19.29% clinopyroxene + 1.31% ilmenite. While present

in the assumed parental magma, orthopyroxene does not seem to play a significant role in fractional crystallization.

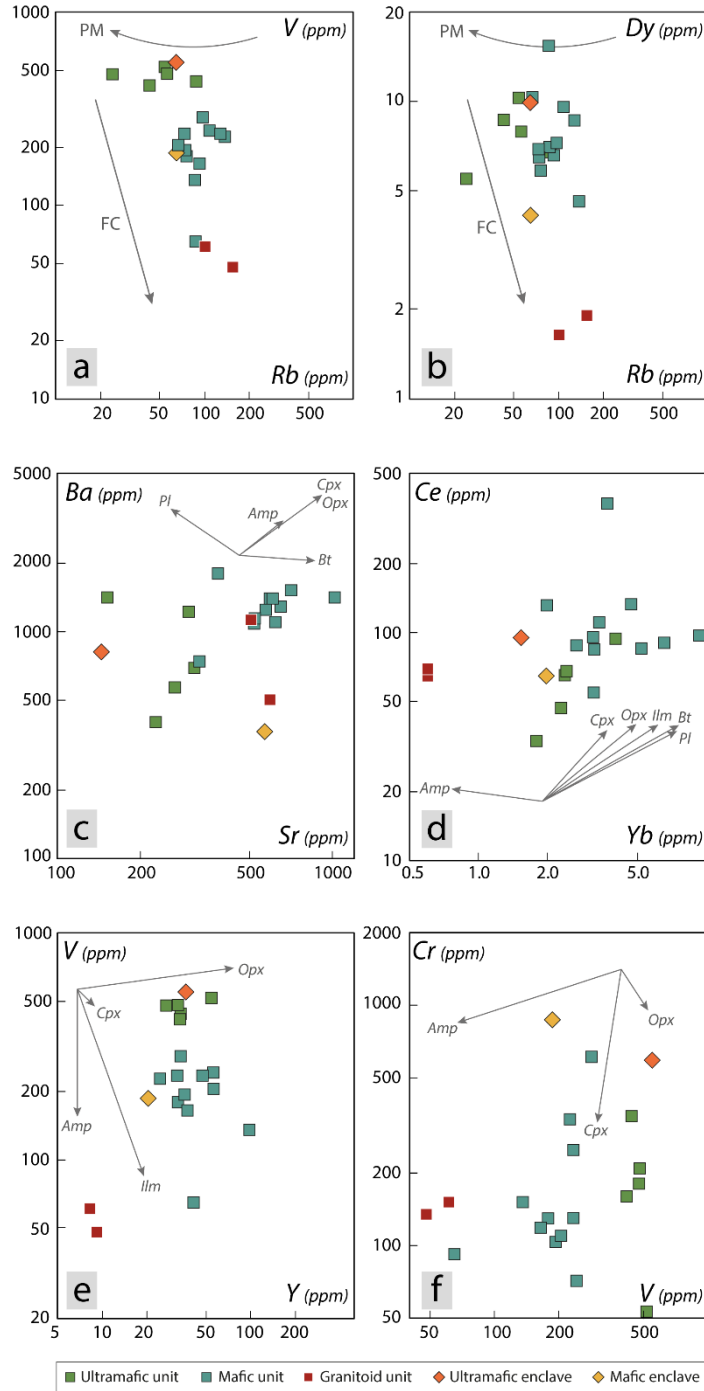


Figure III.9- Petrogenetic discrimination diagrams for rocks from the Capela pluton. Log-log plots of (a) Rb vs. V and (b) Rb vs. Dy with the trends produced by partial melting (PM) and fractional crystallization (FC). Log-log vector plots of (c) Sr vs. Ba, (d) Yb vs. Ce, (e) Y vs. V, and (f) V vs. Cr illustrating the influence of fractional crystallization of clinopyroxene (Cpx), orthopyroxene (Opx), amphibole (Amp), biotite (Bt), plagioclase (Pl), and ilmenite (Ilm). Mineral/melt partition coefficients are listed in Supplementary Material 1.

Despite excellent fits for major elements, modeling constrained by the mass balance results fails to explain the trace element composition of granitoids (Supplementary Table S2). The calculated bulk coefficient partition (D) for the more incompatible trace elements is below unity. This behavior should produce daughter liquids richer in incompatible elements than their parental mafic magma, which is invalid for the studied granitoids. Furthermore, the granitoid sample PC084C records the less radiogenic Sr isotope composition ($^{87}\text{Sr}/^{86}\text{Sr}_{(630\text{ Ma})} = 0.7054$), precluding its derivation from isotopically evolved precursors. Thus, although fractional crystallization has operated mainly among the mafic members, the associated granitoids do not represent the final products of this process.

8.3 EVOLUTION OF CUMULATES

All ultramafic samples, including the UME, have similar mineral assemblages and elemental compositions. Pereira et al. (2019) recognized a genetic relationship between the UME and hornblendites based on the overall compositional coherence between the main forming minerals from both units. The similar composition and behavior regarding major and trace elements corroborate this assumption. Accordingly, we infer that ultramafic enclaves may represent fragments formed through brecciation of early-solidified hornblendites.

They show low SiO_2 (~43 wt%) and high MgO (~10 wt%), Cr (~257 ppm), and V (~482 ppm) contents. Whole-rock data lie near the amphibole pole in the variation diagrams (Fig. 5), demonstrating the role exerted by hornblende accumulation. In a plot of major elements normalized to the average amphibole composition from the Capela pluton, all oxides have normalized values close to unity, with the exception of K_2O (Supplementary Figure 1). Such behavior implies that bulk rock mimics the composition of the main modal constituent, at least in terms of principal oxides.

The chemistry of cumulate plutonic rocks is mainly governed by the proportions of cumulus minerals and melt entrapped during crystallization. This relationship is illustrated for the Capela ultramafic rocks by the heterogeneous contents of incompatible elements linked with the volume of interstitial phases. Those samples with large cumulus hornblende crystals and scarce interstitial phases typically have the lowest LILE concentrations and REE sums. Zircon, apatite, and titanite are the main accessory phases responsible for the REE budget. Negative Eu and Sr anomalies suggest plagioclase fractionation near the final stages of crystallization (Fig. 4a and 4d). The similarity between whole-rock Sr–Nd–Pb, and zircon Lu–Hf data for ultramafic and mafic rocks demonstrates that they share the same parental magma (Fig. 8). These

inferences, allied with the transition from hornblendites to hornblende gabbros and hornblende diorites, may indicate that the former represent partial cumulates derived from fractionation of a hydrous basaltic magma, from which the gabbros and diorites were created.

8.4 CRUSTAL CONTAMINATION VERSUS ENRICHMENT OF THE MANTLE SOURCE

The high contents of fluid-soluble elements (K, LILE, and LREE), radiogenic Sr-Pb, and unradiogenic Nd-Hf isotope compositions imply a crustal fingerprint in mantle-derived rocks from the Capela pluton. At first glance, the abundance of incompatible elements prevents an asthenospheric mantle source because obtaining such enriched compositions from a depleted mantle would require minimal degrees of partial melting. For instance, considering the Ba concentration of 1145 ppm (sample SOS-940) in the melt, the partial melting degree would be $\sim 0.04\%$, considering $C_0 = 0.563$ and $D_{Ba} = 0.00012$ for a depleted mantle (Workman and Hart, 2005). Therefore, two main processes can be envisaged to generate the enriched geochemical and isotopic features in mantle-derived rocks of the Capela pluton: (i) the enrichment of a geochemical and isotopically depleted basaltic magma through assimilation of crustal rocks and fractional crystallization and (ii) partial melting of an enriched mantle source.

Since the basalt liquidus temperature (~ 1200 °C) is above the melting points of the main rock-forming minerals, melting of the surrounding rocks is likely during ascent or storage in the crust (Watson, 1982; Xu et al., 2017). The presence of partially molten and disaggregated metasedimentary xenoliths suggests that, even locally, the Capela pluton bulk-rock composition could have been modified by some degree of shallow-level crustal assimilation. Quantitative evaluation of this process is challenging once the metasedimentary sequence of the Macururé Complex is poorly known and the scarce available data show heterogeneous compositions (Fig. 8a). Assimilation of the wall rocks surrounding the magma chamber is generally combined with fractional crystallization (DePaolo, 1981a). The AFC (assimilation-fractional crystallization) model takes into account the modal proportion of the fractionated phases (28.03% Pl + 26.88% Amp + 24.49% Bt + 19.29% Cpx + 1.31% Ilm), remaining melt amount ($F = 15\%$), and assimilation rate/crystallization rate parameter (r), which was fixed at 0.2 and 0.5. The parental mafic component was the average composition of slightly LILE-enriched depleted basaltic magma of the Canindé layered intrusion, interpreted as derived from the subcontinental lithospheric mantle (SCLM; Pinto et al., 2020). As shown in Fig. 10a, AFC processes cannot explain the elemental and isotopic characteristics of the Capela pluton mafic rocks, even when considering high assimilation proportions. This is partly due to the incompatible element

concentrations in the primitive rocks being above those observed in the country rocks (Oliveira et al., 2015a) or even the continental crust (Rudnick and Gao, 2003). As a result, their compositions are relatively insensitive to modification during crustal contamination (Farmer, 2007).

The emplacement of mantle-derived basaltic magmas into the lower crust may induce local anatexis in a MASH zone, where melting, assimilation, storage, and homogenization take place (Hildreth and Moorbath, 1988). Whether mafic and felsic melts mixed and homogenized during ascension and storage in the crust, the variable hybridization degrees could explain the evolved signatures of gabbros-diorites. We tested this hypothesis for Capela rocks assuming a simple binary mixing process. Sample PC-080A, the most radiogenic granitoid in our dataset, was selected as the felsic endmember. Mixing calculations reveal that more than 50% crustal components would have to be incorporated to reproduce the composition of the mafic rocks (Fig. 10b). Unreliable high values are reached when considering the isotopic compositions of the host schists and Paleoproterozoic and Tonian rocks in the SOS, which are feasible contamination sources. These values are strongly unlike because with such a proportion of contaminants, the magma would no longer be mafic (Farmer, 2007).

Because sediments typically have strong negative Nb anomalies [$Nb/Nb^* = Nb_{PM}/\sqrt{(Th_{PM} \times La_{PM})}$], the occurrence of negative Nb anomalies in trace element patterns could be diagnostic of interaction between mafic magmas and continentally derived material. All studied samples exhibit deep troughs at Nb, whose magnitude negatively correlates with MgO (Supplementary Figure 2). Nonetheless, there is no correlation between Nb/Nb^* and $^{87}Sr/^{86}Sr_{(t)}$ (Supplementary Figure 3), indicating that the Nb anomalies were not acquired through contamination with metasedimentary rocks but were probably inherited from the source. The absence of correlations between SiO_2 and $^{87}Sr/^{86}Sr_{(t)}$ and $\epsilon Nd_{(t)}$ corroborates the negligible role played by shallow-level contamination (Fig. 10c and 10d). Lead isotopes show a range of $^{207}Pb/^{204}Pb$ and $^{208}Pb/^{204}Pb$ at a narrow interval of $^{206}Pb/^{204}Pb$, which is unlikely to reflect crustal contamination because sediments typically have a broad range of $^{206}Pb/^{204}Pb$ ratios (e.g., Turner et al., 1996). In addition, the narrow range of $^{177}Hf/^{176}Hf_{(t)}$ on zircon indicates an isotopically homogenous enriched source for the most primitive rocks.

Although there is some evidence for local crustal contamination, different approaches to address this issue fail to explain the geochemical and isotopic behavior of the investigated rocks. These characteristics seem to be inherited from a mantle region that already had an enriched composition before the onset of partial melting.

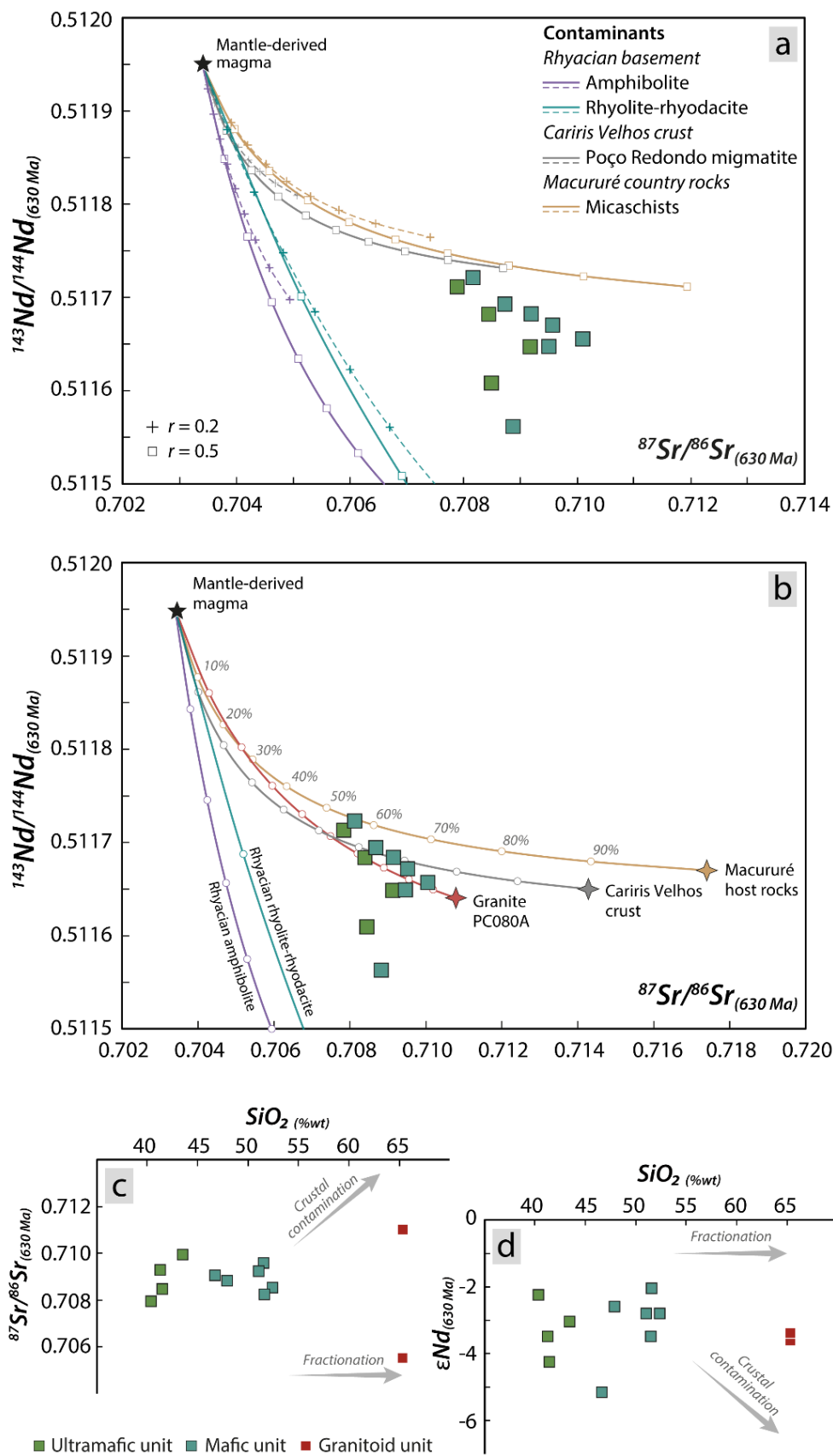


Figure III.10- Initial $^{87}\text{Sr}/^{86}\text{Sr}$ and $^{143}\text{Nd}/^{144}\text{Nd}$ isotope ratios of rocks from the Capela pluton, host schists, and the average of Rhyacian and Cariris Velhos remnants in the SOS. The parameters adopted for (a) AFC and (b) mixing modeling are presented in Table 4.

Table III.4- Parameters of the components used for petrogenetic modeling. Elemental and isotopic compositions relative to average values from n analyses. Values in parentheses correspond to the entire variation range.

Geological unit	[Sr] ppm	$^{87}\text{Sr}/^{86}\text{Sr}_{(630\text{ Ma})}$	[Nd] ppm	$^{143}\text{Nd}/^{144}\text{Nd}_{(630\text{ Ma})}$	$\epsilon\text{Nd}_{(630\text{ Ma})}$	n
<i>Jirau do Ponciano dome^a</i>						
Amphibolite	198	0.7112 (0.7106 - 0.7119)	13.74	0.51120 (0.51167 - 0.51173)	-2.4 (-3.1 to -1.9)	5
Rhyolite-rhyodacite	270	0.7297 (0.7278-0.7303)	17.35	0.51044 (0.51023-0.51105)	-27.1 (-15.2 to -31.3)	5
<i>Poço Redondo Domain^b</i>						
Poço Redondo migmatite	218	0.7143 (0.7106 - 0.7180)	34.66	0.51165 (0.51154 - 0.51175)	-3.5 (-5.6 to -1.4)	2
<i>Canindé Domain^c</i>						
Canindé gabbroic intrusion	410	0.7034 (0.7029 - 0.7040)	9.16	0.51195 (0.51186 - 0.51202)	+2.4 (+0.6 to +3.8)	7
<i>Macururé Domain^b</i>						
Macururé micaschists	163	0.7174 (0.7034 - 0.7630)	28.99	0.51167 (0.51147 - 0.51180)	-3.1 (-7.0 to -0.6)	6
DM ^d	7.664	0.7026	0.581	0.51313	+5.4	-
Glimmerite (EN88-1G) ^e	250.1	0.7227	10.40	0.51053	-25.3	-
Glimmerite (EN88-1Gb) ^e	722.5	0.7117	8.65	0.51045	-26.9	-

^a Lima et al. (2019).

^b Oliveira et al. (2015a).

^c Pinto et al. (2020).

^d Workman and Hart (2005).

^e Carlson and Irving (1994).

8.5 CONSTRAINTS ON MANTLE SOURCE

Experimental studies reveal that potassic liquids may be obtained from metasomatized phlogopite-bearing peridotite (Conceição and Green, 2004; Condamine and Médard, 2014). Similar compositions were attained in melting experiments conducted with peridotite hybridized with granitoid material (Mallik et al., 2015; Rapp et al., 2010). Both experiment types are equivalent from the geochemical view since the second approach results in phlogopite/amphibole-bearing peridotite in equilibrium with K-rich mafic melts (Couzinié et al., 2016). The major element compositions of the investigated mafic rocks match those liquids obtained by partial melting of phlogopite- and amphibole-bearing peridotites (Fig. 11a and 11b). These results agree with recent studies in potassic and ultrapotassic rocks in the SOS, which argue the existence of a K-bearing minor phase in the mantle source buffering the K_2O contents in such rocks (Lisboa et al., 2019; Pereira et al., 2020, 2023; Sousa et al., 2022). Recognition of the trace element signature of residual phlogopite/amphibole in basalt implies derivation or interaction with the SCLM because these phases are unstable at the high temperatures of the convecting upper mantle (Class and Goldstein, 1997; Farmer, 2007).

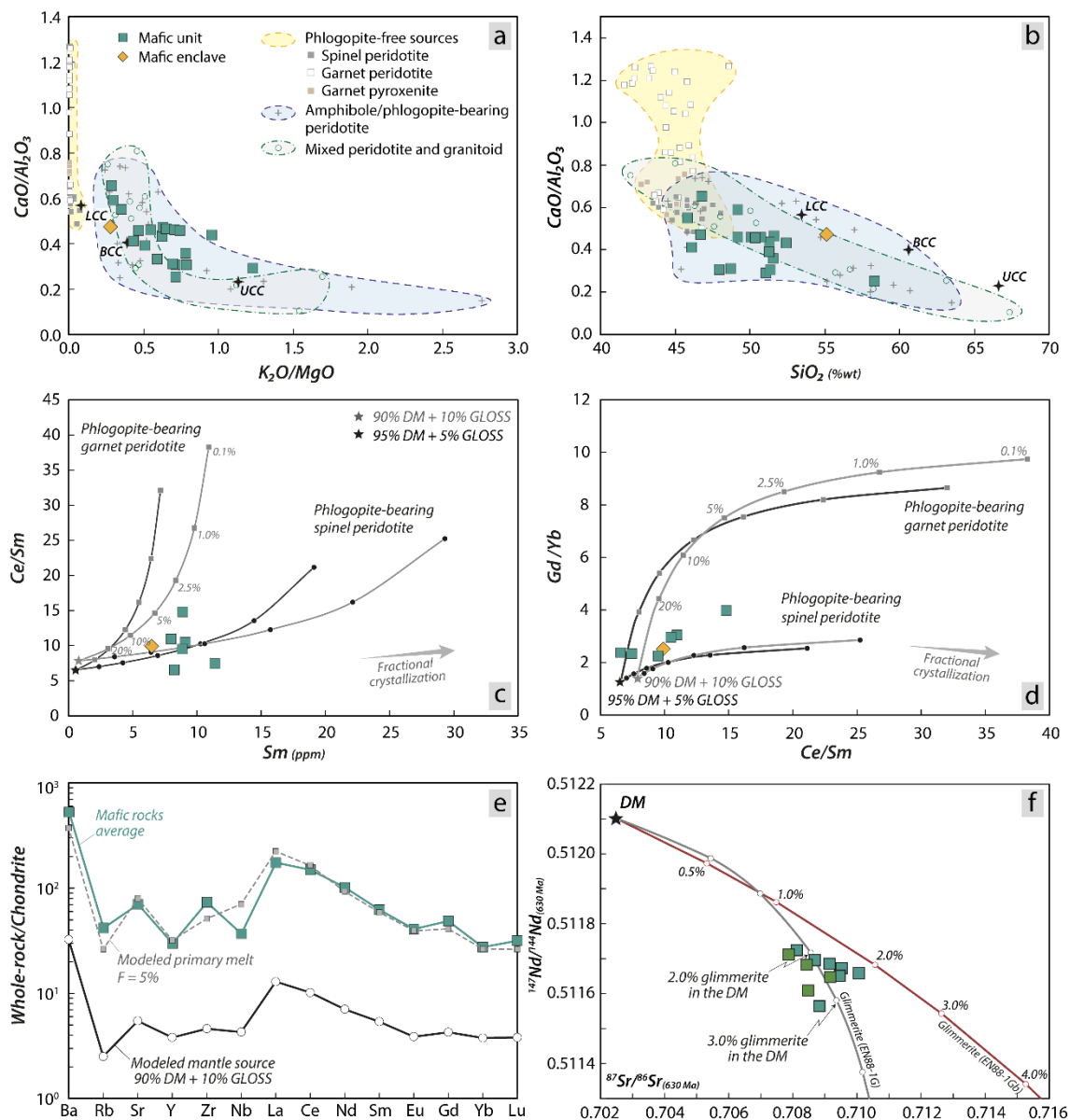


Figure III.11- Elemental and isotopic constraints on mantle source (for samples with 45 wt% < SiO_2 < 60 wt%). (a) $\text{K}_2\text{O}/\text{MgO}$ and (b) SiO_2 vs. $\text{CaO}/\text{Al}_2\text{O}_3$ plots with fields of experimental melts derived from metasomatized phlogopite/amphibole-bearing peridotite (Conceição and Green, 2004; Condamine et al., 2016; Condamine and Médard, 2014), phlogopite/amphibole-free peridotite and pyroxenite (Gaetani and Grove, 1998; Herzberg and Zhang, 1996; Hirschmann et al., 2003; Tenner et al., 2012), and hybridized peridotite and granitoid sources (Mallik et al., 2015; Rapp et al., 2010). Upper (UCC), lower (LCC), and bulk (BCC) continental crusts from Rudnick and Gao (2003). (c) Sm vs. Ce/Sm and (d) Cs/Sm vs. Gd/Yb plots with batch melting curves of phlogopite-bearing garnet and spinel peridotites (for samples with $\text{Mg}\# > 0.5$). Modeled sources assume 95% DM + 5% GLOSS (black) and 90% DM + 10% GLOSS (gray). Values for DM and GLOSS are from Workman and Hart (2005) and Plank and Langmuir (1998), respectively. The modal proportions of residual minerals were 69% olivine + 15% orthopyroxene + 8% clinopyroxene + 7% phlogopite + 1% spinel for spinel peridotite (Condamine and Médard, 2014) and 25% olivine + 50% orthopyroxene + 15% clinopyroxene + 7% garnet + 3% phlogopite for garnet peridotite (Thibault et al., 1992). (e) Chondrite-normalized (McDonough and Sun, 1995) incompatible element pattern showing the composition of the modeled mantle source, mafic rock average, and liquid generated by 5% partial melting (residue = 69% olivine + 15% orthopyroxene + 14% clinopyroxene + 1% spinel + 1% phlogopite). (f) $^{87}\text{Sr}/^{86}\text{Sr}_{(630 \text{ Ma})}$ plotted against $^{147}\text{Nd}/^{144}\text{Nd}_{(630 \text{ Ma})}$. Modeling assumes binary mixing between a depleted mantle source (Workman and Hart, 2005) and two hypothetical glimmerite veins (Carlson and Irving, 1994).

Various mechanisms have been proposed for metasomatism of the mantle. In active continental margins, subduction plays a crucial role in leading crustal components that react with underlying peridotites of the mantle wedge (e.g., Hawkesworth et al., 1997). The infiltration of LILE- and volatile-rich subduction-related melts or fluids contributes to forming enriched domains in the lithospheric mantle, which may contain unusual phases such as apatite, amphibole, phlogopite, and Ti-bearing minerals (Foley, 1992; Guo et al., 2006; Turner et al., 1996). Modal metasomatized regions have lower solidus temperatures than refractory “dry” peridotites (Conceição and Green, 2004; Condamine and Médard, 2014), making them more prone to melt during subsequent reheating episodes.

Depending on the nature of the contaminant agent, mantle-derived magmas present a particular signature of incompatible trace elements and isotopic ratios. The percolation of fluids released from hydrothermally altered oceanic crust results in magmas having low $^{87}\text{Sr}/^{86}\text{Sr}$ ~ 0.7035 and high Sr/Th ratios (Hawkesworth et al., 1997). Conversely, introducing partial melts of slab sediments produces much more radiogenic Sr and low Sr/Th magmas. The analyzed mafic rocks have high $^{87}\text{Sr}/^{86}\text{Sr}$ and Sr/Th ratios, consistent with a sediment-related origin for mantle source enrichment.

In Pb isotope diagrams (Fig. 8b and 8c), the samples plot within the field of GLOSS, suggesting that Pb isotopic compositions may reflect the proportion of sediment in the source. They overlap the area of the Tibetan post-collisional potassic-ultrapotassic volcanic rocks, whose mantle sources have a significant crustal component (Guo et al., 2006; Turner et al., 1996). The radiogenic $^{87}\text{Sr}/^{86}\text{Sr}_{(t)}$ ratios along the negative $\epsilon\text{Nd}_{(t)}$ trend toward the EM-II endmember also indicate the participation of a recycled continental crust component in the mantle (Zindler and Hart, 1986). In addition, the subchondritic $\epsilon\text{Hf}_{(t)}$ values reinforce a long-term enrichment of Hf over Lu in the magma source. Based on these features, we argue that the mantle source region was metasomatized by subducted sediments (bulk or partial melts derived from them) before generating potassic LILE-rich magmas of the Capela pluton.

Rubidium and Ba are strongly incompatible during the partial melting of the mantle. Depletion of Rb relative to Ba in primitive mantle-normalized multielement patterns suggests the presence of a mineral phase that retained Rb rather than Ba. These elements have distinct partition coefficients for pargasite and phlogopite, the main minor phases resulting from metasomatic processes (Class and Goldstein, 1997; Conceição and Green, 2004; Foley, 1992). Phlogopite mainly holds Rb ($K_{\text{Rb}}/K_{\text{Ba}} \sim 2.8$), but amphibole preferentially incorporates Ba ($K_{\text{Rb}}/K_{\text{Ba}} \sim 0.7$) (Rollinson, 1993). Thus, low Rb at relatively high Ba certainly reflects the presence of phlogopite as a melting residue.

The relatively high HREE in mafic rocks, which are dozens of times higher than chondrites, and almost flat HREE patterns preclude garnet as a residual mineral in the mantle source region. Instead, these characteristics are more compatible with the presence of spinel and imply shallower melting depths (Farmer, 2007).

Figures 11c and 11d show batch partial melting curves for two modeled mantle sources. The models assume that parental magmas of the Capela pluton were produced by the partial melting of a metasomatized mantle source in response to mixing of a depleted source (DM; Workman and Hart, 2005) with subducted sediments (Plank and Langmuir, 1998). We found that low partial melting degrees (5-10%) of a mixed source consisting of 90-95% DM and 5-10% GLOSS accounts for the LREE-enriched character of the studied mafic rocks. These plots further suggest that melting took place in a spinel-facies source. Geochemical modeling constrained by these inferences reveals that 5% partial melting of a spinel lherzolite containing 1% residual phlogopite reproduces the behavior of incompatible elements in multielement patterns (Fig. 11e). The smaller extent of negative Nb anomalies in the calculated primary melt may reflect the presence of a Ti-bearing accessory phase.

Phlogopite in mantle peridotites occurs as intergranular material or in veins associated with other metasomatic phases. Vein-plus-wall rock melting produces a variety of potassic magmas in orogenic areas (Becker et al., 1999; Foley, 1992). Experiments at 1-2 GPa of mixed glimmerite and harzburgite demonstrated that melting begins in phlogopite-rich metasomes, producing ultrapotassic melts similar to lamproites (Förster et al., 2017). Melting of adjacent depleted peridotite dilutes the strongly alkaline glimmerite-derived melts, rendering less potassic magmas akin to shoshonites. We propose that a similar scenario was active in the SCLM beneath the southern Borborema Province, where glimmerite veins in peridotites were formed due to modal metasomatism processes by long-term incorporation of metasedimentary components. This proposal was modeled taking the DM isotopic composition as the unmetasomatized mantle endmember and hypothetical phlogopite-rich mafic veins as contaminants (glimmerites EN88-G and EN88-Gb; Carlson and Irving, 1994). The model yields that mixing 2-3% glimmerite veins in a depleted source accounts for the isotope signatures of the Capela pluton mafic rocks (Fig. 11f).

Trace element modeling assumes a homogeneous mixture between the depleted mantle and recycled components. Although this method cannot precisely reproduce the complexity of the melting process of a heterogeneous mantle source, our model explains most geochemical and isotopic features of the Capela pluton.

8.6 MANTLE ENRICHMENT HISTORY

If our interpretations are correct, the SCLM beneath the southern sector of the Borborema Province, at least in its shallowest portions, had enriched trace elements and isotopic signatures. Such features resulted from the incorporation of small amounts of sediments through subduction. Furthermore, the interval between source enrichment and magma generation must have been large enough that the time-integrated evolution of the Hf–Sr–Nd–Pb isotopic systems could reach a crustal-like signature.

Previous studies have proposed that the Borborema Province basement experienced a subduction episode during the Rhyacian Orogeny (2.22–1.96 Ga; Caxito et al., 2020a; Neves, 2021; Neves et al., 2015). Metavolcanic rocks in the Jirau do Ponciano dome, exposed at the northern segment of the SOS, display crystallization ages between 2.07–2.05 Ga (Lima et al., 2019). The period of ~2.0 Ga also marks the final cratonization of the SFC, the emplacement of the Arauá intermediate-acidic dike swarm in its northern margin, and the ultrahigh-temperature metamorphism of the Arapiraca Complex (Barbosa et al., 2018; Oliveira, 2014; Tesser et al., 2021).

Subduction events during the early Tonian (Cariris Velhos event) and late Tonian–Cryogenian (Canindé event) are also postulated by other researchers (Carvalho, 2005; Oliveira et al., 2010; Passos et al., 2022, 2021; Pinto et al., 2020). Both events added juvenile material to the SOS crust, showing positive $\epsilon\text{Nd}(t)$ values indicative of a depleted source.

On the other hand, the Brasiliano Orogeny was dominated by crustal reworking, adding around 15% juvenile material in the Borborema Province (Ganade et al., 2021). Pereira et al. (2023) suggested that the Brasiliano Orogeny in the SOS resulted from widespread lithospheric extension and basin inversion, culminating in the PEAL–SFC collision. These authors determined zircon Hf- T_{DM}^{C} model ages ranging from 2.47 to 2.32 Ga for the 643 Ma Camará mafic pluton. Such old model ages were interpreted as recording the preservation of tracts of the Paleoproterozoic SCLM, which survived since the Rhyacian accretionary event. This work obtained similar Siderian–Rhyacian zircon Hf- T_{DM}^{C} model ages between 2.10 and 2.47 Ga.

Recognition of a Paleoproterozoic subduction-related metasomatic signature in the SCLM sampled by Ediacaran mafic rocks is difficult to reconcile, given that a depleted mantle source was available at 740–680 and 980–960 Ma. A possible explanation is that crustal recycling and consequent mantle enrichment occurred during the Cariris Velhos or Canindé events. Although our data do not allow a straightforward conclusion about this issue, the Paleoproterozoic model ages are consistent with the Rhyacian basement of the SOS (Lima et

al., 2019; Tesser et al., 2021). This scenario favors the intracontinental model for this orogen and the (para)allochthonous derivation of the Canindé and Poço Redondo-Marancó domains.

8.7 ORIGIN OF GRANITOIDS

The granodiorites, quartz monzonites, and granites from the Capela pluton are metaluminous to slightly peraluminous ($A/CNK = 0.94-1.05$; Fig. 3b), akin to I-type granitoids derived from igneous protoliths (Chappell and White, 2001). Their isotopic compositions vary from relatively depleted to evolved $^{87}\text{Sr}/^{86}\text{Sr}_{(t)}$ ratios (0.7051 and 0.7108), with negative $\epsilon\text{Nd}_{(t)}$ values (-3.6 and -3.4) and Nd- T_{DM} ages of ~ 1.3 Ga (Fig. 12a). The lead isotope ratios overlap the range of mafic-ultramafic rocks, indicating a U- and Th-enriched source. These data suggest that their parental magmas were derived from an ancient crustal source, probably related to the Cariris Velhos event (Carvalho, 2005; Oliveira et al., 2015a).

In a plot comparing the compositions of melts produced by experimental dehydration melting (Patiño Douce, 1999), most granitoids lie in the field of amphibolite sources (Fig. 12b), pointing to a mafic source. Dehydration melting experiments demonstrate that metaluminous to slightly peraluminous melts can be obtained from moderately K-enriched amphibolite of basaltic composition (Sen and Dunn, 1994; Ye et al., 2021). These andesitic to rhyolitic liquids generally coexist with a restite assemblage of amphibole, clinopyroxene, plagioclase, and garnet.

The composition of Capela granitoids can be modeled following these experiments, assuming a metabasaltic source. However, some caveats must be raised about the residue nature. The negligible Eu negative anomalies ($\text{Eu}/\text{Eu}^* = 0.8$) preclude a significant involvement of plagioclase as melting residue, further evidenced by the absence of Sr troughs (Fig. 4c and 4f). In addition, the highly fractionated REE patterns suggest that garnet was a residual phase once $Kd_{\text{HREE}} \gg Kd_{\text{LREE}}$ for this mineral (Rollinson, 1993). Multielement patterns display prominent negative Nb anomalies accompanied by small troughs at Ti, suggesting the presence of a minor titanium-bearing phase.

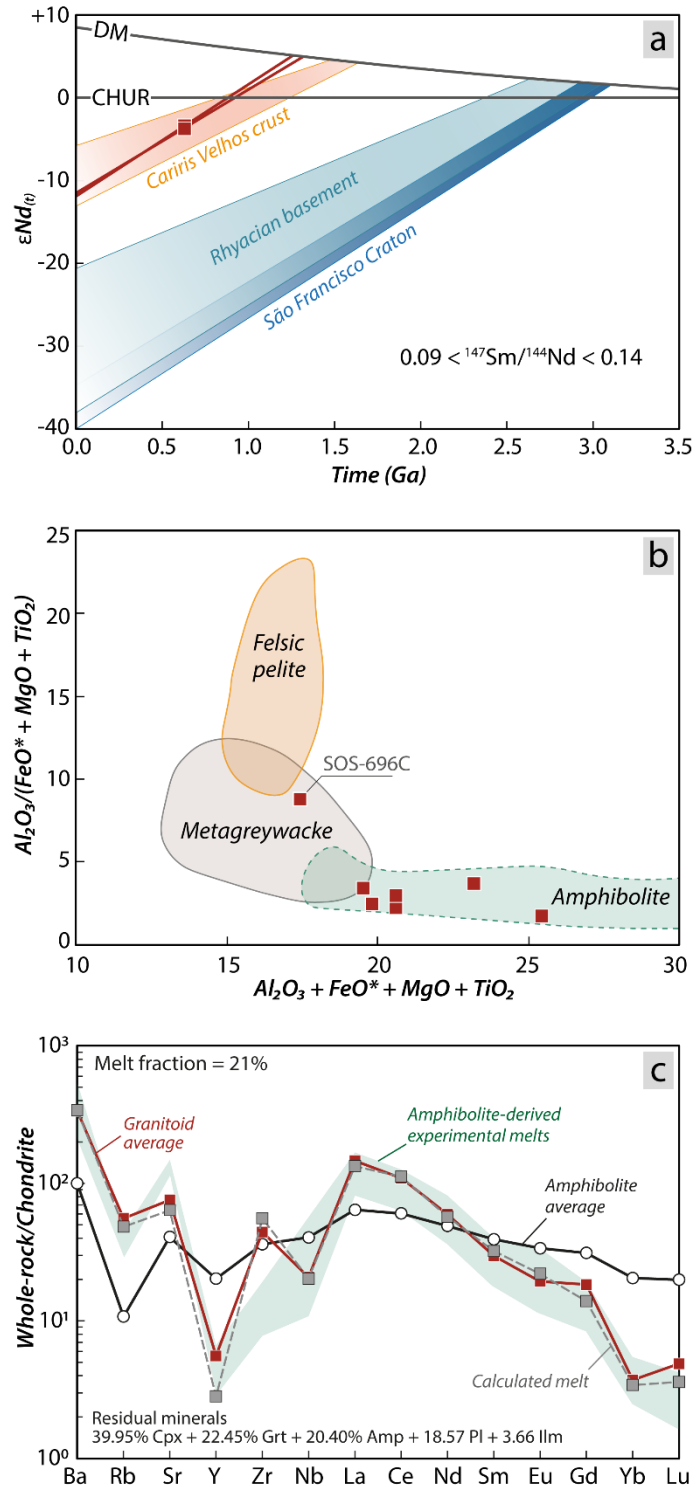


Figure III.12- Origin of the granitoids associated with the Capela pluton. (a) Nd evolution paths compared with those from Cariris Velhos-related orthogneisses and migmatites (Carvalho, 2005), Rhyacian metavolcanic acid rocks (Lima et al., 2019), and Archean gneisses from the SFC (Oliveira et al., 2015b) in the SOS, which show $^{147}\text{Sm}/^{144}\text{Nd}$ between 0.09 and 0.14. Intercepts with the depleted mantle curve of (DePaolo, 1981b) at 1.26 and 1.32 Ga. (b) $\text{Al}_2\text{O}_3 + \text{FeO}^* + \text{MgO} + \text{TiO}_2$ vs. $\text{Al}_2\text{O}_3/(\text{FeO}^* + \text{MgO} + \text{TiO}_2)$ plot with fields of experimental liquids obtained through dehydration melting of amphibolites, metagraywackes, and felsic pelites (Patiño Douce, 1999). (b) Trace element model for granitoid generation by partial melting of a basaltic amphibolite source. The green shaded area corresponds to experimental liquids obtained by dehydration melting of amphibolite at 1.5 GPa and 850-950 °C (Ye et al., 2021). Chondrite normalization values from McDonough and Sun (1995).

We propose a petrogenetic model based on the partial melting of a LILE-enriched basaltic source representing a lower crustal component where granite generation occurred (Table 5). We select the ortho-amphibolites from the Canindé Domain to constrain the source composition of the granitoids even though there is no genetic relationship between them. We assume the average composition of basaltic amphibolites from the Novo Gosto unit (Passos et al., 2021 and references therein) as the unmelted source (C_0) and the average granitoid composition as the final liquid (C_L). Mineral composition data obtained from dehydration melting experiments by Ye et al. (2021) were considered to represent the remaining residue after melting.

The best fit for major elements is reached assuming the rhyolitic melt is in equilibrium with an ilmenite-bearing residue ($\Sigma R^2 = 0.108$, $F = 21\%$) composed of clinopyroxene (39.95%), garnet (22.45%), amphibole (20.40%), plagioclase (18.54%), and ilmenite (3.66%). Trace element modeling based on residual assemblage and melt proportions from mass balance calculations provided satisfactory fits between the observed and modeled liquids, as shown in Fig. 12c. Overall, the calculated magma matches the experimental melts from Ye et al. (2021), indicating the viability of the model.

A heat source to partially melt an amphibolitic lower crust is needed. The migration and emplacement of hot mantle-derived magmas at 643-628 Ma was a potential heat source triggering the melting of the crust (Pereira et al., 2020, 2023). The Zr saturation systematic of Watson and Harrison (1983) provides some insights into this assumption. The Zr concentration in the studied granitoids is less than 200 ppm, rendering low near liquidus temperatures of approximately 770 °C. However, experimental data constrain the partial melting of mafic protoliths by amphibole dehydration at 850-900 °C (Sen and Dunn, 1994; Ye et al., 2021). At 900 °C, contents above 600 ppm of Zr would be necessary for such a metaluminous composition to achieve saturation (Watson and Harrison, 1983). Together with crust fertility, the H₂O content of the basalt heat source is a critical factor in determining the extent of crustal melting (Annen et al., 2015) because hydrous fluids can trigger water-assisted melting, which is considerably more efficient than dehydration melting (Weinberg and Hasalová, 2015 and references therein). The model proposed here suggests the emplacement of hydrous basaltic magmas in the lower crust as mafic underplates released aqueous fluids, which were then transferred to the crust and promoted water-fluxed melting.

Table III.5- Major and trace element modeling for generation of the granitoids of the Capela pluton by partial melting of a basaltic amphibolite source.

<i>Major elements</i> (wt%)	<i>Amphibolite average</i> ^a <i>C₀</i>	<i>Residue</i> <i>C_S</i>	<i>Mineral compositions</i> ^b				<i>Calculated melt</i> <i>C_L'</i>	<i>Granitoid average</i> ^d <i>C_L</i>
			<i>Cpx</i> 39.95%	<i>Grt</i> 22.45%	<i>Amp</i> 20.40%	<i>Pl</i> 18.54%		
SiO ₂	52.05	47.69	51.13	38.79	42.04	62.89	68.46	68.59
TiO ₂	2.09	2.39	0.53	0.26	1.46	0.01	50.00	0.94
Al ₂ O ₃	14.69	14.50	7.07	21.54	12.99	22.36	15.44	14.85
FeO*	12.32	14.48	10.93	22.94	16.72	0.15	50.00	4.18
MgO	5.77	6.71	11.50	2.84	9.20		2.23	1.46
CaO	9.13	10.89	14.96	13.84	8.41	3.46	2.52	2.73
Na ₂ O	3.08	3.02	1.72	0.02	3.45	8.88	3.33	4.45
K ₂ O	0.87	0.33	0.03	0.01	1.02	0.52	2.90	3.01
<i>Trace elements (ppm)</i>								
Ba	241						816	812
Rb	25						111	128
Sr	295						462	549
Y	31.8						4.4	8.7
Zr	138						213	169
Nb	9.7						4.9	5.0
La	15.22				ΣR ² = 0.108		31.63	34.60
Ce	37.04				F = 21%		68.51	66.80
Nd	22.37						26.05	27.20
Sm	5.82						4.77	4.40
Eu	1.94						1.24	1.09
Gd	6.17						2.77	3.66
Yb	3.29						0.55	0.60
Lu	0.49						0.09	0.12

^a Average of 22 samples from Passos et al. (2021) and references therein.

^b Values from Ye et al. (2021).

^c Assumed simplified composition.

^d Average of the samples PC080A and PC084C.

8.8 TOWARD AN INTEGRATED MODEL

We infer that SCLM metasomatism occurred during the Rhyacian accretionary event by incorporating sediments, which led to the development of exotic mineralogy containing minor amounts of phlogopite (Fig. 13a). Because mantle assemblages holding metasomatic phases have lower solidus temperatures due to high concentrations of volatiles and silicate-incompatible elements (Foley, 1992), such domains were more susceptible to melt during the late Cryogenian extensional episode of the Brasiliano Orogeny in the SOS (Pereira et al., 2023). The strongly alkaline melt derived from the veins first melted is then diluted by the melts generated from adjacent peridotites, producing potassic melts (Foley, 1992; Förster et al., 2017). As melting progresses, the basaltic magmas become able to segregate from the regional source and ascend to the crust. The migration toward shallower levels was facilitated by the high water contents in such magmas (Condamine and Médard, 2014; Murphy, 2020), which tend to remain trapped at the mantle-crust boundary (Hildreth and Moorbath, 1988).

High-anorthite plagioclase, orthopyroxene, and clinopyroxene indicate the early crystallization of the gabbro-norites from a deep-seated mush (Fig. 13b). The presence of biotite in these rocks, without post-magmatic transformations and high TiO₂ contents (Pereira et al., 2019), supports that the primitive basaltic magmas were originally water- and potassium-rich. Amphibole in gabbro-norites occurs only as coronas bordering pyroxene crystals, while clinopyroxene is present as relicts within amphibole from hornblende-norites, gabbros, and diorites. These observations suggest increasing p_{H₂O} conditions with differentiation, responsible for expanding the stability field of hornblende relative to the anhydrous phases (Murphy, 2020, 2013).

Amphibole crystallization and precipitation started at deep crustal levels (~8 kbar; Pereira et al., 2019), where ultramafic cumulates typically are found (Annen et al., 2015; Moyen et al., 2021), forming hornblende-norites in association with hornblende-rich gabbros and diorites (Fig. 13c). The reworking and disruption of early-crystallized ultramafic cumulates at depth might have occurred in response to the episodic replenishment of the magma chamber recorded by the MME (Fig. 13d). Plagioclase phenocrysts from host rocks included by MME suggest the entrance of new magma batches into a poorly consolidated crystal mush. The continued rejuvenation is believed to have produced the complex zoning patterns (inverse and oscillatory) recorded by plagioclase from gabbros and diorites (Pereira et al., 2019). On the other hand, skeletal patchy-zoned plagioclase (Fig. 2e) illustrates significant changes in magma composition that led to the resorption of high-anorthite plagioclase and crystallization of outward low-anorthite plagioclase (Bennett et al., 2019 and references therein).

The repeated influxes of mantle-derived magmas as a succession of sills into the lower crust could have developed a deep crustal hot zone (Annen et al., 2015, 2006). Lower crustal mafic rocks of basaltic composition have likely partially melted due to the combined effect of heat supply and aqueous fluids exsolved and released from hydrous basaltic magmas (Weinberg and Hasalová, 2015). Water-fluxed melting gave rise to minor amounts of acid melts, preserved in the Capela pluton as high-K calc-alkaline granodiorites and granites (Fig. 13a).

Angular xenoliths of host schists within gabbros and diorites reveal that the final emplacement occurred at shallower depths (Fig. 13d), where the wall rocks were brittle and cold. At higher structural levels, decreasing pressure drives water saturation of the magmatic system, which explains the predominance of idiomorphic hornblende and pegmatitic textures (Castro et al., 2003; Murphy, 2020, 2013).

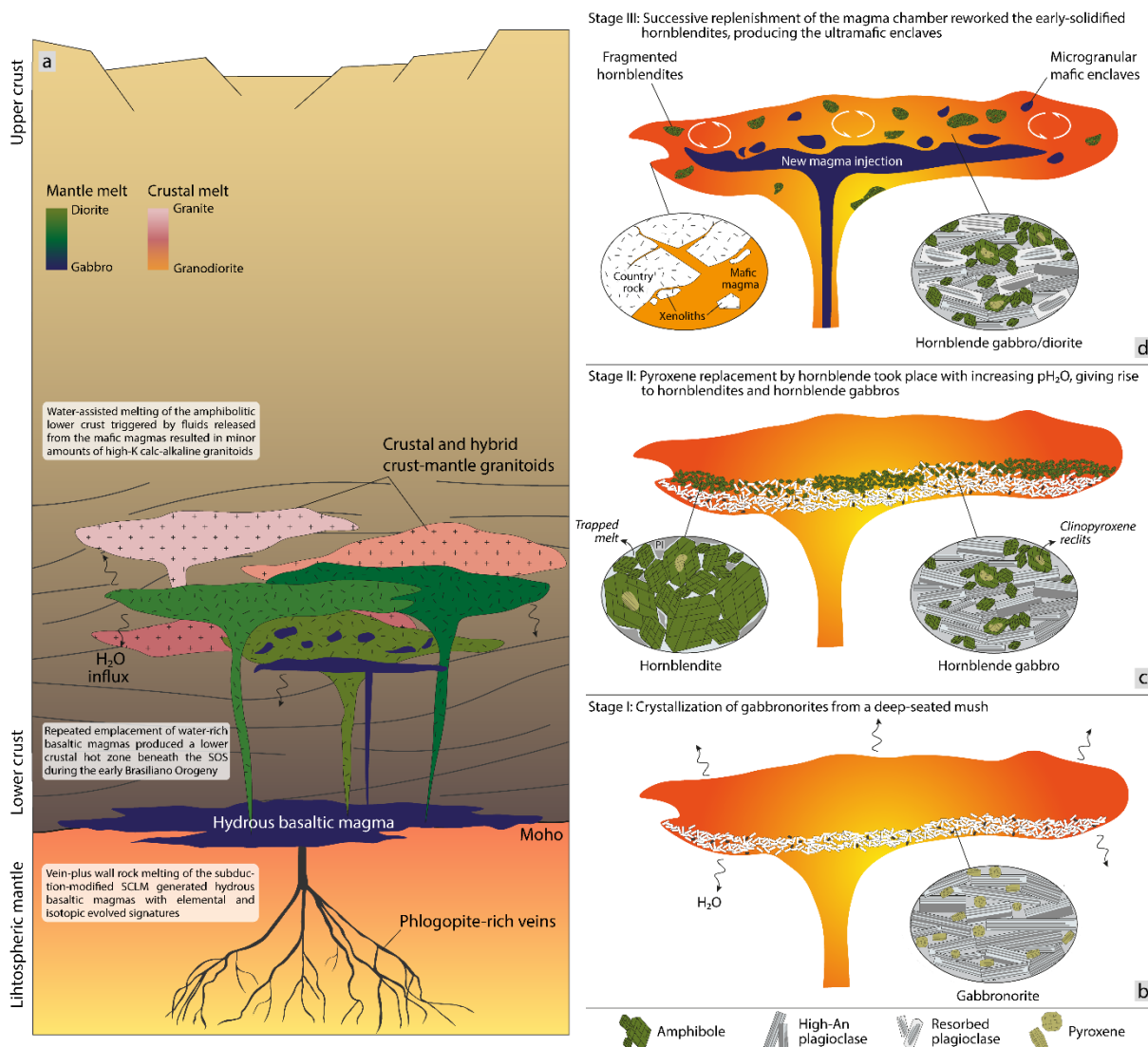


Figure III.13- Conceptual model for generation and assembly of the Capela pluton. (a) Melting of the phlogopite-bearing metasomatized SCLM beneath the southern Borborema Province during the early Brasiliano Orogeny generated water-rich basaltic magmas showing evolved elemental and isotopic features. Underplating and injection of these magmas could have induced the partial melting of the metabasaltic lower crust, forming minor potassic felsic melts. (b), (c) and (d) describe the magmatic evolution of the deep-seated pluton, starting with the crystallization of gabbronorites, followed by cumulate hornblendites, hornblende gabbros, and hornblende diorites. Subsequent pulses of hotter mafic magmas into a growing crystal mush are registered as MME and could have promoted hornblende dismembering.

9 CONCLUSIONS

The early Ediacaran Capela pluton comprises hornblendites, gabbros, diorites, and minor granitoids associated with abundant mafic and ultramafic enclaves. New zircon U–Pb dating of a gabbro sample reveals an extensive range of dates between 631 and 600 Ma, which can be ascribed to ancient Pb-loss instead of a long-lived magmatic history of the pluton.

The mafic rocks present shoshonitic geochemical features, selective enrichments in LILE and LREE, and depletions in HFSE and HREE. Whole-rock isotopic results from mafic and ultramafic rocks broadly overlap, displaying radiogenic Sr-Pb and nonradiogenic Nd-Hf compositions. The intersample compositional coherence describes uniform trends in isotopic and elemental diagrams, which cannot be reconciled with significant crustal contamination. In turn, the evolved isotopic and geochemical characteristics of most primitive samples are consistent with derivation by low degrees of partial melting of an incompatible element-enriched phlogopite-bearing lithospheric mantle in the spinel stability field. The source area is inferred to represent subduction-modified mantle metasomatized by incorporating sedimentary components during the Rhyacian Orogeny.

The associated granitoids show high-K calc-alkaline affiliation and moderately depleted to enriched isotope signatures, precluding derivation by fractional crystallization from mafic magmas. Petrological features of granitoids are consistent with derivation from a heterogeneous amphibolitic lower crustal source. We postulate that the underplating emplacement of hydrous mafic magmas triggered the partial melting of the surrounding lower crust, producing coeval metaluminous to peraluminous granitoids.

ACKNOWLEDGMENTS

This study was financed in part by the Coordenação de Aperfeiçoamento de Pessoal de Nível Superior – Brazil (CAPES) – Finance Code 001. The research was supported with funding from Conselho Nacional de Desenvolvimento Científico e Tecnológico (CNPq; Jean Michel Lafon – grants 312393/2020-2 and 42625/2018-7; Maria de Lourdes Silva Rosa – grant 311023/2021-5; Herbet Conceição – grant 310740/2021-5; Anelise Losangela Bertotti – grant 403797/2016-0). We are grateful to Gilberto Nunes for his support during the fieldwork. The authors acknowledge the Laboratório de Microanálises staff of the Universidade Federal do Pará for image capture by SEM.

REFERENCES

Annen, C., Blundy, J.D., Leuthold, J., Sparks, R.S.J., 2015. Construction and evolution of igneous bodies: Towards an integrated perspective of crustal magmatism. *Lithos* 230, 206–221. <https://doi.org/10.1016/J.LITHOS.2015.05.008>

- Annen, C., Blundy, J.D., Sparks, R.S.J., 2006. The Genesis of Intermediate and Silicic Magmas in Deep Crustal Hot Zones. *Journal of Petrology* 47, 505–539. <https://doi.org/10.1093/PETROLOGY/EGI084>
- Barbosa, J.S.F., Marinho, M.M., Leal, A.B.M., Oliveira, E.M., Souza-Oliveira, J.S., Argollo, R.M., Lana, C., Barbosa, R.G., Santos, L.T.L., 2018. As raízes granulíticas do cinturão Salvador-Esplanada-Boquim, Cráton do São Francisco, Bahia-Sergipe, Brasil. *Geologia USP. Série Científica* 18, 103–128. <https://doi.org/10.11606/issn.2316-9095.v18-134238>
- Becker, H., Wenzel, T., Volker, F., 1999. Geochemistry of Glimmerite Veins in Peridotites from Lower Austria—Implications for the Origin of K-rich Magmas in Collision Zones. *Journal of Petrology* 40, 315–338. <https://doi.org/10.1093/PETROJ/40.2.315>
- Bennett, E.N., Lissenberg, C.J., Cashman, K. V., 2019. The significance of plagioclase textures in mid-ocean ridge basalt (Gakkel Ridge, Arctic Ocean). *Contributions to Mineralogy and Petrology* 174, 1–22. <https://doi.org/10.1007/S00410-019-1587-1/FIGURES/14>
- Brito Neves, B.B., Van Schmus, W.R., Santos, E.J., Campos Neto, M.C., Kozuch, M., 1995. O evento Cariris Velhos na Província Borborema: intergração de dados, implicações e perspectivas. *Revista Brasileira de Geociências* 25, 279–296.
- Bueno, J.F., Oliveira, E.P., McNaughton, N.J., Laux, J.H., 2009. U–Pb dating of granites in the Neoproterozoic Sergipano Belt, NE-Brazil: implications for the timing and duration of continental collision and extrusion tectonics in the Borborema Province. *Gondwana Research* 15, 86–97. <https://doi.org/10.1016/J.GR.2008.06.003>
- Carlson, R.W., Irving, A.J., 1994. Depletion and enrichment history of subcontinental lithospheric mantle: An Os, Sr, Nd and Pb isotopic study of ultramafic xenoliths from the northwestern Wyoming Craton. *Earth Planet Sci Lett* 126, 457–472. [https://doi.org/10.1016/0012-821X\(94\)90124-4](https://doi.org/10.1016/0012-821X(94)90124-4)
- Carvalho, M.J., 2005. Evolução tectônica do Domínio Marancó-Poço Rendido: registro das orogêneses Cariris Velhos e Brasiliana na Faixa Sergipana, NE do Brasil (Ph.D. thesis). Universidade de Campinas, Campinas.
- Castro, A., Corretgé, L.G., de la Rosa, J.D., Fernández, C., López, S., García-Moreno, O., Chacón, H., 2003. The Appinite–Migmatite Complex of Sanabria, NW Iberian Massif, Spain. *Journal of Petrology* 44, 1309–1344. <https://doi.org/10.1093/PETROLOGY/44.7.1309>

Caxito, F.A., Santos, L.C.M.L., Ganade, C.E., Bendaoud, A., Fettous, E., Bouyo, M.H., 2020a. Toward an integrated model of geological evolution for NE Brazil-NW Africa: The Borborema Province and its connections to the Trans-Saharan (Benino-Nigerian and Tuareg shields) and Central African orogens. *Brazilian Journal of Geology* 50, e20190122. <https://doi.org/10.1590/2317-4889202020190122>

Caxito, F.A., Santos, L.C.M.L., Uhlein, A., Dantas, E.L., Alkmim, A.R., Lana, C., 2020b. New U-Pb (SHRIMP) and first Hf isotope constraints on the Tonian (1000-920 Ma) Cariris Velhos event, Borborema Province, NE Brazil. *Brazilian Journal of Geology* 50, e20190082. <https://doi.org/10.1590/2317-4889202020190082>

Chappell, B.W., White, A.J.R., 2001. Two contrasting granite types: 25 years later. *Australian Journal of Earth Sciences* 48, 489–499. <https://doi.org/10.1046/j.1440-0952.2001.00882.x>

Class, C., Goldstein, S.L., 1997. Plume-lithosphere interactions in the ocean basins: constraints from the source mineralogy. *Earth Planet Sci Lett* 150, 245–260. [https://doi.org/10.1016/S0012-821X\(97\)00089-7](https://doi.org/10.1016/S0012-821X(97)00089-7)

Cocherie, A., 1986. Systematic use of trace element distribution patterns in log-log diagrams for plutonic suites. *Geochim Cosmochim Acta* 50, 2517–2522. [https://doi.org/10.1016/0016-7037\(86\)90034-7](https://doi.org/10.1016/0016-7037(86)90034-7)

Coleman, D.S., Gray, W., Glazner, A.F., 2004. Rethinking the emplacement and evolution of zoned plutons: Geochronologic evidence for incremental assembly of the Tuolumne Intrusive Suite, California. *Geology* 32, 433–436. <https://doi.org/10.1130/G20220.1>

Conceição, J.A., 2019. Magmatismo leucogranítico do Domínio Macururé, Sistema Orogênico Sergipano, NE do Brasil (Ph.D. thesis). Universidade Federal da Bahia, Salvador.

Conceição, J.A., 2014. Petrologia do Stock Granítico Glória Sul, Faixa Sergipana, setor sul da Província Borborema, Sergipe (M.S. dissertation). Universidade Federal de Sergipe, São Cristóvão.

Conceição, R. V., Green, D.H., 2004. Derivation of potassic (shoshonitic) magmas by decompression melting of phlogopite+pargasite lherzolite. *Lithos* 72, 209–229. <https://doi.org/10.1016/J.LITHOS.2003.09.003>

Condamine, P., Médard, E., 2014. Experimental melting of phlogopite-bearing mantle at 1 GPa: Implications for potassic magmatism. *Earth Planet Sci Lett* 397, 80–92. <https://doi.org/10.1016/J.EPSL.2014.04.027>

- Condamine, P., Médard, E., Devidal, J.L., 2016. Experimental melting of phlogopite-peridotite in the garnet stability field. *Contributions to Mineralogy and Petrology* 2016 171:11 171, 1–26. <https://doi.org/10.1007/S00410-016-1306-0>
- Corfu, F., 2003. Atlas of zircon textures. *Rev Mineral Geochem* 53, 469–500. <https://doi.org/10.2113/0530469>
- Costa, F.G., Klein, E.L., Lafon, J.M., Milhomem Neto, J.M., Galarza, M.A., Rodrigues, J.B., Naletto, J.L.C., Corrêa Lima, R.G., 2018. Geochemistry and U–Pb–Hf zircon data for plutonic rocks of the Troia Massif, Borborema Province, NE Brazil: Evidence for reworking of Archean and juvenile Paleoproterozoic crust during Rhyacian accretionary and collisional tectonics. *Precambrian Res* 311, 167–194. <https://doi.org/10.1016/J.PRECAMRES.2018.04.008>
- Couzinié, S., Laurent, O., Moyen, J.F., Zeh, A., Bouilhol, P., Villaros, A., 2016. Post-collisional magmatism: Crustal growth not identified by zircon Hf–O isotopes. *Earth Planet Sci Lett* 456, 182–195. <https://doi.org/10.1016/J.EPSL.2016.09.033>
- Davison, I., Santos, R.A., 1989. Tectonic evolution of the Sergipano Fold Belt, NE Brazil, during the Brasiliano Orogeny. *Precambrian Res* 45, 319–342. [https://doi.org/10.1016/0301-9268\(89\)90068-5](https://doi.org/10.1016/0301-9268(89)90068-5)
- DePaolo, D.J., 1981a. Trace element and isotopic effects of combined wallrock assimilation and fractional crystallization. *Earth Planet Sci Lett* 53, 189–202. [https://doi.org/10.1016/0012-821X\(81\)90153-9](https://doi.org/10.1016/0012-821X(81)90153-9)
- DePaolo, D.J., 1981b. Nd Isotopic Studies: Some new perspectives on Earth structure and evolution. *Eos, Transactions American Geophysical Union* 62, 137–137. <https://doi.org/10.1029/EO062I014P00137-01>
- Farmer, G.L., 2007. Continental Basaltic Rocks. *Treatise on Geochemistry* 1–39. <https://doi.org/10.1016/B0-08-043751-6/03019-X>
- Faure, G., 2001. *Origin of Igneous Rocks: The Isotopic Evidence*, 1st ed, *Origin of Igneous Rocks*. Springer Berlin Heidelberg. <https://doi.org/10.1007/978-3-662-04474-2>
- Foley, S., 1992. Vein-plus-wall-rock melting mechanisms in the lithosphere and the origin of potassic alkaline magmas. *Lithos* 28, 435–453. [https://doi.org/10.1016/0024-4937\(92\)90018-T](https://doi.org/10.1016/0024-4937(92)90018-T)
- Förster, M.W., Prelević, D., Schmück, H.R., Buhre, S., Veter, M., Mertz-Kraus, R., Foley, S.F., Jacob, D.E., 2017. Melting and dynamic metasomatism of mixed harzburgite + glimmerite

mantle source: Implications for the genesis of orogenic potassic magmas. *Chem Geol* 455, 182–191. <https://doi.org/10.1016/J.CHEMGEO.2016.08.037>

Fowler, M.B., Kocks, H., Darbyshire, D.P.F., Greenwood, P.B., 2008. Petrogenesis of high Ba–Sr plutons from the Northern Highlands Terrane of the British Caledonian Province. *Lithos* 105, 129–148. <https://doi.org/10.1016/J.LITHOS.2008.03.003>

Gaetani, G.A., Grove, T.L., 1998. The influence of water on melting of mantle peridotite. *Contributions to Mineralogy and Petrology* 1998 131:4 131, 323–346. <https://doi.org/10.1007/S004100050396>

Ganade, C.E., Weinberg, R.F., Caxito, F.A., Lopes, L.B.L., Tesser, L.R., Costa, I.S., 2021. Decratonization by rifting enables orogenic reworking and transcurrent dispersal of old terranes in NE Brazil. *Scientific Reports* 2021 11:1 11, 1–13. <https://doi.org/10.1038/s41598-021-84703-x>

Gerdes, A., Zeh, A., 2009. Zircon formation versus zircon alteration — New insights from combined U–Pb and Lu–Hf in-situ LA-ICP-MS analyses, and consequences for the interpretation of Archean zircon from the Central Zone of the Limpopo Belt. *Chem Geol* 261, 230–243. <https://doi.org/10.1016/J.CHEMGEO.2008.03.005>

Guimarães, I.P., Lara de Brito, M.F., Lages, G.A., Silva Filho, A.F., Santos, L., Brasilino, R.G., 2016. Tonian granitic magmatism of the Borborema Province, NE Brazil: A review. *J South Am Earth Sci* 68, 97–112. <https://doi.org/10.1016/J.JSAMES.2015.10.009>

Guo, Z., Wilson, M., Liu, J., Mao, Q., 2006. Post-collisional, Potassic and Ultrapotassic Magmatism of the Northern Tibetan Plateau: Constraints on Characteristics of the Mantle Source, Geodynamic Setting and Uplift Mechanisms. *Journal of Petrology* 47, 1177–1220. <https://doi.org/10.1093/PETROLOGY/EGL007>

Hawkesworth, C.J., Turner, S.P., McDermott, F., Peate, D.W., van Calsteren, P., 1997. U–Th isotopes in arc magmas: implications for element transfer from the subducted crust. *Science* (1979) 276, 551–555. <https://doi.org/10.1126/science.276.5312.551>

Herzberg, C., Zhang, J., 1996. Melting experiments on anhydrous peridotite KLB-1: Compositions of magmas in the upper mantle and transition zone. *J Geophys Res Solid Earth* 101, 8271–8295. <https://doi.org/10.1029/96JB00170>

- Hildreth, W., Moorbath, S., 1988. Crustal contributions to arc magmatism in the Andes of Central Chile. *Contributions to Mineralogy and Petrology* 98, 455–489. <https://doi.org/10.1007/BF00372365/METRICS>
- Hirschmann, M.M., Kogiso, T., Baker, M.B., Stolper, E.M., 2003. Alkalic magmas generated by partial melting of garnet pyroxenite. *Geology* 31, 481–484. [https://doi.org/10.1130/0091-7613\(2003\)031<0481:AMGBPM>2.0.CO;2](https://doi.org/10.1130/0091-7613(2003)031<0481:AMGBPM>2.0.CO;2)
- Hofmann, A.W., 2007. Sampling Mantle Heterogeneity through Oceanic Basalts: Isotopes and Trace Elements. *Treatise on Geochemistry* 2–9, 1–44. <https://doi.org/10.1016/B0-08-043751-6/02123-X>
- Irvine, T.N., Baragar, W.R.A., 1971. A guide to the chemical classification of the common volcanic rocks. *Can J Earth Sci* 8, 523–548. <https://doi.org/10.1139/e71-055>
- Lima, H.M., Pimentel, M.M., Santos, L.C.M.L., Dantas, E.L., 2019. Isotopic and geochemical characterization of the metavolcano-sedimentary rocks of the Jirau do Ponciano Dome: A structural window to a Paleoproterozoic continental arc root within the Southern Borborema Province, Northeast Brazil. *J South Am Earth Sci* 90, 54–69. <https://doi.org/10.1016/J.JSAMES.2018.12.002>
- Lisboa, V.A.C., Conceição, H., Rosa, M.L.S., Fernandes, D.M., 2019. The onset of post-collisional magmatism in the Macururé Domain, Sergipano Orogenic System: The Glória Norte Stock. *J South Am Earth Sci* 89, 173–188. <https://doi.org/10.1016/J.JSAMES.2018.11.005>
- Long, L.E., Castellana, C.H., Sial, A.N., 2005. Age, origin and cooling history of the Coronel João Sá Pluton, Bahia, Brazil. *Journal of Petrology* 46, 255–273. <https://doi.org/10.1093/petrology/egh070>
- Mallik, A., Nelson, J., Dasgupta, R., 2015. Partial melting of fertile peridotite fluxed by hydrous rhyolitic melt at 2–3 GPa: implications for mantle wedge hybridization by sediment melt and generation of ultrapotassic magmas in convergent margins. *Contributions to Mineralogy and Petrology* 2015 169:5 169, 1–24. <https://doi.org/10.1007/S00410-015-1139-2>
- McDonough, W.F., Sun, S.S., 1995. The composition of the Earth. *Chem Geol* 120, 223–253. [https://doi.org/10.1016/0009-2541\(94\)00140-4](https://doi.org/10.1016/0009-2541(94)00140-4)
- Middlemost, E.A.K., 1994. Naming materials in the magma/igneous rock system. *Earth Sci Rev* 37, 215–224. [https://doi.org/10.1016/0012-8252\(94\)90029-9](https://doi.org/10.1016/0012-8252(94)90029-9)

- Miller, J.S., Matzel, J.E.P., Miller, C.F., Burgess, S.D., Miller, R.B., 2007. Zircon growth and recycling during the assembly of large, composite arc plutons. *Journal of Volcanology and Geothermal Research* 167, 282–299. <https://doi.org/10.1016/j.jvolgeores.2007.04.019>
- Morrison, G.W., 1980. Characteristics and tectonic setting of the shoshonite rock association. *Lithos* 13, 97–108. [https://doi.org/10.1016/0024-4937\(80\)90067-5](https://doi.org/10.1016/0024-4937(80)90067-5)
- Moyen, J.F., Janoušek, V., Laurent, O., Bachmann, O., Jacob, J.B., Farina, F., Fiannacca, P., Villaros, A., 2021. Crustal melting vs. fractionation of basaltic magmas: Part 1, granites and paradigms. *Lithos* 402–403, 106291. <https://doi.org/10.1016/J.LITHOS.2021.106291>
- Murphy, J.B., 2020. Appinite suites and their genetic relationship with coeval voluminous granitoid batholiths. *Int Geol Rev* 62, 683–713. <https://doi.org/10.1080/00206814.2019.1630859>
- Murphy, J.B., 2013. Appinite suites: A record of the role of water in the genesis, transport, emplacement and crystallization of magma. *Earth Sci Rev* 119, 35–59. <https://doi.org/10.1016/J.EARSCIREV.2013.02.002>
- Neves, S.P., 2021. Comparative geological evolution of the Borborema Province and São Francisco Craton (eastern Brazil): Decratonization and crustal reworking during West Gondwana assembly and implications for paleogeographic reconstructions. *Precambrian Res* 355, 106119. <https://doi.org/10.1016/J.PRECAMRES.2021.106119>
- Neves, S.P., Bruguier, O., Silva, J.M.R., Mariano, G., Silva Filho, A.F., Teixeira, C.M.L., 2015. From extension to shortening: Dating the onset of the Brasiliano Orogeny in eastern Borborema Province (NE Brazil). *J South Am Earth Sci* 58, 238–256. <https://doi.org/10.1016/J.JSAMES.2014.06.004>
- Oliveira, E.M., 2014. Petrografia, litogeoquímica e geocronologia das rochas granulíticas da parte norte do Cinturão Salvador-Esplanada-Boquim, Bahia-Sergipe (Ph.D. thesis). Universidade Federal da Bahia, Salvador.
- Oliveira, E.P., 2012. Geologia da Faixa Sergipana no Estado da Bahia, in: Barbosa, J., Mascarenhas, J.F., Correa Gomes, L.C., Dominguez, J.M.L., S, S.J. (Eds.), *Geologia Da Bahia. Pesquisa e Atualização*. Companhia Baiana de Pesquisa Mineral, pp. 179–190.
- Oliveira, E.P., Bueno, J.F., McNaughton, N.J., Silva Filho, A.F., Nascimento, R.S., Donatti-Filho, J.P., 2015a. Age, composition, and source of continental arc- and syn-collision granites

of the Neoproterozoic Sergipano Belt, Southern Borborema Province, Brazil. *J South Am Earth Sci* 58, 257–280. <https://doi.org/10.1016/j.jsames.2014.08.003>

Oliveira, E.P., McNaughton, N.J., Windley, B.F., Carvalho, M.J., Nascimento, R.S., 2015b. Detrital zircon U–Pb geochronology and whole-rock Nd-isotope constraints on sediment provenance in the Neoproterozoic Sergipano Orogen, Brazil: from early passive margins to late foreland basins. *Tectonophysics* 662, 183–194. <https://doi.org/10.1016/J.TECTO.2015.02.017>

Oliveira, E.P., Windley, B.F., Araújo, M.N.C., 2010. The Neoproterozoic Sergipano Orogenic Belt, NE Brazil: a complete plate tectonic cycle in Western Gondwana. *Precambrian Res* 181, 64–84. <https://doi.org/10.1016/J.PRECAMRES.2010.05.014>

Passos, L.H., Fuck, R.A., Chemale, F., Lenz, C., Pimentel, M.M., Machado, A., Pinto, V.M., 2021. Neoproterozoic (740–680 Ma) arc-back-arc magmatism in the Sergipano Belt, southern Borborema Province, Brazil. *J South Am Earth Sci* 109, 103280. <https://doi.org/10.1016/J.JSAMES.2021.103280>

Passos, L.H., Fuck, R.A., Junior, F.C., Lenz, C., Porcher, C.C., Pinto, V.M., Santos, L.C.M.L., 2022. Neoproterozoic pre-collisional events recorded in the Sergipano belt, Southern Borborema Province, West Gondwana. *Int Geol Rev* 64, 1–19. <https://doi.org/10.1080/00206814.2022.2054029>

Patiño Douce, A.E., 1999. What do experiments tell us about the relative contributions of crust and mantle to the origin of granitic magmas? Geological Society, London, Special Publications 168, 55–75. <https://doi.org/10.1144/GSL.SP.1999.168.01.05>

Peccerillo, A., Taylor, S.R., 1976. Geochemistry of eocene calc-alkaline volcanic rocks from the Kastamonu area, Northern Turkey. *Contributions to Mineralogy and Petrology* 58, 63–81. <https://doi.org/10.1007/BF00384745>

Pereira, F.S., 2019. Petrogênese da Suíte Máfica do Domínio Macururé, Sistema Orogênico Sergipano, setor sul da Província Borborema (M.S. dissertation). Universidade Federal de Sergipe, São Cristóvão.

Pereira, F.S., Conceição, H., Rosa, M.L.S., Marinho, M.M., Tassinari, C.C.G., Milhomem Neto, J.M., Lafon, J.M., 2023. Late Cryogenian–Ediacaran magmatism in southern Borborema Province, NE Brazil: Ages, sources, petrogenesis, and tectonic setting. *Geoscience Frontiers* 14, 101626. <https://doi.org/10.1016/j.gsf.2023.101626>

- Pereira, F.S., Rosa, M.L.S., Conceição, H., 2019. Condições de colocação do magmatismo máfico do Domínio Macururé, Sistema Orogênico Sergipano: Maciço Capela. *Revista Geologia USP. Série Científica* 19, 3–29. <https://doi.org/10.11606/issn.2316-9095.v19-151464>
- Pereira, F.S., Rosa, M.L.S., Conceição, H., Bertotti, A.L., 2020. Age, composition, and source of the Macururé Mafic Suite, Southern Borborema Province, Brazil. *Brazilian Journal of Geology* 50, e20190105. <https://doi.org/10.1590/2317-4889202020190105>
- Pinto, V.M., Koester, E., Debruyne, D., Chemale, F., Marques, J.C., Porcher, C.C., Passos, L.H., Lenz, C., 2020. Petrogenesis of the mafic-ultramafic Canindé layered intrusion, Sergipano Belt, Brazil: Constraints on the metallogenesis of the associated Fe–Ti oxide ores. *Ore Geol Rev* 122, 103535. <https://doi.org/10.1016/j.oregeorev.2020.103535>
- Plank, T., Langmuir, C.H., 1998. The chemical composition of subducting sediment and its consequences for the crust and mantle. *Chem Geol* 145, 325–394. [https://doi.org/10.1016/S0009-2541\(97\)00150-2](https://doi.org/10.1016/S0009-2541(97)00150-2)
- Rapp, R.P., Norman, M.D., Laporte, D., Yaxley, G.M., Martin, H., Foley, S.F., 2010. Continent Formation in the Archean and Chemical Evolution of the Cratonic Lithosphere: Melt–Rock Reaction Experiments at 3–4 GPa and Petrogenesis of Archean Mg-Diorites (Sanukitoids). *Journal of Petrology* 51, 1237–1266. <https://doi.org/10.1093/PETROLOGY/EGQ017>
- Rollinson, H., 1993. Using geochemical data: evaluation, presentation, interpretation. Longman, Essex.
- Rosa, M.L.S., Conceição, J.A., Marinho, M.M., Pereira, F.S., Conceição, H., 2020. U-Pb SHRIMP dating of the Itabaiana Dome: a Mesoarchean basement inlier (2.83 Ga) in the Sergipano Orogenic System, Borborema Province. *Brazilian Journal of Geology* 50, e20190106. <https://doi.org/10.1590/2317-4889202020190106>
- Rubatto, D., 2017. Zircon: the metamorphic mineral. *Rev Mineral Geochem* 83, 261–295. <https://doi.org/10.2138/rmg.2017.83.9>
- Rudnick, R.L., Gao, S., 2003. Composition of the continental crust. *Treatise on Geochemistry* 1–64. <https://doi.org/10.1016/B0-08-043751-6/03016-4>
- Santos, E.J., Schmus, W.R. Van, Kozuch, M., Neves, B.B. de B., 2010. The Cariris Velhos tectonic event in Northeast Brazil. *J South Am Earth Sci* 29, 61–76. <https://doi.org/10.1016/J.JSAMES.2009.07.003>

Santos, R.A., Martins, A.A.M., Neves, J.P., Leal, R.A., 1998. Programa de Levantamentos Geológicos Básicos do Brasil: Geologia e recursos minerais do Estado de Sergipe. Escala 1:250.000. Texto explicativo do mapa geológico do Estado de Sergipe. CPRM/DIEDIG/DEPAT;CODISE, Salvador.

Sen, C., Dunn, T., 1994. Dehydration melting of a basaltic composition amphibolite at 1.5 and 2.0 GPa: implications for the origin of adakites. *Contributions to Mineralogy and Petrology* 117, 394–409. <https://doi.org/10.1007/BF00307273>

Shand, S.J., 1943. *The Eruptive Rocks*, 2nd ed. John Wiley, New York.

Silva Filho, M.A., Bomfim, L.F.C., Santos, R.A., Leal, R.A., Santana, A.C., Filho, P.A.B., 1979. Geologia da Geossinclinal Sergipana e do seu embasamento - Alagoas, Sergipe e Bahia: Projeto Baixo São Francisco/Vaza-Barris. DNPM/CPRM, Brasília.

Sousa, C.S., Soares, H.S., Rosa, M.L.S., Conceição, H., 2022. Injection of enriched lithospheric mantle magmas explains the formation of microgranular enclaves in the Rio Jacaré Batholith, Borborema Province, Brazil. *Brazilian Journal of Geology* 52, e2022033. <https://doi.org/10.1590/2317-4889202220220033>

Spencer, C.J., Kirkland, C.L., Taylor, R.J.M., 2016. Strategies towards statistically robust interpretations of in situ U-Pb zircon geochronology. *Geoscience Frontiers* 7, 581–589. <https://doi.org/10.1016/j.gsf.2015.11.006>

Teixeira, L.R., 2014. Mapa Geológico e de Recursos Minerais do Estado de Sergipe, escala 1:250.000. CPRM/CODISE, Salvador.

Tenner, T.J., Hirschmann, M.M., Humayun, M., 2012. The effect of H₂O on partial melting of garnet peridotite at 3.5 GPa. *Geochemistry, Geophysics, Geosystems* 13, 3016. <https://doi.org/10.1029/2011GC003942>

Tesser, L.R., Ganade, C.E., Weinberg, R.F., Basei, M.A.S., Moraes, R., Batista, L.A., 2021. Ultrahigh-temperature Palaeoproterozoic rocks in the Neoproterozoic Borborema Province, implications for São Francisco Craton dispersion in NE Brazil. *Journal of Metamorphic Geology*. <https://doi.org/10.1111/JMG.12632>

Thibault, Y., Edgar, A.D., Lloyd, F.E., 1992. Experimental investigation of melts from a carbonated phlogopite lherzolite: Implications for metasomatism in the continental lithospheric mantle. *American Mineralogist* 77, 784–794.

- Trompette, R., 1997. Neoproterozoic (~600 Ma) aggregation of Western Gondwana: a tentative scenario. *Precambrian Res* 82, 101–112. [https://doi.org/10.1016/S0301-9268\(96\)00045-9](https://doi.org/10.1016/S0301-9268(96)00045-9)
- Turner, S., Arnaud, N., Liu, J., Rogers, N., Hawkesworth, C., Harris, N., Kelley, S., Van Calsteren, P., Deng, W., 1996. Post-collision, shoshonitic volcanism on the tibetan plateau: implications for convective thinning of the lithosphere and the source of ocean island basalts. *Journal of Petrology* 37, 45–71. <https://doi.org/10.1093/petrology/37.1.45>
- Van Schmus, W.R., Oliveira, E.P., Silva Filho, A.F., Toteu, S.F., Penaye, J., Guimarães, I.P., Silva Filho, A.F., Toteu, S.F., Penaye, J., Guimarães, I.P., 2008. Proterozoic links between the Borborema Province, NE Brazil, and the Central African fold belt. *Geol Soc Spec Publ* 294, 69–99. <https://doi.org/10.1144/SP294.5>
- Watson, E.B., 1982. Basalt contamination by continental crust: some experiments and models. *Contributions to Mineralogy and Petrology* 80, 73–87. <https://doi.org/10.1007/BF00376736>
- Watson, E.B., Harrison, T.M., 1983. Zircon saturation revisited: temperature and composition effects in a variety of crustal magma types. *Earth Planet Sci Lett* 64, 295–304. [https://doi.org/10.1016/0012-821X\(83\)90211-X](https://doi.org/10.1016/0012-821X(83)90211-X)
- Weinberg, R.F., Hasalová, P., 2015. Water-fluxed melting of the continental crust: A review. *Lithos* 212–215, 158–188. <https://doi.org/10.1016/J.LITHOS.2014.08.021>
- Workman, R.K., Hart, S.R., 2005. Major and trace element composition of the depleted MORB mantle (DMM). *Earth Planet Sci Lett* 231, 53–72. <https://doi.org/https://doi.org/10.1016/j.epsl.2004.12.005>
- Xu, W., Xu, X., Zeng, G., 2017. Crustal contamination versus an enriched mantle source for intracontinental mafic rocks: Insights from early Paleozoic mafic rocks of the South China Block. *Lithos* 286–287, 388–395. <https://doi.org/10.1016/J.LITHOS.2017.06.023>
- Ye, Z., Wan, F., Jiang, N., Xu, J., Wen, Y., Fan, D., Zhou, W., 2021. Dehydration melting of amphibolite at 1.5 GPa and 800–950 °C: Implications for the Mesozoic potassium-rich adakite in the eastern North China Craton. *Geoscience Frontiers* 12, 896–906. <https://doi.org/10.1016/J.GSF.2020.03.008>
- Zartman, R.E., Doe, B.R., 1981. Plumbotectonics—the model. *Tectonophysics* 75, 135–162. [https://doi.org/10.1016/0040-1951\(81\)90213-4](https://doi.org/10.1016/0040-1951(81)90213-4)
- Zindler, A., Hart, S., 1986. Chemical Geodynamics. *Annu Rev Earth Planet Sci* 14, 493–571. <https://doi.org/10.1146/annurev.ea.14.050186.002425>

SUPPLEMENTARY MATERIAL

ANALYTICAL PROCEDURES

Sampling and data compilation

Mineral chemistry and whole-rock data for the Capela pluton have been compiled from published literature (Pereira, 2019; Pereira et al., 2020, 2019). New geochemical analyses of twelve samples were conducted to complement the existing dataset. *In situ* Lu–Hf isotope analyses were carried out on zircon crystals from two samples (SOS-696F and SOS-696G). U–Pb ages for the sample SOS-696F, previously dated by Pereira et al. (2020), were used to calculate the $\varepsilon_{\text{Hf}(t)}$ and Hf- T_{DM}^{C} model ages. Whole-rock Sr–Nd–Pb isotope compositions were determined in 13 samples encompassing the ultramafic ($n = 4$), mafic ($n = 7$), and granitoid ($n = 2$) units.

Textural and mineral investigation

Backscattered electron (BSE) images were obtained at the Laboratório de Microanálises, Universidade Federal do Pará (LABMEV/UFPA), using a scanning electron microscope (SEM) Zeiss model Sigma-VP, working at a constant accelerating voltage of 20 kV and beam current of 80 μA .

Semiquantitative determinations of mineral compositions were performed with an energy dispersive X-ray spectrometer (Oxford Instruments model x-act) coupled to an SEM Tescan model LMU Vega3 at the Condomínio Laboratorial das Geociências, Universidade Federal de Sergipe (CLGeo-UFS). The operating conditions were an accelerating voltage of 15 kV, a beam current of 15–17 nA, and an electron beam diameter of 280–430 nm. Equipment calibration procedures employed natural minerals and synthetic oxides. The ZAF (atomic number-absorption-fluorescence) correction procedure was applied to chemical data treatment. Mineral abbreviations in micrographic and BSE images follow the recommendations of Warr (2021).

Geochemistry

An X-ray fluorescence spectrometer X Rigaku model ZSX Primus II was used to analyze major elements using lithium tetraborate fused glass disks at the Núcleo de Estudos Geoquímicos, Universidade Federal de Pernambuco (NEG-UFPE). Loss on ignition (LOI) was

determined in previously dried rock powders (110 °C) by calcinating in a muffle furnace at 1000 °C for 2 hours.

The trace elements were measured by inductively coupled plasma–mass spectrometry at SGS GEOSOL Laboratory, Belo Horizonte, Brazil. The analytical procedures included sodium peroxide fusion followed by measuring the elemental concentrations (<https://www.sgsgroup.com.br/>). Geochemical data handling and diagram elaboration were performed using the Geochemical Data Toolkit (Janoušek et al., 2006).

Geochemical modeling

We perform modeling tests to elucidate the petrogenetic processes involved in generating and differentiating the Capela pluton. Major element mass balance was performed using the software GENESIS 4.0 (Teixeira, 2005), which employs the equations of Stormer and Nicholls (1978). This algorithm uses linear regression and adjusts the proportion of residual mineral phases to reproduce the composition of the considered melt. The sum of the residual squares (ΣR^2) is the statistical parameter used to evaluate the adjustment quality between the theoretical model and observed data. When $\Sigma R^2 \gg 1$, the model is not acceptable, while $\Sigma R^2 < 1$ indicates a good correlation between the geological hypothesis and the data (Janoušek et al., 2015). Following Janoušek et al. (2015), geochemical analyses were recalculated to 100 wt%, and minor oxides MnO and P₂O₅ were disregarded in mass balance calculations. All iron is reported as FeO*.

Elemental and isotopic mixture calculations follow the equations derived by Faure (2001). Equilibrium partial melting (Wilson, 1989), fractional crystallization (Rayleigh, 1896), and assimilation and fractional crystallization (AFC; DePaolo, 1981a) equations were applied for trace element and isotopic modeling. The mineral/liquid partition coefficients (K_d) used in the modeling were obtained from Rollinson (1993) and the Geochemical Earth Reference Model – GERM database (<https://earthref.org/KDD/>), and they are listed in Table A.

Table A- Mineral/melt partition coefficients used in geochemical modeling.

Mineral phase	Trace elements													
	Ba	Rb	Sr	Y	Zr	Nb	La	Ce	Nd	Sm	Eu	Gd	Yb	Lu
<i>Basaltic liquids</i>														
Olivine	0.0003	0.0002	0.00036	0.001	0.001	0.001	0.0003	0.0003	0.0002	0.00018	0.0002	0.00025	0.00522	0.00852
Clinopyroxene	0.001	0.001	0.1283	0.412	0.26	0.008	0.0536	0.0858	0.1873	0.291	0.3288	0.367	0.43	0.433
Orthopyroxene	0.0005	0.0002	0.0012	0.095	0.032	0.0013	0.0008	0.0016	0.0056	0.015	0.03	0.034	0.22	0.22
Spinel	0.0004	0.029	0.0047	0.002	0.0009	0.86	0.01	0.01	0.01	0.01	0.01	0.01	0.01	0.01
Garnet	7E-12	0.0002	0.0023	3.9	0.12	0.00054	0.0014	0.03	0.07	0.29	0.49	0.97	11.5	11.9
Plagioclase	0.4586	0.015	1.83	0.026	0.04	0.03	0.124	0.117	0.068	0.058	0.22	0.035	0.0097	0.008
Amphibole	0.43	0.11	0.49	2.58	0.83	0.76	0.2	0.43	1.23	2.03	1.73	2.51	2.96	2.59
Phlogopite	3.9139	4.7588	0.0879	0.036	0.0151	0.0853	0.0004	0.0007	0.0019	0.0045	0.0095	0.0096	0.033	0.0395
<i>Dacitic and rhyolitic liquids</i>														
Amphibole	0.044	0.0077	0.0224	2.46	0.91	1.5	0.68	0.899	2.89	3.99	5.14	5.48	4.89	4.53
Clinopyroxene	0.08	0.009	0.02	1.2	0.1841	0.21	0.0154	0.044	0.1661	0.4574	0.4108	0.7028	0.64	0.683
Plagioclase	0.36	0.048	2.84	0.1	0.1	0.06	0.38	0.24	0.17	0.13	2.15	0.097	0.049	0.046
Garnet	0.0172	0.00851	0.0154	35	1.2	-	0.37	0.51	0.27	0.76	0.214	5.3	26.9	24.6
Ilmenite	-	-	-	-	-	-	1.223	1.64	2.267	2.833	1.013	-	1.467	1.203

Zircon U–Pb geochronology

Obtaining zircon concentrates involved conventional crushing, grinding, panning, and magnetic separation techniques. The best zircon grains were hand-picked and mounted in an epoxy disc with a diameter of 25 mm, which was polished to reveal the internal domains of the crystals. The mount was gold-coated, and the inner structures were evaluated by cathodoluminescence (CL) images using a scanning electron microscope before analysis.

U–Pb dating was carried out with a high-resolution ion microprobe (SHRIMP IIe) from the Centro de Pesquisas Geocronológicas of the Universidade de São Paulo (CPGeo-USP), according to the procedures of Sato et al. (2014). The operation conditions were a 30 μm spot size and an O^{-2} beam density of approximately 2.5–7.0 ηA . The U concentration was determined based on SL-13 (238 ppm; Williams, 1997). Uranium and lead isotope ratios were obtained by normalizing the unknown samples to the Temora 2 zircon reference (416.78 ± 0.33 Ma; Black et al., 2004). Raw data reduction was performed using SQUID software (Ludwig, 2009a). Decay constants for U isotopes are from Steiger and Jäger (1977). The age calculations and graphic representation were performed using Excel Add-in Isoplot (Ludwig, 2009b), with error ellipses reflecting 2σ uncertainty.

Zircon Lu–Hf isotope analyses

Lu–Hf isotope composition was carried out on previously dated zircon crystals in the same area where the concordant to subconcordant U–Pb age was determined. Analyses were performed at the Laboratório de Geologia Isotópica of the Universidade Federal do Pará (Pará-Iso/UFPA) and Laboratório de Geoquímica Isotópica of the Universidade Federal de Ouro Preto (UFOP). Detailed analytical procedures for both laboratories can be found in Milhomem Neto and Lafon (2019) and Santos et al. (2022), respectively. The equipment in the Pará-Iso/UFPA was a multicollector high-resolution ICP–MS Thermo Finnigan Neptune, combined with a laser ablation microprobe CETAC Nd:YAG 213 nm model LSX-213 G2. The analytical conditions were 50 μm spot diameter, 10–12 Hz frequency, 50–60% power, and 60 s counting. At the UFOP, the samples were analyzed using a ThermoScientific Neptune Plus multicollector ICP–MS coupled to a Photon Machines 193 ($\lambda = 193$ nm) ArF excimer laser ablation system. Data were collected during 60 s ablation, with a spot size of 40 μm and a repetition rate of 8 Hz.

Lu, Hf, and Yb isotopes were measured concomitantly. The isotope ratios of Yb and Hf were normalized assuming the values of $^{173}\text{Yb}/^{171}\text{Yb} = 1.12346$ (Thirlwall and Anczkiewicz, 2004) and $^{179}\text{Hf}/^{177}\text{Hf} = 0.7325$ (Patchett and Tatsumoto, 1981), following the exponential law. Natural abundances for isotopes ^{175}Lu ($^{176}\text{Lu}/^{175}\text{Lu} = 0.02659$; Chu et al., 2002) and ^{173}Yb

($^{176}\text{Yb}/^{173}\text{Yb} = 0.786956$; Thirlwall and Anczkiewicz, 2004) were considered to correct the isobaric interferences. $^{176}\text{Hf}/^{177}\text{Hf}$ ratios measured in unknown crystals were normalized based on the average values of $^{176}\text{Hf}/^{177}\text{Hf}$ obtained from the Mud Tank reference zircon and their respective certified ratios (Morel et al., 2008). The GJ-1, Plešovice, Blue Berry, and Temora reference zircons were used as secondary standards to monitor the accuracy and external reproducibility of the method. Repeated analyses yielded $^{176}\text{Hf}/^{177}\text{Hf}$ ratios ($\pm 2\text{SD}$) of 0.282023 ± 28 for GJ-1 ($n = 5$), 0.282484 ± 28 for Plešovice ($n = 5$), 0.281668 ± 31 for Blue Berry ($n = 5$), and 0.282687 ± 41 for Temora ($n = 4$). These results agree with recommended values (Morel et al., 2008; Santos et al., 2017; Sláma et al., 2008; Woodhead and Hergt, 2005). Data from reference zircons are listed in Table B.

Table B- Lu–Hf isotope composition determined on the zircon reference materials.

Spot ID	$^{176}\text{Yb}/^{177}\text{Hf}$	2 σ	$^{176}\text{Lu}/^{177}\text{Hf}$	2 σ	$^{178}\text{Hf}/^{177}\text{Hf}$	$^{180}\text{Hf}/^{177}\text{Hf}$	2 σ	$^{176}\text{Hf}/^{177}\text{Hf}$	2 σ
GJ-1 (0.282000 ± 0.000005; Morel et al., 2008)									
GJ1 006	0.0065	5	0.00025	1	1.46719	1.88676	6	0.282020	25
GJ1 007	0.0064	5	0.00025	1	1.46732	1.88697	6	0.282016	24
GJ1 008	0.0065	5	0.00025	1	1.46714	1.88679	6	0.282031	25
GJ1 009	0.0064	5	0.00025	1	1.46719	1.88691	6	0.282005	20
GJ1 010	0.0063	5	0.00025	1	1.46714	1.88688	6	0.282045	22
Average $\pm 2\text{SD}$								0.282023 ± 28	
PLEŠOVICE (0.282482 ± 0.000013; Sláma et al., 2008)									
Plešovice 016	0.0028	2	0.00007	0	1.46719	1.88683	10	0.282490	19
Plešovice 017	0.0021	2	0.00005	0	1.46723	1.88687	10	0.282488	19
Plešovice 018	0.0020	2	0.00005	0	1.46724	1.88683	10	0.282462	16
Plešovice 019	0.0028	2	0.00007	0	1.46719	1.88682	10	0.282504	19
Plešovice 020	0.0025	2	0.00007	0	1.46724	1.88687	10	0.282478	20
Average $\pm 2\text{SD}$								0.282484 ± 28	
BB (0.281674 ± 0.000018; Santos et al., 2017)									
BB 011	0.0045	4	0.00015	1	1.46727	1.88700	8	0.281687	25
BB 012	0.0044	4	0.00015	1	1.46723	1.88692	8	0.281658	24
BB 013	0.0044	4	0.00015	1	1.46722	1.88693	8	0.281661	21
BB 014	0.0045	4	0.00015	1	1.46725	1.88680	8	0.281673	20
BB 015	0.0044	4	0.00015	1	1.46719	1.88702	8	0.281662	23
Average $\pm 2\text{SD}$								0.281669 ± 21	
TEMORA 2 (0.282686 ± 0.000008; Woodhead and Hergt, 2005)									
Temora 001	0.0109	9	0.00043	3	1.46717	1.88680	9	0.282662	20
Temora 002	0.0330	30	0.00123	10	1.46696	1.88744	2	0.282682	169
Temora 003	0.0207	17	0.00081	5	1.46720	1.88701	7	0.282719	25
Temora 005	0.0250	21	0.00095	6	1.46722	1.88697	8	0.282686	23
Average $\pm 2\text{SD}$								0.282687 ± 41	

Figure A shows no relationship between the $^{176}\text{Hf}/^{177}\text{Hf}$ and $^{176}\text{Yb}/^{177}\text{Hf}$ ratios, indicating that the correction of the Yb interferent did not affect the zircon Hf isotope composition. In addition, the $^{176}\text{Yb}/^{177}\text{Hf}$ ratios of the analyzed zircon crystals are low (< 0.09),

as recommended by Griffin et al. (2002). The calculated ϵ_{Hf} values overlap within uncertainties, suggesting that zircon crystals crystallized from a homogeneous source.

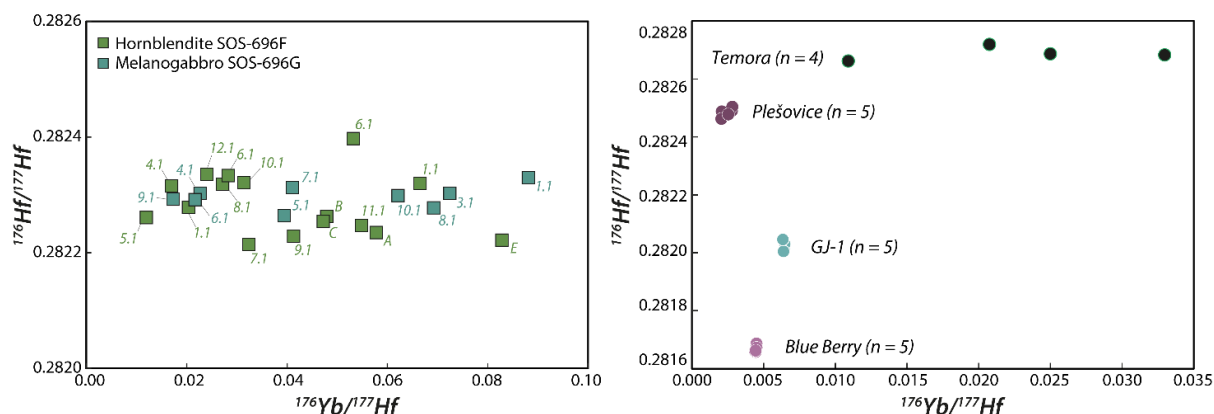


Figure A: $^{176}\text{Hf}/^{177}\text{Hf}$ versus $^{176}\text{Yb}/^{177}\text{Hf}$ diagrams for the analyzed samples and zircon reference materials.

Isotope ratios were back-calculated to crystallization age using the decay constant $1.867 \times 10^{-11} \text{ years}^{-1}$ (Söderlund et al., 2004). The epsilon hafnium parameter (ϵ_{Hf}) and the two-stage depleted mantle model ages ($\text{Hf-T}_{\text{DM}}^{\text{C}}$) consider the values for the chondritic uniform reservoir (CHUR) and the depleted mantle (DM) from Bouvier et al. (2008) and Andersen et al. (2009), respectively. A $^{176}\text{Lu}/^{177}\text{Hf}$ ratio of 0.022 is assumed for the $\text{Hf-T}_{\text{DM}}^{\text{C}}$ calculation, consistent with a mafic crust (Pietranik et al., 2008).

Sr, Nd, and Pb isotopes

Whole-rock isotope analyses were achieved at the Laboratório de Geologia Isotópica (LGI) of the Centro de Estudos em Petrologia e Geoquímica (CPGq), Universidade Federal do Rio Grande do Sul (UFRGS). Approximately 100 μg of sample powder was mixed with a ^{149}Sm - ^{150}Nd spike solution in Savillex vials. The mixture was attacked with HNO_3 , HF , and HCl acids on a hot plate until complete dissolution. Chemical separation was undertaken through conventional ion exchange techniques in Teflon columns. The first stage consisted of separating Sr and rare earth elements (REE) using a Bio-Rad AG50W-X8 resin. Sm and Nd were separated from the other REE using HDEHP LN resin. Pb was separated with Dowex AG-1X8 cation exchange resin. Sr, Sm, and Nd concentrates were evaporated to dryness, dissolved with H_3PO_4 , and deposited on double Re filaments. Collected Pb aliquots were deposited on single Re filaments using a mixture of H_3PO_4 and silica gel.

All isotopic analyses were performed in a Thermo Scientific Triton plus thermal ionization mass spectrometer. Sr isotope compositions were determined based on a mean of 120 measurements with an intensity of 1.0 V for ^{88}Sr . The normalization of the Sr ratios was made with $^{86}\text{Sr}/^{88}\text{Sr} = 0.1194$ adjusted for bias based on NBS-987 ($^{87}\text{Sr}/^{86}\text{Sr} = 0.71026 \pm 0.000011$). The $^{87}\text{Rb}/^{86}\text{Sr}$ ratio was calculated from Rb and Sr elemental data. Sm–Nd isotopic analyses were carried out with a mean of 100 measurements in isotope ratios and an intensity of 1.0 V for ^{146}Nd . The values were normalized to the ratio $^{146}\text{Nd}/^{144}\text{Nd} = 0.7219$ and adjusted for bias based on Nd SPEX, assuming $^{143}\text{Nd}/^{144}\text{Nd} = 0.511110$, and calibrated against JNdi assuming a $^{143}\text{Nd}/^{144}\text{Nd}$ value of 0.511859 ± 0.000010 . Pb–Pb ratios were obtained through a mean of 50 measurements with an intensity of 0.5 V for the ^{206}Pb isotope. Pb was corrected for fractionation in 0.1% amu⁻¹ based on NBS-982 standard analyses ($^{206}\text{Pb}/^{204}\text{Pb} = 36.618609 \pm 0.0100$). The errors for all isotopic data are under 24 ppm for $^{87}\text{Sr}/^{86}\text{Sr}$ and 11 ppm for $^{143}\text{Nd}/^{144}\text{Nd}$. Typical analytical errors for $^{87}\text{Rb}/^{86}\text{Sr}$, $^{147}\text{Sm}/^{144}\text{Nd}$, and the $^{206}\text{Pb}/^{204}\text{Pb}$ ratio were equal to or lower than 0.1%. Single-stage depleted mantle model ages (Nd- T_{DM}) were calculated according to DePaolo (1981). Chronometric calculations applied the decay constants recommended by Steiger and Jäger (1977) and Wasserburg et al. (1981).

References

- Andersen, T., Andersson, U.B., Graham, S., Åberg, G., Simonsen, S.L., 2009. Granitic magmatism by melting of juvenile continental crust: new constraints on the source of Palaeoproterozoic granitoids in Fennoscandia from Hf isotopes in zircon. *J Geol Soc London* 166, 233–247. <https://doi.org/10.1144/0016-76492007-166>
- Black, L.P., Kamo, S.L., Allen, C.M., Davis, D.W., Aleinikoff, J.N., Valley, J.W., Mundil, R., Campbell, I.H., Korsch, R.J., Williams, I.S., Foudoulis, C., 2004. Improved $^{206}\text{Pb}/^{238}\text{U}$ microprobe geochronology by the monitoring of a trace-element-related matrix effect; SHRIMP, ID–TIMS, ELA–ICP–MS and oxygen isotope documentation for a series of zircon standards. *Chem Geol* 205, 115–140. <https://doi.org/10.1016/J.CHEMGEO.2004.01.003>
- Bouvier, A., Vervoort, J.D., Patchett, P.J., 2008. The Lu–Hf and Sm–Nd isotopic composition of CHUR: Constraints from unequilibrated chondrites and implications for the bulk composition of terrestrial planets. *Earth Planet Sci Lett* 273, 48–57. <https://doi.org/https://doi.org/10.1016/j.epsl.2008.06.010>
- Chu, N.C., Taylor, R.N., Chavagnac, V., Nesbitt, R.W., Boella, R.M., Milton, J.A., German, C.R., Bayon, G., Burton, K., 2002. Hf isotope ratio analysis using multi-collector inductively coupled plasma mass spectrometry: an evaluation of isobaric interference corrections. *J Anal At Spectrom* 17, 1567–1574. <https://doi.org/10.1039/B206707B>

- DePaolo, D.J., 1981a. Trace element and isotopic effects of combined wallrock assimilation and fractional crystallization. *Earth Planet Sci Lett* 53, 189–202. [https://doi.org/10.1016/0012-821X\(81\)90153-9](https://doi.org/10.1016/0012-821X(81)90153-9)
- DePaolo, D.J., 1981b. Nd Isotopic Studies: Some new perspectives on Earth structure and evolution. *Eos, Transactions American Geophysical Union* 62, 137–137. <https://doi.org/10.1029/EO062I014P00137-01>
- Faure, G., 2001. *Origin of Igneous Rocks: The Isotopic Evidence*, 1st ed, Origin of Igneous Rocks. Springer Berlin Heidelberg. <https://doi.org/10.1007/978-3-662-04474-2>
- Griffin, W.L., Wang, X., Jackson, S.E., Pearson, N.J., O'Reilly, S.Y., Xu, X., Zhou, X., 2002. Zircon chemistry and magma mixing, SE China: In-situ analysis of Hf isotopes, Tonglu and Pingtan igneous complexes. *Lithos* 61, 237–269. [https://doi.org/10.1016/S0024-4937\(02\)00082-8](https://doi.org/10.1016/S0024-4937(02)00082-8)
- Janoušek, V., Farrow, C.M., Erban, V., 2006. Interpretation of whole-rock geochemical data in igneous geochemistry: introducing Geochemical Data Toolkit (GCDkit). *Journal of Petrology* 47, 1255–1259. <https://doi.org/10.1093/petrology/egl013>
- Janoušek, V., Moyen, J.F., Martin, H., Erban, V., Farrow, C., 2015. Geochemical modelling of igneous processes - principles and recipes in R language: Bringing the power of R to a geochemical community. *Geochemical Modelling of Igneous Processes - Principles and Recipes in R Language: Bringing the Power of R to a Geochemical Community* 1–346. <https://doi.org/10.1007/978-3-662-46792-3/COVER>
- Ludwig, K., 2009a. *SQUID 2: A User's Manual*, Spec. Pub. ed, Berkeley Geochronology Center, Berkeley.
- Ludwig, K., 2009b. *User's Manual for Isoplot 3.70*, Spec. Pub. ed, Berkeley Geochronology Center, Berkeley.
- Milhomem Neto, J.M., Lafon, J.M., 2019. Zircon U-Pb and Lu-Hf isotope constraints on Archean crustal evolution in Southeastern Guyana Shield. *Geoscience Frontiers* 10, 1477–1506. <https://doi.org/10.1016/J.GSF.2018.09.012>
- Morel, M.L.A., Nebel, O., Nebel-Jacobsen, Y.J., Miller, J.S., Vroon, P.Z., 2008. Hafnium isotope characterization of the GJ-1 zircon reference material by solution and laser-ablation MC-ICPMS. *Chem Geol* 255, 231–235. <https://doi.org/10.1016/J.CHEMGEO.2008.06.040>
- Patchett, P.J., Tatsumoto, M., 1981. A routine high-precision method for Lu-Hf isotope geochemistry and chronology. *Contributions to Mineralogy and Petrology* 75, 263–267. <https://doi.org/10.1007/BF01166766>
- Pereira, F.S., 2019. *Petrogênese da Suíte Máfica do Domínio Macururé, Sistema Orogênico Sergipano, setor sul da Província Borborema* (M.S. dissertation). Universidade Federal de Sergipe, São Cristóvão.
- Pereira, F.S., Rosa, M.L.S., Conceição, H., 2019. Condições de colocação do magmatismo máfico do Domínio Macururé, Sistema Orogênico Sergipano: Maciço Capela. *Revista Geologia USP. Série Científica* 19, 3–29. <https://doi.org/10.11606/issn.2316-9095.v19-151464>

- Pereira, F.S., Rosa, M.L.S., Conceição, H., Bertotti, A.L., 2020. Age, composition, and source of the Macururé Mafic Suite, Southern Borborema Province, Brazil. *Brazilian Journal of Geology* 50, e20190105. <https://doi.org/10.1590/2317-4889202020190105>
- Pietranik, A.B., Hawkesworth, C.J., Storey, C.D., Kemp, A.I.S., Sircombe, K.N., Whitehouse, M.J., Bleeker, W., 2008. Episodic, mafic crust formation from 4.5 to 2.8 Ga: New evidence from detrital zircons, Slave craton, Canada. *Geology* 36, 875–878. <https://doi.org/10.1130/G24861A.1>
- Rayleigh, J.W.S., 1896. Theoretical considerations respecting the separation of gases by diffusion and similar processes. *Philosophical Magazine* 42, 493–498. <https://doi.org/10.1080/14786449608620944>
- Rollinson, H., 1993. Using geochemical data: evaluation, presentation, interpretation. Longman, Essex.
- Santos, C., Zincone, S.A., Queiroga, G.N., Bersan, S.M., Lana, C.C., Oliveira, E.P., 2022. Evidence for change in crust formation process during the Paleoproterozoic in the São Francisco Craton (Gavião Block): Coupled zircon Lu-Hf and U-Pb isotopic analyses and tectonic implications. *Precambrian Res* 368, 106472. <https://doi.org/10.1016/J.PRECAMRES.2021.106472>
- Santos, M.M., Lana, C., Scholz, R., Buick, I., Schmitz, M.D., Kamo, S.L., Gerdes, A., Corfu, F., Tapster, S., Lancaster, P., Storey, C.D., Basei, M.A.S., Tohver, E., Alkmim, A., Nalini, H., Krambrock, K., Fantini, C., Wiedenbeck, M., 2017. A New Appraisal of Sri Lankan BB Zircon as a Reference Material for LA-ICP-MS U-Pb Geochronology and Lu-Hf Isotope Tracing. *Geostand Geoanal Res* 41, 335–358. <https://doi.org/10.1111/GGR.12167>
- Sato, K., Tassinari, C., Basei, M.A.S., Júnior, O.S., Onoe, A., Souza, M., 2014. Microsonda Iônica de Alta Resolução e de Alta Sensibilidade (SHRIMP IIe/MC) do Instituto de Geociências da Universidade de São Paulo, Brasil: método analítico e primeiros resultados. *Revista Geologia USP. Série Científica* 14, 3–18. <https://doi.org/10.5327/Z1519-874X201400030001>
- Sláma, J., Košler, J., Condon, D.J., Crowley, J.L., Gerdes, A., Hanchar, J.M., Horstwood, M.S.A., Morris, G.A., Nasdala, L., Norberg, N., Schaltegger, U., Schoene, B., Tubrett, M.N., Whitehouse, M.J., 2008. Plešovice zircon — A new natural reference material for U–Pb and Hf isotopic microanalysis. *Chem Geol* 249, 1–35. <https://doi.org/10.1016/J.CHEMGEO.2007.11.005>
- Söderlund, U., Patchett, P.J., Vervoort, J.D., Isachsen, C.E., 2004. The ^{176}Lu decay constant determined by Lu–Hf and U–Pb isotope systematics of Precambrian mafic intrusions. *Earth Planet Sci Lett* 219, 311–324. [https://doi.org/10.1016/S0012-821X\(04\)00012-3](https://doi.org/10.1016/S0012-821X(04)00012-3)
- Steiger, R.H., Jäger, E., 1977. Subcommittee on geochronology: convention on the use of decay constants in geo- and cosmochronology. *Earth Planet Sci Lett* 36, 359–362. [https://doi.org/10.1016/0012-821X\(77\)90060-7](https://doi.org/10.1016/0012-821X(77)90060-7)
- Stormer, J.C., Nicholls, J., 1978. XLFRAC: a program for the interactive testing of magmatic differentiation models. *Comput Geosci* 4, 143–159. [https://doi.org/10.1016/0098-3004\(78\)90083-3](https://doi.org/10.1016/0098-3004(78)90083-3)

- Teixeira, L., 2005. GENESIS 4.0: Modelos geoquímicos.
- Thirlwall, M.F., Anczkiewicz, R., 2004. Multidynamic isotope ratio analysis using MC-ICP-MS and the causes of secular drift in Hf, Nd and Pb isotope ratios. *Int J Mass Spectrom* 235, 59–81. <https://doi.org/https://doi.org/10.1016/j.ijms.2004.04.002>
- Warr, L.N., 2021. IMA–CNMNC approved mineral symbols. *Mineral Mag* 85, 291–320. <https://doi.org/10.1180/MGM.2021.43>
- Wasserburg, G.J., Jacobsen, S.B., DePaolo, D.J., McCulloch, M.T., Wen, T., 1981. Precise determination of SmNd ratios, Sm and Nd isotopic abundances in standard solutions. *Geochim Cosmochim Acta* 45, 2311–2323. [https://doi.org/10.1016/0016-7037\(81\)90085-5](https://doi.org/10.1016/0016-7037(81)90085-5)
- Williams, I.S., 1997. U-Th-Pb geochronology by ion microprobe, in: *Applications of Microanalytical Techniques to Understanding Mineralizing Processes*. Society of Economic Geologists.
- Wilson, M., 1989. *Igneous Petrogenesis: a Global Tectonic Approach*. Springer Netherlands, Dordrecht. <https://doi.org/10.1007/978-1-4020-6788-4>
- Woodhead, J.D., Hergt, J.M., 2005. A preliminary appraisal of seven natural zircon reference materials for in situ Hf isotope determination. *Geostand Geoanal Res* 29, 183–195. <https://doi.org/10.1111/j.1751-908X.2005.tb00891.x>

SUPPLEMENTARY TABLES

Supplementary Table S1- Summary of whole-rock geochemical data.

Sample	Location ^a		Ref. ^b	Field name	Chemical nomenclature ^c	Unit	Major elements (wt%)										Na ₂ O+K ₂ O	K ₂ O/Na ₂ O	K/Na	A/CNK	Mg#	
	X	Y					SiO ₂	TiO ₂	Al ₂ O ₃	Fe ₂ O ₃ *	MgO	MnO	CaO	K ₂ O	Na ₂ O	P ₂ O ₅						LOI
PC003B	713925	8841800	[1]	Grt-bearing bt diorite	Monzogabbro	Mafic	47.90	1.13	18.08	13.84	3.46	0.45	5.55	2.46	2.37	0.54	1.56	4.83	1.04	0.68	1.09	0.38
PC008A	714692	8842100	[1]	Bt hornblende	Foid gabbro	Ultramafic	41.26	2.73	12.48	16.00	8.39	0.20	8.75	2.22	2.05	0.31	2.82	4.27	1.08	0.71	0.58	0.56
PC033A	710688	8842290	[1]	Bt qz diorite	Gabbroic diorite	Mafic	52.38	1.24	14.67	10.10	4.24	0.17	6.33	2.64	2.52	0.37	3.83	5.16	1.05	0.69	0.79	0.50
PC037A	715999	8841284	[1]	Hornblende	Gabbro	Ultramafic	43.46	1.78	9.61	12.47	13.08	0.19	9.08	2.63	1.68	0.40	3.53	4.31	1.57	1.03	0.43	0.72
PC039A	716002	8841526	[1]	Bt diorite	Monzogabbro	Mafic	46.66	2.06	15.07	11.90	5.17	0.16	7.13	3.26	2.41	0.92	2.62	5.67	1.35	0.89	0.74	0.51
PC054A	714464	8841648	[1]	Grt-bearing bt qz diorite	Monzodiorite	Mafic	51.49	1.28	16.66	9.70	3.52	0.18	5.96	2.74	3.05	0.54	2.61	5.79	0.90	0.59	0.89	0.47
PC055A	714653	8841768	[1]	Grt-bearing bt diorite	Monzodiorite	Mafic	51.04	0.87	19.76	8.99	1.98	0.20	5.74	2.43	3.88	0.38	2.00	6.31	0.63	0.41	1.02	0.35
PC076A	710031	8844048	[1]	Hbl gabbro	Monzodiorite	Mafic	51.59	1.27	14.76	10.58	4.84	0.19	6.88	3.14	2.58	0.52	1.22	5.72	1.22	0.80	0.73	0.53
PC080A	710700	8845353	[1]	Bt granodiorite	Quartz monzonite	Granitic	65.35	0.42	14.07	4.58	1.20	0.05	2.21	3.77	3.97	0.14	2.68	7.74	0.95	0.62	0.96	0.39
PC084A	711516	8845158	[1]	Px hornblende	Foid gabbro	Ultramafic	40.34	2.46	11.41	14.94	10.41	0.16	10.02	1.75	1.98	0.16	3.84	3.73	0.88	0.58	0.49	0.63
PC084C	711516	8845158	[1]	Bt granodiorite	Granodiorite	Granitic	65.32	0.54	14.23	4.74	1.57	0.05	2.98	1.96	4.50	0.17	2.00	6.46	0.44	0.29	0.95	0.45
PC084E	711516	8845158	[1]	Qz diorite	-	Mafic	n.d	1.36	17.40	9.77	6.36	0.14	5.78	3.74	n.d	0.51	n.d	-	-	-	-	0.61
SOS-696A	711418	8845143	[2]	Granite	Quartz monzonite	Granitic	65.51	0.35	15.42	3.51	1.69	0.04	2.90	4.62	3.69	0.24	0.42	8.32	1.25	0.82	0.94	0.54
SOS-696B	711418	8845143	[2]	Grt-bearing gabbro	Foid gabbro	Ultramafic	44.10	1.62	13.62	15.36	10.38	0.18	8.06	3.29	1.86	0.60	1.20	5.15	1.77	1.16	0.64	0.62
SOS-696C	711418	8845143	[2]	Tonalite pocket	Granite	Granitic	70.49	0.16	15.66	1.15	0.59	0.02	2.08	5.32	3.52	0.06	0.51	8.84	1.51	1.00	1.02	0.56
SOS-696D	711418	8845143	[2]	Hbl gabbro	Foid gabbro	Ultramafic	42.77	2.21	12.99	18.06	9.83	0.17	9.53	2.32	1.80	0.30	1.30	4.11	1.29	0.85	0.57	0.57
SOS-696E	711418	8845143	[2]	Bt grt diorite	Foid gabbro	Ultramafic	43.32	1.69	14.98	16.94	8.33	0.29	8.04	2.91	1.91	0.74	1.05	4.82	1.53	1.00	0.72	0.54
SOS-696F*	711418	8845143	[2]	Bt hornblende	Foid gabbro	Ultramafic	41.47	2.29	13.21	18.28	9.75	0.16	10.23	2.15	1.78	0.70	1.34	3.92	1.21	0.80	0.55	0.56
SOS-696G*	711418	8845143	[2]	Hbl gabbro	Foid gabbro	Mafic	40.81	2.28	12.87	19.37	10.50	0.19	10.28	2.03	1.62	0.44	1.39	3.65	1.25	0.82	0.55	0.57
SOS-919A	713920	8841801	[2]	Grt-bearing bt diorite	Monzogabbro	Mafic	48.63	1.02	18.35	12.21	4.32	0.29	5.71	2.98	2.57	0.81	0.71	5.56	1.16	0.76	1.03	0.46
SOS-919B	713920	8841801	[2]	Microgranular mafic enclave	Gabbroic diorite	MME	55.09	0.62	14.13	9.33	8.77	0.13	6.68	2.44	2.08	0.30	0.77	4.51	1.17	0.77	0.78	0.70
SOS-919C	713920	8841801	[2]	Grt-bearing bt diorite	Monzogabbro	Mafic	49.12	1.45	15.98	12.02	5.35	0.16	7.33	2.48	2.70	0.92	0.58	5.18	0.92	0.61	0.78	0.52
SOS-920A	713863	8841890	[2]	Bt-hbl gabbro	Gabbro	Mafic	46.73	1.36	13.98	14.45	7.99	0.20	9.14	2.28	1.73	0.84	0.84	4.01	1.32	0.87	0.64	0.57
SOS-920B	713863	8841890	[2]	Grt-bearing bt granodiorite	Monzodiorite	Mafic	51.30	1.01	18.11	8.89	4.05	0.15	5.55	3.18	2.95	0.89	0.80	6.13	1.08	0.71	0.99	0.53
SOS-924A	714376	8841931	[2]	Granite	Quartz monzonite	Granitic	61.44	0.37	18.26	4.04	0.93	0.04	4.67	2.81	4.45	0.28	0.90	7.26	0.63	0.42	0.97	0.36
SOS-924B	714376	8841931	[2]	Grt-bearing bt hornblende	Foid gabbro	Ultramafic	44.85	1.40	19.40	12.17	5.16	0.13	5.50	4.34	2.61	1.15	0.78	6.95	1.66	1.09	1.02	0.51
SOS-925	714677	8842092	[2]	Bt hornblende	Foid gabbro	Ultramafic	41.29	2.42	13.68	18.91	9.35	0.20	9.39	2.62	1.74	0.46	0.80	4.36	1.50	0.99	0.60	0.55
SOS-928A	715128	8842308	[2]	Grt-bearing bt diorite	Monzodiorite	Mafic	51.23	1.42	15.51	10.64	5.97	0.12	6.06	3.04	2.59	0.65	0.96	5.63	1.17	0.77	0.84	0.58
SOS-929	715221	8842175	[2]	Grt-bearing bt diorite	Monzogabbro	Mafic	46.03	1.46	16.70	14.39	6.43	0.29	6.87	2.76	2.15	0.88	0.42	4.92	1.28	0.84	0.88	0.52
SOS-930A	715311	8842153	[2]	Grt-bearing bt diorite	Foid gabbro	Ultramafic	43.91	1.65	16.93	14.72	6.81	0.25	7.52	3.37	1.86	1.02	0.79	5.23	1.82	1.19	0.83	0.53
SOS-930B	715311	8842153	[2]	Ultramafic enclave	Gabbro	UME	45.28	1.61	12.19	17.67	9.95	0.18	8.35	2.46	1.17	1.19	0.94	3.64	2.10	1.38	0.62	0.58
SOS-930C	715311	8842153	[2]	Ultramafic enclave	Foid gabbro	UME	41.47	2.31	16.15	15.36	9.31	0.11	6.90	4.16	1.57	1.14	1.69	5.73	2.65	1.74	0.82	0.60

Continues on the next page

Sample	Location ^a		Ref. ^b	Field name	Chemical classification ^c	Unit	Major elements (wt.%)										Na ₂ O+K ₂ O	K ₂ O/Na ₂ O	K/Na	A/CNK	Mg#	
	X	Y					SiO ₂	TiO ₂	Al ₂ O ₃	Fe ₂ O ₃ *	MgO	MnO	CaO	K ₂ O	Na ₂ O	P ₂ O ₅						LOI
SOS-930D	715311	8842153	[2]	Ultramafic enclave	Foid gabbro	UME	44.24	1.70	12.01	18.75	10.24	0.19	8.69	2.26	1.13	1.18	1.07	3.39	2.01	1.32	0.60	0.57
SOS-931	715447	8841922	[2]	Grt-bearing bt diorite	Monzogabbro	Ultramafic	44.96	1.44	18.33	13.34	5.21	0.25	6.97	3.42	2.30	1.05	0.61	5.72	1.49	0.98	0.91	0.49
SOS-932	715284	8841913	[2]	Bt-hbl gabbro	Foid gabbro	Ultramafic	42.87	2.28	15.04	15.88	8.42	0.16	8.53	2.90	2.37	0.44	0.72	5.27	1.22	0.81	0.67	0.56
SOS-934A	714694	8842007	[2]	Hb gabbro	Gabbro	Ultramafic	47.36	1.13	9.74	13.50	12.99	0.19	12.00	0.85	1.60	0.24	0.95	2.46	0.53	0.35	0.38	0.70
SOS-934B	714694	8842007	[2]	Hornblendite	Gabbro	Ultramafic	46.27	1.05	9.23	14.55	13.98	0.21	12.26	0.83	1.20	0.45	1.06	2.03	0.69	0.45	0.37	0.70
SOS-938	709818	8845024	[2]	Grt-bearing bt diorite	Granodiorite	Granitic	61.86	0.57	16.19	6.54	2.80	0.09	3.96	2.74	3.17	0.53	0.48	5.92	0.86	0.57	1.05	0.51
SOS-939	710024	8844044	[2]	Bt diorite	Monzodiorite	Mafic	51.24	1.19	15.84	10.35	4.37	0.14	6.93	4.16	2.18	0.66	0.25	6.34	1.91	1.25	0.77	0.51
SOS-940	710340	8844360	[2]	Bt-hbl gabbro	Monzodiorite	Mafic	50.66	1.35	15.50	10.94	5.51	0.15	7.12	3.01	2.48	0.62	0.29	5.49	1.21	0.80	0.76	0.55
SOS-941A	710580	8844798	[2]	Bt diorite	Gabbro	Mafic	45.74	1.69	15.54	14.48	6.70	0.15	8.58	2.35	2.31	0.78	0.54	4.66	1.02	0.67	0.71	0.53
SOS-941B	710580	8844798	[2]	Grt-bearing bt granite	Diorite	Mafic	58.29	0.93	15.45	9.58	4.72	0.11	3.90	3.36	2.47	0.47	0.39	5.84	1.36	0.90	1.04	0.54
SOS-943A	710695	8845349	[2]	Bt granite	Quartz monzonite	Granitic	66.89	0.31	15.08	3.01	1.42	0.04	2.72	4.48	3.78	0.23	0.32	8.26	1.19	0.78	0.94	0.53
SOS-944	711011	8844016	[2]	Bt diorite	Monzodiorite	Mafic	50.01	1.33	16.36	10.87	4.58	0.15	7.54	3.23	2.40	0.63	0.11	5.64	1.35	0.89	0.77	0.51
SOS-945	712244	8844770	[2]	Bt hornblendite	Foidolite	Ultramafic	40.24	2.23	13.35	19.33	9.91	0.23	10.98	1.93	1.65	0.41	1.30	3.57	1.17	0.77	0.54	0.55
SOS-946	712203	8845025	[2]	Bt diorite	Monzodiorite	Mafic	50.30	1.28	16.22	10.78	4.54	0.15	7.43	3.37	2.43	0.61	0.07	5.80	1.38	0.91	0.77	0.51
SOS-947	711371	8845371	[2]	Bt-hbl gabbro	Gabbro	Mafic	49.14	1.30	13.30	12.31	9.02	0.17	7.87	2.67	2.06	0.45	1.06	4.73	1.30	0.85	0.65	0.64

Continues on the next page

^a Universal Transverse Mercator (UTM) coordinate system, South American Datum, 24S zone^b [1] This study, [2] Pereira (2023)^c According to Middlemost (1994)

* Samples used for U-Pb dating and Lu-Hf isotope composition on zircon

n.d = not determined

LOI = loss on ignition

Mg# = Mg/(Mg + Fe²⁺), calculated assuming Fe₂O₃/(Fe₂O₃ + FeO) = 0.20A/CNK = molar [Al₂O₃/(CaO + Na₂O + K₂O)]

Sample	Trace elements (ppm)																										Rb/ Ba	Sr/ Th	Nb/ Nb*	La/ Yb _{CN}	La/ Sm _{CN}	Gd/ Yb _{CN}	Eu/ Eu*		
	Ba	Rb	Sr	Cs	Ga	U	Th	Zr	Hf	Nb	Y	Cr	Ni	V	La	Ce	Pr	Nd	Sm	Eu	Gd	Tb	Dy	Ho	Er	Tm								Yb	Lu
PC003B	1253	86	573	3.80	22	2.01	14.00	611.8	14	5	98.30	151	46	136	43.50	97.00	11.37	43.70	8.70	2.26	13.39	2.30	15.40	3.48	10.67	1.58	9.60	1.86	0.07	40.93	0.07	3.08	3.12	1.13	0.64
PC008A	1227	54	300	1.90	25	0.69	5.50	168.4	6	12	54.11	53	28	519	27.00	94.00	13.94	64.90	13.50	3.18	14.36	1.85	10.33	2.09	5.69	0.72	4.00	0.62	0.04	54.55	0.34	4.59	1.25	2.90	0.70
PC033A	1087	76	519	4.40	19	2.26	11.10	226.2	6	11	32.26	129	21	179	43.70	87.80	10.72	43.80	8.00	2.09	8.24	1.09	5.85	1.24	3.40	0.49	2.70	0.48	0.07	46.76	0.17	10.99	3.41	2.47	0.78
PC037A	1415	88	152	1.70	18	0.45	1.80	70.5	4	5	33.76	345	69	441	18.20	65.10	10.55	51.40	11.70	2.52	11.42	1.34	6.78	1.37	3.50	0.45	2.40	0.38	0.06	84.44	0.30	5.15	0.97	3.85	0.66
PC039A	1809	108	383	3.60	25	1.47	5.10	199.7	6	12	55.83	71	23	243	31.30	84.90	12.13	55.40	11.40	2.72	12.18	1.64	9.58	2.14	6.40	0.91	5.20	0.85	0.06	75.10	0.33	4.09	1.71	1.90	0.70
PC054A	1527	93	706	3.70	24	2.43	9.60	396.2	10	10	37.57	119	33	165	41.40	111.10	13.02	52.60	9.70	2.41	9.81	1.27	6.61	1.44	3.99	0.57	3.40	0.57	0.06	73.54	0.17	8.27	2.67	2.33	0.75
PC055A	1415	87	1020	2.90	24	2.26	50.00	611.7	15	5	41.17	92	21	65	202.40	367.70	39.43	131.50	15.50	3.28	12.88	1.55	7.05	1.47	4.26	0.58	3.70	0.62	0.06	20.40	0.02	37.16	8.15	2.82	0.71
PC076A	1406	74	591	3.40	19	1.80	7.40	118.2	3	5	35.93	103	22	194	45.00	95.50	11.95	48.70	9.10	2.65	9.48	1.21	6.49	1.37	3.87	0.54	3.20	0.51	0.05	79.86	0.09	9.55	3.09	2.40	0.87
PC080A	1124	155	506	12.10	24	2.98	9.80	159.1	5	5	9.19	135	17	48	32.70	64.50	7.12	26.00	4.40	1.12	3.78	0.42	1.91	0.34	0.89	0.11	0.60	0.12	0.14	51.63	0.10	37.02	4.64	5.10	0.84
PC084A	399	24	228	2.10	15	0.38	1.90	54.6	2	5	26.98	181	30	479	10.10	33.40	5.62	29.50	7.60	1.93	8.38	1.00	5.48	1.08	2.83	0.33	1.80	0.28	0.06	120.00	0.39	3.81	0.83	3.77	0.74
PC084C	500	101	592	6.10	24	3.29	10.00	178.7	5	5	8.24	152	19	61	36.50	69.10	7.81	28.40	4.40	1.06	3.54	0.40	1.64	0.29	0.83	0.12	0.60	0.11	0.20	59.20	0.09	41.33	5.18	4.77	0.82
PC084E	1286	137	650	8.10	29	2.77	16.60	310.0	8	5	24.47	336	92	227	69.10	131.90	14.97	56.50	8.90	2.06	7.98	0.98	4.62	0.92	2.56	0.34	2.00	0.58	0.11	39.16	0.05	23.47	4.85	3.23	0.75
SOS-696D	569	56	267	3.56	23	1.18	1.90	127.0	5	10	32.30	210	-	481	14.30	46.60	7.43	37.90	10.35	2.58	9.47	1.30	7.93	1.34	3.38	0.40	2.31	0.37	0.10	140.53	0.63	4.21	0.86	3.32	0.79
SOS-696F	693	43	315	2.26	24	0.67	2.73	173.0	6	9	33.40	160	-	418	22.20	67.80	10.15	48.70	12.45	2.98	11.05	1.57	8.69	1.41	3.40	0.45	2.44	0.32	0.06	115.38	0.40	6.18	1.11	3.66	0.77
SOS-919B	363	65	567	2.47	23	1.20	5.08	171.0	5	9	20.40	870	-	187	28.80	64.50	7.81	31.80	6.48	1.57	5.01	0.68	4.14	0.75	2.17	0.30	1.99	0.26	0.18	111.61	0.25	9.83	2.78	2.04	0.84
SOS-919C	1100	67	619	2.42	26	1.45	4.55	212.0	6	15	56.40	110	-	206	34.80	90.20	12.35	55.50	12.35	2.69	10.80	1.67	10.35	2.02	6.25	0.96	6.56	0.98	0.06	136.04	0.42	3.60	1.76	1.33	0.71
SOS-930B	816	64	145	1.83	26	0.89	3.83	55.0	3	12	36.60	590	-	551	32.00	95.00	14.45	70.90	17.65	3.16	15.30	1.98	9.91	1.49	3.35	0.34	1.54	0.17	0.08	37.73	0.37	14.12	1.13	8.04	0.59
SOS-939	1405	128	605	7.35	25	3.34	16.40	256.0	7	17	47.40	130	-	235	63.50	133.50	15.30	59.80	12.40	2.75	10.35	1.53	8.64	1.77	4.89	0.68	4.71	0.66	0.09	36.89	0.18	9.16	3.20	1.78	0.74
SOS-940	1145	74	522	2.89	23	1.35	5.69	239.0	6	13	31.90	250	-	235	38.90	84.20	10.00	39.80	8.86	1.97	7.30	1.09	6.94	1.33	3.41	0.53	3.24	0.42	0.06	91.74	0.30	8.16	2.74	1.82	0.75
SOS-947	740	97	328	14.00	22	1.81	5.07	199.0	6	13	33.80	610	-	286	20.10	54.30	7.54	34.50	8.25	2.11	7.68	1.19	7.28	1.30	3.81	0.51	3.22	0.44	0.13	64.69	0.43	4.24	1.52	1.93	0.81

CN = chondrite normalized (McDonough and Sun, 1995)

PM = primitive mantle normalized (McDonough and Sun, 1995)

$Eu/Eu^* = Eu_{CN}/\sqrt{(Sm_{CN} \times Gd_{CN})}$

$Nb/Nb^* = Nb_{PM}/\sqrt{(Th_{PM} \times La_{PM})}$

References

McDonough, W.F., Sun, S.S., 1995. The composition of the Earth. *Chemical Geology* 120, 223–253.

Middlemost, E.A.K., 1994. Naming materials in the magma/igneous rock system. *Earth-Science Reviews* 37, 215–224.

Pereira, F.S., 2019. Petrogênese da Suíte Máfica do Domínio Macururé, Sistema Orogênico Sergipano, setor sul da Província Borborema. Universidade Federal de Sergipe, São Cristóvão.

Supplementary Table S2- Fractional crystallization model for major and trace elements.

Major elements (wt%)	Parent magma SOS-940 C_0	Residue C_S	Mineral compositions ^a					Calculated melt C_L'	Daughter magma PC080A C_L
			28.03% Pl	26.88% Amp	24.49% Bt	19.29% Cpx	1.31% Ilm ^b		
			$n = 44$	$n = 24$	$n = 27$	$n = 14$			
SiO ₂	53.07	45.92	53.36	42.36	36.91	50.99	66.94	66.57	
TiO ₂	1.41	1.97		1.32	3.31	0.51	0.34	0.43	
Al ₂ O ₃	16.24	17.18	30.11	14.20	16.61	3.07	14.41	14.33	
FeO*	10.30	11.75	0.08	16.05	16.97	11.82	7.49	7.31	
MgO	5.77	8.29		9.75	12.25	12.71	0.88	1.22	
CaO	7.46	10.10	11.65	10.94		19.77	2.34	2.25	
Na ₂ O	2.60	2.11	4.95	2.17	0.03	0.61	3.55	4.04	
K ₂ O	3.15	2.69	0.20	0.96	9.23		4.05	3.84	
Trace elements (ppm)									
Ba	1145						2199	1124	
Rb	74						95	155	
Sr	522						630	506	
Y	31.90						34.47	9.19	
Zr	239.0						430.2	159.1	
Nb	13						18	5	
La	38.9						82.0	32.7	
Ce	84.2						170.3	64.5	
Nd	39.8						44.6	26.0	
Sm	8.86						6.83	4.40	
Eu	1.97						0.61	1.12	
Gd	7.30						3.65	3.78	
Yb	3.24						1.93	0.60	
Lu	0.42						0.28	0.12	

^a Average mineral compositions calculated from n analyzes (Pereira, 2019)

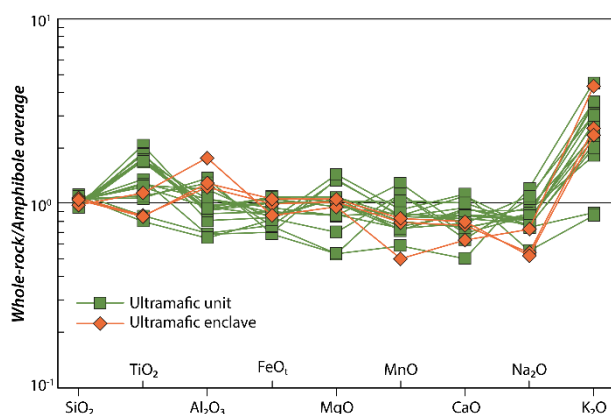
^b Assumed simplified composition

Cumulate = 34.47% $(1 - F) = 65.53\%$ $\sum R^2 = 0.056$
--

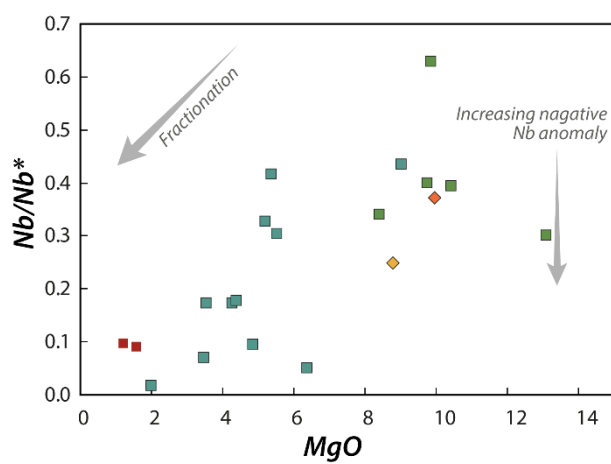
Reference

Pereira, F.S., 2019. Petrogênese da Suíte Máfica do Domínio Macururé, Sistema Orogênico Sergipano, setor sul da Província Borborema. Universidade Federal de Sergipe, São Cristóvão.

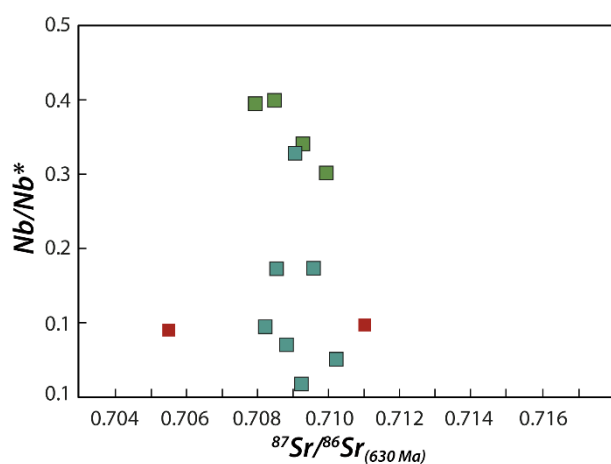
SUPPLEMENTARY FIGURES



Supplementary Figure 1- Ultramafic rocks major elements normalized to the average amphibole composition.



Supplementary Figure 2- Nb anomaly expressed as Nb/Nb^* parameter versus MgO .



Supplementary Figure 3- Nb anomaly expressed as Nb/Nb^* parameter versus $^{87}\text{Sr}/^{86}\text{Sr}_{(630 \text{ Ma})}$.

CAPÍTULO IV DETRITAL ZIRCON U–Pb–Hf GEOCHRONOLOGY AND GEOCHEMICAL CONSTRAINTS ON THE PROVENANCE AND TECTONIC SETTING OF THE MACURURÉ COMPLEX, SOUTHERN BORBOREMA PROVINCE, NE BRAZIL

Periódico pretendido: International Geology Review

Fábio dos Santos Pereira^{1,*}, Jean-Michel Lafon¹, Maria de Lourdes Silva Rosa², Herbet Conceição², João Marinho Milhomem Neto¹, Moacyr Moura Marinho³

¹ Programa de Pós-Graduação em Geologia e Geoquímica (PPGG), Laboratório de Geologia Isotópica (Pará-Iso), Instituto de Geociências (IG), Universidade Federal do Pará (UFPA), 66075-110 Belém, Pará, Brazil

² Programa de Pós-Graduação em Geociências e Análise de Bacias (PGAB), Universidade Federal de Sergipe (UFS), 49100-000 São Cristóvão, Sergipe, Brazil

³ Instituto de Geociências, Universidade Federal da Bahia (UFBA), 40170-290 Ondina, Salvador, Bahia, Brazil

*Corresponding author: Programa de Pós-Graduação em Geologia e Geoquímica, Instituto de Geociências, Universidade Federal do Pará, 66075-110 Belém, Pará, Brazil

E-mail address: fabio.pereira@ig.ufpa.br (F.S. Pereira)

1 INTRODUCTION

Zircon is a common minor component of clastic rocks that survive the sedimentary cycle due to its physicochemical stability and refractory character, ultimately becoming the only record of eroded ancient areas (e.g., Wilde et al., 2001). The high concentration of U-Th-Pb makes this heavy mineral a powerful tool in geochronological studies applied to sedimentary provenance and crustal evolution (Cawood et al., 2012; Gehrels, 2011; Hoskin and Schaltegger, 2003).

The standard application of this technique aims to provide time constraints on the sedimentation period, for which the youngest clastic constituent provides an estimate of the maximum deposition age (Coutts et al., 2019; Vermeesch, 2021). This approach is especially important for Precambrian strata, where biostratigraphic age control is absent (Gehrels, 2011). Potential source areas may be recognized by matching detrital ages with known igneous and metamorphic zircon-forming events (Andersen et al., 2018a). In addition, age pattern distribution in detrital zircon spectra has a straight relationship with the tectonic setting of the basin where detritus were deposited (Cawood et al., 2012), enabling the elucidate broad aspects of the geodynamic evolution of a region.

Besides the distribution of ages, the proportion of juvenile and recycled material has a key role in understanding the genesis of a crustal segment. Once zircon preserves the Hf isotope signature of the magma source from which it crystallized, combining detrital ages and Lu-Hf isotope compositions is a valuable tool for distinguishing protosources with the same crystallization age (Griffin et al., 2004). This is particularly useful in deeply eroded orogenic belts where specific source rock units may no longer be accessible.

The Sergipano Orogenic System (SOS), the southernmost segment of the Borborema Province, is part of a large Brasiliano/Pan-African orogen stretching out to the Central African Orogenic Belt (CAOB) (Caxito et al., 2020a; Oliveira et al., 2006; Van Schmus et al., 2008). Most geodynamic reconstruction of this area has been based on geochemical and isotopic signatures of magmatic rocks, limiting these interpretations to the rifting event related to the break-up of the Rodinia supercontinent and convergence of landmasses during the Gondwana assembly (Oliveira et al., 2010; Pereira et al., 2023). In a pioneering work, Oliveira et al. (2015b) defined the general provenance framework for the main metasedimentary successions composing the SOS. Subsequent studies (Lima et al., 2018; Neves et al., 2019; Passos et al., 2022) fed the regional database with U-Pb zircon ages of igneous and sedimentary rocks, and a large number of in situ analyses are now available.

The Macururé Domain is the most prominent geological unit of the SOS, consisting mainly of phyllites and schists metamorphized under greenschist and amphibolite-facies conditions (Davison and Santos, 1989; Silva et al., 1995), interlayered with thick successions of quartzite. In this work, we report the first coupled U-Pb and Lu-Hf analyses on detrital zircon of the from metasedimentary rocks of the SOS. Newly acquired data are integrated with the existent database to investigate the timing of sedimentation, tectonic setting of deposition, and nature of the source areas.

2 GEOLOGICAL SETTING

2.1 BORBOREMA PROVINCE

The Borborema Province in NE Brazil formed from the convergence between the Amazonian, São Luís-West Africa, and São Francisco-Congo cratons during the Western Gondwana assembly in the course of the Brasiliano/Pan-African Orogeny (Fig. 1a; Brito Neves et al., 2000; Caxito et al., 2020a).

The basement of the Borborema Province is mainly composed of Paleoproterozoic orthogneisses related to the Rhyacian Orogeny (2.3-1.9 Ga), which ultimately led to the building of the Columbia Supercontinent. Late Paleoproterozoic associations in the central and northern subprovinces are interpreted as extension-related magmatism emplaced at the Statherian-Calymmian transition (Amaral et al., 2015; Lages et al., 2019). Metavolcanic-sedimentary sequences and orthogneisses, correlated with the Cariris Velhos event (1.0-0.9 Ga), have been recognized in the central and southern sectors of the province (Brito Neves et al., 1995; Carvalho, 2005; Caxito et al., 2020b; Guimarães et al., 2016). In addition, late Neoproterozoic supracrustal successions covering the basement were intruded by widespread Brasiliano/Pan-African magmatism (650-530 Ma) represented by several batholiths, stocks, and dike swarms.

The continental-scale Patos and Pernambuco shear zones have been considered important crustal limits that divide the Borborema Province into northern, central, and southern subprovinces (Fig. 1b; Van Schmus et al., 2011, 2008). The southern subprovince is bounded by the Pernambuco shear zone and the São Francisco Craton (SFC), comprising the Pernambuco-Alagoas Domain (PEAL), Sergipano, and Riacho do Pontal orogenic belts.

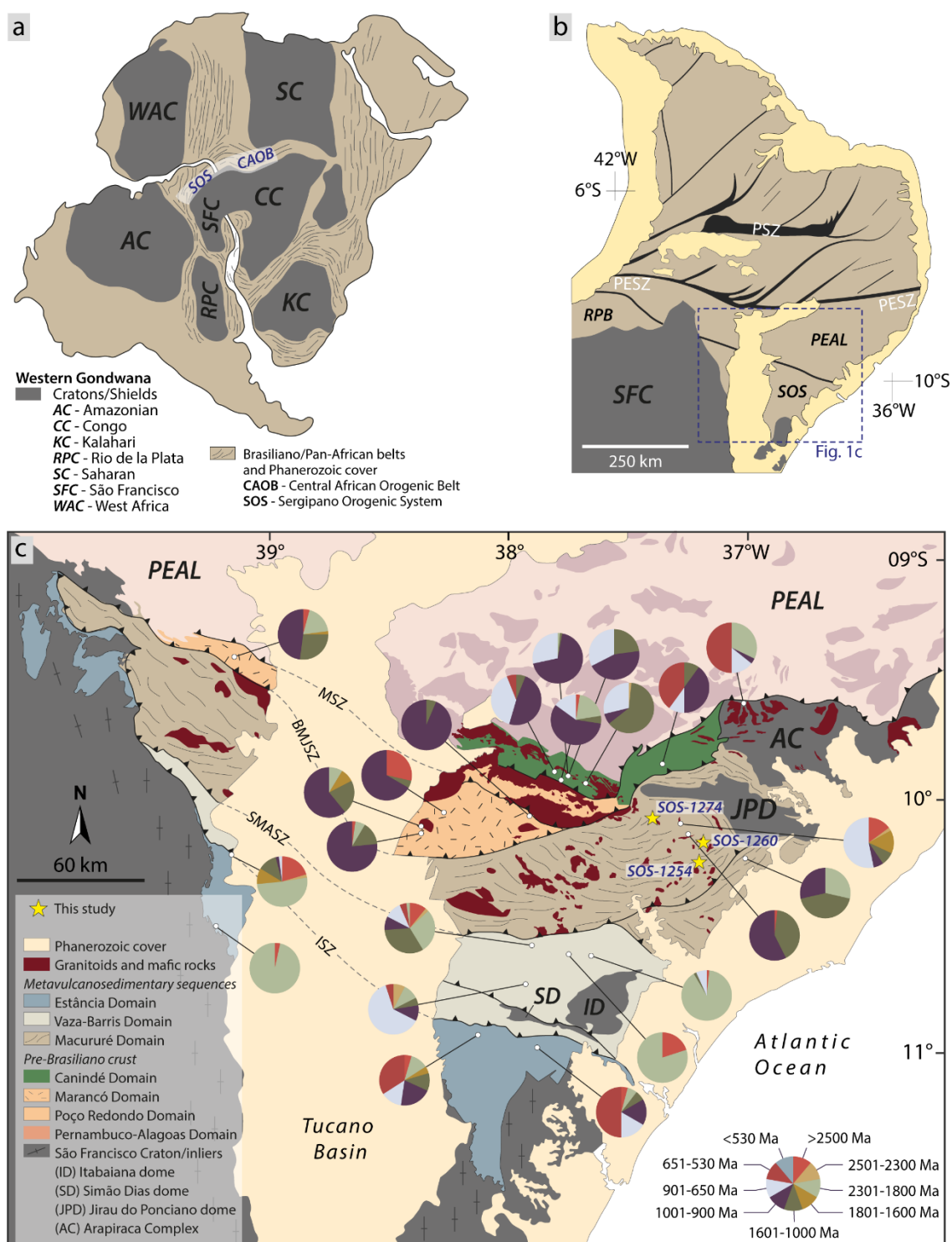


Figure IV.1- Geological background of the study area. (a) South America-Africa connection along the western margin of the Gondwana supercontinent with the position of the main cratonic blocks. The outlined area corresponds to the extent of the Sergipano and Central Africa orogenic belts. (b) Division of the Borborema Province in northern, central, and southern subprovinces, bounded by the Patos (PSZ) and Pernambuco (PESZ) shear zone systems (Van Schmus et al., 2011, 2008). PEAL = Pernambuco-Alagoas Domain, RPB = Riacho do Pontal Belt. (c) Tectonic compartmentalization of the SOS (Davison and Santos, 1989). The Itaporanga (ISZ), São Miguel do Aleixo (SMASZ), Belo Monte-Jeremoabo (BMJSZ), and Macururé (MSZ) shear zones mark the limits between the domains. Pie plots represent the location and age distribution of detrital zircon from metasedimentary samples.

2.2 SERGIPANO OROGENIC SYSTEM

The SOS has a triangular shape and stands between the PEAL and SFC, corresponding to the western sector CAOB in pre-drift reconstructions (Castaing et al., 1994; Caxito et al., 2020a). This orogen was formed by the amalgamation of different units with ages ranging from Rhyacian to late Ediacaran during the closure of a basin along the northern margin of the São Francisco Craton (Oliveira et al., 2010; Pereira et al., 2023).

Davison and Santos (1989) recognized six domains in the SOS, namely from north to south: Canindé, Poço Redondo, Marancó, Macururé, Vaza Barris, and Estância (Fig. 1c). The Macururé, Belo Monte-Jeremoabo, São Miguel do Aleixo, and Itaporanga shear zones separate these domains. The Estância, Vaza Barris, and Macururé domains comprise cratonic to distal deposits interpreted as ancient passive margins (D'el-Rey Silva, 1999). In contrast, the northernmost Marancó, Poço Redondo, and Canindé are allochthonous domains accreted to the north margin of the São Francisco paleoplate and deformed during the Neoproterozoic Brasiliano/Pan-African Orogeny (Carvalho, 2005; Oliveira et al., 2010). Toward the north from the São Miguel do Aleixo shear zone, a voluminous plutonism that records different stages of the Brasiliano Orogeny intruded the SOS crust, showing crystallization ages between 643 and 603 Ma (Oliveira et al., 2015a; Pereira et al., 2023, 2020).

Structural windows of the Archean-Paleoproterozoic basement have been identified within the metavolcanic-sedimentary succession of the Vaza Barris and Macururé domains. The Mesoarchean crystalline cores of Simão Dias and Itabaiana domes provide crystallization ages between 2.86 and 2.83 Ga (Oliveira, 2012; Rosa et al., 2020). The Paleoproterozoic basement units are exposed in the Rhyacian-Orosirian Jirau do Ponciano Dome and Arapiraca Complex (Lima et al., 2019; Tesser et al., 2021). Tesser et al. (2021) interpreted the Arapiraca Complex as a continental fragment pulled away from the São Francisco-Congo paleocontinent during the Neoproterozoic.

A brief description of each domain composing the SOS is presented below, summarizing the available detrital zircon geochronological data for the metasedimentary successions (Table 1). A simplified stratigraphy is shown in Figure 2.

2.2.1 Canindé Domain

The Canindé Domain is made up of the (i) basement slices formed during the Cariris Velhos event at 1006-989 Ma (Passos et al., 2022); (ii) Canindé Complex, which includes the metavolcano-sedimentary rocks of the Novo Gosto unit and the bimodal association of the

Gentileza unit. Novo Gosto amphibolites and Gentileza metavolcanic rocks produce U-Pb zircon concordia ages of 743 ± 3 and 701 ± 5 Ma, respectively (Passos et al., 2022, 2021); (iii) Canindé layered gabbroic complex build-up between 719-704 Ma (Passos et al., 2022; Pinto et al., 2020); and (iv) Brasileiro diorites, granodiorites, and granites, crosscutting the older units with crystallization ages from 640 to 611 Ma (Oliveira et al., 2015a; Santos, 2016; Soares et al., 2019).

Tonian detrital zircon grains dominate the age distribution of the Novo Gosto unit, with less expressive Rhyacian to Cryogenian contributions (Oliveira et al., 2015b; Passos et al., 2022). The youngest detrital zircon displays an age of 625 Ma, suggesting that sedimentation may have occurred synchronously with the early stages of the Brasileiro Orogeny.

Table VI.1- Summary of available detrital U-Pb zircon data for the SOS.

Sample	Unit	Lithology	Concordant ^a / analyzed grains	YSG ^b (Ma)	Reference ^c
Canindé Domain					
FS-136	Novo Gosto	Metagrewacke	33/34	625 ± 4	[1]
AC05	Araticum Complex	Schist	20/29	603 ± 14	[2]
DDLH-9A	Novo Gosto	Quartzite	63/90	808 ± 9	[3]
DDLH-9B	Novo Gosto	Quartzite	83/90	665 ± 8	[3]
DDLH-11A	Novo Gosto	Phyllite	79/100	804 ± 9	[3]
DDLH-15A	Novo Gosto	Paragneiss	58/61	666 ± 7	[3]
Marancó Domain					
MMC-311	Minuim	Quartzite	47/47	914 ± 8	[1]
MMC-332	Morro Bugi	Metaconglomerate	21/22	954 ± 16	[1]
MMC-19.2	Belém	Quartzite	47/48	936 ± 10	[1]
MMC-328-A	Belém	Metaconglomerate	23/24	948 ± 12	[1]
Macururé Domain					
BR92-09	Undivided	Metaturbidite	54/68	923 ± 11	[4]
FS-89	Undivided	Quartzite	48/49	930 ± 5	[1]
FS-68	Undivided	Garnet mica schist	47/49	910 ± 10	[1]
MAC-02	Undivided	Quartzite	28/41	936 ± 18	[5]
Vaza Barris Domain					
FS-118	Frei Paulo Fm.	Metarenite	46/46	615 ± 4	[1]
FS-104	Ribeirópolis Fm.	Metarenite	59/59	789 ± 5	[1]
FS-113	Itabaiana Fm.	Quartzite	25/25	1965 ± 13	[1]
FS-123	Palestina Fm.	Metadiamictite	40/40	615 ± 3	[1]
FS-166	Rosário Fm.	Metadiamictite	49/50	875 ± 10	[1]
Estância Domain					
FS-95	Palmares Fm.	Sandstone	44/44	575 ± 8	[1]
FS-F	Lagarto Fm.	Sandstone	48/49	550 ± 3	[1]
JP-159	Juetê Fm.	Diamictite	29/33	2072 ± 9	[1]
Arapiraca Complex					
BC-10	Undivided	Pelitic mesosome	28/35	603 ± 3	[6]
Jirau do Ponciano Dome					
NCG35	Nicolau-Campo Grande Complex	Paragneiss	41/41	2028 ± 60	[7]

^a Considering a 90-110% concordance cutoff.

^b Youngest single grain with Th/U ratio > 0.1.

^c [1] Oliveira et al. (2015b), [2] Lima et al. (2018), [3] Passos et al. (2022), [4] Van Schmus et al. (2011), and [5] Neves et al. (2019), [6] Lima et al. (2019), [7] Neves et al. (2016).

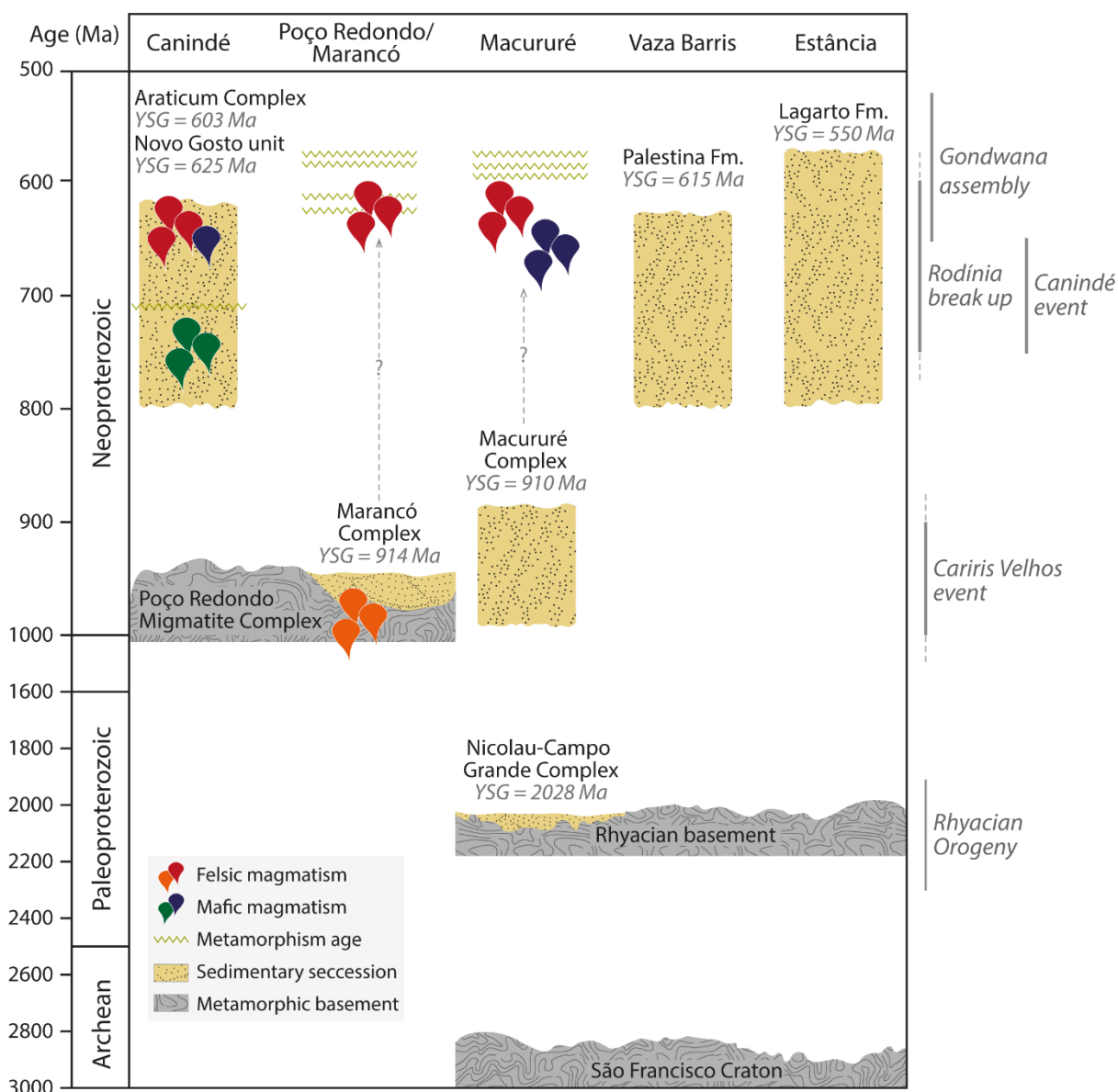


Figure IV.2- Simplified stratigraphy of the SOS based on available geochronological data for igneous and metasedimentary rocks (Carvalho, 2005; Lima et al., 2019, 2018; Oliveira, 2012; Oliveira et al., 2015a; Passos et al., 2022, 2021; Pereira et al., 2023; Rosa et al., 2020; Tesser et al., 2021). The maximum depositional age of a particular domain is assumed to be that of its younger metasedimentary unit. Values are shown as in the original works listed in Table 1. Metamorphic ages are from Oliveira et al. (2010) and Passos et al. (2022).

2.2.2 Poço Redondo and Marancó domains

The Marancó and Poço Redondo domains compose NE-SW trending crustal segments formed during the Cariris Velhos event. Carvalho (2005) and Oliveira et al. (2010) described occurrences of Tonian migmatites (980 ± 4 Ma) in the Poço Redondo Domain and A-type granitic orthogneiss (952 ± 2 Ma) in the Marancó Domain. Such ages overlap those obtained by Passos et al. (2022) for the crystallization of the protolith of orthogneisses (957 ± 12 Ma) and for an inherited zircon population (990 ± 7 Ma) from an intrusive granite in the Poço

Redondo Domain. The basement rocks of the Poço Redondo Domain units were intruded by Brasiliano granitoids at 636-617 Ma (Lima, 2016; Oliveira et al., 2015a; Passos et al., 2022). Quartzite and meta-conglomerate samples from the Marancó Domain yielded an almost unimodal distribution of detrital zircon data at 1000-980 Ma, indicating massive erosion of Cariris Velhos-like source areas (Oliveira et al., 2015b).

2.2.3 Macururé Domain

The Macururé Domain stretches 350 km from eastern Sergipe and northern Bahia, divided into two segments by the Phanerozoic Tucano basin. It is constituted of the supracrustal sequence of the Macururé Complex, metamorphosed in greenschist to amphibolite facies, and an intrusive suite ranging from mafic-ultramafic to granitic rocks (643-603 Ma; Oliveira et al., 2015a; Pereira et al., 2023, 2020).

The Macururé Complex comprises a basal quartzite layer, the Santa Cruz Formation, which defines topographic highs surrounding the Jirau do Ponciano Dome (Silva Filho et al., 1979). Other expressive exposures of quartzites occur in the Nossa Senhora de Lourdes and Porto da Folha areas. This unit is overlaid by a thick package of garnet-bearing micaschists, phyllites, metasandstones, and metagraywackes, intercalated with thin levels of acid metavolcanics, amphibolite, quartzite, marble, and calc-silicate rocks (Oliveira et al., 2010; Santos et al., 1998). U-Pb detrital zircon data of four samples reveal a heterogeneous provenance dominated by Rhyacian and Tonian contributions (Neves et al., 2019; Oliveira et al., 2015b; Van Schmus et al., 2011). The absence of zircon grains younger than 900 Ma suggests a pre-Brasiliano deposition for this sedimentary succession (Oliveira et al., 2015b).

2.2.4 Vaza Barris Domain

The Vaza Barris Domain encompasses a low-grade psammo-pelitic and carbonate series (Davison and Santos, 1989). Following Oliveira et al. (2010), the basal Miaba Group consists of conglomerates and quartzites of the Itabaiana Formation, followed by metagraywackes, phyllites, and chlorite schists of the Ribeirópolis Formation, capped by the carbonates of the Jacoca Formation. The overlying Vaza Barris Group comprises metasandstones and phyllites of the Frei Paulo Formation, succeeded by diamictites and phyllites of the Palestina Formation and carbonates of the Olhos D'Água Formation. Detrital U-Pb zircon data reveals distinctive contributions from base to top. The lowermost units of the Miaba Group have a predominance

of Rhyacian ages. In contrast, Tonian and Cryogenian ages become more common toward the top (Oliveira et al., 2015b).

2.2.5 Estância Domain

The Estância Domain is the least deformed of the SOS and rests unconformably on the São Francisco Craton (Davison and Santos, 1989). According to Oliveira et al. (2010), it contains, from base to top: (i) conglomerate, argillites, sandstones, and diamictites of the Juetê Formation, (ii) carbonates and shales of the Acauã Formation, (iii) fine clastic and red shales of the Lagarto Formation, and (iv) graywackes to conglomerates of the Palmares Formation. A diamictite sample from the Juetê Formation provided homogenous Rhyacian zircon ages, whereas detritus for the uppermost Lagarto and Palmares formations were mainly derived from Ediacaran and Tonian sources (Oliveira et al., 2015b).

3 ANALYTICAL APPROACH

3.1 WHOLE-ROCK GEOCHEMISTRY

The major element composition of nineteen samples was measured from pressed pellets by X-ray spectrometry fluorescence (XRF) using a Shimadzu XRF-1800 installed at the Condomínio de Laboratórios das Geociências of the Universidade Federal de Sergipe (CLGeo-UFS). The samples were mechanically crushed and milled to a granulometric fraction below 100 mesh. The mixture of approximately 2.5 g of sample powder and 0.8 g of boric acid (H_3BO_3) was homogenized, deposited in steel disks, and compacted in a hydraulic press. Calibration curves for the used XRF incorporate 20 geochemical reference materials comprising a wide range of rock types. The quality control was monitored by analyzing duplicate samples and reference materials different from those applied to calibration curve construction. The precision was better than 1.2% for all analyzed oxides except for P_2O_5 , which provided a precision estimate of around 2.6%. Loss of mass on ignition (LOI) was determined from previously dried sample powder ($\sim 120^\circ\text{C}$) by calcination in a muffle furnace at 1000°C for 2 h.

In addition, the analysis of 10 metasedimentary rocks was performed by inductively coupled plasma-mass spectrometry at SGS GEOSOL Laboratory, Belo Horizonte, Brazil. The analytical procedures encompassed sodium peroxide fusion before elemental measuring. More details about analytical methods can be accessed at <https://www.sgsgroup.com.br/>.

All oxides were recalculated to a 100% sum on a volatile-free basis for comparative purposes. Geochemical data treatment and diagram elaboration were carried out using the Geochemical Data Toolkit – GCDkit (Janoušek et al., 2006). Major and trace element results are given in Supplementary Table S1.

3.2 ZIRCON U-Pb DATING

Zircon grains were separated from around 5 kg of three samples of quartzite collected from fresh outcrops of the Macururé Complex. Concentration techniques involved the crushing, grinding, and water sieving of the granulometric fraction between 250 and 75 μm . Heavy minerals aliquot was concentrated using a gold pan repeated times. Magnetic and non-magnetic fractions were separated using a neodymium magnet and an isodynamic separator Frantz. Approximately 300 grains hand-picked in each sample were mounted in 25 mm epoxy discs. The mounts were polished and coated with gold to investigate the internal structures of zircon grains.

Cathodoluminescence (CL) images of two samples were obtained using a scanning electron microscope (SEM) Tescan LMU model Vega3 at the CLGeo-UFS. The operating conditions were an acceleration voltage of 20 kV, a beam current between 10-20 nA, and an electron beam diameter varying from 0.4-1.0 μm . Zircon grains from the third sample were imaged by an SEM Zeiss EVO LS-15 installed at the Geological Survey of Brazil, Pará, Belém. Analyses applied a voltage of 15 kV and a beam current of 10 nA in a work distance of 12 mm. Investigation of internal structures employed the classification of Corfu (2003).

Zircon U-Pb dating was performed using an iCAP-Q single quadrupole inductively coupled plasma mass spectrometer associated with a laser ablation system Nd:YAG LSX-213 G2 CETAC (LA-Q-ICP-MS) at the Laboratório de Geologia Isotópica of the Universidade Federal do Pará (Pará-Iso/UFPa), Belém, Brazil. The signal of the masses $^{204}\text{(Pb + Hg)}$, ^{206}Pb , ^{207}Pb , ^{208}Pb , ^{238}U , and ^{232}Th were measured during the analyses. ^{235}U signal was calculated assuming $^{238}\text{U}/^{235}\text{U} = 138.77$. Isotope data were acquired during 40 s zircon ablation after 20 s background measurement. Laser beam parameters were 25 μm spot size, 10 Hz frequency, and 4 J/cm^2 fluency. Time-resolved raw data were corrected offline for background signal and common Pb using an in-house Excel spreadsheet modified by Milhomem Neto and Lafon (2019). Common ^{206}Pb estimation applied the Hg-corrected measurement of ^{204}Pb for each spot, using the lead composition predicted by Stacey and Kramers (1975). Laser-induced elemental fractionation and instrumental mass discrimination were corrected by normalizing relative to

the reference zircon GJ-1 (608.5 ± 1.5 Ma; Jackson et al., 2004). Blue Berry (560.0 ± 0.4 Ma; Santos et al., 2017) and 91500 (1065.4 ± 0.3 Ma; Wiedenbeck et al., 1995) reference zircons were used as secondary standards to monitor the reliability and reproducibility of the method.

All quoted uncertainties are reported at 1σ level (Supplementary Table S2). Decay constants are those recommended by Steiger and Jäger (1977). The age calculations and graphic representation of the U-Pb data were made using the IsoplotR (Vermeesch, 2018) and detzrcr R-package (Andersen et al., 2018b), with error ellipses reflecting 2σ uncertainty.

The concordance of isotopic ages was determined considering the $^{206}\text{Pb}/^{238}\text{U}$ and $^{207}\text{Pb}/^{206}\text{Pb}$ dates (Spencer et al., 2016). Dates with a discordance degree above $\pm 10\%$ have been excluded from interpretations. The $^{206}\text{Pb}/^{238}\text{U}$ date has been assumed for grains younger than 1.5 Ga, whereas the $^{207}\text{Pb}/^{206}\text{Pb}$ date was used for grains older than 1.5 Ga (Spencer et al., 2016). Dated zircon grains were split into eight age groups: Archean (>2500 Ma), early Paleoproterozoic (2500-2301 Ma), middle Paleoproterozoic (2300-1801 Ma) corresponding to the Rhyacian-Orosirian Orogeny, late Paleoproterozoic (1800-1601 Ma), Mesoproterozoic (1600-1001 Ma), early Neoproterozoic (1000-901 Ma) corresponding to the Cariris Velhos event in the Borborema Province, middle Neoproterozoic (900-651 Ma), late Neoproterozoic to early Cambrian (650-530 Ma), corresponding to the Brasiliano/Pan-African Orogeny.

3.3 LA-ICP-MS ZIRCON Lu-Hf ISOTOPE ANALYSES

Zircon Lu-Hf analyses were carried out in the grains previously dated for U-Pb in the same domain where the age was determined. Only the grains with concordant and subconcordant ages within 10% discordance were analyzed for Lu-Hf if their sizes were sufficient. Isotope data were measured with a Thermo Finnigan Neptune multi-collector inductively coupled plasma mass spectrometer coupled with a Photon-Machines 193 nm ArF Excimer laser ablation system (LA-MC-ICP-MS) at Pará-Iso/UFPA, following the modified protocols of Milhomem Neto and Lafon (2019).

Data were obtained in static mode during 50 s of ablation, with a spot size of 40 μm . During data collection, the isotopes of Lu, Hf, and Yb were monitored concomitantly. Isotope ratios of Yb and Hf were normalized by assuming the values of $^{173}\text{Yb}/^{171}\text{Yb} = 1.12346$ (Thirlwall and Anczkiewicz, 2004) and $^{179}\text{Hf}/^{177}\text{Hf} = 0.7325$ (Patchett and Tatsumoto, 1981), according to the exponential law. Isobaric corrections were performed using the natural abundances of ^{175}Lu ($^{176}\text{Lu}/^{175}\text{Lu} = 0.02659$; Chu et al., 2002) and ^{173}Yb ($^{176}\text{Yb}/^{173}\text{Yb} = 0.786956$; Thirlwall and Anczkiewicz, 2004). $^{176}\text{Hf}/^{177}\text{Hf}$ ratios of unknown grains were

normalized to the average values obtained for the Mud Tank reference zircon and their certified ratios (Morel et al., 2008). The Blue Berry (Santos et al., 2017), 91500 (Woodhead and Hergt, 2005), and GJ-1 (Morel et al., 2008) reference zircons were employed as secondary standards to monitor the external reproducibility of the method. All Lu-Hf isotope data are listed in Supplementary Table S3.

Isotope ratios calculations back to crystallization age used the decay constant $^{176}\text{Lu} = 1.867 \times 10^{-11} \text{ years}^{-1}$ (Söderlund et al., 2004). Present-day values for the chondritic uniform reservoir (CHUR; Bouvier et al., 2008) were employed to calculate the epsilon hafnium parameter (ϵHf). Two-stage depleted mantle model ages ($\text{Hf-T}_{\text{DM}}^{\text{C}}$) are calculated using the values for depleted mantle (DM) of Andersen et al. (2009), assuming a $^{176}\text{Lu}/^{177}\text{Hf}$ ratio of 0.015 as a continental crust average (Griffin et al., 2004, 2002).

4 GEOLOGICAL CONTEXT OF THE STUDY AREA

The study area is located in the eastern portion of the SOS, Sergipe state. In this sector, garnet-bearing muscovite-chlorite-biotite phyllites and metarythmites predominate, with minor occurrences of metagraywackes and metacarbonate rocks. Centimeter-thick calc-silicate levels typically contain plagioclase, amphibole, epidote, and quartz. Near intrusions, the calc-silicate rocks and metapelite hosts give place to a more massive structure and porphyroblastic texture, marked by the development of large crystals of amphibole and garnet.

The **phyllites** are gray, brown, or reddish and have a lustrous appearance (Fig. 3a). They comprise idioblastic garnet phenoblasts with 0.2 to 0.5 mm in size. Reddish brown biotite crystals (~0.5 mm), partially transformed to chlorite, define the rock foliation. The matrix consists of very fine-grained (<0.01 mm) quartz, plagioclase, and microcline. Muscovite and chlorite occur associated with the matrix, oriented along the schistosity. Opaque mineral and green tourmaline prisms occur as accessory phases disseminated in the rock. Garnet-bearing micaschists show the same mineral assemblage of the phyllites, differing by the coarser granulation (Fig. 3b).

The **metarythmites** are characterized by a bimodal alternation of millimeter-thick layers of metapelite and metapsammite (Fig. 3c). The latter comprises very fine-grained quartz and feldspar in a matrix containing abundant muscovite, chlorite, and minor biotite. The metapelite layers are essentially composed of brown biotite and muscovite with disseminated rare detrital grains. The preferred alignment of mica blasts defines a slaty cleavage. Opaque minerals are the accessories.

The **metagraywackes** (Fig. 3d) comprise poorly sorted quartz grains and subordinate feldspar, with varying granulation from very fine to very coarse, predominating those with 0.3 mm. They are immersed in a recrystallized quartz-felspathic matrix with chlorite, muscovite, and biotite. Rare tiny grains of green tourmaline, zircon, and rutile are disseminated. Some samples contain carbonate and secondary opaque minerals associated with the matrix.

Metacarbonate rocks correspond to light- to medium-gray marls, with centimeter-thick intercalations of dark-gray impure carbonates. Metamarls are composed of fine-grained muscovite and chlorite (~0.2 mm), strongly oriented, between a polygonal calcite mosaic and quartz. Rare opaque minerals follow the mica orientation. Calcite veinlets are injected along the foliation. Impure metalimestones have very fine granulation (<0.1 mm) and consist of a polygonal mosaic of calcite, with interstices occupied by muscovite, quartz, and feldspar.

Quartzites are light gray to yellowish and medium-grained (Fig. 3e and 3f). They consist of quartz, muscovite, and feldspar. Minor amounts of opaque minerals and biotite are associated with muscovite, which defines a spaced anastomosing foliation. Fine-grained muscovite blasts are hypidiomorphic, anastomosing around porphyroclasts of plagioclase and microcline, which are widely altered into sericite. Quartz grains are xenoblastic and inequigranular. The larger grains have patchy undulose extinction and deformation lamellae, with grain boundaries interlobate and ameboid. Aggregates of fine-grained recrystallized grains surround these grain boundaries. Such features indicate that dynamic recrystallization of quartz occurred by bulging and subgrain rotation, implying low to moderate temperatures (Passchier and Trouw, 2005).

Table IV.1- Petrographic aspects of the metasedimentary rocks from the Macururé Complex. Mineral abbreviation names follow the recommendation of Warr (2021).

Rock group	Texture	Mineral assembly	
		Major	Accessory
Phyllite/Schist	Lepidoblastic, porphyroblastic	Qz + Pl + Ms + Bt + Chl + Grt ± Opq	Tur ± Opq
Metarythmite	Lepidoblastic, porphyroblastic	Ms + Chl + Bt + Qz + Fsp + Grt + Opq	Zrn ± Opq
Metagraywacke	Porphyroclastic	Qz + Pl + Afs + Ms + Chl ± Opq ± Cal	Rt + Zrn ± Tur
Carbonate	Granoblastic, lepidoblastic	Cal + Ms + Chl + Qz + Afs + Pl + Opq	Zrn ± Opq
Quartzite	Granoblastic, porphyroclastic, lepidoblastic	Qz + Pl + Afs + Ms	Bt + Chl ± Ap ± Rt ± Zrn

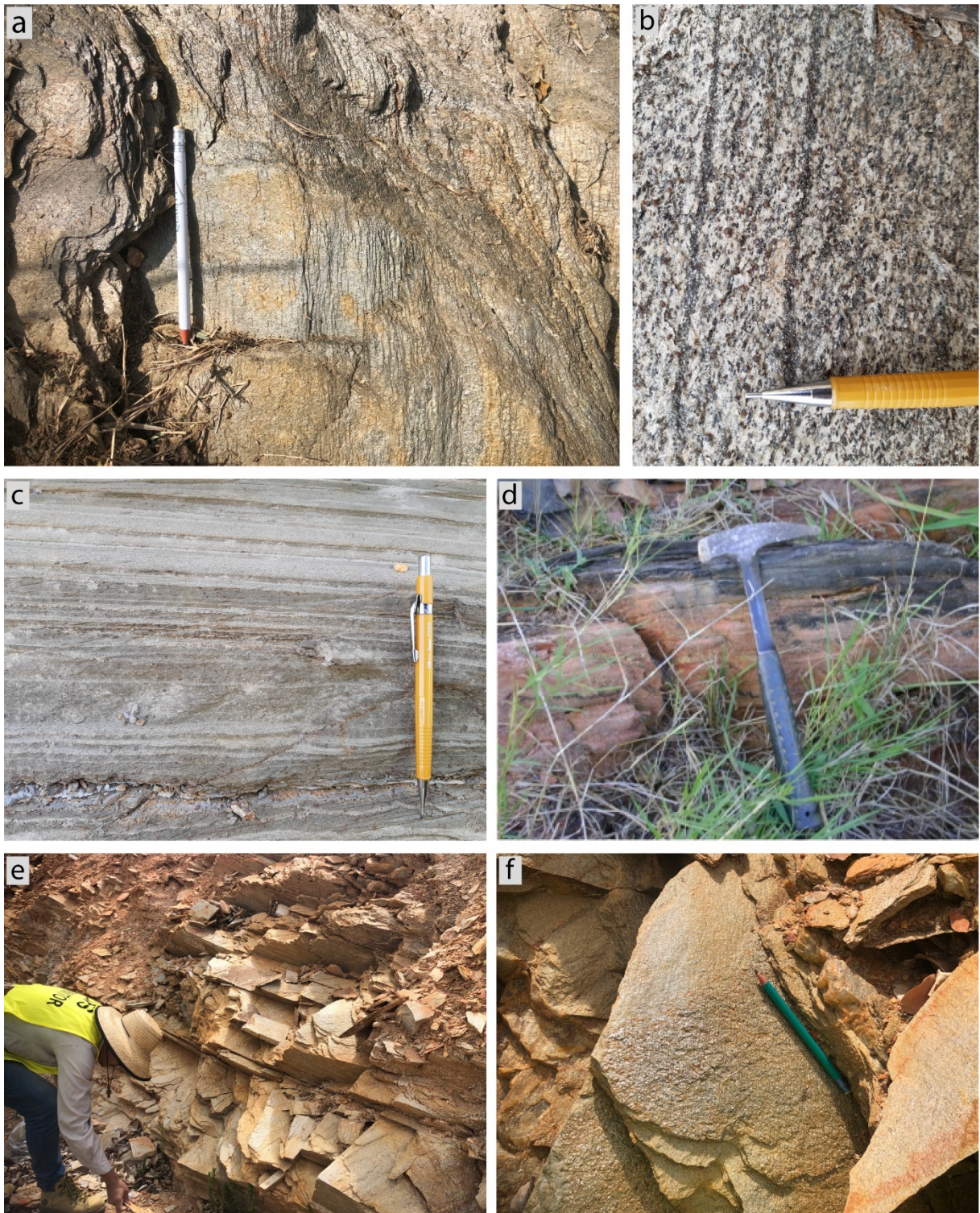


Figure IV.3- Rocks of the study area. (a) Lustrous appearance of phyllites, with a well-developed foliation defined by muscovite, chlorite, and biotite orientation. (b) Schist with porphyroblasts of garnet and biotite. (c) Alternating fine-grained arenite (light gray) and siltite (dark gray) intercalations in metarythmite. Tinny black points in the siltite layers are oxidized garnet porphyroblasts. (d) Reddish metagraywacke. (e) Exposure of quartzite on the road to Escorial village. (f) A detailed view of the sample in (e) shows the high concentration of muscovite along foliation planes, giving quartzite a golden aspect.

5 MAJOR AND TRACE ELEMENTS

Whole-rock geochemical data for phyllites, schists, and graywackes show variable contents of SiO₂ (55.00-77.11 wt.%), TiO₂ (0.57-1.16 wt.%), Al₂O₃ (10.68-22.62 wt.%), Fe₂O₃ (4.34-12.95 wt.%), MgO (0.45-5.51 wt.%), CaO (0.07-7.21 wt.%), Na₂O (0.98-3.52 wt.%), K₂O (1.47-4.95 wt.%), and P₂O₅ (0.02-0.28 wt.%). Compared to the upper continental crust (UCC; Rudnick and Gao, 2003), metapelites show most values close to unity. Based on major elements, the protolith of these samples can be classified as shale and wacke (Herron, 1988).

Quartzite samples differ from the others by the greater contents of SiO₂ (88.64-92.33 wt.%), moderate Al₂O₃ (4.76-7.00 wt.%), and K₂O (1.90-2.82 wt.%), along with very low TiO₂ (<0.14 wt.%), Fe₂O₃* (<1.17 wt.%), MgO (<0.11 wt.%), CaO (<0.01), Na₂O (<0.55 wt.%), and P₂O₅ (<0.01 %). Regarding major elements, quartzites lie in the field of the subarkose (Fig. 4a; Herron, 1988).

In Harker diagrams (Fig. 5), there are strong negative correlations of SiO₂ with TiO₂ ($r = -0.91$), Al₂O₃ ($r = -0.95$), Fe₂O₃* ($r = 0.91$), and MgO ($r = -0.77$), and less expressive against K₂O ($r = -0.57$), Na₂O ($r = -0.46$), and CaO ($r = -0.38$).

The abundance of rare earth elements (REE) ranges from 89 to 305 ppm, with an average value of ~128 ppm, lower than the Post-Archean Australian Shale (PAAS = 184.8 ppm; Taylor and McLennan, 1985). Relative to the chondrites (McDonough and Sun, 1995), the analyzed rocks have about 100 times the light REE (LREE) and 10 times the heavy REE (HREE), yielding La/Yb_{CN} ratios between 3.6 and 13.4 (Fig. 4b), where the subscript "CN" means chondrite-normalized. The fractionation degree is moderate among LREE (La/Sm_{CN} = 2.5-4.1), and HREE patterns are flat with Gd/Yb_{CN} in the range of 0.9-2.3. They also have pronounced negative Eu anomalies (Eu/Eu* = 0.42-0.77) and almost absent Ce anomalies (Ce/Ce* = 0.86-1.10). All features are essentially identical to typical PAAS.

The UCC-normalized plot for incompatible elements is shown in Fig. 4c. Despite the highly variable concentration of trace elements, the patterns are arranged close to unity, with deep troughs for Sr and P. Average composition for large ion lithophile elements (LILE), high-field strength elements (HFSE), and compatible elements is depleted relatively to PAAS.

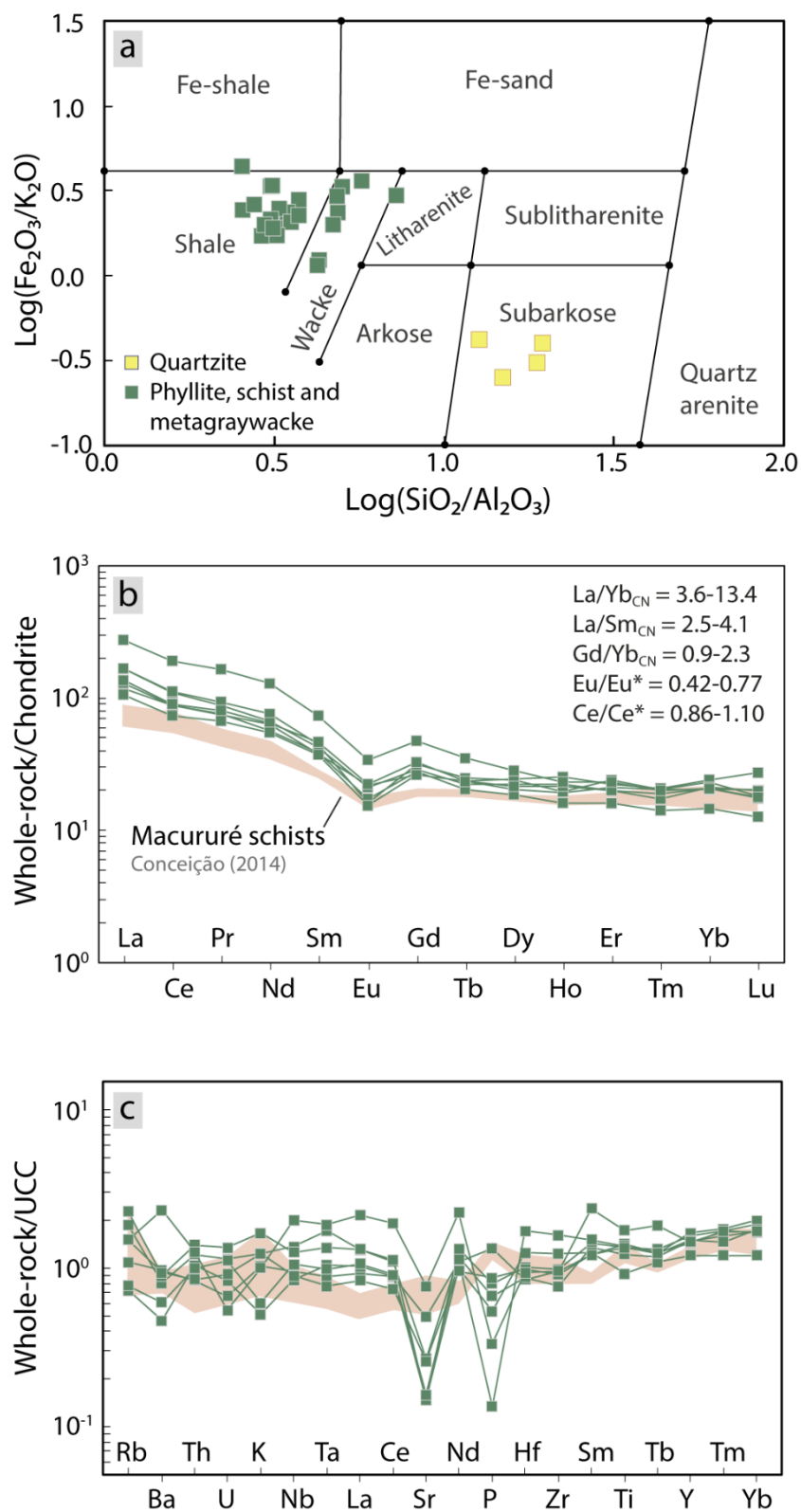


Figure IV.4- Whole-rock geochemical data for paraderived metamorphic rocks of the Macururé Domain. (a) $\text{Log}(\text{SiO}_2/\text{Al}_2\text{O}_3)$ vs. $\text{log}(\text{Fe}_2\text{O}_3/\text{K}_2\text{O})$ after Herron (1988). REE and multi-element patterns normalized to the chondrite (McDonough and Sun, 1995) and upper continental crust (UCC; Rudnick and Gao, 2003). The composition of Macururé schists (Conceição, 2014) is displayed for comparison.

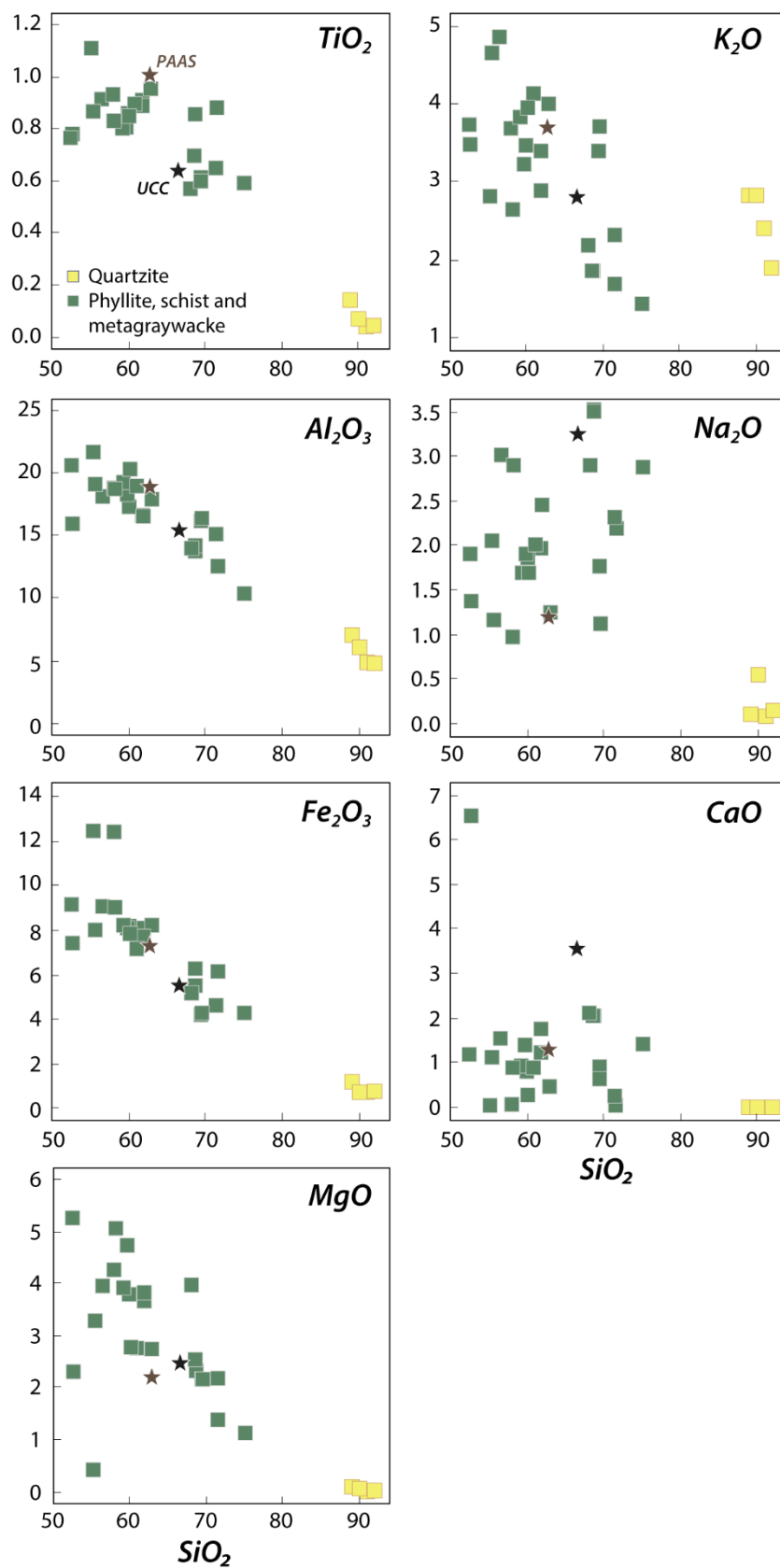


Figure IV.5- Harker diagrams for selected major oxides (wt.%) from the metasedimentary rocks of the Macururé Complex. PAAS = Post Archean Australian Shale (Taylor and McLennan, 1985), UCC = Upper Continental Crust (Rudnick and Gao, 2003).

6 U-Pb AND Lu-Hf DETRITAL ZIRCON GEOCHRONOLOGY

A total of 370 detrital zircon grains were analyzed in three samples of micaceous quartzites from the Macururé Complex, but only a subset of 247 grains showed less than 10% discordance. Among these, 113 had their Lu-Hf isotope composition determined. A synthesis of the U-Pb and Lu-Hf results are presented in Table 2 and 3.

2.1 SAMPLE SOS-1254

Sample SOS-1254 is a muscovite quartzite cropping out as a 50 cm-thick layer intercalated with garnet-bearing biotite-muscovite phyllites near the external ring of the Nossa Senhora de Lourdes interference structure (Fig. 1c).

Zircon grains are colorless, pale pink or light gray, translucent, and rarely limpid. Their sizes range from 310 to 80 μm . Most are rounded to subrounded, with length/width ratios between 1:1 and 3:1. Only rare grains preserve a prismatic shape.

From 120 analyzed grains, 80 yielded concordant results within 10% (Fig. 6a). They are mainly anhedral to subhedral with regular broad or fine oscillatory zoning (50%). Remaining crystals are homogeneous (14%) in CL images or reveal complex internal structures, dominated by irregular diffuse (11%) and concentric (8%) patterns, chaotic (6%), convolute (5%), patchy (5%), and sectorial (1%) zoning. Th/U ratios vary from 3.17 to 0.24.

Ages range from the Siderian to Tonian (Fig. 6b), with the youngest single grain yielding 808 ± 13 Ma. The Kernel density estimate (KDE) plot for the concordant and subconcordant populations shows almost bimodal age distribution with prominent clusters in 2100-1900 Ma and 1200-800 Ma. Early Paleoproterozoic zircons make up 1% of the total. About 40% of the grains are in the Rhyacian-Orosirian age interval, with a peak at 2000 Ma. They show subchondritic initial $^{176}\text{Hf}/^{177}\text{Hf}$ ratios between 0.281075-0.281517, equivalent to $\varepsilon\text{Hf}_{(t)}$ values from -15.6 to -0.7, with Hf- T_{DM}^{C} model ages ranging from 3.5 to 2.6 Ga (Fig. 7).

The second cluster has a peak at ca. 950 Ma, encompassing grains of the Mesoproterozoic (20%), early Neoproterozoic (28%), and middle Neoproterozoic (11%) interval ages. Initial $^{176}\text{Hf}/^{177}\text{Hf}$ ratios of the Mesoproterozoic grains vary in the interval of 0.281949-0.282289, recording negative to positive $\varepsilon\text{Hf}_{(t)}$ values between -7.1 and +5.1, with Hf- T_{DM}^{C} model ages from 2.2 to 1.6 Ga. The early Neoproterozoic population has varying initial $^{176}\text{Hf}/^{177}\text{Hf}$ ratios (0.281851-0.282252), which correspond to sub- and suprachondritic $\varepsilon\text{Hf}_{(t)}$ values (-12.3 to +3.5). Hf- T_{DM}^{C} model ages range from 2.5 to 1.6 Ga. The youngest zircon

population registers unradiogenic initial $^{176}\text{Hf}/^{177}\text{Hf}$ ratios (0.281558-0.282069) and $\epsilon\text{Hf}(t)$ values from -24.7 to -6.0, with Hf- T_{DM}^{C} model ages from 3.2 to 2.1 Ga.

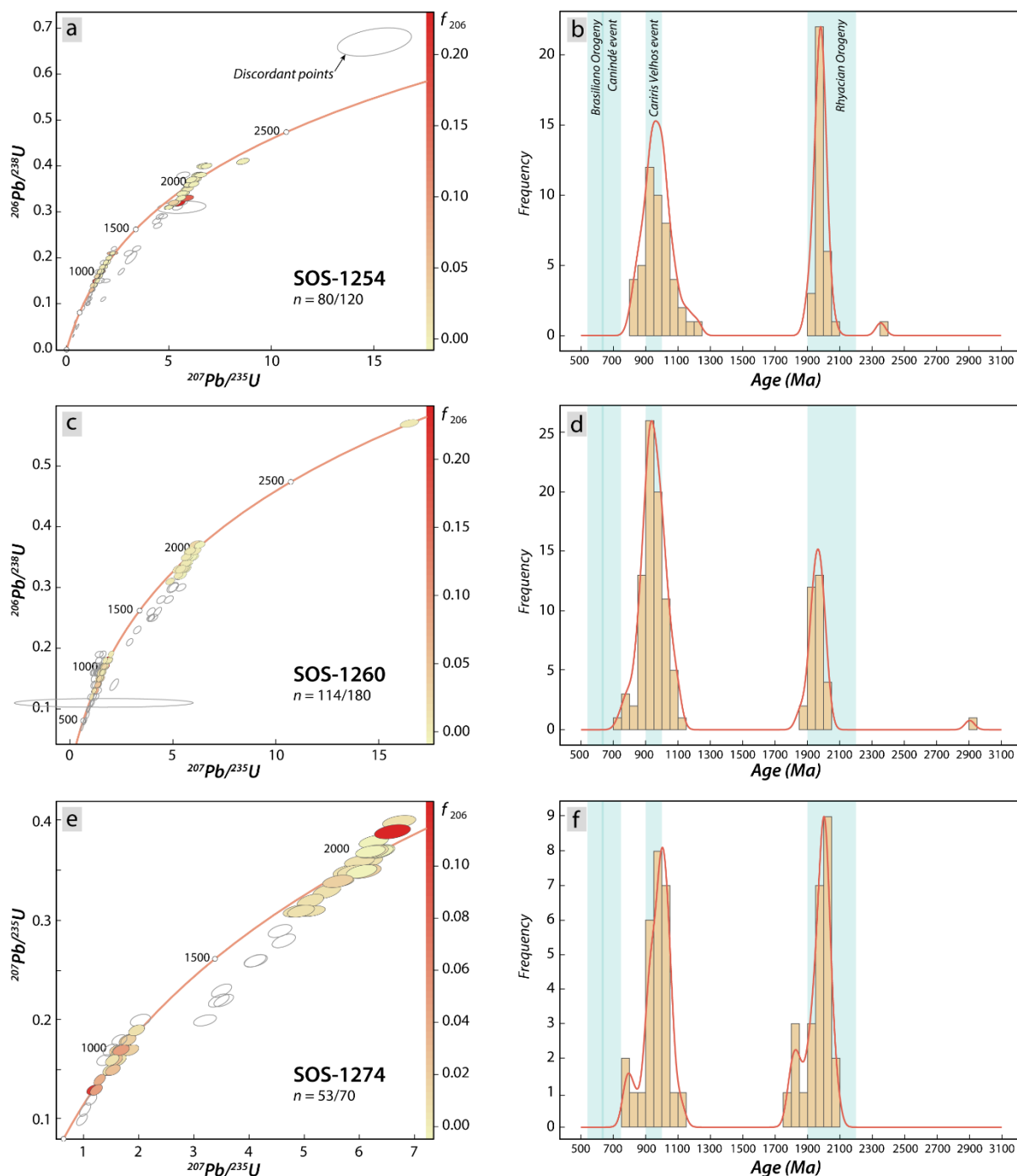


Figure IV.6- Concordia and KDE plots of the analyzed quartzites from the Macururé Complex. (a-b) Sample SOS-1254. (c-d) Sample SOS-1260. (e-f) Sample SOS-1274. Error ellipses in (a), (c), and (e) are shaded according to the proportion of common Pb of each analyzed spot, expressed in terms of absolute values of the parameter $f_{206} = (^{206}\text{Pb}/^{238}\text{U})_{\text{common}} / (^{206}\text{Pb}/^{238}\text{U})_{\text{sample}}$.

Table IV.2- Summary of U-Pb and Lu-Hf analyses on detrital zircon from quartzite samples of the Macururé Complex.

Sample ID	Coordinates ^a	Concordant ^{b/} analyzed grains		900-701 Ma	1000-901 Ma	1600-1001 Ma	1800-1601 Ma	2300-1801 Ma	2500-2301 Ma	> 2500 Ma
SOS-1254	718420/8879989	80/120	%	11.3	27.5	20.0	-	40.0	1.2	-
			$\epsilon\text{Hf}_{(t)}$	-24.7 to -6.0	-12.3 to +3.5	-7.1 to +5.1		-15.6 to -0.7		
			Hf-T _{DM} ^C (Ga)	3.2-2.1	2.5-1.6	2.2-1.5		3.5-2.6		
SOS-1260	720250/8889560	114/180	%	16.7	40.3	14.9	-	27.2	-	0.9
			$\epsilon\text{Hf}_{(t)}$	-5.2 to +3.3	-10.3 to +4.4	-8.9 to +8.4		-10.4 to 0		
			Hf-T _{DM} ^C (Ga)	1.9-1.5	2.4-1.5	2.4-1.3		3.1-2.5		
SOS-1274	693659/8901596	53/70	%	7.5	26.4	17.0	-	49.1	-	-
			$\epsilon\text{Hf}_{(t)}$	-2.3	-1.0 to +7.7	-10.0 to +2.7		-9.0 to +0.5		
			Hf-T _{DM} ^C (Ga)	1.8	1.8-1.3	2.4-1.7		3.1-2.5		

^a Universal Transverse Mercator coordinate system, South American 1969 datum, 24S zone.

^b 90-110% concordance.

(-) Not sampled age interval.

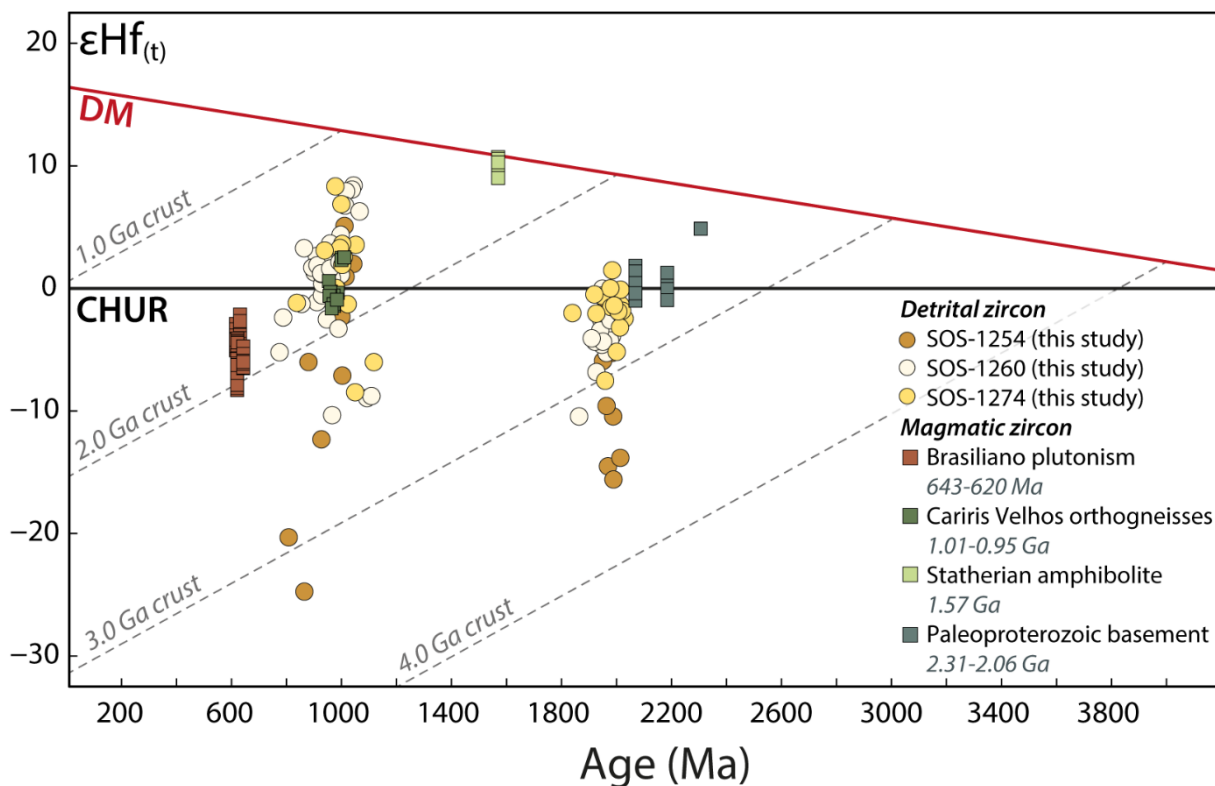


Figure IV.7- Lu-Hf isotope composition on detrital zircon from quartzite samples of the Macururé Complex, compared with zircon data of the main tectonic event recorded in the Borborema Province. Data source: Paleoproterozoic granitoids of the Troia Massif (Costa et al., 2018), amphibolite protoliths of the Forquilha eclogite zone (Amaral et al., 2015), Cariris Velhos orthogneisses of the Riacho do Pontal Belt (Caxito et al., 2020b), Brasiliano granitoids and mafic rocks of the Macururé Domain (Pereira et al., 2023).

6.2 SAMPLE SOS-1260

This sample is a mylonitic muscovite quartzite exposed in an operating quarry located in the external ring of the Nossa Senhora de Lourdes interference structure on the road to the Escurial village (Fig. 1c).

Zircon grains exhibit pale pink and light gray color. They are mostly clear and less commonly translucent or opaque, with sizes between 380 and 133 μm . The larger grains show subrounded shapes, with the original prismatic habit still recognizable. In contrast, the smaller ones are rounded and sub-spherical. Length/width ratios range from 3:1 to 1:1.

U-Pb zircon analyses performed on 180 detrital zircon grains returned 114 concordant ages (Fig. 6c). Zircon grains mostly display regular oscillatory zoning (63%). Homogeneous unzoned grains comprise 15% of the analyzed population, followed by more complex patterns of zonation, which represent 22% of the total (irregular concentric 8% and diffuse 5%, convolute 4%, sector 3%, chaotic, cross-bedding, and patchy ~2%). Despite the wide variation of internal structures, there are no significant variations of Th/U ratios among the zircon populations, ranging from 0.10 to 1.73.

Concordant and subconcordant U-Pb data spread from Mesoarchean to Cryogenian, with two significant clusters at 2100-1900 and 1150-700 Ma (Fig. 6d). The older group encloses 27% of the grains, which produce a peak at ca. 2000 Ma. Middle Paleoproterozoic aged grains yielded initial $^{176}\text{Hf}/^{177}\text{Hf}$ in the range of 0.281302-0.281541, corresponding to subchondritic to chondritic $\epsilon\text{Hf}(t)$ values from -10.4 to 0.0. Archean Hf- T_{DM}^{C} model ages vary from 3.1 to 2.5 Ga (Fig. 7).

The younger cluster peaks at ca. 940 Ma and represents 72% of the analyzed population, from which 15% is Mesoproterozoic, 40% is early Neoproterozoic, and 17% is middle Neoproterozoic. The Mesoproterozoic population displayed initial $^{176}\text{Hf}/^{177}\text{Hf}$ ratios of 0.281836-0.282366, consistent with negative to positive $\epsilon\text{Hf}(t)$ values between -8.9 and +8.4. Hf- T_{DM}^{C} model ages range from Siderian to Ectasian (2.4-1.3 Ga). Representative grains of the early Neoproterozoic age interval provided initial $^{176}\text{Hf}/^{177}\text{Hf}$ ratios between 0.281883-0.282285, equivalent to sub- and suprachondritic $\epsilon\text{Hf}(t)$ values ranging from -10.3 to +4.4. Hf- T_{DM}^{C} model ages vary from 2.4 to 1.3 Ga. The younger group encloses grains with initial $^{176}\text{Hf}/^{177}\text{Hf}$ ratios between 0.282150-0.282333. These values correspond to $\epsilon\text{Hf}(t)$ values from -5.2 to +3.3. Hf- T_{DM}^{C} model ages spread from late Orosirian to Calymmian (1.8-1.5 Ga). One zircon grain yielded an Archean $^{207}\text{Pb}/^{206}\text{Pb}$ age of 2904 ± 29 Ma. The youngest single grain provided an age of 739 ± 14 Ma.

6.3 SAMPLE SOS-1274

The sample SOS-1274 consists of a muscovite-bearing quartzite exposed on the road near the Iguaçu locality (Fig. 1c). This rock belongs to a thick quartzite package outcropping as hills between the cities of Gararu and Porto da Folha.

Detrital zircon grains are mostly clear and pale pink colored. Translucent and opaque brown grains are uncommon. They are prismatic to spherical, predominating those with subrounded shapes. Length/width ratios are between 4:1 and 1:1. Some grains contain inclusions of opaque minerals.

Seventy detrital zircon grains were dated in this sample, from which 53 were concordant (Fig. 6e). They are anhedral to subhedral. Internal structures under CL reveal the dominance of regular oscillatory zoning (37%) and homogeneous unzoned (30%). Grains showing irregular concentric (17%) and diffuse (9%), chaotic (4), convolute (2%), and sector patterns (1%) are less common. Th/U ratios range from 0.07 to 1.54.

A bimodal distribution characterizes this sample in a KDE plot (Fig. 6f). Almost half of the zircons (49%) show middle Paleoproterozoic ages, which define two peaks at ca. 2000 Ma and 1800 Ma. The initial $^{176}\text{Hf}/^{177}\text{Hf}$ ratios range is 0.281283-0.281533, corresponding to $\epsilon\text{Hf}_{(t)}$ values between -9.0 to +0.5, with $\text{Hf-T}_{\text{DM}}^{\text{C}}$ model ages from 3.1 to 2.5 Ga (Fig. 7).

Mesoproterozoic grains make up 17% of the analyzed concordant population. These grains show initial $^{176}\text{Hf}/^{177}\text{Hf}$ ratios between 0.282071-0.282196, equivalent to negative to positive $\epsilon\text{Hf}_{(t)}$ values from -10.0 to +2.7. $\text{Hf-T}_{\text{DM}}^{\text{C}}$ model ages range from 2.4 to 1.7 Ga.

The remaining 34% of detrital grains are clustered in the early (26%) and middle (8%) Neoproterozoic interval ages, marking a prominent peak at ca. 950 Ma and a subordinate at 750 Ma. Early Neoproterozoic aged zircons display initial $^{176}\text{Hf}/^{177}\text{Hf}$ ratios in the range of 0.282137-0.282385, which corresponds to subchondritic to suprachondritic $\epsilon\text{Hf}_{(t)}$ values between -1.0 and +7.7. $\text{Hf-T}_{\text{DM}}^{\text{C}}$ model ages oscillate from 1.8 to 1.3 Ga. One grain belonging to the middle Neoproterozoic cluster was analyzed for Lu-Hf, which provided a negative $\epsilon\text{Hf}_{(t)}$ value of -2.3 ($^{176}\text{Hf}/^{177}\text{Hf}_{(t)} = 0.282192$) and an Orosirian $\text{Hf-T}_{\text{DM}}^{\text{C}}$ model age of 1.8 Ga. The youngest single grain records an age of 782 ± 12 Ma.

3 PRELIMINARY DISCUSSION

A careful assessment of the internal structures of the dated grains demonstrates the dominance of regular concentric zoning, typical of magmatic zircon crystals (Corfu, 2003). The homogenous unzoned pattern is the second most common internal feature, followed by more complex structures, such as convolute, chaotic, and diffuse patterns (Supplementary Table S2). In order to access the meaning of obtained zircon ages and identify possible Pb loss events, we compare the proportion of common lead (expressed as f_{206}), Th/U ratios, and concordance degree with the best age of each grain. Among the Paleoproterozoic cluster, the younger ages are recorded by the less concordant grains, reflecting the adopted filter of 10% discordance. Overall, there is no significant correlation between the contents of common lead and Th/U ratios with age, which means that the obtained intervals represent those of their sources instead of being produced by lead loss. It is worth noting that there is no relationship between the investigated parameters and internal structures of the grains.

7.1 DEPOSITIONAL AGES

There are many ways to access the maximum depositional age (MDA) of a sedimentary siliciclastic rock using U-Pb geochronology, which is assumed as the age of the youngest

detrital component (Coutts et al., 2019; Gehrels, 2014, 2011). The widely used methods to derive MDA from detrital zircon populations (e.g., youngest single grain, youngest graphical peak, youngest grain cluster at 1σ or 2σ) in general drift for younger or too-old age estimates (Coutts et al., 2019; Vermeesch, 2021). To overcome this issue, Vermeesch (2021) proposed the use of maximum likelihood ages (MLA), a purely statistical method that employs a maximum likelihood model originally developed for fission-track thermochronology (Galbraith and Laslett, 1993). MLA calculated from detrital zircon data were 802 Ma for the sample SOS-1254, 760 Ma for the sample SOS-1260, and 789 Ma for the sample SOS-1274. These estimates are similar to those obtained by the youngest single grain approach (808, 782, 739 Ma) but significantly younger than those of previous studies in the Macururé Complex, which obtained MDA around 900 Ma (Neves et al., 2019; Oliveira et al., 2015b; Van Schmus et al., 2011). These new data indicate that quartzite protoliths deposition could have occurred ca. 150 Ma later than previously believed, synchronously with the sedimentation of the Novo Gosto unit in the Canindé Domain (Oliveira et al., 2015b; Passos et al., 2022), and before the onset of the Brasiliano Orogeny. The oldest intrusive body in the Macururé Domain shows a crystallization age of 643 Ma (Pereira et al., 2023), giving a minimum age estimate for deposition.

7.2 SOURCE CHARACTERISTICS

Bulk rock geochemistry of siliciclastic rocks is controlled by provenance, source rock characteristics, and tectonic setting (Fedó et al., 1995; McLennan et al., 1993; Nesbitt and Young, 1982; Taylor and McLennan, 1985). The parameter chemical index of alteration (Nesbitt and Young, 1982), defined as $CIA = 100 \times \text{molar} [Al_2O_3 / (Al_2O_3 + CaO^* + Na_2O + K_2O)]$, where CaO^* corresponds to CaO in the silicate fraction. Because CO_2 was not determined to correct the CaO in the carbonates, all CaO^* is assumed to be CaO . CIA values for the metapelitic and coexisting psammitic rocks vary from 47 to 77, with an average of 65 ± 7 . Although CIA values have significant variations, they are similar to the PAAS ($CIA = 69$; Taylor and McLennan, 1985), suggesting derivation from weakly weathered sources. In the CN-A-K compositional space (where $CN = CaO + Na_2O$, $A = Al_2O_3$, and $K = K_2O$, all in molecular proportion), the schists, phyllites, and metagraywackes mainly plot along the weathering line of granodiorite composition (Fig. 8a), indicating intermediate to acidic source area.

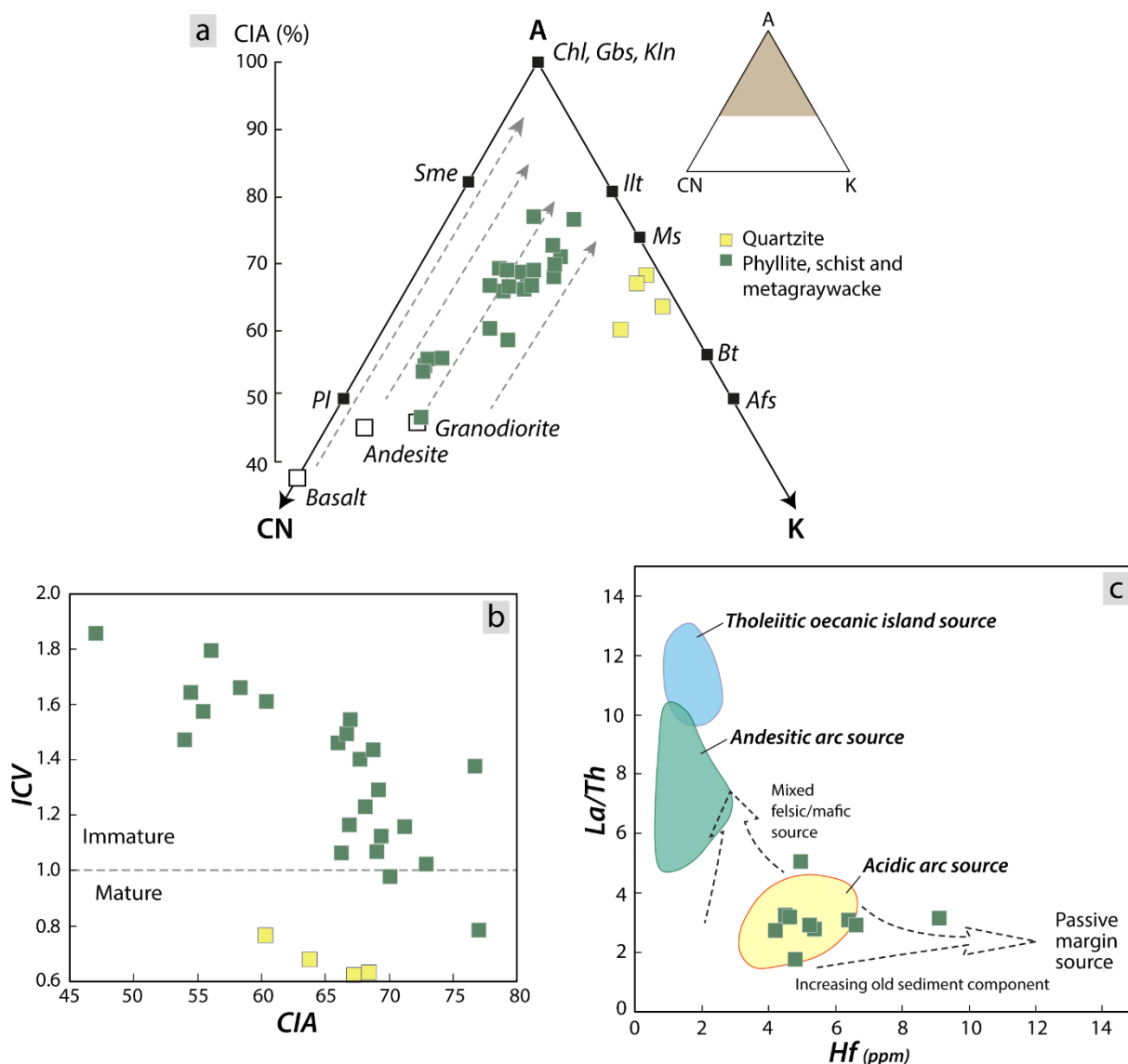


Figure IV.8- Geochemical constraints on the source. (a) CN-A-K ternary diagram with compositional poles of the main minerals and typical rock types. Dashed arrows correspond to the general trends of weathering (Fedo et al., 1995; McLennan et al., 1993; Nesbitt and Young, 1984). (b) CIA versus ICV parameters to infer the degree of weathering and maturity of the source areas (Cox et al., 1995; Nesbitt and Young, 1982). (c) Source and compositional discrimination diagram in terms of La/Th ratio and Hf contents (Floyd and Leveridge, 1987).

On the other hand, the index of compositional variability, $ICV = (Fe_2O_3 + K_2O + Na_2O + CaO + MgO + MnO + TiO_2)/Al_2O_3$, stands out as an efficient measure of compositional maturity of the source rocks (Cox et al., 1995). The analyzed rocks show variable ICV values between 0.62 and 1.86. The quartzites have uniform ICV lesser than unity (0.62-0.77, with an average of 0.68 ± 0.06), suggesting source areas dominated by mature materials that experienced sedimentary recycling (Fig. 8b). Conversely, the higher values are those from metapelite and metagraywacke samples (0.98-1.86, with an average of 1.36 ± 0.27), implying compositionally immature sources (Cox et al., 1995; Nesbitt and Young, 1982). This

compositionally immature rock types is typically found in tectonically active settings and are first-cycle deposits (Cox et al., 1995, and references therein).

In active continental margins, igneous rocks show variable contents of incompatible elements, which is reflected in the sedimentary rocks derived from them. The studied rocks show REE patterns moderately enriched in LREE, modest negative Eu anomalies, and almost flat HREE. These features match with the observed in felsic-intermediate rocks from active continental margins. In a diagram comparing the Hf contents with the La/Th ratios (Floyd and Leveridge, 1987), geochemical data for metapelite samples indicate that the source materials were dominated by felsic igneous rocks from a magmatic arc (Fig. 8c), instead of recycled sedimentary materials.

7.3 POTENTIAL SOURCE AREAS

The age distribution patterns of the zircon grain from the micaceous quartzites of the Macururé Complex record significant Rhyacian-Orosirian and Tonian contributions, in agreement with previous works (Neves et al., 2019; Oliveira et al., 2015b; Van Schmus et al., 2011). These results contrast with provenance data obtained for the adjacent Canindé, Vaza Barris, and Estância domains, whose age distribution shows high proportion of Brasiliano grains (Fig. 1c).

The most likely candidate as a source area for the Paleoproterozoic population is the Jirau do Ponciano Dome, which has been interpreted as the basement above which the Macururé Complex lies unconformably (Oliveira et al., 2015b, 2010). Lima et al. (2019) obtained U-Pb zircon ages between 2.07 and 2.05 Ga for amphibolites and acidic metavolcanic rocks from the Nicolau-Campo Grande Complex in the Jirau do Ponciano, with an important inherited Mesoarchean component (3.05-2.84 Ma). Rhyacian ages are also documented by detrital zircon grains from a hornblende-biotite paragneiss of this complex, which show the youngest graphic peak at 2027 Ma (Fig. 2; Lima et al., 2019). In recent work, Tesser et al. (2021) determined U-Pb ages between 2.03 and 1.96 Ga for neoblastic zircons from Arapiraca Complex diatexites, making this another potential source area.

Archean and early Paleoproterozoic intervals are each represented by one zircon grain, which probably reflects the recycling of Siderian and Mesoarchean grains of the metasupracrustal sequence of the Jirau do Ponciano Dome (Lima et al., 2019).

The zircon grains with ages between 900 and 1000 Ma are correlatable with the Cariris Velhos event, primarily recognized in the Alto Pajeú Domain of the Central Subprovince (Brito Neves et al., 1995; Kozuch, 2003). Remnants of this event were later identified in the PEAL

(Cruz et al., 2014) and Riacho do Pontal Belt (Caxito et al., 2020b, 2014). The Cariris Velhos-like crust is represented in the SOS by the Poço Redondo Migmatite Complex and Serra Negra A-type orthogneisses in the Poço Redondo and Marancó domains (Carvalho, 2005; Oliveira et al., 2010). The tectonic setting of the Cariris Velhos event remains debated. The predominance of bimodal volcanic rocks and granitoids with A-type filiation argues in favor of an extensional origin for the magmatism in an intraplate environment (Guimarães et al., 2016, 2012, 2011; Neves, 2003). Conversely, an orogenic origin has been proposed based on the volcanic arc signature of the magmatic rocks (Carvalho, 2005; Caxito et al., 2020b; Oliveira et al., 2010).

The zircon ages around 1.1 Ga have a more enigmatic origin once rocks with these ages restricted occurrence in the Borborema Province. U-Pb zircon data from felsic volcanic rock within the Riacho Gravatá Complex of the Alto Pajeú Domain record a crystallization age of 1091 ± 13 Ma (Guimarães et al., 2012). These researchers interpreted this age as an early rifting stage preceding the Cariris Velhos event.

Middle Neoproterozoic zircon grains cluster ca. 840 Ma but show a continuum spectrum of ages from ca. 880 to 800 Ma. Crystallization U-Pb ages on zircon in the range of 870-850 Ma are recorded by orthogneisses from the Rio Capibaribe Domain of the Central Subprovince and eastern PEAL of the Southern Subprovince (Neves et al., 2021).

The most intriguing zircon population encloses grains as young as 740 Ma, which had not been identified until now. Zircon grains from an amphibolite of the Novo Gosto unit produce a concordia age of 743 ± 3 Ma (Passos et al., 2021), which is so far the only one documented in southern Borborema Province.

In summary, our data support that Borborema Province, further north, was the main source of detritus for the Macururé Complex.

7.4 TECTONIC SETTING

D'el-Rey Silva (1999) argued that the Macururé Complex and the low-grade Vaza Barris and Estância domains should represent distal and proximal facies of platformal sediments deposited in a passive margin of the SFC. Subsequently, Carvalho (2005) suggested that the sedimentary succession of this domain was deposited in a basin adjacent to the Poço Redondo-Marancó arc, developed in the course of the Cariris Velhos event. This interpretation is supported by the abundance of Tonian zircon grains, the absence of Archean detritus, and the Nd- T_{DM} model ages between 1.8 and 1.3 Ga (Oliveira et al., 2015b). In the widely accepted geodynamic evolutive model for the SOS (Oliveira et al., 2010), the Macururé Domain was once again interpreted as a passive margin but now of the PEAL.

Cawood et al. (2012) demonstrated that detrital zircon spectra have distinctive age distribution patterns that reflect the tectonic setting of the basin in which they are deposited. Figure 9 displays the cumulative distribution of zircon ages plotted against the difference between the zircon crystallization and depositional ages for the studied samples from the Macururé Complex. The difference between crystallization and depositional ages is less than 150 Ma for the 5% youngest grains and above 100 Ma for the 30% youngest grains. Although this distribution is inconclusive, it seems more compatible with a collisional or extensional tectonic setting than with a convergent environment.

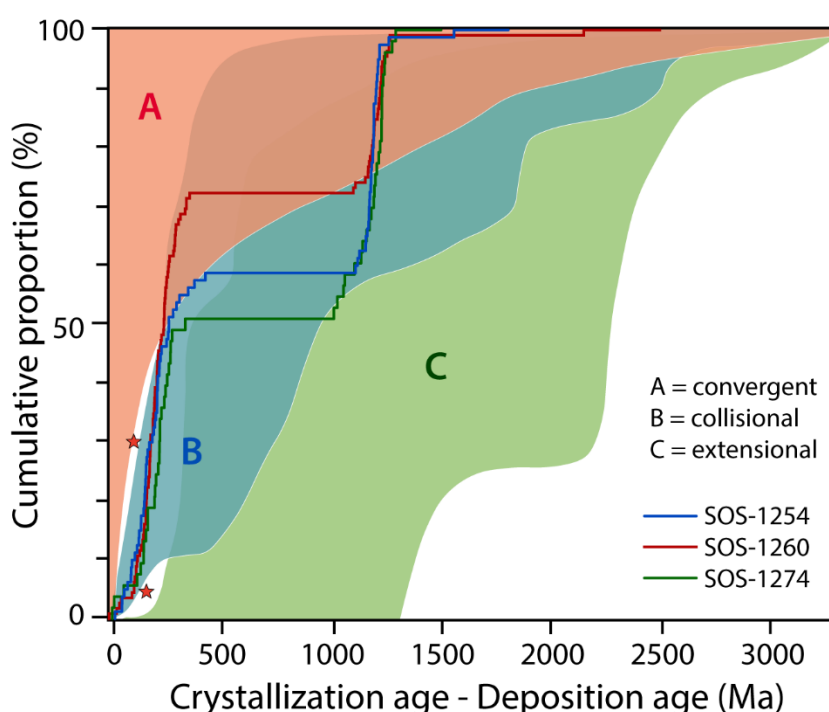


Figure IV.9- Cumulative age proportion plotted against the difference between the crystallization age for a detrital zircon grain and the depositional age of the succession (Cawood et al., 2012).

7.5 CRUSTAL GROWTH AND REWORKING

In Borborema Province, Lu-Hf isotope data on zircon is still scarce, especially in the southern subprovince. Figure 7 compares the newly acquired Hf isotope composition with potential zircon-forming events.

Zircon grains from the Middle Paleoproterozoic show strongly negative to slightly positive $\epsilon\text{Hf}(t)$ values between -15.6 and +0.5, with Hf- T_{DM}^{C} model ages spreading from 3.5 to 2.5 Ga. The predominance of subchondritic $\epsilon\text{Hf}(t)$ points to significant crustal reworking during the formation of rocks that constitute the basement of the Borborema Province. Two concordant and one near concordant grains provided the oldest Hf- T_{DM}^{C} model age between 3.4-3.5 Ga, implying some crust generation in the Paleoproterozoic, which was subsequently reworked into the

granitoid crust at ca. 2.0 Ga. Most Hf- T_{DM}^C model ages for Rhyacian-Orosirian grains are concentrated around 2.7 Ga, suggesting an important event of crust generation during the Neoproterozoic. In addition, chondritic to low-positive $\epsilon Hf_{(1.95-1.98 \text{ Ga})}$ values from 0 to +1.5 with Hf- T_{DM}^C model ages of ~ 2.5 Ga point to partial melting of a Neoproterozoic juvenile source. Granitoids of the Troia Massif in the Northern Subprovince record $\epsilon Hf_{(2.31-2.07 \text{ Ga})}$ values slightly negative and positive between +4.87 and -0.98, with Archean Hf- T_{DM}^C model ages between 2.5 and 2.8 Ga (Costa et al., 2018).

On the other hand, the Hf isotope signature of the late Mesoproterozoic, early Neoproterozoic, and middle Neoproterozoic populations are characterized by suprachondritic to subchondritic $\epsilon Hf_{(t)}$ values between -24.7 and +8.4. Strongly positive $\epsilon Hf_{(t)}$ values are accompanied by the younger Hf- T_{DM}^C model ages around 1.3-1.4 Ga, implying the addition of juvenile crust during the Cariris Velhos event. The $\epsilon Hf_{(t)}$ values become progressively more negative toward younger ages, illustrating the increasing role of reworking processes with time. The large number of low-positive $\epsilon Hf_{(t)}$ values with 1.5-1.6 suggests that the Cariris Velhos event may have reworked a Statherian crust, represented in Borborema Province by the Forquilha eclogite zone. In $\epsilon Hf_{(t)}$ versus time diagram, the alignment of the evolutive trends supports this hypothesis. Tonian granitic orthogneisses of the Riacho do Pontal Belt in the Southern Subprovince show zircon U-Pb crystallization ages between 966 and 1002 Ma. These grains show moderately juvenile to weakly evolved Hf signature ($\epsilon Hf_{(t)} = -1.5$ to +2.5), with Hf- T_{DM}^C model ages ranging from 1.7 to 1.9 Ga (Caxito et al., 2020b).

8 FINAL REMARKS

New geochemical and U-Pb-Hf isotope data on zircon allowed us to understand better how the crustal evolution processes operated in the southern Borborema Province. Pelitic protoliths from the Macururé Complex probably come from acidic, weakly weathered, immature sources with signatures of magmatic arc. On the other hand, micaceous quartzite protoliths had a subarkose composition, representing recycled sedimentary deposits. Detrital zircon from quartzite samples shows a bimodal age distribution dominated by Tonian and Rhyacian-Orosirian sources, with prominent peaks at ca. 950 and 2000 Ma. Mostly Rhyacian-Orosirian zircon grains record subchondritic Hf isotope composition and Paleoproterozoic to Neoproterozoic Hf- T_{DM}^C model ages, pointing to an important reworking of ancient continental crust during the formation of the Borborema Province basement. Tonian grains are characterized by suprachondritic to strongly subchondritic $\epsilon Hf_{(t)}$ values, indicating the addition of juvenile material and reworking during the Cariris Velhos event. Such inferences are

compatible with relatively proximal source areas, where the Borborema Province further north acted as the main detritus supplier.

REFERENCES

- Amaral, W., Santos, T.J., Ancelmi, M.F., Fuck, R.A., Dantas, E.L., Matteini, M., Moreto, C.P., 2015. 1.57 Ga protolith age of the Neoproterozoic Forquilha eclogites, Borborema Province, NE-Brazil, constrained by U–Pb, Hf and Nd isotopes. *J. South Am. Earth Sci.* 58, 210–222. <https://doi.org/10.1016/J.JSAMES.2014.10.001>
- Andersen, T., Andersson, U.B., Graham, S., Åberg, G., Simonsen, S.L., 2009. Granitic magmatism by melting of juvenile continental crust: new constraints on the source of Palaeoproterozoic granitoids in Fennoscandia from Hf isotopes in zircon. *J. Geol. Soc.* 166, 233–247. <https://doi.org/10.1144/0016-76492007-166>
- Andersen, T., Elburg, M.A., van Niekerk, H.S., Ueckermann, H., 2018a. Successive sedimentary recycling regimes in southwestern Gondwana: Evidence from detrital zircons in Neoproterozoic to Cambrian sedimentary rocks in southern Africa. *Earth-Sci. Rev.* 181, 43–60. <https://doi.org/10.1016/j.earscirev.2018.04.001>
- Andersen, T., Kristoffersen, M., Elburg, M.A., 2018b. Visualizing, interpreting and comparing detrital zircon age and Hf isotope data in basin analysis – a graphical approach. *Basin Res.* 30, 132–147. <https://doi.org/10.1111/BRE.12245>
- Bouvier, A., Vervoort, J.D., Patchett, P.J., 2008. The Lu–Hf and Sm–Nd isotopic composition of CHUR: Constraints from unequilibrated chondrites and implications for the bulk composition of terrestrial planets. *Earth Planet. Sci. Lett.* 273, 48–57. <https://doi.org/10.1016/j.epsl.2008.06.010>
- Brito Neves, B.B., Santos, E.J., Van Schmus, W.R., 2000. Tectonic history of the Borborema Province, in: Cordani, U.G., Milani, E.J., Thomaz Filho, A., Campos, D.A. (Eds.), *Tectonic Evolution of South America*. 31st International Geological Congress, Rio de Janeiro, pp. 151–182.
- Brito Neves, B.B., Van Schmus, W.R., Santos, E.J., Campos Neto, M.C., Kozuch, M., 1995. O evento Cariris Velhos na Província Borborema: intergração de dados, implicações e perspectivas. *Rev. Bras. Geociências* 25, 279–296.

Carvalho, M.J., 2005. Evolução tectônica do Domínio Marancó-Poço Rendido: registro das orogêneses Cariris Velhos e Brasiliana na Faixa Sergipana, NE do Brasil. Universidade de Campinas, Campinas.

Castaing, C., Feybesse, J.L., Thiéblemont, D., Triboulet, C., Chèvremont, P., 1994. Palaeogeographical reconstructions of the Pan-African/Brasiliano orogen: closure of an oceanic domain or intracontinental convergence between major blocks? *Precambrian Res.* 69, 327–344. [https://doi.org/10.1016/0301-9268\(94\)90095-7](https://doi.org/10.1016/0301-9268(94)90095-7)

Cawood, P.A., Hawkesworth, C.J., Dhuime, B., 2012. Detrital zircon record and tectonic setting. *Geology* 40, 875–878. <https://doi.org/10.1130/G32945.1>

Caxito, F.A., Santos, L.C.M.L., Ganade, C.E., Bendaoud, A., Fettous, E., Bouyo, M.H., 2020a. Toward an integrated model of geological evolution for NE Brazil-NW Africa: The Borborema Province and its connections to the Trans-Saharan (Benino-Nigerian and Tuareg shields) and Central African orogens. *Braz. J. Geol.* 50, e20190122. <https://doi.org/10.1590/2317-4889202020190122>

Caxito, F.A., Santos, L.C.M.L., Uhlein, A., Dantas, E.L., Alkmim, A.R., Lana, C., 2020b. New U-Pb (SHRIMP) and first Hf isotope constraints on the Tonian (1000-920 Ma) Cariris Velhos event, Borborema Province, NE Brazil. *Braz. J. Geol.* 50, e20190082. <https://doi.org/10.1590/2317-4889202020190082>

Caxito, F.A., Uhlein, A., Dantas, E.L., 2014. The Afeição augen-gneiss Suite and the record of the Cariris Velhos Orogeny (1000–960 Ma) within the Riacho do Pontal fold belt, NE Brazil. *J. South Am. Earth Sci.* 51, 12–27. <https://doi.org/10.1016/j.jsames.2013.12.012>

Chu, N.C., Taylor, R.N., Chavagnac, V., Nesbitt, R.W., Boella, R.M., Milton, J.A., German, C.R., Bayon, G., Burton, K., 2002. Hf isotope ratio analysis using multi-collector inductively coupled plasma mass spectrometry: an evaluation of isobaric interference corrections. *J. Anal. At. Spectrom.* 17, 1567–1574. <https://doi.org/10.1039/B206707B>

Conceição, J.A., 2014. Petrologia do Stock Granítico Glória Sul, Faixa Sergipana, setor sul da Província Borborema, Sergipe. Universidade Federal de Sergipe, São Cristóvão.

Corfu, F., 2003. Atlas of zircon textures. *Rev. Mineral. Geochem.* 53, 469–500. <https://doi.org/10.2113/0530469>

Costa, F.G., Klein, E.L., Lafon, J.M., Milhomem Neto, J.M., Galarza, M.A., Rodrigues, J.B., Naletto, J.L.C., Corrêa Lima, R.G., 2018. Geochemistry and U–Pb–Hf zircon data for plutonic

rocks of the Troia Massif, Borborema Province, NE Brazil: Evidence for reworking of Archean and juvenile Paleoproterozoic crust during Rhyacian accretionary and collisional tectonics. *Precambrian Res.* 311, 167–194. <https://doi.org/10.1016/J.PRECAMRES.2018.04.008>

Coutts, D.S., Matthews, W.A., Hubbard, S.M., 2019. Assessment of widely used methods to derive depositional ages from detrital zircon populations. *Geosci. Front.* 10, 1421–1435. <https://doi.org/10.1016/j.gsf.2018.11.002>

Cox, R., Lowe, D.R., Cullers, R.L., 1995. The influence of sediment recycling and basement composition on evolution of mudrock chemistry in the southwestern United States. *Geochim. Cosmochim. Acta* 59, 2919–2940. [https://doi.org/10.1016/0016-7037\(95\)00185-9](https://doi.org/10.1016/0016-7037(95)00185-9)

Cruz, R.F.D., Pimentel, M.M., Accioly, A.C.D.A., Rodrigues, J.B., 2014. Geological and isotopic characteristics of granites from the Western Pernambuco-Alagoas Domain: implications for the crustal evolution of the Neoproterozoic Borborema Province. *Braz. J. Geol.* 44, 627–652. <https://doi.org/10.5327/Z23174889201400040008>

Davison, I., Santos, R.A., 1989. Tectonic evolution of the Sergipano Fold Belt, NE Brazil, during the Brasiliano Orogeny. *Precambrian Res.* 45, 319–342. [https://doi.org/10.1016/0301-9268\(89\)90068-5](https://doi.org/10.1016/0301-9268(89)90068-5)

D’el-Rey Silva, L.J.H., 1999. Basin infilling in the southern-central part of the Sergipano Belt (NE Brazil) and implications for the evolution of Pan-African/Brasiliano cratons and Neoproterozoic sedimentary cover. *J. South Am. Earth Sci.* 12, 453–470. [https://doi.org/10.1016/S0895-9811\(99\)00034-6](https://doi.org/10.1016/S0895-9811(99)00034-6)

Fedo, C.M., Wayne Nesbitt, H., Young, G.M., 1995. Unraveling the effects of potassium metasomatism in sedimentary rocks and paleosols, with implications for paleoweathering conditions and provenance. *Geology* 23, 921. [https://doi.org/10.1130/0091-7613\(1995\)023<0921:UTEOPM>2.3.CO;2](https://doi.org/10.1130/0091-7613(1995)023<0921:UTEOPM>2.3.CO;2)

Floyd, P.A., Leveridge, B.E., 1987. Tectonic environment of the Devonian Gramscatho basin, south Cornwall: framework mode and geochemical evidence from turbiditic sandstones. *J. Geol. Soc.* 144, 531–542. <https://doi.org/10.1144/gsjgs.144.4.0531>

Galbraith, R.F., Laslett, G.M., 1993. Statistical models for mixed fission track ages. *Nucl. Tracks Radiat. Meas.* 21, 459–470. [https://doi.org/10.1016/1359-0189\(93\)90185-C](https://doi.org/10.1016/1359-0189(93)90185-C)

Gehrels, G., 2014. Detrital Zircon U-Pb Geochronology Applied to Tectonics. *Annu. Rev. Earth Planet. Sci.* 42, 127–149. <https://doi.org/10.1146/annurev-earth-050212-124012>

- Gehrels, G., 2011. Detrital Zircon U-Pb Geochronology: Current Methods and New Opportunities, in: *Tectonics of Sedimentary Basins*. John Wiley & Sons, Ltd, pp. 45–62. <https://doi.org/10.1002/9781444347166.ch2>
- Griffin, W.L., Belousova, E.A., Shee, S.R., Pearson, N.J., O'Reilly, S.Y., 2004. Archean crustal evolution in the northern Yilgarn Craton: U–Pb and Hf-isotope evidence from detrital zircons. *Precambrian Res.* 131, 231–282. <https://doi.org/10.1016/j.precamres.2003.12.011>
- Griffin, W.L., Wang, X., Jackson, S.E., Pearson, N.J., O'Reilly, S.Y., Xu, X., Zhou, X., 2002. Zircon chemistry and magma mixing, SE China: In-situ analysis of Hf isotopes, Tonglu and Pingtan igneous complexes. *Lithos* 61, 237–269. [https://doi.org/10.1016/S0024-4937\(02\)00082-8](https://doi.org/10.1016/S0024-4937(02)00082-8)
- Guimarães, I.P., Lara de Brito, M.F., Lages, G.A., Silva Filho, A.F., Santos, L., Brasilino, R.G., 2016. Tonian granitic magmatism of the Borborema Province, NE Brazil: A review. *J. South Am. Earth Sci.* 68, 97–112. <https://doi.org/10.1016/J.JSAMES.2015.10.009>
- Guimarães, I.P., Silva Filho, A.F., Almeida, C.N., Macambira, M.B., Armstrong, R., 2011. U–Pb SHRIMP data constraints on calc-alkaline granitoids with 1.3–1.6 Ga Nd TDM model ages from the central domain of the Borborema province, NE Brazil. *J. South Am. Earth Sci.* 31, 383–396. <https://doi.org/10.1016/J.JSAMES.2011.03.001>
- Guimarães, I.P., Van Schmus, W.R., De Brito Neves, B.B., Bretas Bittar, S.M., Silva Filho, A.F., Armstrong, R., 2012. U–Pb zircon ages of orthogneisses and supracrustal rocks of the Cariris Velhos belt: Onset of Neoproterozoic rifting in the Borborema Province, NE Brazil. *Precambrian Res.* 192–195, 52–77. <https://doi.org/10.1016/J.PRECAMRES.2011.10.008>
- Herron, M.M., 1988. Geochemical classification of terrigenous sands and shales from core or log data. *J. Sediment. Res.* 58, 820–829. <https://doi.org/10.1306/212F8E77-2B24-11D7-8648000102C1865D>
- Hoskin, P.W.O., Schaltegger, U., 2003. The composition of zircon and igneous and metamorphic petrogenesis. *Rev. Mineral. Geochem.* 53, 27–62. <https://doi.org/10.2113/0530027>
- Jackson, S.E., Pearson, N.J., Griffin, W.L., Belousova, E.A., 2004. The application of laser ablation-inductively coupled plasma-mass spectrometry to in situ U–Pb zircon geochronology. *Chem. Geol.* 211, 47–69. <https://doi.org/10.1016/j.chemgeo.2004.06.017>

- Janoušek, V., Farrow, C.M., Erban, V., 2006. Interpretation of whole-rock geochemical data in igneous geochemistry: introducing Geochemical Data Toolkit (GCDkit). *J. Petrol.* 47, 1255–1259. <https://doi.org/10.1093/petrology/egl013>
- Kozuch, M., 2003. Isotopic and trace element geochemistry of early Neoproterozoic gneissic and metavolcanic rocks in the Cariris Velhos orogen of the Borborema Province, Brazil, and their bearing on tectonic setting. University of Kansas, Lawrence.
- Lages, G.A., Santos, L.C.M.L., Brasilino, R.G., Rodrigues, J.B., Dantas, E.L., 2019. Statherian-Calymmian (ca. 1.6 Ga) magmatism in the Alto Moxotó Terrane, Borborema Province, northeast Brazil: Implications for within-plate and coeval collisional tectonics in West Gondwana. *J. South Am. Earth Sci.* 91, 116–130. <https://doi.org/10.1016/j.jsames.2019.02.003>
- Lima, D.R., 2016. Caracterização petrológica e geoquímica do pluton Curitiba, Domínio Poço Redondo-Marancó, Cinturão Sergipano. Universidade Federal de Pernambuco, Recife.
- Lima, H.M., Pimentel, M.M., Fuck, R.A., Santos, L.C.M.L., Dantas, E.L., 2018. Geochemical and detrital zircon geochronological investigation of the metavolcanosedimentary Araticum complex, Sergipano Fold Belt: Implications for the evolution of the Borborema Province, NE Brazil. *J. South Am. Earth Sci.* 86, 176–192. <https://doi.org/10.1016/J.JSAMES.2018.06.013>
- Lima, H.M., Pimentel, M.M., Santos, L.C.M.L., Dantas, E.L., 2019. Isotopic and geochemical characterization of the metavolcano-sedimentary rocks of the Jirau do Ponciano Dome: A structural window to a Paleoproterozoic continental arc root within the Southern Borborema Province, Northeast Brazil. *J. South Am. Earth Sci.* 90, 54–69. <https://doi.org/10.1016/J.JSAMES.2018.12.002>
- McDonough, W.F., Sun, S.S., 1995. The composition of the Earth. *Chem. Geol.* 120, 223–253. [https://doi.org/10.1016/0009-2541\(94\)00140-4](https://doi.org/10.1016/0009-2541(94)00140-4)
- McLennan, S.M., Hemming, S., McDaniel, D.K., Hanson, G.N., 1993. Geochemical approaches to sedimentation, provenance, and tectonics, in: Geological Society of America Special Papers. Geological Society of America, pp. 21–40. <https://doi.org/10.1130/SPE284-p21>
- Milhomem Neto, J.M., Lafon, J.M., 2019. Zircon U-Pb and Lu-Hf isotope constraints on Archean crustal evolution in Southeastern Guyana Shield. *Geosci. Front.* 10, 1477–1506. <https://doi.org/10.1016/J.GSF.2018.09.012>

- Morel, M.L.A., Nebel, O., Nebel-Jacobsen, Y.J., Miller, J.S., Vroon, P.Z., 2008. Hafnium isotope characterization of the GJ-1 zircon reference material by solution and laser-ablation MC-ICPMS. *Chem. Geol.* 255, 231–235. <https://doi.org/10.1016/J.CHEMGEO.2008.06.040>
- Nesbitt, H.W., Young, G.M., 1984. Prediction of some weathering trends of plutonic and volcanic rocks based on thermodynamic and kinetic considerations. *Geochim. Cosmochim. Acta* 48, 1523–1534. [https://doi.org/10.1016/0016-7037\(84\)90408-3](https://doi.org/10.1016/0016-7037(84)90408-3)
- Nesbitt, H.W., Young, G.M., 1982. Early Proterozoic climates and plate motions inferred from major element chemistry of lutites. *Nature* 299, 715–717. <https://doi.org/10.1038/299715a0>
- Neves, S.P., 2003. Proterozoic history of the Borborema province (NE Brazil): Correlations with neighboring cratons and Pan-African belts and implications for the evolution of western Gondwana. *Tectonics* 22, 1–14. <https://doi.org/10.1029/2001TC001352>
- Neves, S.P., Silva, J.M.R., Bruguier, O., 2019. The metasedimentary Macururé Complex (Sergipano Belt, Borborema Province, Brazil) in southern Alagoas state: geology and geochronology. *J. Geol. Surv. Braz.* 2, 17–25. <https://doi.org/10.29396/jgsb>
- Neves, S.P., Teixeira, C.M.L., Bruguier, O., 2021. 870–850 Ma-old magmatic event in eastern Borborema Province, NE Brazil: Another Tonian failed attempt to break up the São Francisco Paleoplate? *J. South Am. Earth Sci.* 105, 102917. <https://doi.org/10.1016/J.JSAMES.2020.102917>
- Oliveira, E.P., 2012. Geologia da Faixa Sergipana no Estado da Bahia, in: Barbosa, J., Mascarenhas, J.F., Correa Gomes, L.C., Dominguez, J.M.L., S, S.J. (Eds.), *Geologia Da Bahia. Pesquisa e Atualização*. Companhia Baiana de Pesquisa Mineral, pp. 179–190.
- Oliveira, E.P., Bueno, J.F., McNaughton, N.J., Silva Filho, A.F., Nascimento, R.S., Donatti-Filho, J.P., 2015a. Age, composition, and source of continental arc- and syn-collision granites of the Neoproterozoic Sergipano Belt, Southern Borborema Province, Brazil. *J. South Am. Earth Sci.* 58, 257–280. <https://doi.org/10.1016/j.jsames.2014.08.003>
- Oliveira, E.P., McNaughton, N.J., Windley, B.F., Carvalho, M.J., Nascimento, R.S., 2015b. Detrital zircon U–Pb geochronology and whole-rock Nd-isotope constraints on sediment provenance in the Neoproterozoic Sergipano Orogen, Brazil: from early passive margins to late foreland basins. *Tectonophysics* 662, 183–194. <https://doi.org/10.1016/J.TECTO.2015.02.017>
- Oliveira, E.P., Toteu, S.F., Araújo, M.N.C., Carvalho, M.J., Nascimento, R.S., Bueno, J.F., McNaughton, N., Basilici, G., 2006. Geologic correlation between the Neoproterozoic

Sergipano belt (NE Brazil) and the Yaoundé belt (Cameroon, Africa). *J. Afr. Earth Sci.* 44, 470–478. <https://doi.org/10.1016/J.JAFREARSCI.2005.11.014>

Oliveira, E.P., Windley, B.F., Araújo, M.N.C., 2010. The Neoproterozoic Sergipano Orogenic Belt, NE Brazil: a complete plate tectonic cycle in Western Gondwana. *Precambrian Res.* 181, 64–84. <https://doi.org/10.1016/J.PRECAMRES.2010.05.014>

Passchier, C.W., Trouw, R.A.J., 2005. *Microtectonics*. Springer-Verlag, Berlin. <https://doi.org/10.1007/3-540-29359-0>

Passos, L.H., Fuck, R.A., Chemale, F., Lenz, C., Pimentel, M.M., Machado, A., Pinto, V.M., 2021. Neoproterozoic (740–680 Ma) arc-back-arc magmatism in the Sergipano Belt, southern Borborema Province, Brazil. *J. South Am. Earth Sci.* 109, 103280. <https://doi.org/10.1016/J.JSAMES.2021.103280>

Passos, L.H., Fuck, R.A., Junior, F.C., Lenz, C., Porcher, C.C., Pinto, V.M., Santos, L.C.M.L., 2022. Neoproterozoic pre-collisional events recorded in the Sergipano belt, Southern Borborema Province, West Gondwana. *Int. Geol. Rev.* 64, 1–19. <https://doi.org/10.1080/00206814.2022.2054029>

Patchett, P.J., Tatsumoto, M., 1981. A routine high-precision method for Lu-Hf isotope geochemistry and chronology. *Contrib. Mineral. Petrol.* 75, 263–267. <https://doi.org/10.1007/BF01166766>

Pereira, F.S., Conceição, H., Rosa, M.L.S., Marinho, M.M., Tassinari, C.C.G., Milhomem Neto, J.M., Lafon, J.M., 2023. Late Cryogenian–Ediacaran magmatism in southern Borborema Province, NE Brazil: Ages, sources, petrogenesis, and tectonic setting. *Geosci. Front.* 14, 101626. <https://doi.org/10.1016/j.gsf.2023.101626>

Pereira, F.S., Rosa, M.L.S., Conceição, H., Bertotti, A.L., 2020. Age, composition, and source of the Macururé Mafic Suite, Southern Borborema Province, Brazil. *Braz. J. Geol.* 50, e20190105. <https://doi.org/10.1590/2317-4889202020190105>

Pinto, V.M., Koester, E., Debruyne, D., Chemale, F., Marques, J.C., Porcher, C.C., Passos, L.H., Lenz, C., 2020. Petrogenesis of the mafic-ultramafic Canindé layered intrusion, Sergipano Belt, Brazil: Constraints on the metallogenesis of the associated Fe–Ti oxide ores. *Ore Geol. Rev.* 122, 103535. <https://doi.org/10.1016/j.oregeorev.2020.103535>

Rosa, M.L.S., Conceição, J.A., Marinho, M.M., Pereira, F.S., Conceição, H., 2020. U–Pb SHRIMP dating of the Itabaiana Dome: a Mesoarchean basement inlier (2.83 Ga) in the

- Sergipano Orogenic System, Borborema Province. *Braz. J. Geol.* 50, e20190106. <https://doi.org/10.1590/2317-4889202020190106>
- Rudnick, R.L., Gao, S., 2003. Composition of the continental crust. *Treatise Geochem.* 1–64. <https://doi.org/10.1016/B0-08-043751-6/03016-4>
- Santos, L.R., 2016. *Petrologia do Stock Canindé Velho, Sistema Orogênico Sergipano, NE Brasil.* Universidade Federal de Sergipe, São Cristóvão.
- Santos, M.M., Lana, C., Scholz, R., Buick, I., Schmitz, M.D., Kamo, S.L., Gerdes, A., Corfu, F., Tapster, S., Lancaster, P., Storey, C.D., Basei, M.A.S., Tohver, E., Alkmim, A., Nalini, H., Krambrock, K., Fantini, C., Wiedenbeck, M., 2017. A New Appraisal of Sri Lankan BB Zircon as a Reference Material for LA-ICP-MS U-Pb Geochronology and Lu-Hf Isotope Tracing. *Geostand. Geoanalytical Res.* 41, 335–358. <https://doi.org/10.1111/GGR.12167>
- Santos, R.A., Martins, A.A.M., Neves, J.P., Leal, R.A., 1998. Programa de Levantamentos Geológicos Básicos do Brasil: Geologia e recursos minerais do Estado de Sergipe. Escala 1:250.000. Texto explicativo do mapa geológico do Estado de Sergipe. CPRM/DIEDIG/DEPAT;CODISE, Salvador.
- Silva Filho, M.A., Bomfim, L.F.C., Santos, R.A., Leal, R.A., Santana, A.C., Filho, P.A.B., 1979. Geologia da Geossinclinal Sergipana e do seu embasamento - Alagoas, Sergipe e Bahia: Projeto Baixo São Francisco/Vaza-Barris. DNPM/CPRM, Brasília.
- Silva, J.M.R., Campos Neto, M.C., Brito Neves, B.B., 1995. Deformação e metamorfismo principais de uma parte da Faixa Sul-Alagoana (Complexo Macururé), Sistema de Dobramentos Sergipano, Nordeste do Brasil. *Rev. Bras. Geociências* 25, 343–350.
- Soares, H.S., Sousa, C.S., Rosa, M.L.S., Conceição, H., 2019. Petrologia dos stocks Santa Maria, Monte Pedral, Bom Jardim, Boa Esperança e Niterói, Suíte Intrusiva Serra do Catu, estado de Sergipe, NE Brasil. *Rev. Geol. USP Sér. Científica* 19, 63–84. <https://doi.org/10.11606/issn.2316-9095.v19-156598>
- Söderlund, U., Patchett, P.J., Vervoort, J.D., Isachsen, C.E., 2004. The ^{176}Lu decay constant determined by Lu–Hf and U–Pb isotope systematics of Precambrian mafic intrusions. *Earth Planet. Sci. Lett.* 219, 311–324. [https://doi.org/10.1016/S0012-821X\(04\)00012-3](https://doi.org/10.1016/S0012-821X(04)00012-3)
- Spencer, C.J., Kirkland, C.L., Taylor, R.J.M., 2016. Strategies towards statistically robust interpretations of in situ U-Pb zircon geochronology. *Geosci. Front.* 7, 581–589. <https://doi.org/10.1016/j.gsf.2015.11.006>

- Stacey, J.S., Kramers, J.D., 1975. Approximation of terrestrial lead isotope evolution by a two-stage model. *Earth Planet. Sci. Lett.* 26, 207–221. [https://doi.org/10.1016/0012-821X\(75\)90088-6](https://doi.org/10.1016/0012-821X(75)90088-6)
- Steiger, R.H., Jäger, E., 1977. Subcommittee on geochronology: convention on the use of decay constants in geo- and cosmochemistry. *Earth Planet. Sci. Lett.* 36, 359–362. [https://doi.org/10.1016/0012-821X\(77\)90060-7](https://doi.org/10.1016/0012-821X(77)90060-7)
- Taylor, S.R., McLennan, S.M., 1985. *The Continental Crust: its Composition and Evolution. An Examination of the Geochemical Record Preserved in Sedimentary Rocks*. Blackwell Scientific, Oxford.
- Tesser, L.R., Ganade, C.E., Weinberg, R.F., Basei, M.A.S., Moraes, R., Batista, L.A., 2021. Ultrahigh-temperature Palaeoproterozoic rocks in the Neoproterozoic Borborema Province, implications for São Francisco Craton dispersion in NE Brazil. *J. Metamorph. Geol.* <https://doi.org/10.1111/JMG.12632>
- Thirlwall, M.F., Anczkiewicz, R., 2004. Multidynamic isotope ratio analysis using MC–ICP–MS and the causes of secular drift in Hf, Nd and Pb isotope ratios. *Int. J. Mass Spectrom.* 235, 59–81. <https://doi.org/10.1016/j.ijms.2004.04.002>
- Van Schmus, W.R., Kozuch, M., Brito Neves, B.B., 2011. Precambrian history of the Zona Transversal of the Borborema Province, NE Brazil: Insights from Sm–Nd and U–Pb geochronology. *J. South Am. Earth Sci.* 31, 227–252. <https://doi.org/10.1016/J.JSAMES.2011.02.010>
- Van Schmus, W.R., Oliveira, E.P., Silva Filho, A.F., Toteu, S.F., Penaye, J., Guimarães, I.P., Silva Filho, A.F., Toteu, S.F., Penaye, J., Guimarães, I.P., 2008. Proterozoic links between the Borborema Province, NE Brazil, and the Central African fold belt. *Geol. Soc. Spec. Publ.* 294, 69–99. <https://doi.org/10.1144/SP294.5>
- Vermeesch, P., 2021. Maximum depositional age estimation revisited. *Geosci. Front.* 12, 843–850. <https://doi.org/10.1016/J.GSF.2020.08.008>
- Vermeesch, P., 2018. IsoplotR: A free and open toolbox for geochronology. *Geosci. Front.* 9, 1479–1493. <https://doi.org/10.1016/J.GSF.2018.04.001>
- Warr, L.N., 2021. IMA–CNMNC approved mineral symbols. *Mineral. Mag.* 85, 291–320. <https://doi.org/10.1180/MGM.2021.43>

Wilde, S.A., Valley, J.W., Peck, W.H., Graham, C.M., 2001. Evidence from detrital zircons for the existence of continental crust and oceans on the Earth 4.4 Gyr ago. *Nature* 409, 175–178. <https://doi.org/10.1038/35051550>

Woodhead, J.D., Hergt, J.M., 2005. A preliminary appraisal of seven natural zircon reference materials for in situ Hf isotope determination. *Geostand. Geoanalytical Res.* 29, 183–195. <https://doi.org/10.1111/j.1751-908X.2005.tb00891.x>

SUPPLEMENTARY TABLE

Supplementary Table S1- Major and trace elements data for metasedimentary rocks of the Macururé Complex.

Ref. ^a	FDS-09C	FDS-63	FDS-68A	FDS-331B	GsSe 222A	GeSe 245A	GeSe 230B	GeSe 511	GeSe 372	GeSe 284A
	[1]	[1]	[1]	[2]	[2]	[2]	[2]	[2]	[2]	[2]
<i>Major elements (%wt.)</i>										
SiO ₂	68.68	56.52	68.65	61.85	52.70	55.52	75.09	71.55	60.01	55.28
TiO ₂	0.85	0.91	0.69	0.91	0.78	0.87	0.59	0.88	0.86	1.11
Al ₂ O ₃	13.70	18.07	14.16	16.64	15.90	19.17	10.40	12.56	17.34	21.72
Fe ₂ O ₃ ^b	6.19	8.98	5.46	8.08	7.37	7.98	4.25	6.12	8.17	12.43
MnO	0.12	0.17	0.11	0.12	0.10	0.06	0.11	0.05	0.14	0.09
MgO	2.31	3.93	2.52	3.67	2.30	3.30	1.13	1.38	3.78	0.43
CaO	2.03	1.51	2.01	1.22	6.54	1.12	1.42	0.06	0.80	0.03
Na ₂ O	3.50	3.00	3.48	1.97	1.38	1.16	2.88	2.19	1.87	2.06
K ₂ O	1.85	4.83	1.85	2.88	3.48	4.65	1.43	1.69	3.46	2.81
P ₂ O ₅	0.17	0.22	0.18	0.20	0.10	0.12	0.08	0.02	0.13	0.05
LOI	0.40	1.60	0.70	n.a.	n.a.	n.a.	n.a.	n.a.	n.a.	n.a.
<i>Trace elements (ppm)</i>										
Ba	438	595	480	609	504	563	292	382	586	1460
Rb	55.6	180.3	61.8	89.5	153.3	186.5	59.4	63.6	124.1	124.1
Sr	210.5	162.4	287.6	157.4	86.1	47.3	47.2	50.9	82.6	246.2
U	1.90	3.20	1.60	1.80	3.08	3.63	2.25	3.02	2.48	1.46
Th	7.10	11.10	5.50	8.80	12.80	14.70	10.90	10.50	8.90	13.30
Pb	2.10	12.10	2.60	2.20	20.60	17.00	20.40	6.00	2.70	3.60
Zr	223.5	167.70	152.70	183.30	148.10	189.80	238.00	312.00	176.20	184.80
Hf	6.40	4.80	4.20	4.50	4.64	5.37	6.63	9.11	5.22	4.96
Nb	12.60	11.80	7.30	11.50	16.42	15.08	10.12	12.64	10.74	24.03
Ta	0.80	0.80	0.50	0.80	1.55	1.21	0.94	0.89	0.69	1.69
Ni	41.00	74.00	46.00	62.00	44.30	52.60	16.40	41.00	58.70	38.60
Co	13.20	24.80	14.20	22.90	15.30	15.80	6.40	8.20	19.70	45.10
V	114	184	103	140	130	148	68	107	129	95
Zn	72	148	75	101	85	99	41	92	107	85
Sc	15	22	13	19	n.a.	n.a.	n.a.	n.a.	n.a.	n.a.
Cu	16.30	33.10	17.90	31.40	32.90	45.90	10.90	26.00	48.10	27.20
Cs	4.20	18.40	3.40	5.40	6.99	8.50	2.67	3.87	6.58	3.60
Ga	14.90	23.00	15.10	20.30	23.20	27.40	11.80	13.60	23.00	30.50
La	21.50	18.90	14.80	28.60	40.60	40.80	31.80	33.10	25.90	67.10
Ce	50.10	43.10	34.50	55.60	69.10	71.00	55.90	57.10	46.40	120.70
Pr	5.61	5.02	4.08	7.09	8.48	8.93	7.25	7.71	6.44	15.81
Nd	22.20	20.80	16.20	29.70	31.70	35.70	26.80	30.60	25.90	60.60
Sm	4.39	4.33	3.76	5.75	6.40	6.80	5.90	7.10	5.70	11.20
Eu	1.03	0.86	0.94	1.26	1.23	0.92	1.00	1.30	0.89	1.98
Gd	4.20	4.05	3.68	5.40	5.90	6.46	5.66	6.69	5.37	9.71
Tb	0.75	0.70	0.66	0.88	0.82	0.92	0.76	0.87	0.87	1.30
Dy	4.62	4.71	4.19	5.13	5.67	6.08	4.72	6.17	5.43	7.14
Ho	0.96	1.02	0.86	1.08	1.25	1.10	0.90	1.42	1.21	1.30
Er	2.84	3.14	2.57	3.46	3.26	3.94	2.63	3.67	3.31	3.83
Tm	0.44	0.53	0.39	0.52	0.48	0.52	0.36	0.53	0.44	0.51
Yb	2.76	3.54	2.43	3.36	3.40	3.80	2.40	4.00	3.50	3.40
Lu	0.42	0.51	0.35	0.51	0.44	0.46	0.32	0.69	0.50	0.45
Y	26.40	27.10	24.20	30.30	31.15	33.65	25.29	35.00	31.39	30.84
∑REE	121.82	111.21	89.41	148.34	178.73	187.43	146.40	160.95	131.86	305.03
La/Yb _{CN}	5.3	3.6	4.1	5.8	8.1	7.3	9.0	5.6	5.0	13.4
La/Sm _{CN}	3.1	2.7	2.5	3.1	4.0	3.7	3.4	2.9	2.8	3.7
Gd/Yb _{CN}	1.2	0.9	1.2	1.3	1.4	1.4	1.9	1.4	1.2	2.3
Eu/Eu*	0.73	0.63	0.77	0.69	0.61	0.42	0.53	0.57	0.49	0.58
Ce/Ce*	1.10	1.07	1.07	0.94	0.90	0.90	0.89	0.86	0.87	0.90

Continue on the next page.

Ref. ^a	SOS-1249	SOS-1250	SOS-1252	SOS-1254	SOS-1260	SOS-1264B	SOS-1265	SOS-1271	SOS-1272	SOS-1273	SOS-1274	SOS-1275	SOS-1276	SOS-1277	SOS-1278	SOS-1279	SOS-1282
	[2]	[2]	[2]	[2]	[2]	[2]	[2]	[2]	[2]	[2]	[2]	[2]	[2]	[2]	[2]	[2]	[2]
<i>Major elements (%wt.)</i>																	
SiO ₂	69.43	52.52	59.78	91.00	89.00	68.13	58.04	59.26	62.97	90.00	92.00	61.90	60.95	58.20	71.46	69.53	60.15
TiO ₂	0.61	0.77	0.81	0.04	0.14	0.57	0.93	0.80	0.95	0.07	0.04	0.89	0.90	0.83	0.65	0.60	0.85
Al ₂ O ₃	16.20	20.60	18.30	4.86	7.03	14.03	18.81	19.30	17.88	6.06	4.74	16.61	19.02	18.76	15.14	16.46	20.29
Fe ₂ O ₃ ^b	4.20	9.12	8.05	0.74	1.18	5.16	12.41	8.20	8.20	0.70	0.76	7.70	7.11	8.99	4.60	4.29	7.85
MnO	0.06	0.11	0.07	0.00	0.00	0.11	0.29	0.12	0.09	0.00	0.00	0.09	0.07	0.08	0.07	0.10	0.08
MgO	2.16	5.26	4.73	0.00	0.11	3.97	4.26	3.92	2.75	0.05	0.04	3.83	2.76	5.07	2.18	2.15	2.77
CaO	0.91	1.20	1.39	0.01	0.01	2.13	0.07	0.92	0.47	0.01	0.01	1.75	0.90	0.90	0.26	0.64	0.27
Na ₂ O	1.77	1.91	1.91	0.08	0.10	2.89	0.98	1.70	1.26	0.55	0.14	2.45	2.01	2.89	2.32	1.12	1.69
K ₂ O	3.39	3.73	3.22	2.41	2.83	2.18	3.69	3.83	3.99	2.83	1.90	3.40	4.13	2.65	2.32	3.71	3.95
P ₂ O ₅	0.16	0.27	0.26	0.00	0.01	0.26	0.03	0.24	0.17	0.01	0.01	0.26	0.27	0.24	0.21	0.20	0.05
LOI	1.76	3.56	2.69	0.26	0.49	0.97	2.21	3.10	2.71	0.09	0.29	1.46	2.57	3.19	2.44	2.36	3.62

LOI = Loss on ignition.

n.a. = Not analyzed

CN = Chondrite normalized (McDonough and Sun, 1995).

Eu/Eu* = $Eu_{CN}/\sqrt{(Sm_{CN} \times Gd_{CN})}$.

Ce/Ce* = $Ce_{CN}/\sqrt{(La_{CN} \times Pr_{CN})}$.

^a [1] Conceição (2014), [2] This study.

^b All iron expressed as Fe³⁺.

References

- Conceição, J.A., 2014. Petrologia do Stock Granítico Glória Sul, Faixa Sergipana, setor sul da Província Borborema, Sergipe. Universidade Federal de Sergipe, São Cristóvão.
- McDonough, W.F., Sun, S.S., 1995. The composition of the Earth. *Chemical Geology* 120, 223–253.

Supplementary Table S2- U-Pb data for detrital zircon grains from quartzite samples of the Macururú Domain.

Spot ID	Site	f_{206}^a	Th [ppm]	U [ppm]	Th/U ^b	Isotope ratios ^c						Ages (Ma)				Conc. ^c 6/8-7/6 (%)			
						²⁰⁷ Pb/ ²³⁵ U	1 s (%)	²⁰⁶ Pb/ ²³⁸ U	1 s (%)	Rho ^c	²⁰⁷ Pb/ ²⁰⁶ Pb	1 s (%)	²⁰⁶ Pb/ ²³⁸ U	1 s (abs)	²⁰⁷ Pb/ ²³⁵ U		1 s (abs)	²⁰⁷ Pb/ ²⁰⁶ U	1 s (abs)
<i>Sample SOS-1254</i>																			
1254-1 A1	Irregular concentric	0.003	5.5	11.3	0.49	6.58	1.46	0.40	0.49	0.34	0.12	1.38	2155	10.6	2056.1	30.1	1959	27.0	110
1254-1 A3	Chaotic	0.006	24.2	41.7	0.58	4.55	1.67	0.29	0.89	0.53	0.11	1.41	1626	14.5	1739.9	29.1	1880	26.5	87
1254-1 A4	Patchy	0.094	812.1	439.2	1.86	0.33	4.98	0.03	4.21	0.85	0.07	2.66	218	9.2	285.8	14.2	884	23.5	25
1254-1 A7	Fine oscillatory	0.015	25.9	55.4	0.47	1.17	2.96	0.12	1.45	0.49	0.07	2.58	724	10.5	787.2	23.3	972	25.0	74
1254-1 A8	Fine oscillatory	0.131	11.5	11.0	1.06	1.92	4.42	0.15	1.11	0.25	0.09	4.28	886	9.9	1087.3	48.1	1515	64.8	59
1254-1 A9	Fine oscillatory	0.049	22.8	29.1	0.79	1.07	3.30	0.10	1.60	0.49	0.08	2.88	626	10.0	740.2	24.4	1104	31.8	57
1254-1 B9	Irregular concentric	0.222	182.4	224.9	0.82	5.70	2.28	0.38	0.74	0.33	0.11	2.16	2056	15.3	1931.3	44.0	1800	38.8	114
1254-1 B8	Fine oscillatory	0.009	12.6	15.2	0.84	1.79	2.55	0.18	0.92	0.36	0.07	2.38	1073	9.9	1042.7	26.6	981	23.3	109
1254-1 B6	Homogeneous	0.017	10.6	16.1	0.66	3.02	2.84	0.21	1.18	0.42	0.11	2.58	1210	14.3	1412.0	40.1	1731	44.7	70
1254-1 B5	Convolute	0.040	11.8	10.2	1.17	1.40	4.17	0.15	1.16	0.28	0.07	4.01	882	10.3	890.6	37.2	912	36.6	97
1254-1 B4	Homogeneous	0.698	99.7	38.2	2.63	5.62	8.62	0.31	1.77	0.21	0.13	8.43	1757	31.2	1919.9	165.5	2101	177.2	84
1254-1 B3	Irregular diffuse	0.004	10.1	17.5	0.58	6.69	1.67	0.40	0.68	0.41	0.12	1.53	2156	14.8	2071.7	34.7	1989	30.4	108
1254-1 B2	Fine oscillatory	0.009	43.9	37.9	1.17	1.59	2.96	0.17	1.11	0.37	0.07	2.75	990	10.9	965.3	28.6	910	25.0	109
1254-1 B1	Fine oscillatory	0.006	16.9	24.7	0.69	1.74	2.76	0.18	1.05	0.38	0.07	2.55	1054	11.1	1025.1	28.3	963	24.6	110
1254-1 C2	Fine oscillatory	0.003	17.2	36.2	0.48	6.07	1.72	0.36	0.80	0.47	0.12	1.52	1997	16.0	1985.9	34.2	1975	30.1	101
1254-1 C3	Fine oscillatory	0.128	55.8	81.1	0.69	1.35	3.30	0.14	1.30	0.39	0.07	3.03	825	10.7	867.7	28.6	977	29.6	84
1254-1 C4	Irregular diffuse	0.003	8.7	20.6	0.43	6.83	1.63	0.40	0.59	0.36	0.12	1.53	2183	12.9	2089.7	34.2	1999	30.5	109
1254-1 C6	Fine oscillatory	0.005	23.0	38.5	0.60	8.61	1.48	0.41	0.68	0.46	0.15	1.31	2234	15.2	2297.4	34.0	2354	30.9	95
1254-1 C7	Convolute	0.007	11.7	16.3	0.72	1.77	2.91	0.19	1.00	0.34	0.07	2.73	1104	11.1	1035.8	30.1	894	24.4	124
1254-1 D7	Irregular diffuse	0.009	32.3	63.7	0.51	1.58	2.77	0.16	1.14	0.41	0.07	2.52	949	10.8	962.8	26.7	994	25.1	95
1254-1 D6	Irregular diffuse	0.001	54.9	126.4	0.44	4.97	1.74	0.31	0.65	0.37	0.12	1.61	1730	11.3	1815.0	31.5	1914	30.8	90
1254-1 D5	Homogeneous	0.007	33.7	36.3	0.94	4.71	1.88	0.29	0.78	0.41	0.12	1.71	1637	12.7	1769.2	33.3	1929	33.1	85
1254-1 D1	Fine oscillatory	0.011	78.1	61.2	1.29	1.03	3.24	0.10	1.72	0.53	0.07	2.74	640	11.0	719.7	23.3	977	26.8	65
1254-1 E1	Patchy	0.011	168.1	82.8	2.04	1.52	2.87	0.15	1.21	0.42	0.07	2.60	909	11.0	937.6	26.9	1006	26.1	90
1254-1 E2	Fine oscillatory	0.019	110.7	98.2	1.14	1.41	2.84	0.14	1.25	0.44	0.07	2.55	838	10.5	894.2	25.4	1037	26.4	81
1254-1 E4	Fine oscillatory	0.005	136.1	133.7	1.03	1.34	2.90	0.14	1.22	0.42	0.07	2.63	839	10.3	865.3	25.1	932	24.5	90
1254-1 E5	Fine oscillatory	0.072	302.6	226.6	1.34	1.30	2.95	0.13	1.35	0.46	0.07	2.62	772	10.4	845.9	24.9	1045	27.4	74
1254-1 E6	Fine oscillatory	0.005	123.2	161.2	0.77	1.57	2.80	0.16	1.09	0.39	0.07	2.57	950	10.4	959.3	26.8	982	25.3	97
1254-1 E7	Fine oscillatory	0.008	23.8	22.4	1.07	1.60	3.00	0.16	1.12	0.37	0.07	2.79	984	11.0	972.0	29.2	946	26.4	104
1254-1 E9	Irregular diffuse	0.005	25.5	58.9	0.44	1.54	2.91	0.16	1.14	0.39	0.07	2.68	956	10.9	948.2	27.6	930	24.9	103
1254-1 F8	Fine oscillatory	0.079	5.7	5.9	0.97	2.24	4.88	0.21	0.74	0.15	0.08	4.82	1251	9.2	1195.2	58.3	1095	52.8	114

Spot ID	Site	f_{206}^a	Th [ppm]	U [ppm]	Th/U ^b	Isotope ratios ^c							Ages (Ma)					Conc. ^c 6/8-7/6 (%)	
						²⁰⁷ Pb/ ²³⁵ U	1 s (%)	²⁰⁶ Pb/ ²³⁸ U	1 s (%)	Rho ^c	²⁰⁷ Pb/ ²⁰⁶ Pb	1 s (%)	²⁰⁶ Pb/ ²³⁸ U	1 s (abs)	²⁰⁷ Pb/ ²³⁵ U	1 s (abs)	²⁰⁷ Pb/ ²⁰⁶ U		1 s (abs)
1254-1 F4	Homogeneous	0.033	1331.3	543.4	2.47	0.41	4.12	0.05	3.04	0.74	0.06	2.78	287	8.7	347.3	14.3	774	21.5	37
1254-1 F2	Fine oscillatory	0.002	23.3	42.2	0.56	5.70	1.61	0.34	0.60	0.37	0.12	1.50	1888	11.4	1931.6	31.2	1979	29.6	95
1254-1 F1	Fine oscillatory	0.003	40.4	70.0	0.58	5.00	1.66	0.31	0.66	0.40	0.12	1.52	1730	11.4	1818.7	30.1	1922	29.2	90
1254-1 G1	Irregular concentric	0.008	20.8	38.8	0.54	2.67	2.35	0.17	1.73	0.73	0.11	1.59	1005	17.3	1320.6	31.0	1877	29.9	54
1254-1 G2	Fine oscillatory	0.009	4.6	11.6	0.40	2.24	2.52	0.21	0.77	0.30	0.08	2.40	1220	9.4	1195.1	30.1	1150	27.6	106
1254-1 G3	Fine oscillatory	0.018	27.3	50.1	0.55	1.59	2.71	0.16	0.97	0.36	0.07	2.53	953	9.3	967.4	26.2	1001	25.3	95
1254-1 G4	Fine oscillatory	0.016	6.2	8.4	0.75	1.73	2.89	0.18	0.84	0.29	0.07	2.76	1050	8.8	1019.2	29.5	954	26.4	110
1254-1 G9	Fine oscillatory	0.003	19.4	33.5	0.58	6.34	1.60	0.38	0.63	0.39	0.12	1.47	2059	12.9	2023.5	32.4	1988	29.2	104
1254-1 H6	Chaotic	0.103	53.1	85.5	0.62	1.70	2.62	0.17	0.89	0.34	0.07	2.46	999	8.9	1009.3	26.4	1032	25.4	97
1254-1 H4	Irregular concentric	0.005	31.0	57.5	0.54	1.91	2.20	0.18	0.90	0.41	0.08	2.00	1088	9.8	1084.4	23.8	1078	21.6	101
1254-1 H3	Chaotic	0.366	20.3	28.1	0.73	15.03	4.92	0.67	1.88	0.38	0.16	4.55	3293	62.0	2817.2	138.7	2492	113.3	132
1254-1 H2	Irregular diffuse	0.221	43.9	38.5	1.15	5.51	2.19	0.32	1.00	0.46	0.12	1.95	1808	18.2	1902.2	41.6	2006	39.0	90
1254-1 H1	Fine oscillatory	0.024	25.1	19.1	1.32	1.27	2.85	0.13	1.33	0.47	0.07	2.52	787	10.5	832.6	23.7	957	24.1	82
1254-1 I2	Homogeneous	0.163	84.4	68.6	1.24	1.49	3.16	0.15	1.06	0.33	0.07	2.98	899	9.5	924.9	29.3	988	29.5	91
1254-1 I4	Patchy	0.003	24.8	36.0	0.69	5.67	1.42	0.34	0.65	0.46	0.12	1.27	1870	12.1	1927.1	27.4	1989	25.2	94
1254-2 I5	Convolute	0.004	37.4	99.4	0.38	1.53	2.36	0.16	1.03	0.44	0.07	2.13	942	9.7	943.8	22.3	948	20.2	99
1254-1 I7	Fine oscillatory	0.075	33.7	46.1	0.74	1.62	2.80	0.16	1.15	0.41	0.07	2.55	964	11.1	976.8	27.3	1006	25.6	96
1254-1 I8	Convolute	0.003	10.5	27.1	0.39	6.31	1.46	0.38	0.69	0.48	0.12	1.28	2054	14.2	2020.3	29.5	1987	25.5	103
1254-1 I9	Fine oscillatory	0.027	79.1	95.2	0.84	1.53	2.45	0.15	1.07	0.44	0.07	2.20	926	9.9	943.2	23.1	983	21.6	94
1254-1 I10	Fine oscillatory	0.011	42.4	54.9	0.78	1.66	2.64	0.16	1.23	0.47	0.07	2.34	978	12.1	992.8	26.2	1027	24.0	95
1254-1 J9	Broad oscillatory	0.001	51.7	102.3	0.51	6.35	1.45	0.37	0.56	0.39	0.12	1.33	2049	11.6	2025.4	29.3	2001	26.7	102
1254-1 J8	Fine oscillatory	0.002	29.8	42.2	0.71	6.44	1.54	0.38	0.74	0.48	0.12	1.36	2074	15.3	2038.4	31.5	2003	27.2	104
1254-1 J7	Fine oscillatory	0.001	79.8	93.0	0.87	6.16	1.47	0.36	0.62	0.42	0.12	1.34	1984	12.3	1998.8	29.4	2014	26.9	99
1254-1 J6	Fine oscillatory	0.006	14.2	19.8	0.72	2.31	2.30	0.22	0.84	0.36	0.08	2.14	1274	10.6	1215.0	28.0	1112	23.8	115
1254-1 I6	Irregular diffuse	0.006	15.4	36.2	0.43	2.02	2.49	0.19	1.11	0.44	0.08	2.23	1141	12.6	1121.3	27.9	1084	24.2	105
1254-1 J5	Homogeneous	0.136	372.4	200.7	1.87	1.15	3.04	0.11	1.69	0.56	0.08	2.53	654	11.1	777.0	23.6	1149	29.0	57
1254-1 J4	Fine oscillatory	0.003	20.7	38.9	0.54	6.40	1.51	0.38	0.66	0.44	0.12	1.36	2067	13.7	2032.2	30.7	1997	27.1	104
1254-1 J3	Irregular diffuse	0.079	31.5	54.1	0.59	1.77	2.95	0.17	1.07	0.36	0.07	2.75	1020	11.0	1035.1	30.6	1066	29.3	96
1254-1 J2	Fine oscillatory	0.004	27.9	61.9	0.45	1.75	2.40	0.17	1.08	0.45	0.08	2.14	1002	10.8	1027.3	24.6	1081	23.1	93
1254-2 A1	Chaotic	0.011	4	9	0.51	1.69	3.31	0.17	1.30	0.39	0.07	3.04	1003	13.1	1004.2	33.2	1007	30.6	100
1254-2 A4	Patchy	0.026	14	11	1.25	1.79	2.82	0.11	1.88	0.67	0.12	2.10	689	13.0	1041.8	29.4	1881	39.5	37
1254-2 A5	Irregular concentric	0.157	2	5	0.44	5.86	2.42	0.33	0.81	0.33	0.13	2.28	1861	15.0	1954.9	47.3	2056	46.9	90
1254-2 A6	Homogeneous	0.008	3	5	0.65	5.72	1.99	0.34	0.73	0.37	0.12	1.85	1901	13.9	1934.1	38.5	1970	36.5	97

Spot ID	Site	f_{206}^a	Th [ppm]	U [ppm]	Th/U ^b	Isotope ratios ^c						Ages (Ma)				Conc. ^c 6/8-7/6 (%)			
						²⁰⁷ Pb/ ²³⁵ U	1 s (%)	²⁰⁶ Pb/ ²³⁸ U	1 s (%)	Rho ^c	²⁰⁷ Pb/ ²⁰⁶ Pb	1 s (%)	²⁰⁶ Pb/ ²³⁸ U	1 s (abs)	²⁰⁷ Pb/ ²³⁵ U		1 s (abs)	²⁰⁷ Pb/ ²⁰⁶ U	1 s (abs)
1254-2-A7	Sectorial	0.019	2	4	0.54	1.67	3.56	0.17	1.24	0.35	0.07	3.34	1036	12.8	995.8	35.5	909	30.4	114
1254-2-A10	Broad oscillatory	0.095	151	98	1.54	0.53	5.89	0.05	5.06	0.86	0.08	3.01	307	15.6	433.5	25.5	1175	35.4	26
1254-2-B10	Chaotic	0.056	9	10	0.91	1.37	3.78	0.14	1.47	0.39	0.07	3.48	865	12.7	877.3	33.2	908	31.6	95
1254-2-B9	Homogeneous	0.004	2	7	0.33	5.87	2.03	0.35	0.90	0.45	0.12	1.82	1944	17.6	1956.1	39.7	1969	35.8	99
1254-2-B7	Irregular concentric	0.007	2	6	0.34	6.09	1.96	0.36	0.72	0.37	0.12	1.82	1991	14.4	1989.2	38.9	1988	36.1	100
1254-2-B6	Homogeneous	0.016	3	4	0.61	1.76	3.44	0.18	1.24	0.36	0.07	3.21	1054	13.0	1029.7	35.5	979	31.5	108
1254-2-B5	Irregular diffuse	0.003	3	7	0.46	6.18	1.94	0.37	0.65	0.34	0.12	1.83	2051	13.4	2002.2	38.8	1952	35.7	105
1254-2-B4	Irregular diffuse	0.059	5	8	0.65	3.42	2.40	0.22	1.12	0.47	0.11	2.12	1281	14.3	1509.4	36.2	1847	39.1	69
1254-2-B1	Homogeneous	0.046	258	94	2.76	0.43	5.17	0.06	3.51	0.68	0.06	3.80	346	12.1	362.3	18.7	466	17.7	74
1254-2-C2	Fine oscillatory	0.011	3	6	0.53	2.07	3.08	0.20	1.06	0.34	0.08	2.90	1170	12.4	1140.1	35.1	1084	31.4	108
1254-2-C3	Irregular diffuse	0.378	3	4	0.77	1.65	4.72	0.15	1.53	0.32	0.08	4.47	883	13.5	989.1	46.7	1223	55.1	72
1254-2-C4	Fine oscillatory	0.011	2	10	0.24	5.92	1.95	0.35	0.81	0.42	0.12	1.77	1946	15.9	1963.7	38.2	1983	35.1	98
1254-2-C5	Fine oscillatory	0.004	4	8	0.57	5.64	1.95	0.34	0.76	0.39	0.12	1.80	1882	14.4	1922.2	37.5	1966	35.3	96
1254-2-C7	Homogeneous	0.014	3	5	0.52	1.53	3.45	0.16	1.35	0.39	0.07	3.17	943	12.7	944.2	32.5	947	30.0	100
1254-2-C8	Convolute	0.004	3	6	0.46	6.54	1.90	0.38	0.61	0.32	0.12	1.80	2088	12.8	2050.9	39.0	2014	36.3	104
1254-2-C9	Homogeneous	0.020	16	28	0.58	5.32	2.04	0.32	0.92	0.45	0.12	1.82	1781	16.4	1871.7	38.2	1974	35.9	90
1254-2-D10	Broad oscillatory	0.020	43	39	1.11	1.41	3.74	0.15	1.51	0.40	0.07	3.42	880	13.3	894.7	33.4	931	31.9	94
1254-2-D9	Fine oscillatory	0.011	21	32	0.66	1.75	3.37	0.18	1.14	0.34	0.07	3.17	1043	11.9	1026.9	34.6	992	31.4	105
1254-2-D8	Fine oscillatory	0.002	64	163	0.40	6.05	1.97	0.36	0.66	0.34	0.12	1.86	1982	13.1	1983.1	39.1	1984	36.9	100
1254-2-D7	Fine oscillatory	0.008	49	64	0.76	1.37	3.52	0.14	1.40	0.40	0.07	3.23	850	11.9	874.5	30.8	938	30.3	91
1254-2-D3	Irregular diffuse	0.012	8	13	0.62	6.17	2.16	0.37	0.70	0.33	0.12	2.04	2047	14.4	1999.7	43.2	1951	39.8	105
1254-2-D1	Irregular diffuse	0.011	299	167	1.81	1.51	3.48	0.16	1.30	0.37	0.07	3.23	938	12.1	933.5	32.5	923	29.9	102
1254-2-E7	Fine oscillatory	0.059	68	71	0.96	1.22	3.98	0.13	1.61	0.41	0.07	3.63	808	13.0	810.0	32.2	817	29.7	99
1254-2-E8	Fine oscillatory	0.233	29	38	0.77	5.53	2.75	0.32	0.85	0.31	0.13	2.62	1773	15.0	1906.0	52.5	2054	53.8	86
1254-2-E10	Broad oscillatory	0.014	600	311	1.95	0.81	3.99	0.09	2.24	0.56	0.07	3.30	541	12.1	603.9	24.1	846	27.9	64
1254-2-F9	Homogeneous	0.051	3	7	0.44	1.56	4.88	0.17	1.20	0.25	0.07	4.73	1021	12.2	953.0	46.5	799	37.8	128
1254-2-F8	Irregular concentric	0.014	99	82	1.21	1.14	3.54	0.12	1.73	0.49	0.07	3.09	729	12.6	774.0	27.4	907	28.0	80
1254-2-F7	Fine oscillatory	0.170	51	38	1.35	1.41	4.00	0.15	1.43	0.36	0.07	3.73	885	12.7	892.6	35.7	912	34.1	97
1254-2-F5	Patchy	0.109	780	248	3.17	0.32	6.71	0.04	5.09	0.76	0.06	4.38	247	12.6	279.4	18.8	561	24.5	44
1254-2-F3	Fine oscillatory	0.005	52	106	0.49	5.42	1.84	0.31	0.79	0.43	0.13	1.67	1754	13.8	1888.0	34.8	2038	33.9	86
1254-2-F2	Chaotic	0.028	477	158	3.04	1.13	3.81	0.12	2.06	0.54	0.07	3.21	734	15.1	766.0	29.2	862	27.6	85
1254-2-F1	Irregular concentric	0.020	16	50	0.33	5.99	1.96	0.36	0.80	0.41	0.12	1.79	1959	15.7	1973.9	38.8	1989	35.7	99
1254-2-G1	Chaotic	0.006	14	36	0.41	6.00	1.89	0.36	0.68	0.36	0.12	1.77	1986	13.4	1975.4	37.4	1964	34.8	101

Spot ID	Site	f_{206}^a	Th [ppm]	U [ppm]	Th/U ^b	Isotope ratios ^c						Ages (Ma)					Conc. ^c 6/8-7/6 (%)		
						²⁰⁷ Pb/ ²³⁵ U	1 s (%)	²⁰⁶ Pb/ ²³⁸ U	1 s (%)	Rho ^c	²⁰⁷ Pb/ ²⁰⁶ Pb	1 s (%)	²⁰⁶ Pb/ ²³⁸ U	1 s (abs)	²⁰⁷ Pb/ ²³⁵ U	1 s (abs)		²⁰⁷ Pb/ ²⁰⁶ U	1 s (abs)
1254-2 G2	Fine oscillatory	0.010	37	48	0.77	1.63	3.31	0.17	1.29	0.39	0.07	3.05	1000	12.9	980.6	32.5	938	28.6	107
1254-2 G3	Fine oscillatory	0.054	244	124	1.99	1.15	3.56	0.12	1.78	0.50	0.07	3.09	702	12.5	777.0	27.7	999	30.9	70
1254-2 G6	Fine oscillatory	0.010	39	70	0.57	1.09	3.49	0.11	1.92	0.55	0.07	2.92	672	12.9	747.0	26.1	978	28.5	69
1254-2 G8	Fine oscillatory	0.006	44	42	1.04	1.69	2.82	0.17	1.26	0.45	0.07	2.52	1009	12.7	1005.7	28.3	998	25.2	101
1254-2 G9	Fine oscillatory	0.032	41	38	1.06	1.26	3.61	0.14	1.54	0.43	0.07	3.27	840	13.0	829.3	30.0	801	26.2	105
1254-2 G10	Homogeneous	0.029	53	54	1.00	1.49	3.05	0.15	1.38	0.45	0.07	2.72	927	12.8	926.2	28.2	924	25.1	100
1254-2 H9	Convolute	0.004	16	51	0.32	4.40	1.91	0.28	1.00	0.52	0.11	1.63	1602	16.0	1712.3	32.7	1849	30.1	87
1254-2 H8	Homogeneous	0.012	19	49	0.40	1.67	2.91	0.17	1.30	0.45	0.07	2.61	1015	13.2	998.8	29.1	963	25.1	105
1254-2 H5	Fine oscillatory	0.004	23	42	0.55	6.09	1.77	0.37	0.75	0.42	0.12	1.61	2010	15.1	1988.8	35.3	1967	31.6	102
1254-2 H4	Fine oscillatory	0.004	102	116	0.88	1.63	2.82	0.17	1.28	0.45	0.07	2.51	994	12.7	983.0	27.7	959	24.1	104
1254-2 I1	Fine oscillatory	0.004	61	105	0.58	1.70	2.78	0.17	1.25	0.45	0.07	2.48	1011	12.7	1007.9	28.0	1001	24.9	101
1254-2 I5	Fine oscillatory	0.014	24	33	0.75	1.61	3.00	0.17	1.29	0.43	0.07	2.71	1000	12.9	974.8	29.3	918	24.9	109
1254-2 I6	Broad oscillatory	0.017	21	25	0.84	1.51	3.19	0.16	1.35	0.42	0.07	2.89	945	12.8	933.3	29.7	905	26.1	104
1254-2 I7	Fine oscillatory	0.008	26	37	0.72	1.91	2.78	0.19	1.15	0.41	0.07	2.53	1102	12.7	1084.0	30.2	1048	26.5	105
1254-2 I9	-	0.016	18	43	0.41	1.46	3.20	0.15	1.45	0.45	0.07	2.85	916	13.3	914.5	29.2	911	25.9	101
1254-2 J10	-	0.005	24	35	0.69	5.59	1.72	0.33	0.75	0.44	0.12	1.55	1859	13.9	1915.0	32.9	1976	30.6	94
1254-2 J7	-	0.027	24	49	0.48	0.86	3.85	0.10	2.16	0.56	0.07	3.18	590	12.8	631.1	24.3	782	24.9	75
1254-2 J3	Homogeneous	0.173	46	33	1.41	3.15	3.65	0.20	2.71	0.74	0.11	2.45	1175	31.8	1444.3	52.8	1867	45.7	63
1254-2 J1	Fine oscillatory	0.008	123	102	1.21	1.52	2.91	0.15	1.36	0.47	0.07	2.57	918	12.5	939.9	27.4	992	25.5	93
1254-2 I2	Irregular concentric	0.003	24	91	0.27	6.21	1.65	0.36	0.68	0.41	0.12	1.51	2003	13.5	2005.2	33.2	2008	30.3	100
1254-2 I3	Homogeneous	0.006	79	67	1.18	4.45	1.87	0.27	0.89	0.48	0.12	1.65	1565	13.9	1720.9	32.2	1916	31.5	82
1254-2 I4	Patchy	0.036	23	34	0.67	5.22	1.97	0.32	0.75	0.38	0.12	1.82	1813	13.7	1856.0	36.6	1905	34.8	95
1254-2 H3	Fine oscillatory	0.031	39	55	0.72	1.48	3.41	0.16	1.35	0.40	0.07	3.13	947	12.8	922.5	31.5	865	27.1	109
Sample SOS-1260																			
006-1260-A1	Broad oscillatory	1.027	0.0	0.0	1.13	156.12	135.32	1.47	135.05	1.00	0.77	8.50	5836.2	7881.7	5134.8	6948.3	4865.1	413.5	120
007-1260-A2	Fine oscillatory	0.239	2.0	4.4	0.46	1.64	108.33	0.11	2.70	0.02	0.10	108.30	701.4	19.0	986.2	1068.4	1688.9	1829.1	42
008-1260-A3	Patchy	0.034	143.9	433.1	0.33	0.91	3.77	0.10	2.48	0.66	0.07	2.84	610.8	15.1	654.4	24.7	807.9	22.9	76
009-1260-A5	Fine oscillatory	0.020	60.7	140.5	0.44	1.39	3.21	0.14	1.80	0.56	0.07	2.66	856.3	15.4	883.2	28.3	951.2	25.3	90
010-1260-A6	Broad oscillatory	0.074	38.8	75.0	0.52	1.46	3.49	0.15	1.69	0.49	0.07	3.05	898.7	15.2	914.8	31.9	953.8	29.1	94
011-1260-A7	Fine oscillatory	0.009	52.7	101.5	0.52	1.38	3.21	0.14	1.80	0.56	0.07	2.65	847.7	15.3	881.2	28.2	966.2	25.6	88
012-1260-A9	Fine oscillatory	0.019	42.5	63.4	0.68	1.35	3.62	0.15	1.76	0.49	0.07	3.17	878.9	15.4	865.7	31.3	832.3	26.3	106
013-1260-A10	Fine oscillatory	0.005	53.8	104.5	0.52	1.47	3.13	0.15	1.72	0.55	0.07	2.62	894.7	15.4	916.8	28.7	970.4	25.4	92
014-1260-A11	Parallel banding, homogeneous	0.007	18.8	49.6	0.38	5.35	1.83	0.32	0.94	0.51	0.12	1.57	1772.0	16.6	1876.2	34.3	1993.6	31.3	89

Spot ID	Site	f_{206}^a	Th [ppm]	U [ppm]	Th/U ^b	Isotope ratios ^c							Ages (Ma)				Conc. ^c 6/8-7/6 (%)		
						²⁰⁷ Pb/ ²³⁵ U	1 s (%)	²⁰⁶ Pb/ ²³⁸ U	1 s (%)	Rho ^c	²⁰⁷ Pb/ ²⁰⁶ Pb	1 s (%)	²⁰⁶ Pb/ ²³⁸ U	1 s (abs)	²⁰⁷ Pb/ ²³⁵ U	1 s (abs)		²⁰⁷ Pb/ ²⁰⁶ U	1 s (abs)
015 1260 B2	Fine oscillatory	0.003	69.2	170.2	0.41	5.64	1.73	0.33	0.84	0.49	0.12	1.51	1836.2	15.5	1921.5	33.2	2014.9	30.4	91
019 1260 B3	Cross-bedding	0.010	11.3	28.4	0.40	5.39	1.99	0.33	0.82	0.41	0.12	1.81	1823.3	14.9	1883.1	37.4	1949.7	35.3	94
020 1260 B4	Convolute	0.046	15.2	50.4	0.30	0.71	5.20	0.08	3.23	0.62	0.07	4.08	478.5	15.5	546.5	28.4	840.9	34.3	57
021 1260 B5	Parallel banding, homogeneous	0.020	40.0	89.7	0.45	1.18	3.59	0.12	1.99	0.55	0.07	2.99	721.6	14.4	792.6	28.5	998.0	29.8	72
022 1260 B6	Broad oscillatory	0.043	8.5	11.1	0.78	1.52	4.37	0.15	1.60	0.37	0.07	4.06	926.2	14.8	940.0	41.0	972.5	39.5	95
023 1260 B7	Fine oscillatory	0.032	92.3	62.1	1.50	1.40	3.61	0.15	1.60	0.44	0.07	3.24	900.2	14.4	887.0	32.0	854.1	27.6	105
024 1260 B9	Fine oscillatory	0.073	36.4	61.7	0.59	1.34	3.98	0.14	1.76	0.44	0.07	3.57	842.9	14.8	863.1	34.4	915.4	32.7	92
025 1260 B10	Homogeneous	0.018	167.1	167.3	1.01	1.41	3.34	0.14	1.68	0.50	0.07	2.89	866.0	14.6	894.6	29.9	966.0	27.9	90
026 1260 B12	Fine oscillatory	0.004	26.5	75.8	0.35	5.68	1.90	0.34	0.82	0.43	0.12	1.72	1887.7	15.6	1928.0	36.7	1971.5	33.8	96
027 1260 C1	Fine oscillatory	0.057	224.1	236.9	0.95	1.09	3.72	0.11	2.10	0.56	0.07	3.07	687.4	14.4	746.3	27.8	927.1	28.5	74
028 1260 C2	Fine oscillatory	0.006	57.2	111.3	0.52	1.61	3.22	0.16	1.51	0.47	0.07	2.84	963.5	14.5	975.7	31.4	1003.2	28.5	96
032 1260 C3	Convolute	0.004	33.6	87.0	0.39	5.02	1.92	0.30	0.99	0.52	0.12	1.64	1678.7	16.6	1822.3	35.0	1990.5	32.7	84
033 1260 C5	Fine oscillatory	0.009	53.0	124.9	0.43	1.04	3.62	0.11	2.18	0.60	0.07	2.89	652.4	14.2	724.3	26.2	953.7	27.6	68
034 1260 C7	Fine oscillatory	0.092	119.8	498.0	0.24	0.86	3.86	0.09	2.64	0.68	0.07	2.82	528.1	13.9	630.1	24.3	1015.5	28.7	52
035 1260 C8	Fine oscillatory	0.025	31.5	52.2	0.61	1.63	3.31	0.16	1.45	0.44	0.07	2.97	957.5	13.8	981.5	32.4	1035.6	30.8	92
036 1260 C9	Homogeneous	0.057	50.5	160.7	0.32	0.59	4.91	0.07	3.50	0.71	0.07	3.44	406.4	14.2	468.1	23.0	783.3	27.0	52
037 1260 C11	Broad oscillatory	0.007	145.9	149.9	0.98	1.35	3.30	0.14	1.74	0.53	0.07	2.81	833.5	14.5	868.0	28.7	956.9	26.8	87
038 1260 C12	Irregular concentric	0.004	35.8	84.1	0.43	5.42	1.86	0.32	0.85	0.46	0.12	1.65	1788.6	15.3	1887.5	35.1	1998.2	33.0	90
039 1260 D1	Fine oscillatory	0.018	124.0	177.5	0.70	1.27	3.33	0.13	1.76	0.53	0.07	2.83	790.0	13.9	832.2	27.7	946.7	26.8	83
040 1260 D2	Homogeneous	0.010	10.7	25.1	0.43	5.54	1.92	0.33	0.76	0.40	0.12	1.76	1853.2	14.2	1906.9	36.6	1965.8	34.6	94
041 1260 D3	Fine oscillatory	0.006	26.5	80.6	0.33	4.43	2.01	0.28	0.93	0.46	0.12	1.78	1583.8	14.7	1717.3	34.5	1884.1	33.6	84
045 1260 D4	Fine oscillatory	0.075	112.2	109.4	1.03	1.29	3.50	0.13	1.49	0.43	0.07	3.17	815.0	12.2	840.8	29.4	909.7	28.8	90
046 1260 D5	Fine oscillatory	0.018	15.2	33.0	0.46	5.39	1.82	0.30	0.82	0.45	0.13	1.62	1708.3	14.0	1883.5	34.2	2082.6	33.8	82
047 1260 D6	Fine oscillatory	0.006	54.4	118.6	0.46	1.54	3.01	0.16	1.27	0.42	0.07	2.73	944.4	12.0	947.4	28.5	954.5	26.1	99
048 1260 D7	Fine oscillatory	0.010	50.8	89.3	0.57	1.60	3.03	0.16	1.21	0.40	0.07	2.77	978.0	11.9	969.0	29.3	948.6	26.3	103
049 1260 D8	Fine oscillatory	0.025	22.0	27.1	0.82	1.45	3.45	0.15	1.37	0.40	0.07	3.17	908.9	12.4	908.5	31.4	907.5	28.8	100
050 1260 D9	Convolute	0.005	18.2	47.1	0.39	5.78	1.79	0.35	0.67	0.37	0.12	1.66	1919.2	12.8	1943.6	34.8	1969.8	32.7	97
051 1260 D10	Convolute	0.013	58.0	97.7	0.60	1.66	3.05	0.18	1.14	0.37	0.07	2.83	1050.0	12.0	993.3	30.3	870.0	24.6	121
052 1260 D11	Fine oscillatory	0.014	50.9	150.5	0.34	1.19	3.34	0.13	1.50	0.45	0.07	2.99	786.2	11.8	794.5	26.6	817.7	24.4	96
053 1260 D12	Sector	0.016	12.9	29.0	0.45	1.69	3.13	0.17	1.19	0.38	0.07	2.90	995.9	11.8	1005.2	31.5	1025.5	29.7	97
054 1260 E1	Fine oscillatory	0.004	131.1	173.3	0.76	1.55	2.95	0.16	1.26	0.43	0.07	2.66	939.2	11.9	949.8	28.0	974.6	25.9	96
058 1260 E2	Fine oscillatory	0.026	26.4	29.4	0.90	1.47	3.58	0.16	1.28	0.36	0.07	3.34	939.4	12.0	917.4	32.8	864.7	28.9	109
059 1260 E3	Fine oscillatory	0.022	39.9	86.1	0.47	1.26	3.34	0.13	1.76	0.53	0.07	2.83	789.2	13.9	829.4	27.7	938.9	26.6	84

Spot ID	Site	f_{206}^a	Th [ppm]	U [ppm]	Th/U ^b	Isotope ratios ^c							Ages (Ma)					Conc. ^c 6/8-7/6 (%)	
						²⁰⁷ Pb/ ²³⁵ U	1 s (%)	²⁰⁶ Pb/ ²³⁸ U	1 s (%)	Rho ^c	²⁰⁷ Pb/ ²⁰⁶ Pb	1 s (%)	²⁰⁶ Pb/ ²³⁸ U	1 s (abs)	²⁰⁷ Pb/ ²³⁵ U	1 s (abs)	²⁰⁷ Pb/ ²⁰⁶ Pb		1 s (abs)
060 1260 E4	Fine oscillatory	0.047	63.6	80.0	0.80	1.64	3.16	0.17	1.20	0.38	0.07	2.92	989.0	11.9	985.9	31.1	979.0	28.6	101
061 1260 E6	Irregular diffuse	0.006	22.1	52.3	0.43	5.75	1.82	0.35	0.73	0.40	0.12	1.67	1936.2	14.1	1938.8	35.4	1941.5	32.5	100
062 1260 E7	Fine oscillatory	0.012	45.5	92.0	0.50	1.43	3.19	0.15	1.35	0.42	0.07	2.90	908.8	12.2	899.5	28.7	876.6	25.4	104
063 260 E8	Fine oscillatory	0.006	48.3	82.7	0.59	1.56	3.04	0.16	1.25	0.41	0.07	2.77	974.2	12.2	955.8	29.1	913.7	25.3	107
064 1260 E9	Convolute	0.005	23.1	51.7	0.45	5.97	1.79	0.36	0.70	0.39	0.12	1.64	1962.0	13.8	1971.3	35.3	1981.0	32.6	99
065 1260 E10	Convolute	0.009	9.4	65.1	0.14	1.76	2.99	0.18	1.19	0.40	0.07	2.75	1042.5	12.4	1029.8	30.8	1003.1	27.6	104
066 1260 E12	Fine oscillatory	0.032	18.7	39.4	0.48	1.36	3.60	0.14	1.43	0.40	0.07	3.31	862.2	12.3	870.4	31.4	891.1	29.5	97
067 1260 F1	Fine oscillatory	0.014	32.7	53.6	0.61	1.47	3.33	0.15	1.34	0.40	0.07	3.05	928.2	12.4	917.6	30.5	892.2	27.2	104
071 1260 F2	Homogeneous	0.348	29.8	71.2	0.42	2.15	4.00	0.14	2.80	0.70	0.11	2.85	847.0	23.7	1164.2	46.5	1814.4	51.8	47
072 1260 F4	Fine oscillatory	0.020	17.3	46.0	0.38	1.74	2.84	0.17	1.11	0.39	0.07	2.61	1036.1	11.5	1023.0	29.0	995.0	26.0	104
073 1260 F5	Fine oscillatory	0.014	26.3	41.9	0.63	1.40	3.02	0.15	1.24	0.41	0.07	2.76	906.2	11.3	887.5	26.8	840.9	23.2	108
074 1260 F6	Sector	0.049	5.5	12.8	0.44	1.45	3.80	0.15	1.26	0.33	0.07	3.58	910.6	11.5	910.5	34.6	910.3	32.6	100
075 1260 F7	Fine oscillatory	0.037	56.7	84.8	0.67	1.38	3.07	0.15	1.33	0.43	0.07	2.77	885.0	11.8	879.3	27.0	865.1	23.9	102
076 1260 F8	Homogeneous	0.019	21.9	40.2	0.55	1.46	3.21	0.16	1.15	0.36	0.06	2.99	982.5	11.3	913.0	29.3	748.5	22.4	131
077 1260 F9	Fine oscillatory	0.010	75.7	172.3	0.44	1.60	2.69	0.16	1.18	0.44	0.07	2.41	959.1	11.3	971.5	26.1	999.9	24.1	96
078 1260 F10	Fine oscillatory	0.011	27.6	52.0	0.53	1.54	2.87	0.16	1.19	0.41	0.07	2.61	958.6	11.4	945.4	27.1	914.9	23.9	105
079 1260 F11	Homogeneous	0.032	46.3	61.7	0.76	1.14	3.52	0.13	1.51	0.43	0.06	3.18	772.8	11.7	770.8	27.1	765.0	24.3	101
080 1260 F12	Homogeneous	0.015	7.9	25.5	0.31	3.93	2.01	0.25	0.85	0.42	0.11	1.82	1462.4	12.4	1619.0	32.5	1829.0	33.3	80
084 1260 G3	Homogeneous	0.014	27.7	81.3	0.34	3.93	1.71	0.25	0.98	0.57	0.12	1.40	1423.2	13.9	1620.6	27.7	1887.4	26.4	75
085 1260 G5	Homogeneous	0.006	23.7	51.6	0.46	5.50	1.51	0.33	0.69	0.45	0.12	1.35	1826.2	12.5	1900.4	28.7	1982.3	26.7	92
086 1260 G6	Fine oscillatory	0.013	20.3	55.7	0.37	1.71	2.53	0.17	1.16	0.46	0.07	2.24	1014.7	11.8	1012.6	25.6	1008.1	22.6	101
087 1260 G7	Sector	0.020	13.6	21.9	0.63	1.49	2.86	0.16	1.23	0.43	0.07	2.58	944.7	11.6	926.8	26.5	884.3	22.8	107
088 1260 G8	Homogeneous	0.019	28.8	91.2	0.32	1.21	2.84	0.13	1.61	0.57	0.07	2.34	759.3	12.2	803.8	22.8	929.4	21.7	82
089 1260 G9	Fine oscillatory	0.027	16.1	28.0	0.58	1.43	2.96	0.15	1.27	0.43	0.07	2.67	919.8	11.7	903.3	26.7	863.1	23.0	107
090 1260 G10	Fine oscillatory	0.017	20.6	46.0	0.45	1.39	2.81	0.15	1.31	0.46	0.07	2.49	892.3	11.6	882.6	24.8	858.4	21.3	104
091 1260 G11	Convolute	0.017	19.2	56.5	0.34	1.25	2.89	0.13	1.62	0.56	0.07	2.39	775.2	12.6	824.1	23.8	958.3	22.9	81
092 1260 G12	Fine oscillatory	0.005	29.3	78.9	0.37	1.55	2.54	0.16	1.27	0.50	0.07	2.20	941.8	12.0	950.1	24.1	969.3	21.3	97
093 1260 H1	Fine oscillatory	0.071	81.9	173.9	0.47	1.42	2.70	0.14	1.35	0.50	0.07	2.34	869.0	11.7	896.8	24.2	965.9	22.6	90
097 1260 H2	Irregular diffuse	0.007	130.8	270.1	0.49	4.26	1.81	0.26	1.18	0.66	0.12	1.36	1466.3	17.4	1684.8	30.4	1968.7	26.8	74
098 1260 H3	Fine oscillatory	0.026	29.7	53.8	0.56	1.54	2.85	0.16	1.29	0.45	0.07	2.54	945.5	12.2	946.0	27.0	947.2	24.1	100
099 1260 H5	Fine oscillatory	0.033	337.1	196.3	1.73	1.44	2.56	0.14	1.34	0.52	0.07	2.18	849.8	11.4	906.5	23.2	1047.1	22.8	81
100 1260 H6	Fine oscillatory	0.013	15.0	39.4	0.38	1.67	2.74	0.17	1.15	0.42	0.07	2.49	1011.4	11.6	997.3	27.3	966.3	24.1	105
101 1260 H7	Fine oscillatory	0.003	123.2	163.4	0.76	1.69	2.45	0.17	1.14	0.47	0.07	2.17	995.2	11.4	1005.6	24.7	1028.4	22.3	97

Spot ID	Site	f_{206}^a	Th [ppm]	U [ppm]	Th/U ^b	Isotope ratios ^c							Ages (Ma)					Conc. ^c 6/8-7/6 (%)	
						²⁰⁷ Pb/ ²³⁵ U	1 s (%)	²⁰⁶ Pb/ ²³⁸ U	1 s (%)	Rho ^c	²⁰⁷ Pb/ ²⁰⁶ Pb	1 s (%)	²⁰⁶ Pb/ ²³⁸ U	1 s (abs)	²⁰⁷ Pb/ ²³⁵ U	1 s (abs)	²⁰⁷ Pb/ ²⁰⁶ U		1 s (abs)
102 1260 H8	Chaotic	0.003	13.2	75.9	0.17	6.17	1.53	0.37	0.67	0.44	0.12	1.38	2017.5	13.5	2000.1	30.6	1982.2	27.3	102
103 1260 H9	Fine oscillatory	0.008	32.6	54.7	0.60	5.53	1.58	0.33	0.78	0.49	0.12	1.37	1839.8	14.4	1905.9	30.1	1978.7	27.2	93
104 1260 H10	Irregular concentric	0.003	18.2	48.7	0.38	5.76	1.53	0.34	0.63	0.41	0.12	1.39	1909.6	12.0	1941.0	29.6	1974.6	27.5	97
105 1260 H11	Irregular diffuse	0.027	38.9	66.4	0.59	0.74	3.96	0.08	2.51	0.63	0.06	3.06	524.2	13.2	560.4	22.2	710.4	21.7	74
106 1260 H12	Sector	0.028	21.7	28.7	0.76	1.45	3.08	0.15	1.28	0.42	0.07	2.80	927.3	11.9	909.1	28.0	865.0	24.2	107
110 1260 I2	Fine oscillatory	0.033	12.5	22.8	0.55	1.32	4.43	0.16	1.28	0.29	0.06	4.24	972.3	12.5	854.7	37.8	560.7	23.8	173
111 1260 I3	Fine oscillatory	0.005	110.0	304.7	0.36	1.50	2.98	0.15	1.37	0.46	0.07	2.65	911.5	12.5	929.5	27.7	972.5	25.8	94
112 1260 I4	Fine oscillatory	0.045	15.3	31.5	0.49	1.47	3.91	0.15	1.39	0.36	0.07	3.65	908.8	12.6	918.1	35.9	940.6	34.3	97
113 1260 I6	Irregular concentric	0.003	26.4	63.9	0.42	5.91	1.80	0.36	0.70	0.39	0.12	1.66	1961.7	13.7	1962.0	35.3	1962.4	32.6	100
114 1260 I7	Irregular concentric	0.003	17.3	42.7	0.41	6.00	1.74	0.35	0.70	0.40	0.12	1.59	1946.1	13.6	1975.7	34.3	2006.8	31.9	97
115 1260 I8	Fine oscillatory	0.018	19.3	39.9	0.49	1.50	3.26	0.16	1.35	0.41	0.07	2.97	939.4	12.7	928.6	30.3	903.1	26.8	104
116 1260 I9	Fine oscillatory	0.009	18.9	42.7	0.45	1.61	3.18	0.16	1.36	0.43	0.07	2.87	963.0	13.1	973.5	30.9	997.4	28.6	97
117 1260 I10	Fine oscillatory	0.007	48.5	104.7	0.47	1.52	3.03	0.15	1.38	0.46	0.07	2.70	928.4	12.8	939.8	28.5	966.7	26.1	96
118 1260 I11	Irregular diffuse	0.004	30.3	61.5	0.50	5.92	1.82	0.35	0.84	0.46	0.12	1.62	1916.0	16.0	1964.1	35.8	2015.2	32.7	95
119 1260 I12	Fine oscillatory	0.025	18.7	37.9	0.50	1.48	3.47	0.15	1.39	0.40	0.07	3.18	925.0	12.8	922.8	32.0	917.5	29.2	101
123 1260 J1	Irregular diffuse	0.018	12.0	119.6	0.10	3.27	2.29	0.23	1.10	0.48	0.11	2.01	1308.3	14.4	1473.9	33.8	1721.2	34.6	76
124 1260 J2	Broad oscillatory	0.124	29.6	33.8	0.88	1.26	4.53	0.12	1.87	0.41	0.07	4.13	753.9	14.1	829.4	37.6	1037.3	42.8	73
125 1260 J3	Fine oscillatory	0.027	14.1	28.4	0.50	1.14	4.57	0.14	1.67	0.37	0.06	4.25	844.7	14.1	773.4	35.3	572.8	24.3	147
126 1260 J5	Homogeneous	0.019	13.0	30.0	0.44	4.04	2.22	0.25	0.97	0.44	0.12	2.00	1453.8	14.1	1641.7	36.4	1891.5	37.8	77
127 1260 J7	Fine oscillatory	0.017	116.8	222.9	0.53	1.40	3.24	0.14	1.56	0.48	0.07	2.84	857.9	13.4	888.4	28.8	965.2	27.4	89
128 1260 J8	Irregular diffuse	0.008	44.0	90.1	0.49	1.94	2.97	0.18	1.25	0.42	0.08	2.69	1091.1	13.7	1094.5	32.5	1101.1	29.6	99
129 1260 J9	Broad oscillatory	0.017	212.7	196.9	1.09	1.07	3.79	0.12	1.82	0.48	0.06	3.32	757.3	13.8	738.4	28.0	681.3	22.6	111
130 1260 J10	Sector	0.235	13.8	27.0	0.51	1.29	7.68	0.13	1.87	0.24	0.07	7.44	767.0	14.3	840.3	64.5	1039.3	77.4	74
131 1260 J11	Fine oscillatory	0.010	21.6	45.3	0.48	5.63	1.92	0.34	0.78	0.40	0.12	1.76	1897.0	14.7	1920.0	36.9	1944.9	34.2	98
132 1260 J12	Fine oscillatory	0.016	19.6	40.4	0.49	1.45	3.60	0.16	1.47	0.41	0.07	3.29	940.4	13.8	908.9	32.7	833.0	27.4	113
006 1260 2 A3	Fine oscillatory	0.056	10.3	16.6	0.63	1.16	4.74	0.15	1.45	0.31	0.05	4.51	927.3	13.5	783.3	37.1	392.6	17.7	236
007 1260 2 A4	Fine oscillatory	0.030	11.9	23.6	0.51	1.27	4.37	0.17	1.33	0.31	0.06	4.16	1000.7	13.4	834.3	36.5	413.5	17.2	242
008 1260 2 A5	Fine oscillatory	0.023	13.3	41.2	0.32	1.47	3.44	0.16	1.39	0.40	0.07	3.15	973.1	13.5	917.6	31.6	786.4	24.8	124
009 1260 2 A6	Homogeneous	0.031	21.4	35.4	0.61	1.25	4.04	0.16	1.37	0.34	0.06	3.80	973.4	13.3	825.2	33.3	444.5	16.9	219
010 1260 2 A7	Fine oscillatory	0.077	7.2	14.8	0.49	1.29	4.93	0.16	1.49	0.30	0.06	4.70	930.6	13.8	842.3	41.6	616.3	29.0	151
011 1260 2 A9	Broad oscillatory	0.029	12.0	24.7	0.49	1.37	4.10	0.17	1.35	0.33	0.06	3.87	1002.2	13.5	875.3	35.8	566.5	21.9	177
012 1260 2 A11	Fine oscillatory	0.042	16.8	20.6	0.82	1.13	5.31	0.16	1.42	0.27	0.05	5.12	953.7	13.5	767.5	40.8	257.5	13.2	370
013 1260 2 A12	Fine oscillatory	0.039	6.0	14.9	0.40	1.60	3.99	0.19	1.19	0.30	0.06	3.80	1119.0	13.4	971.1	38.7	649.8	24.7	172

Spot ID	Site	f_{206}^a	Th [ppm]	U [ppm]	Th/U ^b	Isotope ratios ^c						Ages (Ma)					Conc. ^c 6/8-7/6 (%)		
						²⁰⁷ Pb/ ²³⁵ U	1 s (%)	²⁰⁶ Pb/ ²³⁸ U	1 s (%)	Rho ^c	²⁰⁷ Pb/ ²⁰⁶ Pb	1 s (%)	²⁰⁶ Pb/ ²³⁸ U	1 s (abs)	²⁰⁷ Pb/ ²³⁵ U	1 s (abs)		²⁰⁷ Pb/ ²⁰⁶ U	1 s (abs)
014 1260-2 A13	Fine oscillatory	0.018	11.7	14.8	0.80	5.23	1.91	0.33	0.85	0.45	0.11	1.71	1854.1	15.8	1858.0	35.5	1862.4	31.8	100
015 1260-2 A14	Fine oscillatory	0.023	33.1	83.4	0.40	1.56	2.91	0.16	1.39	0.48	0.07	2.56	956.8	13.3	953.6	27.8	946.0	24.2	101
019 1260-2 B1	Fine oscillatory	0.040	4.4	11.3	0.39	1.42	5.47	0.19	1.07	0.20	0.05	5.36	1136.1	12.2	897.0	49.1	346.0	18.6	328
020 1260-2 B4	Broad oscillatory	0.072	179.0	134.5	1.34	0.87	3.69	0.10	2.07	0.56	0.07	3.05	588.9	12.2	637.1	23.5	812.2	24.8	73
021 1260-2 B9	Fine oscillatory	0.012	30.5	36.0	0.85	4.87	1.82	0.31	0.71	0.39	0.11	1.68	1749.8	12.4	1797.3	32.7	1852.9	31.1	94
022 1260-2 B10	Irregular diffuse	0.007	16.3	43.5	0.38	5.27	1.71	0.32	0.72	0.42	0.12	1.56	1799.6	12.9	1864.1	32.0	1936.9	30.2	93
023 1260-2 B11	Fine oscillatory	0.020	9.1	20.5	0.44	1.62	3.08	0.17	1.19	0.39	0.07	2.85	986.9	11.7	978.4	30.2	959.4	27.3	103
024 1260-2 B12	Fine oscillatory	0.033	9.0	17.8	0.51	1.27	4.16	0.16	1.29	0.31	0.06	3.96	932.2	12.0	831.2	34.6	569.8	22.5	164
025 1260-2 B13	Fine oscillatory	0.015	17.8	31.5	0.57	1.49	3.16	0.16	1.21	0.38	0.07	2.92	971.5	11.7	925.3	29.3	816.9	23.9	119
026 1260-2 B14	Fine oscillatory	0.047	16.8	37.9	0.45	0.96	4.30	0.12	1.58	0.37	0.06	4.00	757.0	11.9	684.5	29.4	452.8	18.1	167
027 1260-2 B15	Fine oscillatory	0.011	12.5	32.2	0.39	1.85	2.79	0.18	1.14	0.41	0.07	2.54	1064.4	12.2	1063.0	29.7	1060.1	27.0	100
028 1260-2 C1	Fine oscillatory	0.011	51.6	72.2	0.72	1.52	2.94	0.16	1.26	0.43	0.07	2.66	948.7	11.9	940.0	27.6	919.7	24.5	103
032 1260-2 C2	Fine oscillatory	0.010	16.6	28.1	0.59	1.99	2.97	0.19	1.22	0.41	0.08	2.70	1106.7	13.5	1110.6	32.9	1118.3	30.2	99
033 1260-2 C4	Irregular concentric	0.006	11.6	32.3	0.36	6.17	1.88	0.37	0.78	0.42	0.12	1.71	2008.5	15.7	2000.8	37.5	1992.8	34.0	101
034 1260-2 C7	Irregular concentric	0.025	97.8	83.9	1.17	1.29	3.38	0.14	1.52	0.45	0.07	3.02	852.5	13.0	843.2	28.5	818.9	24.7	104
035 1260-2 B8	Homogeneous	0.009	7.1	23.2	0.31	5.89	1.93	0.36	0.74	0.38	0.12	1.79	1999.4	14.9	1960.4	37.9	1919.5	34.3	104
036 1260-2 C11	Fine oscillatory	0.013	120.1	117.2	1.03	1.49	3.13	0.15	1.40	0.45	0.07	2.80	923.8	12.9	928.0	29.0	938.0	26.3	98
037 1260-2 C13	Broad oscillatory	0.025	152.9	91.4	1.68	4.80	1.87	0.28	0.90	0.48	0.13	1.63	1580.1	14.3	1785.6	33.3	2034.9	33.3	78
038 1260-2 C14	Fine oscillatory	0.223	17.9	40.5	0.45	1.75	3.81	0.17	1.32	0.35	0.08	3.58	991.5	13.1	1027.8	39.2	1105.9	39.6	90
039 1260-2 C15	Fine oscillatory	0.010	30.2	46.1	0.66	5.38	1.93	0.33	0.84	0.44	0.12	1.74	1843.9	15.5	1882.4	36.3	1925.2	33.4	96
040 1260-2 D2	Irregular concentric	0.015	7.4	11.9	0.62	6.11	1.93	0.37	0.69	0.36	0.12	1.80	2042.7	14.1	1991.6	38.4	1939.0	35.0	105
041 1260-2 D7	Homogeneous	0.232	35.5	66.6	0.54	1.80	3.79	0.18	1.35	0.35	0.07	3.55	1055.7	14.2	1047.1	39.7	1029.2	36.5	103
045 1260-2 D8	Homogeneous	0.014	16.7	42.0	0.40	1.55	3.21	0.16	1.36	0.42	0.07	2.91	956.8	13.0	949.8	30.5	933.6	27.2	102
046 1260-2 D9	Fine oscillatory	0.020	66.7	96.3	0.70	1.43	3.21	0.15	1.36	0.42	0.07	2.90	923.9	12.6	900.0	28.9	841.6	24.4	110
047 1260-2 D10	Homogeneous	0.016	58.3	82.1	0.71	1.59	3.13	0.17	1.28	0.41	0.07	2.86	993.3	12.7	966.9	30.3	907.5	26.0	109
048 1260-2 D12	Fine oscillatory	0.036	38.3	65.3	0.59	1.52	3.28	0.16	1.30	0.39	0.07	3.02	967.8	12.5	937.1	30.8	865.7	26.1	112
049 1260-2 D14	Homogeneous	0.012	16.1	47.7	0.34	1.60	3.19	0.17	1.26	0.39	0.07	2.93	991.2	12.5	968.9	30.9	918.7	26.9	108
050 1260-2 D15	Homogeneous	0.012	11.4	28.4	0.41	6.12	1.85	0.37	0.69	0.37	0.12	1.71	2009.9	13.9	1993.1	36.8	1975.8	33.9	102
051 1260-2 E1	Fine oscillatory	0.016	26.3	35.3	0.75	1.49	3.56	0.17	1.24	0.35	0.06	3.34	1024.8	12.7	928.2	33.1	705.4	23.6	145
052 1260-2 E2	Convolute	0.004	14.8	49.2	0.30	5.72	1.83	0.35	0.71	0.39	0.12	1.68	1922.9	13.7	1934.7	35.4	1947.3	32.8	99
053 1260-2 E6	Irregular concentric	0.027	15.2	31.5	0.49	6.08	1.86	0.37	0.75	0.40	0.12	1.70	2024.1	15.2	1987.0	36.9	1948.6	33.1	104
054 1260-2 E7	Fine oscillatory	0.016	28.8	42.0	0.69	1.53	3.34	0.17	1.30	0.39	0.07	3.08	990.2	12.9	942.0	31.5	831.0	25.6	119
058 1260-2 E10	Fine oscillatory	0.013	13.2	23.4	0.57	1.62	3.05	0.17	1.31	0.43	0.07	2.76	991.0	12.9	978.0	29.8	948.9	26.2	104

Spot ID	Site	f_{206}^a	Th [ppm]	U [ppm]	Th/U ^b	Isotope ratios ^c							Ages (Ma)				Conc. ^c 6/8-7/6 (%)		
						²⁰⁷ Pb/ ²³⁵ U	1 s (%)	²⁰⁶ Pb/ ²³⁸ U	1 s (%)	Rho ^c	²⁰⁷ Pb/ ²⁰⁶ Pb	1 s (%)	²⁰⁶ Pb/ ²³⁸ U	1 s (abs)	²⁰⁷ Pb/ ²³⁵ U	1 s (abs)		²⁰⁷ Pb/ ²⁰⁶ U	1 s (abs)
059 1260-2 E11	Fine oscillatory	0.021	30.2	39.6	0.77	3.94	2.07	0.26	1.03	0.50	0.11	1.79	1471.2	15.2	1621.3	33.6	1822.0	32.7	81
060 1260-2 E15	Fine oscillatory	0.033	47.9	67.2	0.72	1.43	3.31	0.15	1.39	0.42	0.07	3.01	918.8	12.8	901.7	29.9	860.1	25.9	107
061 1260-2 F2	Fine oscillatory	0.026	28.4	68.6	0.42	1.55	3.12	0.16	1.39	0.44	0.07	2.79	948.1	13.2	948.7	29.6	950.1	26.6	100
062 1260-2 F5	Fine oscillatory	0.190	20.1	37.0	0.55	4.99	2.30	0.30	1.15	0.50	0.12	1.99	1681.2	19.3	1817.3	41.7	1977.1	39.3	85
063 1260-2 F9	Irregular concentric	0.006	12.5	42.2	0.30	6.10	1.79	0.36	0.74	0.41	0.12	1.63	1995.7	14.7	1990.6	35.7	1985.2	32.5	101
064 1260-2 F10	Fine oscillatory	0.022	9.1	24.6	0.37	1.44	3.65	0.16	1.41	0.39	0.06	3.37	965.8	13.6	907.0	33.1	766.5	25.8	126
065 1260-2 F11	Fine oscillatory	0.017	11.8	33.6	0.35	1.71	3.09	0.17	1.26	0.41	0.07	2.82	1032.7	13.0	1012.7	31.3	969.5	27.3	107
066 1260-2 F12	Broad oscillatory	0.027	88.8	119.3	0.75	1.43	3.18	0.15	1.40	0.44	0.07	2.85	922.9	12.9	899.8	28.6	843.7	24.0	109
067 1260-2 F13	Fine oscillatory	0.022	7.8	15.9	0.49	1.52	3.60	0.17	1.32	0.37	0.06	3.35	1018.5	13.4	939.2	33.8	757.6	25.4	134
071 1260-2 G3	Broad oscillatory	0.019	27.7	29.0	0.96	1.67	3.09	0.17	1.37	0.44	0.07	2.77	1005.9	13.8	997.8	30.9	980.0	27.2	103
072 1260-2 F4	Irregular diffuse	0.029	27.2	21.0	1.31	1.43	3.58	0.15	1.44	0.40	0.07	3.28	906.3	13.1	901.9	32.3	891.2	29.2	102
073 1260-2 G5	Fine oscillatory	0.013	67.0	61.2	1.10	1.60	3.09	0.17	1.35	0.44	0.07	2.77	988.9	13.4	970.4	29.9	928.6	25.7	106
074 1260-2 G6	Fine oscillatory	0.016	17.6	23.6	0.75	1.76	3.08	0.17	1.30	0.42	0.07	2.79	1039.4	13.5	1029.4	31.7	1008.1	28.1	103
075 1260-2 G7	Fine oscillatory	0.012	16.5	113.4	0.15	2.90	2.24	0.21	1.15	0.51	0.10	1.92	1242.1	14.3	1381.3	30.9	1603.5	30.8	77
076 1260-2 G11	Fine oscillatory	0.007	28.2	53.3	0.53	1.67	2.96	0.17	1.36	0.46	0.07	2.63	1000.2	13.6	998.5	29.5	994.8	26.1	101
077 1260-2 G12	Irregular concentric	0.012	5.6	15.7	0.36	5.81	1.90	0.36	0.79	0.42	0.12	1.73	1972.5	15.6	1947.3	37.0	1920.5	33.1	103
078 1260-2 G13	Fine oscillatory	0.012	20.5	38.7	0.53	1.86	2.86	0.18	1.20	0.42	0.07	2.60	1085.5	13.0	1066.0	30.5	1026.3	26.7	106
079 1260-2 G14	Homogeneous	0.071	137.7	84.9	1.63	1.34	3.32	0.14	1.57	0.47	0.07	2.93	852.3	13.4	862.9	28.7	890.1	26.0	96
080 1260-2 G15	Fine oscillatory	0.023	14.1	29.9	0.47	1.05	3.87	0.12	1.85	0.48	0.06	3.40	738.8	13.7	731.3	28.3	708.4	24.1	104
084 1260-2 H1	Fine oscillatory	0.032	18.3	30.6	0.60	1.53	3.30	0.16	1.20	0.36	0.07	3.08	984.0	11.8	944.0	31.2	852.0	26.2	115
085 1260-2 H3	Homogeneous	0.047	37.7	42.6	0.89	1.19	3.68	0.14	1.38	0.38	0.06	3.41	843.5	11.6	796.6	29.3	667.5	22.7	126
086 1260-2 H4	Irregular concentric	0.057	6.9	9.2	0.75	1.20	5.88	0.16	1.26	0.22	0.05	5.74	965.4	12.2	801.2	47.1	368.4	21.1	262
087 1260-2 H5	Broad oscillatory	0.012	27.8	28.1	1.00	1.72	3.01	0.17	1.13	0.38	0.07	2.78	1039.3	11.8	1016.8	30.6	968.6	27.0	107
088 1260-2 H7	Homogeneous	0.007	43.1	88.1	0.49	1.71	2.89	0.18	1.13	0.39	0.07	2.66	1043.7	11.8	1012.5	29.2	945.6	25.1	110
089 1260-2 H8	Homogeneous	0.025	22.5	34.8	0.65	1.34	3.74	0.16	1.22	0.33	0.06	3.54	960.1	11.7	864.8	32.4	627.9	22.2	153
090 1260-2 H9	-	0.020	14.3	21.7	0.66	1.63	3.29	0.17	1.18	0.36	0.07	3.07	1001.7	11.8	981.4	32.3	936.2	28.7	107
091 1260-2 H14	Homogeneous	0.031	10.3	15.2	0.68	1.58	3.73	0.17	1.16	0.31	0.07	3.54	1027.4	11.9	961.8	35.9	814.6	28.9	126
092 1260-2 H6	Fine oscillatory	0.016	52.5	32.8	1.61	1.38	3.51	0.16	1.24	0.35	0.06	3.28	949.0	11.8	880.4	30.9	711.6	23.4	133
093 1260-2 H10	Homogeneous	0.042	7.5	19.9	0.38	1.40	4.47	0.18	1.12	0.25	0.06	4.33	1057.9	11.8	890.7	39.9	495.4	21.5	214
097 1260-2 I1	Fine oscillatory	0.009	36.4	75.1	0.49	1.57	2.93	0.16	1.27	0.43	0.07	2.65	972.0	12.3	956.6	28.1	921.3	24.4	106
098 1260-2 J4	Fine oscillatory	0.002	33.1	69.7	0.48	6.31	1.67	0.37	0.62	0.37	0.12	1.55	2020.8	12.6	2020.5	33.7	2020.1	31.3	100
099 1260-2 J5	Irregular concentric	0.026	3.9	12.4	0.32	1.68	3.17	0.17	1.09	0.34	0.07	2.98	1009.1	11.0	1000.1	31.7	980.5	29.2	103
100 1260-2 J8	Homogeneous	0.008	5.7	11.0	0.53	16.49	1.12	0.57	0.48	0.43	0.21	1.01	2907.3	14.1	2905.6	32.6	2904.4	29.4	100

Spot ID	Site	f_{206}^a	Th [ppm]	U [ppm]	Th/U ^b	Isotope ratios ^c							Ages (Ma)					Conc. ^c 6/8-7/6 (%)	
						²⁰⁷ Pb/ ²³⁵ U	1 s (%)	²⁰⁶ Pb/ ²³⁸ U	1 s (%)	Rho ^c	²⁰⁷ Pb/ ²⁰⁶ Pb	1 s (%)	²⁰⁶ Pb/ ²³⁸ U	1 s (abs)	²⁰⁷ Pb/ ²³⁵ U	1 s (abs)	²⁰⁷ Pb/ ²⁰⁶ U		1 s (abs)
101 1260-2 J10	Fine oscillatory	0.006	9.9	27.4	0.36	5.64	1.75	0.35	0.68	0.39	0.12	1.62	1916.8	13.0	1922.9	33.7	1929.6	31.2	99
102 1260-2 J11	Broad oscillatory	0.125	29.8	34.9	0.86	1.45	3.77	0.16	1.17	0.31	0.07	3.58	939.9	11.0	910.4	34.3	839.6	30.1	112
103 1260-2 J12	Fine oscillatory	0.013	11.4	28.3	0.41	1.93	2.79	0.18	1.02	0.37	0.08	2.60	1091.1	11.2	1089.9	30.5	1087.4	28.3	100
104 1260-2 J15	Homogeneous	0.021	27.5	41.4	0.67	1.18	3.61	0.13	1.38	0.38	0.07	3.33	793.6	11.0	793.0	28.6	791.3	26.3	100
105 1260-2 F15	Irregular diffuse	0.011	20.1	29.4	0.69	5.85	1.78	0.36	0.65	0.36	0.12	1.66	1998.9	12.9	1954.5	34.9	1907.7	31.7	105
106 1260-2 F7	Homogeneous	0.050	3.3	8.8	0.37	1.35	4.62	0.14	1.32	0.29	0.07	4.43	862.0	11.4	869.7	40.2	889.2	39.4	97
Sample SOS-1274																			
006 1274-2 A3	Chaotic	0.010	20	45	0.46	4.56	1.92	0.29	0.92	0.48	0.12	1.68	1627.4	14.9	1741.2	33.4	1880.7	31.6	87
007 1274-2 A4	Homogeneous	0.015	79	59	1.35	1.77	2.92	0.17	1.30	0.45	0.07	2.61	1020.2	13.3	1032.7	30.2	1059.3	27.7	96
008 1274-2 A6	Fine oscillatory	0.012	18	59	0.31	3.50	2.14	0.23	1.18	0.55	0.11	1.79	1345.8	15.9	1526.5	32.7	1786.9	31.9	75
009 1274-2 A10	Homogeneous	0.011	4	23	0.18	1.63	3.03	0.16	1.35	0.45	0.07	2.71	974.8	13.1	980.3	29.7	992.5	26.9	98
010 1274-2 B10	Fine oscillatory	0.206	109	195	0.56	0.97	4.11	0.10	2.35	0.57	0.07	3.37	633.1	14.9	688.4	28.3	873.9	29.4	72
011 1274-2 B9	Sector	0.009	48	39	1.23	1.58	3.06	0.16	1.32	0.43	0.07	2.77	982.1	12.9	961.3	29.4	913.9	25.3	107
012 1274-2 B8	Fine oscillatory	0.037	33	54	0.61	1.49	3.17	0.15	1.50	0.47	0.07	2.79	911.9	13.7	926.0	29.3	959.7	26.8	95
013 1274-2 B7	Fine oscillatory	0.008	20	39	0.51	1.65	2.97	0.17	1.32	0.44	0.07	2.66	1000.3	13.2	988.8	29.4	963.4	25.6	104
014 1274-2 B6	Irregular concentric	0.014	32	76	0.42	1.22	3.32	0.13	1.79	0.54	0.07	2.80	777.1	13.9	811.5	27.0	906.9	25.4	86
015 1274-2 B4	Irregular diffuse	0.009	48	60	0.80	5.92	1.71	0.35	0.71	0.42	0.12	1.55	1925.5	13.7	1963.5	33.5	2003.8	31.1	96
019 1274-2 B3	Irregular concentric	0.014	14	37	0.37	5.77	1.76	0.35	0.76	0.43	0.12	1.59	1934.6	14.7	1942.1	34.2	1950.2	31.0	99
020 1274-2 B2	Fine oscillatory	0.005	13	27	0.47	6.01	1.75	0.36	0.74	0.42	0.12	1.58	1988.8	14.7	1977.8	34.5	1966.3	31.1	101
021 1274-2 C2	Irregular concentric	0.008	7	29	0.24	6.16	1.74	0.36	0.73	0.42	0.12	1.58	2000.0	14.5	1998.4	34.8	1996.7	31.6	100
022 1274-2 C3	Broad oscillatory	0.028	3	10	0.29	1.80	3.13	0.18	1.29	0.41	0.07	2.85	1054.7	13.6	1044.6	32.7	1023.7	29.2	103
023 1274-2 C4	Fine oscillatory	0.039	17	92	0.19	1.29	3.35	0.14	1.68	0.50	0.07	2.90	835.4	14.0	840.2	28.1	853.2	24.7	98
024 1274-2 C5	Fine oscillatory	0.029	21	55	0.38	3.54	2.05	0.22	1.14	0.56	0.12	1.70	1279.5	14.6	1535.5	31.5	1908.4	32.5	67
025 1274-2 C7	Homogeneous	0.006	9	22	0.42	6.24	1.79	0.37	0.75	0.42	0.12	1.62	2035.2	15.3	2010.2	35.9	1984.7	32.1	103
026 1274-2 D10	Fine oscillatory	0.005	13	27	0.49	6.26	1.74	0.38	0.69	0.40	0.12	1.59	2075.5	14.4	2012.8	34.9	1949.2	31.0	106
027 1274-2 D9	Homogeneous	0.006	9	19	0.46	6.25	1.79	0.37	0.72	0.40	0.12	1.64	2028.0	14.6	2011.8	36.1	1995.1	32.7	102
028 1274-2 D8	Fine oscillatory	0.097	6	23	0.26	1.65	3.74	0.17	1.36	0.36	0.07	3.48	997.1	13.6	990.7	37.0	976.7	34.0	102
032 1274-2 D7	Fine oscillatory	0.024	21	75	0.28	4.63	1.87	0.28	1.00	0.53	0.12	1.59	1571.5	15.7	1755.6	32.9	1982.2	31.5	79
033 1274-2 D6	Fine oscillatory	0.110	55	82	0.68	1.50	3.70	0.15	1.57	0.42	0.07	3.35	926.1	14.5	929.4	34.4	937.3	31.4	99
034 1274-2 D5	Irregular diffuse	0.010	112	102	1.10	4.11	1.95	0.26	1.00	0.51	0.12	1.67	1484.7	14.8	1656.6	32.3	1882.0	31.5	79
035 1274-2 D3	Homogeneous	0.022	11	19	0.61	1.50	3.97	0.17	1.49	0.37	0.06	3.68	1022.0	15.2	931.7	36.9	723.5	26.6	141
036 1274-2 D2	Homogeneous	0.009	38	43	0.90	1.65	3.12	0.16	1.53	0.49	0.07	2.72	977.6	14.9	988.0	30.8	1011.3	27.5	97
037 1274-2 E2	Fine oscillatory	0.003	14	32	0.44	6.36	1.82	0.37	0.79	0.44	0.12	1.64	2051.8	16.3	2027.3	36.8	2002.4	32.7	102

Spot ID	Site	f_{206}^a	Th [ppm]	U [ppm]	Th/U ^b	Isotope ratios ^c						Ages (Ma)				Conc. ^c 6/8-7/6 (%)			
						²⁰⁷ Pb/ ²³⁵ U	1 s (%)	²⁰⁶ Pb/ ²³⁸ U	1 s (%)	Rho ^c	²⁰⁷ Pb/ ²⁰⁶ Pb	1 s (%)	²⁰⁶ Pb/ ²³⁸ U	1 s (abs)	²⁰⁷ Pb/ ²³⁵ U		1 s (abs)	²⁰⁷ Pb/ ²⁰⁶ U	1 s (abs)
038 1274-2 E3	Fine oscillatory	0.018	21	27	0.78	1.79	3.25	0.18	1.39	0.43	0.07	2.94	1048.9	14.6	1041.0	33.9	1024.6	30.1	102
039 1274-2 E4	Irregular diffuse	0.012	9	17	0.52	5.41	1.94	0.33	0.92	0.47	0.12	1.71	1819.8	16.7	1887.2	36.6	1962.2	33.5	93
040 1274-2 E6	Homogeneous	0.030	6	10	0.54	2.03	3.70	0.20	1.26	0.34	0.07	3.48	1181.6	14.9	1127.1	41.7	1023.7	35.6	115
041 1274-2 E7	Fine oscillatory	0.074	116	97	1.21	1.03	4.00	0.11	2.52	0.63	0.07	3.10	658.2	16.6	721.4	28.8	923.2	28.6	71
045 1274-2 E8	Fine oscillatory	0.014	31	102	0.31	1.46	3.16	0.15	1.46	0.46	0.07	2.81	896.5	13.1	913.3	28.9	954.0	26.8	94
046 1274-2 E9	Fine oscillatory	0.039	169	215	0.79	1.14	3.54	0.12	1.85	0.52	0.07	3.01	717.3	13.3	770.8	27.3	929.2	28.0	77
047 1274-2 E10	Broad oscillatory	0.012	13	22	0.58	1.65	3.18	0.17	1.31	0.41	0.07	2.90	999.9	13.1	990.9	31.5	971.1	28.2	103
048 1274-2 F10	Fine oscillatory	0.007	26	52	0.51	1.64	3.09	0.17	1.31	0.42	0.07	2.80	1006.5	13.2	985.9	30.5	940.5	26.3	107
049 1274-2 F9	Homogeneous	0.007	11	20	0.54	6.26	1.81	0.37	0.69	0.38	0.12	1.68	2051.2	14.1	2012.5	36.5	1972.9	33.1	104
050 1274-2 F8	Fine oscillatory	0.024	19	25	0.74	1.78	3.19	0.18	1.31	0.41	0.07	2.91	1041.5	13.6	1036.5	33.1	1026.0	29.8	102
051 1274-2 F6	Convolute	0.023	20	40	0.51	1.81	3.16	0.18	1.24	0.39	0.07	2.90	1046.7	13.0	1050.8	33.2	1059.5	30.8	99
052 1274-2 F3	Chaotic	0.004	11	27	0.43	6.30	1.80	0.37	0.65	0.36	0.12	1.67	2050.5	13.3	2018.3	36.2	1985.5	33.2	103
053 1274-2 F2	Irregular concentric	0.007	13	23	0.55	6.00	1.85	0.36	0.68	0.37	0.12	1.72	1992.6	13.6	1975.3	36.5	1957.3	33.6	102
054 1274-2 F1	Homogeneous	0.006	18	67	0.27	5.11	1.94	0.32	0.91	0.47	0.11	1.71	1805.7	16.5	1837.4	35.6	1873.6	32.0	96
058 1274-2 G1	Homogeneous	0.005	23	25	0.92	5.87	1.87	0.35	0.75	0.40	0.12	1.71	1936.1	14.4	1956.3	36.5	1977.6	33.8	98
059 1274-2 G3	Irregular diffuse	0.009	32	84	0.39	5.14	1.93	0.31	0.70	0.36	0.12	1.80	1748.9	12.3	1843.4	35.6	1951.9	35.1	90
060 1274-2 G4	Fine oscillatory	0.003	12	27	0.45	6.34	1.78	0.37	0.72	0.40	0.12	1.63	2049.0	14.8	2024.0	36.1	1998.6	32.6	103
061 1274-2 G6	Irregular diffuse	0.009	13	30	0.44	5.65	1.86	0.34	0.69	0.37	0.12	1.73	1883.3	12.9	1924.3	35.8	1968.8	34.0	96
062 1274-2 G7	Fine oscillatory	0.010	29	65	0.45	18.06	19.61	0.75	3.48	0.18	0.18	19.30	3595.9	125.1	2992.9	587.1	2609.7	503.8	138
063 1274-2 G8	Homogeneous	0.007	47	86	0.56	1.52	3.10	0.16	1.33	0.43	0.07	2.80	944.0	12.5	940.0	29.2	930.7	26.1	101
064 1274-2 G9	Irregular concentric	0.108	73	75	0.98	1.17	3.98	0.13	1.55	0.39	0.07	3.67	782.1	12.1	788.7	31.4	807.3	29.6	97
065 1274-2 G10	Broad oscillatory	0.005	13	25	0.54	6.24	1.87	0.37	0.74	0.40	0.12	1.71	2035.3	15.1	2009.6	37.5	1983.4	34.0	103
066 1274-2 H10	Homogeneous	0.004	11	27	0.40	6.20	1.79	0.37	0.67	0.37	0.12	1.66	2020.8	13.5	2003.8	35.8	1986.3	33.0	102
067 1274-2 H9	Homogeneous	0.005	12	26	0.44	6.72	1.84	0.40	0.66	0.36	0.12	1.71	2170.8	14.3	2075.1	38.1	1981.4	34.0	110
071 1274-2 H8	Irregular concentric	0.023	15	21	0.72	6.09	2.05	0.35	0.83	0.40	0.12	1.87	1956.2	16.2	1988.6	40.7	2022.5	37.8	97
072 1274-2 H7	Homogeneous	0.008	20	31	0.65	1.96	3.04	0.19	1.19	0.39	0.08	2.79	1115.4	13.2	1102.4	33.5	1076.9	30.1	104
073 1274-2 H6	Fine oscillatory	0.121	17	31	0.56	6.60	2.03	0.39	0.76	0.37	0.12	1.88	2103.1	16.0	2058.8	41.8	2014.8	38.0	104
074 1274-2 H5	Irregular concentric	0.036	32	49	0.66	3.45	2.23	0.22	1.24	0.56	0.12	1.85	1256.3	15.6	1515.7	33.8	1899.5	35.2	66
075 1274-2 H4	Homogeneous	0.019	21	14	1.54	1.61	3.65	0.17	1.34	0.37	0.07	3.40	998.3	13.4	975.2	35.6	923.4	31.4	108
076 1274-2 H3	Irregular concentric	0.026	37	59	0.63	1.58	3.31	0.16	1.46	0.44	0.07	2.97	944.0	13.8	962.3	31.9	1004.3	29.9	94
077 1274-2 H2	Homogeneous	0.004	9	24	0.39	6.04	1.89	0.35	0.79	0.42	0.12	1.71	1937.7	15.3	1981.9	37.4	2028.2	34.7	96
078 1274-2 I5	Fine oscillatory	0.020	6	12	0.52	1.85	3.34	0.17	1.31	0.39	0.08	3.08	1033.0	13.5	1062.2	35.5	1122.6	34.6	92
079 1274-2 I6	Irregular concentric	0.016	11	29	0.40	5.61	2.02	0.34	0.76	0.38	0.12	1.87	1890.8	14.4	1916.9	38.8	1945.3	36.4	97

Spot ID	Site	f_{206}^a	Th [ppm]	U [ppm]	Th/U ^b	Isotope ratios ^c						Ages (Ma)						Conc. ^e 6/8-7/6 (%)	
						²⁰⁷ Pb/ ²³⁵ U	1 s (%)	²⁰⁶ Pb/ ²³⁸ U	1 s (%)	Rho ^c	²⁰⁷ Pb/ ²⁰⁶ Pb	1 s (%)	²⁰⁶ Pb/ ²³⁸ U	1 s (abs)	²⁰⁷ Pb/ ²³⁵ U	1 s (abs)	²⁰⁷ Pb/ ²⁰⁶ Pb		1 s (abs)
080 1274-2 J7	Irregular concentric	0.015	64	144	0.45	4.12	2.10	0.26	0.96	0.46	0.12	1.87	1477.7	14.1	1658.7	34.8	1896.1	35.4	78
084 1274-2 J10	Fine oscillatory	0.006	36	60	0.61	1.64	3.14	0.17	1.37	0.44	0.07	2.83	991.9	13.6	985.2	31.0	970.3	27.5	102
085 1274-2 J10	Homogeneous	0.053	5	15	0.34	1.68	3.62	0.17	1.29	0.36	0.07	3.38	1024.7	13.2	999.2	36.2	943.6	31.9	109
086 1274-2 J8	Irregular diffuse	0.031	8	12	0.64	1.53	3.59	0.15	1.47	0.41	0.07	3.27	924.8	13.6	943.5	33.8	987.6	32.3	94
087 1274-2 J9	Homogeneous	0.005	5	81	0.07	4.85	1.96	0.31	0.78	0.40	0.11	1.80	1728.4	13.5	1792.9	35.1	1868.8	33.6	92
088 1274-2 J6	Irregular concentric	0.048	29	24	1.21	1.38	4.18	0.16	1.39	0.33	0.06	3.94	952.2	13.2	878.5	36.7	697.0	27.5	137
089 1274-2 J5	Homogeneous	0.019	24	25	0.99	1.65	3.38	0.18	1.25	0.37	0.07	3.14	1046.0	13.1	991.3	33.6	872.0	27.4	120
090 1274-2 J4	Irregular concentric	0.166	21	43	0.49	3.20	2.64	0.20	1.15	0.43	0.11	2.38	1191.7	13.7	1457.6	38.5	1870.0	44.5	64
091 1274-2 J3	Homogeneous	0.011	16	37	0.45	1.52	3.31	0.16	1.41	0.43	0.07	2.99	936.0	13.2	937.9	31.0	942.4	28.2	99
092 1274-2 J1	Homogeneous	0.009	9	22	0.40	4.94	2.03	0.31	0.82	0.40	0.12	1.86	1737.6	14.3	1809.1	36.8	1892.6	35.2	92
093 1274-2 G2	Chaotic	0.046	30	53	0.57	1.23	3.70	0.13	1.70	0.46	0.07	3.28	791.1	13.5	812.8	30.0	872.9	28.6	91

Strikethrough analytical points are outside the 10% discordance filter.

Internal structures following Corfu (2003).

^a Fraction of the non-radiogenic ²⁰⁶Pb in the analyzed spot, where $f_{206} = (^{206}\text{Pb}/^{204}\text{Pb})_{\text{common}} / (^{206}\text{Pb}/^{204}\text{Pb})_{\text{sample}}$.

^b Th/U ratios and Pb, Th and U concentrations are calculated relative to GJ-1 reference zircon.

^c Error correlation defined as the quotient of the propagated errors of ²⁰⁶Pb/²³⁸U and ²⁰⁷Pb/²³⁵U ratios.

^d Corrected for mass-bias by normalizing to GJ-1 reference zircon and common Pb using the model of Stacey and Kramers (1975).

^e Concordance degree = $100 \times (^{206}\text{Pb}/^{238}\text{U} \text{ age}) / (^{207}\text{Pb}/^{206}\text{Pb} \text{ age})$ according to Spencer et al. (2016).

References

Corfu, F., 2003. Atlas of zircon textures. *Reviews in Mineralogy and Geochemistry* 53, 469–500.

Spencer, C.J., Kirkland, C.L., Taylor, R.J.M., 2016. Strategies towards statistically robust interpretations of in situ U-Pb zircon geochronology. *Geoscience Frontiers* 7, 581–589.

Stacey, J.S., Kramers, J.D., 1975. Approximation of terrestrial lead isotope evolution by a two-stage model. *Earth and Planetary Science Letters* 26, 207–221.

Supplementary Table S3- Lu-Hf data for detrital zircon grains from quartzite samples of the Macururé Domain.

Spot ID	$^{176}\text{Hf}/^{177}\text{Hf}$	2σ	$^{176}\text{Lu}/^{177}\text{Hf}$	2σ	$^{176}\text{Yb}/^{177}\text{Hf}$	2σ	$\epsilon\text{Hf}(0)$	U-Pb age (Ma)	$^{176}\text{Hf}/^{177}\text{Hf}(0)$	$\epsilon\text{Hf}(0)$	2σ	T_{DM}^c (Ga)
<i>Sample SOS-1260</i>												
004 1260-1 B12	0.281446	0.000040	0.000263	0.000001	0.011149	0.000086	-47.3	1972 ± 34	0.281436	-3.1	1.4	2.8
005 1260-1 B7	0.282266	0.000043	0.000773	0.000025	0.031402	0.000904	-18.4	900 ± 15	0.282253	1.3	1.5	1.7
006 1260-1 C2	0.281900	0.000053	0.000935	0.000106	0.042831	0.003879	-31.3	964 ± 15	0.281883	-10.3	1.9	2.4
007 1260-1 D6	0.282225	0.000065	0.001193	0.000137	0.053339	0.004737	-19.8	944 ± 12	0.282204	0.6	2.3	1.7
008 1260-1 D7	0.282185	0.000056	0.000706	0.000068	0.031035	0.001953	-21.2	978 ± 12	0.282172	0.2	2.0	1.8
009 1260-1 D8	0.282191	0.000050	0.000742	0.000080	0.033138	0.002768	-21.0	909 ± 12	0.282178	-1.1	1.8	1.8
010 1260-1 D9	0.281475	0.000040	0.000514	0.000037	0.022012	0.001124	-46.3	1970 ± 33	0.281456	-2.5	1.4	2.7
011 1260-1 D11	0.282238	0.000050	0.001121	0.000072	0.050942	0.002597	-19.3	786 ± 12	0.282221	-2.4	1.8	1.8
012 1260-1 D12	0.282196	0.000062	0.000533	0.000022	0.019458	0.000614	-20.8	996 ± 12	0.282186	1.1	2.2	1.7
013 1260-1 E12	0.282345	0.000179	0.000760	0.000054	0.034162	0.001490	-15.5	862 ± 12	0.282333	3.3	6.4	1.5
017 1260-1 E1	0.282265	0.000056	0.000377	0.000027	0.030257	0.001156	-18.4	939 ± 12	0.282258	2.4	2.0	1.6
018 1260-1 E6	0.281480	0.000056	0.000189	0.000014	0.016834	0.000372	-46.1	1942 ± 33	0.281473	-2.5	2.0	2.7
019 1260-1 E7	0.282294	0.000075	0.000526	0.000102	0.043589	0.003189	-17.3	909 ± 12	0.282285	2.7	2.7	1.6
020 1260-1 E9	0.281428	0.000093	0.000208	0.000036	0.018857	0.001137	-48.0	1981 ± 33	0.281420	-3.5	3.3	2.8
021 1260-1 E10	0.282370	0.000073	0.000394	0.000190	0.033285	0.005802	-14.7	1042 ± 12	0.282362	8.4	2.6	1.3
022 1260-1 F11	0.282153	0.000083	0.000229	0.000042	0.020485	0.001279	-22.4	773 ± 12	0.282150	-5.2	3.0	2.0
023 1260-1 F10	0.282236	0.000064	0.000215	0.000005	0.019182	0.000113	-19.4	959 ± 11	0.282232	1.9	2.3	1.7
024 1260-1 F9	0.282225	0.000049	0.000283	0.000040	0.025623	0.001245	-19.8	959 ± 11	0.282220	1.5	1.7	1.7
025 1260-1 F4	0.282361	0.000060	0.000219	0.000030	0.017971	0.000809	-15.0	1036 ± 12	0.282357	8.1	2.1	1.3
026 1260-1 F1	0.281829	0.000712	0.000403	0.000177	0.046069	0.011053	-33.8	928 ± 12	0.281822	-13.3	25.4	2.6
034 1260-1 G6	0.282377	0.000058	0.000583	0.000045	0.026617	0.001198	-14.4	1015 ± 12	0.282365	7.9	2.1	1.3
035 1260-1 G10	0.282280	0.000040	0.000664	0.000035	0.032862	0.000857	-17.9	892 ± 12	0.282269	1.7	1.4	1.6
036 1260-1 G12	0.282199	0.000063	0.000909	0.000208	0.055295	0.009440	-20.7	942 ± 12	0.282183	-0.2	2.3	1.8
037 1260-1 H10	0.281417	0.000049	0.000356	0.000012	0.018884	0.000398	-48.4	1975 ± 27	0.281403	-4.2	1.8	2.8
038 1260-1 H8	0.281448	0.000059	0.001028	0.000100	0.054502	0.004542	-47.3	1982 ± 27	0.281409	-3.9	2.1	2.8
039 1260-1 H7	0.282289	0.000057	0.000553	0.000064	0.025958	0.001860	-17.5	995 ± 11	0.282279	4.4	2.0	1.5
040 1260-1 H6	0.282352	0.000046	0.000843	0.000082	0.042885	0.002436	-15.3	1011 ± 12	0.282336	6.8	1.7	1.4
041 1260-1 H3	0.282130	0.000060	0.000797	0.000035	0.042882	0.002070	-23.2	945 ± 12	0.282116	-2.5	2.2	1.9
042 1260-1 I6	0.281398	0.000059	0.000399	0.000033	0.022165	0.001292	-49.0	1962 ± 33	0.281383	-5.3	2.1	2.9
043 1260-1 I7	0.281465	0.000042	0.000326	0.000010	0.017269	0.000252	-46.7	2007 ± 32	0.281453	-1.7	1.5	2.7
048 1260-1 I9	0.282208	0.000059	0.000479	0.000018	0.025547	0.000562	-20.4	963 ± 13	0.282200	0.9	2.1	1.7
049 1260-1 I10	0.282221	0.000043	0.000716	0.000039	0.039983	0.001970	-19.9	928 ± 13	0.282209	0.4	1.5	1.7

Spot ID	$^{176}\text{Hf}/^{177}\text{Hf}$	2σ	$^{176}\text{Lu}/^{177}\text{Hf}$	2σ	$^{176}\text{Yb}/^{177}\text{Hf}$	2σ	$\epsilon\text{Hf}(t)$	U-Pb age (Ma)	$^{176}\text{Hf}/^{177}\text{Hf}(t)$	$\epsilon\text{Hf}(t)$	2σ	T_{DM}^{C} (Ga)
050 1260-1 I11	0.281472	0.000055	0.000459	0.000013	0.024750	0.000465	-46.4	2015 ± 33	0.281455	-1.5	2.0	2.7
051 1260-1 I12	0.282243	0.000049	0.000581	0.000045	0.029872	0.001876	-19.2	925 ± 13	0.282233	1.2	1.8	1.7
052 1260-1 J11	0.281428	0.000047	0.000408	0.000014	0.021393	0.000526	-48.0	1945 ± 34	0.281413	-4.6	1.7	2.8
053 1260-1 J8	0.281855	0.000060	0.000662	0.000141	0.036393	0.006614	-32.9	1091 ± 14	0.281841	-9.0	2.1	2.4
054 1260-1 I3	0.282272	0.000051	0.000571	0.000093	0.031215	0.004080	-18.1	911 ± 12	0.282263	1.9	1.8	1.6
055 1260-1 H9	0.281452	0.000047	0.000366	0.000009	0.019518	0.000482	-47.1	1979 ± 27	0.281438	-2.9	1.7	2.8
056 1260-1 H12	0.282196	0.000056	0.000753	0.000340	0.043680	0.016080	-20.8	927 ± 12	0.282183	-0.5	2.0	1.8
057 1260-1 G5	0.281488	0.000041	0.000404	0.000036	0.021891	0.001613	-45.9	1982 ± 27	0.281472	-1.6	1.5	2.7
062 1260-2 A14	0.282293	0.000061	0.000571	0.000084	0.029809	0.003524	-17.4	957 ± 13	0.282283	3.7	2.2	1.6
063 1260-2 A13	0.281318	0.000063	0.000445	0.000008	0.022513	0.000417	-51.9	1862 ± 32	0.281302	-10.4	2.3	3.1
064 1260-2 B15	0.282303	0.000040	0.000730	0.000073	0.032978	0.002114	-17.0	1064 ± 12	0.282288	6.3	1.4	1.5
065 1260-2 B11	0.282081	0.000044	0.000717	0.000046	0.039756	0.001291	-24.9	987 ± 12	0.282068	-3.3	1.6	2.0
066 1260-2 B8	0.281473	0.000050	0.001002	0.000199	0.049449	0.006275	-46.4	1920 ± 34	0.281437	-4.3	1.8	2.8
067 1260-2 C1	0.283318	0.002296	0.001420	0.000378	0.126761	0.034951	18.9	949 ± 12	0.283293	39.3	82.0	-0.7
068 1260-2 C2	0.281852	0.000057	0.000780	0.000039	0.041028	0.001824	-33.0	1107 ± 14	0.281836	-8.8	2.0	2.4
069 1260-2 C4	0.281452	0.000048	0.000406	0.000022	0.022329	0.001144	-47.1	1993 ± 34	0.281437	-2.7	1.7	2.8
070 1260-2 C7	0.282223	0.000048	0.000808	0.000063	0.042141	0.002520	-19.9	853 ± 13	0.282210	-1.3	1.7	1.8
071 1260-2 C11	0.282249	0.000050	0.000799	0.000071	0.045828	0.002787	-19.0	924 ± 13	0.282235	1.2	1.8	1.7
076 1260-2 C15	0.281398	0.000045	0.000944	0.000078	0.048050	0.003127	-49.1	1925 ± 33	0.281363	-6.8	1.6	3.0
077 1260-2 D15	0.281466	0.000057	0.000445	0.000044	0.026007	0.002135	-46.7	1976 ± 34	0.281449	-2.6	2.0	2.7
079 1260-2 D8	0.282236	0.000062	0.000594	0.000069	0.033069	0.004498	-19.4	957 ± 13	0.282226	1.6	2.2	1.7
080 1260-2 D2	0.281467	0.000040	0.000465	0.000004	0.024796	0.000366	-46.6	1939 ± 35	0.281450	-3.4	1.4	2.8
081 1260-2 E2	0.281561	0.000066	0.000544	0.000103	0.027102	0.002651	-43.3	1947 ± 33	0.281541	0.0	2.4	2.6
082 1260-2 E6	0.281449	0.000047	0.000846	0.000026	0.045127	0.001364	-47.2	1949 ± 33	0.281418	-4.3	1.7	2.8
083 1260-2 E10	0.282232	0.000044	0.000729	0.000048	0.040649	0.002318	-19.6	991 ± 13	0.282218	2.2	1.6	1.7
084 1260-2 F15	0.281463	0.000042	0.000306	0.000013	0.015942	0.000505	-46.8	1908 ± 32	0.281452	-4.1	1.5	2.8
085 1260-2 F13	0.282166	0.000046	0.000563	0.000021	0.030302	0.000612	-21.9	1006 ± 14	0.282155	0.3	1.6	1.8
Sample SOS-1254												
46 SOS-1254 (2) A6	0.281431	0.000063	0.000386	0.000014	0.016222	0.000442	-47.9	1970 ± 36	0.281417	-3.9	2.2	2.8
47 SOS-1254 (2) A1	0.281968	0.000049	0.001018	0.000114	0.045089	0.003457	-28.9	1003 ± 13	0.281949	-7.1	1.8	2.3
48 SOS-1254 (2) B5	0.281541	0.000062	0.000637	0.000151	0.032084	0.007408	-44.0	1952 ± 36	0.281517	-0.7	2.2	2.6
49 SOS-1254 (2) B7	0.281251	0.000052	0.000813	0.000005	0.033381	0.000388	-54.2	1988 ± 36	0.281220	-10.4	1.8	3.2
50 SOS-1254 (2) B9	0.281149	0.000054	0.000817	0.000073	0.035366	0.002268	-57.9	1969 ± 36	0.281118	-14.5	1.9	3.5
51 SOS-1254 (2) B10	0.281558	0.000051	0.001163	0.000269	0.059090	0.010888	-43.4	856 ± 13	0.281540	-24.9	1.8	3.2

Spot ID	$^{176}\text{Hf}/^{177}\text{Hf}$	2σ	$^{176}\text{Lu}/^{177}\text{Hf}$	2σ	$^{176}\text{Yb}/^{177}\text{Hf}$	2σ	$\epsilon\text{Hf}(t)$	U-Pb age (Ma)	$^{176}\text{Hf}/^{177}\text{Hf}(t)$	$\epsilon\text{Hf}(t)$	2σ	T_{DM}^{C} (Ga)
52 SOS-1254 (2) C8	0.281122	0.000060	0.000363	0.000018	0.015253	0.000740	-58.8	2014 ± 36	0.281108	-13.8	2.1	3.5
53 SOS-1254 (2) C7	0.282251	0.000075	0.000520	0.000060	0.020208	0.001665	-18.9	943 ± 13	0.282242	1.9	2.7	1.7
54 SOS-1254 (2) C5	0.281461	0.000095	0.001381	0.000335	0.079494	0.015854	-46.8	1966 ± 35	0.281409	-4.2	3.4	2.8
55 SOS-1254 (2) C4	0.281486	0.000073	0.001305	0.000193	0.057646	0.005434	-45.9	1983 ± 35	0.281436	-2.9	2.6	2.8
60 SOS-1254 (2) D3	0.281389	0.000057	0.000469	0.000016	0.020393	0.000555	-49.4	1951 ± 40	0.281372	-5.9	2.0	2.9
61 SOS-1254 (2) D8	0.281387	0.000053	0.000484	0.000047	0.020947	0.001638	-49.4	1984 ± 37	0.281369	-5.3	1.9	2.9
62 SOS-1254 (2) D9	0.282188	0.000065	0.000369	0.000017	0.016012	0.000657	-21.1	1043 ± 12	0.282181	2.0	2.3	1.7
63 SOS-1254 (2) D10	0.282069	0.000067	0.000633	0.000024	0.027522	0.000896	-25.3	880 ± 13	0.282059	-6.0	2.4	2.1
64 SOS-1254 (2) E7	0.281707	0.000060	0.000438	0.000050	0.016666	0.001497	-38.1	808 ± 13	0.281701	-20.3	2.1	2.9
65 SOS-1254 (2) F1	0.281101	0.000037	0.000703	0.000032	0.029458	0.000824	-59.5	1989 ± 36	0.281075	-15.6	1.3	3.6
66 SOS-1254 (2) G1	0.281274	0.000079	0.000369	0.000048	0.015784	0.001712	-53.4	1964 ± 36	0.281260	-9.6	2.8	3.2
67 SOS-1254 (2) G2	0.282113	0.000060	0.001429	0.000032	0.059968	0.001250	-23.8	1000 ± 13	0.282086	-2.3	2.1	2.0
68 SOS-1254 (2) G10	0.281860	0.000069	0.000549	0.000024	0.023275	0.000693	-32.7	927 ± 13	0.281851	-12.3	2.5	2.5
69 SOS-1254 (2) H8	0.282195	0.000059	0.001380	0.000087	0.064182	0.003143	-20.8	1015 ± 13	0.282169	1.0	2.1	1.8
74 SOS-1254 (2) H5	0.281395	0.000057	0.000372	0.000026	0.015785	0.000734	-49.1	1967 ± 32	0.281382	-5.2	2.0	2.9
75 SOS-1254 (2) H4	0.282216	0.000063	0.000701	0.000069	0.032224	0.003038	-20.1	994 ± 13	0.282203	1.7	2.3	1.7
76 SOS-1254 (2) I1	0.282301	0.000066	0.000635	0.000022	0.024975	0.000705	-17.1	1011 ± 13	0.282289	5.1	2.4	1.5
77 SOS-1254 (2) I5	0.282261	0.000052	0.000521	0.000073	0.021412	0.001850	-18.5	1000 ± 13	0.282252	3.5	1.9	1.6
78 SOS-1254 (2) I6	0.282254	0.000066	0.000581	0.000019	0.025038	0.000725	-18.8	945 ± 13	0.282244	2.0	2.4	1.6
79 SOS-1254 (2) J10	0.281468	0.000047	0.000309	0.000026	0.012977	0.000697	-46.6	1976 ± 31	0.281456	-2.4	1.7	2.7
80 SOS-1254 (2) J1	0.282256	0.000064	0.001157	0.000127	0.050255	0.005594	-18.7	918 ± 13	0.282236	1.1	2.3	1.7
Sample SOS-1274												
04 SOS-1274 (2) J3	0.282264	0.000062	0.000513	0.000012	0.023578	0.000427	-18.4	936 ± 13	0.282255	2.2	2.2	1.6
05 SOS-1274 (2) I10	0.282239	0.000056	0.000728	0.000073	0.032953	0.002555	-19.3	992 ± 14	0.282225	2.4	2.0	1.7
06 SOS-1274 (2) I6	0.281533	0.000056	0.000441	0.000027	0.019625	0.000803	-44.3	1917 ± 36	0.281517	-1.6	2.0	2.6
07 SOS-1274 (2) H2	0.281545	0.000050	0.000321	0.000033	0.013966	0.000985	-43.9	1982 ± 35	0.281533	0.5	1.8	2.6
08 SOS-1274 (2) H7	0.281883	0.000057	0.000583	0.000041	0.022609	0.001122	-31.9	1115 ± 13	0.281870	-7.4	2.0	2.4
09 SOS-1274 (2) H10	0.281429	0.000047	0.000265	0.000005	0.011601	0.000222	-47.9	2004 ± 33	0.281419	-3.0	1.7	2.8
10 SOS-1274 (2) G10	0.281398	0.000039	0.000576	0.000019	0.025791	0.000564	-49.0	2010 ± 34	0.281376	-4.4	1.4	2.9
11 SOS-1274 (2) H8	0.281461	0.000065	0.000461	0.000029	0.020584	0.000720	-46.8	1989 ± 38	0.281443	-2.5	2.3	2.7
12 SOS-1274 (2) G6	0.281507	0.000060	0.001127	0.000083	0.049885	0.002330	-45.2	1924 ± 34	0.281466	-3.2	2.1	2.7
13 SOS-1274 (2) G1	0.281295	0.000049	0.000336	0.000010	0.015410	0.000219	-52.7	1956 ± 34	0.281283	-9.0	1.7	3.1
20 SOS-1274 (2) F1	0.281539	0.000043	0.000426	0.000047	0.018722	0.001563	-44.1	1837 ± 32	0.281524	-3.2	1.6	2.7
21 SOS-1274 (2) F2	0.281505	0.000048	0.000303	0.000014	0.013142	0.000338	-45.3	1975 ± 34	0.281494	-1.0	1.7	2.6

Spot ID	$^{176}\text{Hf}/^{177}\text{Hf}$	2σ	$^{176}\text{Lu}/^{177}\text{Hf}$	2σ	$^{176}\text{Yb}/^{177}\text{Hf}$	2σ	$\epsilon\text{Hf}(0)$	U-Pb age (Ma)	$^{176}\text{Hf}/^{177}\text{Hf}(0)$	$\epsilon\text{Hf}(0)$	2σ	T_{DM}^{C} (Ga)
22 SOS-1274 (2) F3	0.281440	0.000059	0.000743	0.000014	0.032544	0.000431	-47.6	2018 ± 33	0.281412	-3.0	2.1	2.8
23 SOS-1274 (2) F6	0.281853	0.000068	0.000604	0.000047	0.023634	0.000995	-33.0	1047 ± 13	0.281841	-10.0	2.4	2.5
24 SOS-1274 (2) F9	0.281480	0.000051	0.000365	0.000010	0.015584	0.000299	-46.1	2012 ± 33	0.281466	-1.2	1.8	2.7
25 SOS-1274 (2) F10	0.282202	0.000044	0.000418	0.000027	0.018282	0.000883	-20.6	1006 ± 13	0.282194	1.6	1.6	1.7
26 SOS-1274 (2) E10	0.282249	0.000056	0.000997	0.000038	0.044094	0.001077	-19.0	1000 ± 13	0.282230	2.8	2.0	1.6
27 SOS-1274 (2) E3	0.282206	0.000062	0.000471	0.000023	0.018216	0.000686	-20.5	1049 ± 15	0.282196	2.7	2.2	1.7
28 SOS-1274 (2) E2	0.281399	0.000062	0.000309	0.000012	0.013285	0.000286	-49.0	2027 ± 33	0.281387	-3.6	2.2	2.8
29 SOS-1274 (2) D2	0.282145	0.000062	0.000415	0.000020	0.018201	0.000708	-22.6	978 ± 15	0.282137	-1.0	2.2	1.9
33 SOS-1274 (2) D9	0.281442	0.000042	0.000314	0.000009	0.012965	0.000222	-47.5	2012 ± 33	0.281430	-2.5	1.5	2.8
34 SOS-1274 (2) D8	0.282339	0.000048	0.000600	0.000022	0.023391	0.000739	-15.8	997 ± 14	0.282328	6.2	1.7	1.4
35 SOS-1274 (2) C7	0.281424	0.000052	0.000331	0.000004	0.014152	0.000248	-48.1	2010 ± 32	0.281411	-3.2	1.8	2.8
36 SOS-1274 (2) C4	0.282211	0.000052	0.001186	0.000088	0.050716	0.002625	-20.3	835 ± 14	0.282192	-2.3	1.9	1.8
37 SOS-1274 (2) C2	0.281372	0.000060	0.001234	0.000163	0.054761	0.006409	-50.0	1998 ± 32	0.281325	-6.5	2.1	3.0
38 SOS-1274 (2) B2	0.281459	0.000049	0.000330	0.000009	0.013693	0.000357	-46.9	1978 ± 31	0.281446	-2.7	1.8	2.7
39 SOS-1274 (2) B3	0.281515	0.000052	0.000486	0.000030	0.020657	0.000914	-44.9	1942 ± 31	0.281497	-1.7	1.8	2.7
40 SOS-1274 (2) B7	0.282189	0.000062	0.000516	0.000029	0.022005	0.000937	-21.1	1000 ± 13	0.282179	1.0	2.2	1.8
41 SOS-1274 (2) A10	0.282395	0.000048	0.000569	0.000028	0.019396	0.000864	-13.8	975 ± 13	0.282385	7.7	1.7	1.3
42 SOS-1274 (2) A4	0.282085	0.000063	0.000729	0.000091	0.030233	0.002960	-24.7	1020 ± 13	0.282071	-2.4	2.2	2.0

CAPÍTULO V CONCLUSÕES

O Domínio Macururé compõe-se por uma grande variedade de rochas que possuem um papel-chave no entendimento da evolução geodinâmica da Província Borborema sul e, por consequência, da margem oeste do Supercontinente Gondwana.

Uma sucessão de rochas metassedimentares composta de filitos, xistos, quartzitos e metarenitos constituem o Complexo Macururé. Geocronologia U-Pb de zircões detríticos revelam um padrão bimodal de distribuição de idades, dominado por contribuições riacianas-orosirianas e tonianas. Os zircões de idade paleoproterozoica são correlacionáveis com o embasamento da Província Borborema, que na área de estudo está representado pelo Domo Jirau do Ponciano e pelo Complexo Arapiraca. A população de grãos de zircão tonianos mostram idades similares às aquelas identificadas em ortognaisses e migmatitos relacionados ao evento Cariris Velhos. Esse evento tem como principais representantes no SOS o Complexo Migmatítico de Poço Redondo e o ortognaisse Serra Negra, de afinidade geoquímica com granitos do tipo-A, no Domínio Marancó. Dados isotópicos pontuais Lu-Hf em zircão demonstram que o retrabalhamento de crosta arqueana foi predominante durante a Orogenia Riacciana na Província Borborema, com subordinadas adições de material juvenil. Por outro lado, as assinaturas de Hf dos grãos de zircão tonianos indicam que esse foi um importante de geração de crosta e de retrabalhamento de componentes paleoproterozoicos e arqueanos.

A sequência metassupracrustal do Domínio Macururé foi intrudida por numerosos plútons de naturezas diversas durante a Orogenia Brasileira/Pan-Africana. As rochas plutônicas mais antigas da região são gabros e dioritos, com hornblenditos e termos félsicos ocorrendo de forma subordinada. As rochas plutônicas desse primeiro grupo apresentam idades de cristalização U-Pb em zircão e titanita entre 643 e 628 Ma. Elas mostram uma foliação tectônica definida pela orientação preferencial de cristais de biotita, hornblenda e plagioclásio, e evidências de deformação no estado sólido compatíveis com as condições das fácies xisto verde-anfibolito. Essas inferências apontam para a colocação em estágio pré- a cedo-colisional desses magmas. Dados geoquímicos indicam que uma natureza essencialmente magnésiana e uma afinidade com as suítes cálcio-alcalina de alto K e shoshonítica. Os padrões de multielementos e de ETR revelam enriquecimento em LILE e ETRL em relação a HFSE e ETRP, assim como importantes anomalias negativas em Ti-Nb-Ta. O fraco ou ausente fracionamento entre ETRP são indicativos de uma fonte relativamente rasa, no campo de estabilidade do espinélio. Os magmas basálticos do Domínio Macururé também apresentam características isotópicas de Sr-Nd-Pb-Hf evoluídas, pontuando para derivação a partir de uma fonte mantélica

metassomatizada pela entrada de sedimentos via processos de subducção. A interação dos peridotitos mantélicos com material crustal resultou na formação de flogopita como principal fase metassomática, o que é sustentado por meio de modelamento isotópico e geoquímico. Esses dados dão conta que baixas taxas de fusão de um manto lherzolítico contendo flogopita no campo de estabilidade do espinélio é capaz de reproduzir as principais características composicionais das rochas mais primitivas. Os termos intermediários, por sua vez, resultam da mistura e hibridização dos magmas basálticos com magmas graníticos de origem crustal.

Granodioritos e granitos leucocráticos registram idades de cristalização U-Pb em zircão e titanita entre 630 e 624 Ma. Esses corpos ocorrem como *stocks* e *sheets* colocados ao longo da xistosidade das rochas encaixantes metassedimentares, com suas estruturas magmáticas paralelas a essa foliação. Essas observações sugerem uma colocação sincrônica ao evento colisional no SOS. Os cristais de biotita e muscovita que coexistem nos leucogranitos exibem formas subédricas em contatos retos com as fases adjacentes, indicando uma origem magmática. Os dados geoquímicos para esse grupo indicam um caráter predominantemente peraluminoso e afinidade com a suíte cálcio-alcálica de alto K. Eles são magnesianos a ferrosos, sobrepondo o campo ocupado por leucogranitos himalaianos. Os padrões de ETR são caracterizados por elevado fracionamento de ETRL em relação aos ETRP, o que sugere presença de granada residual na fonte. Ao comparar a composição química dessas rochas com a de líquidos experimentais, os leucogranitos posicionam-se no campo dos fundidos gerados por fusão parcial de metagrauvas. Uma origem predominantemente metassedimentar é suportada por (i) uma mineralogia aluminosa, (ii) presença de abundantes enclaves surmicócos, (iii) abundância de zircões herdados de idades variadas, similar aos obtidos em rochas detríticas, e (iv) composição isotópica de Sm-Nd similar a das rochas encaixantes metassedimentares.

O grupo magmático mais jovem exibe idades de cristalização U-Pb em zircão e titanita entre 625 e 603 Ma, compreendendo rochas de composição monzonítica, granodiorítica e granítica. Elas são em sua maioria isotrópicas e truncam as estruturas das encaixantes metamórficas, indicando colocação em estágio tardio em relação ao evento colisional entre o CFS e o PEAL. Esses granitoides contêm hornblenda e biotita como principais fases máficas, são metaluminosos, magnesianos e mostram filiação geoquímica com rochas das suítes cálcio-alcálica de alto K e shoshonítica. Os espectros de ETR e multielementares são fracionados, com enriquecimento seletivo de ETRL e LILE em relação a ETRL e HFSE, com importantes anomalias negativas em Ti-Nb-Ta. Modelamento geoquímico de elementos traços demonstram que as composições dos granodioritos podem ser obtidas por fusão parcial de uma fonte basáltica moderadamente enriquecida em elementos incompatíveis. A sobreposição parcial dos

dados Lu-Hf em zircão com o *trend* evolutivo de ortognaisses tonianos da Faixa Riacho do Pontal sugerem que os granitoides mais jovens do Domínio Macururé podem ter se formado a partir do retrabalhamento de uma crosta relacionada ao evento Cariris Velhos.

Os resultados apresentados nesse volume e disponíveis na literatura revelam um cenário dominado por retrabalhamento e sem aporte significativo de material juvenil durante o Brasiliano no SOS, o que contrasta com o esperado para um ambiente de arco magmático. Aliado a isso, a ausência de rochas com afinidades cálcio-alcálica de médio e baixo K, de rochas de alta pressão e de remanescentes de ofiolitos não suportam a existência de um oceano nessa região. Desse modo, propõe-se que a evolução do SOS no Neoproterozoico resultou de uma extensão litosférica do embasamento, seguido por inversão da bacia e colisão continental em decorrência de esforços vindos de outras regiões na Província Borborema.

REFERÊNCIAS

- Aleinikoff J.N., Wintsch R.P., Fanning C.M., Dorais M.J. 2002. U–Pb geochronology of zircon and polygenetic titanite from the Glastonbury Complex, Connecticut, USA: an integrated SEM, EMPA, TIMS, and SHRIMP study. *Chemical Geology*, **188**: 188, 125-147.
- Almeida F.F.M., Hasui Y., Brito Neves B.B., Fuck R.A. 1981. Brazilian structural provinces: An introduction. *Earth-Science Reviews*, **17**: 1-29.
- Amaral W., Santos T.J., Ancelmi M.F., Fuck R.A., Dantas E.L., Matteini M., Moreto C.P. 2015. 1.57 Ga protolith age of the Neoproterozoic Forquilha eclogites, Borborema Province, NE-Brazil, constrained by U–Pb, Hf and Nd isotopes. *Journal of South American Earth Sciences*, **58**: 210-222.
- Andersen T., Andersson U.B., Graham S., Åberg G., Simonsen S.L. 2009. Granitic magmatism by melting of juvenile continental crust: new constraints on the source of Palaeoproterozoic granitoids in Fennoscandia from Hf isotopes in zircon. *Journal of the Geological Society*, **166**: 233-247.
- Andersen T., Elburg M.A., van Niekerk H.S., Ueckermann H. 2018. Successive sedimentary recycling regimes in southwestern Gondwana: Evidence from detrital zircons in Neoproterozoic to Cambrian sedimentary rocks in southern Africa. *Earth-Science Reviews*, **181**: 43-60.
- Andersen T., Kristoffersen M., Elburg M.A. 2018. Visualizing, interpreting and comparing detrital zircon age and Hf isotope data in basin analysis – a graphical approach. *Basin Research*, **30**: 132-147.
- Annen C., Blundy J.D., Sparks R.S.J. 2006. The Genesis of Intermediate and Silicic Magmas in Deep Crustal Hot Zones. *Journal of Petrology*, **47**: 505-539.
- Annen C., Blundy J.D., Leuthold J., Sparks R.S.J. 2015. Construction and evolution of igneous bodies: Towards an integrated perspective of crustal magmatism. *Lithos*, **230**: 206-221.
- Arndt N.T. & Goldstein S.L. 1987. Use and abuse of crust-formation ages. *Geology*, **15**: 893-895.
- Barbarin B. 1999. A review of the relationships between granitoid types, their origins and their geodynamic environments. *Lithos*, **46**: 605-626.
- Barbarin B. & Didier J. 1991. Macroscopic features of mafic microgranular enclaves. In: Didier, J. & Barbarin, B. *Enclaves and Granite Petrology*. Amsterdam, Elsevier, p. 253-262.

Barbosa J.S.F., Marinho M.M., Leal A.B.M., Oliveira E.M., Souza-Oliveira J.S., Argollo R.M., Lana C., Barbosa R.G., Santos L.T.L. 2018. As raízes granulíticas do cinturão Salvador-Esplanada-Boquim, Cráton do São Francisco, Bahia-Sergipe, Brasil. *Geologia USP. Série Científica*, **18**: 103-128.

Baxter S. & Feely M. 2002. Magma mixing and mingling textures in granitoids: examples from the Galway Granite, Connemara, Ireland. *Mineralogy and Petrology*, **76**: 63-74.

Becker H., Wenzel T., Volker F. 1999. Geochemistry of Glimmerite Veins in Peridotites from Lower Austria – Implications for the Origin of K-rich Magmas in Collision Zones. *Journal of Petrology*, **40**: 315-338.

Bennett E.N., Lissenberg C.J., Cashman K. V. 2019. The significance of plagioclase textures in mid-ocean ridge basalt (Gakkel Ridge, Arctic Ocean). *Contributions to Mineralogy and Petrology*, **174**: 1-22.

Black L.P., Kamo S.L., Allen C.M., Davis D.W., Aleinikoff J.N., Valley J.W., Mundil R., Campbell I.H., Korsch R.J., Williams I.S., Foudoulis C. 2004. Improved $^{206}\text{Pb}/^{238}\text{U}$ microprobe geochronology by the monitoring of a trace-element-related matrix effect; SHRIMP, ID-TIMS, ELA-ICP-MS and oxygen isotope documentation for a series of zircon standards. *Chemical Geology*, **205**: 115-140.

Bouvier A., Vervoort J.D., Patchett P.J. 2008. The Lu-Hf and Sm-Nd isotopic composition of CHUR: Constraints from unequilibrated chondrites and implications for the bulk composition of terrestrial planets. *Earth and Planetary Science Letters*, **273**: 48-57.

Brito Neves B.B., Van Schmus W.R., Santos E.J., Campos Neto M.C., Kozuch M. 1995. O evento Cariris Velhos na Província Borborema: intergração de dados, implicações e perspectivas. *Revista Brasileira de Geociências*, **25**: 279-296.

Brito Neves B.B., Santos E.J., Van Schmus W.R. 2000. Tectonic history of the Borborema Province. In: Cordani, U.G., Milani, E.J., Thomaz Filho, A., Campos, D.A. (eds.). *Tectonic Evolution of South America*. Rio de Janeiro, 31st International Geological Congress, p. 151-182.

Bueno J.F., Oliveira E.P., McNaughton N.J., Laux J.H. 2009. U-Pb dating of granites in the Neoproterozoic Sergipano Belt, NE-Brazil: implications for the timing and duration of continental collision and extrusion tectonics in the Borborema Province. *Gondwana Research*, **15**: 86-97.

Carlson R.W. & Irving A.J. 1994. Depletion and enrichment history of subcontinental

lithospheric mantle: An Os, Sr, Nd and Pb isotopic study of ultramafic xenoliths from the northwestern Wyoming Craton. *Earth and Planetary Science Letters*, **126**: 457-472.

Carvalho M.J. 2005. *Evolução tectônica do Domínio Marancó-Poço Rondonio: registro das orogêneses Cariris Velhos e Brasiliana na Faixa Sergipana, NE do Brasil*. PhD Thesis. Universidade de Campinas, Campinas, 202 p.

Castaing C., Feybesse J.L., Thiéblemont D., Triboulet C., Chèvremont P. 1994. Palaeogeographical reconstructions of the Pan-African/Brasiliano orogen: closure of an oceanic domain or intracontinental convergence between major blocks? *Precambrian Research*, **69**: 327-344.

Castro A., Corretgé L.G., de la Rosa J.D., Fernández C., López S., García-Moreno O., Chacón H. 2003. The Appinite–Migmatite Complex of Sanabria, NW Iberian Massif, Spain. *Journal of Petrology*, **44**: 1309-1344.

Cawood P.A., Hawkesworth C.J., Dhuime B. 2012. Detrital zircon record and tectonic setting. *Geology*, **40**: 875-878.

Caxito F.A., Uhlein A., Dantas E.L. 2014. The Afeição augen-gneiss Suite and the record of the Cariris Velhos Orogeny (1000–960 Ma) within the Riacho do Pontal fold belt, NE Brazil. *Journal of South American Earth Sciences*, **51**: 12-27.

Caxito F.A., Uhlein A., Dantas E.L., Stevenson R., Salgado S.S., Dussin I.A., Sial A.N. 2016. A complete Wilson Cycle recorded within the Riacho do Pontal Orogen, NE Brazil: implications for the Neoproterozoic evolution of the Borborema Province at the heart of West Gondwana. *Precambrian Research*, **282**: 97-120.

Caxito F.A., Santos L.C.M.L., Ganade C.E., Bendaoud A., Fettous E., Bouyo M.H. 2020. Toward an integrated model of geological evolution for NE Brazil-NW Africa: The Borborema Province and its connections to the Trans-Saharan (Benino-Nigerian and Tuareg shields) and Central African orogens. *Brazilian Journal of Geology*, **50**: e20190122.

Caxito F.A., Santos L.C.M.L., Uhlein A., Dantas E.L., Alkmim A.R., Lana C. 2020. New U-Pb (SHRIMP) and first Hf isotope constraints on the Tonian (1000-920 Ma) Cariris Velhos event, Borborema Province, NE Brazil. *Brazilian Journal of Geology*, **50**: e20190082.

Chapman J.B., Ducea M.N., Kapp P., Gehrels G.E., DeCelles P.G. 2017. Spatial and temporal radiogenic isotopic trends of magmatism in Cordilleran orogens. *Gondwana Research*, **48**: 189-204.

Chappell B.W. & White A.J.R. 2001. Two contrasting granite types: 25 years later. *Australian Journal of Earth Sciences*, **48**: 489-499.

Chu N.C., Taylor R.N., Chavagnac V., Nesbitt R.W., Boella R.M., Milton J.A., German C.R., Bayon G., Burton K. 2002. Hf isotope ratio analysis using multi-collector inductively coupled plasma mass spectrometry: an evaluation of isobaric interference corrections. *Journal of Analytical Atomic Spectrometry*, **17**: 1567-1574.

Class C. & Goldstein S.L. 1997. Plume-lithosphere interactions in the ocean basins: constraints from the source mineralogy. *Earth and Planetary Science Letters*, **150**: 245-260.

Clemens J.D. 2018. Granitic magmas with I-type affinities, from mainly metasedimentary sources: the Harcourt batholith of southeastern Australia. *Contributions to Mineralogy and Petrology*, **173**: 1-20.

Clemens J.D., Stevens G., Farina F. 2011. The enigmatic sources of I-type granites: The peritectic connexion. *Lithos*, **126**: 174-181.

Cocherie A. 1986. Systematic use of trace element distribution patterns in log-log diagrams for plutonic suites. *Geochimica et Cosmochimica Acta*: **50**, 2517-2522.

Coleman D.S., Gray W., Glazner A.F. 2004. Rethinking the emplacement and evolution of zoned plutons: Geochronologic evidence for incremental assembly of the Tuolumne Intrusive Suite, California. *Geology*, **32**: 433-436.

Conceição R.V. & Green D.H. 2004. Derivation of potassic (shoshonitic) magmas by decompression melting of phlogopite + pargasite lherzolite. *Lithos*, **72**: 209-229.

Conceição H., Rosa M.L.S., Conceição J.A., Lisboa V.A.C., Pereira F.S., Teles D.S., Fernandes D.M., Sousa E.S., Cruz J.W.S., Rezende H.J.C., Oliveira I.R., Souza J.M.D., Oliveira I.L. 2017. Magmatismos no Domínio Macururé, Sistema Orogênico Sergipano: estado do conhecimento. In: SBG, XXVII Simpósio de Geologia do Nordeste, João Pessoa, *Anais[...]*. Disponível em: http://geologiadonordeste.com.br/2017/anais/index_sessao.php#resumos. Acesso em 19 set. 2023.

Conceição J.A. 2014. *Petrologia do Stock Granítico Glória Sul, Faixa Sergipana, setor sul da Província Borborema, Sergipe*. MS Dissertation, Universidade Federal de Sergipe, São Cristóvão, 145 p.

Conceição J.A. 2019. *Magmatismo leucogranítico do Domínio Macururé, Sistema Orogênico Sergipano, NE do Brasil*. ThD Thesis, Universidade Federal da Bahia, Salvador, 62 p.

- Conceição J.A., Rosa M.L.S., Conceição H. 2016. Sienogranitos leucocráticos do Domínio Macururé, Sistema Orogênico Sergipano, Nordeste do Brasil: Stock Glória Sul. *Brazilian Journal of Geology*, **46**: 63-77.
- Condamine P. & Médard E. 2014. Experimental melting of phlogopite-bearing mantle at 1 GPa: Implications for potassic magmatism. *Earth and Planetary Science Letters*, **397**: 80-92.
- Condamine P., Médard E., Devidal J.L. 2016. Experimental melting of phlogopite-peridotite in the garnet stability field. *Contributions to Mineralogy and Petrology*, **171**(11): 1-26.
- Corfu F. 2003. Atlas of zircon textures. *Reviews in Mineralogy and Geochemistry*. **53**: 469-500.
- Costa F.G., Klein E.L., Lafon J.M., Milhomem Neto J.M., Galarza M.A., Rodrigues J.B., Naletto J.L.C., Corrêa Lima R.G. 2018. Geochemistry and U–Pb–Hf zircon data for plutonic rocks of the Troia Massif, Borborema Province, NE Brazil: Evidence for reworking of Archean and juvenile Paleoproterozoic crust during Rhyacian accretionary and collisional tectonics. *Precambrian Research*, **311**: 167-194.
- Coutts D.S., Matthews W.A., Hubbard S.M. 2019. Assessment of widely used methods to derive depositional ages from detrital zircon populations. *Geoscience Frontiers*, **10**: 1421-1435.
- Couzinié S., Laurent O., Moyen J.F., Zeh A., Bouilhol P., Villaros A. 2016. Post-collisional magmatism: Crustal growth not identified by zircon Hf–O isotopes. *Earth and Planetary Science Letters*, **456**: 182-195.
- Cox R., Lowe D.R., Cullers R.L. 1995. The influence of sediment recycling and basement composition on evolution of mudrock chemistry in the southwestern United States. *Geochimica et Cosmochimica Acta*, **59**: 2919-2940.
- Cruz R.F.D., Pimentel M.M., Accioly A.C.D.A., Rodrigues J.B. 2014. Geological and isotopic characteristics of granites from the Western Pernambuco-Alagoas Domain: implications for the crustal evolution of the Neoproterozoic Borborema Province. *Brazilian Journal of Geology*, **44**: 627-652.
- D’el-Rey Silva L.J.H. 1999. Basin infilling in the southern-central part of the Sergipano Belt (NE Brazil) and implications for the evolution of Pan-African/Brasiliano cratons and Neoproterozoic sedimentary cover. *Journal of South American Earth Sciences*, **12**: 453-470.
- Davison I. & Santos R.A. 1989. Tectonic evolution of the Sergipano Fold Belt, NE Brazil, during the Brasiliano Orogeny. *Precambrian Research*, **45**: 319-342.

- DePaolo D.J. 1981. Nd Isotopic Studies: Some new perspectives on Earth structure and evolution. *Eos, Transactions American Geophysical Union*, **62**: 137-137.
- DePaolo D.J. 1981. Trace element and isotopic effects of combined wallrock assimilation and fractional crystallization. *Earth and Planetary Science Letters*, **53**: 189-202.
- DePaolo D.J. 1988. *Neodymium Isotope Geochemistry: An Introduction*. Berlin, Springer-Verlag, 187 p.
- Farmer G.L. 2007. Continental Basaltic Rocks. In: Holland H.D. & Turekian K.K. *Treatise on Geochemistry*. Oxford, Elsevier-Pergamon, p. 1-39.
- Faure G. 2001. *Origin of Igneous Rocks: The Isotopic Evidence*. Berlin, Springer Berlin Heidelberg, 496 p.
- Fedo C.M., Wayne Nesbitt H., Young G.M. 1995. Unraveling the effects of potassium metasomatism in sedimentary rocks and paleosols, with implications for paleoweathering conditions and provenance. *Geology*, **23**: 921-924.
- Fernandes D.M., Lisboa V.A.C., Rosa M.L.S., Conceição H. 2020. Petrologia e idade do Stock Fazenda Lagoas, Domínio Macururé, Sistema Orogênico Sergipano, NE-Brasil. *Geologia USP. Série Científica*, **20**: 39-60.
- Ferreira V.P., Neves C.H.S., Silva T.R., Lima M.M.C., Sial A.N., Silva Filho A.F. 2021. Neoproterozoic high magmatic addition rate episode building a composite batholith in northeastern Brazil, and implications for the western Gondwana assembly. *Precambrian Research*, **363**: 106331.
- Ferry J.M. & Watson E.B. 2007. New thermodynamic models and revised calibrations for the Ti-in-zircon and Zr-in-rutile thermometers. *Contributions to Mineralogy and Petrology*, **154**: 429-437.
- Fettes D. & Desmons J. 2014. *Rochas Metamórficas - classificação e glossário*. Oficina de Textos. 328 p.
- Fisher C.M., Bauer A.M., Luo Y., Sarkar C., Hanchar J.M., Vervoort J.D., Tapster S.R., Horstwood M., Pearson D.G. 2020. Laser ablation split-stream analysis of the Sm-Nd and U-Pb isotope compositions of monazite, titanite, and apatite – Improvements, potential reference materials, and application to the Archean Saglek Block gneisses. *Chemical Geology*, **539**: 119493.
- Floyd P.A. & Leveridge B.E. 1987. Tectonic environment of the Devonian Gramscatho basin,

south Cornwall: framework mode and geochemical evidence from turbiditic sandstones. *Journal of the Geological Society*, **144**: 531-542.

Foley S. 1992. Vein-plus-wall-rock melting mechanisms in the lithosphere and the origin of potassic alkaline magmas. *Lithos*, **28**: 435-453.

Fontes M.P., Conceição H., Rosa M.L.S., Lisboa V.A.C. 2018. Minettes do Stock Monzonítico Glória Norte: evidência de magmatismo ultrapotássico pós-orogênico, com assinatura de subducção, no Sistema Orogênico Sergipano. *Revista Geologia USP. Série Científica*, **18**: 51-66.

Förster M.W., Prelević D., Schmück H.R., Buhre S., Veter M., Mertz-Kraus R., Foley S.F., Jacob D.E. 2017. Melting and dynamic metasomatism of mixed harzburgite + glimmerite mantle source: Implications for the genesis of orogenic potassic magmas. *Chemical Geology*, **455**: 182-191.

Fourcade S. & Allegre C.J. 1981. Trace elements behavior in granite genesis: A case study The calc-alkaline plutonic association from the Querigut complex (Pyrénées, France). *Contributions to Mineralogy and Petrology*, **76**(2): 177-195.

Fowler M.B., Kocks H., Darbyshire D.P.F., Greenwood P.B. 2008. Petrogenesis of high Ba–Sr plutons from the Northern Highlands Terrane of the British Caledonian Province. *Lithos*, **105**: 129-148.

Frost B.R., Barnes C.G., Collins W.J., Arculus R.J., Ellis D.J., Frost C.D. 2001. A geochemical classification for granitic rocks. *Journal of Petrology*, **42**: 2033-2048.

Frost B.R., Chamberlain K.R., Schumacher J.C. 2001. Sphene (titanite): phase relations and role as a geochronometer. *Chemical Geology*, **172**: 131-148.

Furman T. & Graham D. 1999. Erosion of lithospheric mantle beneath the East African Rift system: geochemical evidence from the Kivu volcanic province. *Lithos*, **48**: 237-262.

Galbraith R.F. & Laslett G.M. 1993. Statistical models for mixed fission track ages. *Nuclear tracks and radiation measurements*, **21**: 459-470.

Gaetani G.A. & Grove T.L. 1998. The influence of water on melting of mantle peridotite. *Contributions to Mineralogy and Petrology*, **131**: 323-346.

Ganade C.E., Weinberg R.F., Caxito F.A., Lopes L.B.L., Tesser L.R., Costa I.S. 2021. Decratonization by rifting enables orogenic reworking and transcurrent dispersal of old terranes in NE Brazil. *Scientific Reports*, **11**: 1-13.

- Ganade de Araujo C.E., Weinberg R.F., Cordani U.G. 2013. Extruding the Borborema Province (NE-Brazil): a two-stage Neoproterozoic collision process. *Terra Nova*, **26**: 157-168.
- Gehrels G. 2011. Detrital Zircon U-Pb Geochronology: Current Methods and New Opportunities. In: Busby C. & Azor A (eds.). *Tectonics of Sedimentary Basins*. Oxford, John Wiley & Sons, p. 45-62.
- Gehrels G. 2014. Detrital Zircon U-Pb Geochronology Applied to Tectonics. *Annual Review of Earth and Planetary Sciences*, **42**: 127-149.
- Gerdes A. & Zeh A. 2009. Zircon formation versus zircon alteration — New insights from combined U–Pb and Lu–Hf in-situ LA-ICP-MS analyses, and consequences for the interpretation of Archean zircon from the Central Zone of the Limpopo Belt. *Chemical Geology*, **261**: 230-243.
- Gray D.R., Foster D.A., Maas R., Spaggiari C. v., Gregory R.T., Goscombe B., Hoffmann K.H. 2007. Continental growth and recycling by accretion of deformed turbidite fans and remnant ocean basins: Examples from Neoproterozoic and Phanerozoic orogens. *Memoir of the Geological Society of America*: **200**: 63-92.
- Griffin W.L., Wang X., Jackson S.E., Pearson N.J., O'Reilly S.Y., Xu X., Zhou X. 2002. Zircon chemistry and magma mixing, SE China: In-situ analysis of Hf isotopes, Tonglu and Pingtan igneous complexes. *Lithos*, **61**: 237-269.
- Griffin W.L., Belousova E.A., Shee S.R., Pearson N.J., O'Reilly S.Y. 2004. Archean crustal evolution in the northern Yilgarn Craton: U–Pb and Hf-isotope evidence from detrital zircons. *Precambrian Research*, **131**: 231-282.
- Guimarães I.P., Silva Filho A.F., Almeida C.N., Macambira M.B., Armstrong R. 2011. U–Pb SHRIMP data constraints on calc-alkaline granitoids with 1.3–1.6 Ga Nd TDM model ages from the central domain of the Borborema province, NE Brazil. *Journal of South American Earth Sciences*, **31**: 383-396.
- Guimarães I.P., Van Schmus W.R., Brito Neves B.B., Bretas Bittar S.M., Silva Filho A.F., Armstrong R. 2012. U–Pb zircon ages of orthogneisses and supracrustal rocks of the Cariris Velhos belt: Onset of Neoproterozoic rifting in the Borborema Province, NE Brazil. *Precambrian Research*, **192-195**: 52-77.
- Guimarães I.P., Lara de Brito M.F., Lages G.A., Silva Filho A.F., Santos L., Brasilino R.G. 2016. Tonian granitic magmatism of the Borborema Province, NE Brazil: A review. *Journal of*

South American Earth Sciences, **68**: 97-112.

Guo Z., Wilson M., Liu J., Mao Q. 2006. Post-collisional, Potassic and Ultrapotassic Magmatism of the Northern Tibetan Plateau: Constraints on Characteristics of the Mantle Source, Geodynamic Setting and Uplift Mechanisms. *Journal of Petrology*, **47**: 1177-1220.

Hao H., Campbell I.H., Park J.W. 2022. Nd-Hf isotopic systematics of the arc mantle and their implication for continental crust growth. *Chemical Geology*, **602**: 120897.

Hawkesworth C.J., Turner S.P., McDermott F., Peate D.W., van Calsteren P. 1997. U-Th isotopes in arc magmas: implications for element transfer from the subducted crust. *Science*, **276**: 551-555.

Heaman L.M. 2009. The application of U–Pb geochronology to mafic, ultramafic and alkaline rocks: An evaluation of three mineral standards. *Chemical Geology*, **261**: 43-52.

Herron M.M. 1988. Geochemical classification of terrigenous sands and shales from core or log data. *Journal of Sedimentary Research*, **58**: 820-829.

Herzberg C. & Zhang J. 1996. Melting experiments on anhydrous peridotite KLB-1: Compositions of magmas in the upper mantle and transition zone. *Journal of Geophysical Research: Solid Earth*, **101**: 8271-8295.

Hildreth W. & Moorbath S. 1988. Crustal contributions to arc magmatism in the Andes of Central Chile. *Contributions to Mineralogy and Petrology*, **98**: 455-489.

Hirschmann M.M., Kogiso T., Baker M.B., Stolper E.M. 2003. Alkalic magmas generated by partial melting of garnet pyroxenite. *Geology*, **31**: 481-484.

Hofmann A.W., Jochum K.P., Seufert M., White W.M. 1986. Nb and Pb in oceanic basalts: new constraints on mantle evolution. *Earth and Planetary Science Letters*, **79**: 33-45.

Hofmann A.W. 2007. Sampling Mantle Heterogeneity through Oceanic Basalts: Isotopes and Trace Elements. In: Holland H.D. & Turekian K.K. *Treatise on Geochemistry*. Oxford, Elsevier-Pergamon, p. 1-44.

Hoskin P.W.O. & Schaltegger U. 2003. The composition of zircon and igneous and metamorphic petrogenesis. *Reviews in Mineralogy and Geochemistry*, **53**: 27-62.

Hoskin P.W.O. 2005. Trace-element composition of hydrothermal zircon and the alteration of Hadean zircon from the Jack Hills, Australia. *Geochimica et Cosmochimica Acta*, **69**: 637-648.

- Humphrey L. & Allard G.O. 1969. *Geologia da área do Domo de Itabaiana (Sergipe) e sua relação com a geologia do Geossinclinal de Propriá: um elemento tectônico recém-reconhecido no escudo brasileiro*. Rio de Janeiro, PETROBRÁS/CENPES, 160 p.
- Irvine T.N. & Baragar W.R.A. 1971. A guide to the chemical classification of the common volcanic rocks. *Canadian Journal of Earth Sciences*, **8**: 523-548.
- Jackson S.E., Pearson N.J., Griffin W.L., Belousova E.A. 2004. The application of laser ablation-inductively coupled plasma-mass spectrometry to in situ U–Pb zircon geochronology. *Chemical Geology*, **211**: 47-69.
- Janoušek V., Farrow C.M., Erban V. 2006. Interpretation of whole-rock geochemical data in igneous geochemistry: introducing Geochemical Data Toolkit (GCDkit). *Journal of Petrology*, **47**: 1255-1259.
- Kohn M.J. 2017. Titanite petrochronology. *Reviews in Mineralogy and Geochemistry*, **83**: 419-441.
- Kourim F., Wang K.L., Beinlich A., Chieh C.J., Dygert N., Lafay R., Kovach V., Michibayashi K., Yarmolyuk V., Iizuka Y. 2021. Metasomatism of the off-cratonic lithospheric mantle beneath Hangay Dome, Mongolia: Constraints from trace-element modelling of lherzolite xenoliths. *Lithos*, **400-401**: 106407.
- Kozuch M. 2003. *Isotopic and trace element geochemistry of early Neoproterozoic gneissic and metavolcanic rocks in the Cariris Velhos orogen of the Borborema Province, Brazil, and their bearing on tectonic setting*. PhD Thesis, University of Kansas, Lawrence, 199 p.
- Lages G.A., Santos L.C.M.L., Brasilino R.G., Rodrigues J.B., Dantas E.L., 2019. Statherian-Calymmian (ca. 1.6 Ga) magmatism in the Alto Moxotó Terrane, Borborema Province, northeast Brazil: Implications for within-plate and coeval collisional tectonics in West Gondwana. *Journal of South American Earth Sciences*, **91**: 116-130.
- Lameyre J. & Bowden P. 1982. Plutonic rock types series: discrimination of various granitoid series and related rocks. *Journal of Volcanology and Geothermal Research*, **14**: 169-186.
- Le Maitre R.W., Streckeisen A., Zanettin B., le Bas M.J., Bonin B., Bateman P. (eds.). 2002. *Igneous Rocks: a classification and glossary of terms, recommendations of the International Union of Geological Sciences Subcommission on the Systematics of Igneous Rocks*. 2nd ed. Cambridge, Cambridge University Press, 256 p.
- Lima A.L.R. 2021. *Petrologia do Stock Altos Verdes, Domínio Macururé, Província*

Borborema. MS Dissertation, Universidade Federal de Sergipe, São Cristóvão, 246 p.

Lima D.R. 2016. *Caracterização petrológica e geoquímica do pluton Curitiba, Domínio Poço Redondo-Marancó, Cinturão Sergipano*. MS Dissertation, Universidade Federal de Pernambuco, Recife, 111 p.

Lima H.M., Pimentel M.M., Fuck R.A., Santos L.C.M.L., Dantas E.L. 2018. Geochemical and detrital zircon geochronological investigation of the metavolcanosedimentary Araticum complex, Sergipano Fold Belt: Implications for the evolution of the Borborema Province, NE Brazil. *Journal of South American Earth Sciences*, **86**: 176-192.

Lima H.M., Pimentel M.M., Santos L.C.M.L., Dantas E.L. 2019. Isotopic and geochemical characterization of the metavolcano-sedimentary rocks of the Jirau do Ponciano Dome: A structural window to a Paleoproterozoic continental arc root within the Southern Borborema Province, Northeast Brazil. *Journal of South American Earth Sciences*, **90**: 54-69.

Lima J. V., Guimarães I.P., Neves S.P., Basei M.A.S., Silva Filho A.F., Brainer C.C.G. 2021. Post-collisional, high-Ba-Sr Teixeira Batholith granites: Evidence for recycling of Paleoproterozoic crust in the Alto Pajeú domain, Borborema Province – NE-Brazil. *Lithos*, **404-405**: 106469.

Lima M.M.C., Ferreira V.P., Silva T.R., Sial A.N., Carvalho B.M.B. 2021. Crustal growth during Western Gondwana amalgamation and onset of the Brasiliano orogeny: Insights from geochemistry and Pb–Sr–Nd–O isotopes from granites in northeastern Brazil. *Lithos*, **396-397**: 106223.

Lisboa V.A.C., Conceição H., Rosa M.L.S., Fernandes D.M. 2019. The onset of post-collisional magmatism in the Macururé Domain, Sergipano Orogenic System: The Glória Norte Stock. *Journal of South American Earth Sciences*, **89**: 173-188.

Long L.E., Castellana C.H., Sial A.N. 2005. Age, origin and cooling history of the Coronel João Sá Pluton, Bahia, Brazil. *Journal of Petrology*, **46**: 255-273.

Ludwig K. 2009. *User's Manual for Isoplot 3.70*. Berkeley, Berkeley Geochronology Center Special Publication, 74 p.

Ludwig K. 2009. *SQUID 2: A User's Manual*. Berkeley, Berkeley Geochronology Center Special Publication.

Mallik A., Nelson J., Dasgupta R. 2015. Partial melting of fertile peridotite fluxed by hydrous rhyolitic melt at 2–3 GPa: implications for mantle wedge hybridization by sediment melt and

generation of ultrapotassic magmas in convergent margins. *Contributions to Mineralogy and Petrology*, **169**: 1-24.

McDonough W.F. & Sun S.S. 1995. The composition of the Earth. *Chemical Geology*, **120**: 223-253.

McLennan S.M., Hemming S., McDaniel D.K., Hanson G.N. 1993. Geochemical approaches to sedimentation, provenance, and tectonics. *In: Johnsson M.J. & Basu A. Processes Controlling the Composition of Clastic Sediments*, Geological Society of America Special Papers, Colorado, p. 21-40.

Mendes V.A. & Brito M.F.L. 2016. *Geologia e recursos minerais da folha Arapiraca SC.24-X-D: escala 1:250.000: estados de Pernambuco, Alagoas e Sergipe*. Recife, CPRM, 254 p.

Menzies M.A., Rogers N., Tindle A.G., Hawkesworth C.J. 1987. Metasomatic and enrichment processes in lithospheric peridotites, an effect of asthenosphere-lithosphere interaction. *In: Menzies, M.A. & Hawkesworth, C.J. (eds.). Mantle Metasomatism*. London, Academic Press, p. 313-361.

Middlemost E.A.K. 1994. Naming materials in the magma/igneous rock system. *Earth-Science Reviews*, **37**: 215-224.

Milhomem Neto J.M. & Lafon J.M. 2019. Zircon U-Pb and Lu-Hf isotope constraints on Archean crustal evolution in Southeastern Guyana Shield. *Geoscience Frontiers*, **10**: 1477-1506.

Miller C.F., McDowell S.M., Mapes R.W. 2003. Hot and cold granites? Implications of zircon saturation temperatures and preservation of inheritance. *Geology*, **31**: 529-532.

Miller J.S., Matzel J.E.P., Miller C.F., Burgess S.D., Miller R.B. 2007. Zircon growth and recycling during the assembly of large, composite arc plutons. *Journal of Volcanology and Geothermal Research*, **167**: 282-299.

Morel M.L.A., Nebel O., Nebel-Jacobsen Y.J., Miller J.S., Vroon P.Z. 2008. Hafnium isotope characterization of the GJ-1 zircon reference material by solution and laser-ablation MC-ICPMS. *Chemical Geology*, **255**: 231-235.

Morrison G.W. 1980. Characteristics and tectonic setting of the shoshonite rock association. *Lithos*, **13**: 97-108.

Moyen J.F., Janoušek V., Laurent O., Bachmann O., Jacob J.B., Farina F., Fiannacca P., Villaros A. 2021. Crustal melting vs. fractionation of basaltic magmas: Part 1, granites and

paradigms. *Lithos*, **402-403**: 106291.

Murphy J.B. 2013. Appinite suites: A record of the role of water in the genesis, transport, emplacement and crystallization of magma. *Earth-Science Reviews*, **119**: 35-59.

Murphy J.B. 2020. Appinite suites and their genetic relationship with coeval voluminous granitoid batholiths. *International Geology Review*, **62**: 683-713.

Nesbitt H.W. & Young G.M. 1982. Early Proterozoic climates and plate motions inferred from major element chemistry of lutites. *Nature*, **299**: 715-717.

Nesbitt H.W. & Young G.M. 1984. Prediction of some weathering trends of plutonic and volcanic rocks based on thermodynamic and kinetic considerations. *Geochimica et Cosmochimica Acta*, **48**: 1523-1534.

Newbury D.E. 2009. Mistakes encountered during automatic peak identification of minor and trace constituents in electron-excited energy dispersive X-ray microanalysis. *Scanning*, **31**: 91-101.

Neves S.P. 2003. Proterozoic history of the Borborema province (NE Brazil): Correlations with neighboring cratons and Pan-African belts and implications for the evolution of western Gondwana. *Tectonics*, **22**: 1-14.

Neves S.P. 2021. Comparative geological evolution of the Borborema Province and São Francisco Craton (eastern Brazil): Decratonization and crustal reworking during West Gondwana assembly and implications for paleogeographic reconstructions. *Precambrian Research*, **355**: 106119.

Neves S.P., Bruguier O., Bosch D., da Silva J.M.R., Mariano G. 2008. U–Pb ages of plutonic and metaplutonic rocks in southern Borborema Province (NE Brazil): Timing of Brasiliano deformation and magmatism. *Journal of South American Earth Sciences*, **25**: 285-297.

Neves S.P., Bruguier O., Silva J.M.R., Mariano G., Silva Filho A.F., Teixeira C.M.L. 2015. From extension to shortening: Dating the onset of the Brasiliano Orogeny in eastern Borborema Province (NE Brazil). *Journal of South American Earth Sciences*, **58**: 238-256.

Neves S.P., Rangel da Silva J.M., Bruguier O. 2016. The transition zone between the Pernambuco-Alagoas Domain and the Sergipano Belt (Borborema Province, NE Brazil): geochronological constraints on the ages of deposition, tectonic setting and metamorphism of metasedimentary rocks. *Journal of South American Earth Sciences*, **72**: 266-278.

Neves S.P., Silva J.M.R., Bruguier O. 2019. The metasedimentary Macururé Complex

(Sergipano Belt, Borborema Province, Brazil) in southern Alagoas state: geology and geochronology. *Journal of the Geological Survey of Brazil*, **2**: 17-25.

Neves S.P., Teixeira C.M.L., Bruguier O. 2021. 870-850 Ma-old magmatic event in eastern Borborema Province, NE Brazil: Another Tonian failed attempt to break up the São Francisco Paleoplate? *Journal of South American Earth Sciences*, **105**: 102917.

Ohta T. & Arai H. 2007. Statistical empirical index of chemical weathering in igneous rocks: A new tool for evaluating the degree of weathering. *Chemical Geology*, **240**: 280-297.

Oliveira E.M. 2014. *Petrografia, litogeoquímica e geocronologia das rochas granulíticas da parte norte do Cinturão Salvador-Esplanada-Boquim, Bahia-Sergipe*. PhD Thesis, Universidade Federal da Bahia, Salvador, 220 p.

Oliveira E.P. & Tarney J. 1990. Petrogenesis of the Canindé de São Francisco complex: A major Late Proterozoic gabbroic body in the Sergipe Foldbelt, northeastern Brazil. *Journal of South American Earth Sciences*, **3**: 125-140.

Oliveira E.P., Toteu S.F., Araújo M.N.C., Carvalho M.J., Nascimento R.S., Bueno J.F., McNaughton N., Basilici G. 2006. Geologic correlation between the Neoproterozoic Sergipano belt (NE Brazil) and the Yaoundé belt (Cameroon, Africa). *Journal of South American Earth Sciences*, **44**: 470-478.

Oliveira E.P., Windley B.F., Araújo M.N.C. 2010. The Neoproterozoic Sergipano Orogenic Belt, NE Brazil: a complete plate tectonic cycle in Western Gondwana. *Precambrian Research*, **81**: 64-84.

Oliveira E.P., Bueno J.F., McNaughton N.J., Silva Filho A.F., Nascimento R.S., Donatti-Filho J.P. 2015. Age, composition, and source of continental arc- and syn-collision granites of the Neoproterozoic Sergipano Belt, Southern Borborema Province, Brazil. *Journal of South American Earth Sciences*, **58**: 257-280.

Oliveira E.P., McNaughton N.J., Windley B.F., Carvalho M.J., Nascimento R.S. 2015. Detrital zircon U–Pb geochronology and whole-rock Nd-isotope constraints on sediment provenance in the Neoproterozoic Sergipano Orogen, Brazil: from early passive margins to late foreland basins. *Tectonophysics*, **662**: 183-194.

Oliveira E.P., Windley B.F., McNaughton N.J., Bueno J.F., Nascimento R.S., Carvalho M.J., Araújo M.N.C. 2017. The Sergipano Belt. In: Heilbron, M., Cordani, U.G., Alkmim, F.F. (eds.).

- São Francisco Craton, Eastern Brazil: Tectonic Genealogy of a Miniature Continent*. Cham, Springer International Publishing, p. 241-254.
- Oliveira E.P. 2012. Geologia da Faixa Sergipana no Estado da Bahia. *In*: Barbosa, J., Mascarenhas, J.F., Correa Gomes, L.C., Dominguez, J.M.L., Souza, J.S. (eds.). *Geologia da Bahia: pesquisa e atualização*. Salvador, CBPM, p. 179-190.
- Oliveira I.R. 2020. *Petrogênese dos stocks Mocambo e Frutuoso, Domínio Macururé, Sistema Orogênico Sergipano*. MS Dissertation, Universidade Federal de Sergipe, São Cristóvão, 206 p.
- Orejana D., Villaseca C., Kristoffersen M. 2020. Geochemistry and geochronology of mafic rocks from the Spanish Central System: Constraints on the mantle evolution beneath central Spain. *Geoscience Frontiers*, **11**: 1651-1667.
- Othman D.B., Polvé M., Allègre C.J. 1984. Nd-Sr isotopic composition of granulites and constraints on the evolution of the lower continental crust. *Nature*, **307**, 510-515.
- Passchier C.W. & Trouw R.A.J. 2005. *Microtectonics*. Berlin, Springer-Verlag, 366 p.
- Passos L.H., Fuck R.A., Chemale F., Lenz C., Pimentel M.M., Machado A., Pinto V.M. 2021. Neoproterozoic (740-680 Ma) arc-back-arc magmatism in the Sergipano Belt, southern Borborema Province, Brazil. *Journal of South American Earth Sciences*, **109**: 103280.
- Passos L.H., Fuck R.A., Junior F.C., Lenz C., Porcher C.C., Pinto V.M., Santos L.C.M.L. 2022. Neoproterozoic pre-collisional events recorded in the Sergipano belt, Southern Borborema Province, West Gondwana. *International Geology Review*, **64**: 1-19.
- Patiño Douce A.E. & Beard J.S. 1995. Dehydration-melting of Biotite Gneiss and Quartz Amphibolite from 3 to 15 kbar. *Journal of Petrology*, **36**: 707-738.
- Patiño Douce A.E. 1999. What do experiments tell us about the relative contributions of crust and mantle to the origin of granitic magmas? *In*: Castro A., Fernández C., Vigneresse J.L. *Understanding Granites: Integrating New and Classical Techniques*. London, Geological Society of London, p. 55-75. (Special Publications, 168).
- Patchett P.J. & Tatsumoto M. 1981. A routine high-precision method for Lu-Hf isotope geochemistry and chronology. *Contributions to Mineralogy and Petrology*, **75**: 263-267.
- Pe-Piper G., Piper D.J.W., Koukouvelas I., Dolansky L.M., Kokkalas S. 2009. Postorogenic shoshonitic rocks and their origin by melting underplated basalts: The Miocene of Limnos, Greece. *Geological Society of America Bulletin*, **121**: 39-54.

- Peccerillo A. & Taylor S.R. 1976. Geochemistry of eocene calc-alkaline volcanic rocks from the Kastamonu area, Northern Turkey. *Contributions to Mineralogy and Petrology*, **58**: 63-81.
- Pereira F.S. 2019. *Petrogênese da Suíte Máfica do Domínio Macururé, Sistema Orogênico Sergipano, setor sul da Província Borborema*. MS Dissertation, Universidade Federal de Sergipe, São Cristóvão, 280 p.
- Pereira F.S., Rosa M.L.S., Conceição H. 2019. Condições de colocação do magmatismo máfico do Domínio Macururé, Sistema Orogênico Sergipano: Maciço Capela. *Revista Geologia USP. Série Científica*, **19**: 3-29.
- Pereira F.S., Rosa M.L.S., Conceição H., Bertotti A.L. 2020. Age, composition, and source of the Macururé Mafic Suite, Southern Borborema Province, Brazil. *Brazilian Journal of Geology*, **50**: e20190105.
- Pereira F.S., Conceição H., Rosa M.L.S., Marinho M.M., Tassinari C.C.G., Milhomem Neto J.M., Lafon J.M. 2023. Late Cryogenian–Ediacaran magmatism in southern Borborema Province, NE Brazil: Ages, sources, petrogenesis, and tectonic setting. *Geoscience Frontiers*, **14**: 101626.
- Pietranik A.B., Hawkesworth C.J., Storey C.D., Kemp A.I.S., Sircombe K.N., Whitehouse M.J., Bleeker W. 2008. Episodic, mafic crust formation from 4.5 to 2.8 Ga: New evidence from detrital zircons, Slave craton, Canada. *Geology*, **36**: 875-878.
- Pinto V.M., Koester E., Debruyne D., Chemale F., Marques J.C., Porcher C.C., Passos L.H., Lenz C. 2020. Petrogenesis of the mafic-ultramafic Canindé layered intrusion, Sergipano Belt, Brazil: Constraints on the metallogensis of the associated Fe–Ti oxide ores. *Ore Geology Reviews*, **122**: 103535.
- Pinto J.A.E. 2023. *U–Pb em titanita por LA-ICP-MS no Laboratório Pará-Iso (UFPA): Metodologia e aplicação em rochas do sudeste do Escudo das Guianas e Província Borborema*. MS Dissertation, Universidade Federal do Pará, Belém, 108 p.
- Plank T. & Langmuir C.H. 1998. The chemical composition of subducting sediment and its consequences for the crust and mantle. *Chemical Geology*, **145**: 325-394.
- Rapp R.P., Norman M.D., Laporte D., Yaxley G.M., Martin H., Foley S.F. 2010. Continent Formation in the Archean and Chemical Evolution of the Cratonic Lithosphere: Melt–Rock Reaction Experiments at 3–4 GPa and Petrogenesis of Archean Mg-Diorites (Sanukitoids). *Journal of Petrology*, **51**: 1237-1266.

- Roberts N.M.W. & Spencer C.J. 2015. The zircon archive of continent formation through time. *In: Roberts N.M.W., Van Kranendonk M.J., Parman S., Clift P.D. Continent Formation Through Time*. London, Geological Society, p. 197-225. (Special Publications, 389).
- Rollinson H. 1993. *Using geochemical data: evaluation, presentation, interpretation*. Essex, Longman, 352 p.
- Rosa M.L.S., Conceição J.A., Marinho M.M., Pereira F.S., Conceição H. 2020. U-Pb SHRIMP dating of the Itabaiana Dome: a Mesoarchean basement inlier (2.83 Ga) in the Sergipano Orogenic System, Borborema Province. *Brazilian Journal of Geology*, **50**: e20190106.
- Rubatto, D. 2017. Zircon: the metamorphic mineral. *Reviews in Mineralogy and Geochemistry*, **83**: 261-295.
- Rudnick R.L. & Gao S. 2003. Composition of the continental crust. *In: Holland H.D. & Turekian K.K. Treatise on Geochemistry*. Oxford, Elsevier-Pergamon, p. 1-64.
- Rushmer T. 1991. Partial melting of two amphibolites: contrasting experimental results under fluid-absent conditions. *Contributions to Mineralogy and Petrology*, **107**: 41-59.
- Santos R.A., Martins A.A.M., Neves J.P., Leal R.A. 1998. *Programa de Levantamentos Geológicos Básicos do Brasil: Geologia e recursos minerais do Estado de Sergipe*. Escala 1:250.000. Texto explicativo do mapa geológico do Estado de Sergipe. Salvador, CPRM/DIEDIG/DEPAT;CODISE, 156 p.
- Santos E.J., Van Schmus W.R., Kozuch M., Neves B.B.B. 2010. The Cariris Velhos tectonic event in Northeast Brazil. *Journal of South American Earth Sciences*, **29**: 61-76.
- Santos L.R. 2016. *Petrologia do Stock Canindé Velho, Sistema Orogênico Sergipano, NE Brasil*. MS Dissertation, Universidade Federal de Sergipe, São Cristóvão, 146 p.
- Santos M.M., Lana C., Scholz R., Buick I., Schmitz M.D., Kamo S.L., Gerdes A., Corfu F., Tapster S., Lancaster P., Storey C.D., Basei M.A.S., Tohver E., Alkmim A., Nalini H., Krambrock K., Fantini C., Wiedenbeck M. 2017. A New Appraisal of Sri Lankan BB Zircon as a Reference Material for LA-ICP-MS U-Pb Geochronology and Lu-Hf Isotope Tracing. *Geostandards and Geoanalytical Research*, **41**: 335-358.
- Santos I.S., Conceição H., Rosa M.L.S., Marinho M.M. 2019. Magmatismos shoshonítico e cálcio-alcalino de alto potássio pós-orogênico (615 Ma) na porção leste do Domínio Macururé, Sistema Orogênico Sergipano: Stocks Propriá, Amparo do São Francisco e Fazenda Alvorada. *Geologia USP. Série Científica*, **19**: 99-116.

- Santos L.Q.S. 2021. *Petrogênese do Stock Fazenda Alvorada, Domínio Macururé, Sistema Orogênico Sergipano*. MS Dissertation, Universidade Federal de Sergipe, São Cristóvão.
- Santos C., Zincone S.A., Queiroga G.N., Bersan S.M., Lana C.C., Oliveira E.P. 2022. Evidence for change in crust formation process during the Paleoproterozoic in the São Francisco Craton (Gavião Block): Coupled zircon Lu-Hf and U-Pb isotopic analyses and tectonic implications. *Precambrian Research*, **368**: 106472.
- Sato K., Tassinari C.C.G., Basei M.A.S., Siga O., Onoe A.T., Souza M.D. 2014. Sensitive High Resolution Ion Microprobe (SHRIMP IIe/MC) of the Institute of Geosciences of the University of São Paulo, Brazil: Analytical method and first results. *Geologia USP - Serie Científica*, **14**: 3-18.
- Sato K., Junior O.S., Basei M.A.S., Tassinari C.C.G., Onoe A.T. 2016. SHRIMP U-Th-Pb Analyses of titanites: Analytical techniques and examples of Terranes of the South-Southeast of Brazil - Geoscience Institute of the University of São Paulo. *Geologia USP - Serie Científica*, **16**: 3-18.
- Sen C. & Dunn, T. 1994. Dehydration melting of a basaltic composition amphibolite at 1.5 and 2.0 GPa: implications for the origin of adakites. *Contributions to Mineralogy and Petrology*, **117**: 394-409.
- Shand S.J. 1943. *The Eruptive Rocks*. 2nd ed. New York, John Wiley, 444 p.
- Shaw S.E. & Flood R.H. 2009. Zircon Hf Isotopic Evidence for Mixing of Crustal and Silicic Mantle-derived Magmas in a Zoned Granite Pluton, Eastern Australia. *Journal of Petrology*, **50**: 147-168.
- Silva C.C. 2014. *Petrologia e geocronologia do stock granodiorítico Lagoa do Roçado, Domínio Macururé, Faixa Sergipana-SE*. MS Dissertation, Universidade Federal de Sergipe, São Cristóvão, 92 p.
- Silva J.M.R., Campos Neto M.C., Brito Neves B.B. 1995. Deformação e metamorfismo principais de uma parte da Faixa Sul-Alagoana (Complexo Macururé), Sistema de Dobramentos Sergipano, Nordeste do Brasil. *Revista Brasileira de Geociências*, **25**: 343-350.
- Silva J.P.A., Lana C., Mazoz A., Buick I., Scholz, R. 2022. U-Pb Saturn: New U-Pb/Pb-Pb Data Reduction Software for LA-ICP-MS. *Geostandards and Geoanalytical Research*, 1-18.

Silva Filho M.A., Bomfim L.F.C., Santos R.A., Leal R.A., Santana A.C., Filho P.A.B. 1979. *Geologia da Geossinclinal Sergipana e do seu embasamento - Alagoas, Sergipe e Bahia: Projeto Baixo São Francisco/Vaza-Barris*. Brasília, DNPM/CPRM, 134 p.

Silva Filho M.A. & Torres H. 2002. A new interpretation on the Sergipano Belt Domain. *Anais da Academia Brasileira de Ciências*, **74**: 556-557.

Silva Filho A.F., Guimarães I.P., Van Schmus W.R., Armstrong R.A., Rangel da Silva J.M., Osako L.S., Cocentino L.M. 2014. SHRIMP U–Pb zircon geochronology and Nd signatures of supracrustal sequences and orthogneisses constrain the Neoproterozoic evolution of the Pernambuco–Alagoas domain, southern part of Borborema Province, NE Brazil. *International Journal of Earth Sciences*, **103**: 2155-2190.

Silva Filho A.F., Guimarães I.P., Santos L., Armstrong R., Van Schmus W.R. 2016. Geochemistry, U–Pb geochronology, Sm–Nd and O isotopes of ca. 50 Ma long ediacaran high-K syn-collisional magmatism in the Pernambuco Alagoas Domain, Borborema Province, NE Brazil. *Journal of South American Earth Sciences*, **68**: 134-154.

Silva Filho A.F., Guimarães I.P., Armstrong R.A., Silva J.R.M., Van Schmus W.R., Farias D.S., Ferreira V.P., Amorim J.V.A., Souza K., Cocentino L.M. 2021. A major neoproterozoic crustal boundary in the Borborema province of NE Brazil. *International Geology Review*, **64**: 1981-2007.

Sisson T.W., Ratajeski K., Hankins W.B., Glazner A.F. 2005. Voluminous granitic magmas from common basaltic sources. *Contributions to Mineralogy and Petrology*, **148**: 635-661.

Sláma J., Košler J., Condon D.J., Crowley J.L., Gerdes A., Hanchar J.M., Horstwood M.S.A., Morris G.A., Nasdala L., Norberg N., Schaltegger U., Schoene B., Tubrett M.N., Whitehouse M.J. 2008. Plešovice zircon – A new natural reference material for U–Pb and Hf isotopic microanalysis. *Chemical Geology*, **249**: 1-35.

Soares H.S., Sousa C.S., Rosa M.L.S., Conceição H. 2019. Petrologia dos stocks Santa Maria, Monte Pedral, Bom Jardim, Boa Esperança e Niterói, Suíte Intrusiva Serra do Catu, estado de Sergipe, NE Brasil. *Geologia USP. Série Científica*, **19**: 63-84.

Söderlund U., Patchett P.J., Vervoort J.D., Isachsen C.E. 2004. The ¹⁷⁶Lu decay constant determined by Lu–Hf and U–Pb isotope systematics of Precambrian mafic intrusions. *Earth and Planetary Science Letters*, **219**: 311-324.

Sousa C.S., Soares H.S., Rosa M.L.S., Conceição H. 2019. Petrologia e geocronologia do

Batólito Rio Jacaré, Domínio Poço Redondo, Sistema Orogênico Sergipano, NE do Brasil. *Geologia USP. Série Científica*, **19**: 171-194.

Sousa E.S. 2020. *Petrologia do magmatismo ediacarano na porção central do Domínio Macururé: stocks Graccho Cardoso e Queimadinha*. MS Dissertation, Universidade Federal de Sergipe, São Cristóvão, 205 p.

Sousa C.S., Soares H.S., Rosa M.L.S., Conceição H., 2022. Injection of enriched lithospheric mantle magmas explains the formation of microgranular enclaves in the Rio Jacaré Batholith, Borborema Province, Brazil. *Brazilian Journal of Geology*, **52**: e2022033.

Spalletta B.M. & Oliveira E.P. 2017. Idades LA-SF-ICPMS em zircão dos quartzitos da Formação Santa Cruz, Orógeno Sergipano, Alagoas. In: SBG, XXVII Simpósio de Geologia do Nordeste, João Pessoa, *Anais[...]*. Disponível em: http://geologiadonordeste.com.br/2017/anais/index_sessao.php#resumos. Acesso em 19 set. 2023.

Spencer C.J., Kirkland C.L., Taylor R.J.M. 2016. Strategies towards statistically robust interpretations of in situ U-Pb zircon geochronology. *Geoscience Frontiers*, **7**: 581-589.

Spencer C.J., Kirkland C.L., Roberts N.M.W., Evans N.J., Liebmann J. 2020. Strategies towards robust interpretations of in situ zircon Lu-Hf isotope analyses. *Geoscience Frontiers*, **11**: 843-853.

Stacey J.S. & Kramers J.D. 1975. Approximation of terrestrial lead isotope evolution by a two-stage model. *Earth and Planetary Science Letters*, **26**: 207-221.

Steiger R.H. & Jäger E. 1977. Subcommittee on geochronology: convention on the use of decay constants in geo- and cosmochemistry. *Earth and Planetary Science Letters*, **36**: 359-362.

Streckeisen A. 1976. To each plutonic rock its proper name. *Earth-Science Reviews*, **12**: 1-33.

Taylor S.R. & McLennan S.M. 1985. The Continental Crust: its Composition and Evolution. An Examination of the Geochemical Record Preserved in Sedimentary Rocks, The Continental Crust: its Composition and Evolution. In: Taylor S.R. *An Examination of the Geochemical Record Preserved in Sedimentary Rocks*. Oxford, Blackwell Scientific, 312 p.

Teixeira L. 2005. GENESIS 4.0: Modelos geoquímicos. Software de livre distribuição para modelagem geoquímica.

Teixeira L.R. 2014. *Mapa Geológico e de Recursos Minerais do Estado de Sergipe*. Salvador, CPRM/CODISE. 1 mapa. Escala 1:250.000.

- Tenner T.J., Hirschmann M.M., Humayun M. 2012. The effect of H₂O on partial melting of garnet peridotite at 3.5 GPa. *Geochemistry, Geophysics, Geosystems*, **13**: Q03016.
- Tesser L.R., Ganade C.E., Weinberg R.F., Basei M.A.S., Moraes R., Batista L.A. 2021. Ultrahigh-temperature Palaeoproterozoic rocks in the Neoproterozoic Borborema Province, implications for São Francisco Craton dispersion in NE Brazil. *Journal of Metamorphic Geology*, **40**: 359-387
- Thibault Y., Edgar A.D., Lloyd F.E. 1992. Experimental investigation of melts from a carbonated phlogopite lherzolite: Implications for metasomatism in the continental lithospheric mantle. *American Mineralogist*, **77**: 784-794.
- Thirlwall M.F. & Anczkiewicz, R. 2004. Multidynamic isotope ratio analysis using MC-ICP-MS and the causes of secular drift in Hf, Nd and Pb isotope ratios. *International Journal of Mass Spectrometry*, **235**: 59-81.
- Trompette R. 1997. Neoproterozoic (~600 Ma) aggregation of Western Gondwana: a tentative scenario. *Precambrian Research*, **82**: 101-112.
- Turner S., Arnaud N., Liu J., Rogers N., Hawkesworth C., Harris N., Kelley S., Van Calsteren P., Deng W. 1996. Post-collision, shoshonitic volcanism on the tibetan plateau: implications for convective thinning of the lithosphere and the source of ocean island basalts. *Journal of Petrology*, **37**: 45-71.
- Van Schmus W.R., Oliveira E.P., Silva Filho A.F., Toteu S.F., Penaye J., Guimarães I.P., Silva Filho A.F., Toteu S.F., Penaye J., Guimarães I.P. 2008. Proterozoic links between the Borborema Province, NE Brazil, and the Central African fold belt. In: Pankhurst R.J., Trouw R. A. J., Brito Neves, B.B., Wit M.J. *West Gondwana: Pre-Cenozoic Correlations Across the South Atlantic Region*. Geological Society, London, Special Publications, 294, p. 69-99.
- Van Schmus W.R., Kozuch M., Brito Neves B.B. 2011. Precambrian history of the Zona Transversal of the Borborema Province, NE Brazil: Insights from Sm-Nd and U-Pb geochronology. *Journal of South American Earth Sciences*, **31**: 227-252.
- Vermeesch P. 2021. Maximum depositional age estimation revisited. *Geoscience Frontiers*, **12**: 843-850.
- Vermeesch P. 2018. IsoplotR: A free and open toolbox for geochronology. *Geoscience Frontiers*, **9**(5): 1479-1493.
- Vervoort J.D. & Kemp A.I.S. 2016. Clarifying the zircon Hf isotope record of crust-mantle

- evolution. *Chemical Geology*, **425**: 65-75.
- Warr L.N. 2021. IMA–CNMNC approved mineral symbols. *Mineralogical Magazine*, **85**: 291-320.
- Wasserburg G.J., Jacobsen S.B., DePaolo D.J., McCulloch M.T., Wen T. 1981. Precise determination of SmNd ratios, Sm and Nd isotopic abundances in standard solutions. *Geochimica et Cosmochimica Acta*, **45**: 2311-2323.
- Watson E.B. 1982. Basalt contamination by continental crust: some experiments and models. *Contributions to Mineralogy and Petrology*, **80**: 73-87.
- Watson E.B. & Harrison T.M. 1983. Zircon saturation revisited: temperature and composition effects in a variety of crustal magma types. *Earth and Planetary Science Letters*, **64**: 295-304.
- Watson E.B., Wark D.A., Thomas J.B. 2006. Crystallization thermometers for zircon and rutile. *Contributions to Mineralogy and Petrology*, **151**: 413-433.
- Weinberg R.F. & Hasalová P. 2015. Water-fluxed melting of the continental crust: A review. *Lithos*, **212-215**: 158-188.
- Weaver B.L., Tarney J., Windley B.F., Leake B.E. 1982. Geochemistry and petrogenesis of Archaean metavolcanic amphibolites from Fiskenaasset, S. W. Greenland. *Geochimica et Cosmochimica Acta*, **46**: 2203-2215.
- Wiedenbeck M., Allé P., Corfu F., Griffin W.L., Meier M., Oberli F., Quadt A.V.O.N., Roddick J.C., Spiegel W. 1995. Three natural zircon standards for U-Th-Pb, Lu-Hf, trace element and REE analyses. *Geostandards Newsletter*, **19**: 1-23.
- Wilde S.A., Valley J.W., Peck W.H., Graham C.M. 2001. Evidence from detrital zircons for the existence of continental crust and oceans on the Earth 4.4 Gyr ago. *Nature*, **409**: 175-178.
- Williams I.S. 1997. U-Th-Pb geochronology by ion microprobe. In: McKibben M.A., Shanks W.C., Ridley I.W. *Applications of Microanalytical Techniques to Understanding Mineralizing Processes*. Society of Economic Geologists, 7, p. 1-36.
- Wilson M. 1989. *Igneous Petrogenesis: a global tectonic approach*. Dordrecht, Springer Netherlands, 466 p.
- Workman R.K. & Hart S.R. 2005. Major and trace element composition of the depleted MORB mantle (DMM). *Earth and Planetary Science Letters*, **231**: 53-72.
- Woodhead J.D., Hergt J.M., Davidson J.P., Eggins S.M. 2001. Hafnium isotope evidence for

‘conservative’ element mobility during subduction zone processes. *Earth and Planetary Science Letters*, **192**: 331-346.

Woodhead J.D. & Hergt J.M. 2005. A preliminary appraisal of seven natural zircon reference materials for in situ Hf isotope determination. *Geostandards and Geoanalytical Research*, **29**: 183-195.

Xu W., Xu X., Zeng G. 2017. Crustal contamination versus an enriched mantle source for intracontinental mafic rocks: Insights from early Paleozoic mafic rocks of the South China Block. *Lithos*, **286-287**: 388-395.

Ye Z., Wan F., Jiang N., Xu J., Wen Y., Fan D., Zhou W. 2021. Dehydration melting of amphibolite at 1.5 GPa and 800–950 °C: Implications for the Mesozoic potassium-rich adakite in the eastern North China Craton. *Geoscience Frontiers*, **12**: 896-906.

Zartman R.E. & Doe B.R. 1981. Plumbotectonics—the model. *Tectonophysics*, **75**: 135-162.

Zindler A. & Hart S. 1986. Chemical Geodynamics. *Annual Review of Earth and Planetary Sciences*, **14**: 493-571.



UNIVERSIDADE FEDERAL DO PARÁ
INSTITUTO DE GEOCIÊNCIAS
PROGRAMA DE PÓS-GRADUAÇÃO EM GEOLOGIA E GEOQUÍMICA

PARECER

Sobre a Defesa Pública da Tese de Doutorado de **FÁBIO DOS SANTOS PEREIRA**

A banca examinadora da Tese de Doutorado de **FÁBIO DOS SANTOS PEREIRA** orientando do Prof. Dr. Jean Michel Lafon (UFPA), com a coorientação da Prof.^a Dr.^a Maria de Lourdes da Silva Rosa (UFS) e composta pelos professores doutores Ignez Pinho Guimarães (UFPE), Valdecir de Assis Janasi (USP), Moacir José Buenano Macambira (UFPA), Candido Augusto Veloso Moura (UFPA) após apresentação da sua tese intitulada **“EVOLUÇÃO CRUSTAL DO SETOR SUL DA PROVÍNCIA BORBOREMA: DOMÍNIO MACURURÉ, SISTEMA OROGÊNICO SERGIPANO, NORDESTE DO BRASIL”**, emite o seguinte parecer:

O candidato realizou sua apresentação de forma clara, bem organizada e segura no tempo estipulado. Na arguição mostrou domínio da temática abordada e respondeu às perguntas formuladas pela banca. O trabalho escrito foi apresentado na forma de três artigos, sendo um já publicado, um submetido, ambos a periódicos de impacto internacional, e um outro em fase final de elaboração. Dessa forma, o documento apresentado atende às exigências básicas para uma tese de doutorado.

Finalmente, a banca examinadora decidiu por unanimidade aprovar a tese de doutorado com **DISTINÇÃO**.

Belém, 29 de setembro de 2023.

Prof. Dr. Jean Michel Lafon (Orientador – UFPA)

Prof.^a Dr.^a Ignez Pinho Guimarães (Membro – UFPE)

Prof. Dr. Valdecir de Assis Janasi (Membro – USP)

Prof. Dr. Moacir José Buenano Macambira (Membro – UFPA)

Prof. Dr. Candido Augusto Veloso Moura (Membro – UFPA)



Ministério da Educação
Universidade Federal do Pará
Sistema de Bibliotecas

DECLARAÇÃO DE AUTORIA

Autor: Fábio dos Santos Pereira
CPF: 042.735.855-88 Matrícula: 201901780005
Telefone (99) 99959-3144 e-mail: fabio.santos.pereira@hotmail.com
Curso/Programa: Programa de Pós-Graduação em Geologia e Geoquímica
Orientador: Jean-Michel Hofen
Coorientador: Maura de Lourdes da Silva Rosa
Data da Defesa: 29/09/2023
Título/Subtítulo: Evolução crustal do setor sul da Província Borborema: Domínio Macurú, Sistema Araximo Sergipano, Nordeste do Brasil
Tipo do documento: () TCC¹ () TCCE² () Dissertação () Tese () Artigo Científico
() Livro () Capítulo de livro () Outro: _____

Declaro que, para os devidos fins, o presente trabalho é de minha autoria e que estou ciente:

- Dos Artigos 297 a 299 do Código Penal, Decreto-Lei n. 2.848 de 7 de dezembro de 1940;
- Da Lei n. 9.610, de 19 de fevereiro de 1998, que dispõe sobre os Direitos Autorais;
- Do Regimento Interno da Universidade Federal do Pará;
- Da lei 12.527 de novembro de 2011, que trata da Lei de Acesso à Informação;
- Da utilização da licença pública internacional *Creative Commons 4.0*;
- Que plágio consiste na reprodução de obra alheia e submissão da mesma como trabalho próprio ou na inclusão, em trabalho próprio, de ideias, textos, tabelas ou ilustrações transcritos de obras de terceiros sem a devida e correta citação referencial.

Fábio dos Santos Pereira

Autor

Belém, 25 de setembro de 2023

Local e Data

¹ Trabalho de Conclusão de Curso

² Trabalho de Conclusão de Especialização



Ministério da Educação
Universidade Federal do Pará
Sistema de Bibliotecas

**TERMO DE AUTORIZAÇÃO E DECLARAÇÃO DE DISTRIBUIÇÃO NÃO EXCLUSIVA PARA
PUBLICAÇÃO DIGITAL NO PORTAL INSTITUCIONAL DE ACESSO ABERTO DA UFPA**

1. Tipo de documento: () TCC³ () TCCE⁴ () Dissertação (X) Tese () Artigo
Científico () Livro () Capítulo de Livro () Trabalho Apresentado em evento

2. Informações sobre a obra:

Autor: Fábio dos Santos Pereira
RG: 10162534 CPF: 042.735.855-88 E-mail: fabio.santos.pereira@hotmail.com
Telefone: (99) 99959-3144 Curso/Programa: Pós Graduação em Geologia e Geoquímica
Orientador: Jean-Michel Lapon Coorientador: Maria de Lourdes da Silva Rosa

Título do documento:

Evolução crustal do setor Sul da Província Borboroma: Domínio
Mocimé, Sistema Orogênico Serapióno, Nordeste do Brasil

Data da defesa: 29/09/2023 Área do Conhecimento: Geoquímica e Petrologia

Agência de Fomento (se houver): CADES (Bolsa de pesquisa), CNPq (Projetos orientados)

3. Informação de disponibilização do documento:

Restrição para publicação: () Total () Parcial (X) Sem restrição

Justificativa de restrição total*: _____

Em caso de restrição parcial, especifique os capítulos restritos: _____

A partir de qual data esse documento poderá ser disponibilizado: ___/___/___

4. Permissões⁵

Permite o uso comercial da obra? () Sim (X) Não / Permitir modificações na obra? () Sim (X) Não

O documento está sujeito a patentes? () Sim (X) Não

5. T&D defendidas fora da instituição

É Tese ou Dissertação defendida fora da UFPA? () Sim (X) Não

Belém, 25 de setembro de 2023
Local e Data

Fábio dos Santos Pereira
Assinatura do autor

³ Trabalho de Conclusão de Curso

⁴ Trabalho de Conclusão de Curso em Especialização

⁵ Creative Commons Internacional 4.0